

# **Synthesis and Applications of Self-Assembled Nanostructured Gel Materials**

**Ph.D. Thesis**

By  
**REENA**



**DEPARTMENT OF CHEMISTRY  
INDIAN INSTITUTE OF TECHNOLOGY INDORE**

**August 2023**



# Synthesis and Applications of Self-Assembled Nanostructured Gel Materials

A THESIS

*Submitted in partial fulfillment of the requirements for the award of the degree of*  
**DOCTOR OF PHILOSOPHY**

*by*

**REENA**



**DEPARTMENT OF CHEMISTRY**  
**INDIAN INSTITUTE OF TECHNOLOGY INDORE**

August 2023





# INDIAN INSTITUTE OF TECHNOLOGY INDORE

## CANDIDATE'S DECLARATION

I hereby certify that the work which is being presented in the thesis entitled **SYNTHESIS AND APPLICATIONS OF SELF-ASSEMBLED NANOSTRUCTURED GEL MATERIALS** in the partial fulfillment of the requirements for the award of the degree of **DOCTOR OF PHILOSOPHY** and submitted in the **DEPARTMENT OF CHEMISTRY, Indian Institute of Technology Indore**, is an authentic record of my own work carried out during the time period from **July 2018** to **August 2023** under the supervision of Dr. Suman Mukhopadhyay, Professor, Department of Chemistry, Indian Institute of Technology Indore.

The matter presented in this thesis has not been submitted by me for the award of any other degree of this or any other institute.

signature of the student with date  
**REENA**

---

This is to certify that the above statement made by the candidate is correct to the best of my/our knowledge.

Signature of Thesis Supervisor with date  
**Prof. SUMAN MUKHOPADHYAY**

---

**Ms. REENA** has successfully given his/her Ph.D. Oral Examination held on **18 October 2023**.

Signature of Thesis Supervisor with date  
**Prof. SUMAN MUKHOPADHYAY**

---

## ACKNOWLEDGEMENTS

From the bottom of my heart, I am grateful to God for giving me blessings, perseverance, and courage to reach my dream and destination as a researcher. It's my pleasure to dedicate the achievement to my loving and hardworking parents and husband.

The research as a Ph.D. thesis in its present form, which is possible due to several people's continuous support and encouragement. I am pleased to sincerely thank everyone who has been a momentous part of this unforgettable Ph.D. journey.

First and elite, I want to express my sincere thanks and profound gratitude to my supervisor, Professor Suman Mukhopadhyay, for his constant support, continuous guidance, belief, and encouragement throughout my work. Due to his effort, this research journey from the very first to the present day turned into a conclusive doctoral thesis. I will never forget his greatness, kindness, and caring nature toward every student. He has always given me the perfect environment for research and patiently brings out my capabilities toward research work.

I wish to express my esteemed gratitude to Prof. Suhas S. Joshi, Director, IIT Indore, for giving me the opportunity to complete my dream in IIT Indore. I would like to thank Council of Scientific & Industrial Research (CSIR) for financial support during my Ph.D. I am grateful to Sophisticated Instrument Centre (SIC), IIT Indore for instrumentation facility. It's my pleasure to express my sincere thanks to my PSPC members Prof. Sanjay Kumar Singh and prof. Sudeshna Chattopadhyay for their valuable suggestions and guidance throughout my Ph.D. journey in IIT Indore. I would like to acknowledge my collaborators, Dr. Bidyut Kumar Kundu, Dr. Sivaranjana Reddy Vennapusa and Mr. Probal Nag for their active support for DFT studies. I would like to acknowledge SAIF IIT Bombay for TEM and ICP-AES analysis, MNIT Jaipur and SAPTARSHI IIT Jammu for XPS

analysis. I would like to thank all faculty members of the Department of Chemistry, IIT Indore for their guidance and help during various activities. I am very happy to thank teaching and non-teaching staff from bottom of my heart. It's my pleasure to express my sincere regards to Mr. Kinny Pandey, Dr. Ravinder, Mr. Nitin, Mr. Ghanshyam Bhavsar, Mr. Atul Singh, Mrs. Mitali Dave, Mr. Ranjeet Raghuvanshi from SIC and Mr. Manish Kushwaha, Mr. Rameshwar Dohare, Mrs. Vinita Kothari and Mr. P. K. Parthiban from Chemistry office IIT Indore.

My seniors and juniors strengthened my Ph.D. journey and was with me in my ups and downs. I would like to give my deepest thanks to my senior Dr. Rishi Ranjan for giving me continuous moral support like a family. I am thankful to my lab mates Ms. Pragti porwal, Mr. Argha Chakraborty and Mr. Sayantan Sarkar for giving me favourable environment around my workplace. I am happy to thank my beloved and supportive juniors Ms. Ritika Munjal, Mr. Amardeep Kumar, Ms. Mamta Kunwar, Mr. Priyanshu Nautiyal, Ms. Srestha Nayak, Ms. Srijita Pal, Mr. Ritik, Mr. Ashish Bora, and Mr. Prince Kumar for giving me cheerful surroundings like my family. I would like to express my heartiest gratitude to my friends Ms. Aparna Gangwar, Ms. Likhi Dhruv, Dr. Bhawna Saini, Mr. Meher Prakash, Ms. Manavi Rajan, Mr. Aditya Prasun, Ms. Moupia Mukherjee, Mr. Ashvani K. Patel, Mr. S. Banuprakash goud, Mr. Kriti Prasanna, Ms. Shruti Bagel, Ms. Ruchi Singh, Mrs. Rakhi, Mr. Durgesh Sarothiya, Ms. Rajni Lodhi, Ms. Shikha S. Rathor, Ms. Poonam Rani, Mr. Raju L. Dhakar, Ms. Nisha Kumari and to all beloved friends in IIT Indore for their love and support with me. I would also like to thank my childhood and college friends Ms. Reena Verma, Ms. Priyanka Isser and Ms. Julie Saini for their love and blessings.

I am very happy to express my love and thank to one who never leave me alone from my graduation to now when I am going to become a Ph.D. holder, who is always with me like my strength, she is my best friend Ms.

Sandhya Kapurwan. I would like to take this opportunity to express my gratitude towards my respected teachers of “Rajkiya Madhyamik Vidyalaya Rishikesh”, “Government girl inter college (GGIC) Rishikesh” and “Pt. L.M.S. post graduate college Rishikesh, HNBGU Uttarakhand” for making me able to think about my aim.

The most important part of my life and each journey, i.e., my family; nothing would have been possible without their support. I am extremely fortunate to have hardworking and lovely parents, Mr. Jay Lal Kyarikwal and Mrs. Vindeshwari Devi. They did everything unconditionally to complete my studies with love and care. I am very happy to have a supportive and caring husband, Mr. Shiv Darshan Kumar, and my lovely parents-in-law, Mr. Ramesh Kandara, and Mrs. Ganeshi Devi, and grandfather-in-law Mr. Beerbal Kandara, in this journey. I would like to express my respect and thanks to my mama and mami ji, Mr. Ram Lal Bhatiyana and Mrs. Rameshwari Devi, my supportive uncles Mr. Suryaprakash Kapurwan and Late Mr. Balwant Singh Bendwal, my aunts, Mrs. Sarla Devi, and Mrs. Saroj Bendwal and my jaithi maa Mrs. Sateshwari devi for giving me blessings and support. I am happy to mention the thanks and respect to my brothers-in-law Mr. Mukesh ji and Mr. Girish ji, my sisters-in-law Mrs. Seema Devi and Mrs. Suman Devi, love and blessings to my brothers, Mr. Sandeep Kumar, Mr. Sonu, Mr. Pradeep, Mr. Kuldeep, Mr. Sunil, and my sisters Mrs. Beena Sharma, Ms. Soni, Ms. Moni, and Ms. Jyoti. They all are a memorable part of my life and a supportive system for my Ph.D. journey.

Finally, I would like to thank all the others who supported me and encouraged me to make my Ph.D. journey successful.



**Dedicated to  
My Beloved Parents  
and  
Husband**





## ABSTRACT

A semi-solid material with the viscoelastic behavior and properties of both solid and liquid materials is known as gel. Gels are a vital part of soft materials, showing several applications in recently advanced fields. The basic unit of gel is gelator molecules. Gels can be formed by high molecular weight (HMW) or low molecular weight (LMW,  $M < 3000$  Da) gelator components. The supramolecular gel is a significant area of research in today's material chemistry. The formation of gels is greatly influenced by the self-assembly of low-molecular-weight gelators (LMWGs) in a proper solvent forming a 3D network. Gels are a central research point under soft materials due to their susceptibility to chemical stimuli like temperature, light, pH, and other chemical entities. Based on the previous research reports, to design a prospective gelator molecule incorporations of specific functional groups viz. carboxylic acid, carboxamide, amine, alcohol, pyridine, tetrazole, imidazole, nitrile, and aromatics ring in the structure are found to be crucial. These entities can provide the sites for non-covalent interactions, like  $\pi$ - $\pi$  interactions, hydrogen bonding interactions, van der Waals forces, intercolumnar stacking, etc., which are crucial for gel formation. It is impossible to confirm the gelation behavior of any molecule or gelator without its experimental analysis. Therefore, experimentally, the fabrication of a gel by a gelator molecule is supposed to be investigated to confirm such a process. Incorporating metal ions within the gel matrix can change the gelation behaviour significantly. Researchers are also investigating the incorporation of metal nanoparticles inside the gel matrix to form nanometallogels or synthesize a nanostructured metallogel<sup>6</sup>. These modifications or development pushes the boundary of applications and paves the way for advanced functional materials.

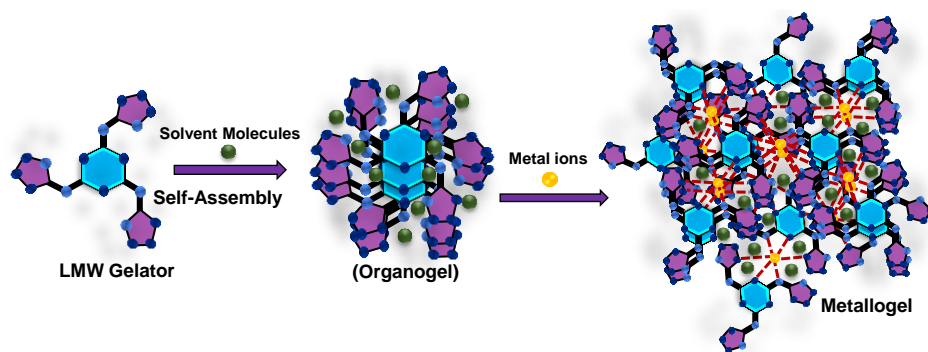


**Figure 1.** Fabrication of organogel and metallogel from gelator components.

In the present thesis, the synthesis and fabrication of the following material have been done:

- Synthesis of BTA-based gelator molecule **G7**
- Synthesis of triazine-based gelator molecule **G8**
- Synthesis of BTA-based gelation enhancer molecule **GE**
- Fabrications of nanostructured organogel and metallogels of **G7** with transition metal salts, organogels of **G8** with isomers of aminopyridine, organogel and metallogels of **G8GE** with heavy metal salts and metallogels of **G8** with PdCl<sub>2</sub> and **G8PdNPs** nanocomposite.
- Applications of fabricated organogels and metallogels in applied fields like catalysis, sensing, and water remediation.

The present work aims to synthesize gelator molecules, fabricate organo- and metallogels and apply the low molecular weight nanostructured organogels and metallogels in various fields.

## OBJECTIVES

The primary objectives for this thesis are the following:

- To design suitable low molecular weight organic molecules containing functional groups like carboxylic acid, tetrazole, amide, amine, and aromatic rings. The synthesis and characterization of those gelator organic

molecules (given below) as low molecular weight gelators (LMWGs) for fabricating organogels and metallogels are explored.

**Gelator molecule G7:** Gelator molecule **G7** (triethylammonium 5-(3,5-bis((1H-tetrazol-5-yl)carbamoyl)benzamido) tetrazol-1-ide) has been synthesized. It contains an aromatic ring in core, amide, and tetrazole groups around the tripodal side of the core which provide the sites for non-covalent interactions.

**Gelator molecule G8:** Gelator molecule **G8** ( $N^2, N^4, N^6$ -tri(1H-tetrazol-5-yl)-1,3,5-triazine-2,4,6-triamine) contained secondary amine and tetrazole ring with triazine ring as a core which shows alternative hydrogen bond donor-acceptor sites with isomers of aminopyridine and fabricates mixed organogels.

**Gelator component GE:** Gelator component **GE** ((3,3',3''-(benzenetricarbonyltris(azanediyl)) tris (4-aminobenzoic acid)) contains carboxamide, carboxylic acid, amine and aromatic benzene ring as core which act as gelation property enhancer molecule to enhance the rheological and fluorometric properties of organogel and metallogels with mixed gel system **G8GE**.

● To explore the gelation properties of synthesized gelator molecules **G7** and **G8**. Gelator molecules **G7** form organogel in DMSO:H<sub>2</sub>O mixture. Further, it shows metallogel formation with perchlorate salts of Fe(II), Co(II), Ni(II), Cu(II), Zn(II), Ag(I), and Fe(III). The other gelator molecule, **G8**, forms organogels **G8-3AP**, **G8-2AP**, and **G8-4AP** with isomers of aminopyridine. Another synthesized organic molecule, **GE**, does not form organogel or metallogel itself, but it enhances organogel and metallogel formation as gelator components with gelator molecule **G8**. Therefore, the mixed **G8GE** system formed metallogels with heavy metal salts of HgCl<sub>2</sub>, Hg(OAc)<sub>2</sub>, HgSO<sub>4</sub>, CdCl<sub>2</sub>, Cd(OAc)<sub>2</sub>, CdSO<sub>4</sub>, PbCl<sub>2</sub> and Pb(OAc)<sub>2</sub>. Gelator molecule **G8** also formed nanostructured metallogel **G8PdCl<sub>2</sub>** and

nanometallogel **G8PdNPs**.

● To explore the properties of fabricated organogels and metallogels of gelator molecules **G7**, **G8**, and mixed gelator components **G8GE**. The significant effect can be seen on the gel strength with the rheological behavior of organogels and metallogels of all the synthesized gelator components. Metallogels of **G7** show enhanced strength compared to their organogel due to the additional metal coordinate bonds within the gel matrix. While in the case of organogels of **G8** with isomers of aminopyridine, the **G8-3AP** organogel shows greater storage modulus as compared to **G8**, **G8-2AP**, and **G8-4AP** due to the presence of complementary hydrogen bond donor-acceptor sites in **G8-3AP**. In the case of **G8GE**, the method of gel fabrication affects the strength of all the metallogels. Metallogels formed by the adsorption method show notable enhancement in the strength of gels because, here, the insertion of metal ions does not affect the non-covalent interactions significantly between **G8** and **GE**.

● To explore the applicability of fabricated organogels and metallogels based on their properties. Metallogels of **G7** with a series of transition metal perchlorate salts were used to synthesize and stabilize silver nanoparticles and formed silver nanocomposite **M<sup>1</sup>G7AgNPs** which was used as a catalyst for reducing nitroaromatic into amino aromatics. The organogel **G8** is used for the discrimination between isomers of aminopyridine and provide the possibility of modification in gel properties by changing gel formation conditions and components. Further, the hydrophobic organogel **G8GE** is used for the remediation of water from the contamination of heavy metal salts viz. Hg(II), Cd(II), and Pb(II). The reusability of xerogel of **G8GE** is also explored for further purification. The thesis further investigated the possibilities of the formation of palladium embedded **G8** metallogel as prospective catalysts. Here, the xerogel of nanostructured metallogel **G8PdCl<sub>2</sub>** and

nanometallogel **G8PdNPs** act as catalysts for cycloaddition reaction for tetrazole formation and Suzuki–Miyaura coupling reactions, respectively.

● To investigate the possible structure of interactions of gelator components with each other and with metal ions. FTIR, mass, and PXRD analysis are utilized for the structure prediction for **M<sup>1</sup>G7 metallogel**. The interactions of **G8** with isomers of aminopyridine and the possible interaction between **G8** and **GE** in **G8GE** organogel have been examined by DFT analysis.

### **Summary of Research Work**

The contents of each chapter included in the thesis are discussed briefly as follows:

#### **Chapter 1: General Introduction and Background**

A brief introduction to the field of gel, the design of gelator molecules, their basic concepts, and recent scientific developments towards advanced applications in the field of sensor, catalysis, and environmental science is presented. A summary of the research work done, which is reported in this thesis, has also been mentioned in this chapter.

#### **Chapter 2: Preparation of tris-tetrazole-based metallogels (G7) and stabilization of silver nanoparticles: studies on reduction catalysis and self-healing property.**

An ionic multifunctional gelator molecule triethylammonium 5-(3,5-bis((1H-tetrazol-5-yl)carbamoyl)benzamido)tetrazol-1-ide (**G7**) is synthesized and characterized by spectroscopic tools and mass spectrometry. **G7** forms a stable organogel in a mixture of DMSO and water. Introduction of different metal perchlorate salts in a DMSO solution of **G7** furnished a series of metallogels **M<sup>1</sup>G7**, **M<sup>2</sup>G7**, **M<sup>3</sup>G7**, **M<sup>4</sup>G7**, **M<sup>5</sup>G7**, **M<sup>6</sup>G7** and **M<sup>7</sup>G7** [ $M^1 = \text{Fe(III)}$ ,  $M^2 = \text{Co(II)}$ ,  $M^3 = \text{Cu(II)}$ ,  $M^4 = \text{Zn(II)}$ ,  $M^5 = \text{Ag(I)}$ ,  $M^6 = \text{Ni}$ , and  $M^7 = \text{Fe(II)}$ ]. Among them, **M<sup>1</sup>G7**, **M<sup>3</sup>G7**, **M<sup>4</sup>G7**, **M<sup>6</sup>G7**, and **M<sup>7</sup>G7** help individually to synthesize and

stabilize bimetallic nanocomposites containing silver nanoparticles (AgNPs). Iron(III)-containing nanocomposite  $M^1G7AgNPs$  has been utilized as catalysts in the reduction reaction of nitroaromatic compounds to corresponding amines with a quantitative yield. The organogel **G7** has also shown the ability to absorb different metal ions from aqueous solutions and allow selective transition of  $M^1G7$  from the gel state to the crystalline state. Furthermore, the nanocomposite  $M^1G7AgNPs$  gets converted into a nanostructured metallogel, which shows exclusive self-healing properties. The  $M^1G7AgNPs$  nanocomposite is the first example where a nanocomposite powder contains the dual metal system (Fe(III) and Ag(0)) and shows a reduction catalytic property, and its nanostructured dual-metallogel form manifests the self-healing property.

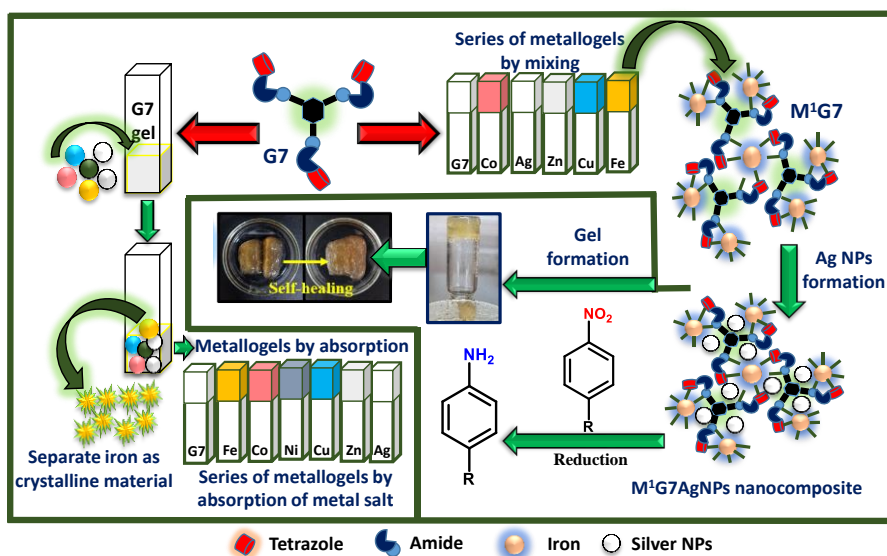


**Figure 2.** Fabrication of series of metallogel of **G7**, silver nanocomposite formation with  $M^1G7$  and their use in reduction of nitroaromatic.

### Chapter 3: Another tris-tetrazole (**G8**) based nanostructured soft material: studies on self-healing, AIEE, rheological and fluorometric detection of 3-aminopyridine.

The tetrazole-based gelator molecule  $N^2, N^4, N^6$ -tri(1H-tetrazol-5-yl)-1,3,5-triazine-2,4,6-triamine (**G8**) has been synthesized and characterized using

ESI-MS, NMR and FTIR techniques. **G8** itself formed an organogel which shows aggregation-induced enhanced emission (AIEE). It also shows fluorescence in the concentrated solution state due to the intramolecular charge transfer (ICT) within the planar structure of the compound. To analyse the possibility of discrimination between various isomers of the organic compound depending upon their hydrogen bonding sites, **G8** is used to interact with the isomers of aminopyridine (AP) and three mixed organogels, viz. **G8-2AP**, **G8-3AP**, and **G8-4AP** have formed. The interactions of the isomers of aminopyridines and the predicted structures of **G8-2AP**, **G8-3AP**, and **G8-4AP** have been investigated by fluorescence, <sup>1</sup>H NMR, PXRD, FT-IR, and DFT studies. Of these three aminopyridines, **G8** shows selective sensing of 3-AP with notable changes in terms of fluorescence primarily due to the stronger restriction of intramolecular rotation (RIR) within the **G8** molecule, thus blocking the non-radiative pathway. 3-AP also gets recognized by a higher storage modulus than the other organogels due to the formation of stronger hydrogen bonds (N–H...N) within **G8** and 3-AP molecules.

Furthermore, **G8** can also distinguish 3-AP by visual color changes concerning other aminopyridines. The time oscillation sweep (TOS) experiment shows that the thixotropic behaviour of **G8-3AP** decreases with an increasing number of cycles due to the greater storage modulus value of **G8-3AP**. The selective results due to the interactions of the isomers of aminopyridine with **G8** confirm the effect of the isomeric positions on the different properties of the mixed organogels.

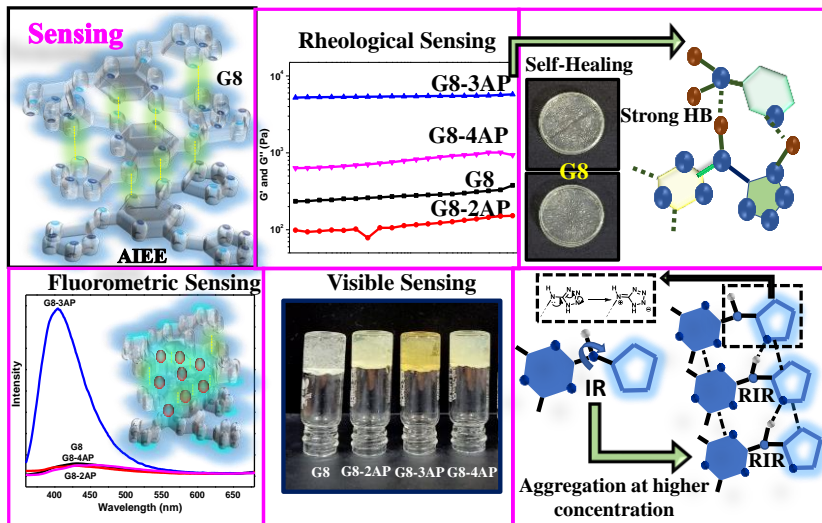


**Figure 3.** Fabrication of organogels of **G8**, effect of isomeric position on physical and chemical properties of gel.

#### **Chapter 4: Palladium nanoparticles and palladium ion embedded nanostructured metallogel: effective catalyst for Suzuki-Miyaura coupling and cycloaddition reaction for tetrazole formation.**

The gelator molecule **G8** is utilized as a component for the preparation of a gel matrix for the stabilization of palladium nanoparticles and the fabrication of its nanometallogel. For the formation of catalyst **G8PdCl<sub>2</sub>**, the metallogel fabrication has been carried out in DMSO: H<sub>2</sub>O mixture. After the fabrication of **G8PdCl<sub>2</sub>** metallogel, it was converted into xerogel by lyophilization. This xerogel is used as a catalyst for the cycloaddition reaction of nitrile substituent and sodium azide to form respective tetrazoles. Further, the palladium nanocomposite has been synthesized from **G8** and **PdCl<sub>2</sub>** in THF solvent with its treatment with NaBH<sub>4</sub>. The synthesized palladium nanocomposite **G8PdNPs** treated with **G8** in DMSO: H<sub>2</sub>O mixture and fabrication of nanoparticles containing metallogel **G8PdNPs** is achieved. It was further converted into xerogel by its lyophilization. The synthesized xerogel was used as a catalyst for the Suzuki-Miyaura coupling reaction for various substrates with good product yield. The catalytic reaction products were examined by ESI-MS and NMR

techniques. The synthesis and fabrication of palladium nanocomposite, metallogels, and its xerogels have been analysed by FTIR, PXRD, XPS, SEM, TEM, UV-Vis, and fluorescence analysis.

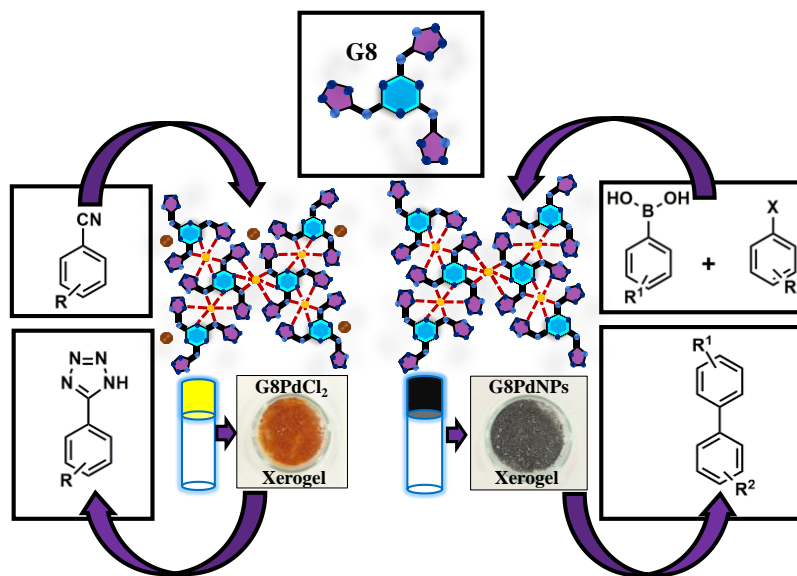


**Figure 4.** Fabrication of nanostructured metallogel and nanoparticles containing metallogel of Palladium with **G8** molecules and their use as catalyst in organic catalytic reactions.

### Chapter 5: Design and synthesis of hydrophobic mixed organogel with complementary hydrogen-bond donor-acceptor sites: removal of heavy metal ions $\text{Hg}^{2+}$ , $\text{Cd}^{2+}$ and $\text{Pb}^{2+}$ from aqueous solution.

The incorporation of metal ions in gelator systems can generate different kinds of metallogels. However, capturing heavy metal ions by gel structures is scarcely investigated by researchers. In an earlier chapter, one LMWG molecule viz  $N^2, N^4, N^6$ -tri(1*H*-tetrazol-5-yl)-1,3,5-triazine-2,4,6-triamine (**G8**) was introduced for discrimination between various isomers of aminopyridines. However, the gel strength was found to be moderate, and it was unstable in water. Herein, the introduction of another molecule, viz. 3,3',3''-(benzenetricarbonyltris(azanediyl))tris(4-aminobenzoic acid) (**GE**) along with **G8** has been done to impart greater stability and make the mixed-gel water stable. The design of the **GE** is strategized with the

presence of complementary hydrogen bond donor-acceptor sites with respect to **G8**. The resultant organogel **G8GE** has shown the ability to form metallogels with Hg(II), Cd(II), and Pb(II) salts. The hydrophobic nature of the gel **G8GE** is observed with the retention of the disc-shaped gel structure in an aqueous medium for an extended period. Metallogels are fabricated with two different approaches, viz. mixing and adsorption methods. Rheological experiments indicated that in the adsorption method, the slow diffusion of metal ions does not substantially disturb the interactions between **G8** and **GE**, proving it a more efficient process for gel formation. DFT-based optimization of the structure supports the complementary hydrogen bond formation hypothesis between **G8** and **GE**. The mixed organogel shows the capacity to efficiently remove toxic metal ions like Hg(II), Cd(II), and Pb(II) from their aqueous solutions. The material can be recycled for further water remediation by treating the mercury-contained mixed organogel with excess KI.

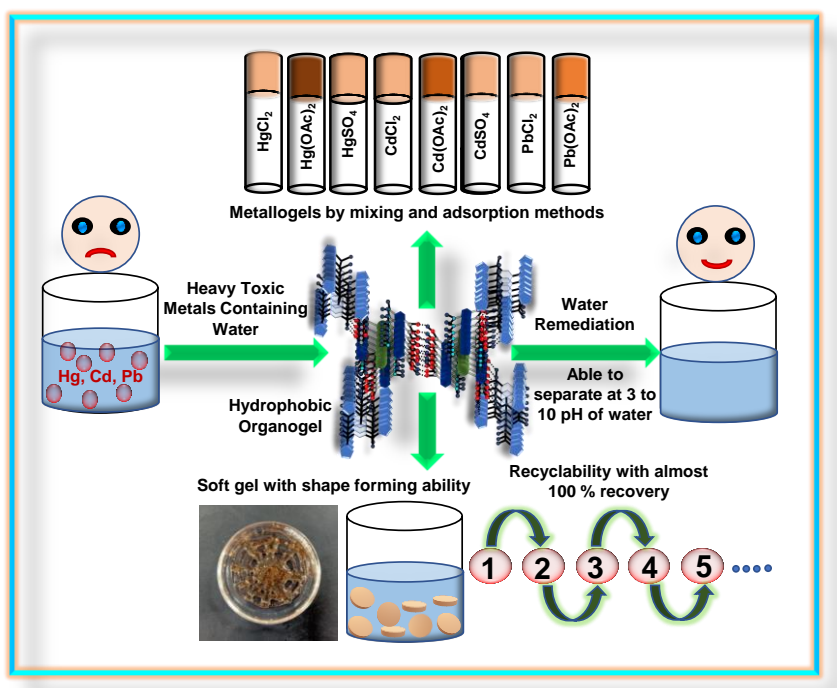


**Figure 5.** Fabrication of hydrophobic organogels **G8GE** and its use in remediation of water.

## **Chapter 6: General Conclusions and Future Scope**

In this thesis, two LMW gelator molecules, **G7**, **G8**, and one gelation enhancer molecule **GE**, have been introduced with their remarkable ability to form organogels and metallogels with various metal ions and organic substrates. The derived properties of all the fabricated organogels and metallogels make them useful for various applications, viz. stabilization of nanoparticles, catalysis, sensing, and environmental remediation. Besides this, the thesis focused on modification in the rheological properties of gels and the formation of multi-applicable gel materials. Apart from that, the future applications of this thesis have been discussed.



# LIST OF PUBLICATIONS

## (A) Outcomes from MS (R)/ PhD. Thesis work:

### A1. In refereed journals:

#### Papers published:

- 1. Kyarikwal, R.,** Malviya, N., Chakraborty, A. and Mukhopadhyay, S. (2021), Preparation of tris-tetrazole-based metallogels and stabilization of silver nanoparticles: studies on reduction catalysis and self-healing property, ACS Appl. Mater. Interfaces, **13**, 59567-59579. (D.O.I. **10.1021/acsami.1c19217**) (I.F: **9.5**)
- 2. Kyarikwal, R.,** Kundu, B.K., Chakraborty, A. and Mukhopadhyay, S. (2022), A tris-tetrazole based nanostructured soft material: Studies on self-healing, AIEE, and rheological and fluorometric detection of 3-aminopyridine. Mater. Chem. Front., **6**, 2835-2847 (D.O.I. **10.1039/D2QM00520D**) (I.F: **7**)
- 3. Kyarikwal, R.,** Munjal, R., Nag, P., Vennapusa, S.R. and Mukhopadhyay, S. (2023), Design and synthesis of hydrophobic mixed organogels with complementary hydrogen-bond donor–acceptor sites: removal of heavy metal ions  $\text{Hg}^{2+}$ ,  $\text{Cd}^{2+}$  and  $\text{Pb}^{2+}$  from aqueous solution, Mater. Adv., **4**, 3603-3618 (DOI: **10.1039/D3MA00300K**) (I.F: **5**)

## **Papers under review:**

**4. Kyarikwal, R.,** Munjal, R. and Mukhopadhyay, S., Palladium nanoparticles and palladium ion embedded nanostructured metallogel: effective catalyst for suzuki-miyaura coupling and cycloaddition reaction for tetrazole formation (Manuscript under preparation)

## **A2. In refereed conferences:**

**Papers published in conference proceedings: Nil**

**Papers presented in international/ national conference of high repute:**

Poster presentation in CASM 2022 held at CSIR-NIIST Thiruvananthapuram, India, on 25<sup>th</sup>-27<sup>th</sup> July 2022. The poster presentation was based on “A tris-tetrazole based nanostructured soft material: Studies on self-healing, AIEE, and rheological and fluorometric detection of 3-aminopyridine.”

**A3. Book Chapters (published/: under review: Nil**

**A4. Patent (filed/ published/ granted): Nil**

**A5. Any other relevant information: Nil**

**(B) Other outcomes outside of the MS (R)/ PhD. Thesis work:**

**B1. In refereed journals:**

**Papers published:**

5. Kundu, B.K., Pragti, **Kyarikwal, R.**, Mobin, S.M. and Mukhopadhyay, S. (2019), Mechanistic and thermodynamic aspects of a pyrene-based fluorescent probe to detect picric acid. *New J. Chem.*, **43**, 11483-11492. **(D.O.I. 10.1039/C9NJ02342A) (I.F: 3.3)**

6. Chakraborty, A., Sarkar, S., **Kyarikwal, R.**, Nag, P., Vennapusa, S.R. and Mukhopadhyay, S. (2022), Piperazine-linked covalent triazine polymer as an efficient platform for the removal of toxic mercury (II) ions from wastewater. *ACS Appl. Polym. Mater.*, **4**, 8118-8126. **(D.O.I. 10.1021/acsapm.2c01085) (I.F: 5)**

7. Ranjan, R., Chakraborty, A., **Kyarikwal, R.**, Ganguly, R. and Mukhopadhyay, S. (2022), A binuclear Cu (ii) complex as an efficient photocatalyst for N-alkylation of aromatic amines. *Dalton Trans.*, **51**, 13288-13300. **(D.O.I. 10.1039/D2DT01771G) (I.F: 4)**

8. Ranjan, R., Kundu, B.K., **Kyarikwal, R.**, Ganguly, R. and Mukhopadhyay, S. (2022), Synthesis of Cu (II) complexes by N, O-donor ligand transformation and their catalytic role in visible-light-driven alcohol oxidation. *Appl. Organomet. Chem.*, **36**, e6450. **(D.O.I. 10.1002/aoc.6450) (I.F: 3.9)**

**Papers under review:**

**9.** Nautiyal, P., **Kyarikwal, R.**, Munjal, R. Nag, P., Vennapusa, S.R. and Mukhopadhyay, S., Enhancing gel strength for increased catalytic stability of a nanocomposite catalyst by incorporating reinforcing component with H-bond donor-acceptor sites (Manuscript under preparation)

**B2. In refereed conferences:**

**Papers published in conference proceedings: Nil**

**Papers presented in international/ national conference of high repute: Nil**

**B3. Book Chapters (published/: under review: Nil**

**B4. Patent (filed/ published/ granted): Nil**

**B5. Any other relevant information: Nil**

## LIST OF CONFERENCES

1. Poster presentation in CASM 2022 held at CSIR-NIIST Thiruvananthapuram, India, on 25<sup>th</sup>-27<sup>th</sup> July 2022.
2. Poster presentation in CHEM 2020, “Chemistry Day and In-House Symposium” organized by IIT Indore, Feb 12, 2020.
3. Participated in CHEM 2022, “Chemistry Day and In-House Symposium” organized by IIT Indore, March 11, 2022.
4. Oral presentation in CHEM 2023, “Chemistry Day and In-House Symposium” organized by IIT Indore, March 6, 2023.
5. Oral presentation in RSC-IITI Indore symposium on “Materials Science towards New Horizons-2023, held at IIT Indore, India on Jan 19-20, 2023.



# TABLE OF CONTENTS

List of Nomenclature.....	xxxi
List of Acronyms.....	xxxiii
List of Figures.....	xxxv
List of Schemes.....	lv
List of Tables.....	lix
<b>Chapter 1</b>	
General introduction and background.....	1
1.1 Introduction.....	3
1.1.1 Types of gels based on different parameters.....	6
1.1.2 General characterization methods and basic properties of gels.....	8
1.2 Design and synthesis of low molecular weight gelator Molecules.....	11
1.2.1 Benzene and triazine ring based tripodal amide and Amine.....	13
1.2.2 Tetrazole.....	14
1.2.3 Aromatic primary and secondary amine.....	15
1.3 Gels formation by tripodal aromatic amide, amine and tetrazole based moieties.....	16
1.4 Different Methods of fabrication of various organogels and metallogels.....	18
1.5 Importance of LMW soft organo-metallogels and their Applications .....	19
1.5.1 Soft materials as sensor: sensing ability of gels for cation, anion, biomolecules, and different pollutant.....	20
1.5.2 Self-healing materials: thixotropic nature of gels.....	22

1.5.3 Gels and xerogels as adsorbent: act as environmental remediator .....	24
1.5.4 Nanostructured metallogels as catalyst for various organic Reactions.....	26
1.6 Aim and objective of the current thesis.....	27
1.7 References.....	30

## **Chapter 2**

<b>Preparation of tris-tetrazole-based metallogels and stabilization of silver nanoparticles: studies on reduction catalysis and self-healing property.....</b>	<b>57</b>
2.1 Introduction.....	59
2.2 Experimental section.....	60
2.2.1 Material and method.....	60
2.2.2 Synthesis of gelator molecule <b>G7</b> [triethylammonium 5-(3,5- bis((1H-tetrazol-5-yl) carbamoyl) benzamido)tetrazol-1- ide].....	61
2.2.3 Gel Preparation.....	61
2.2.4 Gel Melting Temperature.....	62
2.2.5 Formation of AgNPs.....	62
2.2.6 Reduction catalysis by <b>M<sup>1</sup>G7AgNPs</b> .....	63
2.2.7 Conversion of AgNPs Containing Nanocomposite Material <b>M<sup>1</sup>G7AgNPs</b> into NanostructuredMetallogel.....	63
2.2.8 Characterization.....	63
2.3 Results and discussion.....	65
2.4 Conclusions.....	103
2.5 Declaration.....	104

2.6 References.....	104
---------------------	-----

### Chapter 3

<b>Another tris-tetrazole based nanostructured soft material: studies on self-healing, AIEE, and rheological and fluorometric detection of 3-aminopyridine.....</b>	<b>115</b>
3.1 Introduction.....	117
3.2 Experimental section.....	118
3.2.1 Material and method.....	118
3.2.2 Synthesis of gelator <b>G8</b> [N <sup>2</sup> , N <sup>4</sup> , N <sup>6</sup> -tri(1H-tetrazol-5-yl)-1,3,5-triazine-2,4,6-triamine].....	118
3.2.3 Preparation of gels.....	119
3.2.4 Gel melting temperature.....	121
3.2.5 Interactions of <b>G8</b> with isomers of aminopyridine.....	121
3.2.6 Characterization.....	121
3.3 Results and discussion.....	122
3.4 Conclusions.....	150
3.5 Declaration.....	151
3.6 References.....	152

### Chapter 4

<b>Palladium Nanoparticles and Palladium Ions Embedded Nanostructured Metallogel: Effective Catalyst for Suzuki-Miyaura Coupling and Cycloaddition Reaction for Tetrazole Formation.....</b>	<b>159</b>
4.1 Introduction.....	161
4.2 Experimental section.....	163
4.2.1 Materials and methods.....	163
4.2.2 Synthesis of <b>G8</b> , <b>G8PdCl<sub>2</sub></b> and <b>G8PdNPs</b> .....	164

4.2.3 Gels preparation.....	165
4.2.4 Characterization.....	165
4.2.5 General method of synthesis of tetrazole substituent (3+2 cycloaddition reaction).....	165
4.2.6 General method of Suzuki-Miyaura coupling reaction.....	179
4.3 Results and discussion.....	197
4.4 Conclusion.....	211
4.5 References.....	212
<b>Chapter 5</b>	
<b>Design and Synthesis of Hydrophobic Mixed Organogel with Complementary Hydrogen-bond Donor-acceptor Sites: Removal of Heavy Metal Ions Hg<sup>+2</sup>, Cd<sup>+2</sup> and Pb<sup>+2</sup> from Aqueous Solution.....</b>	
	<b>223</b>
5.1 Introduction.....	225
5.2 Experimental section.....	228
5.2.1 Materials and methods.....	228
5.2.2 Synthesis of gelator component <b>G8</b> (N <sup>2</sup> , N <sup>4</sup> , N <sup>6</sup> -tri(1H-tetrazol-5- yl)-1,3,5-triazine-2,4,6-triamine) and <b>GE</b> [3,3',3''- (benzenetricarbonyltris(azanediyl)) tris (4-aminobenzoic acid)].....	228
5.2.3 Gels preparation.....	229
5.2.4 Gel melting temperature.....	230
5.2.5 Characterization.....	230
5.3 Results and discussion.....	231
5.4 Conclusion.....	273
5.5 Declaration.....	275
5.6 References.....	275

<b>Chapter 6</b>	
<b>General Conclusions and Future Scope.....</b>	<b>287</b>
6.1 General Conclusion.....	289
6.2 Future scope.....	292



## LIST OF NOMENCLATURE

$\text{\AA}$	Angstrom
$\lambda$	Wavelength
$\mu$	Micro
$\pi$	Pi
nm	Nanometer
mM	Milli Molar
cm	Centimeter
$^{\circ}$	Degree
mL	Milliliter
$\mu\text{L}$	Microliter
a. u.	Arbitrary Unit
$\lambda_{\text{ex}}$	Excitation Wavelength
$\lambda_{\text{em}}$	Emission Wavelength
pH	The negative logarithm of hydronium-ion concentration
$G'$	Storage Modulus
$G''$	Loss Modulus
Pa	Pascal
$T_{\text{gel}}$	Gel-sol phase transition temperature
$\delta$	Chemical shift



## LIST OF ACRONYMS

AIEE	Aggregation Induced Enhanced Emission
ACQ	Aggregation Caused Quenching
BTA	1,3,5-Benzene Tricarboxamide
CDCl <sub>3</sub>	Chloroform - <i>d</i>
CGC	Critical Gel Concentration
DMF	Dimethylformamide
DMSO- <i>d</i> <sub>6</sub>	Dimethyl sulfoxide- <i>d</i> <sub>6</sub>
DNA	Deoxyribonucleic acid
ESI-MS	Electron Spin Ionization Mass Spectrometry
FE-SEM	Field Emission Scanning Electron Microscope
FT-IR	Fourier Transform Infrared
FS	Frequency Sweep
LMW	Low Molecular Weight
LVE	Linear Visco Elastic
NMR	Nuclear Magnetic Resonance
MOF	Metal Organic Framework
PXRD	Powder X-Ray Diffraction
PPM	Parts Per Million

TEM Transmission Electron Microscopy

THF Tetrahydrofuran

# LIST OF FIGURES

## Chapter 1

<b>Figure 1.1</b> Common gels found in daily life.....	<b>5</b>
<b>Figure 1.2</b> Various application areas of gel (brown circle contains initial applications and blue circle contain increasing area of applications with modifications in properties of gel).....	<b>6</b>
<b>Figure 1.3</b> Classification of gels.....	<b>8</b>
<b>Figure 1.4</b> Technology used for the characterization of gels.....	<b>9</b>
<b>Figure 1.5</b> Basic properties of gels.....	<b>10</b>
<b>Figure 1.6</b> Factor behind sensing properties of LMW gels.....	<b>21</b>
<b>Figure 1.7</b> Schematic diagram for self-assembly after reformation of bonds.....	<b>23</b>
<b>Figure 1.8</b> Water contamination due to environmental pollution and their remediation by different methods.....	<b>25</b>
<b>Figure 1.9</b> Nanostructured metallogels as catalyst for different organic reactions.....	<b>27</b>

## Chapter 2

<b>Figure 2.1.</b> IR data of gelator powder <b>G7</b> .....	<b>66</b>
<b>Figure 2.2.</b> $^1\text{H}$ NMR of gelator <b>G7</b> .....	<b>66</b>
<b>Figure 2.3.</b> $^{13}\text{C}$ NMR of gelator <b>G7</b> .....	<b>67</b>
<b>Figure 2.4.</b> ESI-MS of gelator <b>G7</b> in positive mode.....	<b>67</b>
<b>Figure 2.5.</b> Confirmation of gel formation by test tube inversion method.....	<b>68</b>

<b>Figure 2.6.</b> Formation of metallogels by mixing and by absorption of metal ions from aqueous solution.....	<b>69</b>
<b>Figure 2.7.</b> TGA analysis data of gelator <b>G7</b> , Xerogel <b>G7</b> and metallogel <b>M<sup>1</sup>G7</b> .....	<b>71</b>
<b>Figure 2.8.</b> BET analysis of (a) powder <b>G7</b> , (b) organogel <b>G7</b> , and (c) Fe(III) metallogel <b>M<sup>1</sup>G7</b> .....	<b>72</b>
<b>Figure 2.9.</b> ESI-MS of metallogel <b>M<sup>1</sup>G7</b> .....	<b>73</b>
<b>Figure 2.10.</b> FT-IR of gelator <b>G7</b> and <b>M<sup>1</sup>G7</b> .....	<b>74</b>
<b>Figure 2.11.</b> AFM image of <b>M<sup>1</sup>G7AgNPs</b> nanocomposite.....	<b>75</b>
<b>Figure 2.12.</b> EDX analysis of <b>M<sup>1</sup>G7AgNPs</b> nanocomposite.....	<b>75</b>
<b>Figure 2.13.</b> UV-Vis spectra of reaction of AgNO <sub>3</sub> with series of metallogels during silver nanoparticles synthesis after 12 hrs.....	<b>76</b>
<b>Figure 2.14.</b> (a) Synthesis of <b>M<sup>1</sup>G7AgNPs</b> at 6 hrs. and 12 hrs. reaction time with same condition (b) UV-vis data showing changes in wavelength from <b>M<sup>1</sup>G7</b> to <b>M<sup>1</sup>G7AgNPs</b> nanocomposite.....	<b>77</b>
<b>Figure 2.15.</b> (a) UV-vis spectra of <b>M<sup>1</sup>G7AgNPs</b> , to show the synthesis of silver nanoparticles inside the nanocomposite system at different conditions (b) FE-SEM image of <b>M<sup>1</sup>G7AgNPs</b> with the condition 80 °C, 0.5 g of gel, and 12 hrs.....	<b>77</b>
<b>Figure 2.16.</b> (a) Total XPS spectra of composite <b>M<sup>1</sup>G7AgNPs</b> (b) C 1s XPS spectra (c) N 1s XPS spectra (d) O 1s XPS spectra and (e) Fe 2p XPS spectra of catalyst <b>M<sup>1</sup>G7AgNPs</b> .....	<b>78</b>
<b>Figure 2.17.</b> Ag 3d XPS spectra of synthesized silver nanoparticles in nanocomposite <b>M<sup>1</sup>G7AgNPs</b> .....	<b>79</b>

<b>Figure 2.18.</b> FT-IR data of <b>G7</b> , Xerogel of <b>G7</b> , <b>M<sup>1</sup>G7</b> and <b>M<sup>1</sup>G7AgNPs</b> .....	<b>80</b>
<b>Figure 2.19.</b> PXRD analysis of <b>M<sup>1</sup>G7</b> and <b>M<sup>1</sup>G7AgNPs</b> nanocomposite.....	<b>80</b>
<b>Figure 2.20.</b> UV-Vis spectra of reduction of (a) NB (b) 4-NP (c) 4-NA (d) 4-NBA catalyzed by <b>M<sup>1</sup>G7AgNPs</b> nanocomposite.....	<b>82</b>
<b>Figure 2.21.</b> Control reduction experiment of 4-nitrophenol by NaBH <sub>4</sub> without using nanocomposite catalyst <b>M<sup>1</sup>G7AgNPs</b> .....	<b>82</b>
<b>Figure 2.22.</b> <sup>1</sup> H NMR of reduction of (a) NB (b) 4-NP (c) 4-NA and (d) 4-NBA.....	<b>84</b>
<b>Figure 2.23.</b> GC-MS spectra of analyzed data of reduction of nitro aromatics to corresponding amino compounds.....	<b>85</b>
<b>Figure 2.24.</b> UV-vis analysis of <b>M<sup>1</sup>G7AgNPs</b> catalyst during five cycles of catalytic reaction.....	<b>87</b>
<b>Figure 2.25.</b> FE-SEM and EDX analysis of <b>M<sup>1</sup>G7AgNPs</b> catalyst after reduction of 4-NP.....	<b>88</b>
<b>Figure 2.26.</b> PXRD analysis of <b>M<sup>1</sup>G7AgNPs</b> catalyst showing recovery of catalyst.....	<b>88</b>
<b>Figure 2.27.</b> Fe(III) uptake study by UV-Vis analysis.....	<b>89</b>
<b>Figure 2.28.</b> (a) Selective get to crystal transition of iron during absorption of different metal ions (b) Formation of stable dual metallogel of Fe(III) and Zn(II) with <b>G7</b> at 2:1 metals-G7 ratio.....	<b>91</b>
<b>Figure 2.29.</b> PXRD analysis of Crystalline <b>M<sup>1</sup>G7</b> .....	<b>91</b>

**Figure 2.30.** Rheological measurement of (a) linear viscoelastic behavior for the Fe-Zn dual metallogel (b) dynamic frequency sweep for the Fe-Zn dual metallogel.....92

**Figure 2.31.** concentration dependent <sup>1</sup>H NMR spectra of gelator **G7** at (a) 97 mM (b) 195 mM (c) 243 mM.....94

**Figure 2.32.** FTIR of **G7** (Powder) and **G7** (Xerogel).....95

**Figure 2.33.** (a) FT-IR spectra of **G7** (powder) and **G7** (Xerogel) (b) PXRD pattern of Xerogel **G7**.....95

**Figure 2.34.** (a) FE-SEM image of organogel **G7** under micro and (b) nano scale.....95

**Figure 2.35.** (a) Linear viscoelastic (LVE) range of organogel **G7** (b) dynamic frequency sweep for the organogel **G7**.....97

**Figure 2.36.** (a) linear viscoelastic behavior for the **M<sup>1</sup>G7-M<sup>6</sup>G7** (b) dynamic frequency sweep for the **M<sup>1</sup>G7-M<sup>6</sup>G7**.....97

**Figure 2.37.** Rheological measurement of (a) linear viscoelastic behavior for the **M<sup>7</sup>G7** (b) dynamic frequency sweep for the **M<sup>7</sup>G7**.....97

**Figure 2.38.** FTIR of (a) **M<sup>1</sup>G7** (b) **M<sup>2</sup>G7** (c) **M<sup>3</sup>G7** (d) **M<sup>4</sup>G7** (e) **M<sup>5</sup>G7** (f) **M<sup>6</sup>G7**.....98

**Figure 2.39.** PXRD pattern of Xerogel **G7**, Metallogel **M<sup>1</sup>G7** and Silver Nanocomposite **M<sup>1</sup>G7AgNPs**.....100

**Figure 2.40.** PXRD of Xerogel **G7** and metallogels **M<sup>1</sup>G7**, **M<sup>2</sup>G7**, **M<sup>3</sup>G7**, **M<sup>4</sup>G7**, **M<sup>5</sup>G7** and **M<sup>6</sup>G7**.....101

**Figure 2.41.** SEM image of (a) **M<sup>1</sup>G7** (Fe (III) gel) (b) **M<sup>2</sup>G7** (Co (II) gel) (c) **M<sup>3</sup>G7** (Cu (II) gel) (d) **M<sup>4</sup>G7** (Zn (II) gel) (e) **M<sup>5</sup>G7** (Ag (I) gel) (f) **M<sup>6</sup>G7** (Ni (II) gel).....101

**Figure 2.42.** (a) Image showing self-healing property of **M<sup>1</sup>G7AgNPs**

nano-metallogel (b) Time oscillation strain sweep experiment (Thixotropic behavior) of **M<sup>1</sup>G7AgNPs** gel at minimum (0.5 %) and maximum (100 %) strain. (c), (d), (e) The TEM images of **M<sup>1</sup>G7AgNPs** gel at 100 nm, 50 nm and 10 nm respectively.....103

### Chapter 3

**Figure 3.1.** Optimization of gelation condition of **G8**.....120

**Figure 3.2.** Confirmation of gel formation by test tube inversion method.....121

**Figure 3.3.** FTIR data of gelator powder **G8** and xerogel of **G8**.....123

**Figure 3.4.** <sup>13</sup>C NMR of gelator **G8**.....123

**Figure 3.5.** ESI-MS of gelator **G8**.....124

**Figure 3.6.** (a) Solid-state UV-Vis analysis of **G8** (b) Excitation and emission wavelength of **G8** by fluorometer.....125

**Figure 3.7.** Fluorescent images of organogel **G8** under UV chamber (a) Fluorescence data showing aggregation induced enhanced emission (AIEE) of gelator molecule **G8**.....125

**Figure 3.8.** Notable Color change of **G8-3AP** organogel after three weeks at normal condition.....126

**Figure 3.9.** Fluorescence analysis of interaction of (a) **G8**, **G8-2AP**, **G8-3AP** and **G8-4AP** (b) **G8** and **G8-2AP** (c) **G8** and **G8-3AP** (d) **G8** and **G8-4AP**.....127

**Figure 3.10.** Controlled experiment of interaction of **G8** with different pyridine compounds.....128

**Figure 3.11.** Schematic representation of intramolecular charge transfer in planar molecule **G8**.....129

<b>Figure 3.12.</b> Effect of solvent on wavelength of <b>G8</b> molecule.....	<b>130</b>
<b>Figure 3.13.</b> Gelator molecule <b>G8</b> (a) Mapped with ESP and (b) Mulliken atomic charge distribution.....	<b>130</b>
<b>Figure 3.14.</b> <b>G8</b> molecule Mapped with ESP. Isovalue for new surfaces: MO, 0.04, density 0.001, and Laplacian, 0.00.....	<b>130</b>
<b>Figure 3.15.</b> (a) Fluorescence spectra of <b>G8-2AP</b> at different concentration (b) Jobs plot to shows maximum intensity ratio of <b>G8- 2AP</b> .....	<b>132</b>
<b>Figure 3.16.</b> Concentration dependent <sup>1</sup> H NMR of 2-aminopyriine with increasing amount of gelator molecule <b>G8</b> .....	<b>132</b>
<b>Figure 3.17.</b> (a) Fluorescence spectra of <b>G8-3AP</b> at different concentration ratio (b) Jobs plot to shows the maximum intensity ratio of <b>G8-3AP</b> .....	<b>133</b>
<b>Figure 3.18.</b> Concentration dependent <sup>1</sup> H NMR of 3-aminopyriine with increasing amount of gelator molecule <b>G8</b> .....	<b>133</b>
<b>Figure 3.19.</b> (a) Fluorescence spectra of <b>G8-4AP</b> at different concentration ratio (b) Jobs plot to shows the maximum intensity ratio of <b>G8-4AP</b> .....	<b>133</b>
<b>Figure 3.20.</b> Concentration dependent <sup>1</sup> H NMR of 4-aminopyriine with increasing amount of gelator molecule <b>G8</b> showing participation of hydrogen and nitrogen for hydrogen bonding.....	<b>134</b>
<b>Figure 3.21.</b> (a) Fluorescence spectra of <b>G8-3AP</b> at different concentration ratio in DMSO: H <sub>2</sub> O (b) Jobs plot to shows the ratio of amount of interaction of <b>G8-3AP</b> at maximum intensity.....	<b>135</b>
<b>Figure 3.22.</b> (a) Fluorescence spectra of <b>G8-3AP</b> at different concentration ratio in DMSO: CH <sub>3</sub> CH <sub>2</sub> OH (b) Jobs plot to shows the ratio of amount of interaction of <b>G8-3AP</b> at maximum intensity.....	<b>135</b>

<b>Figure 3.23.</b> (a) Fluorescence spectra of <b>G8-3AP</b> at different concentration ratio in DMSO: CH <sub>3</sub> CN (b) Jobs plot to shows the ratio of amount of interaction of <b>G8-3AP</b> at maximum intensity.....	<b>135</b>
<b>Figure 3.24.</b> (a) Fluorescence spectra of <b>G8-3AP</b> at different concentration ratio in DMSO: CH <sub>3</sub> Cl (b) Jobs plot to shows the ratio of amount of interaction of <b>G8-3AP</b> at maximum intensity.....	<b>136</b>
<b>Figure 3.25.</b> (a) Fluorescence spectra of <b>G8-3AP</b> at different concentration ratio in DMSO: CH <sub>3</sub> COOCH <sub>2</sub> CH <sub>3</sub> (b) Jobs plot to shows the ratio of amount of interaction of <b>G8-3AP</b> at maximum intensity.....	<b>136</b>
<b>Figure 3.26.</b> Possible predicted structure of <b>G8-2AP</b> , <b>G8-3AP</b> and <b>G8-4AP</b> organogels.....	<b>136</b>
<b>Figure 3.27.</b> HOMO and LUMO orbital demonstration of gelator molecule <b>G8</b> by DFT study.....	<b>138</b>
<b>Figure 3.28.</b> HOMO-LUMO energy orbitals of gelator molecule <b>G8</b> studied by DFT analysis.....	<b>138</b>
<b>Figure 3.29.</b> Energy band gap calculation by UV-Visible analysis (200- 400 nm) of <b>G8</b> in DMSO: H <sub>2</sub> O mixture.....	<b>138</b>
<b>Figure 3.30.</b> Structure confirmation of (a) <b>G8</b> (b) <b>G8-2AP</b> (c) <b>G8-3AP</b> (d) <b>G8-4AP</b> by DFT study.....	<b>139</b>
<b>Figure 3.31.</b> (a) LVE Angular sweep (AS) and (b) Frequency sweep (FS) of organogel <b>G8</b> .....	<b>141</b>
<b>Figure 3.32.</b> (a) LVE Angular sweep (AS) and (b) Frequency sweep (FS) of organogel <b>G8-2AP</b> .....	<b>141</b>
<b>Figure 3.33.</b> (a) LVE Angular sweep (AS) and (b) Frequency sweep (FS) of organogel <b>G8-3AP</b> .....	<b>142</b>

**Figure 3.34.** (a) LVE Angular sweep (AS) and (b) Frequency sweep (FS) of organogel **G8-4AP**.....142

**Figure 3.35.** (a) Series of organogels synthesized from **G8** (b) Comparative study of storage modulus of **G8-2AP**, **G8-3AP** and **G8-4AP** gels with **G8** by Frequency sweep experiment.....142

**Figure 3.36.** Images showing the self-healing property of LMWG organogels (a) **G8**, (b) **G8-2AP**, (c) **G8-3AP** and (d) **G8-4AP**.....143

**Figure 3.37.** Strain sweep experiment of (a) Organogel **G8** (b) Organogel **G8-2AP** and (c) Organogel **G8-3AP** (d) Organogel **G8-4AP**.....144

**Figure 3.38.** FE-SEM images of (a) **G8** powder (b) Organogel **G8** (c) Organogel **G8-2AP** (d) Organogel **G8-3AP** (e) **G8-3AP** with nano measurement and (f) Organogel **G8-4AP** at 200 nm.....145

**Figure 3.39.** FE-SEM images of (a) Organogel **G8** and (b) Xerogel of Organogel **G8** at 200 nm.....145

**Figure 3.40.** FE-SEM images of (a) Organogel **G8-2AP** and (b) Xerogel of Organogel **G8-2AP** at 200 nm.....145

**Figure 3.41.** FE-SEM images of (a) Organogel **G8-3AP** and (b) Xerogel of Organogel **G8-3AP** at 200 nm.....146

**Figure 3.42.** FE-SEM images of (a) Organogel **G8-4AP** and (b) Xerogel of Organogel **G8-4AP** at 200 nm.....146

**Figure 3.43.** FT-IR data of xerogel of **G8**, **G8-2APX**, **G8-3APX** and **G8-4APX**.....147

**Figure 3.44.** PXRD data of (a) gelator powder G8 and Xerogel of (b) G8, (c) G8-2AP, (d) G8-3AP, (e) G8-4AP.....148

**Figure 3.45.** TGA data of gelator molecule G8 and xerogels of organogels of G8, G8-2AP, G8-3AP and G8-4AP.....150

## **Chapter 4**

**Figure 4.1.** ESI-MS of 5-phenyl-1H-tetrazole in negative mode.....166

**Figure 4.2.** FTIR data of benzonitrile and 5-phenyl-1H-tetrazole.....167

**Figure 4.3.** <sup>1</sup>H NMR data of 5-phenyl-1H-tetrazole.....167

**Figure 4.4.** <sup>13</sup>C NMR data of 5-phenyl-1H-tetrazole.....168

**Figure 4.5.** ESI-MS data of 4-(1H-tetrazol-5-yl)aniline in negative mode.....168

**Figure 4.6.** FTIR data of 4-aminobenzonitrile and 4-(1H-tetrazol-5-yl)aniline.....169

**Figure 4.7.** <sup>1</sup>H NMR data of 4-(1H-tetrazol-5-yl)aniline.....169

**Figure 4.8.** <sup>13</sup>C NMR data of 4-(1H-tetrazol-5-yl)aniline.....170

**Figure 4.9.** ESI-MS data of 3-(1H-tetrazol-5-yl)aniline in negative mode.....170

**Figure 4.10.** FTIR data of 3-aminobenzonitrile and 3-(1H-tetrazol-5-yl)aniline.....171

**Figure 4.11.** <sup>1</sup>H NMR data of 3-(1H-tetrazol-5-yl)aniline.....171

**Figure 4.12.** <sup>13</sup>C NMR data of 3-(1H-tetrazol-5-yl)aniline.....172

<b>Figure 4.13.</b> ESI-MS data of 4-(1H-tetrazol-5-yl)benzaldehyde in negative mode.....	<b>172</b>
<b>Figure 4.14.</b> FTIR data of 4-cyanobenzaldehyde and 4-(1H-tetrazol-5-yl)benzaldehyde.....	<b>173</b>
<b>Figure 4.15.</b> <sup>1</sup> H NMR data of 4-(1H-tetrazol-5-yl)benzaldehyde.....	<b>173</b>
<b>Figure 4.16.</b> <sup>13</sup> C NMR data of 4-(1H-tetrazol-5-yl)benzaldehyde.....	<b>174</b>
<b>Figure 4.17.</b> ESI-MS data of 2-(1H-tetrazol-5-yl)aniline in negative mode.....	<b>174</b>
<b>Figure 4.18.</b> FTIR data of 2-aminobenzonitrile and 2-(1H-tetrazol-5-yl)aniline.....	<b>175</b>
<b>Figure 4.19.</b> <sup>1</sup> H NMR data of 2-(1H-tetrazol-5-yl)aniline.....	<b>175</b>
<b>Figure 4.20.</b> <sup>13</sup> C NMR data of 2-(1H-tetrazol-5-yl)aniline.....	<b>176</b>
<b>Figure 4.21.</b> ESI-MS data of 5-(4-nitrophenyl)-1H-tetrazole in negative mode.....	<b>176</b>
<b>Figure 4.22.</b> FTIR data of 4-nitrobenzonitrile and 5-(4-nitrophenyl)-1H-tetrazole.....	<b>177</b>
<b>Figure 4.23.</b> <sup>1</sup> H NMR data of 5-(4-nitrophenyl)-1H-tetrazole.....	<b>177</b>
<b>Figure 4.24.</b> <sup>13</sup> C NMR data of 5-(4-nitrophenyl)-1H-tetrazole.....	<b>178</b>
<b>Figure 4.25.</b> <sup>1</sup> H NMR data of 4,4'-dimethoxy-1,1'-biphenyl when reaction done in methanol.....	<b>180</b>
<b>Figure 4.26.</b> <sup>13</sup> C NMR data of 4,4'-dimethoxy-1,1'-biphenyl when reaction done in methanol.....	<b>180</b>
<b>Figure 4.27.</b> <sup>1</sup> H NMR data of 4,4'-dimethoxy-1,1'-biphenyl when reaction done in DMF.....	<b>181</b>

<b>Figure 4.28.</b> $^{13}\text{C}$ NMR data of 4,4'-dimethoxy-1,1'-biphenyl when reaction done in DMF.....	<b>181</b>
<b>Figure 4.29.</b> $^1\text{H}$ NMR data of 4,4'-dimethoxy-1,1'-biphenyl when reaction done in acetonitrile.....	<b>182</b>
<b>Figure 4.30.</b> $^{13}\text{C}$ NMR data of 4,4'-dimethoxy-1,1'-biphenyl when reaction done in acetonitrile.....	<b>182</b>
<b>Figure 4.31.</b> $^1\text{H}$ NMR data of 4,4'-dimethoxy-1,1'-biphenyl when reaction done in ethanol.....	<b>183</b>
<b>Figure 4.32.</b> $^{13}\text{C}$ NMR data of 4,4'-dimethoxy-1,1'-biphenyl when reaction done in ethanol.....	<b>183</b>
<b>Figure 4.33.</b> $^1\text{H}$ NMR data of 4,4'-dimethoxy-1,1'-biphenyl when reaction done in tetrahydrofuran.....	<b>184</b>
<b>Figure 4.34.</b> $^{13}\text{C}$ NMR data of 4,4'-dimethoxy-1,1'-biphenyl when reaction done in tetrahydrofuran.....	<b>184</b>
<b>Figure 4.35.</b> FTIR analysis of formation of 1,1'-biphenyl from iodobenzene and phenylboronic acid.....	<b>185</b>
<b>Figure 4.36.</b> $^1\text{H}$ NMR analysis of 1,1'-biphenyl.....	<b>186</b>
<b>Figure 4.37.</b> $^{13}\text{C}$ NMR analysis of 1,1'-biphenyl.....	<b>186</b>
<b>Figure 4.38.</b> FTIR analysis of formation of 4-methoxy-1,1'-biphenyl from 1-iodo-4-methoxybenzene and phenylboronic acid.....	<b>187</b>
<b>Figure 4.39.</b> $^1\text{H}$ NMR analysis of 4-methoxy-1,1'-biphenyl.....	<b>188</b>
<b>Figure 4.40.</b> $^{13}\text{C}$ NMR analysis of 4-methoxy-1,1'-biphenyl.....	<b>188</b>
<b>Figure 4.41.</b> FTIR analysis of formation of 4-methyl-1,1'-biphenyl from 1-iodo-4-methylbenzene and phenylboronic acid.....	<b>189</b>

<b>Figure 4.42.</b> $^1\text{H}$ NMR analysis of 4-methyl-1,1'-biphenyl.....	<b>190</b>
<b>Figure 4.43.</b> $^{13}\text{C}$ NMR analysis of 4-methyl-1,1'-biphenyl.....	<b>190</b>
<b>Figure 4.44.</b> FTIR analysis of formation of 4,4'-dimethoxy-1,1'-biphenyl from 1-iodo-4-methoxybenzene and (4-methoxyphenyl) boronic acid.....	<b>191</b>
<b>Figure 4.45.</b> $^1\text{H}$ NMR analysis of 4,4'-dimethoxy-1,1'-biphenyl.....	<b>192</b>
<b>Figure 4.46.</b> $^{13}\text{C}$ NMR analysis of 4,4'-dimethoxy-1,1'-biphenyl.....	<b>192</b>
<b>Figure 4.47.</b> FTIR analysis of formation of 4-methoxy-4'-methyl-1,1'-biphenyl from 1-iodo-4-methylbenzene and (4-methoxyphenyl)boronic acid.....	<b>193</b>
<b>Figure 4.48.</b> $^1\text{H}$ NMR analysis of 4-methoxy-4'-methyl-1,1'-biphenyl.....	<b>194</b>
<b>Figure 4.49.</b> $^{13}\text{C}$ NMR analysis of 4-methoxy-4'-methyl-1,1'-biphenyl.....	<b>194</b>
<b>Figure 4.50.</b> FTIR analysis of formation of 4-(trifluoromethyl)-1,1'-biphenyl from iodobenzene and (4-(trifluoromethyl)phenyl)boronic acid.....	<b>195</b>
<b>Figure 4.51.</b> $^1\text{H}$ NMR analysis of 4-(trifluoromethyl)-1,1'-biphenyl.....	<b>196</b>
<b>Figure 4.52.</b> $^{12}\text{C}$ NMR analysis of 4-(trifluoromethyl)-1,1'-biphenyl.....	<b>196</b>
<b>Figure 4.53.</b> Use of <b>G8</b> for the formation of two type of catalyst i.e., used in two different types of reactions.....	<b>198</b>
<b>Figure 4.54.</b> FTIR analysis of xerogels of <b>G8</b> , <b>G8PdCl<sub>2</sub></b> and <b>G8PdNPs</b> .....	<b>200</b>
<b>Figure 4.55.</b> PXRD analysis of xerogels of <b>G8</b> , <b>G8PdCl<sub>2</sub></b> and <b>G8PdNPs</b> .....	<b>201</b>

<b>Figure 4.56.</b> (a) XPS survey spectra of xerogel of <b>G8PdNPs</b> and XPS analysis of (b) Pd 3d (c) C 1s (d) PdO (e) N 1s.....	<b>202</b>
<b>Figure 4.57.</b> FE-SEM images of (a) <b>G8PdCl<sub>2</sub></b> gel (b) <b>G8PdNPs</b> powder and (c) <b>G8PdNPs</b> gel.....	<b>203</b>
<b>Figure 4.58.</b> EDX and mapping analysis of <b>G8PdNPs</b> gel.....	<b>203</b>
<b>Figure 4.59.</b> TEM analysis of <b>G8PdNPs</b> gel.....	<b>204</b>
<b>Figure 4.60.</b> Angular sweep experiment of (a) <b>G8</b> (c) <b>G8PdCl<sub>2</sub></b> and <b>G8PdNPs</b> , frequency sweep experiment of (b) <b>G8</b> and (d) <b>G8PdCl<sub>2</sub></b> and <b>G8PdNPs</b> .....	<b>205</b>
<b>Figure 4.61.</b> Time oscillation sweep experiment of (a) <b>G8</b> (b) <b>G8PdCl<sub>2</sub></b> and (c) <b>G8PdNPs</b> .....	<b>206</b>
<b>Figure 4.62.</b> Schematic representation of self-assembly of <b>G8</b> molecules and their components for gel formation.....	<b>207</b>
<b>Figure 4.63.</b> (a) Isolated yield of product 4-(1H-tetrazol-5-yl)benzaldehyde during recyclability of catalyst <b>G8PdCl<sub>2</sub></b> till five cycle of reaction (b) Bar graph showing the recyclability of catalyst.....	<b>209</b>
<b>Figure 4.64.</b> FTIR data of catalyst <b>G8PdCl<sub>2</sub></b> before use and after using till five cycles of reaction.....	<b>209</b>
<b>Figure 4.65.</b> (a) Isolated yield of Suzuki-Miyaura coupling product 4,4'-dimethoxy-1,1'-biphenylduring, recyclability of catalyst <b>G8PdNPs</b> till five cycles of reaction. (b) Bar graph showing the recyclability of catalyst.....	<b>210</b>
<b>Figure 4.66.</b> FTIR data of catalyst <b>G8PdNPs</b> before use and after using till five cycles of reaction.....	<b>211</b>

## Chapter 5

<b>Figure 5.1.</b> FTIR data of gelator enhancer molecule <b>GE</b> .....	<b>232</b>
<b>Figure 5.2.</b> ESI-MS data of gelator component <b>GE</b> .....	<b>232</b>
<b>Figure 5.3.</b> <sup>1</sup> H NMR data of gelator component <b>GE</b> .....	<b>233</b>
<b>Figure 5.4.</b> <sup>13</sup> C NMR data of gelator component <b>GE</b> .....	<b>233</b>
<b>Figure 5.5.</b> (a) Formation of gel <b>G8GE</b> at different concentration (b) 3D graph showing best gelation concentration for <b>G8GE</b> organogel (c) images of organogel <b>G8GE</b> at 1:1 and 3:2 ratio (d) linear viscoelastic (LVE) experiment for <b>G8GE</b> at 0.03: 0.03 mmol condition (e) LVE experiment for <b>G8GE</b> at 0.03: 0.02 mmol condition.....	<b>235</b>
<b>Figure 5.6.</b> Angular sweep experiment of organogel <b>G8GE</b> with (a) 0.01: 0.01 mmol (b) 0.02: 0.02 mmol in 1:1 ratio of 2 mL DMSO: H <sub>2</sub> O mixture.....	<b>236</b>
<b>Figure 5.7.</b> Angular sweep experiment of organogel <b>G8GE</b> with (a) 0.03: 0.03 mmol (b) 0.04: 0.04 mmol in 1:1 ratio of 2 mL DMSO: H <sub>2</sub> O mixture.....	<b>236</b>
<b>Figure 5.8.</b> Angular sweep experiment of organogel <b>G8GE</b> with (a) 0.07: 0.07 mmol (b) 0.1: 0.1 mmol in 1:1 ratio of 2 mL DMSO: H <sub>2</sub> O mixture.....	<b>236</b>
<b>Figure 5.9.</b> (a) Addition of organogel <b>G8GE</b> in water by syringe (b) Image showing hydrophobic nature of <b>G8GE</b> gels in water (c) shape formation showing soft and viscoelastic nature of gel (d) formation of metallogel of <b>G8GE</b> with heavy metal salts by mixing (e) formation of metallogel of <b>G8GE</b> with heavy metal salts by adsorption method.....	<b>238</b>
<b>Figure 5.10.</b> UV-Vis spectrum of (a) <b>GE</b> and (c) <b>G8GE</b> .....	<b>239</b>

**Figure 5.11.** Fluorescence spectrum of (a) **G8**, **GE**, **G8GE** (b) 1 mM solution of **G8**, **GE** and **G8GE** under UV chamber.....239

**Figure 5.12.** (a) Fluorescence analysis of **G8**, **GE** and **G8GE** in DMSO: H<sub>2</sub>O mixture (b) Fluorescence analysis of **G8**, **GE** and **G8GE** in DMSO (c) AIEE phenomenon for **G8GE** gelation component and (d) Job's plot showing ratio of interaction between **G8** and **GE**.....241

**Figure 5.13.** (a) Fluorescence study of **G8GE** gelator component with different polar protic and polar aprotic solvents (b) 0.03 mM solution of **G8GE** component in different solvents under UV chamber.....241

**Figure 5.14.** Fluorescence study of **G8GE** organogel and metallogels formed by (a) mixing method and (b) adsorption method.....242

**Figure 5.15.** Fluorescence study of (a) 1 mM solution of **G8GE** (in DMSO) and HgCl<sub>2</sub> (in H<sub>2</sub>O) and (b) 1 mM solution of **G8GE** (in DMSO: H<sub>2</sub>O) and HgCl<sub>2</sub> (in DMSO: H<sub>2</sub>O).....243

**Figure 5.16.** (a) Organogel **G8GE** at different concentration (b) Ratio of interaction of **G8** and **GE** (c) FE-SEM image of **G8GE** (gel of 0.03: 0.03 mmol of **G8** and **GE**) and (d) FE-SEM image of **G8GE** (gel of 0.1: 0.1 mmol of **G8** and **GE**).....244

**Figure 5.17.** FE-SEM images of (a) **M1G8GECl<sub>2</sub>** (b) **M1G8GE(OAc)<sub>2</sub>** (c) **M1G8GESO<sub>4</sub>** (d) **M2G8GECl<sub>2</sub>** (e) Gelatinous solution of **M2G8GE(OAc)<sub>2</sub>** (f) Gelatinous solution of **M2G8GESO<sub>4</sub>** (g) **M3G8GECl<sub>2</sub>** and (h) **M3G8GE(OAc)<sub>2</sub>**.....245

**Figure 5.18.** FE-SEM images of (a) **M1G8GECl<sub>2</sub>Ads** (b) **M1G8GE(OAc)<sub>2</sub>Ads** (c) **M1G8GESO<sub>4</sub>Ads** (d) **M2G8GECl<sub>2</sub>Ads** (e) **M2G8GE(OAc)<sub>2</sub>Ads** (f) **M2G8GESO<sub>4</sub>Ads** (g) **M3G8GECl<sub>2</sub>Ads** and (h) **M3G8GE(OAc)<sub>2</sub>Ads** formed by adsorption method.....245

<b>Figure 5.19.</b> EDX and Mapping analysis of <b>M1G8GEC1<sub>2</sub></b> showing the presence of C, N, O, Hg and Cl inside gel matrix.....	<b>245</b>
<b>Figure 5.20.</b> EDX and Mapping analysis of <b>M1G8GE(OAc)<sub>2</sub></b> showing the presence of C, N, O and Hg inside gel matrix.....	<b>246</b>
<b>Figure 5.21.</b> EDX and Mapping analysis of <b>M1G8GESO<sub>4</sub></b> showing the presence of C, N, O, Hg and S inside gel matrix.....	<b>246</b>
<b>Figure 5.22.</b> EDX and Mapping analysis of <b>M2G8GEC1<sub>2</sub></b> showing the presence of C, N, O, Cd and Cl inside gel matrix.....	<b>246</b>
<b>Figure 5.23.</b> EDX and Mapping analysis of <b>M2G8GE(OAc)<sub>2</sub></b> showing the presence of C, N, O and Cd inside gel matrix.....	<b>247</b>
<b>Figure 5.24.</b> EDX and Mapping analysis of <b>M2G8GESO<sub>4</sub></b> showing the presence of C, N, O, Cd and S inside gel matrix.....	<b>247</b>
<b>Figure 5.25.</b> EDX and Mapping analysis of <b>M3G8GEC1<sub>2</sub></b> showing the presence of C, N, O, Pb and Cl inside gel matrix.....	<b>247</b>
<b>Figure 5.26.</b> EDX and Mapping analysis of <b>M3G8GE(OAc)<sub>2</sub></b> showing the presence of C, N, O and Pb inside gel matrix.....	<b>248</b>
<b>Figure 5.27.</b> Frequency sweep experiment of organogel <b>G8GE</b> at (a) 1:1 molar ratio (0.03: 0.03 mmol) (b) 3: 2 molar ratio (0.03: 0.02 mmol).....	<b>248</b>
<b>Figure 5.28.</b> (a) Angular sweep experiment of metallogel <b>M1G8GEC1<sub>2</sub></b> (b) Frequency sweep experiment of metallogel <b>M1G8GEC1<sub>2</sub></b> .....	<b>249</b>
<b>Figure 5.29.</b> (a) Angular sweep experiment of metallogel <b>M1G8GE(OAc)<sub>2</sub></b> (b) Frequency sweep experiment of metallogel <b>M1G8GE(OAc)<sub>2</sub></b> .....	<b>249</b>
<b>Figure 5.30.</b> (a) Angular sweep experiment of metallogel <b>M1G8GESO<sub>4</sub></b> (b) Frequency sweep experiment of metallogel <b>M1G8GESO<sub>4</sub></b> .....	<b>249</b>

**Figure 5.31.** (a) Angular sweep experiment of metallogel **M2G8GEC<sub>l2</sub>** (b) Frequency sweep experiment of metallogel **M2G8GEC<sub>l2</sub>**.....250

**Figure 5.32.** (a) Angular sweep experiment of metallogel **M3G8GEC<sub>l2</sub>** (b) Frequency sweep experiment of metallogel **M3G8GEC<sub>l2</sub>**.....250

**Figure 5.33.** (a) Angular sweep experiment of metallogel **M3G8GESO<sub>4</sub>** (b) Frequency sweep experiment of metallogel **M3G8GESO<sub>4</sub>**.....250

**Figure 5.34.** (a) Angular sweep experiment of metallogel **M1G8GEC<sub>l2</sub>Ads** (b) Frequency sweep experiment of metallogel **M1G8GEC<sub>l2</sub>Ads**.....252

**Figure 5.35.** (a) Angular sweep experiment of metallogel **M1G8GE(OAc)<sub>2</sub>Ads** (b) Frequency sweep experiment of metallogel **M1G8GE(OAc)<sub>2</sub>Ads**.....252

**Figure 5.36.** (a) Angular sweep experiment of metallogel **M1G8GESO<sub>4</sub>Ads** (b) Frequency sweep experiment of metallogel **M1G8GESO<sub>4</sub>Ads**.....252

**Figure 5.37.** (a) Angular sweep experiment of metallogel **M2G8GEC<sub>l2</sub>Ads** (b) Frequency sweep experiment of metallogel **M2G8GEC<sub>l2</sub>Ads**.....253

**Figure 5.38.** (a) Angular sweep experiment of metallogel **M2G8GE(OAc)<sub>2</sub>Ads** (b) Frequency sweep experiment of metallogel **M2G8GE(OAc)<sub>2</sub>Ads**.....253

**Figure 5.39.** (a) Angular sweep experiment of metallogel **M2G8GESO<sub>4</sub>Ads** (b) Frequency sweep experiment of metallogel **M2G8GESO<sub>4</sub>Ads**.....253

**Figure 5.40.** (a) Angular sweep experiment of metallogel **M3G8GEC<sub>l2</sub>Ads** (b) Frequency sweep experiment of metallogel **M3G8GEC<sub>l2</sub>Ads**.....254

<b>Figure 5.41.</b> (a) Angular sweep experiment of metallogel <b>M3G8GE(OAc)<sub>2</sub>Ads</b> (b) Frequency sweep experiment of metallogel <b>M3G8GE(OAc)<sub>2</sub>Ads</b> .....	<b>254</b>
<b>Figure 5.42.</b> Comparative study of value of storage modulus (G') of all the metallogels formed by mixing and adsorption methods.....	<b>255</b>
<b>Figure 5.43.</b> (a) FTIR data of <b>G8</b> , <b>GE</b> and <b>G8GE</b> xerogel (b) possible structure of gelator components <b>G8GE</b> interaction (c) PXRD data of <b>G8</b> , <b>GE</b> and <b>G8GE</b> xerogel.....	<b>256</b>
<b>Figure 5.44.</b> (a) DFT structure of (a) <b>G8</b> (b) <b>GE</b> and (c) plausible structure of interaction of <b>G8</b> and <b>GE</b> .....	<b>257</b>
<b>Figure 5.45.</b> DFT structure showing (a, b) Planarity and (c, d) Tilted structure of <b>GE</b> , (e, f) Less tilted structure of <b>G8GE</b> .....	<b>258</b>
<b>Figure 5.46.</b> HOMO-LUMO energy orbitals of (a) <b>G8</b> and (b) <b>GE</b> .....	<b>258</b>
<b>Figure 5.47.</b> FTIR data of (a) <b>M1G8GECl<sub>2</sub></b> (b) <b>M1G8GE(OAc)<sub>2</sub></b> (c) <b>M1G8GESO<sub>4</sub></b> (d) <b>M2G8GECl<sub>2</sub></b> (e) precipitate of <b>M2G8GE(OAc)<sub>2</sub></b> (f) precipitate of <b>M2G8GESO<sub>4</sub></b> (g) <b>M3G8GECl<sub>2</sub></b> (h) <b>M3G8GE(OAc)<sub>2</sub></b> .....	<b>259</b>
<b>Figure 5.48.</b> PXRD data of metallogels (a) <b>M1G8GECl<sub>2</sub></b> (b) <b>M1G8GE(OAc)<sub>2</sub></b> (c) <b>M1G8GESO<sub>4</sub></b> (d) <b>M2G8GECl<sub>2</sub></b> (e) precipitate of <b>M2G8GE(OAc)<sub>2</sub></b> (f) precipitate of <b>M2G8GESO<sub>4</sub></b> (g) <b>M3G8GECl<sub>2</sub></b> (h) <b>M3G8GE(OAc)<sub>2</sub></b> .....	<b>260</b>
<b>Figure 5.49.</b> PXRD data of metallogels (a) <b>M1G8GECl<sub>2</sub>Ads</b> (b) <b>M1G8GE(OAc)<sub>2</sub>Ads</b> (c) <b>M2G8GECl<sub>2</sub>Ads</b> (d) <b>M2G8GE(OAc)<sub>2</sub>Ads</b> (e) <b>M2G8GESO<sub>4</sub>Ads</b> (f) <b>M3G8GECl<sub>2</sub>Ads</b> .....	<b>261</b>
<b>Figure 5.50.</b> Systematic representation of removal of heavy metal salts from contaminated water and their ICP-AES analysis.....	<b>263</b>

<b>Figure 5.51.</b> BET analysis data of (a) Xerogel <b>G8GE</b> (b) mercury-treated <b>G8GE</b> ( <b>mtG8GE</b> ) (c) mercury recovered <b>G8GE</b> ( <b>mrG8GE</b> ).....	<b>265</b>
<b>Figure 5.52.</b> XPS survey spectra of (a) xerogel <b>G8GE</b> (b) <b>mtG8GE</b> (c) <b>mrG8GE</b> and (d) XPS spectrum of <b>mtG8GE</b> showing the presence of Hg 4f.....	<b>266</b>
<b>Figure 5.53.</b> XPS analysis of xerogel <b>G8GE</b> showing (a) C1s spectrum (b) N1s spectrum and (c) O1s spectrum.....	<b>267</b>
<b>Figure 5.54.</b> XPS analysis of xerogel <b>mtG8GE</b> showing (a) C1s spectrum (b) N1s spectrum and (c) O1s spectrum.....	<b>267</b>
<b>Figure 5.55.</b> XPS analysis of xerogel <b>mrG8GE</b> showing (a) C1s spectrum (b) N1s spectrum and (c) O1s spectrum and (d) Hg 4f spectrum.....	<b>268</b>
<b>Figure 5.56.</b> FE-SEM images of (a) <b>M1G8GECl<sub>2</sub></b> gel by mixing (b) <b>M1G8GECl<sub>2</sub>Ads</b> by adsorption (c) <b>M1G8GECl<sub>2</sub>Ads</b> when <b>G8GE</b> inserted inside the aqueous solution of HgCl <sub>2</sub> .....	<b>269</b>
<b>Figure 5.57.</b> (a) Reusability of <b>G8GE</b> for water remediation (b) Heavy metal removal at different pH from 3-10.....	<b>270</b>
<b>Figure 5.58.</b> Time oscillation sweep experiment of organogel <b>G8GE</b> at (a) 0.02: 0.02 mmol (b) 0.03: 0.03 mmol and (c) 0.04: 0.04 mmol.....	<b>271</b>
<b>Figure 5.59.</b> Thixotropic behaviour by Time oscillation sweep experiments for metallogels (a) <b>M1G8GECl<sub>2</sub></b> (b) <b>M1G8GE(OAc)<sub>2</sub></b> (c) <b>M1G8GESO<sub>4</sub></b> , and metallogels (d) <b>M1G8GECl<sub>2</sub>Ads</b> (e) <b>M1G8GE(OAc)<sub>2</sub>Ads</b> and (f) <b>M1G8GESO<sub>4</sub>Ads</b> .....	<b>272</b>
<b>Figure 5.60.</b> Time oscillation sweep experiment of metallogel <b>M3G8GECl<sub>2</sub></b> .....	<b>272</b>
<b>Figure 5.61.</b> Time oscillation sweep experiment of metallogel <b>M2G8GECl<sub>2</sub>Ads</b> .....	<b>272</b>

**Figure 5.62.** Time oscillation sweep experiment of metallogel (a) **M2G8GE(OAc)<sub>2</sub>Ads** and (b) **M2G8GESO<sub>4</sub>Ads**.....**273**

**Figure 5.63.** Time oscillation sweep experiment of metallogel (a) **M3G8GECl<sub>2</sub>Ads** and (b) **M3G8GE(OAc)<sub>2</sub>Ads**.....**273**

## **Chapter 6**

**Figure 6.1.** Future prospective of application of BTA, tetrazole and triazine based gels and their properties modification for different fields.....**293**

# LIST OF SCHEMES

## Chapter 1

**Scheme 1.1:** BTA, cyanuric core and carboxylic acid groups containing gelator molecules.....14

**Scheme 1.2:** Possibility of hydrogen bonding interactions of tetrazole groups with other functional groups.....14

**Scheme 1.3:** Tetrazole with nine bonding sites with metal coordination.....15

**Scheme 1.4:** Possible hydrogen bonding interactions of amine with gelator components and solvents molecules.....16

## Chapter 2

**Scheme 2.1.** Systematic scheme for the synthesis of gelator **G7**.....65

**Scheme 2.2.** Synthesis of AgNPs Inside the Gel Matrix.....73

**Scheme 2.3.** Observation of color change on reaction of **M<sup>I</sup>G7** with AgNO<sub>3</sub> (b) Predicted structure arrangement of Fe (III) G7 metallo gel (**M<sup>I</sup>G7**).....74

**Scheme 2.4.** Reduction of nitroaromatics to corresponding amines by nanocomposite catalysts.....81

## Chapter 3

**Scheme 3.1.** Synthesis of gelator **G8**.....123

**Scheme 3.2.** Representation of synthesis of **G8** and organogels formation.....124

## Chapter 4

- Scheme 4.1.** Synthesis of gelator **G8**.....164
- Scheme 4.2.** Synthesis of nanocomposite material **G8PdNPs**.....164
- Scheme 4.3:** 2+3 cycloaddition reaction for synthesis of tetrazole substituent by catalyst **G8PdCl<sub>2</sub>**.....166
- Scheme 4.4.** Suzuki-Miyaura coupling reaction catalyzed by nanocomposite catalyst xerogel **G8PdNPs**.....179
- Scheme 4.5.** Suzuki-Miyaura coupling for synthesis of 1,1'-biphenyl.....185
- Scheme 4.6.** Suzuki-Miyaura coupling for synthesis of 4-methoxy-1,1'-biphenyl.....187
- Scheme 4.7.** Suzuki-Miyaura coupling for synthesis of 4-methyl-1,1'-biphenyl.....189
- Scheme 4.8.** Suzuki-Miyaura coupling for synthesis of 4,4'-dimethoxy-1,1'-biphenyl.....191
- Scheme 4.9.** Suzuki-Miyaura coupling for synthesis of 4-methoxy-4'-methyl-1,1'-biphenyl.....193
- Scheme 4.10.** Suzuki-Miyaura coupling for synthesis of 4-(trifluoromethyl)-1,1'-biphenyl.....195

## Chapter 5

- Scheme 5.1.** Synthesis of gelator enhancer **GE**.....232
- Scheme 5.2.** **G8** and **GE** showing alternative hydrogen bond donor-acceptor sites.....234

## Chapter 6

<b>Scheme 6.1.</b> Possibilities of addition of second component with <b>G7</b> and <b>G8</b> gelator components to increase the hydrogen bonding interactions.....	<b>292</b>
---	------------



# LIST OF TABLES

## Chapter 2

**Table 2.1.** Gelator: 2.0 % (w/v) [CGCs = 20 mM in DMSO (or DMF) (1mL) / H<sub>2</sub>O (1mL) Mixture]; **G**: Gel; **S**: Soluble; **I**: Insoluble.....**68**

**Table 2.2.** Optimization Table for gelation.....**68**

**Table 2.3.** BET surface area, TOPO and average pore diameter analysis of (a) powder **G7**, (b) Organogel **G7** and (c) Fe (III) metallogel **M<sup>1</sup>G7**.....**72**

**Table 2.4.** Optimization of reduction reaction by GCMS data.....**86**

**Table 2.5.** Recyclability of the nanocomposite catalyst **M<sup>1</sup>G7AgNPs**.....**87**

## Chapter 3

**Table 3.1.** Solubility of **G8** with different organic solvents. **I**: Insoluble, **S**: Soluble, **G**: Gelation.....**120**

**Table 3.2.** Optimization table of gelation condition of **G8**.....**120**

**Table 3.3.** <sup>1</sup>H NMR data of downward shifting of protons of 2-AP, 3-AP and 4-AP during interactions with gelator molecule **G8**.....**132**

**Table 3.4.** Bond lengths and bond angles of structure of planer **G8** molecule from DFT Data.....**137**

**Table 3.5.** Comparative wavenumber range to show the participation of amine and tetrazolic ring for gelation.....**147**

## Chapter 4

**Table 4.1.** CGC experiment for formation of **G8PdCl<sub>2</sub>** nanostructured metallogel.....**179**

**Table 4.2.** CGC experiment for formation of **G8PdNPs** nanostructured metallogel.....197

**Table 4.3.** Activity of different reported catalyst and synthesized catalyst **G8PdCl<sub>2</sub>** for tetrazole formation.....199

**Table 4.4.** Activity of different reported gel catalyst and synthesized catalyst **G8PdNPs** for Suzuki-Miyaura coupling reaction.....199

## **Chapter 5**

**Table 5.1.** Concentration dependent rheological study of organogel **G8GE**.....237

**Table 5.2.** Storage modulus and loss modulus of metallogels formed by mixing method.....251

**Table 5.3.** Storage modulus and loss modulus of metallogels formed by adsorption method.....254

**Table 5.4.** Intermolecular H-bond binding energies of individual sites along with the associated bond lengths of structure **G8GE**.....258

**Table 5.5.** Optimization of heavy metal removal reaction by xerogel of organogel **G8GE**, analysed by ICP-AES.....262

**Table 5.6.** ICP-AES analysis of study of adsorption property of organogel **G8GE**.....263

**Table 5.7.** Adsorption capacity of various gel-based adsorbent.....263

**Table 5.8.** XPS peaks position of various groups for **G8GE**, **mtG8GE** and recovered **mrG8GE**.....268

**Table 5.9.** Recyclability of xerogel **G8GE** for heavy metal separation.....270

**Table 5.10.** Water remediation at different pH by xerogel **G8GE**.....270



**Chapter 1**  
**General Introduction and Background**



## **Chapter 1**

### **General Introduction and Background**

#### **1.1 Introduction**

The interplay of different chemical and physical forces between molecules can present a semi-solid state with mechanical strength, widely known as a gel. As per the IUPAC, the gel is defined as a nonfluid colloidal network or polymer network that is expanded throughout its whole volume by a fluid.<sup>[1,2]</sup> Since the middle of 19th century, the new state of matter arises i.e., gel which contains the properties of both solid and liquid and shows viscoelastic nature of materials. In 1861, Thomas Graham firstly provides a loose material definition for gel. After sixty-five years of this incident, Dr. Dorothy Jordan Lloyd defined “the colloid condition is gel which is easier to recognize than to define” (Jordan Lloyd, 1926). This definition recognized that all gels must be comprised of at least two components, a liquid and a gelling substance (i.e., a solid). Later it is confirmed that not all colloids are gels and not all gels are colloids. Therefore, from previous studies, a gel must contain two features: (1) it has a continuous microscopic structure with macroscopic dimensions (2) it is solid-like in its rheological behavior, despite being comprised mostly of liquid (Weiss & Terech, 2006). Thomas Graham first prepared silicic acid gels in organic liquid with a very small amount of water.<sup>[3]</sup> In 1921, B.S. Neuhausen and W. A. Patrik worked on organogel and prepared silicic acid gel with solvent exchange phenomenon from organic solvent to water and vice versa.<sup>[4]</sup> After this, the work on organogels and their applications started to increase. The insertion of metal makes the field of organogels more attractive and introduces a new area of gel, i.e., metallo gel. The work on metallo gel was started in 2002 when Bengang Xing and their team reported a coordination polymer-based stable organogel with metal-ligand bonding. This gel was known as metallo gel.<sup>[5]</sup> After that, the research on organogels and metallo gels achieved notable impetus and advancement

in various applicable fields. Over the next thirty years, properties, modifications, and applications of organogels and metallogels continuously evolved and generated more interest, particularly in recent times. The supramolecular interactions, viz. hydrogen bond formation, Van der Waals forces,  $\pi$ - $\pi$  stacking, electrostatic and dipole-dipole interactions, ligand-metal coordination, etc., contribute significantly to forming the three-dimensional (3D) networks with solvent molecules entrapped inside. The dynamic noncovalent interactions impart stimuli-responsive characteristics in the supramolecular gels.<sup>[6-9]</sup> The gel-to-sol transformation and associated properties can be modulated and regulated reversibly as the response to external stimuli like temperature, pH, chemicals, light, magnetic and electric field, sound, mechanical force, enzymes, etc.<sup>[10, 11]</sup> Interestingly these soft materials made out of organic polymers or low-molecular-weight gelators (LMWGs) can show extensive applications in fields like sensors, actuators, 3D printing, water remediation, adhesive, electronics, medical implants, drug delivery, tissue engineering, self-healing materials, conductivity etc.<sup>[12-23]</sup> The incorporation of metal ions in such systems can lead to the formation of metallogels arising from discrete coordination complexes, coordination polymers, and cross-linked coordination polymers. The structures and functionalities of such metallogels can vary widely.<sup>[24]</sup> Understanding such self-assembled structures and relating them with their properties manifested in different forms is a great challenge that might lead us to develop more innovative materials with extensive practical uses. Herein, it is important to note that the introduction of metal ions extends the potential application of gels into the field of catalysis,<sup>[25-31]</sup> magnetism,<sup>[32, 33]</sup> stabilization of nanoparticles,<sup>[34-38]</sup> optoelectronics,<sup>[39-41]</sup> semiconducting materials,<sup>[42-45]</sup> smart detector<sup>[46-48]</sup> etc.

Gel materials contain the properties of both solid and liquid and show the viscoelastic nature of materials. The basic unit of gel is gelator molecules. Sometimes there may be more than one type of molecule

considered as gelator components. The heterogeneous gel system contains two parts, i.e., an immobile gelator network and a mobile solvent phase. Gels can be envisaged as rigid liquids, and this rigidity comes from the gel matrix formed by the interlinking of gelator molecules by various types of non-covalent interactions. The difference in the mode of interactions and interlinking within the gel network decides the structure and morphology of gels. In daily life, gels can be seen everywhere, like cosmetic creams, toothpaste, facewash, jam-jelly, etc. (Figure 1.1) The gels contain viscous-elastic behavior, which comes from the liquid and solid parts of the gel, respectively. The viscoelastic behavior of gel can be defined by rheological parameters, i.e., storage modulus ( $G'$ ) and loss modulus ( $G''$ ). The values of  $G'$  of different gels can lead to their classifications as strong and weak gels. Some gels are more viscous than their elastic nature, while some are more elastic than their viscosity. Based on rheology, gels are soft materials where the value of  $G'$  is always greater than that of  $G''$ , and both are parallel to each other with increasing range of angular frequency ( $\text{rad s}^{-1}$ ).



**Figure 1.1** Common gels found in daily life.

Therefore, gels without metal i.e., organogel or hydrogel also shows the wide range of applications in sensing, drug delivery, medicinal therapy etc., while the incorporation of metal ions inside gel matrix promote the soft materials towards another advanced field viz. catalysis,

optoelectronic, magnetism, drug delivery, nanoparticles synthesis, stabilization, and environmental remediation.<sup>[49]</sup> The incorporation of metal ions within the gel matrix increases its applicability in different fields. Nowadays, researchers are trying to incorporate metal nanoparticles inside gel matrix to form nanometallogels or to synthesize a nanostructured metallogel. These modifications or developments in the field of gels open broad areas of applications and get them utilized as advanced functional materials (Figure 1.2).<sup>[50]</sup>

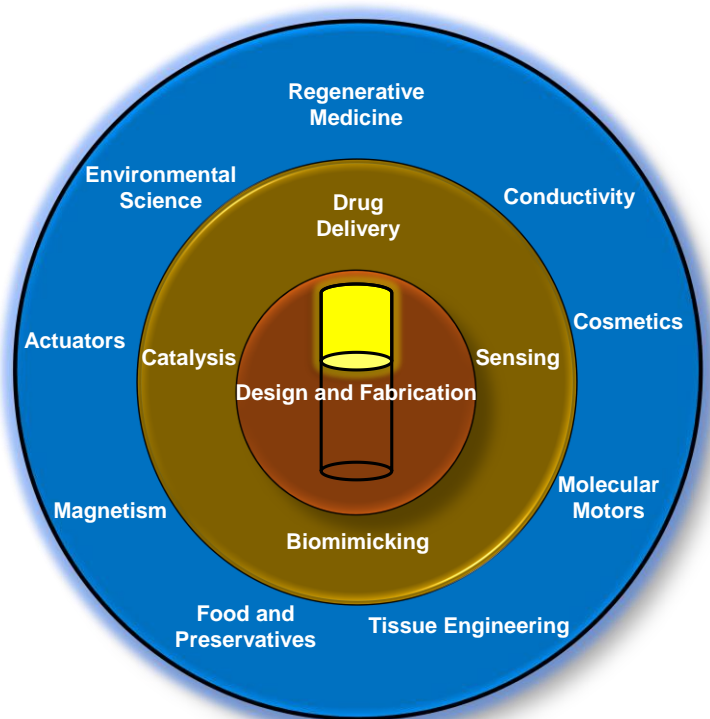


**Figure 1.2** Various application areas of gel (brown circle contains initial applications and blue circle contains increasing area of applications with modifications in properties of gel).

### 1.1.1 Types of gels based on different parameters

There are different types of gel based on various aspects (Figure 1.3). Based on the fabrication of different kinds of gels, they are classified in terms of the sources of the gels, characteristics, presence, and absence of metal ions as well as solvent mediums. Gels can be made from natural or artificial (synthetic) sources. Artificial gels are two kinds,

supramolecular gels, and macromolecular gels. Supramolecular gels get formed by non-covalent interactions; therefore, these are always physical gels. In contrast, macromolecular gels are cross-linked to develop physical and chemical gels. The chemical macromolecular gels are formed when high molecular weight gelators/ polymers are cross-linked by covalent bonds, which cannot form sols from gels. At the same time, when low molecular weight gelators/ polymers are cross-linked with each other by non-covalent interactions, the gel is said to be a physical macromolecular gel, and these gels can show reversibility with gel-sol-gel transition. The characteristics of gels make them segregated into two segments, viz. elastic and nonelastic gels which are based on the reversibility of gel after heating it. Depending upon the presence and absence of metal, gels are metallo gels with the presence of metal ions, and in the absence of it, the gels are considered hydrogel/ organogel. Metallo gels can be further divided into two types. When metal is part of a gelator molecule and gives a self-assembled matrix with entrapment of solvent molecules, in that case, the fabricated gel is said to be a discrete metal complex gel. Here the metal ion does not take part directly in forming the gel network. On the other hand, if the metal and gelator molecule both participate in the fabrication of a gel matrix with solvent molecules, then the resultant metallo gel is said to be coordination polymer gel or coordination metallo gel.<sup>[46]</sup> Further, based on the solvent medium, there are four types of gels, i.e., hydrogel, organogel, xerogel and aerogel.<sup>[51, 52]</sup>

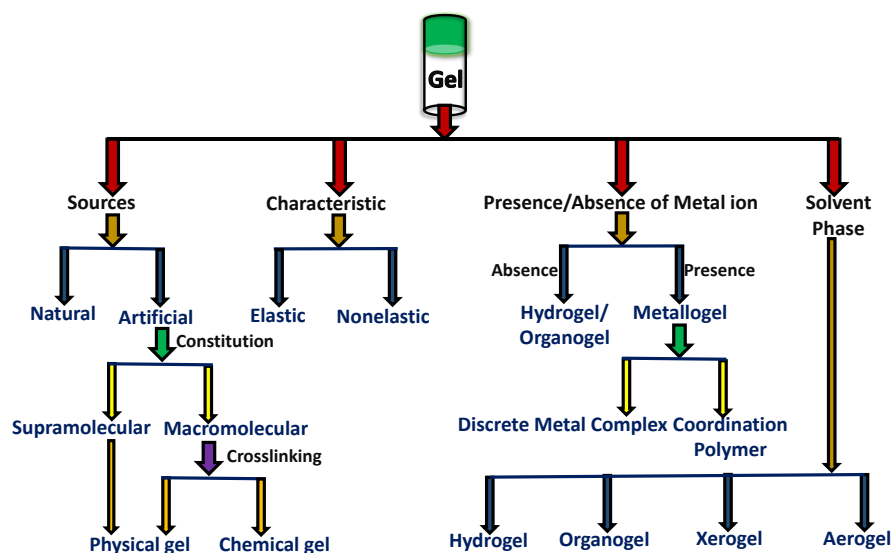


**Figure 1.3** Classification of gels.

### 1.1.2 General characterization methods and basic properties of gels

The preliminary confirmation of gel formation is considered as the test tube inversion method, where the glass vial containing gel has been inverted and tested if the synthesized material sticks to the base of the vial even under gravity. After the initial confirmation, the experimental analysis is carried out in a rheometer to confirm the gel formation by the storage and loss modulus values. The two rheological experiments which are widely used in this connection are angular sweep and frequency sweep experiments. In the angular sweep experiment, the crossover point, and non-deformation range can be examined. Based on the non-deformation range values, the frequency sweep experiment is taken up to obtain the  $G'$  and  $G''$  values. For gel material, the value of  $G'$  is always greater and parallel than  $G''$  with respect to each other throughout the increasing range of angular frequency in  $\text{rad s}^{-1}$ .<sup>[53]</sup> Although there are no direct methods to understand the mechanism of gel formation but various spectroscopic tools like NMR, IR, SEM, and TEM can be used to define its possible mode of assemblies. The self-assembly of gelator molecules is the foremost important factor behind gel formation, and it can be examined extensively by monitoring the shifting of NMR peaks, IR bands, and changes in the SEM and TEM

morphology depicting the 3D changes during aggregation or self-assembly. Other than this, the PXRD analysis also defines the presence of non-covalent bonds within the gel matrix. It indicates if  $\pi$ - $\pi$  stacking, hydrogen bonding, intermolecular stacking, etc., persist inside the gel system. Similarly, the aggregation of gelator molecules or components can also be explored by the UV-Vis and fluorescence experiments which further indicate the nature of the assembly by revealing the changes in wavelength, optical density, and fluorescence intensity (Figure 1.4).<sup>[54]</sup>

55]

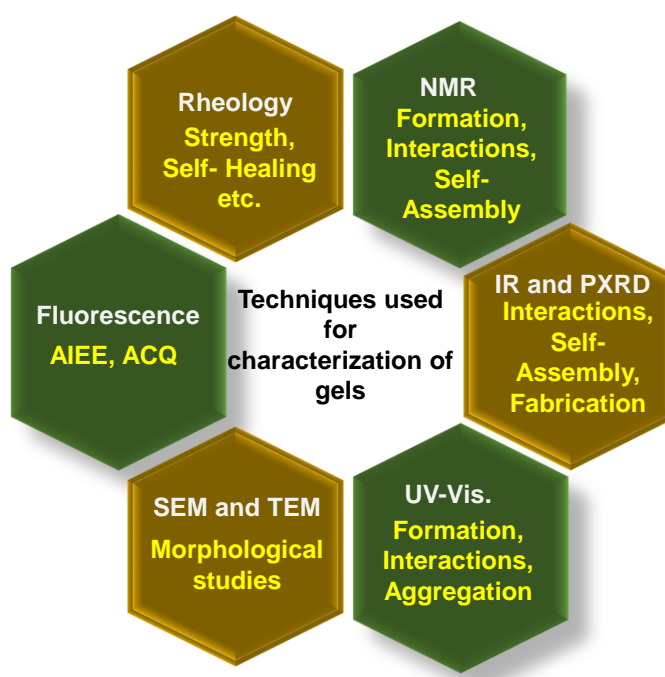


**Figure 1.4** Technology used for the characterization of gels.

The basic properties of gels depend upon the fabrication methods, used gelator components, time, and gel formation temperature, etc. (Figure 1.5). If the components of gel contain groups that can show intramolecular rotation (IR) or intramolecular vibration (IV), then before self-assembly or aggregation, the molecule often remains in a non-fluorescent state. Upon gel formation, the possibilities of IR and IV get decreased and which makes the assembly often fluorescent by aggregation. This property is known as aggregation-induced enhanced emission (AIEE). While some molecules show fluorescence in diluted

systems, the fluorescence gets quenched after aggregation. This type of property is called aggregation-caused quenching (ACQ).<sup>[56-58]</sup> The other main property of gels is their strength which gets measured by rheological experiments. Some gels are fragile, some are moderate in strength, and some gels show very high strength. The strength of the gels can be modified by changing the different factors in gel formation. One crucial property of gels is the self-healing property. Most of the gels show self-healing property. It might be based on the parameters like stability or value of  $G'$  of gel which can be measured by time oscillation sweep experiment under rheological analysis. Other than these mentioned properties, there are many others related to the stimuli-responsiveness of the gels with respect to the changes in temperature, pressure, pH, exposure to light, etc., which is very important to make gels suitable for various advanced applications and technologies.<sup>[59, 60]</sup>

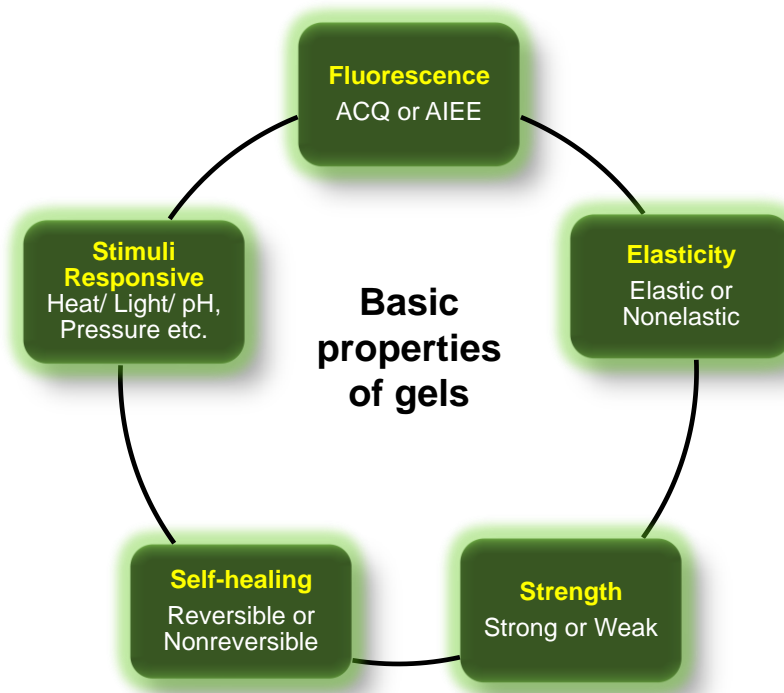


*Figure 1.5 Basic properties of gels.*

## 1.2 Design and synthesis of low molecular weight gelator molecules

Designing a gelator molecule is challenging as it is impossible to accurately predict whether a molecule can form a gel. However, based on previous research and literature reports, it is possible to envisage specific molecular structures with a better chance of forming gels. Incorporation of a few organic functional groups, *viz.* carboxylic acid, carboxamide, amine, alcohol, pyridine, tetrazole, imidazole, nitrile, and aromatics ring, etc., which can provide the sites for extensive non-covalent interactions, enhance the suitability for a molecule to gel formation.<sup>[61-64]</sup> Some molecules require suitable solvent(s) for the fabrication of gels, and that requires extensive searching for the right combinations with the right amount of gelator concentration. Among the synthetic gelator molecules, the self-assembly of low-molecular weight gelators (LMWGs) in a proper solvent to form 3D networks generates lots of interest due to the versatility in the morphology obtained and their response towards various kinds of stimuli and associated properties. Therefore, LMWGs with a molecular weight below then 3000 Da, are extensively researched as they are easy to synthesize, can be modulated with the addition of a number of functional sites, and provide suitable sites for non-covalent interactions, which makes gels reversible and thixotropic in nature. Moreover, the function of these supramolecular gels can be controlled or improved with the introduction of the fine-tuning of the structure. This modification can be further reinforced with additional gelator components, such as the incorporation of metal ions or the addition of a second component or polymer, etc.

In this thesis, specific gelator molecules have been designed and synthesized, taking cues from the previous reports. The designed molecules contain functional groups like amide, amine, tetrazole, carboxylic acid, etc., along with strategically incorporated cyanuric and benzene rings. Deliberate incorporation of such moieties provides ample opportunity for the synthesized molecules to engage in hydrogen

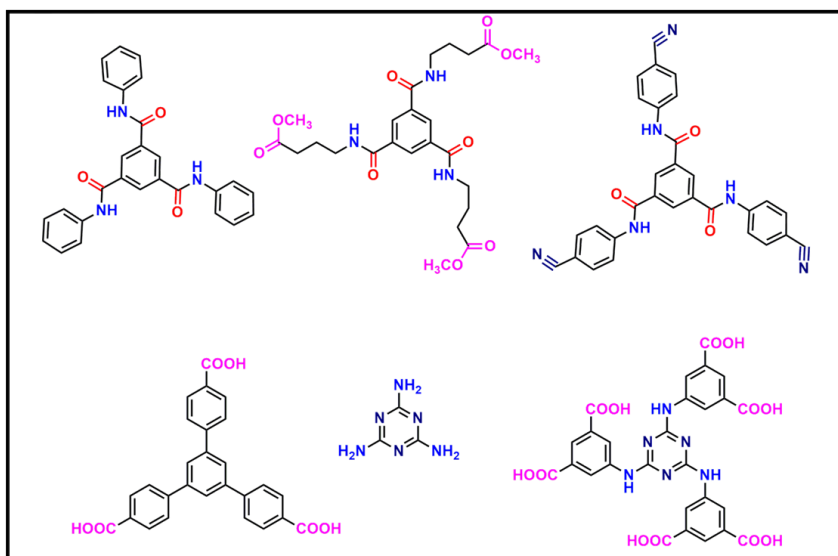
bonding,  $\pi$ - $\pi$  stacking, hydrophobic interactions, and intercolumnar stacking, which are some effective chemical tools for gel fabrication.<sup>[65, 66]</sup> Although gel formation with a tripodal aromatic gelator system has been reported previously, there are only a few reports where the method of gel fabrication is extensively studied to modulate the strength of the gels. Some examples of organogels and metallogels related to tripodal amine moieties and tetrazole are listed below.

- Metallogel formation has been reported with derivatives of nonsteroidal anti-inflammatory drugs (ibuprofen, sulindac, and flurbiprofen) with carboxamide groups. Here, the drug acted as a low molecular weight gelator and formed thirteen metallogels (**MG1-MG13**), out of which **MG9** displayed anticancer response for breast cancer cells.<sup>[67]</sup>
- Two tripodal gelator molecules (TG-1 and TG-2), which contained tripodal amide and pyridine functional groups, formed a coordination polymer metallogel with  $\text{Fe}^{3+}$ . This metallogel shows selective adsorption property for methylene blue (MB) dye with 96 % of adsorption.<sup>[68]</sup>
- One interesting tripodal gelator molecule,  $\text{H}_6\text{L}$ , has been synthesized with the cyanuric ring as a core and secondary amine as a linker, linking the benzene ring as a tripodal branched containing two carboxylic acid groups with each ring. This gelator molecule formed metallogel ( $\text{H}_6\text{L}/\text{Tb}$ ) with stable luminescence. Here, the concept of the heal-set approach was introduced. Hydrogen bonding,  $\pi$ - $\pi$  stacking, and metal-ligand interactions were crucial in forming metallogel.<sup>[69]</sup>
- A tetrazole-based gelator molecule TTB was reported, which shows the metallogel formation with various salts of  $\text{Co}^{2+}$ . This coordination polymer gel  $[(\text{TTB})_2\text{CoBr}_2(\text{MeOH})(\text{DMF})]_n$  exhibit a fluorescence nature, and it was selectively recognized toxic gases of chloride atom such as  $\text{SOCl}_2$ ,  $(\text{COCl})_2$  and  $\text{COCl}_2$ .<sup>[70]</sup> A coordination polymer metallogel of  $\text{Mg}^{2+}$  with pyridine

derivative of tetrazole moieties as end groups has been reported. It has shown remarkable fluorescence enhancement after metallogel formation.<sup>[71]</sup>

### 1.2.1 Benzene and triazine ring based tripodal amide and amine

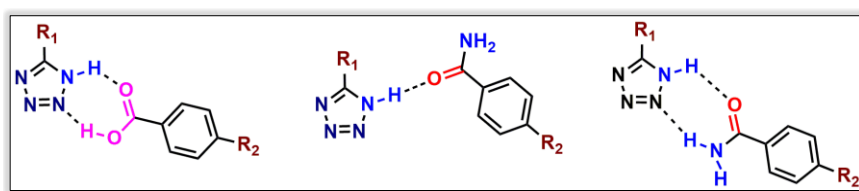
One of the main driving forces behind the fabrication of LMW gels is  $\pi$ - $\pi$  stacking, as it can play a crucial role in the self-assembly of gelator molecules and is also responsible for the strength of gels, albeit partially. Aromatic benzene rings provide the perfect environment for  $\pi$ - $\pi$  stacking between participating molecules; for example, 1,3,5-benzenetricarboxamide (BTA) tends to show gelation properties due to its ability to participate in  $\pi$ - $\pi$  stacking for supramolecular columnar aggregation.<sup>[72, 73]</sup> Other than  $\pi$ - $\pi$  stacking BTA and BTA derivatives provide functional sites for hydrogen bonding and intercolumnar stacking. Notably, several BTA-based gels in combinations of different solvents like polar, nonpolar, protic, and aprotic solvents are reported.<sup>[74-77]</sup> Triazine ring with a similar kind of hexagonal structure is another interesting scaffold to provide a suitable environment for self-assembly by non-covalent and covalent interactions.<sup>[78-80]</sup> Although there are few reports on gels based on a triazine core ring, it shows tremendous potential to explore further with different derivatives for prospective fabrications of organo- and metallogels.<sup>[81-84]</sup> Furthermore, the presence of carboxamide and amine groups increases the possibility of gel formation by several folds (Scheme 1.1).



**Scheme 1.1:** Gelator molecules containing BTA, cyanuric core and carboxylic acid groups.<sup>[74-84]</sup>

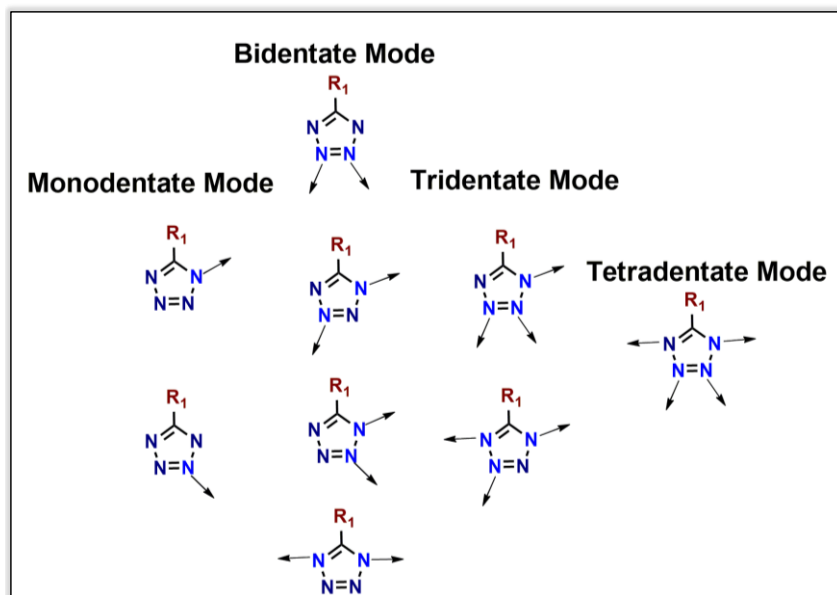
### 1.2.2 Tetrazole

Other than BTA derivatives, nitrogen-rich azole molecules like tetrazole, a five-membered ring containing four nitrogen and one carbon atom in the ring with one hydrogen atom attached to the nitrogen. Therefore, tetrazole itself and sometimes in the presence of other gelator molecules can form strong gels with an increased possibility of hydrogen bond formation (Scheme 1.2).<sup>[85, 86]</sup> Tetrazole shows great improvement and additional properties when introduced with organogel and metallogeles. The multi-binding sites of the tetrazole ring make it suitable linker for forming cross-linking networks,<sup>[87, 88]</sup> which is a critical step in 3D network gel fabrication.<sup>[89]</sup>



**Scheme 1.2:** Possibility of hydrogen bonding interactions of tetrazole groups with other functional groups.

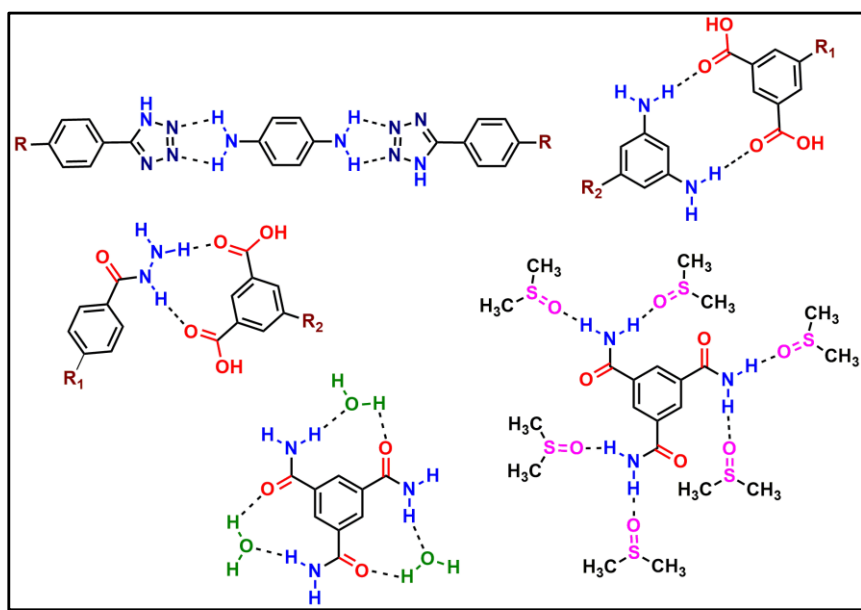
Due to the presence of five nitrogen in tetrazole ring, it shows multi-dentate nature (Scheme 1.3). Therefore, nine possible binding mode can be seen during coordination with metal ion to form metal complexes or during metallogel fabrication.<sup>[90]</sup>



**Scheme 1.3:** Tetrazole with nine bonding sites with metal coordination.  
[90]

### 1.2.3 Aromatic primary and secondary amine

Amines are also known as functional groups for prospective gel formation. Primary, secondary, and tertiary amines provide sites for hydrogen bond formation (Scheme 1.4). Amines are present naturally in various proteins and amino acids. These amino acids also form a gel by self-assembling amino acid groups.<sup>[91-93]</sup> Due to aggregation, the melamine-azobenzene conjugate, which has both primary and secondary amine, shows gelation. The effective force of attraction for gel formation was hydrogen bonding interaction.<sup>[94-96]</sup> Similarly, 3,5-diamino-1,2,4-triazole (DAT), a LMW ligand formed metallogel with  $\text{Co}^{2+}$ . This Co-Gel shows self-healing ability, which arises due to the presence of extensive hydrogen bonding between amine groups and entrapped solvent.<sup>[97]</sup>



*Scheme 1.4: Possible hydrogen bonding interactions of amine with gelator components and solvents molecules.*

### **1.3 Gels formation by tripodal aromatic amide, amine and tetrazole based moieties**

Although several organogels and metallogels have been fabricated and applied in various fields, some notable moieties are discussed here, which show gel formation with different compositions and properties. Nitrile-substituted 1,3,5-tricarboxamide gelator **G4** formed organogel in DMSO: H<sub>2</sub>O mixture. This LMW gelator also formed metallogels with various transition metal ions, out of which Co(II)G4 shows effective sensing for L-tryptophan.<sup>[77]</sup> Other tripodal gelator molecule tris (4-(3-pyridylazo)phenyl)benzene- 1,3,5-tricarboxylate (trans-D) formed multi stimuli responsive organogel which shows the response for heat, light, mechanical shearing, and chemicals.<sup>[74]</sup> The most studied moiety for gel formation is 1,3,5-benzene tricarboxylic acid (BTC) which can form vanadium-based metallogel V gel, in the presence of adenine (Ade) and BTC with vanadium ion. This was applied to detecting counterfeit with a 6% (v/v) methanol composition.<sup>[98]</sup> BTC also formed metallogel with Cu(OAc)<sub>2</sub>.H<sub>2</sub>O in DMF. This metallogel showed semiconducting properties and was fabricated into an electronic

device.<sup>[99]</sup> Other than BTC, triazine-based LMW gelator 5,5',5''-(1,3,5-triazine-2,4,6-triyl) tris (azanediyl) triisophthalate (**H<sub>6</sub>L**) has been synthesized, which formed a heat-set lanthanide-based metallogel with Tb<sup>3+</sup>. This metallogel shows luminescence-stable approach excellent thermal stabilities and good mechanical properties, promising for sensing and security-material applications.<sup>[69]</sup> An aggregation-induced emission (AIE) hydrogel (**PDG**) was fabricated from p-hydroxybenzoic acid-functionalized pillar [5] arene (SPA) and tri-(pyridine-4-yl) functionalized trimesic amide (DTB) in DMSO: H<sub>2</sub>O solvent mixture via non-covalent interactions.<sup>[100]</sup> Other than tripodal gelator molecules, some small molecules with carboxylic acid, carboxamide, and pyridine groups act as gelator molecules, which show gel formation with various applications. For example, 4-biphenylcarboxy capped diphenylalanine formed metallogel with FeCl<sub>3</sub>.<sup>[101]</sup> tetracarboxyl ligand N<sup>1</sup>, N<sup>4</sup> (diterphthalic acid) terephthalamide formed metallogel with chromium (III) which was applicable for specific sorption of dyes.<sup>[102]</sup> 2,3-butanedione bisisonicotinichydrazone (H<sub>2</sub>L) formed metallogel [CPM-Cd] with Cd(OAc)<sub>2</sub>.2H<sub>2</sub>O in DMSO: MeOH mixture and used for dye adsorption.<sup>[103]</sup> FmocFF act as LMW gelator and formed metallogels with different helicity with Zn<sup>2+</sup>, Cu<sup>2+</sup>, Fe<sup>3+</sup>, Al<sup>3+</sup> and showed transformation of self-assembled structures.<sup>[104]</sup> 3, 5-bis ((4-(cyanomethyl) phenyl) carbamoyl) benzoic acid (**G5**) formed organogel and metallogel with ruthenium dimer and showed self-delivery of ruthenium-based anti-cancer drug.<sup>[105]</sup>

Similarly, urea functionalized pyridyl dicarboxylate gelator (PUIA) formed metallogel with transition metal salts, showing anti-inflammatory, anti-cancer, and drug deliverable properties.<sup>[106]</sup> Primary and secondary amines are also notable sites for gel formation as tripeptide-based PA (P1) fabricated metallogel with AgNO<sub>3</sub> shows the formation of silver nanoparticles and silver nanocluster with the different conditions.<sup>[38]</sup> With the series of LMW gelators, 2-phenyl-2-((pyridin-4-ylmethyl) amino) propanoic acid (2-PF), its positional

isomers 3-PF, 4-PF, and BF (BF lacks a pyridine N atom compared with the PF molecule) used for gel formation. The metallo gel (4-PF-Cu-Ag) formation occurred selectively with 4-PF, Cu, and Ag gel components.<sup>[107]</sup> Tetrazoles contain a number of binding sites. Therefore, many metal coordination complexes are reported with tetrazole-based ligand.<sup>[108, 109]</sup> Due to the availability of multi-binding sites, tetrazoles are also played a significant role in gel fabrication by the formation of non-covalent interaction between them and other gelator components. For example, 1,2,4,5-tetra(2H-tetrazole-5 yl)-benzene (TTB) formed metallo gel with  $\text{Co}^{2+}$  salts in an organic solvent which shows sensing of volatile gases containing chloride.<sup>[70]</sup> In another example, di (1H-tetrazole- 5 yl) methane ( $\text{H}_2\text{G6}$ ) formed metallo gels with different lanthanoids and shows applicability towards dye removal and confidential writing.<sup>[110]</sup> The role of the tetrazole-based ligand as gelator molecules is getting continuously explored and investigated.<sup>[111-116]</sup>

## **1.4 Different Methods of fabrication of various organogels and metallo gels**

The main important factors for gel formation are gel components (gelator molecules), suitable solvent combinations, and required conditions like heat, pH, temperature, sonication, stirring, etc. Firstly, the gelator molecules should contain appropriate functional sites to participate in various non-covalent interactions.<sup>[117]</sup> The second most crucial factor is the choice of solvents. Sometimes gel formation occurs with a single solvent system, while the mixture of solvents works better in other systems. The information regarding gel assembly is directly related to the relationship between solvent-gelator interactions. There are three steps during the formation of gel assembly, i.e., solvation power of solvent, intergelator hydrophobic interactions, and intergelator hydrogen-bonding interactions. Solvation power and hydrophobic interactions are critical and compete with hydrogen bonding interactions.<sup>[118, 119]</sup> Apart from gelator molecules and suitable solvent

combinations, other factors influence gel formation in different ways in different systems. For example, some gels are formed by heating/cooling, some by sonication/undisturbed conditions, some at acidic/basic or neutral conditions, and so on. Therefore, there is no optimized or single standard procedure for gel formation. It must be searched for each gel. In general, organogels/hydrogels are formed by the addition of a fixed amount of water into the solution of gelator molecules in the organic solvent, mostly in DMSO or DMF.<sup>[120-123]</sup> After mixing, some gels form spontaneously, but some form after the system is left undisturbed. The formation of metal-containing gels is getting extensively studied in the last couple of decades. The fabrication of metallogels is mostly achieved by the following four methods.

- Self-supported method: Here, the metal salt is added into the solution of the gelator molecule, which is mostly in an organic solvent, forming metallogel.
- Organometallic metallogel: Here, metal and gelator molecules are dissolved in the same solvent and left undisturbed till gel formation.
- Adsorption method: First, organogel or hydrogel is formed, then a solution of the metal salt is layered on the gel bed. After some time, the metal ions get inserted into the organogel and form a stable metallogel.

Mixing method: Here, the gelator molecules and the metal salt are dissolved in a suitable solvent separately. Then the solutions are mixed metallogel formation occurs spontaneously with time, mostly in an undisturbed condition.

## **1.5 Importance of LMW soft organo-metallogels and their applications**

Gels, which are soft materials with flexibility in the structure that external and internal factors can easily modulate, provide a unique opportunity to develop smart materials applicable in a wide range of areas. The LMW gels with more flexibility, easy synthesis, stimuli

response behaviour, reversibility in structure, and self-healable nature have attracted attention recently. It is also pertinent to mention that gels tend to show phenomena like AIEE and ACQ, which can be utilized as probable tools for detection and sensing. Some recent advances in the application of gel materials are discussed below.

### **1.5.1 Soft materials as sensor: sensing ability of gels for cation, anion, biomolecules, and different pollutant**

Supramolecular LMW gels have shown their tremendous impact on sensing anions, cations, biomolecules, and different pollutants. This sensitivity comes due to the reversibility and stimuli-responsive properties of LMW gels as a response to the introduction of external materials.<sup>[124]</sup> Availability of  $\pi$ -electron rich and hydrogen bonding sites environment in the materials make it suitable for sensing for various ions and molecules due to the formation of non-covalent interaction between interactive molecules.<sup>[125]</sup> The LMWGs are engaged in non-covalent interactions between different components, which can get affected in the presence of external molecules. There are reports where gels are employed to detect cyanide,<sup>[126-128]</sup> chiral molecules,<sup>[129]</sup>  $\text{Pb}^{2+}$ ,<sup>[130]</sup> hazardous gas,<sup>[131]</sup> etc. Most often, the sensor property of LMWGs manifest in its spectral changes, gel formation and collapsing, and other visual effects. Some BTC-based organogels and metallogels show sensing for harmful solvents, anions, cations, heavy metals, biological molecules, environmental sensing etc.<sup>[132-135]</sup> Other than BTC-based gelator molecules, other LMWGs show advanced sensing for cyanide, harmful cations, anions, water impurities, etc.<sup>[136, 137]</sup>

A fast and easy way of employing gel materials is to change their colour by introducing the molecules/ions to be sensed. The incoming molecule can disrupt the gel assembly by the formation/disruption of covalent and non-covalent interactions inducing the colour change in the gel system. There are some notable reports related to sensing due to color change. Two rationally designed anion-responsive-organogels OGL1 and OGL2 have been synthesized which shows sensing for  $\text{F}^-$  via reversible color

change.<sup>[138]</sup> Another smart hydrogels of poly(acrylamide-co-dopamine acrylamide) has been reported with a catechol-Fe(III) complex. Due to this metal-ligand coordination, it can dynamically switch between uncoordinated and mono-, bis-, and tris-coordinated states to harvest light energy from the visible spectrum. The products are yellow, green, blue, and red, covering the three primary colors of light.<sup>[139]</sup> In another example, a thermo-responsive colour-changing hydrogel of poly(N-isopropylacrylamide) (PNIPAAm) cross-linked by polydiacetylene (PDA) for visualization and quantification of the power of irradiated microwave has been developed.<sup>[140]</sup> Some LMW gels are used for the detection of isomers of various organic substances.<sup>[141-143]</sup> Other than the color change, there are many reports based on the sensing of cations/anions or molecules by fluorometric studies. In this case, the sensitivity of organogels and metallo gels depends upon the fluorescence property, which might get turned on or turned off by adding a second component (cation/ anion or molecule). Sometimes, an organogel does not have fluorescence, but after the addition of a metal ion, its fluorescence gets turned on, which can further get turned off by the addition of another selective anion. This sensing strategy is known as turn on-turn off sensing of cationic and anionic species.<sup>[144-147]</sup> Metallogel also act as a sensor for various other chemical substances as ammonia, picric acid, hydrogen sulphide and amine derivatives which has been analysed by various spectroscopic tools (Figure 1.6).<sup>[148-151]</sup>

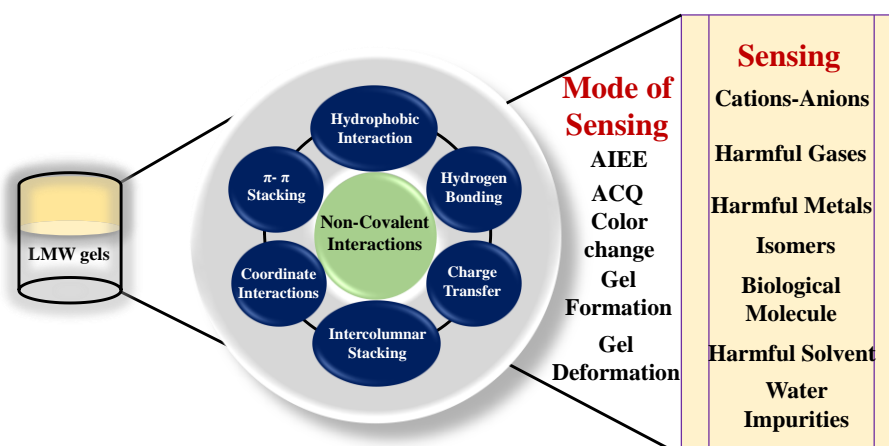


**Figure 1.6** Factor behind sensing properties of LMW gels.

The rheological analysis of gels provides information about the strength of the gels revealing the quantified data for strain, deformation range, frequency, storage modulus, loss modulus, and thixotropic behaviour of gel materials. It is also noted that the position of a functional group, i.e., isomers of gelator molecules, can have a notable effect on the strength and thixotropy of gel.<sup>[123]</sup> However, there is not much study is reported regarding the sensing of isomers and other chemical substances by rheological methods.

## 1.5.2 Self-healing materials: thixotropic nature of gels

Self-healing is the property of materials to repair themselves after any physical damage from the outer or inner environment (Figure 1.7).<sup>[152-157]</sup> Self-healing property has been found in various types of materials like linear polymers, metal-ion polymer, multicomponent system, and gel materials.<sup>[158-162]</sup> The mode of self-healing is different for different materials.<sup>[163-165]</sup> Broadly there are two types of classification, i.e., based on the nature of self-healing and the mechanism of self-healing.

Based on the nature of self-healing, it is of two types: (1) Extrinsic self-healing material where some external component enhances the self-healing. (2) Intrinsic self-healing material where inherently reformation occurred with reversible nature.<sup>[166]</sup>

On the other hand, based on the self-healing mechanism, it is further of two types: (1) Self-healing occurs due to the release of a healing agent after damage to recover the materials, but the process is not showing reversibility continuously. (2) Self-healing occurred due to the repetition of attachment by the reformation of non-covalent interactions, metal coordination, and other interactions between material components. Self-healing by this method shows reversibility.<sup>[167]</sup>

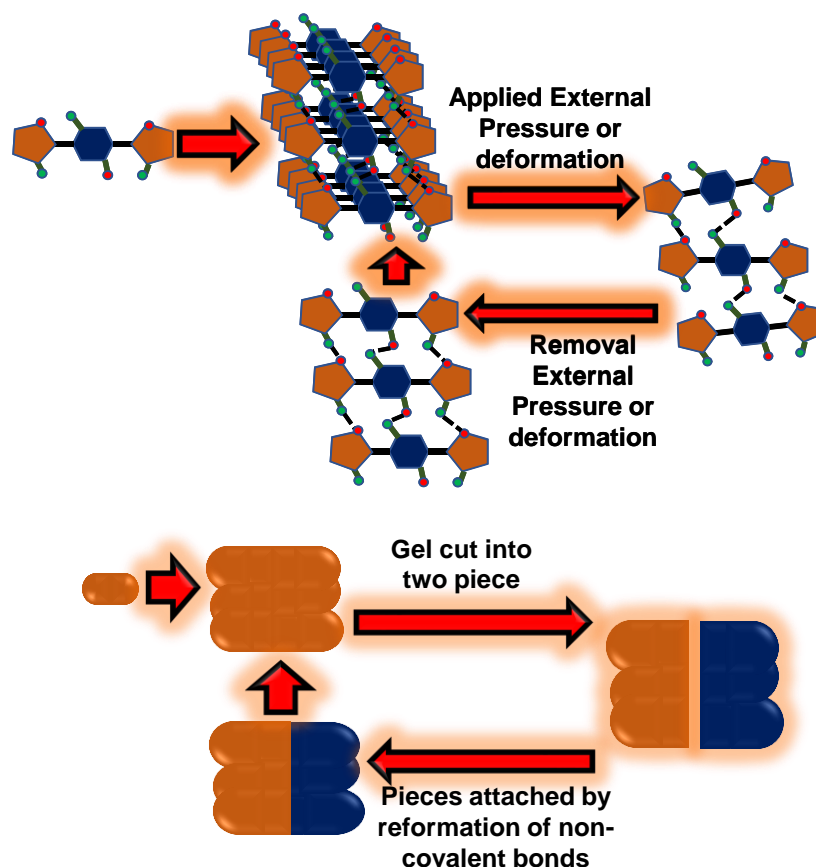


**Figure 1.7** Schematic diagram for self-assembly after reformation of bonds.

In the case of organogel and metallogel, the self-healing property comes due to the recovery of non-covalent interactions like  $\pi$ - $\pi$  stacking, hydrogen bonding, and hydrophobic interaction after any damage to gel materials. Most commonly, the self-healing ability can be seen with low molecular weight physical gels due to their weak interactions, which can recover further after its damage when the environment is suitable for them.<sup>[168-170]</sup> Several reports are present where the self-healing properties of gels are investigated in the bulk phase.<sup>[171-176]</sup>

As noted, gel-sol-gel reversibility depends on the non-covalent bond formation, breaking, and reformation during physical damage; it is crucial to design a gelator molecule that must provide sites for non-covalent bond formation with increased tendencies. For example, supramolecular moldable and self-healing materials were reported by

introducing a series of tetrazole-based ligands with  $\text{Pb}(\text{OAc})_2$ .<sup>[177]</sup> Other than this, there are some other reports where metallo gels of lanthanide series and tetrazole-based organogel and metallo gels have shown their great ability towards self-healing.<sup>[178, 179]</sup> Interestingly, a metallo gel ( $\text{CuA-Ox}$ ) is reported, which can impart self-healing properties to other gel networks without disturbing their previous properties.<sup>[151]</sup> In supramolecular LMW gels, the self-healing property can be defined by a rheological experiment for the thixotropic behaviour of the gel. Thixotropy is the property of gel where gel-sol-gel transition occurs with changes in the value of strain percentage. This test is also known as the time oscillation sweep (TOS) experiment, and it is a confirmatory test for the self-healing property of LMW gels.

### **1.5.3 Gels and xerogels as adsorbent: act as environmental remediator**

The world is developing fast with all the amenities to provide an easy and happy life. But this uncontrolled development continuously impacts the environment. With the presence of an uncontrolled number of industrial hazardous wastes such as heavy metals, dyes and other colorants, pharmaceuticals, petroleum products, pesticides, and fertilizers, the environment is in danger, and mostly the water bodies tend to get highly polluted. Water is an essential part of life. The remediation of wastewater is one of the biggest challenges for today's world. Out of many contaminations in water, the presence of heavy metal salts in water is a very serious issue for human health.<sup>[180]</sup> Heavy metals are those metals that have a density of more than  $5 \text{ gm/ cm}^3$ . These heavy metals are toxic and carcinogenic even at very low concentrations. For the purification of water from heavy metal salts, many methods are developed, e.g., adsorption by porous materials, separation by a membrane, removal by electricity, and several other chemical methods. All these water remediation methods are valuable and applicable but also generate side products such as several non-biodegradable chemicals which get remixed with the environment as

pollutants (Figure 1.8).<sup>[181]</sup> Therefore, it is essential to synthesize a system for water remediation that can be reusable and easy to generate. The adsorption method to remove the pollutants has some specific advantages, as no secondary waste gets generated during wastewater treatment. To develop such an adsorbing material, it is necessary to focus on some functional groups that can mitigate water pollution problems by adsorbing the targeted pollutants. For example, the surface containing amino groups can remove cationic/ anionic impurities by electrostatic or hydrogen bonding interactions, while the impurities of heavy metal species can coordinate with amino sites and come out easily.<sup>[181]</sup>

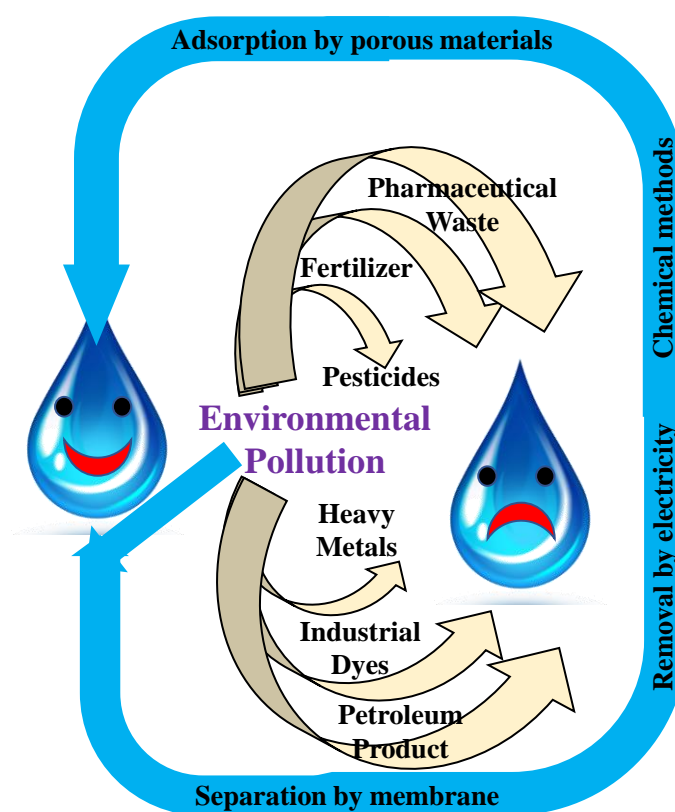


**Figure 1.8** Water contamination due to environmental pollution and their remediation by different methods.

Some reports show that organogels, metallogels, or their xerogels can be used for  $\text{Hg}^{2+}$ ,  $\text{Cd}^{2+}$ ,  $\text{Pb}^{2+}$ , and other heavy metals removal from contaminated water by adsorption method.<sup>[182-185]</sup> However, there are very few reports on such activities with lots of scope for improvement.

#### 1.5.4 Nanostructured metallogels as catalyst for various organic reactions

The application of metallogels as an effective catalyst is explored only with limited examples. However, xerogels of metallogels can act as a suitable catalyst for different reactions due to their heterogeneity towards the reaction systems (Figure 1.9). The heterogeneous nature makes them suitable to recover quickly for further catalysis. Mostly the nanostructured metallogels and nanoparticles containing metallogels of palladium and silver metals are used for organic reaction catalysis like Heck and Suzuki-Miyaura coupling reactions.<sup>[186]</sup> Some examples are reported where nanostructured metallogels of  $\text{Ca}^{2+}$ ,  $\text{Cr}^{3+}$ , and  $\text{Cu}^{2+}$  are used as catalysts for various other organic reactions like phenoxazinone synthase.<sup>[187, 188]</sup> Interestingly as several metalloenzymes can catalyse oxidation reactions like catechol oxidation, few metallogels are reported for that kind of activity.<sup>[189]</sup> Some nanoparticles containing metallogels viz. CoNC-MOG-X is used for oxygen reduction reaction, and TMP@NPCA for oxygen reduction and hydrogen evolution reaction. The vinyl polymer gels (Pd0-loaded VPGs) are used to catalyse oxidation/ disproportionation of benzyl alcohol, while polymer flat-sheet membrane and hollow fibres with palladium nanoparticles as catalyst is reported for hydrogenation reactions.<sup>[190]</sup> Pd(II)-coordination metallogel is used for oxidation of benzyl alcohol and some discrete metallogel catalysts are used for Michael addition reaction.<sup>[191]</sup>

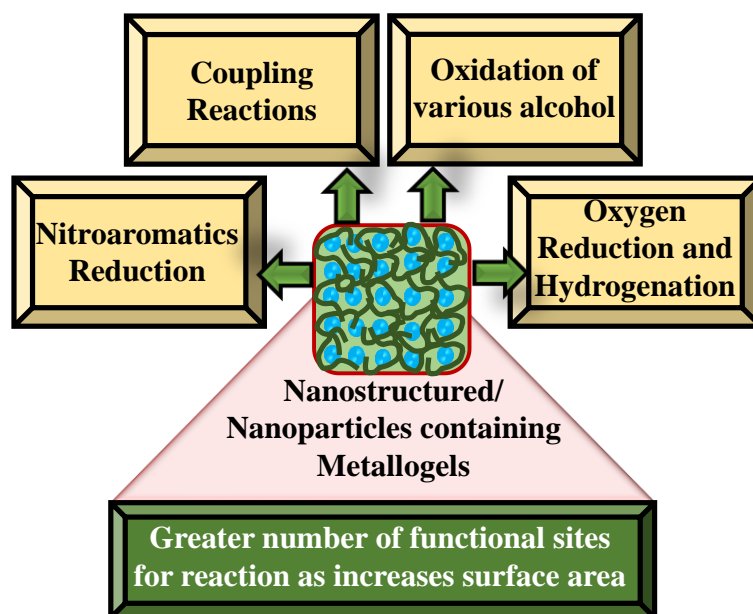


**Figure 1.9** Nanostructured metallogels as catalyst for different organic reactions.

Other than metallogel catalysts, there are also some reports where organogels are used as catalysts for various organic catalytic reactions.<sup>[191]</sup> As mentioned, the nanoparticles containing gels are most effective as a catalyst due to their large surface area provided as a substrate for reaction; some AgNPs containing metallogels are used as a prominent catalyst for reduction of nitroaromatics and further used for optical and antibacterial applications.<sup>[191, 192]</sup> The metallogels of AgNPs are also used for photodegradation of dyes.<sup>[191]</sup> In addition, PdNPs and Pd(II) metallogels are reported for Suzuki-Miyaura and Heck coupling, aerobic oxidation of various alcohols<sup>[191]</sup> and reduction of nitroaromatics.<sup>[193]</sup>

## **1.6 Aim and objective of the current thesis**

The purpose of the present work is to design and synthesize low molecular weight gelators (LMWGs), fabrication of nanostructured organogels, and metallogels fabrication and explore their applications in various fields. The thesis is also intended to correlate the observed properties of the gels and metallogels with their assembled structures. The LMWGs synthesized and explored in this thesis are based on:

- Tetrazole derivative of BTA and triazine ring
- Tetrazole-triazine derivative with isomers of aminopyridine
- Carboxylic acid and amine derivative of BTA with tetrazole-triazine ring

The fabricated nanostructured metallogels of **G7** (triethylammonium 5-(3,5-bis((1H-tetrazol-5-yl)carbamoyl)benzamido)tetrazol-1-ide), **G8** ( $N^2$ ,  $N^4$ ,  $N^6$ -tri(1H-tetrazol-5-yl)-1,3,5-triazine-2,4,6-triamine), and **G8GE** (**GE** is 3,3',3''-(benzenetricarbonyltris(azanediyl))tris(4-aminobenzoic acid)) have been explored for various applications in the presence or absence of different metal ions or nanoparticles. Stabilization of silver nanoparticles in an iron-metallogel furnished a nanocomposite which is used as a heterogeneous catalyst for the reduction reaction. Similarly, the stabilization of palladium nanoparticles and palladium ions in the gel matrix gives heterogeneous catalysts for coupling and cycloaddition reactions, respectively. Furthermore, suitable organogel has shown its properties to discriminate between amino-pyridine isomers. A composite gel structure can provide extra stability to a gel in an aqueous solution, acting as a water remediation agent by heavy metal adsorption.

The current chapter provides a brief description of the field of soft material as gel, its design, fabrication, properties, and applications.

**Chapter 2** presents the preparation of ionic multifunctional gelator molecule triethylammonium 5-(3,5-bis((1H-tetrazol-5-yl)carbamoyl)benzamido)tetrazol-1-ide (**G7**) and their metallogels with  $Fe^{3+}$ ,  $Co^{2+}$ ,  $Ni^{2+}$ ,  $Cu^{2+}$ ,  $Zn^{2+}$ ,  $Ag^+$  and  $Fe^{2+}$ . All the metallogels are used for the stabilization of silver nanoparticles. Out of which Fe(III)G7 metallogel shows stabilization of smaller size of silver nanoparticles and formed silver nanocomposite, which is used as a catalyst for reduction of nitroaromatics. This silver nanocomposite can be again transformed into nanostructured metallogel. The nanoparticle-containing Fe(III)G7 metallogel shows exclusive self-healing properties.

**Chapter 3** talks about the gelator  $N^2, N^4, N^6$ -tri(1H-tetrazol-5-yl)-1,3,5-triazine-2,4,6-triamine (**G8**) and its organogels with isomers of aminopyridine. The isomeric position affects the physical and chemical properties of gel and shows differences in self-healing, AIEE, rheological and fluorometric properties due to the difference in hydrogen bonding present between **G8** and isomers of aminopyridine. The difference leads to the detection of 3-aminopyridine by **G8**.

**Chapter 4** describes the design and Synthesis of 3,3',3''-(benzenetricarbonyltris(azanediyl))tris(4-aminobenzoic acid) (**GE**) as a gelator enhancer molecule. The design of the **GE** is strategically done with the presence of complementary hydrogen bond donor-acceptor sites with respect to **G8**. The resultant organogel **G8GE** has shown the ability to form metallogels with Hg(II), Cd(II), and Pb(II) salts. The hydrophobic nature of the gel **G8GE** is explored with the retention of the disc-shaped gel structure in an aqueous medium for an extended period. These two properties of mixed organogel show the capacity to efficiently remove toxic metal ions like Hg(II), Cd(II), and Pb(II) from aqueous solutions. The adsorbent xerogel **G8GE** shows good heavy metal removal percentage and reusability.

**Chapter 5** presents the use of gelator molecule **G8** for the stabilization of palladium nanoparticles (PdNPs). The fabrication of palladium nanoparticles and palladium ion-embedded nanostructured metallogels (**G8PdNPs** and **G8PdCl<sub>2</sub>**) has been done, which were used as effective catalysts for Suzuki-Miyaura coupling and cycloaddition reaction for tetrazole formation respectively.

**Chapter 6** present the conclusion and future scope of work, which have been done under chapter 2, 3, 4 and 5. This chapter give the brief explanation about the synthesis, fabrication, and applications of organogels and metallogels formed by gelator molecule **G7**, **G8** and gelator enhancer component **GE**.

## 1.7 References

- [1] Kuzina, M.A., Kartsev, D.D., Stratonovich, A.V. and Levkin, P.A. (2023), Organogels versus hydrogels: advantages, challenges, and applications, *Adv. Funct. Mater.*, 2301421 (DOI:10.1002/adfm.202301421)
- [2] Malo de Molina, P., Gradzielski, M. (2017), Gels obtained by colloidal self-assembly of amphiphilic molecules, *Gels*, 3, 30 (DOI:10.3390/gels3030030)
- [3] Graham, T. (1864), On the properties of silicic acid and other analogous colloidal substances, *J. Chem. Soc.*, 17, 318-327 (DOI: 10.1039/JS8641700318)
- [4] Neuhausen, B.S., Patrick, W.A. (1921), Organogels of silicic acid, *J. Am. Chem. Soc.*, 43, 1844-1846 (DOI: 10.1021/ja01441a011)
- [5] Xing, B., Choi, M.F., Xu, B. (2002), A stable metal coordination polymer gel based on a calix [4] arene and its “uptake” of non-ionic organic molecules from the aqueous phase, *Chem. Commun.*, 4, 362-363 (DOI: 10.1039/B111245G)
- [6] Okesola, B.O., Wu, Y., Derkus, B., Gani, S., Wu, D., Knani, D., Smith, D.K., Adams, D.J., Mata, A. (2019), Supramolecular self-assembly to control structural and biological properties of multicomponent hydrogels, *Chem. Mater.*, 31, 7883-7897 (DOI: 10.1021/acs.chemmater.9b01882)
- [7] Díaz, D.D., Kühbeck, D., Koopmans, R.J. (2011), Stimuli-responsive gels as reaction vessels and reusable catalysts, *Chem. Soc. Rev.*, 40, 427-448 (DOI: 10.1039/C005401C)
- [8] Panja, S., Seddon, A., Adams, D.J. (2021), Controlling hydrogel properties by tuning non-covalent interactions in a charge complementary multicomponent system, *Chem. Sci.*, 12, 11197-11203 (DOI: 10.1039/D1SC02854E)
- [9] Sutar, P., Maji, T.K. (2017), Coordination polymer gels with modular nanomorphologies, tunable emissions, and stimuli-

- responsive behavior based on an amphiphilic tripodal gelator, *Inorg. Chem.*, 56, 9417-9425 (DOI: 10.1021/acs.inorgchem.7b01002)
- [10] Jones, C.D., Steed, J.W. (2016), Gels with sense: supramolecular materials that respond to heat, light and sound, *Chem. Soc. Rev.*, 45, 6546-6596 (DOI: 10.1039/C6CS00435K)
- [11] El-Husseiny, H.M., Mady, E.A., Hamabe, L., Abugomaa, A., Shimada, K., Yoshida, T., Tanaka, T., Yokoi, A., Elbadawy, M., Tanaka, R. (2022), Smart/stimuli-responsive hydrogels: Cutting-edge platforms for tissue engineering and other biomedical applications, *Mater. Today Bio*, 13, 100186 (DOI: 10.1016/j.mtbio.2021.100186)
- [12] Roy, S.G., Kumar, A., Misra, N., Ghosh, K. (2022), Pyridoxal-based low molecular weight progelator as a new chemosensor for the recognition of  $\text{Ag}^+$  and  $\text{Hg}^{2+}$  under different conditions, *Mater. Adv.*, 3, 5836-5844 (DOI: 10.1039/D2MA00358A)
- [13] Panja, S., Panja, A., Ghosh, K. (2021), Supramolecular gels in cyanide sensing: A review, *Mater. Chem. Front.*, 5, 584-602 (DOI: 10.1039/D0QM00551G)
- [14] Mommer, S., Wezenberg, S.J. (2022), Anion-induced reversible actuation of squaramide-crosslinked polymer gels, *ACS Appl. Mater. Interfaces*, 14, 43711-43718 (DOI: 10.1021/acsami.2c11136)
- [15] Baruah, K., Dutta, R., Doley, S., Dolui, S.K. (2023), Grafted polymeric organogel using low molecular weight gelator as an effective medium for expulsion and purification of cationic dyes and organic pollutants from contaminated surface water, *Eur. Polym. J.*, 112213 (DOI: 10.1016/j.eurpolymj.2023.112213)
- [16] Tsurumaki, F., Sato, A., Fukai, K., Maruoka, S., Tamesue, S. (2023), Development of an adhesive gel system for changing the structure and properties of its adhesive joint via reactions with amine molecules after adhesion, *ACS Appl. Mater. Interfaces*, 15, 27, 32852–32862 (DOI: 10.1021/acsami.3c03666)

- [17] Long, Y., Jiang, B., Huang, T., Liu, Y., Niu, J., Wang, Z.L., Hu, W. (2023), Super-stretchable, anti-Freezing, anti-drying organogel ionic conductor for multi-mode flexible electronics, *Adv. Funct. Mater.*, 2304625 (DOI: 10.1002/adfm.202304625)
- [18] Adeyemi, S.A., Az-Zamakhshariy, Z., Choonara, Y.E. (2023), In vitro prototyping of a nano-organogel for thermo-sonic intra-cervical delivery of 5-fluorouracil-loaded solid lipid nanoparticles for cervical cancer, *AAPS Pharm. Sci. Tech.*, 24, 123 (DOI: 10.1208/s12249-023-02583-y)
- [19] Singh, B., Sharma, V., Kumar, R., Sharma, D. (2023), Designing biphasic gels from dietary fiber sterculia gum by green approach using high energy radiation for biomedical applications, *Food Hydrocoll. Health*, 3, 100137 (DOI: 10.1016/j.fhfh.2023.100137)
- [20] Zhang, Y., Tang, J., Fang, W., Zhao, Q., Lei, X., Zhang, J., Chen, J., Li, Y., Zuo, Y. (2023), Synergetic effect of electrical and topographical cues in aniline trimer-based polyurethane fibrous scaffolds on tissue regeneration, *J. Funct. Biomater.*, 14, 185 (DOI: 10.3390/jfb14040185)
- [21] Qi, Y., Ayinla, M., Sobkowicz, M.J., Ramström, O. (2023), Self-healable, regenerable, and degradable dynamic covalent nitroalcohol organogels, *Macromol. rapid commun.*, 2300011 (DOI: 10.1002/marc.202300011)
- [22] Zhang, S., Liu, M., Guo, S., Tieu, A.J.K., Yang, J., Adams, S., Tan, S.C. (2023), Strong, compressible, and ultrafast self-recovery organogel with in situ electrical conductivity improvement, *Adv. Funct. Mater.*, 33, 2209129 (DOI: 10.1002/adfm.202209129)
- [23] Zhao, Y., Ohm, Y., Liao, J., Luo, Y., Cheng, H.Y., Won, P., Roberts, P., Carneiro, M.R., Islam, M.F., Ahn, J.H., Walker, L.M. (2023), A self-healing electrically conductive organogel

- composite, *Nat. Electron.*, 6, 206-215 (DOI: 10.1038/s41928-023-00932-0)
- [24] Sutar, P., Maji, T.K. (2020), Recent advances in coordination-driven polymeric gel materials: design and applications, *Dalton Trans.*, 49, 7658-7672 (DOI: 10.1039/D0DT00863J)
- [25] Yang, G., Li, S., Li, N., Zhang, P., Su, C., Gong, L., Chen, B., Qu, C., Qi, D., Wang, T., Jiang, J. (2022), Enhanced photocatalytic CO<sub>2</sub> reduction through hydrophobic microenvironment and binuclear cobalt synergistic effect in metallogels, *Angew. Chem., Int. Ed.*, 61, 202205585 (DOI: 10.1002/anie.202205585)
- [26] Verma, P., Rahimi, F.A., Samanta, D., Kundu, A., Dasgupta, J., Maji, T.K. (2022), Visible-light-driven photocatalytic CO<sub>2</sub> reduction to CO/CH<sub>4</sub> using a metal–organic “Soft” coordination polymer gel, *Angew. Chem. Int. Ed.*, 61, 202116094 (DOI: 10.1002/anie.202116094)
- [27] Sarkar, S., Maji, P.K., Negishi, Y., Dutta, S., Das, T.N., Pan, R., Sarkar, S. (2021), Cu (II)-based nanofibrous metallogel for phenoxazinone synthase-like activity, *ACS Appl. Nano Mater.*, 4, 1455-1466 (DOI: 10.1021/acsanm.0c02984)
- [28] Upadhyay, A., Narula, A., Rao, C.P. (2020), Copper-based metallogel of bovine serum albumin and its derived hybrid biomaterials as aerogel and sheet: comparative study of the adsorption and reduction of dyes and nitroaromatics, *ACS Appl. Bio Mater.*, 3, 8619-8626 (DOI: 10.1021/acsabm.0c01028)
- [29] Verma, P., Samanta, D., Sutar, P., Kundu, A., Dasgupta, J., Maji, T.K. (2022), Biomimetic approach toward visible light-driven hydrogen generation based on a porphyrin-based coordination polymer gel, *ACS Appl. Mater. Interfaces*, 15, 25173-25183 (DOI: 10.1021/acsami.2c14533)
- [30] Guo, H., Feng, Q., Xu, K., Xu, J., Zhu, J., Zhang, C., Liu, T. (2019), Self-templated conversion of metallogel into heterostructured tmp@ carbon quasiaerogels boosting

- bifunctional electrocatalysis, *Adv. Funct. Mater.*, 29, 1903660 (DOI: 10.1002/adfm.201903660)
- [31] Purohit, B., Jeanneau, E., Guyot, Y., Amans, D., Mahler, B., Joubert, M.F., Dujardin, C., Ledoux, G., Mishra, S. (2023), Incorporation of upconverting LiYF<sub>4</sub>: Yb<sup>3+</sup>, Tm<sup>3+</sup> nanoparticles with high quantum yield in TiO<sub>2</sub> metallogels for near infrared-driven photocatalytic dye degradation, *ACS Appl. Nano Mater.*, 6, 2310-2326 (DOI: 10.1021/acsanm.2c04240)
- [32] Saha, S., Pal, B., Sundar Das, K., Kumar Ghose, P., Ghosh, A., De, A., Kumar Das, A., Pratim Ray, P., Mondal, R. (2022), Design of dual purpose Fe-metallogel for magnetic refrigeration and fabrication of schottky barrier diode, *ChemistrySelect*, 7, 202203307 (DOI: 10.1002/slct.202203307)
- [33] Houard, F., Cucinotta, G., Guizouarn, T., Suffren, Y., Calvez, G., Daiguebonne, C., Guillou, O., Artzner, F., Mannini, M., Bernot, K. (2023), Metallogels: a novel approach for the nanostructuring of single-chain magnets, *Mater. Horiz.*, 10, 547-555 (DOI: 10.1039/D2MH01158A)
- [34] Maiti, B., Bhattacharjee, S., Bhattacharya, S. (2019), Palladium-induced transformation of nematic liquid crystals to robust metallogel comprising self-assembled nanowires, *Chem. Commun.*, 55, 12651-12654 (DOI: 10.1039/C9CC05517G)
- [35] Tautz, M., Saldías, C., Lozano-Gorrín, A.D., Díaz, D.D. (2019), Use of a bis-1, 2, 3-triazole gelator for the preparation of supramolecular metallogels and stabilization of gold nanoparticles, *New J. Chem.*, 43, 13850-13856 (DOI: 10.1039/C9NJ03427G)
- [36] Tatikonda, R., Bulatov, E., Özdemir, Z., Haukka, M. (2019), Infinite coordination polymer networks: metallogelation of aminopyridine conjugates and in situ silver nanoparticle formation, *Soft Matter*, 15, 442-451 (DOI: 10.1039/C8SM02006J)

- [37] Nugraha, A.S., Guselnikova, O., Henzie, J., Na, J., Hossain, M.S.A., Dag, O., Rowan, A.E., Yamauchi, Y. (2022), Symmetry-breaking plasmonic mesoporous gold nanoparticles with large pores, *Chem. Mater.*, 34, 7256-7270 (DOI: 10.1021/acs.chemmater.2c01125)
- [38] Bairagi, D., Ghosh, P., Roy, P., Banerjee, A. (2023), Metallogels from Silver Nanoparticles and Peptide Nanofibers as Antimicrobial Surfaces, *ACS Appl. Nano Mater.*, 6, 2299-2309 (DOI: 10.1021/acsanm.2c04144)
- [39] Saha, S., Das, K.S., Pal, P., Hazra, S., Ghosh, A., Bala, S., Ghosh, A., Das, A.K., Mondal, R. (2023), A silver-based integrated system showing mutually inclusive super protonic conductivity and photoswitching behavior, *Inorg. Chem.*, 62, 3485-3497 (DOI: 10.1021/acs.inorgchem.2c03785)
- [40] Lepcha, G., Singha, T., Majumdar, S., Pradhan, A.K., Das, K.S., Datta, P.K., Dey, B. (2022), Adipic acid directed self-healable supramolecular metallogels of Co (II) and Ni (II): intriguing scaffolds for comparative optical-phenomenon in terms of third-order optical non-linearity, *Dalton Trans.*, 51, 13435-13443 (DOI: 10.1039/D2DT01983C)
- [41] Dhibar, S., Dey, A., Majumdar, S., Dey, A., Ray, P.P., Dey, B. (2020), Organic-acid-mediated luminescent supramolecular Tb (III)-metallogel applied in an efficient photosensitive electronic device with excellent charge transport properties, *Ind. Eng. Chem. Res.*, 59, 5466-5473 (DOI: doi.org/10.1021/acs.iecr.9b06032)
- [42] Majumdar, S., Pal, B., Sahu, R., Das, K.S., Ray, P.P., Dey, B. (2022), A croconate-directed supramolecular self-healable Cd (ii)-metallogel with dispersed 2D-nanosheets of hexagonal boron nitride: A comparative outcome of the charge-transport phenomena and non-linear rectifying behaviour of semiconducting diodes, *Dalton Trans.*, 51, 9007-9016 (DOI: 10.1039/D2DT01206E)

- [43] Das, P., Majumdar, S., Dey, A., Mandal, S., Mondal, A., Chakrabarty, S., Ray, P.P., Dey, B. (2021), 4, 4'-Bipyridine-based Ni (ii)-metallogel for fabricating a photo-responsive Schottky barrier diode device, *New J. Chem.*, 45, 15920-15927 (DOI: 10.1039/D1NJ01629F)
- [44] Lepcha, G., Majumdar, S., Pal, B., Ahmed, K.T., Pal, I., Satpati, B., Biswas, S.R., Ray, P.P., Dey, B. (2023), Suberic acid-based supramolecular metallogels of Ni (II), Zn (II), and Cd (II) for anti-pathogenic Activity and Semiconducting Diode Fabrication, *Langmuir*, 39, 21, 7469–7483 (DOI: 10.1021/acs.langmuir.3c00765)
- [45] Dhibar, S., Babu, S., Mohan, A., Chandra, G.K., Bhattacharjee, S., Karmakar, K., Karmakar, P., Rahaman, S.M., Predeep, P., Saha, B. (2023), A novel citric acid facilitated supramolecular Zinc (II)-metallogel: Toward semiconducting device applications, *J. Mol. Liquids*, 375, 121348 (10.1016/j.molliq.2023.121348)
- [46] Verma, P., Singh, A., Maji, T.K. (2021), Photo-modulated wide-spectrum chromism in  $\text{Eu}^{3+}$  and  $\text{Eu}^{3+}/\text{Tb}^{3+}$  photochromic coordination polymer gels: application in decoding secret information, *Chem. Sci.*, 12, 2674-2682 (DOI: 10.1039/D0SC05721E)
- [47] Yao, H., Niu, Y.B., Hu, Y.P., Sun, X.W., Zhang, Q.P., Zhang, Y.M., Wei, T.B., Lin, Q. (2022), Metal-ion-mediated synergistic coordination: construction of AIE-metallogel sensor arrays for anions and amino acids, *New J. Chem.*, 46, 17251-17259 (DOI: 10.1039/D2NJ02992H)
- [48] Liu, Z., Zhao, X., Chu, Q., Feng, Y. (2023), Recent advances in stimuli-responsive metallogels, *Molecules*, 28, 2274 (DOI: 10.3390/molecules28052274)
- [49] Picci, G., Caltagirone, C., Garau, A., Lippolis, V., Milia, J., Steed, J.W. (2023), Metal-based gels: Synthesis, properties, and

- applications, *Coord. Chem. Rev.*, 492, 215225 (DOI: 10.1016/j.ccr.2023.215225)
- [50] Maji, T.K. (2023), Editorial for Forum on Applied Supramolecular Materials, *ACS Appl. Mater. Interfaces*, 15, 25079-25081 (DOI: 10.1021/acsami.3c05952)
- [51] Tripathy, D., Gadtya, A.S., Moharana, S. (2023), Supramolecular gel, its classification, preparation, properties, and applications: A review, *Polym. -Plast. Technol. Mater.*, 62, 306-326 (DOI: 10.1080/25740881.2022.2113892)
- [52] Sangeetha, N.M., Maitra, U. (2005), Supramolecular gels: Functions and uses, *Chem. Soc. Rev.*, 34, 821-836 (DOI: 10.1039/B417081B)
- [53] Draper, E.R., Greeves, B.J., Barrow, M., Schweins, R., Zwijnenburg, M.A., Adams, D.J. (2017), pH-directed aggregation to control photoconductivity in self-assembled perylene bisimides, *Chem.*, 2, 716-731 (DOI: 10.1016/j.chempr.2017.03.022)
- [54] Babu S. S., Praveen V. K., Ajayaghosh A. (2014), Functional  $\pi$ -gelators and their applications, *Chem. Rev.*, 114, 1973-2129 (DOI: 10.1021/cr400195e)
- [55] De Loos M., van Esch J., Stokroos I., Kellogg R. M., Feringa B. L. (1997), Remarkable stabilization of self-assembled organogels by polymerization, *J. Am. Chem. Soc.*, 119, 12675-12676 (DOI: 10.1021/ja972899z)
- [56] Castilla, A.M., Dietrich, B., Adams, D.J. (2018), Using aggregation-induced emission to understand dipeptide gels, *Gels*, 4, 17 (DOI: 10.3390/gels4010017)
- [57] Mei, J., Leung, N.L., Kwok, R.T., Lam, J.W., Tang, B.Z. (2015), Aggregation-induced emission: together we shine, united we soar!, *Chem. Rev.*, 115, 11718-11940 (DOI: 10.1021/acs.chemrev.5b00263)
- [58] Das, P., Kumar, A., Chowdhury, A., Mukherjee, P.S. (2018), Aggregation-induced emission and white luminescence from a

- combination of  $\pi$ -conjugated donor-acceptor organic luminogens, *ACS omega*, 3, 13757-13771 (DOI: 10.1021/acsomega.8b01706)
- [59] Jones, C.D., Steed, J.W. (2016), Gels with sense: supramolecular materials that respond to heat, light and sound, *Chem. Soc. Rev.*, 45, 6546-6596 (DOI: 10.1039/C6CS00435K)
- [60] Chu, C.W., Schalley, C.A. (2021), Recent advances on supramolecular gels: From stimuli-responsive gels to co-assembled and self-sorted systems, *Org. Mater.*, 3, 025-040 (DOI: 10.1055/s-0040-1722263)
- [61] Cantekin S., de Greef T. F., Palmans A. R. (2012), Benzene-1,3,5- tricarboxamide: A versatile ordering moiety for supramolecular chemistry, *Chem. Soc. Rev.*, 41, 8, 6125-6137 (DOI: 10.1039/C2CS35156K)
- [62] Yang X., Fleming F. F. (2017), C-and N-metalated nitriles: The relationship between structure and selectivity, *Acc. Chem. Res.*, 50, 2556-2568 (DOI: 10.1021/acs.accounts.7b00329)
- [63] Gong B., Zheng C., Yan Y. (1999), Structure of N, N', N''-tris (carboxymethyl)- 1, 3, 5-benzenetricarboxamide trihydrate, *J. Chem. Crystallogr.*, 29, 649-652 (DOI: 10.1023/A:1009511501537)
- [64] Lee J. H., Baek Y. E., Kim K. Y., Choi H., Jung J. H. (2016), Metallogel of bis (tetrazole)-appended pyridine derivative with  $\text{CoBr}_2$  as a chemoprobe for volatile gases containing chloride atom, *Supramol. Chem.*, 28, 870-873 (DOI: 10.1080/10610278.2016.1142088)
- [65] Sutar, P., Suresh, V.M., Jayaramulu, K., Hazra, A., Maji, T.K. (2018), Binder driven self-assembly of metal-organic cubes towards functional hydrogels, *Nat. Commun.*, 9, 3587 (DOI: 10.1038/s41467-018-05818-w)
- [66] Nagarajan V., Pedireddi V. R. (2014), Gelation and structural transformation study of some 1, 3, 5-Benzenetricarboxamide

- derivatives, *Cryst. Growth Des.*, 14, 4, 1895-1901 (DOI: 10.1021/cg500026t)
- [67] Sarkar, K., Khasimbi, S., Mandal, S., Dastidar, P. (2018), Rationally developed metallogelators derived from pyridyl derivatives of NSAIDs displaying anti-inflammatory and anticancer activities, *ACS appl. Mater. Interfaces*, 10, 30649-30661 (DOI: 10.1021/acsami.8b09872)
- [68] Liu, J., Gong, G.F., Li, Y.J., Yao, H., Wei, T.B., Lin, Q. (2020), Novel metallogel-based micro-acanthosphere material constructed from two tripodal gelators for efficient separation of organic dyes, *Mater. Lett.*, 274, 128015 (DOI: 10.1016/j.matlet.2020.128015)
- [69] Zhang, B., Dong, X., Xiong, Y., Zhou, Q., Lu, S., Liao, Y., Yang, Y., Wang, H. (2020), A heat-set lanthanide metallogel capable of emitting stable luminescence under thermal, mechanical and water stimuli, *Dalton Trans.*, 49, 2827-2832 (DOI: 10.1039/C9DT04713A)
- [70] Lee, H., Jung, S.H., Han, W.S., Moon, J.H., Kang, S., Lee, J.Y., Jung, J.H., Shinkai, S. (2011), A chromo-fluorogenic tetrazole-based  $\text{CoBr}_2$  coordination polymer gel as a highly sensitive and selective chemosensor for volatile gases containing chloride, *Chem.–A Eur. J.*, 17, 2823-2827 (DOI: 10.1002/chem.201003279)
- [71] Sutar, P., Maji, T.K. (2016), Coordination polymer gels: soft metal–organic supramolecular materials and versatile applications, *Chem. Commun.*, 52, 8055-8074 (DOI: 10.1039/C6CC01955B)
- [72] Stals P. J., Everts J. C., de Bruijn R., Filot I. A., Smulders M. M., Martín-Rapún R., Pidko E. A., de Greef T. F., Palmans A. R., Meijer E. W. (2010), Dynamic supramolecular polymers based on benzene-1,3,5-tricarboxamides: The influence of amide connectivity on aggregate stability and amplification of chirality, *Chem. Eur. J.*, 16, 810-821 (DOI: 10.1002/chem.200902635).

- [73] Van Gorp J. J., Vekemans J. A. J. M., Meijer E. W. (2002), C3-Symmetrical supramolecular architectures: Fibers and organic gels from discotic trisamides and trisureas, *J. Am. Chem. Soc.*, 124, 14759-14769 (DOI: 10.1021/ja020984n)
- [74] Li, B., Xiao, D., Gai, X., Yan, B., Ye, H., Tang, L., Zhou, Q. (2021), A multi-responsive organogel and colloid based on the self-assembly of a Ag (I)-azopyridine coordination polymer, *Soft Matter*, 17, 3654-3663 (DOI: 10.1039/D1SM00013F)
- [75] Zhao, Q., Gong, G.F., Yang, H.L., Zhang, Q.P., Yao, H., Zhang, Y.M., Lin, Q., Qu, W.J., Wei, T.B. (2020), Pillar [5] arene-based supramolecular AIE hydrogel with white light emission for ultrasensitive detection and effective separation of multianalytes, *Polym. Chem.*, 11, 5455-5462 (DOI: 10.1039/D0PY00872A)
- [76] Zhang, Y.M., Zhu, W., Zhao, Q., Qu, W.J., Yao, H., Wei, T.B., Lin, Q. (2020), Th<sup>4+</sup> tuned aggregation-induced emission: A novel strategy for sequential ultrasensitive detection and separation of Th<sup>4+</sup> and Hg<sup>2+</sup>, *Spectrochim. Acta A Mol. Biomol. Spectrosc.*, 229, 117926 (DOI: 10.1016/j.saa.2019.117926)
- [77] Malviya, N., Sonkar, C., Ganguly, R., Mukhopadhyay, S. (2019), Cobalt Metallogel Interface for selectively sensing l-tryptophan among essential amino acids, *Inorg. Chem.*, 58, 7324-7334 (DOI: 10.1021/acs.inorgchem.9b00455)
- [78] Kumar, A., Zangrando, E., Mukherjee, P.S. (2019), Self-assembled Pd<sub>3</sub>L<sub>2</sub> cages having flexible tri-imidazole donors, *Polyhedron*, 172, 67-73 (DOI: 10.1016/j.poly.2019.03.014)
- [79] Kumar, A., Mukherjee, P.S. (2020), Multicomponent self-assembly of PdII/PtII interlocked molecular cages: cage-to-cage conversion and self-sorting in aqueous medium, *Chem.–A Eur. J.*, 26, 4842-4849 (DOI: 10.1002/chem.202000122)

- [80] Chakraborty, D., Modak, R., Howlader, P., Mukherjee, P.S. (2021), De novo approach for the synthesis of water-soluble interlocked and non-interlocked organic cages, *Chem. Commun.*, 57, 3995-3998 (DOI: 10.1039/D1CC00627D)
- [81] Zhang, B., Dong, X., Zhou, Q., Lu, S., Zhang, X., Liao, Y., Yang, Y., Wang, H. (2021), Carboxymethyl chitosan-promoted luminescence of lanthanide metallogel and its application in assay of multiple metal ions, *Carbohydr. Polym.*, 263, 117986 (DOI: 10.1016/j.carbpol.2021.117986)
- [82] Su, H., Zhu, S., Qu, M., Liu, R., Song, G., Zhu, H. (2019), 1, 3, 5-Triazine-based Pt (II) metallogel material: Synthesis, photophysical properties, and optical power-limiting performance, *J. Phys. Chem. C*, 123, 15685-15692 (DOI: 10.1021/acs.jpcc.9b02168)
- [83] Sukul, P.K., Das, P., Dhakar, G.L., Das, L., Malik, S. (2022), Effect of tricarboxylic acids on the formation of hydrogels with melem or melamine: morphological, structural and rheological investigations, *Gels*, 8, 51 (DOI: 10.3390/gels8010051)
- [84] Pan, J., Wang, J. (2020), Boron nitride aerogels consisting of varied superstructures, *Nanoscale Adv.*, 2, 149-155 (DOI: 10.1039/C9NA00702D)
- [85] Liu B., Qiu Y.-C., Peng G., Deng H. (2010), In situ solvothermal syntheses of a heteronuclear copper(I)-alkaline metallic tetrazole-based coordination polymer, *Cryst. Eng. Comm.*, 12, 270-276 (DOI: 10.1039/b910418f)
- [86] Jeong S., Song X., Jeong S., Oh M., Liu X., Kim D., Moon D., Lah M. S. (2011), Metal-organic frameworks based on unprecedented trinuclear and pentanuclear metal-tetrazole clusters as secondary building units, *Inorg. Chem*, 50, 12133-12140 (DOI: 10.1021/ic201883f)
- [87] Howlader, P., Bhandari, P., Chakraborty, D., Clegg, J.K., Mukherjee, P.S. (2020), Self-assembly of a Pd<sub>8</sub> macrocycle and Pd<sub>12</sub> homochiral tetrahedral cages using poly (tetrazolate)

- linkers, *Inorg. Chem.*, 59, 15454-15459 (DOI: 10.1021/acs.inorgchem.0c02452)
- [88] Howlader, P., Zangrando, E., Mukherjee, P.S. (2020), Self-assembly of enantiopure Pd<sub>12</sub> tetrahedral homochiral nanocages with tetrazole linkers and chiral recognition, *J. Am. Chem. Soc.*, 142, 9070-9078 (DOI: 10.1021/jacs.0c03551)
- [89] Peters L., Froehlich R., Boyd A. S. F., Kraft A. (2001), Noncovalent interactions between tetrazole and an N, N'-diethyl-substituted benzamidine, *J. Org. Chem.*, 66, 3291-3298 (DOI: 10.1021/jo005632i)
- [90] Liu B., Qiu Y.-C., Peng G., Deng H., (2010), In situ solvothermal syntheses of a heteronuclear copper(I)-alkaline metallic tetrazole-based coordination polymer, *Cryst. Eng. Comm.*, 12, 270-276 (DOI: 10.1039/b910418f)
- [91] Luo, C., Yang, B., Zhou, Y., Yang, J., Han, F., Baocai, X. (2020), Gelation properties and application based on amino acids gelators with four kinds of edible oils, *Colloids Surf. A: Physicochem. Eng. Asp.*, 585, 124184 (DOI: 10.1016/j.colsurfa.2019.124184)
- [92] Draper, E.R., Morris, K.L., Little, M.A., Raeburn, J., Colquhoun, C., Cross, E.R., McDonald, T.O., Serpell, L.C., Adams, D.J. (2015), Hydrogels formed from Fmoc amino acids, *Cryst. Eng. Comm.*, 17, 8047-8057 (DOI: 10.1039/C5CE00801H)
- [93] Miao, Y., Zhang, J., Zhang, G., He, S., Xu, B. (2022), l-Lysine-based gelators for the formation of gels in water and alcohol-water mixtures, *Gels*, 9, 29 (DOI: 10.3390/gels9010029)
- [94] Ibrahim, N.A., Nada, A.A., Eid, B.M. (2018), Polysaccharide-based polymer gels and their potential applications, *Polym. Gels: Syn. Charact.*, 97-126 (DOI: 10.1007/978-981-10-6083-04)
- [95] Suzuki, M., Nakajima, Y., Yumoto, M., Kimura, M., Shirai, H., Hanabusa, K. (2003), Effects of hydrogen bonding and van der Waals interactions on organogelation using designed low-

- molecular-weight gelators and gel formation at room temperature, *Langmuir*, 19, 8622-8624 (DOI: 10.1021/la034772v)
- [96] Zhou, Q., Dong, L., Wu, J., Shi, Y., Feng, X., Lu, X., Zhu, J., Mu, L. (2021), Versatile ionic gel driven by dual hydrogen bond networks: toward advanced lubrication and self-healing, *ACS Appl. Polym. Mater.*, 3, 5932-5941 (DOI: 10.1021/acsapm.1c01189)
- [97] Saha, E., Karthick, K., Kundu, S., Mitra, J. (2019), Electrocatalytic oxygen evolution in acidic and alkaline media by a multistimuli-responsive Cobalt (II) organogel, *ACS Sustain. Chem. Eng.*, 7, 16094-16102 (DOI: 10.1021/acssuschemeng.9b02858)
- [98] Sedghiniya, S., Soleimannejad, J., Foroutan, M., Ebrahimi, M., Naeini, V.F. (2021), AV (iii)-induced metallogel with solvent stimuli-responsive properties: structural proof-of-concept with MD simulations, *RSC Adv.*, 11, 36801-36813 (DOI: 10.1039/D1RA07055J)
- [99] Kumar, V., Upadhyay, R.K., Bano, D., Chandra, S., Yadav, P.K., Jit, S., Hasan, S.H. (2023), Self-assembly of Cu-TMA based semiconducting fibrous metallogels for fabrication of active electronic device with high rectification ratio, *Mater. Sci. Eng.: B*, 291, 116359 (DOI: 10.1016/j.mseb.2023.116359)
- [100] Zhao, Q., Gong, G.F., Yang, H.L., Zhang, Q.P., Yao, H., Zhang, Y.M., Lin, Q., Qu, W.J., Wei, T.B. (2020), Pillar [5] arene-based supramolecular AIE hydrogel with white light emission for ultrasensitive detection and effective separation of multianalytes, *Polym. Chem.*, 11, 5455-5462. (DOI: 10.1039/D0PY00872A)
- [101] Sasmal, S., Maji, K., Díaz, D.D., Halder, D. (2019), Highly selective metallogel from 4-biphenylcarboxy capped diphenylalanine and FeCl<sub>3</sub>, *Cryst. Eng. Comm.*, 21, 4289-4297 (DOI: 10.1039/C9CE00695H)

- [102] Dietrich, D., Licht, C., Nuhnen, A., Höfert, S.P., De Laporte, L., Janiak, C. (2019), Metal–organic gels based on a bisamide tetracarboxyl ligand for carbon dioxide, sulfur dioxide, and selective dye uptake, *ACS appl. Mater. interfaces*, 11, 19654-19667 (DOI: 10.1021/acsami.9b04659)
- [103] Tom, L., Kurup, M.R.P. (2019), A stimuli responsive multifunctional ZMOF based on an unorthodox polytopic ligand: reversible thermochromism and anion triggered metallogelation, *Dalton Trans.*, 48, 16604-16614 (DOI: 10.1039/C9DT02820J)
- [104] Ji, W., Yuan, C., Zilberzwige-Tal, S., Xing, R., Chakraborty, P., Tao, K., Gilead, S., Yan, X., Gazit, E. (2019), Metal-ion modulated structural transformation of amyloid-like dipeptide supramolecular self-assembly, *ACS nano*, 13(6), 7300-7309 (DOI: 10.1021/acsnano.9b03444)
- [105] Malviya, N., Sonkar, C., Ganguly, R., Bhattacharjee, D., Bhabak, K.P., Mukhopadhyay, S. (2019), Novel approach to generate a self-deliverable Ru (II)-based anticancer agent in the self-reacting confined gel space, *ACS appl. Mater. interfaces*, 11, 47606-47618 (DOI: 10.1021/acsami.9b17075)
- [106] Sarkar, K., Dastidar, P. (2019), Rational approach towards designing metallogels from a urea-functionalized pyridyl dicarboxylate: anti-inflammatory, anticancer, and drug delivery, *Chem. Asian J.*, 14, 194-204 (DOI: 10.1002/asia.201801462)
- [107] Wei, C.W., Wang, X.J., Gao, S.Q., Wen, G.B., Lin, Y.W. (2019), A phenylalanine derivative containing a 4-pyridine group can construct both single crystals and a selective Cu-Ag bimetallohydrogel, *Eur. J. Inorg. Chem.*, 2019, 1349-1353 (DOI: 10.1002/ejic.201900078)
- [108] Horike S., Dincă M., Tamaki K., Long J. R. (2008), Size-selective Lewis acid catalysis in a microporous metal-organic

- framework with exposed  $\text{Mn}^{2+}$  coordination sites, *J. Am. Chem. Soc.*, 130, 5854–5855 (DOI: 10.1021/ja800669j)
- [109] Mota A. J., Rodríguez-Diéguez A., Palacios M. A., Herrera J. M., Luneau D., Colacio E. (2010), Theoretical and experimental study of the effectiveness of the 5-pyrimidyl-tetrazolate bridging ligand in mediating magnetic exchange interactions, *Inorg. Chem.*, 49, 8986-8996 (DOI: 10.1021/ic101322s)
- [110] Malviya, N., Ranjan, R., Sonkar, C., Mobin, S.M., Mukhopadhyay, S. (2019), Self-healable lanthanoid-based metallogels: dye removal and crystallization in the confined gel state, *ACS Appl. Nano Mater.*, 2, 8005-8015 (DOI: 10.1021/acsnm.9b02064)
- [111] Lee J. H., Baek Y. E., Kim K. Y., Choi H., Jung J. H. (2016), Metallogel of bis (tetrazole)-appended pyridine derivative with  $\text{CoBr}_2$  as a chemoprobe for volatile gases containing chloride atom, *Supramol. Chem.*, 28, 870-873 (DOI: 10.1080/10610278.2016.1142088)
- [112] Voitekhovich S. V., Wolf A., Guhrenz C., Lyakhov A. S., Ivashkevich L. S., Adam M., Gaponik N., Kaskel S., Eychmüller A. (2016), 5-(2-Mercaptoethyl)-1H-tetrazole: Facile synthesis and application for the preparation of water-soluble nanocrystals and their gels, *Chem. Eur. J.*, 22, 14746-14752 (DOI: 10.1002/chem.201602980)
- [113] Yan L., Liu C., Shen L., Li J., Liu X., Lv M., Su C., Ye Z. (2018), Visual discrimination of 2-picolinic acid by a supramolecular metallogel, *Chem. Lett.*, 47,640-642 (DOI:10.1246/cl.180065)
- [114] Howlader P., Mukherjee P.S. (2016), Face and edge directed self-assembly of  $\text{Pd}_{12}$  tetrahedral nano-cages and their self-sorting, *Chem. Sci.*, 7, 5893-5899 (DOI: 10.1039/c6sc02012g)
- [115] Lee J. H., Kang S., Lee J. Y., Jung J. H. (2012), A tetrazole-based metallogel induced with  $\text{Ag}^+$  ion and its silver nanoparticle in catalysis, *Soft Matter*, 8, 6557- 6563 (DOI: 10.1039/C2SM25316J)

- [116] Guo M., Yin Q., Li Y., Huang Y., Zhang Z., Zhou L. (2017), Gel-crystal transition during crystallization of cefpiramide, *Chem. Lett*, 46, 1292-1295 (DOI:10.1246/cl.170465)
- [117] Häring, M., Nandi, S.K., Rodríguez-López, J., Haldar, D., Martín, V.S., Lozano-Gorrín, A.D., Saldías, C., Díaz, D.D. (2019), 5-(1 H-1, 2, 3-Triazol-5-yl) isophthalic acid: A versatile ligand for the synthesis of new supramolecular metallogels, *ACS omega*, 4, 2111-2117 (DOI: 10.1021/acsomega.8b03292)
- [118] Zhu, G., Dordick, J.S. (2006), Solvent effect on organogel formation by low molecular weight molecules, *Chem. Mater.*, 18, 5988-5995 (DOI: 10.1021/cm0619297)
- [119] Edwards, W., Lagadec, C.A., Smith, D.K. (2011), Solvent-gelator interactions—using empirical solvent parameters to better understand the self-assembly of gel-phase materials, *Soft Matter*, 7, 110-117 (DOI: 10.1039/C0SM00843E)
- [120] Malviya N., Sonkar C., Kundu B. K., Mukhopadhyay S. (2018), Discotic organic gelators in ion sensing, metallogel formation and bioinspired catalysis, *Langmuir*, 34, 11575-11585 (DOI: 10.1021/acs.langmuir.8b02352)
- [121] Malviya N., Das M., Mandal P., Mukhopadhyay S. (2017), A smart organic gel template as metal cation and inorganic anion sensor, *Soft Matter*, 13, 6243-6249 (DOI: 10.1039/C7SM01199G)
- [122] Kyarikwal, R., Malviya, N., Chakraborty, A., Mukhopadhyay, S. (2021), Preparation of tris-tetrazole-based metallogels and stabilization of silver nanoparticles: studies on reduction catalysis and self-healing property, *ACS Appl. Mater. Interfaces*, 13, 59567-59579 (DOI: 10.1021/acsomega.1c19217)
- [123] Kyarikwal, R., Kundu, B.K., Chakraborty, A., Mukhopadhyay, S. (2022), A tris-tetrazole based nanostructured soft material: Studies on self-healing, AIEE, and rheological and fluorometric detection of 3-aminopyridine, *Mater. Chem. Front.*, 6, 2835-2847 (DOI: 10.1039/D2QM00520D)

- [124] Panja, S., Adams, D.J. (2021), Stimuli responsive dynamic transformations in supramolecular gels, *Chem. Soc. Rev.*, 50, 5165-5200 (DOI: 10.1039/D0CS01166E)
- [125] Gole, B., Shanmugaraju, S., Bar, A.K., Mukherjee, P.S. (2011), Supramolecular polymer for explosives sensing: role of H-bonding in enhancement of sensitivity in the solid state, *Chem. Commun.*, 47, 10046-10048 (DOI: 10.1039/C1CC13925H)
- [126] Ghosh, D., Deepa, Damodaran, K.K. (2020), Metal complexation induced supramolecular gels for the detection of cyanide in water, *Supramol. Chem.*, 32, 276-286 (DOI: 10.1080/10610278.2020.1751845)
- [127] Yin, Z.Y., Hu, J.H., Fu, Q.Q., Gui, K., Yao, Y. (2019), A novel long-alkyl-chained acylhydrazone-based supramolecular polymer gel for the ultrasensitive detection and separation of multianalytes, *Soft Matter*, 15, 4187-4191 (DOI: 10.1039/C9SM00624A)
- [128] Panja, S., Panja, A., Ghosh, K. (2021), Supramolecular gels in cyanide sensing: A review, *Mater. Chem. Front.*, 5, 584-602 (DOI: 10.1039/D0QM00551G)
- [129] Miao, W., Zhang, L., Wang, X., Qin, L., Liu, M. (2013), Gelation-induced visible supramolecular chiral recognition by fluorescent metal complexes of quinolinol-glutamide, *Langmuir*, 29, 5435-5442 (DOI: 10.1021/la400562f)
- [130] Lakshmi, N.V., Mandal, D., Ghosh, S., Prasad, E. (2014), Multi-stimuli-responsive organometallic gels based on ferrocene-linked poly (Aryl Ether) dendrons: reversible redox switching and Pb<sup>2+</sup>-ion sensing, *Chem. Eur. J.*, 20, 9002-9011 (DOI: 10.1002/chem.201400241)
- [131] Biswas, P., Ganguly, S., Dastidar, P. (2018), Stimuli-responsive metallogels for synthesizing Ag nanoparticles and sensing hazardous gases, *Chem. Asian J.*, 13, 1941-1949 (DOI: 10.1002/asia.201800743)

- [132] Yang, Y., Liu, W., Zhong, Q., Zhang, J., Yao, B., Lian, X., Niu, H. (2021), Self-assembly of lanthanide-based metallogel nanoplates into microcubic blocks as self-calibrating luminescent methanol sensors, *ACS Appl. Nano Mater.*, 4, 4735-4745 (DOI: 10.1021/acsnm.1c00343)
- [133] Li, Z.H., Yang, H.L., Adam, K.M., Yao, H., Wei, T.B., Zhang, Y.M., Lin, Q. (2021), Theoretical and experimental insights into the self-assembly and ion response mechanisms of tripodal quinolinamido-based supramolecular organogels, *Chem. Plus. Chem.*, 86, 146-154 (DOI: 10.1002/cplu.202000789)
- [134] Wang, B., Li, J., Shui, S., Xu, J. (2021), An acylhydrazone-based AIE organogel for the selective sensing of submicromolar level  $Al^{3+}$  and Al (iii)-based metallogel formation to detect oxalic acid, *New J. Chem.*, 45, 1899-1903 (DOI: 10.1039/C9NJ06340D)
- [135] Zhao, Q., Gong, G.F., Yang, H.L., Zhang, Q.P., Yao, H., Zhang, Y.M., Lin, Q., Qu, W.J., Wei, T.B. (2020), Pillar [5] arene-based supramolecular AIE hydrogel with white light emission for ultrasensitive detection and effective separation of multianalytes, *Polym. Chem.*, 11, 5455-5462 (DOI: 10.1039/D0PY00872A)
- [136] Ma, Y., Cametti, M., Džolić, Z., Jiang, S. (2019), Selective Cu (ii) sensing by a versatile AIE cyanostilbene-based gel system, *Soft Matter*, 15, 6145-6150 (DOI: 10.1039/C9SM00955H)
- [137] Mohar, M. (2019), A metallogel based on a zwitterionic spirocyclic meisenheimer complex: Sensing of fluoride ions in water and moisture content in organic solvents, *Chem. Select*, 4, 5308-5314 (DOI: 10.1002/slct.201900939)
- [138] Lin, Q., Zhu, X., Fu, Y.P., Zhang, Y.M., Fang, R., Yang, L.Z., Wei, T.B. (2014), Rationally designed anion-responsive-organogels: sensing  $F^-$  via reversible color changes in gel-gel

- states with specific selectivity, *Soft Matter*, 10, 5715-5723 (DOI: 10.1039/C4SM00841C)
- [139] Wen, G.Y., Zhou, X.L., Tian, X.Y., Xie, R., Ju, X.J., Liu, Z., Faraj, Y., Wang, W., Chu, L.Y. (2022), Smart hydrogels with wide visible color tunability, *NPG Asia Mater.*, 14, 29 (DOI: 10.1038/s41427-022-00379-3)
- [140] Nakamitsu, M., Imai, H., Oaki, Y. (2019), Visualization and quantification of microwaves using thermoresponsive color-change hydrogel, *ACS sensors*, 5, 133-139 (DOI: 10.1021/acssensors.9b01900)
- [141] Mukhopadhyay, P., Iwashita, Y., Shirakawa, M., Kawano, S.I., Fujita, N., Shinkai, S. (2006), Spontaneous colorimetric sensing of the positional isomers of dihydroxynaphthalene in a 1D organogel matrix, *Angew. Chem.*, 118, 1622-1625 (DOI: 10.1002/ange.200503158)
- [142] Shi, J., Shen, W., Wang, X., Li, M., Zhang, Y., Xu, P., Li, X., (2023), Simultaneous detection of naphthol isomers with a 3D-graphene-nanostructure-based electrochemical microsensor, *Chemosensors*, 11, 217 (DOI: 10.3390/chemosensors11040217)
- [143] Chattopadhyay, D., Nandi, S.K., Haldar, D. (2022), The impact of the isomerism of peptide mimetics on their assembly and properties: quick and onsite gas phase detection of acids and alcohols, *Mater. Adv.*, 3, 2117-2122 (DOI: 10.1039/D1MA00992C)
- [144] Zhao Z., Lam J. W., Tang B. Z. (2013), Self-assembly of organic luminophores with gelation-enhanced emission characteristics, *Soft Matter*, 9, 4564-4579 (DOI: 10.1039/C3SM27969C)
- [145] Babu S. S., Praveen V. K., Ghosh A. (2014), Functional  $\pi$ -gelators and their applications, *Chem. Rev.*, 114, 1973-2129 (DOI: 10.1021/cr400195e)
- [146] Chen H., Feng Y., Deng G. J., Liu Z. X., He Y. M., Fan Q. H. (2015), Fluorescent dendritic organogels based on 2-(2'-

- Hydroxyphenyl) benzoxazole: Emission enhancement and multiple stimuli-responsive properties, *Chem.-Eur. J.*, 21, 11018-11028 (DOI: 10.1002/chem.201500849)
- [147] Lin Q., Lu T. T., Zhu X., Wei T. B., Li H., Zhang Y. M. (2016), Rationally introduce multi-competitive binding interactions in supramolecular gels: A simple and efficient approach to develop a multi-analyte sensor array, *Chem. Sci.*, 7, 5341-5346 (DOI: 10.1039/C6SC00955G)
- [148] Xue P., Ding J., Shen Y., Gao H., Zhao J., Sun J., Lu R. (2017), Aggregation induced emission nanofiber as dual sensor for aromatic amine and acid vapor, *J. Mater. Chem. C*, 5, 11532-11541 (DOI: 10.1039/C7TC03192K)
- [149] Lee J. H., Baek Y. E., Kim K. Y., Choi H., Jung J. H. (2016), Metallogel of bis (tetrazole)-appended pyridine derivative with  $\text{CoBr}_2$  as a chemoprobe for volatile gases containing chloride atom, *Supramol. Chem.*, 28, 870-873 (DOI: 10.1080/10610278.2016.1142088)
- [150] Hyeoná Kim B. (2006), An insulin-sensing sugar-based fluorescent hydrogel, *Chem. Commun.*, 1842-1844 (DOI: 10.1039/B516632B)
- [151] Feldner T., Häring M., Saha S., Esquena J., Banerjee R., Díaz D. D. (2016), Supramolecular metallogel that imparts self-healing properties to other gel networks, *Chem. Mater*, 28, 3210-3217 (DOI: 10.1021/acs.chemmater.6b01144)
- [152] Bekas, D. G., Tsirka, K., Baltzis, D., Paipetis, A. S. (2016), Self-healing materials: A review of advances in materials, evaluation, characterization and monitoring techniques, *Compos. Part B*, 87, 92– 119 (DOI: 10.1016/j.compositesb.2015.09.057)
- [153] Thakur, V. K., Kessler, M. R. (2015), Self-healing polymer nanocomposite materials: A Review, *Polymer*, 69, 369–38 (DOI: 10.1016/j.polymer.2015.04.086)

- [154] Roy, N., Bruchmann, B., Lehn, J.-M. (2015), Dynamers: dynamic polymers as self-healing materials, *Chem. Soc. Rev.*, 44, 3786–3807 (DOI: 10.1039/C5CS00194C)
- [155] An, S. Y., Arunbabu, D., Noh, S. M., Song, Y. K., Oh, J. K. (2015), Recent strategies to develop self-healable crosslinked polymeric networks, *Chem. Commun.* 51, 13058–13070 (DOI: 10.1039/C5CC04531B)
- [156] Zhang, M., Xu, D., Yan, X., Chen, J., Dong, S., Zheng, B., Huang, F. (2012), Self-healing supramolecular gels formed by crown ether-based host-guest interactions, *Angew. Chem., Int. Ed.*, 51, 7011–7015 (DOI: 10.1002/anie.201203063)
- [157] Ghosh, S.K. (2009), *Self-healing materials: fundamentals, design strategies, and applications*, Weinheim: Wiley-vch, 18, 1-28 (DOI:10.1002/9783527625376)
- [158] Holten-Andersen, N., Harrington, M. J., Birkedal, H., Lee, B. P., Messersmith, P. B., Lee, K. Y. C., Waite, J. H. (2011), PH-induced metal ligand cross-links inspired by mussel yield self-healing polymer networks with near-covalent elastic moduli, *Proc. Natl. Acad. Sci. U. S. A.*, 108, 2651–2655 (DOI: 10.1073/pnas.1015862108)
- [159] Kolmakov, G. V., Revanur, R., Tangirala, R., Emrick, T., Russell, T. P., Crosby, A. J., Balazs, A. C. (2010), Using nanoparticle-filled microcapsules for site-specific healing of damaged substrates: creating a “Repair-and-Go” system, *ACS Nano*, 4, 1115–1123 (DOI: 10.1021/nn901296y)
- [160] Cho, S. H., Braun, P. V., White, S. R. (2009), Self-healing polymer coatings, *Adv. Mater.*, 21, 645–649 (DOI: 10.1002/adma.200802008)
- [161] Burnworth, M., Tang, L., Kumpfer, J. R., Duncan, A. J., Beyer, F. L., Fiore, G. L., Rowan, S. J., Weder, C. (2011), Optically healable supramolecular polymers, *Nature*, 472, 334–337 (DOI: 10.1038/nature09963)

- [162] Cordier, P., Tournilhac, F., Soulie-Ziakovic, C., Leibler, L. (2008), Self-healing and thermoreversible rubber from supramolecular assembly, *Nature*, 451, 977–980 (DOI: 10.1038/nature06669)
- [163] Yao, L., Rong, M. Z., Zhang, M. Q., Yuan, Y. C. (2011), Self-healing of thermoplastics via reversible addition–fragmentation chain transfer polymerization, *J. Mater. Chem.*, 21, 9060–9065 (DOI: 10.1039/C1JM10655D)
- [164] Asoh, T., Kikuchi, A. (2012), Rapid fabrication of reconstructible hydrogels by electrophoretic microbead adhesion, *Chem. Commun.* 48, 10019–10021 (DOI: 10.1039/C2CC35634A)
- [165] Karan, C.K., Bhattacharjee, M. (2016), Self-healing and moldable metallogels as the recyclable materials for selective dye adsorption and separation, *ACS Appl. Mater. Interfaces*, 8, 5526–5535 (DOI: 10.1021/acsami.5b09831)
- [166] Hager M. D., Greil P., Leyens C., van der Zwaag, S., Schubert U. S. (2010), Self-healing materials, *Adv. Mater.*, 22, 5424–5430 (DOI:10.1002/adma.201003036)
- [167] Wen, N., Song, T., Ji, Z., Jiang, D., Wu, Z., Wang, Y., Guo, Z. (2021), Recent advancements in self-healing materials: Mechanicals, performances and features, *React. Funct. Polym.*, 168, 105041 (DOI: 10.1016/j.reactfunctpolym.2021.105041)
- [168] Basak, S., Nanda, J., Banerjee, A. (2014), Multi-stimuli responsive self-healing metallo-hydrogels: tuning of the gel recovery property, *Chem. Commun.*, 50, 2356–2359 (DOI: 10.1039/C3CC48896A)
- [169] Krogsgaard, M., Behrens, M.A., Pedersen, J.S., Birkedal, H. (2013), Self-healing mussel-inspired multi-pH-responsive hydrogels, *Biomacromolecules*, 14, 297–301 (DOI: 10.1021/bm301844u)

- [170] Zhang, Y., Yang, B., Zhang, X., Xu, L., Tao, L., Li, S., Wei, Y. (2012), A magnetic self-healing hydrogel, *Chem. Commun.*, 48, 9305-9307 (DOI: 10.1039/C2CC34745H)
- [171] Shi, Y., Wang, M., Ma, C., Wang, Y., Li, X., Yu, G. (2015), A conductive self-healing hybrid gel enabled by metal–ligand supramolecule and nanostructured conductive polymer, *Nano letters*, 15, 6276-6281 (DOI: 10.1021/acs.nanolett.5b03069)
- [172] Shafiq, Z., Cui, J., Pastor-Pérez, L., San Miguel, V., Gropeanu, R.A., Serrano, C., del Campo, A. (2012), Bioinspired underwater bonding and debonding on demand, *Angew. Chem., Int. Ed.*, 51, 4332-4335 (DOI: 10.1002/ange.201108629)
- [173] Yuan, J., Fang, X., Zhang, L., Hong, G., Lin, Y., Zheng, Q., Xu, Y., Ruan, Y., Weng, W., Xia, H., Chen, G. (2012), Multi-responsive self-healing metallo-supramolecular gels based on “click” ligand, *J. Mater. Chem.*, 22, 11515-11522 (DOI: 10.1039/C2JM31347B)
- [174] Yang, B., Zhang, H., Peng, H., Xu, Y., Wu, B., Weng, W., Li, L. (2014), Self-healing metallo-supramolecular polymers from a ligand macromolecule synthesized via copper-catalyzed azide–alkyne cycloaddition and thiol–ene double “click” reactions, *Polym. Chem.*, 5, 1945-1953 (DOI: 10.1039/C3PY00975K)
- [175] Yuan, J., Fang, X., Zhang, L., Hong, G., Lin, Y., Zheng, Q., Xu, Y., Ruan, Y., Weng, W., Xia, H., Chen, G. (2012), Multi-responsive self-healing metallo-supramolecular gels based on “click” ligand. *J. Mater. Chem.*, 22, 11515-11522 (DOI: 10.1039/C2JM31347B)
- [176] Zhang, M., Xu, D., Yan, X., Chen, J., Dong, S., Zheng, B., Huang, F. (2012), Self-healing supramolecular gels formed by crown ether-based host–guest interactions, *Angew. Chem. Int. Ed.*, 51, 7011-7015 (DOI: 10.1002/anie.201203063)
- [177] Yan, L., Gou, S., Ye, Z., Zhang, S., Ma, L. (2014), Self-healing and moldable material with the deformation recovery ability

- from self-assembled supramolecular metallogels, *Chem. Commun.*, 50, 12847-12850 (DOI: 10.1039/C4CC06154C)
- [178] Martínez-Calvo M., Kotova O., Möbius M. E., Bell A. P., McCabe T., Boland J. J., Gunnlaugsson T. (2015), Healable luminescent self-assembly supramolecular metallogels possessing lanthanide (Eu/Tb) dependent rheological and morphological properties, *J. Am. Chem. Soc.*, 137, 1983-1992 (DOI: 10.1021/ja511799n)
- [179] Haering M., Díaz, D. D. (2016), Supramolecular metallogels with bulk selfhealing properties prepared by in situ metal complexation, *Chem. Commun.*, 52, 13068-13081 (DOI: 10.1039/c6cc06533c)
- [180] Okesola, B.O., Smith, D.K. (2016), Applying low-molecular weight supramolecular gelators in an environmental setting—self-assembled gels as smart materials for pollutant removal, *Chem. Soc. Rev.*, 45, 4226-4251 (DOI: 10.1039/C6CS00124F)
- [181] Gupta, A., Sharma, V., Sharma, K., Kumar, V., Choudhary, S., Mankotia, P., Kumar, B., Mishra, H., Moulick, A., Ekielski, A., Mishra, P.K. (2021), A review of adsorbents for heavy metal decontamination: Growing approach to wastewater treatment, *Materials*, 14, 4702 (DOI: 10.3390/ma14164702)
- [182] De, A., Mondal, R. (2018), Toxic metal sequestration exploiting a unprecedented low-molecular-weight hydrogel-to-metallogel transformation, *ACS omega*, 3, 6022-6030 (DOI: 10.1021/acsomega.8b00758)
- [183] Okesola, B.O., Smith, D.K. (2016), Applying low-molecular weight supramolecular gelators in an environmental setting—self-assembled gels as smart materials for pollutant removal, *Chem. Soc. Rev.*, 45, 4226-4251 (DOI: 10.1039/C6CS00124F)
- [184] Kumar, A., Das, T., Thakur, R.S., Fatima, Z., Prasad, S., Ansari, N.G., Patel, D.K. (2022), Synthesis of biomass-derived activated

- carbons and their immobilization on alginate gels for the simultaneous removal of Cr (VI), Cd (II), Pb (II), As (III), and Hg (II) from water, *ACS omega*, 7, 41997-42011 (DOI: 10.1021/acsomega.2c03786)
- [185] Yang, H.L., Sun, X.W., Zhang, Y.M., Wang, Z.H., Zhu, W., Fan, Y.Q., Wei, T.B., Yao, H., Lin, Q. (2019), A bi-component supramolecular gel for selective fluorescence detection and removal of Hg<sup>2+</sup> in water, *Soft Matter*, 15, 9547-9552 (DOI: 10.1039/C9SM01652J)
- [186] Huang J., He L., Zhang J., Chen L., Su C. Y. (2010), Dynamic functionalised metallogel: An approach to immobilised catalysis with improved activity, *J. Mol. Catal. A: Chem.*, 317, 97-103 (DOI: 10.1016/j.molcata.2009.11.001)
- [187] Mallick A., Schön E. M., Panda T., Sreenivas K., Díaz D. D., Banerjee R. (2012), Fine-tuning the balance between crystallization and gelation and enhancement of CO<sub>2</sub> uptake on functionalized calcium-based MOFs and metallogels, *J. Mater. Chem*, 22, 14951-14963 (DOI: 10.1039/C2JM30866E)
- [188] Tang X. Q., Xiao B. W., Li C. M., Wang D. M., Huang C. Z., Li Y. F. (2017), Co-metal-organic-frameworks with pure uniform crystal morphology prepared via Co<sup>2+</sup> exchange-mediated transformation from Zn-metallogels for luminol catalysed chemiluminescence, *Spectrochim. Acta Part A*, 175, 11-16 (DOI: 10.1016/j.saa.2016.12.014)
- [189] Klabunde T., Eicken C., Sacchettini J. C., Krebs B. (1988), Crystal structure of a plant catechol oxidase containing a dicopper center, *Nat. Struct. Mol. Biol*, 5, 1084-1090 (DOI: 10.1038/4193).
- [190] López-Viveros, M., Favier, I., Gómez, M., Lahitte, J.F., Remigy, J.C. (2021), Remarkable catalytic activity of polymeric membranes containing gel-trapped palladium nanoparticles for hydrogenation reactions, *Catal. Today*, 364, 263-269 (DOI: 10.1016/j.cattod.2020.04.027)

- [191] Fang, W., Zhang, Y., Wu, J., Liu, C., Zhu, H., Tu, T. (2018), Recent advances in supramolecular gels and catalysis, *Chem. Asian J.*, 13, 712-729 (DOI: 10.1002/asia.201800017)
- [192] Sharma, M., Sarma, P.J., Goswami, M.J., Bania, K.K. (2017), Metallogel templated synthesis and stabilization of silver-particles and its application in catalytic reduction of nitro-arene, *J. Colloid Interface Sci.*, 490, 529-541 (DOI: 10.1016/j.jcis.2016.11.065)
- [193] Baran, T., Nasrollahzadeh, M. (2019), Facile synthesis of palladium nanoparticles immobilized on magnetic biodegradable microcapsules used as effective and recyclable catalyst in Suzuki-Miyaura reaction and p-nitrophenol reduction, *Carbohydr. Polym.*, 222, 115029 (DOI: 10.1016/j.carbpol.2019.115029)

## **Chapter 2**

### **Preparation of tris-tetrazole-based metallogels and stabilization of silver nanoparticles: studies on reduction catalysis and self-healing property**



## Chapter 2

### Preparation of tris-tetrazole-based metallogels and stabilization of silver nanoparticles: studies on reduction catalysis and self-healing property

#### 2.1 Introduction

Material science is a developing field where the formation of materials continuously focuses on its targeted synthesis towards the applications with an easy, fast, and economically suitable system. From this point of view, soft materials can be an appropriate class of candidates for fabricating advanced materials as they have tunable physical, chemical, and biological properties.<sup>[1-12]</sup> Although LMWGs have applications in various fields, introducing metal ions or metal nanoparticles within the gel network influences several properties, including gel strength, stability, and other physical and chemical properties. This chapter focuses on introducing metal ions and stabilizing silver nanoparticles within carboxamide-tetrazole gelator molecule **G7**. There are not many reports where nanoparticles are stabilized within a gel matrix. Only a few reports are found,<sup>[13-16]</sup> and furthermore, the use of nanoparticles containing metallogels in the field of catalysis is still rare.<sup>[17]</sup> In this chapter, a tetrazole-based gelator molecule is designed to incorporate metal ions to form metallogels and stabilize metal nanoparticles. Tetrazoles are versatile ligands with diverse coordination modes and gelation properties.<sup>[18, 19]</sup> Reports show tetrazoles can be used to stabilize metal nanoparticles.<sup>[20]</sup> In this work, the carboxamide and tris-tetrazole-based gelator molecule **G7** is used for metallogels formation and dual metal system formation by stabilizing silver nanoparticles within metallogel matrix. For this, a series of metallogels **M<sup>1</sup>G7** (Fe(III)G7), **M<sup>2</sup>G7** (Co(II)G7), **M<sup>3</sup>G7** (Cu(II)G7), **M<sup>4</sup>G7** (Zn(II)G7), **M<sup>5</sup>G7** (Ag(I)G7), **M<sup>6</sup>G7** (Ni(II)G7), and **M<sup>7</sup>G7** (Fe(II)G7) have been fabricated, and their properties are investigated. Certain metallogels are found to be capable of stabilizing silver nanoparticles in situ.

Further, the synthesized AgNPs within the **M<sup>1</sup>G7** network as an **M<sup>1</sup>G7AgNP** nanocomposite has been found to be an effective catalyst for the reduction of nitroaromatics. This **M<sup>1</sup>G7AgNPs** nanocomposite can be further converted into a nanostructured metallogel, which has been investigated for its self-healing property. The organogel **G7** has been tested for its ability to absorb certain transition-metal ions from aqueous solutions.

## **2.2 Experimental section**

### **2.2.1 Material and method**

Used chemicals and solvents were obtained from commercial sources and utilized directly. Each experiment was performed in dimethyl sulfoxide/N,N-dimethylformamide (DMSO/DMF)/MQ-water, or a combination of solvents. Fourier transform infrared (FTIR) analysis was carried out on KBr pellets in a Bruker tensor 27 FTIR spectrophotometer. NMR spectra were obtained by an AVANCE III 400 Ascend Bruker Biospin machine at an ambient temperature using DMSO-d<sup>6</sup>. For electrospray ionization mass spectrometry (ESI-MS) mass data, a Bruker Daltonics micro TOF-QII was used. Morphological data of the gels were recorded in Supra55 Zeiss field emission scanning electron microscopy (FE-SEM). For the data of the surface area, pore volume, and pore size, a Quantachrome, Autosorb iQ2 Brunauer–Emmett–Teller (BET) surface area analyzer was used. The reduction reactions of the nitro group with various substituents were monitored in a quartz cuvette (10 × 10 mm<sup>2</sup>) using a Varian carry 100 Bio UV–vis spectrophotometer. The morphology and size analysis of nanoparticles inside the nanostructured metallogel was performed by transmission electron microscopy (TEM) (PHILIPS CM 200). The iron and silver nanoparticles in the nanocomposite were detected by an X-ray photoelectron (XPS) spectrometer equipped with a Scienta-R4000 electron energy analyzer with a total instrumental resolution of 400 meV.

### 2.2.2 Synthesis of gelator molecule **G7** [triethylammonium 5-(3,5-bis((1H-tetrazol-5-yl) carbamoyl) benzamido)tetrazol-1-ide]

For the synthesis of **G7**, 1.44 g (14 mmol) of 5-aminotetrazole monohydrate and 1.95 mL (14 mmol) of triethylamine were taken in dry dichloromethane (DCM) (40 mL), and the mixture was added dropwise into a  $\text{CHCl}_3$  solution (40 mL) of trimesoyl chloride (1.06 g, 4 mmol) at 0 °C. The reaction mixture was stirred overnight. After completion of the reaction, the precipitate obtained was filtered off, washed with water and methanol, and dried at room temperature under a vacuum. The product formed was the ionic gelator **G7** as one triethylammonium cation remains as a counter ion in one of the tetrazole arms, which gets converted into tetrazolate. Product: yield: 64.5%.  $^1\text{H}$  NMR of **G7** (400.13 MHz, 298 K,  $\text{DMSO-d}_6$ ):  $\delta$  9.05 (3H, amide, s), 9.00 (3H, aromatic, s), 8.75 (1H, triethylammonium, s), 3.15 (6H, triethylammonium, q), 1.22 (9H, triethylammonium, t).  $^{13}\text{C}$  NMR of **G7** (100.16 MHz, 298 K,  $\text{DMSO-d}_6$ ):  $\delta$  166.67 (amide), 164.66 (tetrazole), 151.16 (aromatic), 133.48 (aromatic), 46.22 (triethylammonium), 9.09 (triethylammonium). FTIR of **G7** (KBr): 3442.2, 3245.5, 3094.3, 1687.3, 1588.4, 1457.2, 1391, 1253.5  $\text{cm}^{-1}$ . ESI-MS:  $m/z$   $[\text{M}+\text{H}]^+$  calculated for **G7** ( $\text{C}_{18}\text{H}_{25}\text{N}_{16}\text{O}_3^+$ ): 513.23, found 513.34.

### 2.2.3 Gel Preparation

A total of 40 mM (41 mg) **G7** was taken in 1 mL of dimethyl sulfoxide or dimethylformamide in a glass vial, and 1 mL of Milli-Q water was added homogeneously to it. Within a minute, a stable organogel **G7** was formed instantaneously. For the preparation of metallogels, 40 mM **G7** was dissolved in 1 mL of DMSO, and a 40 mM aqueous solution of metal perchlorate salts (1:1 molar ratio) was added in a glass vial. Within a couple of minutes, stable metallogels Fe(III) (**M<sup>1</sup>G7**), Co(II) (**M<sup>2</sup>G7**), Cu(II) (**M<sup>3</sup>G7**), Zn(II) (**M<sup>4</sup>G7**), Ag(I) (**M<sup>5</sup>G7**), Ni(II) (**M<sup>6</sup>G7**), and Fe(II) (**M<sup>7</sup>G7**) were obtained.

Further, the formation of metallogels were taken up by absorption method. For this, the organogel prepared by the method mentioned

above. In that process 1 mL of 40 mM aqueous solution of metal perchlorate salt was taken in a glass vial, and the prepared gel bed of 2 mL organogel was added into it. After a day, the organogel absorbed metal ions from the solution and formed metallogel.

#### 2.2.4 Gel Melting Temperature

A silicon oil bath was used to detect the gel melting temperature ( $T_{\text{gel}}$ ) and the sol–gel transition behavior. For this experiment, a 15 mL glass vial was used, and the temperature was monitored by a thermometer. A total of 40 mM organogel and metallogels of **G7** (2 mL v/v of DMSO and H<sub>2</sub>O) were taken in a glass vial, a steel ball was placed on the gel surface, and the system was immersed in an oil bath. When the temperature started rising, and the gel started to melt (when downward moment of steel ball is seen), that temperature was noted down as the melting temperature of the gel ( $T_{\text{gel}}$ ). The heating stopped at this point. After 5 min, it was observed that the sol gets converted into a gel again. The gel melting point indicates the sol–gel transition temperature for the organogel and metallogels of **G7**.

#### 2.2.5 Formation of **M<sup>1</sup>G7AgNPs**.

To synthesize and stabilize Ag nanoparticles, 17 mg (0.02 M), 5 mL DMF solution of AgNO<sub>3</sub> was added into 0.5 g of metallogel, and the resultant mixture was refluxed at 80 °C for 12 hrs. After the completion of the reaction, it was found that silver nanoparticles get formed inside the **M<sup>1</sup>G7**, **M<sup>3</sup>G7**, **M<sup>4</sup>G7**, **M<sup>6</sup>G7**, and **M<sup>7</sup>G7**. At the end, a reddish-black precipitate was formed, which was filtered and AgNPs were obtained inside the powdered precipitate. However, the nanoparticle formation was further investigated only with the **M<sup>1</sup>G7** gel because of its ability to stabilize the nanoparticles with desirable sizes. After the formation of silver nanocomposites (**M<sup>1</sup>G7AgNPs**), it was found that iron is also present in the solid composite in a lower amount. FTIR and ESI-MS spectrometric data of **M<sup>1</sup>G7** were utilized to propose a probable structure of the metallogel. The morphology and composition of the

composite were explored by AFM, FE-SEM analysis, energy-dispersive X-ray analysis (EDX), and mapping.

### 2.2.6 Reduction catalysis by M<sup>1</sup>G7AgNPs.

Silver nitrate solution after treatment with M<sup>1</sup>G7, M<sup>3</sup>G7, M<sup>4</sup>G7, M<sup>6</sup>G7, and M<sup>7</sup>G7 formed M<sup>1</sup>G7AgNPs, M<sup>3</sup>G7AgNPs, M<sup>4</sup>G7AgNPs, M<sup>6</sup>G7AgNPs, and M<sup>7</sup>G7AgNPs composites. Among these, M<sup>1</sup>G7AgNPs were explored as a catalyst in reducing nitroaromatics to corresponding amines with different substituents. In a typical experiment, 0.1 mmol of the nitro substituent, 1 mmol of NaBH<sub>4</sub>, and 6 mg of the catalyst were suspended in 10 mL of Milli-Q water and stirred at room temperature. After 25–35 min of reaction, the reduction of the nitro group into the amine gets completed, and this was confirmed with UV–vis, <sup>1</sup>H NMR, and gas chromatography-mass spectrometry (GCMS) analyses. These data show the disappearance of the peak related to the nitro group and the appearance of the peak corresponding to the amine.

### 2.2.7 Conversion of AgNPs Containing Nanocomposite Material M<sup>1</sup>G7AgNPs into Nanostructured Metallogel.

A very small amount (1–2 mg) of M<sup>1</sup>G7AgNP nanocomposite powder was suspended in 1 mL of Milli-Q water, and it was added into 1 mL of DMSO solution of the (41 mg, 0.1 mmol) gelator G7. Immediately, the yellow-colored bimetallic nanostructured metallogel of M<sup>1</sup>G7AgNPs was formed.

### 2.2.8 Characterization

**UV-visible Spectroscopy.** Absorption spectra of synthesis and stabilization of silver nanoparticles and reduction reactions of nitroaromatic compounds have been analyzed by Varian Carry 100 Bio UV-vis spectrophotometer using a quartz cuvette (10×10 mm<sup>2</sup>).

**FT-IR Spectroscopy.** The synthesis of gelator molecules, fabrications of organogel and metallogels, and self-assembly of gels has been analyzed by the study of shifting in wavenumber of functional groups by Bruker (Tensor 27) FTIR spectrophotometer with the help of KBr

pellet. The formation of xerogel was done by solvent removal from gel pores without much disturbing the gel matrix. The drying procedure can affect the morphological analysis because it can change the self-assembled network. The range of wavenumber for the FTIR measurement has been taken around 500-4000  $\text{cm}^{-1}$  over 64 scans at a resolution of 4  $\text{cm}^{-1}$  and interval of 1  $\text{cm}^{-1}$ .

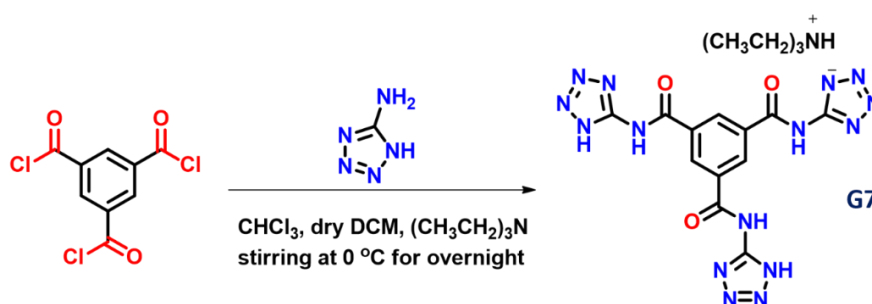
**Powder X-ray Diffraction (PXRD).** The synthesis of the silver nanocomposite, analysis of catalyst recovery, and presence of non-covalent interactions during the fabrication of organogel and metallogels has been studied by powder X-ray diffraction spectra (PXRD). It was taken with the help of Rigaku Smart Lab, an automated multipurpose X-ray diffractometer with Cu  $K\alpha$  source (the wavelength of X-rays was 0.154 nm) with a  $2\theta$  range of 10–50°, step size of 0.02°, and a scan speed of 3°/min.

**Morphological Study.** The morphological study and 3d transformation of gel fabrication, self-assembly of gelator components, and study of shape and size of silver nanoparticles have been done by field-emission scanning electron microscopy (FE-SEM, Carl Zeiss Microscope, model-Supra 55). For sample preparation, a small portion of the gel was spread on the glass slide, dried under vacuum, and subsequently coated (10 nm) with Cu. To keep the morphology undisturbed gel was dried on glass slide by controlled vacuum.

**Rheological Properties.** Oscillating rheology was used to obtain an insight into the mechanical aspects of the organogel and metallogels of **G7** with transition metal salts. The rheological measurements were conducted at 25 °C on an Anton Paar physica MCR 301 rheometer using a 25 mm parallel plate with a true gap of 0.5 mm. Measurement of viscoelasticity was done at 0.1% strain by measuring the storage ( $G'$ ) and loss ( $G''$ ) moduli. The strain-sweep experiment with time or the thixotropic behavior was investigated at minimum (0.5%) and maximum (100%) strains. For measurement, the gel was taken on the stage of the rheometer with the help of a spatula.

### 2.3 Results and discussion

In this work, two organic moieties, viz. carboxamide, and tetrazole, with significant propensities to form gels,<sup>[21, 22]</sup> are combined to synthesize a new ionic gelator molecule **G7**. The synthesis was done by amide bond formation between trimesoyl chloride with 3.5 equivalent of 5-aminotetrazole monohydrate in the presence of triethylamine (Scheme 2.1). The white precipitate obtained was washed with Milli-Q water and methanol and dried over a vacuum. The compound obtained was found to be an ionic gelator. The synthesis of **G7** was confirmed by <sup>1</sup>H and <sup>13</sup>C NMR, IR spectroscopy, CHN elemental analysis and ESI-MS.



**Scheme 2.1.** Systematic scheme for the synthesis of gelator **G7**.

The FTIR of **G7** shows the characteristic band at  $3442\text{ cm}^{-1}$  for carboxamide N–H, while  $1687\text{ cm}^{-1}$  reveals the carboxamide -CO stretching, and  $1588\text{ cm}^{-1}$  shows the presence of the tetrazole group (Figure 2.1). In <sup>1</sup>H NMR, aromatic protons were found at 9.00 ppm, and the peak obtained at 9.05 ppm was assigned to carboxamide protons. A broad peak with less intensity around 6.5 ppm indicates the presence of the tetrazole -NH protons. The peaks obtained at 8.75, 3.15, and 1.22 ppm were assigned to triethylammonium protons (Figure 2.2). In the <sup>13</sup>C NMR spectrum, peaks at 151 and 133 ppm confirm the presence of aromatic carbon. The peak obtained at 166 ppm is assigned to carboxamide carbon, at 164 ppm to tetrazole carbon, and at 46.22 and 9.09 ppm to triethylammonium carbon (Figure 2.3). The ESI-MS spectrum shows a molecular ion peak at  $513.34\text{ [M+H]}^+$  in the positive mode, confirming the synthesis of the ionic gelator **G7** (Figure 2.4). The

CHN elemental analysis has been done for **G7**. The calculated values for C, N, and H are 42.27 %, 43.82 %, 4.53 % respectively and the found values for C, N, and H are 42.06 %, 43.63 % and 4.31 % respectively.

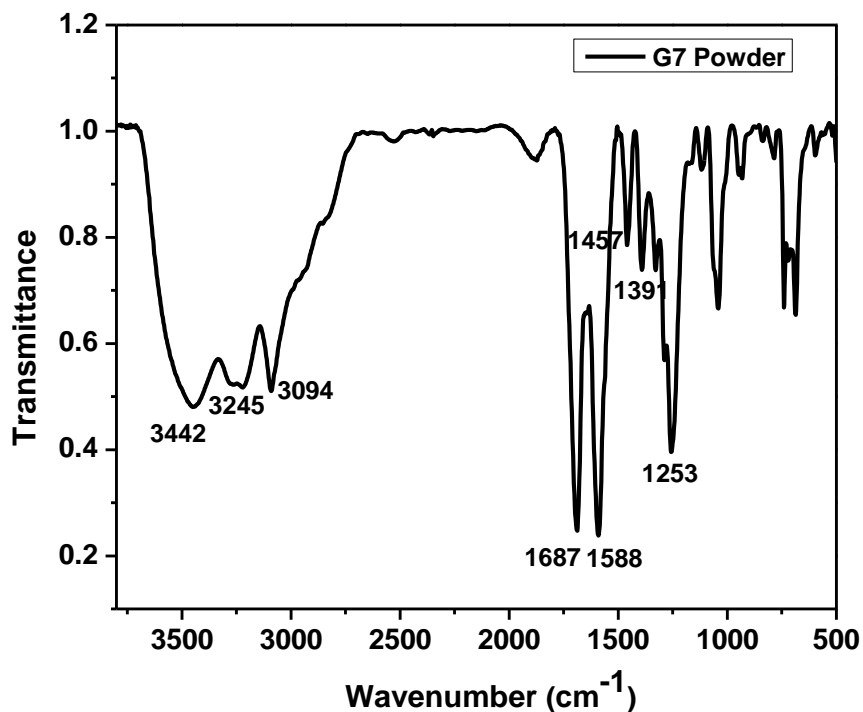


Figure 2.1. IR data of gelator powder **G7**.

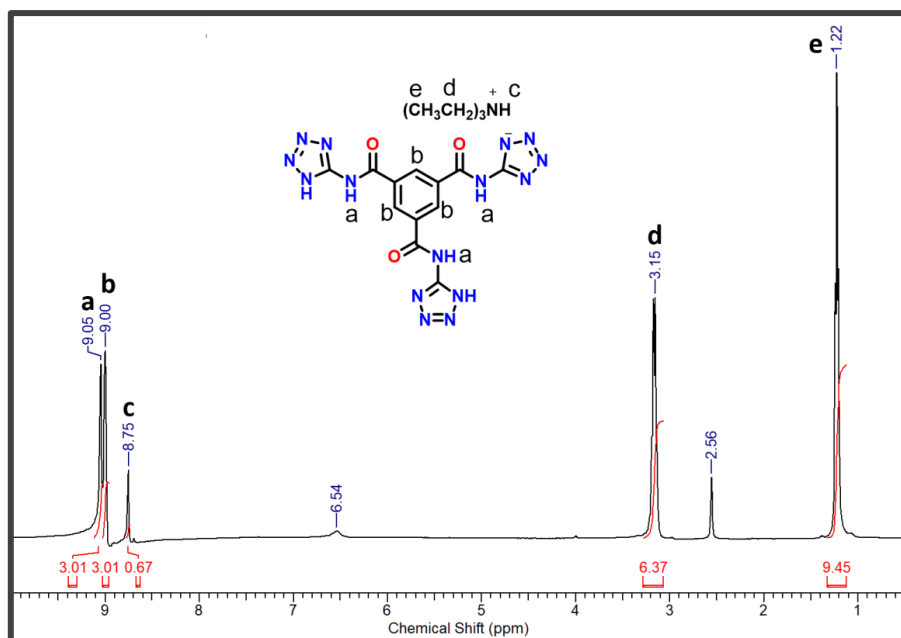


Figure 2.2. <sup>1</sup>H NMR of gelator **G7**.

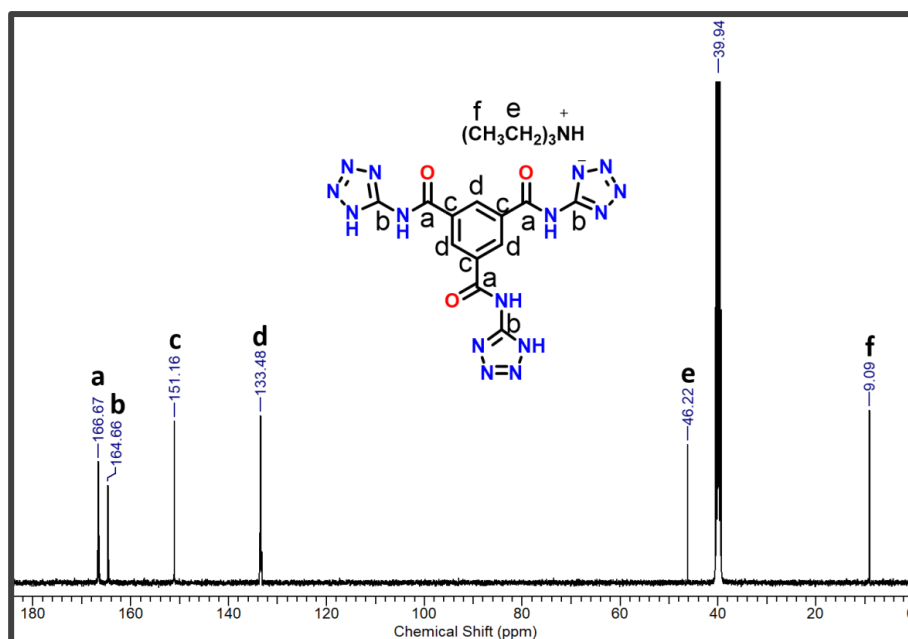


Figure 2.3.  $^{13}\text{C}$  NMR of gelator **G7**.

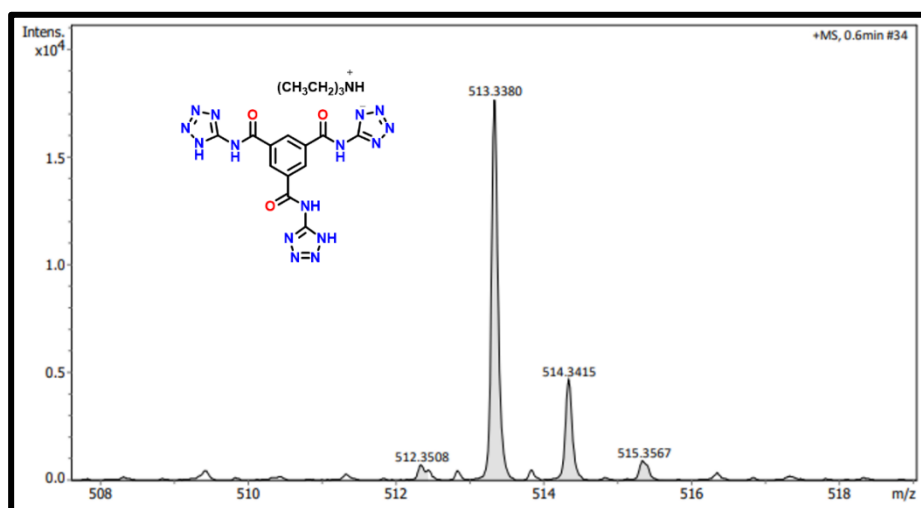


Figure 2.4. ESI-MS of gelator **G7** in positive mode.

**Gelation Behavior of G7 with 3d Metals.** The gelation behavior of **G7** was checked in different organic solvents. Gelator **G7** was found to be soluble in DMF and DMSO. Upon dropwise addition of 1 mL of water into a 1 mL solution of 40 mM of **G7** in DMSO or DMF, the organogel was formed. The critical gel concentration for the gelator molecule of **G7** was found to be 20 mM in a 1:1 ratio of DMSO or DMF and Milli-Q water (Table 2.1 and 2.2). Gel formation was confirmed by the typical “test tube inversion method” (Figure 2.5). The heating–cooling experiment of gel **G7** showed that the transition temperature ( $T_{\text{gel}}$ ) of the

gel-sol conversion is 100 °C, indicating that it is stable at room temperature.

**Table 2.1.** Gelator: 2.0 % (w/v) [CGCs = 20 mM in DMSO (or DMF) (1mL) / H<sub>2</sub>O (1mL) Mixture]; **G**: Gel; **S**: Soluble; **I**: Insoluble.

Solvent	Solubility	Gelation	Solvent	Solubility	Gelation
Cyclohexane	I	-	Toluene	I	-
THF	I	-	Methanol	I	-
N-Hexane	I	-	DMF	S	G
Acetone	I	-	Chloroform	I	-
Petroleum ether	I	-	Dichloromethane	I	-
Ethyl acetate	I	-	DMSO	S	G
Benzene	I	-	Ethanol	I	-

**Table 2.2.** Optimization table for gelation.

Concentration	DMF or DMSO	H <sub>2</sub> O	Gelation
40 mM	500 µL	1500 µL	Solution
	1500 µL	500 µL	Weak Gel
	1000 µL	1000 µL	Strong Gel
↓			
Concentration	DMF or DMSO/ H <sub>2</sub> O		Gelation
10 mM	1 mL/ 1mL		No
20 mM	1 mL/ 1mL		Yes (very weak gel)
30 mM	1 mL/ 1mL		Yes (weak gel)
40 mM	1 mL/ 1mL		Yes (strong gel)

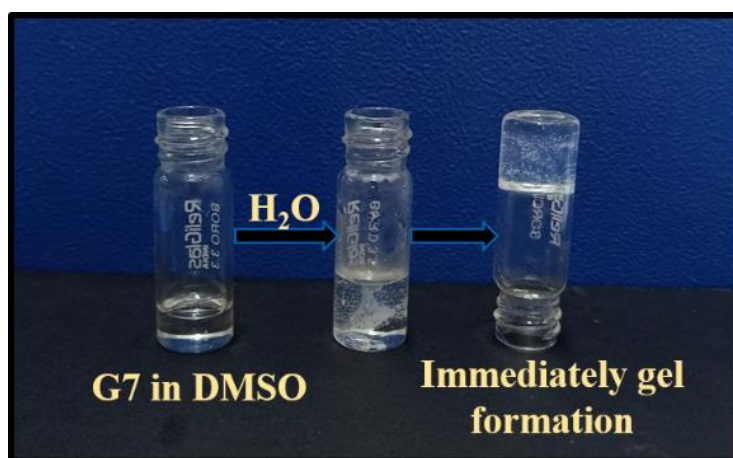


**Figure 2.5.** Confirmation of gel formation by test tube inversion method.

With the availability of so many electron-pair donating centers, it is a matter of interest to check the ability of **G7** to form metallogels with different transition metal ions as they can impart special properties in the gel, including catalysis, absorption, sensing, etc. **G7** was tested for the formation of metallogels with various metal perchlorate salts of 3d-metal ions. It was observed that among the different metal ions, it could form metallogels with perchlorate salts of Fe(III), Co(II), Cu(II), Zn(II), and Fe(II). Furthermore, it was also observed that Ag(I) could also produce metallogel with **G7**. Only nickel was the exception in the 3d-metal series from Fe to Zn, which does not form a metallogel with **G7** in this procedure. However, when an aqueous solution of metal perchlorate salt was taken in a glass vial and then organogel (**G7**) was placed inside the solution, within a day, the organogel absorbed metal ions from the solution and formed metallogels with Fe(III), Co(II), Cu(II), Zn(II), Ag(I), Fe(II), and even with Ni(II) (Figure 2.6). The heating–cooling experiment of a series of metallogels shows that the transition temperatures from the sol to the gel are in the range of 80–100 °C, indicating that all the metallogels are stable at room temperature.

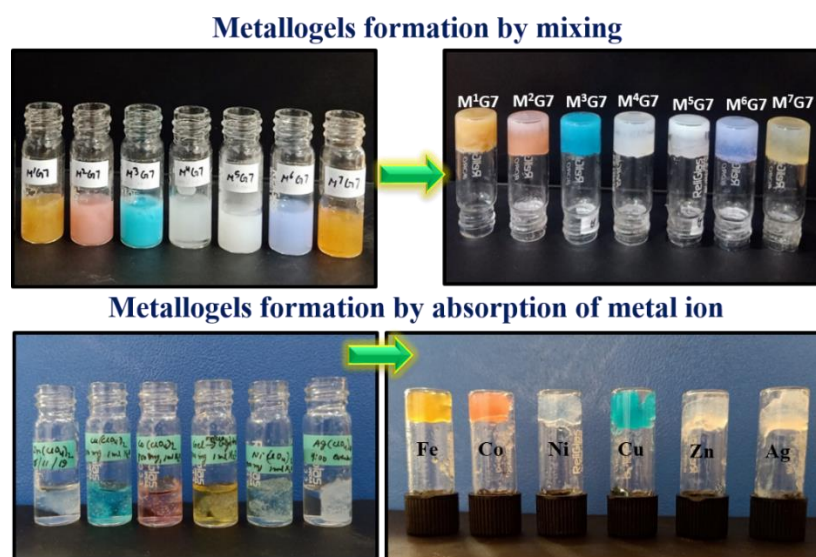


**Figure 2.6.** Formation of metallogels by mixing and by absorption of metal ions from aqueous solution.

**BET Analysis of Gelator Powder G7, Organogel G7, and Fe(III) Metallogel (M<sup>1</sup>G7).** Surface area and porosity are two important physical properties that may reveal the possibilities of utilizing gels in different fields. Generally, it gets analyzed by the well-known Brunauer-Emmett-Teller (BET) technique. The surface area has always been found to be greater for porous structures with rough surfaces as compared to their nonporous structures. Since the surface area is obtained by monolayer coverage of N<sub>2</sub> on the sample surface, the starting points of the isotherm are used for this measurement. Since the maximum amount of condensed N<sub>2</sub> can measure the total pore volume (TOPV), the last points of the isotherm are taken for this calculation. [23, 24] Furthermore, porosity represents the total fraction of void space within the material but does not reveal the size and distribution of voids (pores). This is measured by capillary condensation experiments and by the Kelvin equation. [25] The organogel **G7** shows the absorption of metal ions; thus, to analyze the changes inside the metallogel upon metal-ion absorption, BET analysis was performed for the gelator, organogel, and one metallogel from the series of metallogels. To find out the suitable temperature of xerogels for BET analysis, thermogravimetric analysis (TGA) of **G7** (powder), **G7** (xerogel), and **M<sup>1</sup>G7** (xerogel) was carried out. Weight losses of 4, 8, and 10% were recorded for **G7** (powder), **G7** (xerogel), and **M<sup>1</sup>G7** (xerogel), respectively, up to 200 °C with the removal of moisture from the samples (Figure 2.7).

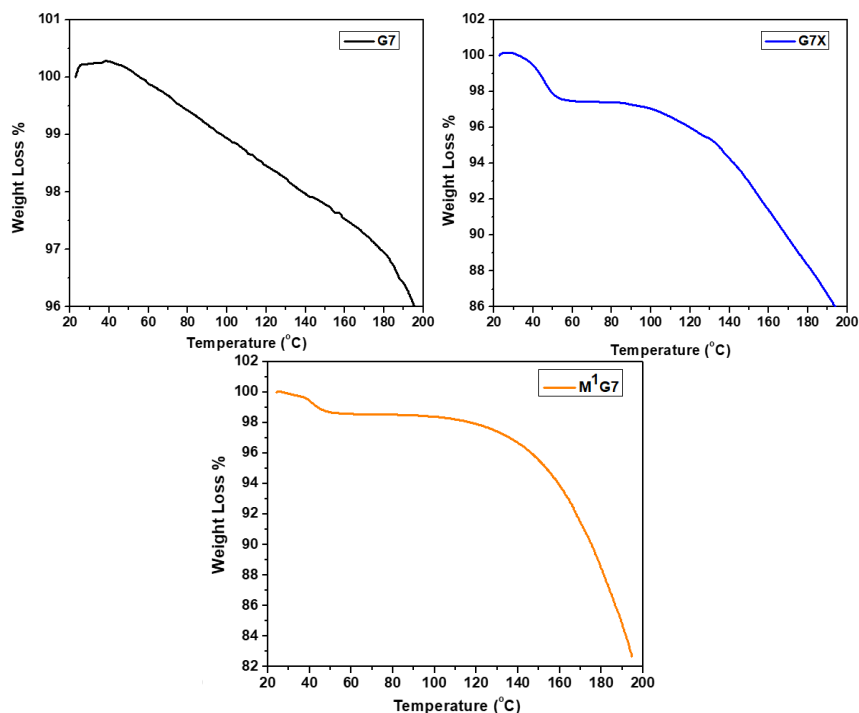


**Figure 2.7.** TGA analysis data of gelator **G7**, Xerogel **G7** and metallogel **M<sup>1</sup>G7**.

The surface areas for the three samples were found to be 6.033, 9.440, and 7.779 m<sup>2</sup>/g, respectively, for **G7**, **G7** (xerogel), and **M<sup>1</sup>G7** (xerogel) (Figure 2.8). The experiments have been repeated thrice and as expected it was found that the surface area increases in the xerogel (**G7**) from the powder (**G7**). In contrast, a slight decrease in surface area is noticed in the metallogel (**M<sup>1</sup>G7**), possibly due to metal ions (Fe) being inserted between pores. The pore volumes, diameter of pores, and average sizes of pores are presented in Table 2.3. This data indicates that an increase in the volume of pores in the gel increases the surface area of the gel. The xerogel with a substantial pore volume can be used to absorb metal ions. The average pore diameters were between 2 and 50 nm, revealing the mesoporous nature of the organogel and metallogel.<sup>[26, 27]</sup> The BET analysis shows deviation from the theoretical type I–V with hysteresis type 3 (H3) because of xerogels' fibrous, leaflike, and platelike morphology.<sup>[28-30]</sup>

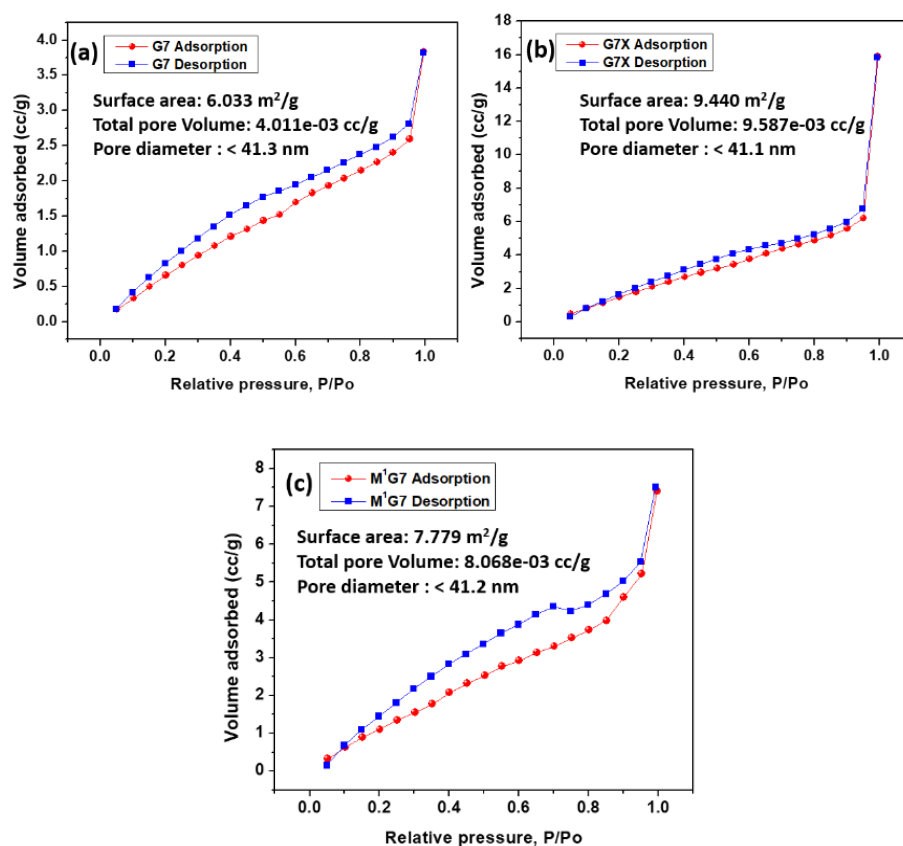


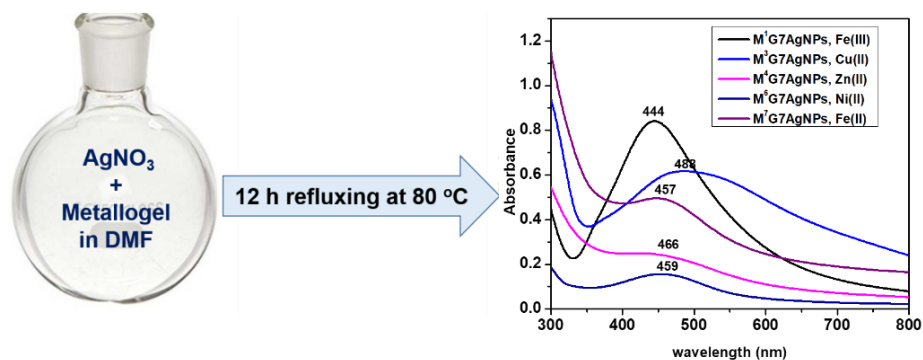
**Figure 2.8.** BET analysis of (a) powder **G7**, (b) organogel **G7**, and (c) **Fe(III)** metallochel **M<sup>1</sup>G7**.

**Table 2.3.** BET surface area, TOPO and average pore diameter analysis of (a) powder **G7**, (b) Organogel **G7** and (c) **Fe (III)** metallochel **M<sup>1</sup>G7**.

BET analysis				
Compound	Surface area (m <sup>2</sup> /g)	Total Pore Volume (cm <sup>3</sup> /g)	Average pore diameter (nm)	Pores smaller than (diameter) (nm)
Powder <b>G7</b>	6.033	0.0040	6.29	41.3 nm
Xerogel of organogel <b>G7</b>	9.440	0.0096	28.06	41.1 nm
Xerogel of metallochel <b>M<sup>1</sup>G7</b>	7.779	0.0081	15.39	41.2 nm

To synthesize and stabilize Ag nanoparticles, 17 mg (0.02 M) of 5 mL of a DMF solution of AgNO<sub>3</sub> was added into 0.5 g of metallochel, and the resultant mixture was refluxed at 80 °C for 12 hrs. After the completion

of the reaction, it was found that silver nanoparticles get formed inside the  $M^1G7$ ,  $M^3G7$ ,  $M^4G7$ ,  $M^6G7$ , and  $M^7G7$ . Ultimately a reddish-black precipitate was formed, which was filtered, and AgNPs were obtained inside the powdered precipitate (Scheme 2.2).



**Scheme 2.2.** Synthesis of AgNPs Inside the Gel Matrix.

However, the nanoparticle formation was further investigated with the  $M^1G7$  gel because of its ability to stabilize the nanoparticles with desirable sizes. After the formation of silver nanocomposites, it was found that iron is also present in the solid composite in a lower amount. FTIR and ESI-MS spectrometric data of  $M^1G7$  were utilized to propose a probable structure of the metallogel (Figure 2.9, 2.10, and Scheme 2.3).

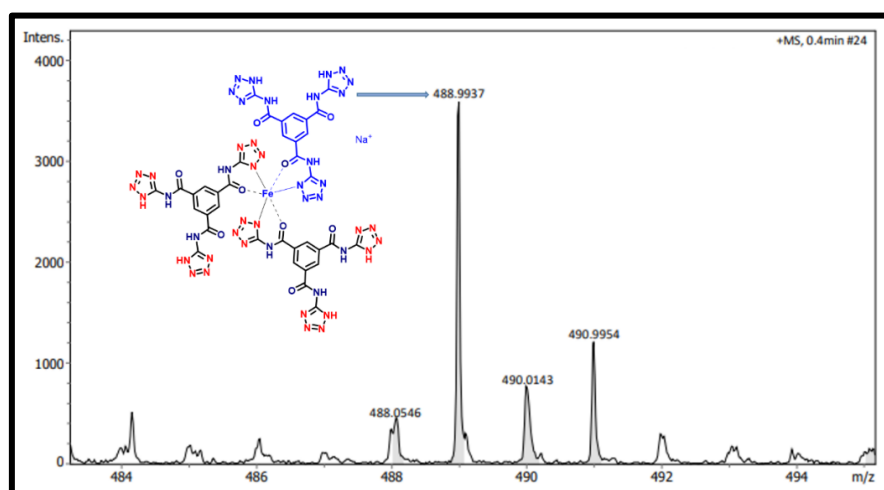


**Figure 2.9.** ESI-MS of metallogel  $M^1G7$ .

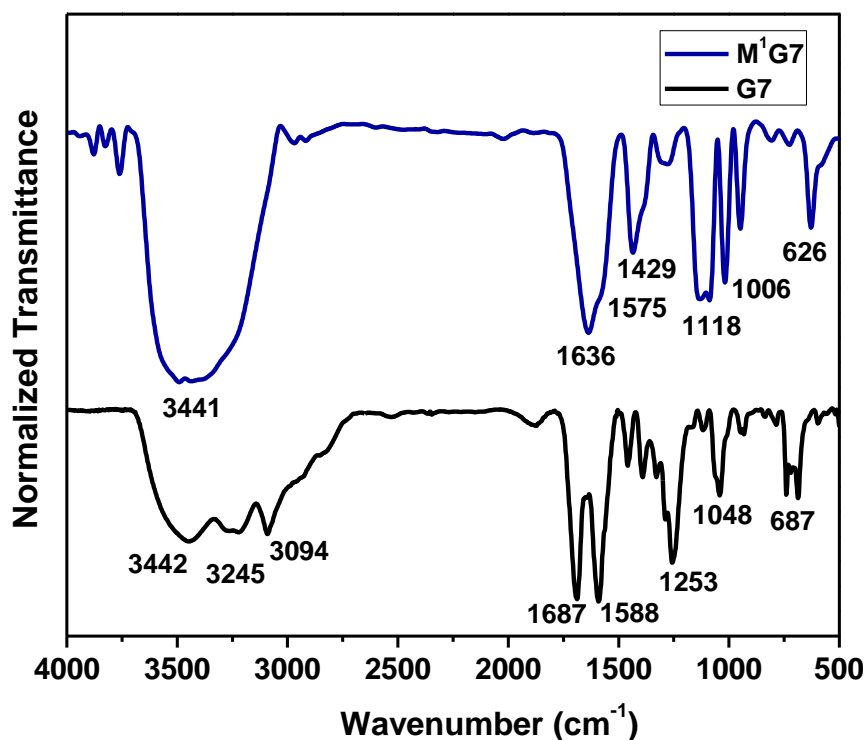
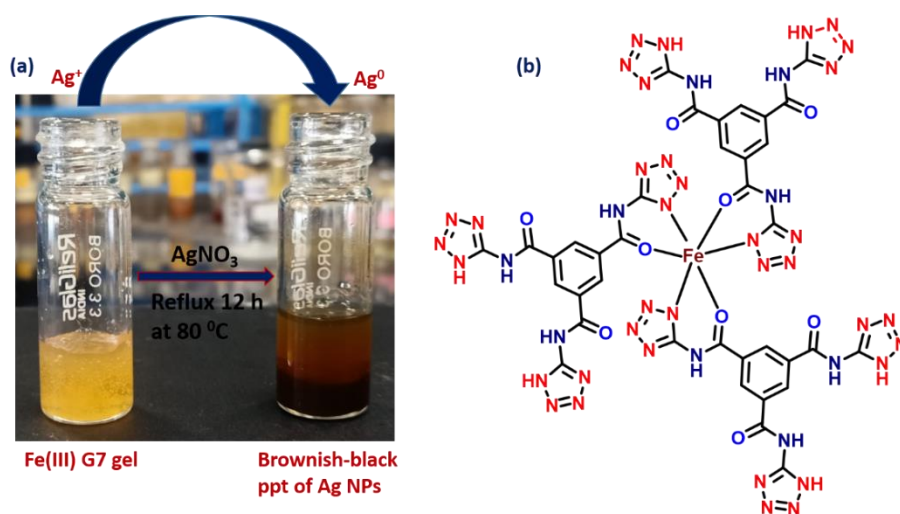


Figure 2.10. FT-IR of gelator **G7** and **M<sup>1</sup>G7**.



Scheme 2.3. Observation of color change on reaction of **M<sup>1</sup>G7** with  $\text{AgNO}_3$  (b) Predicted structure arrangement of Fe (III) G7 metallogel (**M<sup>1</sup>G7**).

The morphology and composition of the composite were explored by AFM, FE-SEM analysis, and energy-dispersive X-ray analysis (EDX) mapping (Figure 2.11 and 2.12).

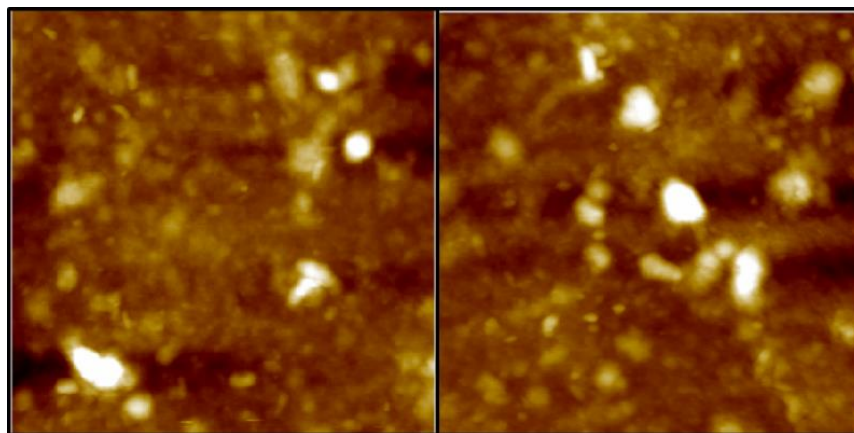


Figure 2.11. AFM image of  $M^1G7AgNPs$  nanocomposite.

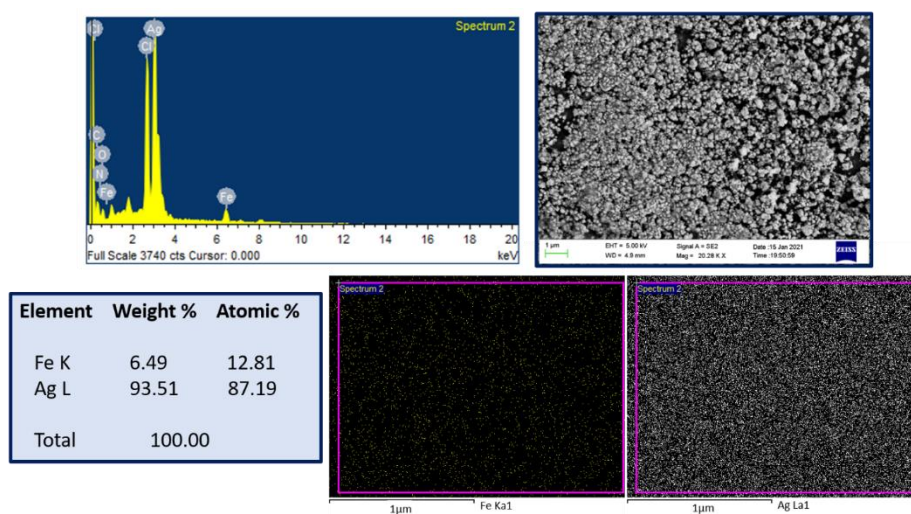
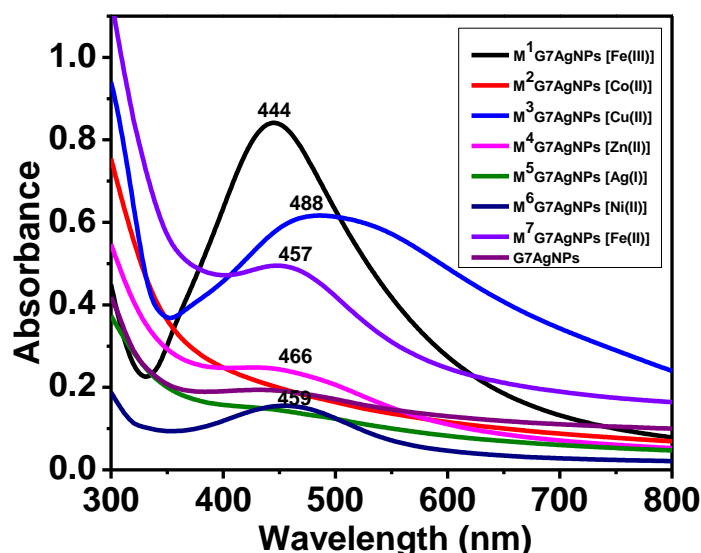


Figure 2.12. EDX analysis of  $M^1G7AgNPs$  nanocomposite.

**Analysis of Synthesis of  $M^1G7AgNPs$ .** Some metallogels have already been reported as prospective catalysts for the reduction reaction.<sup>[31]</sup> However, in this case, the formation of the  $M^1G7AgNPs$  catalyst has provided a unique Fe-Ag bimetallic system that can be utilized as an efficient reduction catalyst in the composite form. The formation and stabilization of silver nanoparticles in the nanocomposite were monitored through UV-Vis spectroscopy. As per literature reports, AgNPs generally show an absorption peak in the range of 410-480 nm, where bigger nanoparticles absorb in higher wavelengths.<sup>[32, 33]</sup> Five nanocomposites, viz.  $M^1G7AgNPs$ ,  $M^3G7AgNPs$ ,  $M^4G7AgNPs$ ,  $M^6G7AgNPs$ , and  $M^7G7AgNPs$ , were synthesized from the precursor metallogel. Although all of them have shown the generation of peaks corresponding to the AgNPs, in most cases, the peaks are very broad,

which might be due to too much aggregation (Figure 2.13). However, interestingly, in the case of  $M^1G7AgNPs$ , a comparatively narrower peak is observed at 444 nm due to the presence of a strong gel matrix of  $M^1G7$  for the stabilization of AgNPs. This might be because  $Fe^{3+}$  is a hard acid as compared to other divalent and monovalent metal ions ( $Fe^{2+}$ ,  $Co^{2+}$ ,  $Ni^{2+}$ ,  $Cu^{2+}$ ,  $Zn^{2+}$ , and  $Ag^+$ ), it makes a stronger metal-ligand interaction with tetrazole containing nitrogen atoms and the amide oxygen center. Due to this strong metal-ligand interaction in the  $Fe(III)G7/M^1G7$  metallogel, it is more stable than the other metallogels. It gives a stable matrix for the synthesis and stabilization of silver nanoparticles. Therefore, further investigation of AgNPs was done with  $M^1G7AgNPs$ .



**Figure 2.13.** UV-Vis spectra of reaction of  $AgNO_3$  with series of metallogels during silver nanoparticles synthesis after 12 hrs.

AgNPs display strong surface plasmon resonance (SPR) due to the collective oscillations of free electrons on the nanoparticle surface. Depending upon the particle size, the oscillation varies, which governs the wavelength range in the visible spectrum. With the increasing size of nanoparticles, the absorption maximum gets red-shifted. Therefore, the absorption wavelength near 452 nm indicates the average particle size of AgNPs around 70 nm in the  $M^1G7AgNP$  composite.<sup>[34]</sup> Different synthetic protocols followed for nanoparticle formation revealed that the

synthesis of AgNPs gets controlled by reaction temperature and time. When the reaction proceeds for 6 hrs.,  $\lambda_{\text{max}}$  was found at 452 nm, while after 12 hrs., it was observed at 444 nm. The optimum conditions for formation and stabilization of **M<sup>1</sup>G7AgNPs** have been found to be 12 hrs. of heating of a mixture of 0.5 g of gel and 0.02 M (5 mL) solution of AgNO<sub>3</sub> in DMF at 80 °C. UV-vis data of AgNO<sub>3</sub>, **M<sup>1</sup>G7**, and **M<sup>1</sup>G7AgNPs** show that the total amount of AgNO<sub>3</sub> used is converted into AgNPs (Figure 2.14). The formation of AgNPs at this condition was further confirmed by FE-SEM analysis. FE-SEM analysis shows that the size of AgNPs formed is between 60 and 110 nm (Figure 2.15).<sup>[17]</sup>

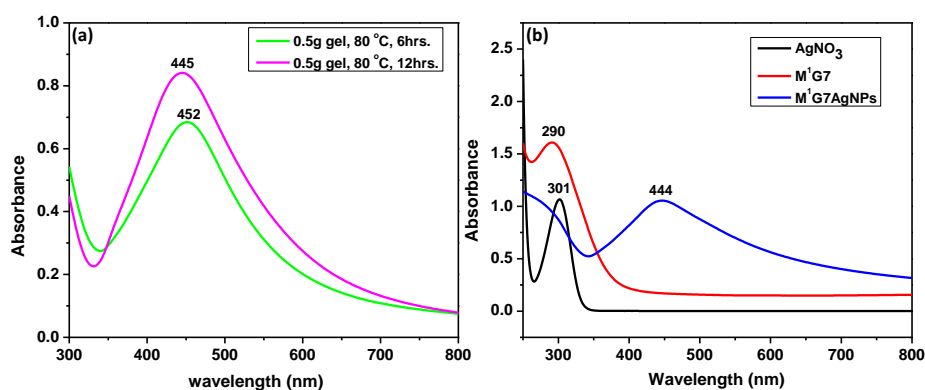


**Figure 2.14.** (a) Synthesis of **M<sup>1</sup>G7AgNPs** at 6 hrs. and 12 hrs. reaction time with same condition (b) UV-vis data showing changes in wavelength from **M<sup>1</sup>G7** to **M<sup>1</sup>G7AgNPs** nanocomposite.

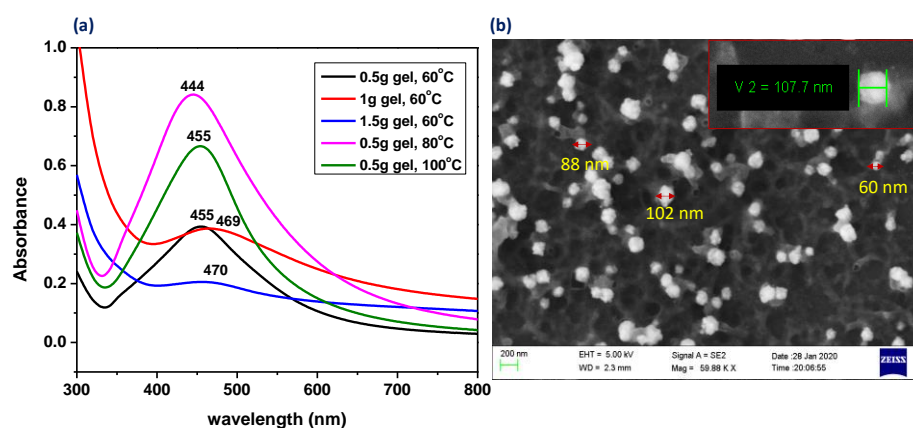


**Figure 2.15.** (a) UV-vis spectra of **M<sup>1</sup>G7AgNPs**, to show the synthesis of silver nanoparticles inside the nanocomposite system at different conditions (b) FE-SEM image of **M<sup>1</sup>G7AgNPs** with the condition 80 °C, 0.5 g of gel, and 12 hrs.

The XPS analysis was also done for the confirmation of the presence of Ag nanoparticles,  $\text{Fe}^{3+}$ , and other elements in  $\text{M}^1\text{G7AgNPs}$ . The full-range XPS spectra of  $\text{M}^1\text{G7AgNPs}$  reveal peaks at 285 (C 1s), 400 (N 1s), 531 (O 1s), 369 (Ag 3d), and 714 eV ( $\text{Fe}$  2p).<sup>[35-37]</sup> The C 1s spectrum has three peaks at 285.2 (CC/C–C), 286.0 (C–N), and 288.0 eV (C=O). The N 1s spectrum exhibits two peaks at 400.1 and 400.9 eV corresponding to N–CO and N–H. The O 1s spectrum presents one peak at 532.5 eV, which introduced the carboxylic group.<sup>[38]</sup> The Fe 2p spectra were deconvoluted in three peaks at 712.3 ( $\text{Fe}(\text{III})$ , Fe 2p<sub>3/2</sub>) and 725.9 ( $\text{Fe}$  2p<sub>1/2</sub>), and a satellite peak was observed at 718.3 eV for  $\text{Fe}^{3+}$  (Figure 2.16).<sup>[39, 40]</sup> The Ag 3d spectrum shows two peaks at 374.6 and 368.6 eV corresponding to the 3d<sub>3/2</sub> and 3d<sub>5/2</sub> orbits of Ag (0) (Figure 2.17).<sup>[17, 41]</sup>

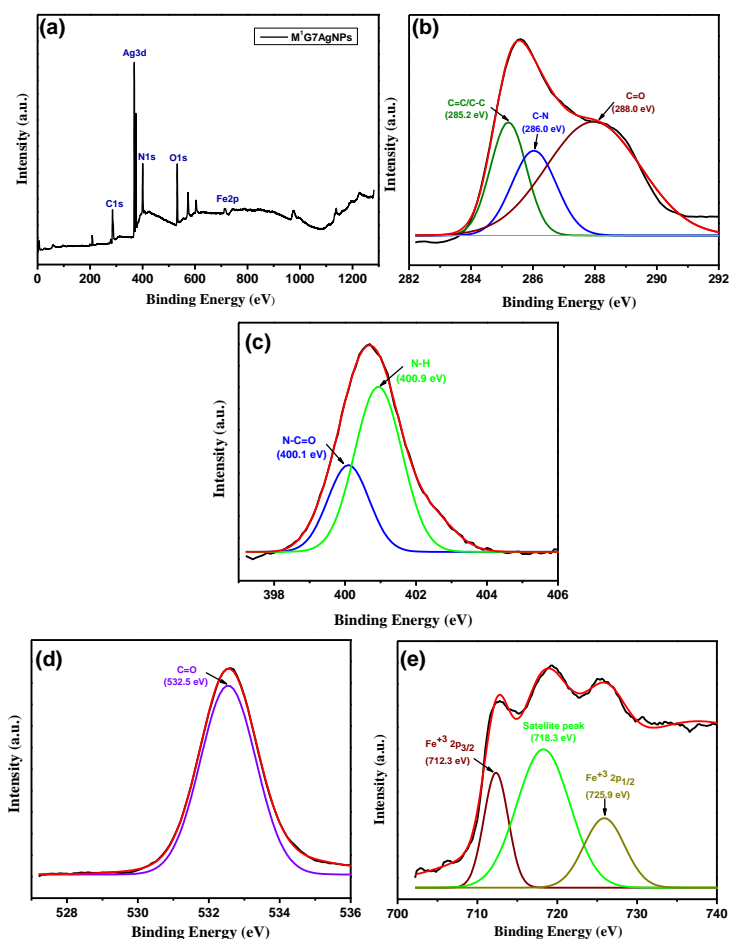


**Figure 2.16.** (a) Total XPS spectra of composite  $\text{M}^1\text{G7AgNPs}$  (b) C 1s XPS spectra (c) N 1s XPS spectra (d) O 1s XPS spectra and (e) Fe 2p XPS spectra of catalyst  $\text{M}^1\text{G7AgNPs}$ .

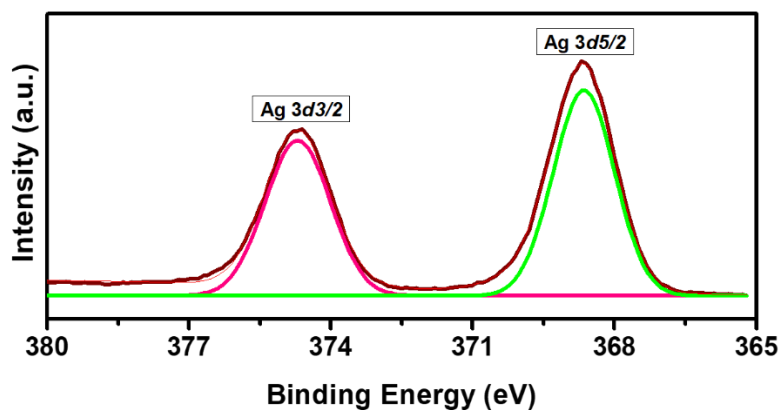


**Figure 2.17.** Ag 3d XPS spectra of synthesized silver nanoparticles in nanocomposite **M<sup>1</sup>G7AgNPs**.

The FTIR data do not show any notable changes in amide and tetrazole IR frequencies for **M<sup>1</sup>G7** and **M<sup>1</sup>G7AgNPs**. The IR bands for amide C=O and tetrazole N–H are found at 1636 and 1575  $\text{cm}^{-1}$  in **M<sup>1</sup>G7** and at 1636 and 1572  $\text{cm}^{-1}$  in **M<sup>1</sup>G7AgNPs**. These data show that Fe is coordinated with amide and tetrazole groups with not much change in the coordination environment. The PXRD data of **M<sup>1</sup>G7AgNPs** reveals the  $2\theta$  values for silver nanoparticles at 38.19, 44.40, 64.55, and 77.41° along with similar peaks like xerogel of the metallogel **M<sup>1</sup>G7** at 11.38, 16.50, 18.97, 23.16, 28.26, and 43.27°. This indicates that Fe(III) remains almost in the same coordination environment with **G7** within the nanocomposite **M<sup>1</sup>G7AgNPs**. Therefore, the synthesized AgNPs stabilized within the **M<sup>1</sup>G7** network do not affect many changes in Fe coordination (Figures 2.18 and 2.19).

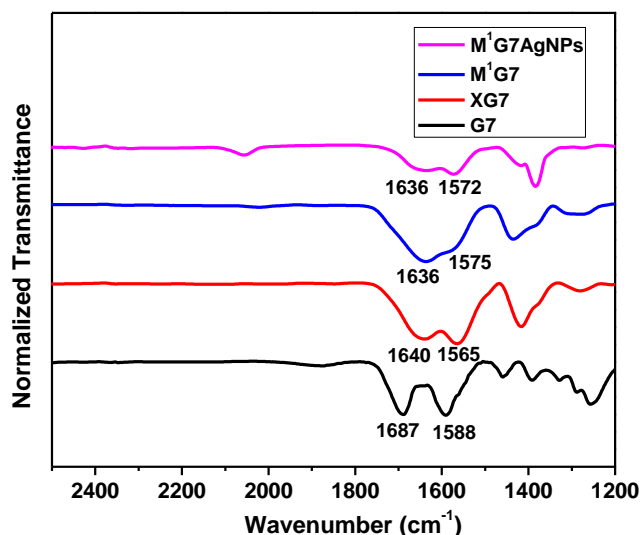


**Figure 2.18.** FT-IR data of **G7**, Xerogel of **G7**, **M¹G7** and **M¹G7AgNPs**.

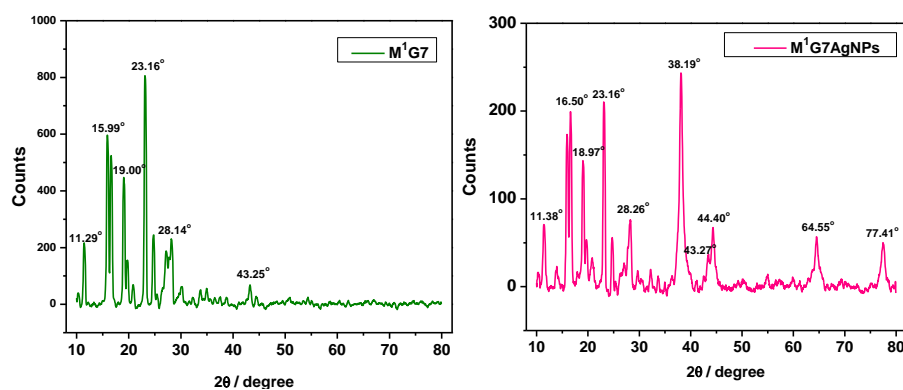
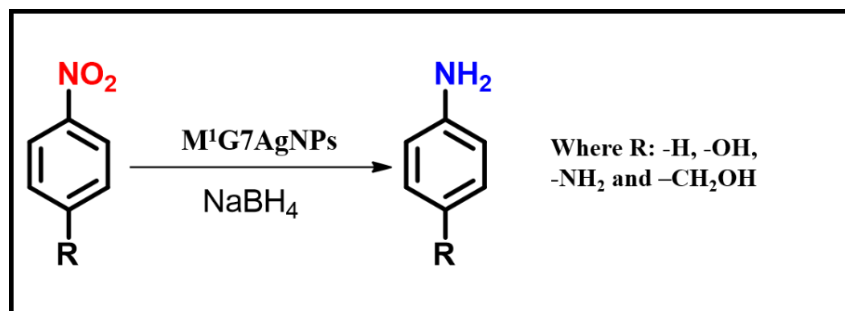


**Figure 2.19.** PXRD analysis of **M¹G7** and **M¹G7AgNPs** nanocomposite.

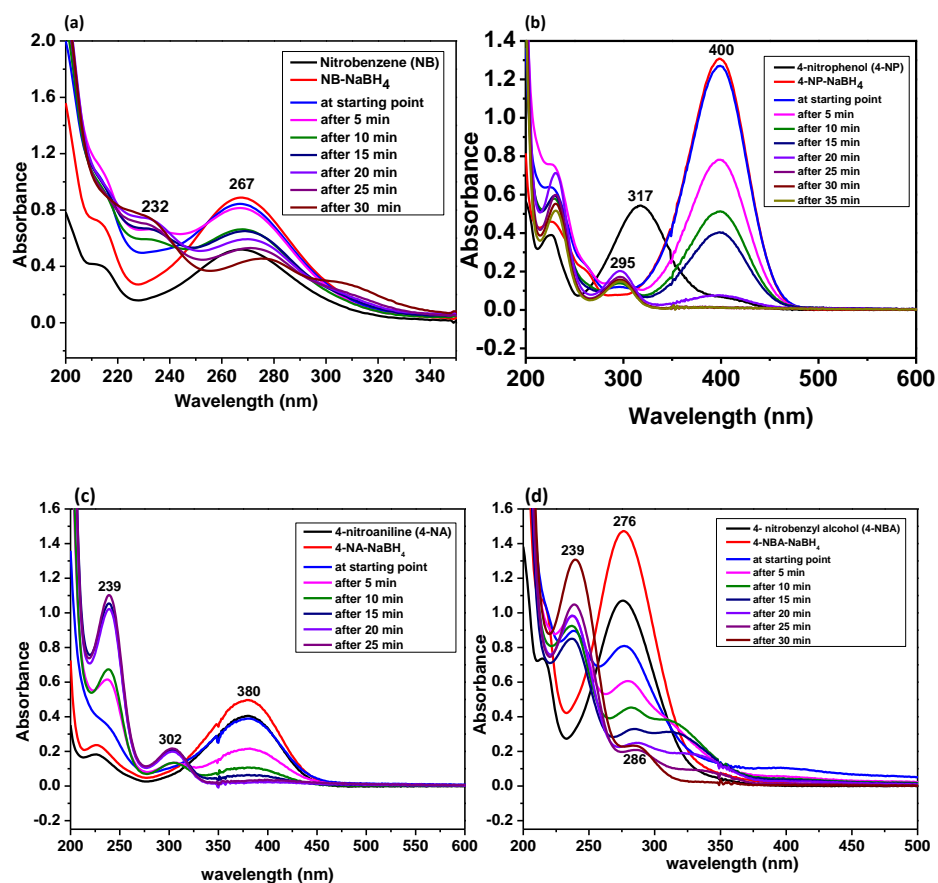
Silver nitrate solution after treatment with **M¹G7**, **M³G7**, **M⁴G7**, **M⁶G7**, and **M⁷G7** formed **M¹G7AgNPs**, **M³G7AgNPs**, **M⁴G7AgNPs**, **M⁶G7AgNPs**, and **M⁷G7AgNPs** composites. Out of these, **M¹G7AgNPs** was explored as a catalyst in reduction of nitroaromatics to corresponding amines with different substituents (Scheme 2.4). In a typical experiment, 0.1 mmol of the nitro substituent, 1 mmol of  $\text{NaBH}_4$ , and 6 mg of the catalyst were suspended in 10 mL of Milli-Q water and stirred at room temperature. After 25–35 min of reaction, the reduction of the nitro group into the amine gets completed, and this was confirmed with UV–vis,  $^1\text{H}$  NMR, and gas chromatography-mass spectrometry (GCMS) analyses. These data show the disappearance of the peak related to the nitro group and the appearance of the peak corresponding to the amine.



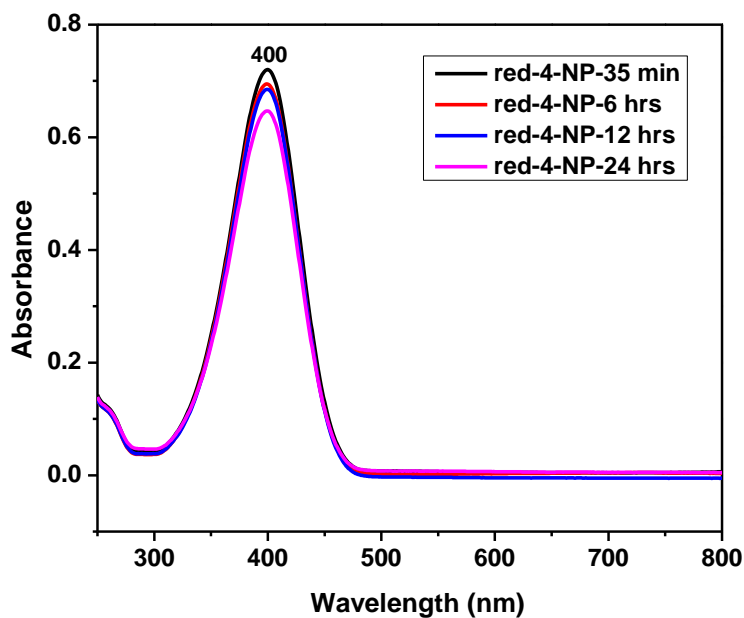
**Scheme 2.4.** Reduction of nitroaromatics to corresponding amines by nanocomposite catalysts.

#### Investigation on the Reduction Reaction of Nitro Aromatics.

Reduction reactions are monitored through UV-vis spectroscopy. In typical monitoring, UV-vis data were taken every 5 min after the start of the reaction, and it was observed that the characteristic peaks for the nitroaromatics get diminished with time, and a new peak appeared for corresponding amine compounds. In the case of nitrobenzene (NB), the characteristic peak at 267 nm reduces, and a new peak appears around 232 nm when catalyzed by **M<sup>1</sup>G7AgNPs**. In the case of 4-nitrophenol(4-NP), the nitro compound itself shows a peak at 317 nm, and after the addition of NaBH<sub>4</sub>, the peak shifts toward 400 nm because of the formation of the phenolate ion. After adding **M<sup>1</sup>G7AgNPs**, the peak at 400 nm get vanished, and a new peak appeared at 295 nm which indicates the formation of 4-aminophenol.<sup>[17,42]</sup> Similarly, the reduction of 4-nitroaniline (4-NA) and 4-nitrobenzylalcohol (4-NBA) was also monitored spectrophotometrically (Figure 2.20). A control experiment was also done with the reduction of 4-nitrophenol by NaBH<sub>4</sub> without using the nanocomposite catalyst **M<sup>1</sup>G7AgNPs**. It reveals that even after 36 hrs., the UV-vis peak at 400 nm shows the presence of the phenoxide ion, but there are no considerable changes that can show the reduction of the nitro compound (Figure 2.21).



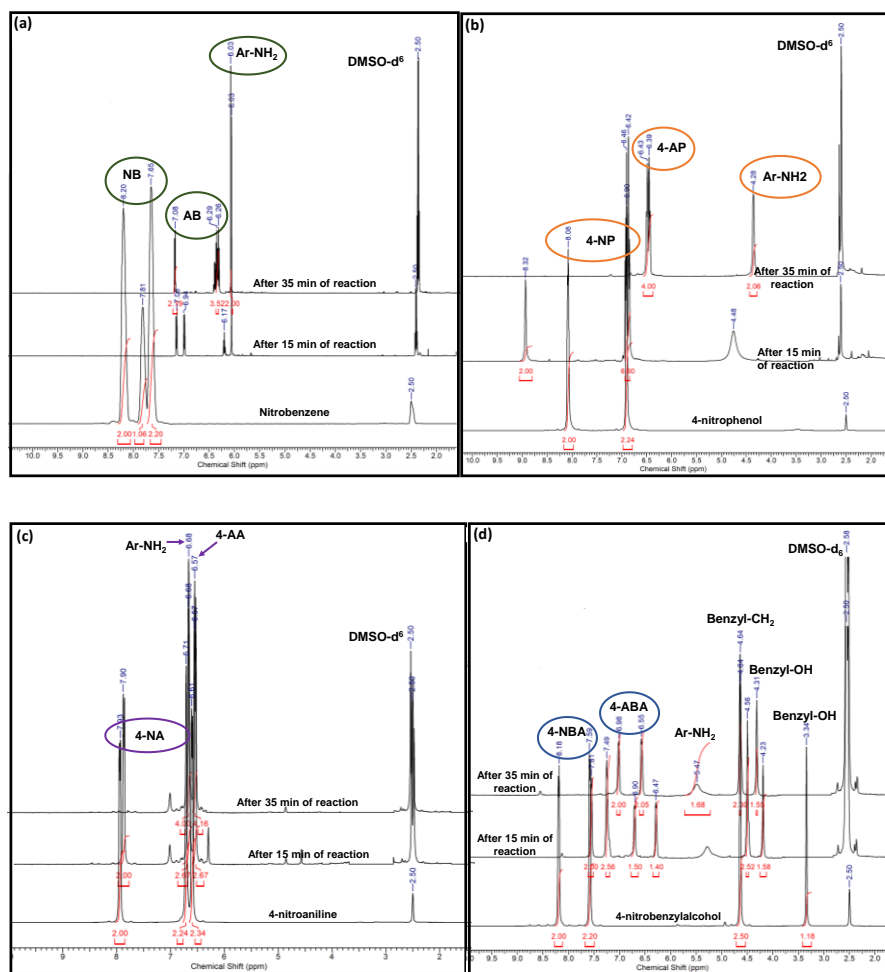
**Figure 2.20.** UV-Vis spectra of reduction of (a) NB (b) 4-NP (c) 4-NA (d) 4-NBA catalyzed by  $M^1G7AgNPs$  nanocomposite.



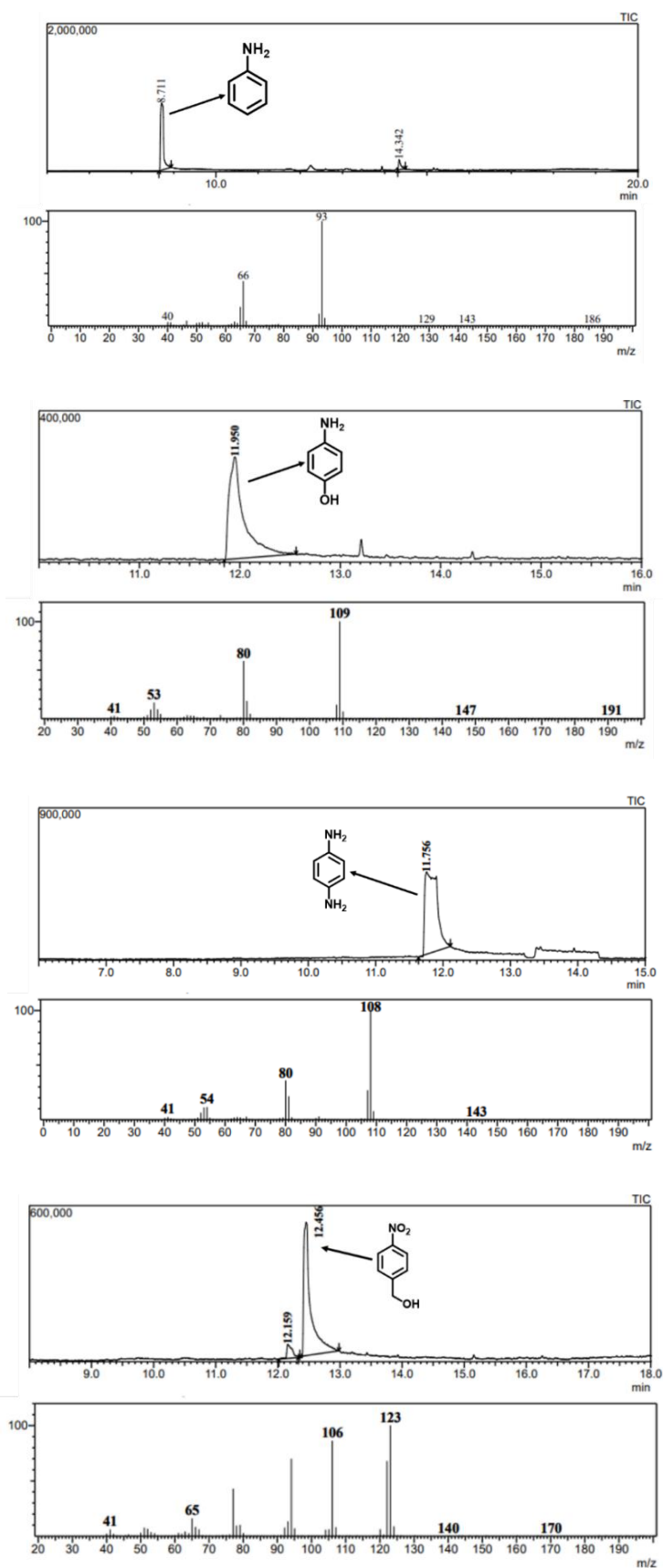
**Figure 2.21.** Control reduction experiment of 4-nitrophenol by  $NaBH_4$  without using nanocomposite catalyst  $M^1G7AgNPs$ .

Proton NMR spectroscopy is also used to monitor the catalytic conversion reaction. The  $^1\text{H}$  NMR of the 4-nitrophenol spectrum was recorded in DMSO, and it furnished two doublets at 6.90 and 8.08 ppm, respectively, due to the aromatic protons. Conversion of 4-nitrophenol to 4-aminophenol in the presence of **M<sup>1</sup>G7AgNPs** was explored in a time-dependent manner as the spectrum was recorded after 15 min. The starting spectrum shows signals for the aromatic protons of 4-nitrophenol (6.90–8.32 ppm) as well as for 4-aminophenol (6.42–6.46 ppm) with a signal at 4.48 ppm due to the presence of the aromatic Ar-NH<sub>2</sub> proton. Along with an increase in the reaction time, the signal for 4-NP becomes weaker, while for 4-AP it becomes stronger. After 35 min, the spectrum was found with signals for 4-aminophenol only, indicating an almost complete reduction of 4-nitrophenol to 4-aminophenol. The  $^1\text{H}$  NMR of nitroaniline (NA) gave three signals at 7.93, 6.61, and 6.71 ppm due to the aromatic protons and Ar-NH<sub>2</sub>. After 15 min, signals were obtained at 7.90 and 6.57 ppm for aromatic protons, with a signal at 6.68 ppm due to Ar-NH<sub>2</sub> protons. While after 35 min, the spectrum reveals the complete conversion of nitroaniline to benzene-1,4-diamine, where the aromatic protons come at 6.57 ppm, and Ar-NH<sub>2</sub> protons come at 6.68 ppm. The conversion of nitrobenzene (NB) and 4-nitrobenzylalcohol (4-NBA) was also confirmed by  $^1\text{H}$  NMR analysis after 15 and 35 min of reaction (Figure 2.22).

The reduction reaction of 4-nitrophenol, nitrobenzene, 4-nitroaniline, and 4-nitrobenzylalcohol was also confirmed by GCMS analysis, and the product yield of the reaction was closely monitored. In most of the cases, the conversion was found to be almost 100% (Figure 2.23 and Table 2.4).

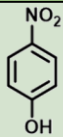
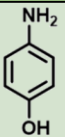
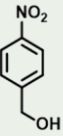
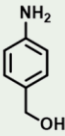
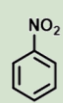
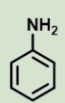
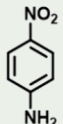
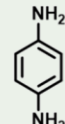


**Figure 2.22.**  $^1\text{H}$  NMR of reduction of (a) NB (b) 4-NP (c) 4-NA and (d) 4-NBA.



*Figure 2.23. GC-MS spectra of analyzed data of reduction of nitro aromatics to corresponding amino compounds.*

Table 2.4. Optimization of reduction reaction by GCMS data.

Entry	Substrate	Product	Time (min)	Con %	Sel %
1			35	100	100
2			30	100	100
3			30	100	90
4			25	100	100

**Recovery of the Catalyst (M<sup>1</sup>G7AgNPs).** The M<sup>1</sup>G7AgNPs nanocomposite acts as a catalyst to reduce the nitro group to the amino group. This was tested for four aromatic nitro compounds, as discussed above. The recyclability of the catalyst was determined by repeat use of the catalysts with the same nitro aromatics. This recyclability was tested with 4-nitrophenol. The catalytic system was found to be effective for 4-5 cycles of reaction and gave products with 100% conversion in the first two cycles. After that, the conversion started to decrease slowly in the third, fourth, and fifth cycles, which has been analyzed by GCMS (Table 2.5). The UV-vis analysis of the catalyst during five consecutive catalytic cycles with increasing time shows an increase in the broadening, indicating the aggregation of silver nanoparticles. However, a shift in the peak position toward lower wavelengths is also observed, which might be due to the leaching out of silver nanoparticles from the composite matrix (Figure 2.24). The stability of the catalyst after the first cycle was confirmed by FE-SEM, EDX, and PXRD analyses (Figure 2.25 and 2.26). The M<sup>1</sup>G7AgNPs nanocomposite powder has been used here as a catalyst. After completion of the reaction, the organic amino compound was extracted by using ethyl acetate. The remaining

water part contains the suspended catalyst. By rotary-evaporator, water was removed, and the catalyst was isolated. The other way is that, after the extraction of the amino compound from the reaction system, the water part can be used directly for the next cycle of the reduction reaction in that case, there is no loss of catalyst, and a very good conversion of the reactant was observed in terms of yield percentage.

**Table 2.5.** Recyclability of the nanocomposite catalyst  $M^1G7AgNPs$ .

Rxn. Cycle	Substrate	Product	Time (min)	Con %
1			35	100
2			35	100
3			35	98
4			35	95
5			35	88

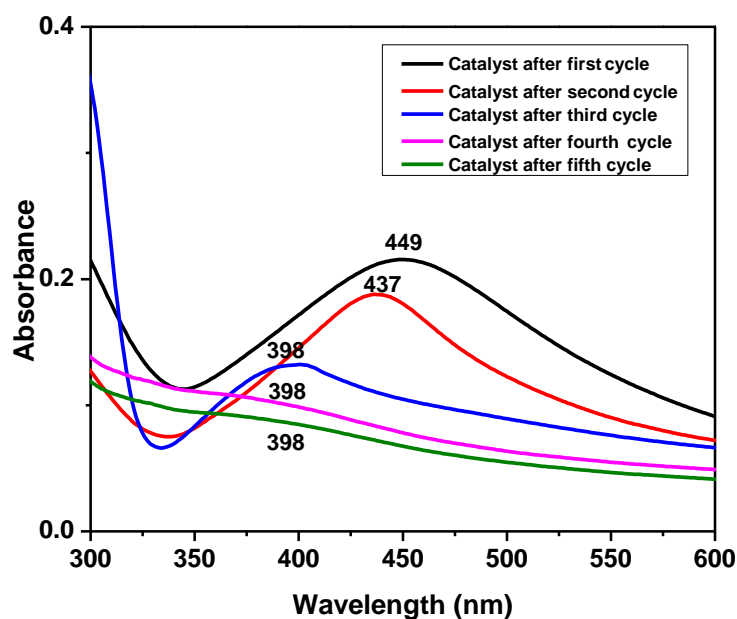


**Figure 2.24.** UV-vis analysis of  $M^1G7AgNPs$  catalyst during five cycles of catalytic reaction.

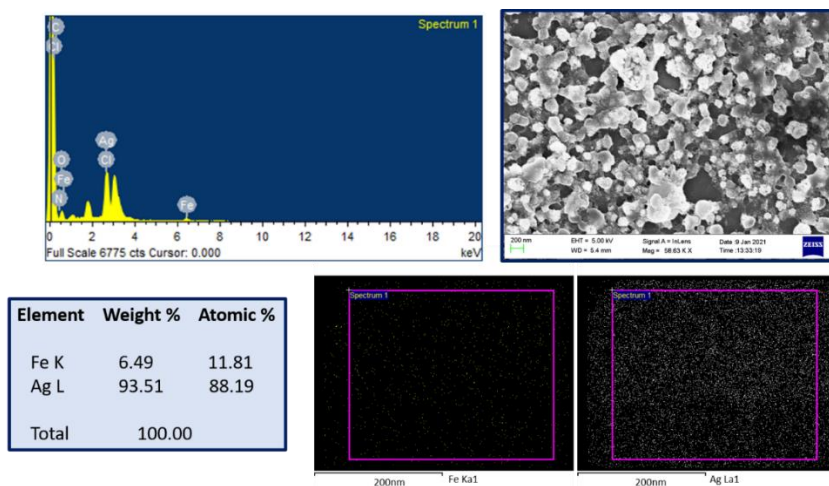


**Figure 2.25.** FE-SEM and EDX analysis of  $M^1G7AgNPs$  catalyst after reduction of 4-NP.

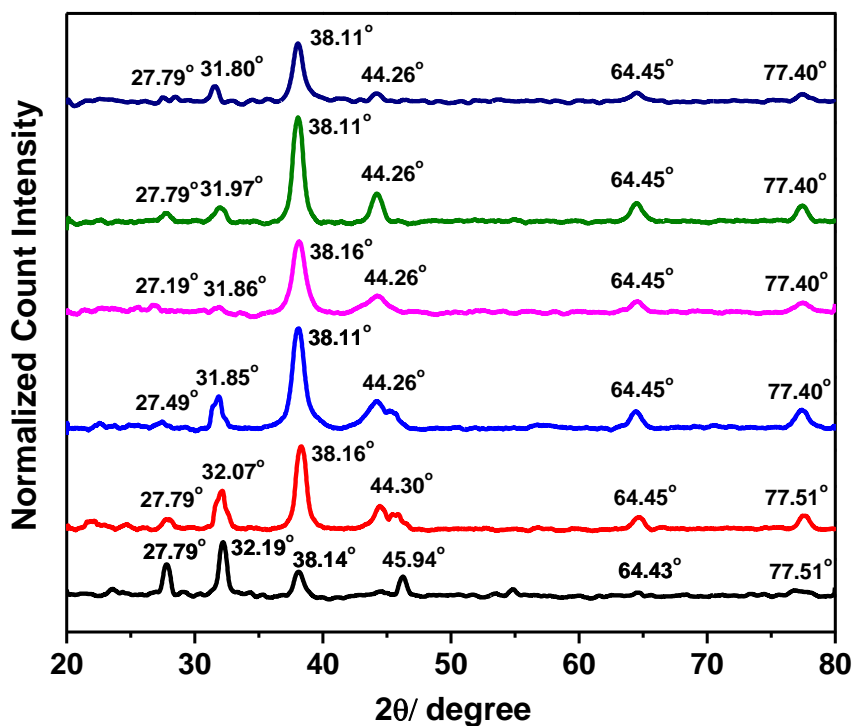


**Figure 2.26.** PXRD analysis of  $M^1G7AgNPs$  catalyst showing recovery of catalyst.

**Metal-Ion Absorption, Selective Gel-to-Crystal Transition ( $M^1G7$ ), and Dual-Metallogel Formation.** The organogel **G7** showed the unique property of absorption of metal ions from metal salts. The metal uptake ability of **G7** was tested only for the case of Fe(III) by the UV-vis analysis in this work. The Fe(III) metal uptake capacity of the organogel

G7 was found to be 73 % in 36 hrs. (Figure 2.27). With increasing time, the Fe(III) metal absorption by organogel G7 has been investigated by the UV-Vis experiment.

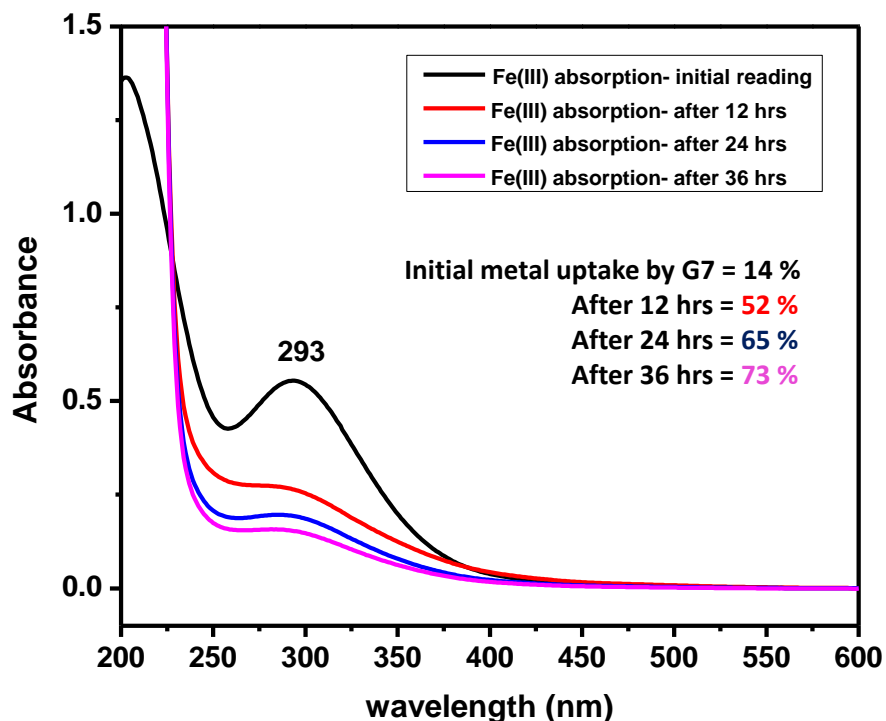


**Figure 2.27.** Fe(III) uptake study by UV-Vis analysis.

Fe(III) concentration = 35 mg in 1 ml H<sub>2</sub>O = 100 mM or 0.1 M

After addition in organogel G7, the upper water layer has been investigated by UV-Vis analysis.

Initial first reading,  $A=0.5529$ , after 12 hrs.,  $A=0.2632$ , after 24 h,  $A=0.1928$ , after 36 hrs.,  $A=0.1512$

Absorption coefficient for solution  $A = \epsilon cl$

$$0.5529 = \epsilon \times 0.1 \times 1, \epsilon = 5.529 \text{ M}^{-1}\text{cm}^{-1}$$

Metal amount after absorption =  $(A/\epsilon) \times$  dilution factor

$$= (0.5529/5.529) \times 301 = 30.1 \text{ mg}$$

Metal absorbed =  $35 - 30.1 = 4.9 \text{ mg}$

Therefore, metal uptake =  $4.9/35 \times 100 = 14\%$

At final reading, after 36 hrs.  $A = 0.1512$

$$\epsilon = 5.529 \text{ M}^{-1}\text{cm}^{-1}, l=1 \text{ cm}, c=?$$

$$\text{Therefore } c = A/\epsilon l = 0.0273 \text{ M} = 27.3 \text{ mM}$$

100 mM solution contain 35 mg in 1 mL.

Therefore, 27.3 mM solution =  $35/100 \times 27.3 = 9.555$  mg in 1mL

Therefore, metal uptake after 36 hrs. =  $35 - 9.555 = 25.5$  mg

$$\text{Metal uptake capacity} = 25.5/35 \times 100 = 73 \%$$

When the organogel was placed under a glass vial in an aqueous solution of metal perchlorate salts, metal ions started to get absorbed by the organogel, and eventually they converted into respective metallogels after a couple of days' time. However, in the case of  $M^I G7$  (Fe(III)G7), the metallogel gradually gets converted into a crystalline product upon standing for a couple of days more (Figure 2.28, a). The PXRD data of crystalline  $M^I G7$  was found to be exactly similar to the PXRD data of the xerogel of  $M^I G7$  (Figure 2.29). Here the used xerogel was formed from gel by lyophilization. This method does not affect gel matrix thus this implies that the lyophilization process has effectively preserved the properties of the original gel matrix. Unfortunately, even with the best efforts, no single crystal could be grown for solid-state structural determination. When the aqueous solutions of the mixture of Fe(III), Co(II), Ni(II), Cu(II), Zn(II), and Ag(I) perchlorate salts were taken inside the vial containing organogel G7, after 1-2 days, the organogel completely absorbs all of the metal ions except iron. The iron gets converted into its crystalline form upon standing with G7 as characterized by its PXRD analysis. The organogel with a mixture of metals confirms the presence of Co(II), Ni(II), Cu(II) Zn(II), and Ag(I) inside it by EDX analysis. Therefore, organogel G7 selectively removed the iron as the crystalline product from a mixture of various metal salts. The possibility of the fabrication of dual metallogels is also explored. For this, the combinations of Fe(III) with Fe(II), Co(II), Ni(II), Cu(II), Zn(II), and Ag(I) perchlorate salts in the presence of G7 were examined with different molar ratios of  $M^I : M_x : G7$ . The stable dual-metallogel formation occurred with Fe(III)/ Zn(II)/G7 at a 1:1:1 ratio. For FE-SEM analysis, the gel can be applied directly on the glass slide and can be taken into a vacuum desiccator. During controlled drying by vacuum, the solvent comes out without disturbing the gel matrix. This technique

gives nearby actual morphology of gels. The discrete flower like morphology of dual metallogel is observed due to dilution of gel during sample preparation (Figure 2.28, b). The value of the storage modulus of the dual gel of Fe(III) and Zn(II) is found to be greater as compared to its Fe ( $M^1G7$ ) and Zn ( $M^5G7$ ) metallogels due to an increase in the number of metal-ligand interaction sites inside the gel matrix (Figure 2.30).

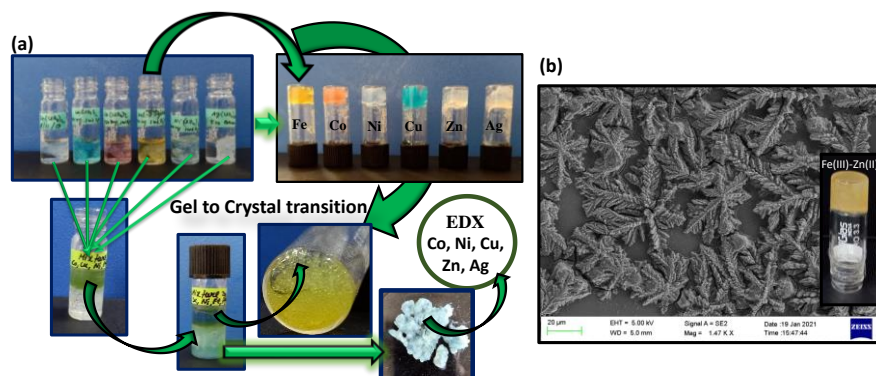


**Figure 2.28.** (a) Selective gel to crystal transition of iron during absorption of different metal ions (b) FE-SEM image of stable dual metallogel of Fe(III) and Zn(II) with  $G7$  at 2:1 metals- $G7$  ratio.

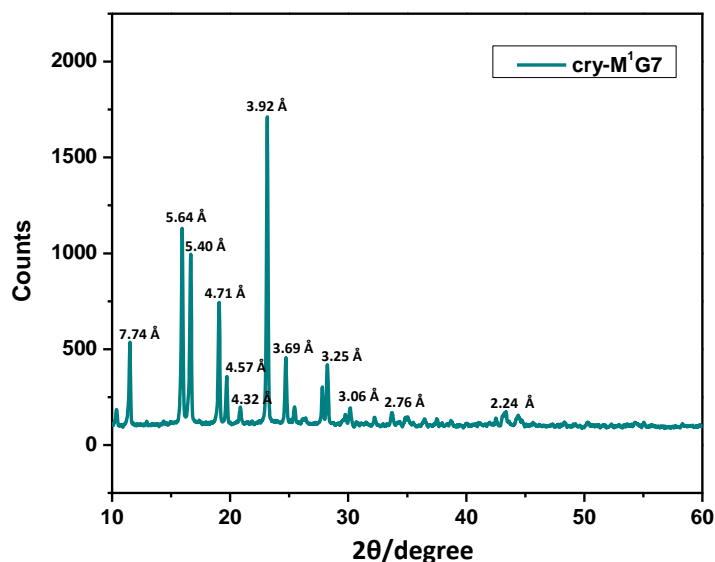


**Figure 2.29.** PXRD analysis of Crystalline  $M^1G7$ .

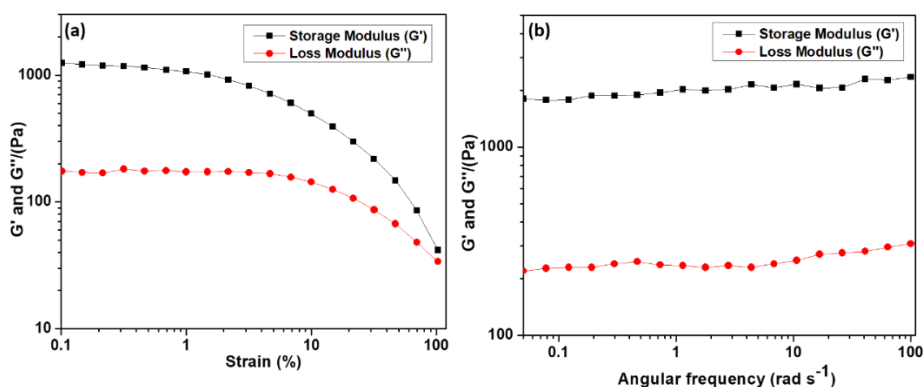


**Figure 2.30.** Rheological measurement of (a) linear viscoelastic behavior for the **Fe-Zn** dual metallogel (b) dynamic frequency sweep for the **Fe-Zn** dual metallogel.

**Role of Self-Assembly in Gelation.** It is well known that discrete gelator molecules can form gels by the self-assembly method, and various spectroscopic tools can investigate the details of interactions. Several noncovalent interactions, viz. H-bonds,  $\pi$ - $\pi$  interactions, etc., can play important roles in inducing gelation. The chemical structure of the gelator molecule plays an important part in bringing about such a kind of interaction for the fabrication of gels.<sup>[43]</sup> On the basis of the literature, the carboxamide and tetrazole moieties are excellent candidates to form H-bonds, while the aromatic rings give an environment for  $\pi$ - $\pi$  stacking.<sup>[44]</sup> The self-assembly of the gelator **G7** is investigated by concentration-dependent <sup>1</sup>H NMR. The result shows that the amide proton -NH is observed only in a high concentration at around 243 mM (50 mg in 500  $\mu$ L of DMSO-d<sub>6</sub>), and with increasing concentration, the amide and aromatic protons show a downfield shift, indicating their involvement in H-bond formation and  $\pi$ - $\pi$  stacking, respectively (Figure 2.31).<sup>[45, 46]</sup> The FTIR method is also used to detect the self-assembly mechanism. For the FTIR analysis, the xerogels are formed by freeze-drying lyophilization, in which the gel converts into xerogel without disturbing the gel network. The IR spectra of the synthesized compound **G7** and xerogel **G7** confirm the emergence of self-assembly in gel formation. The carboxamide N-H band for powder **G7** at 3442 cm<sup>-1</sup> shifts toward a lower wavenumber, 3428 cm<sup>-1</sup>, in the xerogel of **G7**. The carboxamide C=O vibrational band also shifted from

1687 to 1640  $\text{cm}^{-1}$ , indicating hydrogen-bond formation during gelation.<sup>[47, 48]</sup> The band at 1588  $\text{cm}^{-1}$  in **G7** shows the IR band for both the amide and the tetrazole moiety, which also gets shifted to the lower side around 1565  $\text{cm}^{-1}$ . Although it is challenging to clarify the combined effect of amide and tetrazole N–H on hydrogen bonding, shifting in the band shows an essential role of the N–H group in leading to the fabrication of the gel (Figure 2.32). Further, the self-assembled structure is scrutinized through PXRD measurements. In the xerogel of **G7**, an intense peak at  $2\theta = 22.96^\circ$  is observed, which corresponds to the d-spacing value (d value) of 3.95 Å, representing intercolumnar stacking. For **G7**, the peak at  $2\theta = 27.16^\circ$  (d value 3.38 Å) reveals the  $\pi$ – $\pi$  stacking between the benzene rings. Furthermore, the d-spacing at  $2\theta = 33.50^\circ$  (d value 2.79 Å) indicates the H-bond interaction between the NH proton of amide and tetrazole groups (Figure 2.33).<sup>[49-52]</sup> The aggregation due to the gelation process is also examined by FE-SEM technology. The SEM image of organogel **G7** shows a fibrous structure. This gel also shows a clear image upon zooming in to the scale of 200 nm, which clearly indicates the nanofibrous nature of the organogel (**G7**) (Figure 2.34).<sup>[53, 54]</sup>

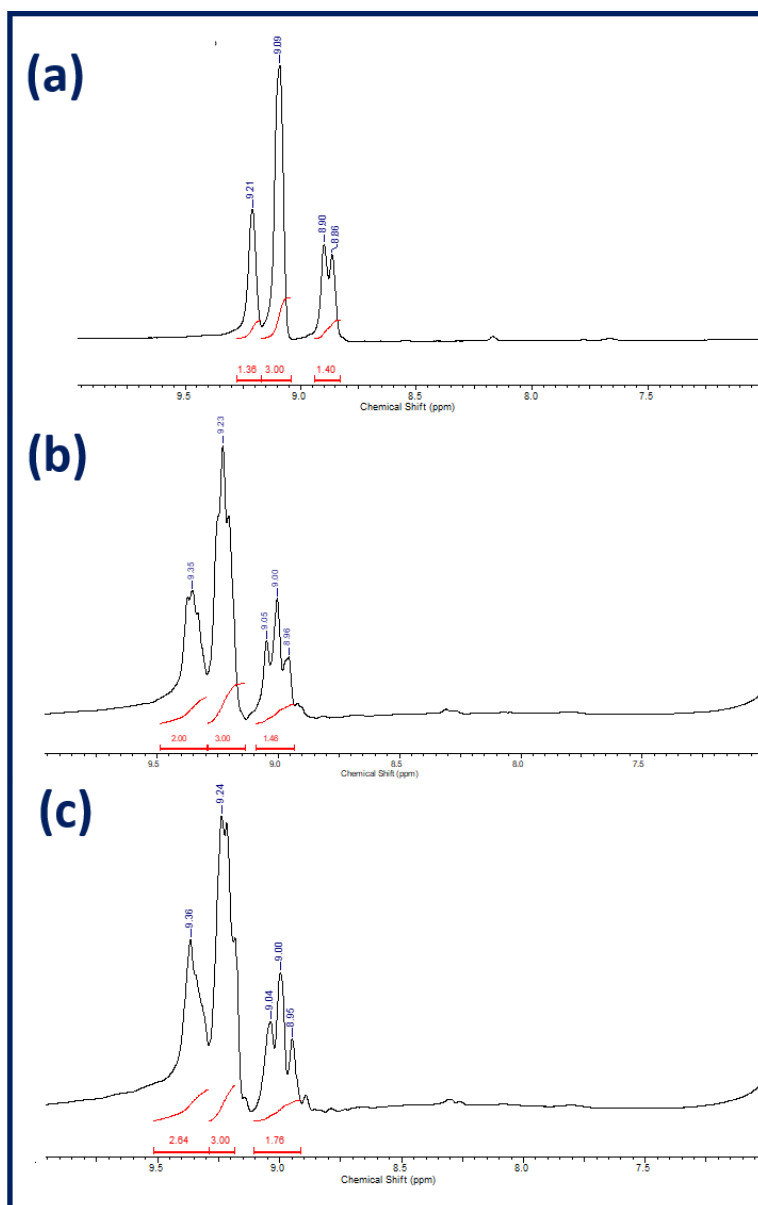


**Figure 2.31.** concentration dependent  $^1\text{H}$  NMR spectra of gelator G7 at (a) 97 mM (b) 195 mM (c) 243 mM.

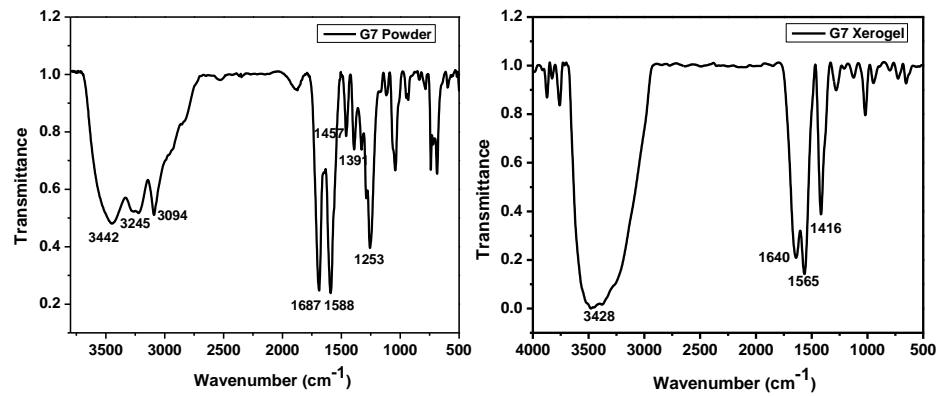


Figure 2.32. FTIR of G7 (Powder) and G7 (Xerogel).

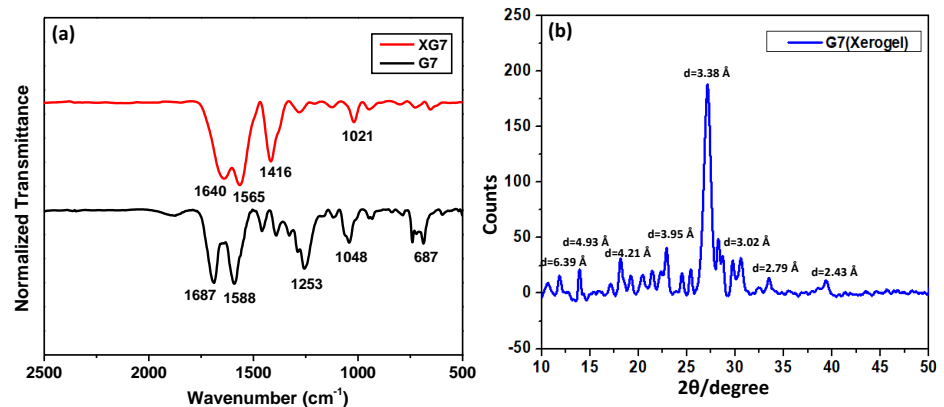


Figure 2.33. (a) FT-IR spectra of G7 (powder) and G7 (Xerogel) (b) PXRD pattern of Xerogel G7.

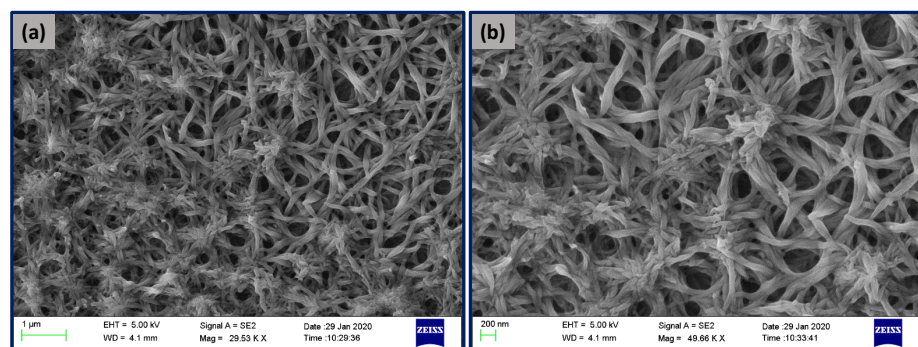
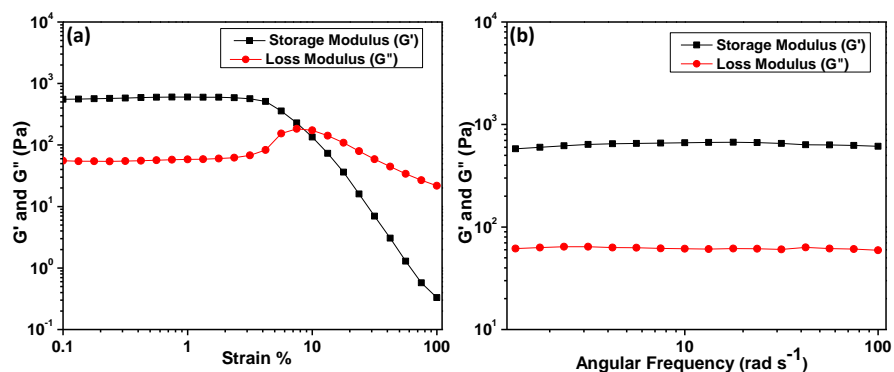


Figure 2.34. (a) FE-SEM image of organogel G7 under micro and (b) nano scale.

**Rheological Study of the Organogel G7 and Its Metallogels.** The rheological study helps find out the strength as well as other properties like the sol–gel transition behavior of gels.<sup>[55-57]</sup> The average storage modulus ( $G'$ ) for the organogel was found to be 586 Pa, and during the experiment,  $G'$  was found to be higher than  $G''$  in most of the ranges. In

the linear viscoelastic (LVE) experiment, upon increasing the strain, the values of  $G'$  and  $G''$  get deviate from linearity (Figure 2.35), and the crossover point is observed around 10% of the strain value. Here, the strain sweep experiment of **G7** shows a notable behavior related to  $G''$ . The  $G''$  first increases at 3 % strain and then decreases at 10 % strain from the crossover point. The phenomenon is known as weak strain overshoot (WSO) when the  $G''$  first increases and then decreases after a certain increase in strain.<sup>[58-60]</sup> The WSO occurs due to the formation of two different types of microstructure orientation inside the gel matrix. The first one is the orientation or alignment of microstructure towards the flow direction, which supports deformation. In contrast, the second one is the formation of complex microstructures which resist deformation up to a certain strain. Therefore, after some increment in  $G''$ , the further decrement starts over the critical strain, after which the complex microstructure aligns with the flow direction. When the metallogels are fabricated out of **G7** with different metal perchlorate salts, the value of the storage modulus was found to be in the range of 200–1000 pa for different metallogels. In most of the cases, it was greater than 600 Pa. The increment in storage modulus indicating an increase in stiffness due to the generation of a metal–organic framework inside gel matrix.<sup>[61]</sup> The nanocomposite gels of **M<sup>1</sup>G7AgNPs** were found to have a storage modulus of around 1000 Pa, which is formed from the synthesized silver nanocomposite **M<sup>1</sup>G7AgNPs**. The crossover points of metallogels were found between 100 and 1000 Pa. The rigidity of metallogels ( $G'-G''$ ) remained mostly parallel in the ongoing sweep range (Figures 2.36 and 2.37).



**Figure 2.35.** (a) Linear viscoelastic (LVE) range of organogel **G7** (b) dynamic frequency sweep for the organogel **G7**.

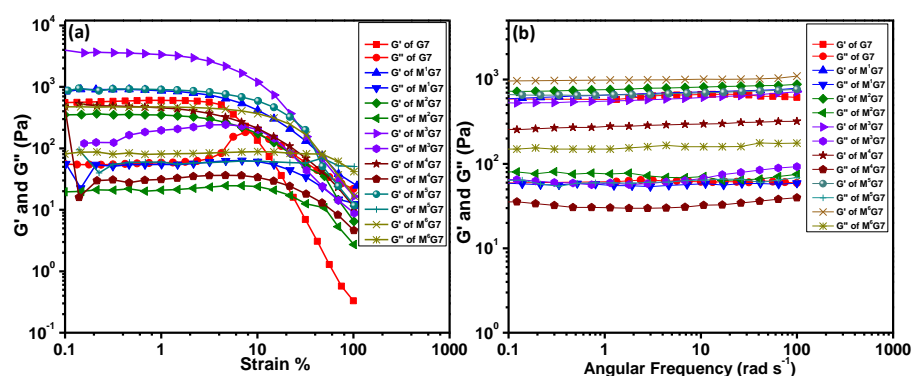


**Figure 2.36.** (a) linear viscoelastic behavior for the  $M^1G7$ - $M^6G7$  (b) dynamic frequency sweep for the  $M^1G7$ - $M^6G7$ .

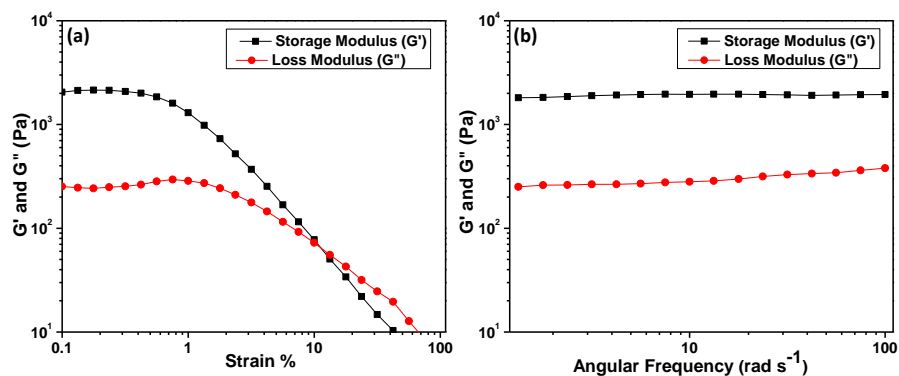


**Figure 2.37.** Rheological measurement of (a) linear viscoelastic behavior for the  $M^7G7$  (b) dynamic frequency sweep for the  $M^7G7$ .

**Interaction between Metal Ions and the Gelator Molecule and their Self-Assembly.** The IR studies of metallogels show the interaction of a metal ions with a ligand (gelator). The IR of the **G7** organogel shows a band at  $1687 \text{ cm}^{-1}$  for the amide bond, and IR spectra of metallogels of

G7 show a significant shift of the stretching frequency of the amide bond to the range of 1600–1650  $\text{cm}^{-1}$ , which reveals the interaction between the amide group and the metal ion. IR data of  $M^1G7$  show that the C=O stretching frequency shifts from 1687 to 1648  $\text{cm}^{-1}$  and for the tetrazole ring from 1588 to 1575  $\text{cm}^{-1}$ . A similar lowering of stretching frequencies for all other metallogels has also been observed. These IR data show that during metallogelation, the metal ion interacts with carboxamide and tetrazole groups (Figure 2.38).

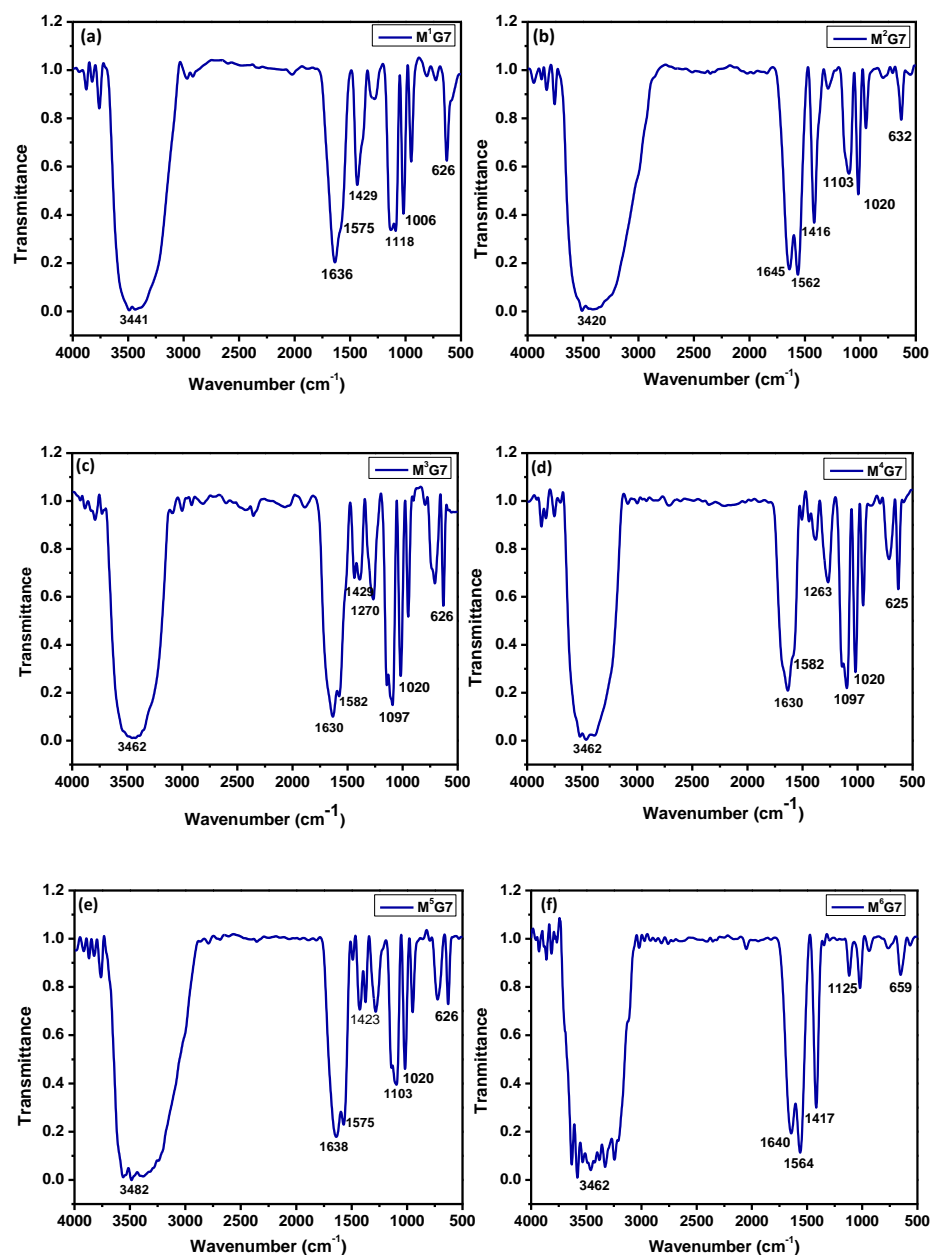
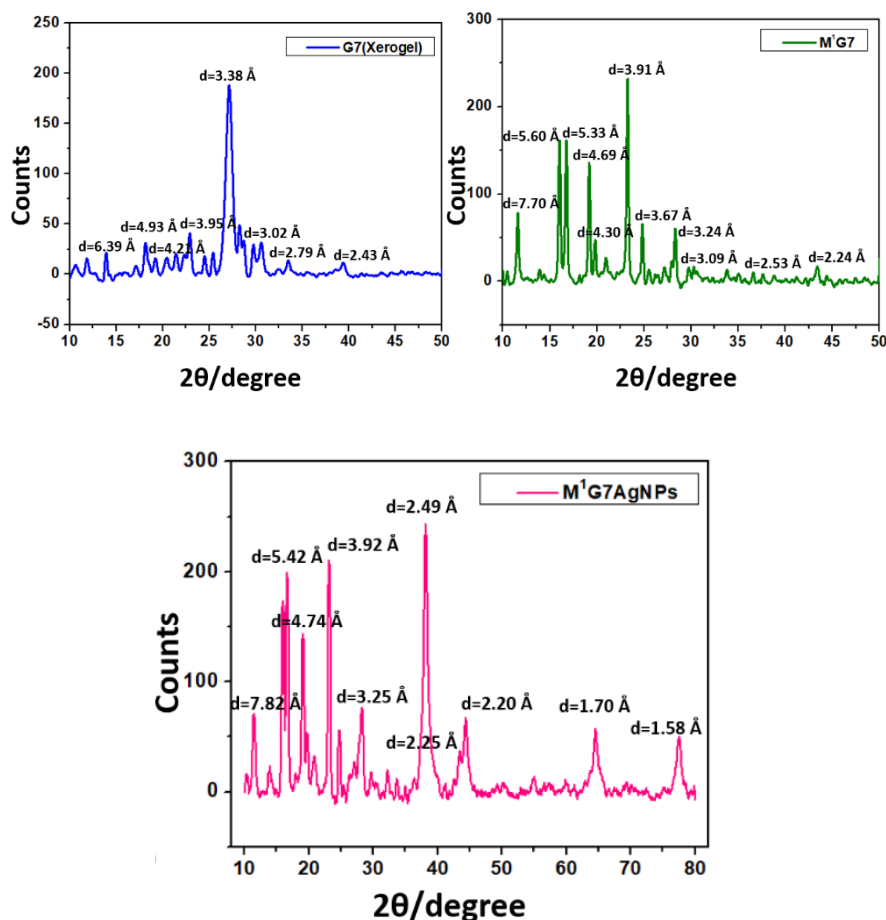


Figure 2.38. FTIR of (a)  $M^1G7$  (b)  $M^2G7$  (c)  $M^3G7$  (d)  $M^4G7$  (e)  $M^5G7$  (f)  $M^6G7$ .

The probable chemical composition of the **M<sup>1</sup>G7** gel was formulated based on the ESI-MS and IR spectroscopic data. A molecular ion peak at 488.9 indicates a composition where three **G7** molecules act as bidentate ligands to form a molecule like  $[\text{Fe}(\text{G7})_3]$  with an octahedral coordination, where the ESI-MS peak stands for  $[\text{Fe}(\text{G7})_3 + \text{Na}]^+$  (Figure 2.9). Although based on the ligand structure, it can be assumed that the oxygen atom of the amide group and the N1 atom of the tetrazole group act as chelating donors; however, it cannot be ascertained if the amide proton is lost or the tetrazole proton, conclusively. Furthermore, in all probability, one **G7** molecule binds three different  $\text{Fe}^{3+}$  centers to act as a bridging ligand and generates a framework structure within the gel network. The PXRD analysis also indicates some remarkable results. The peak of xerogel **G7** at around  $2\theta = 33.50^\circ$  (d value 2.79 Å) shows a hydrogen-bonded structure, which gets shifted toward  $2\theta = 37.55^\circ$  (d value 2.53 Å) in **M<sup>1</sup>G7**, revealing the disruption in the hydrogen-bond network. The peak at  $2\theta = 28.35^\circ$  (d value 3.24 Å) gets weakened, showing a disruption in  $\pi$ - $\pi$  stacking.<sup>[61]</sup> The strong peak at  $2\theta = 23.19^\circ$  (d value 3.91 Å) represents the strong columnar stacking in **M<sup>1</sup>G7**. The  $2\theta = 27.16^\circ$  value of **G7** (d value 3.38 Å) is retained in the case of the xerogel of **M<sup>1</sup>G7AgNPs**, indicating retention of extensive  $\pi$ - $\pi$  stacking between the aromatic rings. The peak at  $2\theta = 33.50^\circ$  with a d value of the peak at 2.79 Å indicates the presence of extensive hydrogen bonding in **M<sup>1</sup>G7AgNPs** (Figure 2.39). In the cases of **M<sup>2</sup>G7**, **M<sup>3</sup>G7**, **M<sup>4</sup>G7**, **M<sup>5</sup>G7**, and **M<sup>6</sup>G7**, the peak ranges from  $2\theta = 22.24$  to  $23.76^\circ$  with the d-spacing ranging from 4.07 to 3.82 Å, showing a columnar stacking. While the peak ranges from  $2\theta = 26.85$  to  $27.79^\circ$  with a d-spacing value from 3.41 to 3.30 Å, showing  $\pi$ - $\pi$  stacking. Here, the peak ranges from  $31.76$  to  $35.82^\circ$  with a d-spacing range from 2.93 to 2.63 Å, showing the presence of hydrogen bonds. The PXRD data of the **M<sup>3</sup>G7** metallo gel shows a peak at  $2\theta = 31.68^\circ$  with a d value of 2.93 Å, which gets shifted with respect to **G7** and represents the disruption in hydrogen bonding. The peak at  $2\theta = 33.50^\circ$  (d value 2.79 Å) in **G7** disappears in the case of **M<sup>4</sup>G7**, showing the absence of hydrogen bonds (Figure 2.40). The

self-assembly of organogelation was also investigated through the FE-SEM technique.<sup>[53, 62-64]</sup>

The morphological studies show that organogel **G7** has a nanofibrous structure, and when metallogels are formed, this fibrous morphology disrupts considerably and gets converted into a dense three-dimensional (3D) leaflike network for **M<sup>I</sup>G7** (Figure 2.41). Interestingly, the other metallogels showed a fibrillar network to some extent similar to the **G7** morphology.



**Figure 2.39.** PXRD pattern of Xerogel **G7**, Metallogel **M<sup>I</sup>G7** and Silver Nanocomposite **M<sup>I</sup>G7AgNPs**.

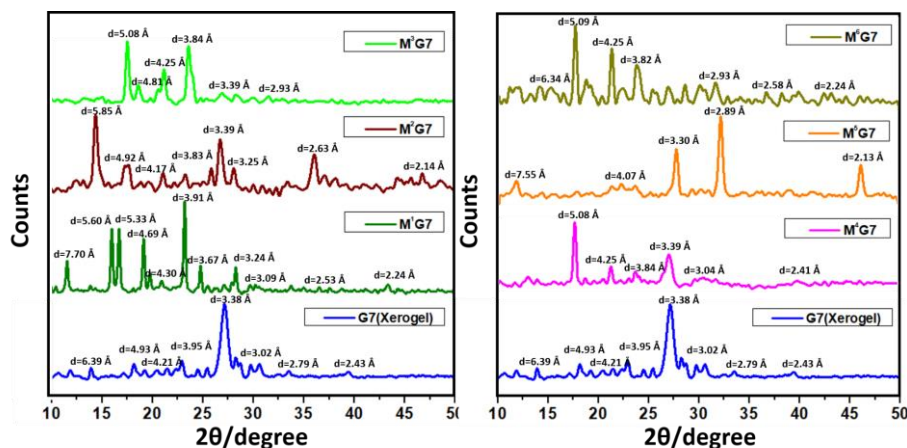


**Figure 2.40.** PXRD of Xerogel  $G7$  and metallogels  $M^1G7$ ,  $M^2G7$ ,  $M^3G7$ ,  $M^4G7$ ,  $M^5G7$  and  $M^6G7$ .

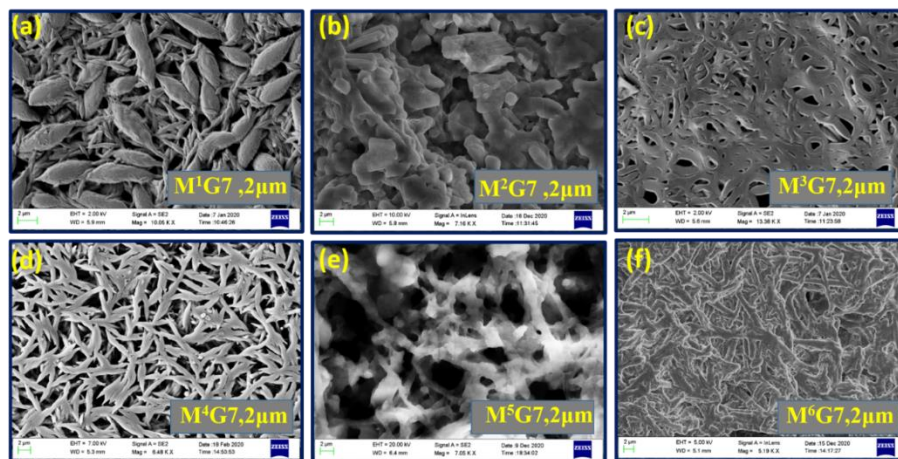


**Figure 2.41.** SEM image of (a)  $M^1G7$  (Fe (III) gel) (b)  $M^2G7$  (Co (II) gel) (c)  $M^3G7$  (Cu (II) gel) (d)  $M^4G7$  (Zn (II) gel) (e)  $M^5G7$  (Ag (I) gel) (f)  $M^6G7$  (Ni (II) gel).

Plant and animal biomaterials show an intrinsic natural self-healing property. Metallogels are found to be potential candidates that can mimic such kinds of properties.<sup>[11]</sup> Tetrazole, with four electronegative N-atoms in the ring, is one of the probable candidates that shows an inherited self-healing property as it forms coordinate covalent bonds with metal centers and is also open for extensive hydrogen bonding.<sup>[65]</sup> The  $M^1G7AgNPs$  nanometallogel has a self-healing nature among all; therefore, it is the most captivating. It is interesting to note that no literature report is available so far on the self-healing property of silver-nanoparticle-containing Fe(III)-metallogels. It is further interesting to

mention that only the bimetallic gel containing the nanoparticles obtained from the precursor composite showed this self-healing ability, indicating an active role of the nanoparticles in repairing the disturbed molecular interactions in the DMSO/water mixture. Therefore, it is quite possible that the metal nanoparticles may act as junctions inducing self-healing properties in this dual nanostructured metallogel. The extra coordination ability due to the presence of Ag nanoparticles with amide and tetrazole groups of gelator **G7** may enhance the noncovalent interactions and driving force behind the unique self-healing ability.<sup>[66]</sup> TEM has been used for the morphological analysis, which reveals the circular shape of the **M<sup>1</sup>G7AgNPs** nanogel. The self-healing property is demonstrated by making a cut in the center of the piece of gel material. It has been observed that upon standing for 30 min to 12 hours, the gel material starts to self-heal without any stimuli, and the cut in the center of the piece of the gel (**M<sup>1</sup>G7AgNPs**) gets plugged over a period of one day. Rheological time oscillation sweep (TOS)/strain sweep experiment was done for the **M<sup>1</sup>G7AgNPs** nanometallogel with minimum and maximum applied strains with a constant angular frequency of 10 rad/s. The TOS/recovery test was performed to confirm the self-healing behavior.<sup>[67]</sup> This recovery test is performed for low-molecular-weight gels to show their thixotropic behavior. A tensile test can explain the self-healing behavior in the polymeric gel system or stretchable gels.<sup>[68]</sup> In the case of reported LMWG, four cycles of TOS tests were done with applied periodic low (0.5% strain) and high (100% strain) strains with an interval of 200 s. In step 1, the strain below the deformation level (a low strain of 0.5%) was applied to the **M<sup>1</sup>G7AgNP** nanometallogel. The result is that the storage modulus ( $G'$ ) was found to be larger than the loss modulus ( $G''$ ) of the nanometallogel, indicating the formation of a stable metallogel by a cross-linked structure. In step 2, after 200 s, a higher strain (100% strain) was applied to the same nanogel, and the result is that the  $G'$  was found to be smaller than  $G''$ , showing the conversion of the gel into a sol (liquidlike), indicating the destruction of the cross-linked system inside the gel matrix. In step 3, when again a low strain (0.5% strain) was applied to the same sample of the

nanometallogel, the broken cross-linked system recovered, and the sol was converted into a gel within 200 s. This experiment was continuously done for four cycles, and due to the regeneration of noncovalent and metal–ligand interactions, the nanogel showed a sol–gel–sol transition, which confirmed the self-healing behavior of the  $M^I G7AgNs$  nanometallogel. No change in gel strength was observed even after 3–4 cycles (Figure 2.42).

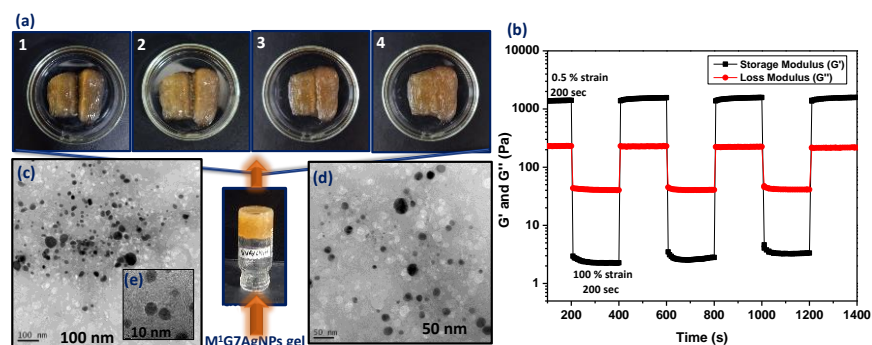


**Figure 2.42.** (a) Image showing self-healing property of  $M^I G7AgNPs$  nano-metallogel (b) Time oscillation strain sweep experiment (Thixotropic behavior) of  $M^I G7AgNPs$  gel at minimum (0.5 %) and maximum (100 %) strain. (c), (d), (e) The TEM images of  $M^I G7AgNPs$  gel at 100 nm, 50 nm and 10 nm respectively.

## 2.4 Conclusions

An ionic gelator molecule **G7** with carboxamide and tetrazole functionalities was synthesized and characterized. A series of metallogels with Fe(III), Fe(II) Co(II), Cu(II), Zn(II), Ag(I), and Ni(II) were fabricated and characterized. Several metallogels showed in situ generation and stabilization of silver nanoparticles to obtain bimetallic nanocomposites. Due to the greater stability and smaller-sized silver nanoparticle formation ability, the iron(III)-containing nanocomposite  $M^I G7AgNPs$  was used as a catalyst to reduce nitroaromatic compounds to the corresponding amines, which showed almost quantitative conversions. The reduction reactions of nitro compounds were investigated by UV–vis, GCMS, and  $^1H$  NMR techniques, and completion of the reaction was achieved in 35 min. The organogel **G7** was found to be capable of absorbing different metal ions from an

aqueous solution due to its porous nature and converting them into metallogels. It was also observed that among all of the metallogels, transition to the crystalline product occurs selectively for the iron(III) ion. Dual metallogels of Fe(III) with Fe(II), Co(II), Cu(II), Zn(II), and Ag(I) can get fabricated. Most interestingly, the nanocomposite **M<sup>1</sup>G7AgNP** in the presence of **G7** gets converted into the **M<sup>1</sup>G7AgNP** nanometallogel, which exclusively shows the self-healing property in the presence of silver nanoparticles and iron ions. This is the first example where the presence of nanoparticles of a different metal atom inside the first metallogel imparts the self-healing property in a metallogel.

## **2.5 Declaration**

This chapter is adapted from ACS Appl. Mater. Interfaces, 2021, 13, 59567-59579. (D.O.I. 10.1021/acscami.1c19217)

## **2.6 References**

- [1] Zhao, X., Chen, X., Yuk, H., Lin, S., Liu, X., Parada, G. (2021), Soft materials by design: Unconventional polymer networks give extreme properties, Chem. Rev., 121, 4309–4372 (DOI: 10.1021/acs.chemrev.0c01088)
- [2] Shim, H.J., Sunwoo, S.H., Kim, Y., Koo, J.H., Kim, D.H. (2021), Functionalized elastomers for intrinsically soft and biointegrated electronics, Adv. Healthcare Mater., 2021, 10, No. 2002105 (DOI: 10.1002/adhm.202002105)
- [3] Panja, S., Adams, D.J. (2021), Stimuli responsive dynamic transformations in supramolecular gels, Chem. Soc. Rev., 2021, 50, 5165– 5200 (DOI: 10.1039/D0CS01166E)
- [4] Shirakawa, M., Fujita, N., Tani, T., Kaneko, K., Shinkai, S. (2005), Organogel of an 8-quinolinol platinum (II) chelate derivative and its efficient phosphorescence emission effected by inhibition of dioxygen quenching, Chem. Commun., 33, 4149–4151 (DOI: 10.1039/B506148B)

- [5] Tan, P., Xie, X.Y., Liu, X.Q., Pan, T., Gu, C., Chen, P.F., Zhou, J.Y., Pan, Y., Sun, L.B. (2017), Fabrication of magnetically responsive HKUST-1/Fe<sub>3</sub>O<sub>4</sub> composites by dry gel conversion for deep desulfurization and denitrogenation, *J. Hazard. Mater.*, 321, 344–352 (DOI: 10.1016/j.jhazmat.2016.09.026)
- [6] Jiang, X.M., Huang, X.J., Song, S.S., Ma, X.Q., Zhang, Y.M., Yao, H., Wei, T.B., Lin, Q. (2018), Tri-pillar [5] arene-based multi-stimuli-responsive supramolecular polymers for fluorescence detection and separation of Hg<sup>2+</sup>, *Polym. Chem.*, 9, 4625–4630 (DOI: 10.1039/C8PY01085D)
- [7] Zhang, P., Sui, Y., Xiao, G., Wang, Y., Wang, C., Liu, B., Zou, G., Zou, B. (2013), Facile fabrication of faceted copper nanocrystals with high catalytic activity for p-nitrophenol reduction, *J. Mater. Chem. A*, 1, 1632–1638 (DOI: 10.1039/C2TA00350C)
- [8] Naseer, F., Ajmal, M., Bibi, F., Farooqi, Z.H., Siddiq, M. (2018), Copper and cobalt nanoparticles containing poly (acrylic acid-co-acrylamide) hydrogel composites for rapid reduction of 4-nitrophenol and fast removal of malachite green from aqueous medium, *Polym. Compos.*, 39, 3187–3198 (DOI: 10.1002/pc.24329)
- [9] Ge, J., Neofytou, E., Cahill III, T.J., Beygui, R.E., Zare, R.N. (2012), Drug release from electric-field-responsive nanoparticles, *ACS Nano*, 6, 227–233 (DOI: 10.1021/nn203430m)
- [10] Feldner, T., Häring, M., Saha, S., Esquena, J., Banerjee, R., Díaz, D.D. (2016), Supramolecular metallogel that imparts self-healing properties to other gel networks, *Chem. Mater.*, 28, 3210–3217 (DOI: 10.1021/acs.chemmater.6b01144)
- [11] Malviya, N., Ranjan, R., Sonkar, C., Mobin, S.M., Mukhopadhyay, S. (2019), Self-healable lanthanoid-based metallogels: dye removal and crystallization in the confined gel state, *ACS Appl. Nano Mater.*, 2, 8005–8015 (DOI: 10.1021/acsanm.9b02064)

- [12] Choudhury, P., Dinda, S., Das, P.K. (2020), Fabrication of soft-nanocomposites from functional molecules with diversified applications, *Soft Matter*, 16, 27–53 (DOI: 10.1039/C9SM01304K)
- [13] Chakrabarty, A., Maitra, U. (2013), Organogels from dimeric bile acid esters: in situ formation of gold nanoparticles, *J. Phys. Chem. B*, 117, 8039–8046 (DOI: 10.1021/jp4029497)
- [14] Guo, H., Feng, Q., Xu, K., Xu, J., Zhu, J., Zhang, C., Liu, T. (2019), Self-templated conversion of metallogel into heterostructured tmp@ carbon quasiaerogels boosting bifunctional electrocatalysis, *Adv. Funct. Mater.*, 29, 1903660 (DOI: 10.1002/adfm.201903660)
- [15] Wei, C.W., Wang, X.J., Gao, S.Q., Wen, G.B., Lin, Y.W. (2019), A Phenylalanine Derivative Containing a 4-Pyridine Group Can Construct Both Single Crystals and a Selective Cu-Ag Bimetallohydrogel, *Eur. J. Inorg. Chem.*, 2019, 1349–1353 (DOI: 10.1002/ejic.201900078)
- [16] Tan, M., He, T., Liu, J., Wu, H., Li, Q., Zheng, J., Wang, Y., Sun, Z., Wang, S., Zhang, Y. (2018), Supramolecular bimetallogels: a nanofiber network for bimetal/nitrogen co-doped carbon electrocatalysts, *J. Mater. Chem. A*, 6, 8227–8232 (DOI: 10.1039/C8TA01898G)
- [17] Sharma, M., Sarma, P.J., Goswami, M.J., Bania, K.K. (2017), Metallogel templated synthesis and stabilization of silver-particles and its application in catalytic reduction of nitro-arene, *J. Colloid Interface Sci.*, 490, 529–541 (DOI: 10.1016/j.jcis.2016.11.065)
- [18] Bai, S.Q., Young, D.J., Hor, T.A. (2011), Nitrogen-rich azoles as ligand spacers in coordination polymers, *Chem. - Asian J.*, 6, 292–304 (DOI: 10.1002/asia.201000698)
- [19] Malviya, N., Mandal, P., Das, M., Ganguly, R., Mukhopadhyay, S. (2017), Nickel tetrazolato complexes synthesized by microwave irradiation: Catecholase like activity and interaction

- with biomolecules, *J. Coord. Chem.*, 70, 261–278 (DOI: 10.1080/00958972.2016.1260121)
- [20] Lee, J.H., Kang, S., Lee, J.Y., Jung, J.H. (2012), A tetrazole-based metallogel induced with Ag<sup>+</sup> ion and its silver nanoparticle in catalysis, *Soft Matter*, 8, 6557–6563 (DOI: 10.1039/C2SM25316J)
- [21] Cantekin, S., de Greef, T.F., Palmans, A.R. (2012), Benzene-1, 3, 5-tricarboxamide: a versatile ordering moiety for supramolecular chemistry, *Chem. Soc. Rev.*, 41, 6125–6137 (DOI: 10.1039/C2CS35156K)
- [22] Xiao, T., Wang, L. (2018), Recent advances of functional gels controlled by pillar [n] arene-based host–guest interactions, *Tetrahedron Lett.*, 59, 1172–1182 (DOI: 10.1016/j.tetlet.2018.02.028)
- [23] Sing, K.S.W., Rouquerol J., Siemieniowska T. (1985), Reporting physisorption data for gas/solid systems with special reference to the determination of surface area and porosity, *Pure Appl. Chem.*, 57, 603–619 (DOI: 10.1351/pac198557040603)
- [24] Zielinski, J.M., Kettle, L. (2013), Physical characterization: surface area and porosity, Intertek Chemicals and Pharmaceuticals, Intertek: London
- [25] Fagerlund, G. (1973), Determination of specific surface by the BET method, *Mat. Constr.*, 6, 239–245 (DOI: 10.1007/BF02479039)
- [26] Sing, K.S., Williams, R.T. (2004), Physisorption hysteresis loops and the characterization of nanoporous materials, *Adsorpt. Sci. Technol.*, 22, 773–782 (DOI: 10.1260/0263617053499032)
- [27] Hu, W.B., Cai, H.R., Hu, W.J., Zhao, X.L., Liu, Y.A., Li, J.S., Jiang, B., Wen, K. (2017), Pillar [5] arene–Py–Cu Gel, the First Pillar [5] arene-Based Metallo (organo) gel, and Adsorption of Sudan III by Its Gel-Precipitate, *Eur. J. Inorg. Chem.*, 2017, 3551–3554 (DOI: 10.1002/ejic.201700602)
- [28] Thommes, M., Kaneko, K., Neimark, A.V., Olivier, J.P., Rodriguez-Reinoso, F., Rouquerol, J., Sing, K.S. (2015),

- Physisorption of gases, with special reference to the evaluation of surface area and pore size distribution (IUPAC Technical Report), *Pure Appl. Chem.*, 87, 1051–1069 (DOI: 10.1515/pac-2014-1117)
- [29] Inglezakis, V.J., Pouloupoulos, S.G., Kazemian, H. (2018), Insights into the S-shaped sorption isotherms and their dimensionless forms, *Microporous Mesoporous Mater.*, 272, 166–176 (DOI: 10.1016/j.micromeso.2018.06.026)
- [30] Coltharp, M.T. (2005), On numerical classification of solution adsorption isotherms, *Langmuir*, 2005, 21, 3475–3479 (DOI: 10.1021/la047539l)
- [31] Song, W., Li, Y., Geng, L., Feng, G., Ren, J., Yu, X. (2021), Polydiacetylene-based gels for solvent discrimination and formation of Au/Ag nanoparticles with embedded photocatalytic performance, *Mater. Des.*, 205, 109744 (DOI: 10.1016/j.matdes.2021.109744)
- [32] Gogoi, N., Babu, P.J., Mahanta, C., Bora, U. (2015), Green synthesis and characterization of silver nanoparticles using alcoholic flower extract of *Nyctanthes arbortristis* and in vitro investigation of their antibacterial and cytotoxic activities, *Mater. Sci., Eng. C*, 46, 463–469 (DOI: 10.1016/j.msec.2014.10.069)
- [33] Bonsak, J., Mayandi, J., Thøgersen, A., Stensrud Marstein, E., Mahalingam, U. (2011), Chemical synthesis of silver nanoparticles for solar cell applications, *Phys. Status Solidi C*, 8, 924–927 (DOI: 10.1002/pssc.201000275)
- [34] Smitha, S.L., Nissamudeen, K.M., Philip, D., Gopchandran, K.G. (2008), Studies on surface plasmon resonance and photoluminescence of silver nanoparticles, *Spectrochim. Acta, Part A*, 71, 186–190 (DOI: 10.1016/j.saa.2007.12.002)
- [35] Wu, X., Wu, L., Cao, X., Li, Y., Liu, A., Liu, S. (2018), Nitrogen-doped carbon quantum dots for fluorescence detection of  $\text{Cu}^{2+}$  and electrochemical monitoring of bisphenol A, *RSC Adv.*, 8, 20000–20006 (DOI: 10.1039/C8RA03180K)

- [36] Malathi, S., Ezhilarasu, T., Abiraman, T., Balasubramanian, S. (2014), One pot green synthesis of Ag, Au and Au–Ag alloy nanoparticles using isonicotinic acid hydrazide and starch, *Carbohydr. Polym.*, 111, 734–743 (DOI: 10.1016/j.carbpol.2014.04.105)
- [37] Xue, C., He, Y., Liu, Y., Saha, P., Cheng, Q. (2019), Controlled synthesis of alkalized Ti<sub>3</sub>C<sub>2</sub> MXene-supported β-FeOOH nanoparticles as anodes for lithium-ion batteries, *Ionics*, 25, 3069–3077 (DOI: 10.1007/s11581-019-02901-0)
- [38] Ding, Y., Zhang, F., Xu, J., Miao, Y., Yang, Y., Liu, X., Xu, B. (2017), Synthesis of short-chain passivated carbon quantum dots as the light emitting layer towards electroluminescence, *RSC Adv.*, 7, 28754–28762 (DOI: 10.1039/C7RA02421E)
- [39] Li, L., Ma, P., Hussain, S., Jia, L., Lin, D., Yin, X., Lin, Y., Cheng, Z., Wang, L. (2019), FeS<sub>2</sub>/carbon hybrids on carbon cloth: a highly efficient and stable counter electrode for dye-sensitized solar cells, *Sustainable Energy Fuels*, 3, 1749–1756 (DOI: 10.1039/C9SE00240E)
- [40] Nasralla, N., Yeganeh, M., Astuti, Y., Piticharoenphun, S., Shahtahmasebi, N., Kompany, A., Karimipour, M., Mendis, B.G., Poolton, N.R.J., Šiller, L. (2013), Structural and spectroscopic study of Fe-doped TiO<sub>2</sub> nanoparticles prepared by sol–gel method, *Sci. Iran.*, 20, 1018–1022 (DOI: 10.1016/j.scient.2013.05.017)
- [41] Wang, X., Shen, Y., Xie, A., Chen, S. (2013), One-step synthesis of Ag@ PANI nanocomposites and their application to detection of mercury, *Mater. Chem. Phys.*, 140, 487–492 (DOI: 10.1016/j.matchemphys.2013.03.058)
- [42] Layek, K., Kantam, M.L., Shirai, M., Nishio-Hamane, D., Sasaki, T., Maheswaran, H. (2012), Gold nanoparticles stabilized on nanocrystalline magnesium oxide as an active catalyst for reduction of nitroarenes in aqueous medium at room temperature, *Green Chem.*, 14, 3164–3174 (DOI: 10.1039/C2GC35917K)

- [43] Suzuki, M., Nakajima, Y., Yumoto, M., Kimura, M., Shirai, H., Hanabusa, K. (2003), Effects of hydrogen bonding and van der Waals interactions on organogelation using designed low-molecular-weight gelators and gel formation at room temperature, *Langmuir*, 19, 8622–8624 (DOI: 10.1021/la034772v)
- [44] Malviya, N., Sonkar, C., Kundu, B.K., Mukhopadhyay, S. (2018), Discotic organic gelators in ion sensing, metallo gel formation, and bioinspired catalysis, *Langmuir*, 34, 11575–11585 (DOI: 10.1021/acs.langmuir.8b02352)
- [45] Hakkarainen, B., Fujita, K., Immel, S., Kenne, L., Sandström, C. (2005), <sup>1</sup>H NMR studies on the hydrogen-bonding network in mono- $\alpha$ -D-glucopyranosyl- $\beta$ -cyclodextrin and its complex with adamantane-1-carboxylic acid, *Carbohydr. Res.*, 340, 1539–1545 (DOI: 10.1016/j.carres.2005.03.016)
- [46] Lin, Q., Fan, Y.Q., Mao, P.P., Liu, L., Liu, J., Zhang, Y.M., Yao, H., Wei, T.B. (2018), Pillar [5] arene-based supramolecular organic framework with multi-guest detection and recyclable separation properties, *Chem. Eur. J.*, 24, 777–783 (DOI: 10.1002/chem.201705107)
- [47] Hu, D., Wang, G., Feng, J., Lu, X. (2016), Exploring supramolecular self-assembly of a bisamide nucleating agent in polypropylene melt: the roles of hydrogen bond and molecular conformation, *Polymer*, 93, 123–131 (DOI: 10.1016/j.polymer.2016.04.033)
- [48] Hirashima, Y., Sato, H., Suzuki, A. (2005), ATR-FTIR spectroscopic study on hydrogen bonding of poly (N-isopropylacrylamide-co-sodium acrylate) gel, *Macromolecules*, 38, 9280–9286 (DOI: 10.1021/ma051081s)
- [49] Beltrán, E., Garzoni, M., Feringán, B., Vancheri, A., Barberá, J., Serrano, J.L., Pavan, G.M., Giménez, R., Sierra, T. (2015), Self-organization of star-shaped columnar liquid crystals with a coaxial nanophase segregation revealed by a combined

- experimental and simulation approach, *Chem. Commun.*, 51, 1811–1814 (DOI: 10.1039/C4CC08602C)
- [50] Zhang, Y., Liang, C., Shang, H., Ma, Y., Jiang, S. (2013), Supramolecular organogels and nanowires based on a V-shaped cyanostilbene amide derivative with aggregation-induced emission (AIE) properties, *J. Mater. Chem. C*, 1, 4472–4480 (DOI: 10.1039/C3TC30545G)
- [51] Ghosh, A., Das, P., Kaushik, R., Damodaran, K.K., Jose, D.A. (2016), Anion responsive and morphology tunable tripodal gelators. *RSC Adv.*, 6, 83303–83311 (DOI: 10.1039/C6RA16345A)
- [52] Xu, Y.L., Li, C.T., Cao, Q.Y., Wang, B.Y., Xie, Y. (2017), A pyrenyl-appended organogel for fluorescence sensing of anions, *Dyes Pigm.*, 139, 681–687 (DOI: <https://doi.org/10.1016/j.dyepig.2016.12.068>)
- [53] Mears, L.L., Draper, E.R., Castilla, A.M., Su, H., Zhuola, Dietrich, B., Nolan, M.C., Smith, G.N., Douth, J., Rogers, S., Akhtar, R. (2017), Drying affects the fiber network in low molecular weight hydrogels, *Biomacromolecules*, 18, 3531–3540 (DOI: 10.1021/acs.biomac.7b00823)
- [54] Du, X., Zhou, J., Shi, J., Xu, B. (2015), Supramolecular hydrogelators and hydrogels: from soft matter to molecular biomaterials, *Chem. Rev.*, 115, 13165–13307 (DOI: 10.1021/acs.chemrev.5b00299)
- [55] Li, L., Aoki, Y. (1997), Rheological images of poly (vinyl chloride) gels. 1. The dependence of sol–gel transition on concentration, *Macromolecules*, 30, 7835–7841 (DOI: 10.1021/ma971045w)
- [56] Wagner, C.E., Turner, B.S., Rubinstein, M., McKinley, G.H., Ribbeck, K. (2017), A rheological study of the association and dynamics of MUC5AC gels, *Biomacromolecules*, 18, 3654–3664 (DOI: 10.1021/acs.biomac.7b00809)
- [57] Argüelles-Monal, W., Goycoolea, F.M., Peniche, C., Higuera-Ciapara, I. (1998), Rheological study of the

- chitosan/glutaraldehyde chemical gel system, *Polym. Gels Networks*, 6, 429–440 (DOI: 10.1016/S0966-7822(98)00032-X)
- [58] Fan, X., Xu, H., Zhang, Q., Song, Y., Zheng, Q. (2019), Insight into the weak strain overshoot of carbon black filled natural rubber, *Polymer*, 167, 109-117 (DOI: 10.1016/j.polymer.2019.01.076)
- [59] Hyun, K., Kim, S.H., Ahn, K.H., Lee, S.J. (2002), Large amplitude oscillatory shear as a way to classify the complex fluids, *J. Non-Newton. Fluid Mech.*, 107, 51-65 (DOI: 10.1016/S0377-0257(02)00141-6)
- [60] Donley, G.J., Singh, P.K., Shetty, A., Rogers, S.A. (2020), Elucidating the  $G''$  overshoot in soft materials with a yield transition via a time-resolved experimental strain decomposition, *Proc. Natl. Acad. Sci.*, 117, 21945-21952 (DOI: 10.1073/pnas.2003869117)
- [61] Piepenbrock, M.O.M., Clarke, N., Steed, J.W. (2011), Rheology and silver nanoparticle templating in a bis (urea) silver metallogel, *Soft Matter*, 7, 2412–2418 (DOI: 10.1039/C0SM00647E)
- [62] Feng, Y., Liu, Z., Wang, L., Chen, H., He, Y., Fan, Q. (2012), Poly (benzyl ether) dendrons without conventional gelation motifs as a new kind of effective organogelators, *Chin. Sci. Bull.*, 57, 4289–4295 (DOI: 10.1007/s11434-012-5479-2)
- [63] Du, X., Zhou, J., Shi, J., Xu, B. (2015), Supramolecular hydrogelators and hydrogels: from soft matter to molecular biomaterials, *Chem. Rev.*, 115, 13165–13307 (DOI: 10.1021/acs.chemrev.5b00299)
- [64] Kartha, K.K., Babu, S.S., Srinivasan, S., Ajayaghosh, A. (2012), Attogram sensing of trinitrotoluene with a self-assembled molecular gelator, *J. Am. Chem. Soc.*, 134, 4834–4841 (DOI: 10.1021/ja210728c)
- [65] Hegarty, I.N. (2020), *Triazole-Pyridine Derivatives: Versatile Building Blocks for Metallosupramolecular Assemblies and Materials* (Doctoral dissertation, The University of Dublin)

- [66] Li, C.H., Zuo, J.L. (2020), Self-healing polymers based on coordination bonds, *Adv. Mater.*, 32, 1903762 (DOI: 10.1002/adma.201903762)
- [67] McCarney, E.P., Byrne, J.P., Twamley, B., Martínez-Calvo, M., Ryan, G., Möbius, M.E., Gunnlaugsson, T. (2015), Self-assembly formation of a healable lanthanide luminescent supramolecular metallogel from 2, 6-bis (1, 2, 3-triazol-4-yl) pyridine (btp) ligands, *Chem. Commun.*, 51, 14123–14126 (DOI: 10.1039/C5CC03139G)
- [68] Zheng, W., Li, Y., Xu, L., Huang, Y., Jiang, Z., Li, B. (2020), Highly stretchable, healable, sensitive double-network conductive hydrogel for wearable sensor, *Polymer*, 211, No. 123095 (DOI: 10.1016/j.polymer.2020.123095)



## Chapter 3

**Another tris-tetrazole based nanostructured soft material: studies on self-healing, AIEE, and rheological and fluorometric detection of 3-aminopyridine**



## Chapter 3

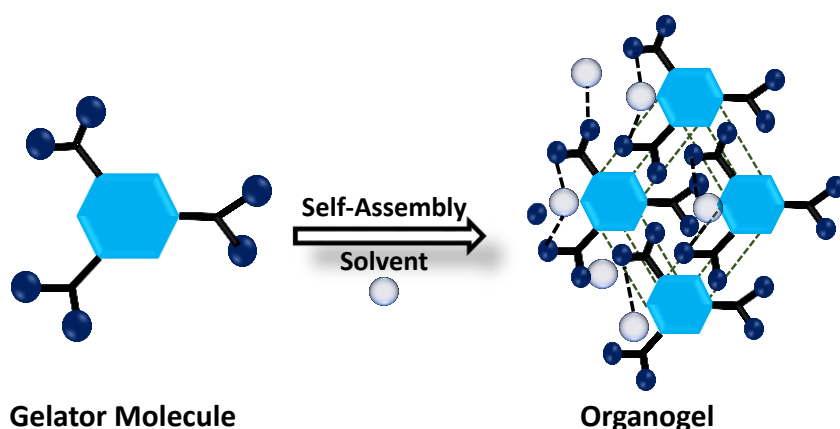
### **Another tris-tetrazole based nanostructured soft material: studies on self-healing, AIEE, and rheological and fluorometric detection of 3-aminopyridine**

#### **3.1 Introduction**

Non-covalent forces generally operate between different molecules and, because of their weak nature, are easily get affected by external stimuli like heat, light, pH, etc.<sup>[1-6]</sup> The associated changes related to these effects in the physical properties of the gels can sometimes be observed by the naked eye or otherwise recorded through different instrumentation techniques. This phenomenon opens up the possibility of utilizing LMWGs as sensing materials.<sup>[7-9]</sup> Interestingly, the position of the complementary donor-accepter sites of hydrogen bonds can play a crucial role in molecular recognition phenomena, as evident in biological molecules like DNA.<sup>[10, 11]</sup> However, only a few studies have been available so far where a gel's properties have been used to discriminate between isomeric organic molecules.<sup>[12-16]</sup> The explanation of the discriminatory behaviour with theoretical studies of the gel structures and the associated properties, which can get influenced by the relative hydrogen bond donor-acceptor sites in the isomers, has rarely been explored. To explore such a possibility, a tetrazole-based gelator molecule, N<sup>2</sup>, N<sup>4</sup>, N<sup>6</sup>-tri(1H-tetrazol-5-yl)-1,3,5-triazine-2,4,6-triamine (**G8**), has been designed and synthesized with a number of hydrogen donor-acceptor sites. The physical properties of the fabricated gel were tested with three different isomers of aminopyridine (2-AP, 3-AP, and 4-AP), also containing hydrogen bond donor-acceptor sites.

Interestingly we have found that the isomeric positions of the functional groups can have a significant impact on different physical properties of the gel. The difference in the interaction between gelator components with varying isomers of aminopyridine in the mixed organogel resulted in substantial differences in gel strength, fluorescence, and visual color

as the signature of molecular recognition. Therefore, this chapter describes the difference in interactions between the gelator and isomers, which leads to such discriminatory behavior in the formation of mixed organogels emission (AIEE). Mixed organogels of **G8** with different aminopyridines have been fabricated, and the differences in the properties of the mixed organogels and subsequent molecular recognition of 3-aminopyridine by the **G8** organogel have been explored and presented herein.



## 3.2 Experimental section

### 3.2.1 Material and method

Chemicals and solvents were purchased from commercial sources and used directly. NMR spectra were obtained using an AVANCE NEO500 Ascend Bruker BioSpin International AG at ambient temperature using DMSO- $d_6$ . DFT analyses were performed in RB3LYP, solvent phase ( $H_2O$ ) with the 6-311++G(d,p) basis set. All the other used instruments for analysis were same as described in 2.2.1 of chapter 2.

### 3.2.2 Synthesis of gelator **G8** [ $N^2$ , $N^4$ , $N^6$ -tri(1H-tetrazol-5-yl)-1,3,5-triazine-2,4,6-triamine]

For the synthesis of **G8**, 2.47 g (24 mmol) of the 5-aminotetrazole monohydrate and 3.34 mL (24 mmol) of triethylamine were taken in 80 mL ethanol under ice-cold conditions, and 8 mmol (1.47 g) solid cyanuric chloride was added into it in small portions. The reaction mixture was refluxed for three hours at 80 °C. After the reaction was

completed, the precipitate obtained was filtered and washed with 3N HCl, water, and methanol before being dried at room temperature under vacuum to isolate the desired gelator molecule **G8**. Product yield: 85%.  $^1\text{H}$  NMR does not show peak for -NH as it is exchangeable proton.  $^{13}\text{C}$  NMR of **G8** (100.16 MHz, 298 K, DMSO- $d_6$ ): d 162.90 (cyanuric aromatic carbon), and 150.38 (tetrazole carbon). FTIR of **G8** (KBr):  $3444\text{ cm}^{-1}$ ,  $1644\text{ cm}^{-1}$ ,  $1534\text{ cm}^{-1}$ ,  $1432\text{ cm}^{-1}$ ,  $1345\text{ cm}^{-1}$ ,  $1253\text{ cm}^{-1}$  and  $1024\text{ cm}^{-1}$ . ESI-MS: m/z  $[\text{M}-\text{H}]^-$  calculated for **G8** ( $\text{C}_6\text{H}_5\text{N}_{18}$ ): 329.09, found 329.12.

### 3.2.3 Preparation of gels

In a glass vial, 1 mL Milli-Q water was added into 33 mg (0.1 mmol), 1 mL DMSO solution of **G8**. In less than a minute, a stable organogel **G8** was formed. The concentration of fabricated organogel is 50 mM (33 mg **G8** in 2 mL solvent). In a glass vial, 33 mg of **G8** dissolved in 1 mL DMSO and 1 mL aqueous solution of 9.4 mg (0.1 mmol) aminopyridine were added (1: 1 molar ratio) to make **G8** organogels with aminopyridines. Stable organogels were obtained within a couple of minutes. Gelator **G8** formed an organogel in DMSO:  $\text{H}_2\text{O}$  (1: 1 v/v).

The gelation behavior of **G8** was investigated in different organic solvents and it can be found that it is soluble in DMSO (Table 3.1). In a 1:1 volume ratio of DMSO and Milli-Q water, the critical gel concentration for the **G8** gelator molecule was found to be 34 mM (22.44 mg **G8** in 2 mL solvent) (Table 3.2 and Figure 3.1). The conventional “test tube inversion procedure” was used to confirm gel formation (Figure 3.2).

**Table 3.1.** Solubility of **G8** with different organic solvent. **I**: Insoluble, **S**: Soluble, **G**: Gelation.

Solvent	Solubility	Gelation	Solvent	Solubility	Gelation
Cyclohexane	I	-	Toluene	I	-
THF	I	-	Methanol	I	-
N-Hexane	I	-	DMF	S after heating	G
Acetone	I	-	Chloroform	I	-
Petroleum ether	I	-	Dichloromethane	I	-
Ethyl acetate	I	-	DMSO	S	G
Benzene	I	-	Ethanol	I	-

**Table 3.2.** Optimization table of gelation condition of **G8**.

Concentration of G8 (in 2 mL solution)	DMSO/ H <sub>2</sub> O	Gelation
17 mM (11.22 mg, 0.03 mmol)	1 mL/ 1mL	No
34 mM (22.44 mg, 0.06 mmol)	1 mL/ 1mL	Yes (weak gel)
50 mM (33 mg, 0.1 mmol)	1 mL/ 1mL	Yes( strong gel)
68 mM (44.88 mg, 0.20 mmol)	1 mL/ 1mL	Yes ( strong but opaque gel)
85 mM (56.1 mg, 0.25 mmol)	1 mL/ 1mL	Yes (very strong but opaque gel)

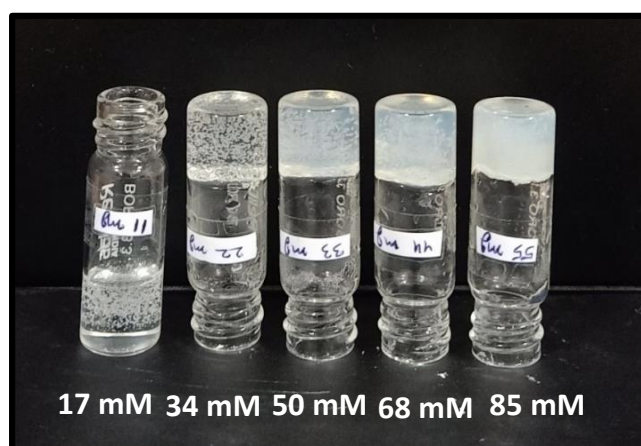


**Figure 3.1.** Optimization of gelation condition of **G8**.

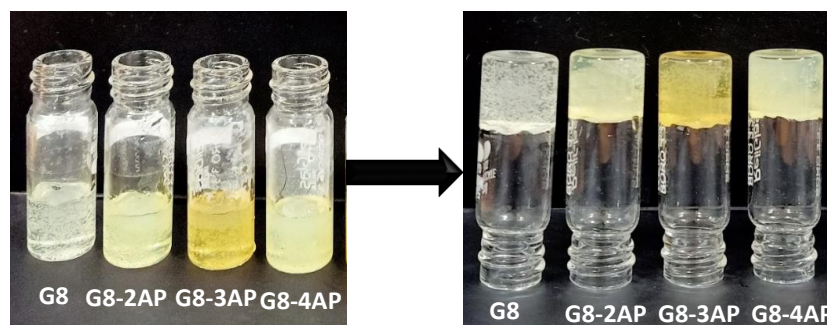


**Figure 3.2.** Confirmation of gel formation by test tube inversion method.

### 3.2.4 Gel melting temperature

The gel melting temperatures ( $T_{\text{gel}}$ ) of organogels **G8** and mixed organogels **G8-2AP**, **G8-3AP**, and **G8-4AP** have been investigated by the same method as mentioned in section 2.2.4 of Chapter 2.

### 3.2.5 Interactions of G8 with isomers of aminopyridine

Further, the mixed-organogels of **G8** with the isomers of aminopyridine were fabricated to analyse the effect of the isomeric positions on gelation behavior. The ratios of the interactions between **G8** and aminopyridines have been derived from the Jobs plot utilizing the fluorescence response of the adduct formation. The optimum ratios of interactions were found from the values of mole fractions at which the fluorescence intensities were found to be maximum.

### 3.2.6 Characterization

The FTIR spectra, UV-vis analysis, NMR studies, powder X-ray diffraction, morphological and rheological analysis of organogels **G8**, **G8-2AP**, **G8-3AP** and **G8-4AP** have been done following similar methods mentioned in section 2.2.5 of chapter 2.

For FE-SEM analysis, the method of drying can change the morphology of gel. Here, two methods are used to take SEM images of gels: -

In first method, the gel was dried by lyophilization, where the gel was converted into its xerogel form without much disturbance in the morphology of the gel. For SEM analysis, the xerogel was further dissolved in a suitable solvent and drop casting was done into a glass

slide and further dried under a desiccator. Due to this further dissolution and drying, the morphology of xerogel is different from the morphology of their gel.

In second method, the gel was applied directly on the glass slide and taken into a vacuum desiccator. During controlled drying by vacuum, the solvent comes out without disturbing the gel matrix. This technique gives nearby actual morphology of gels.

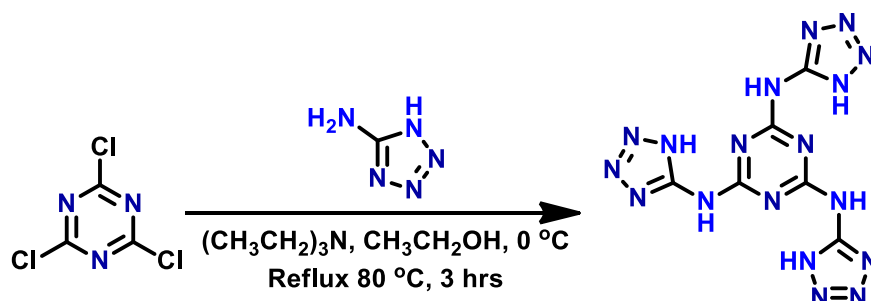
The FE-SEM analysis of **G8**, **G8-2AP**, **G8-3AP** and **G8-4AP** has been done by both methods and found that the morphologies are different for gels (by method 2) and their respective xerogels (by method 1).

The fluorescence spectra of the organogels with aminopyridine were recorded with a FluoroMax-4 spectrofluorometer (HORIBA Jobin Yvon, model: FM-100) in a quartz cuvette (10 mm×10 mm).

### **3.3 Results and discussion**

Tricarboxamide and tetrazole moieties are ideal candidates for gel formation, as evident from our earlier work and other literature reports.<sup>[17-23]</sup> The synthesis of tris(tetrazole) compound **G8** was achieved by secondary amine bond formation between cyanuric chloride and 5-aminotetrazole monohydrate in the presence of triethylamine (Scheme 3.1). A yellowish-white precipitate was obtained. After washing with 3N HCl, Milli-Q water, and methanol, the obtained residue was dried over the vacuum and the final gelator molecule **G8** was formed. The synthesis of **G8** was confirmed by <sup>13</sup>C NMR, IR spectroscopy, CHN elemental analysis and ESI-MS. The FTIR spectrum of **G8** displays distinctive secondary N-H bands at 3444 and 1644 cm<sup>-1</sup>, as well as tetrazole ring bands at 1534, 1432, and 1345 cm<sup>-1</sup> (Figure 3.3). The <sup>1</sup>H NMR of **G8** does not show peak for -NH proton due to its exchangeable nature. The peak at 162 ppm in the <sup>13</sup>C NMR spectrum confirms the presence of cyanuric aromatic carbon, while the peak at 150 ppm is assigned to tetrazole carbon (Figure 3.4). The ESI-MS spectra show a molecular ion peak at 329.12 [M-H]<sup>-</sup> in the negative mode, which confirms the

synthesis of gelator **G8** (Figure 3.5). The CHN elemental analysis has been done for **G8**. The calculated values for C, N, and H are 21.82 %, 76.35 %, 1.83 % respectively and the found values for C, N, and H are 21.48 %, 76.59 % and 1.93 % respectively.



*Scheme 3.1. Synthesis of gelator G8.*

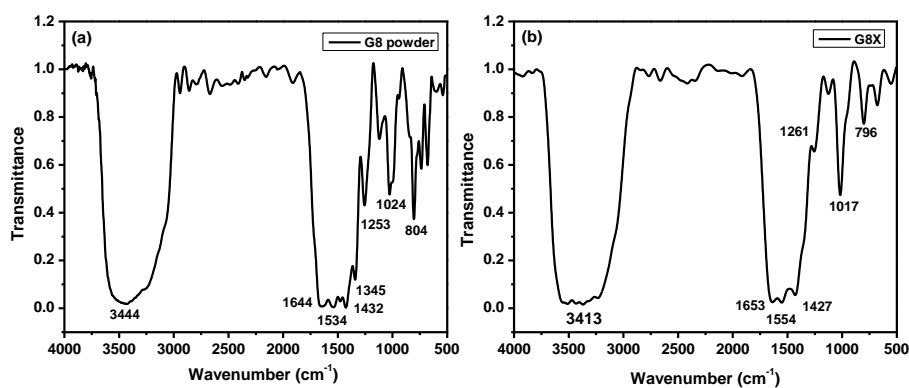


*Figure 3.3. FTIR data of gelator powder G8 and xerogel of G8.*

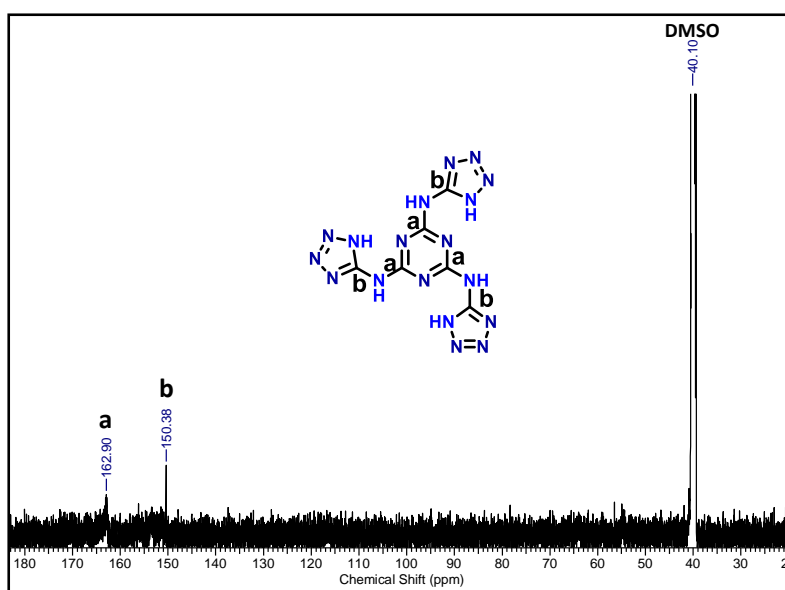


*Figure 3.4.  $^{13}\text{C}$  NMR of gelator G8.*

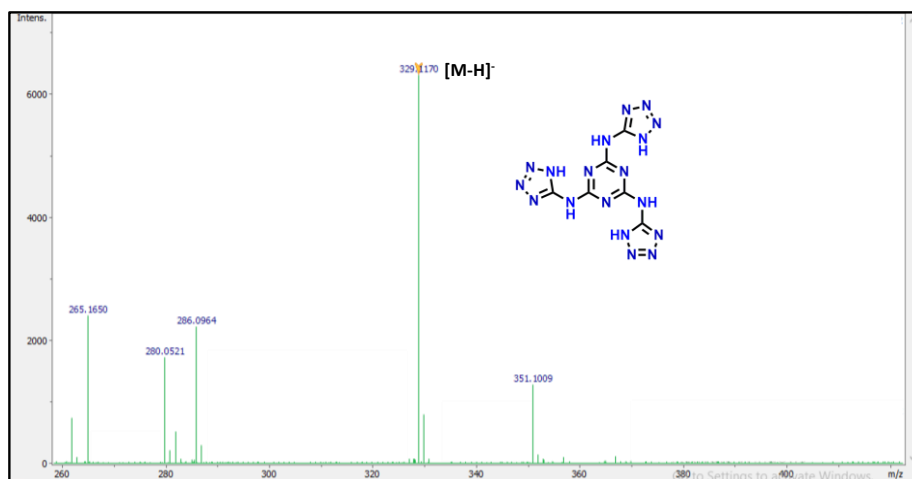
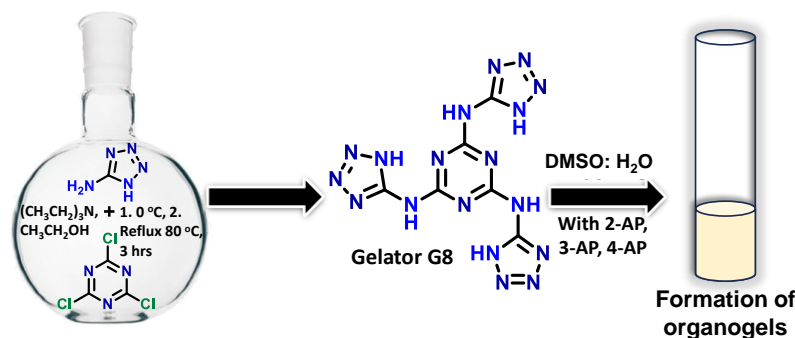


**Figure 3.5.** ESI-MS of gelator **G8**.

**G8** also formed organogels with isomers of aminopyridine with a 1:1 molar ratio (Scheme 3.2). The four synthesized organogels show notable differences in strength, fluorescence intensity, and visual sensing. The heating–cooling experiments of organogels **G8-2AP**, **G8-3AP**, and **G8-4AP** show  $T_{\text{gel}}$  in the range of 100–110 °C for **G8-2AP**, 110–120 °C for **G8-3AP** and 95–100 °C for **G8-4AP**, indicating the stability of all the organogels at room temperature.



**Scheme 3.2.** Representation of synthesis of **G8** and organogels formation.

**Aggregation induced enhanced emission (AIEE), visual and fluorometric sensing analysis.** The solid-state UV-Vis spectrum of **G8** revealed one absorbance peak at 335 nm; however, in the solution state, only a broad shoulder was observable in this range. For emission spectra, the excitation wavelength was fixed at 350 nm, and the emission wavelength was observed at 445 nm (Figure 3.6). **G8** does not show

fluorescence in diluted condition because it contain a flexible arm with secondary -NH group between triazine core and tetrazole ring. When the concentration increases, the **G8** molecules self-assemble to each other by non-covalent interactions and aggregate. This aggregation restricted the intramolecular rotation; thus, excitons follow radiative decay pathway and show fluorescence. Here the gelator molecule **G8** act as an AIEgen. AIEgens show non-emissive nature in the dilute state and the emission appear and increases with increasing concentration of the compound. Therefore, when the number of **G8** molecules increases in solution, it shows an enhancement in emission values, indicating the presence of the aggregation-induced enhanced emission (AIEE) phenomenon. This was confirmed by visual and fluorometric analyses (Figure 3.7).<sup>[24-27]</sup>

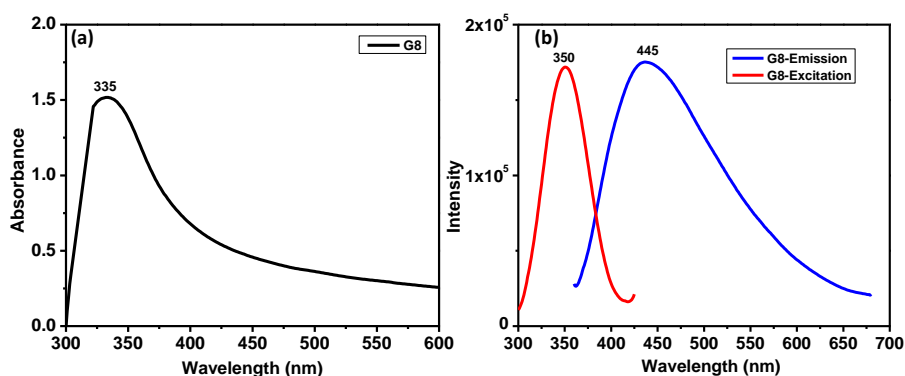


**Figure 3.6.** (a) Solid-state UV-Vis analysis of **G8** (b) Excitation and emission wavelength of **G8** by fluorometer.

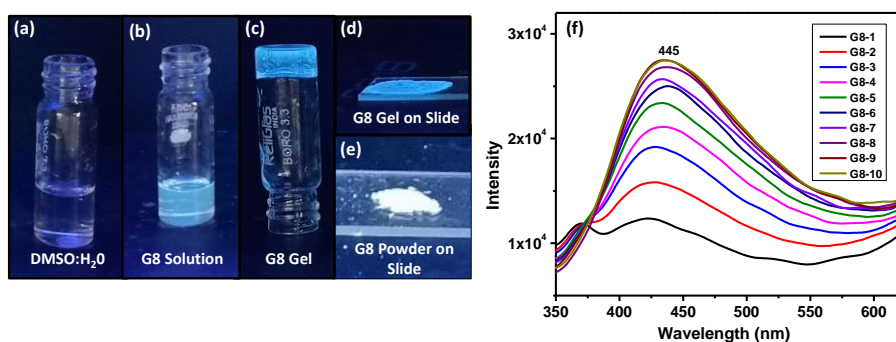


**Figure 3.7.** Fluorescent images of organogel **G8** under UV chamber (a) Fluorescence data showing aggregation induced enhanced emission (AIEE) of gelator molecule **G8**.

The mixed organogels of **G8** and isomers of aminopyridine were formed. The color of the organogels of **G8**, **G8-2AP** and **G8-4AP** was yellowish white, but in the case of **G8-3AP**, a dark yellow color was observed which turned dark red after three weeks. This indicates that **3-AP** can be discriminated by visual color changes from the other isomers with the help of the **G8** organogel (Figure 3.8). When 1 mM solution (DMSO: H<sub>2</sub>O) of **G8** (6.6 mg in 20 mL) combines with 1 mM solution (DMSO: H<sub>2</sub>O) of 2-AP, 3-AP, and 4-AP (1.88 mg in 20 mL) separately, then in the case of **G8-2AP** and **G8-4AP**, a minor enhancement in fluorescence intensity was observed with the highest peak intensity around 429 nm and 458 nm, respectively. However, in the case of **G8-3AP**, a notable enhancement in fluorescence intensity was observed, and the emission peak was recorded around 404 nm (Figure 3.9). These interesting observations show that **G8** can act as a sensor for 3-aminopyridine as it discriminates the same from the other two isomers and indicates that a significant effect of the isomeric positions is perceptible on the combined fluorescence behavior of the mixed organogel. It is envisaged that it might happen because of the presence of a higher number of hydrogen bonds between the gelator molecules and the 3-AP molecules, which restricts the free rotation of tetrazole branches of **G8** and enhances the emission intensity. In this condition, the excitons follow the radiative decay pathway, and the energy loss is minimum in the vibrational level. Due to this, the wavelength decreases.

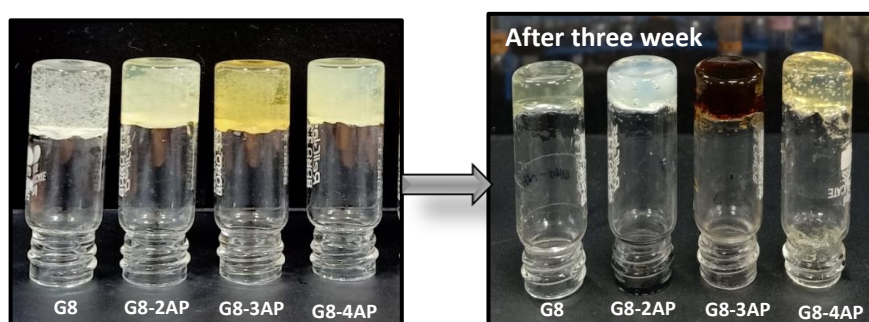


**Figure 3.8.** Notable Color change of **G8-3AP** organogel after three weeks at normal condition.

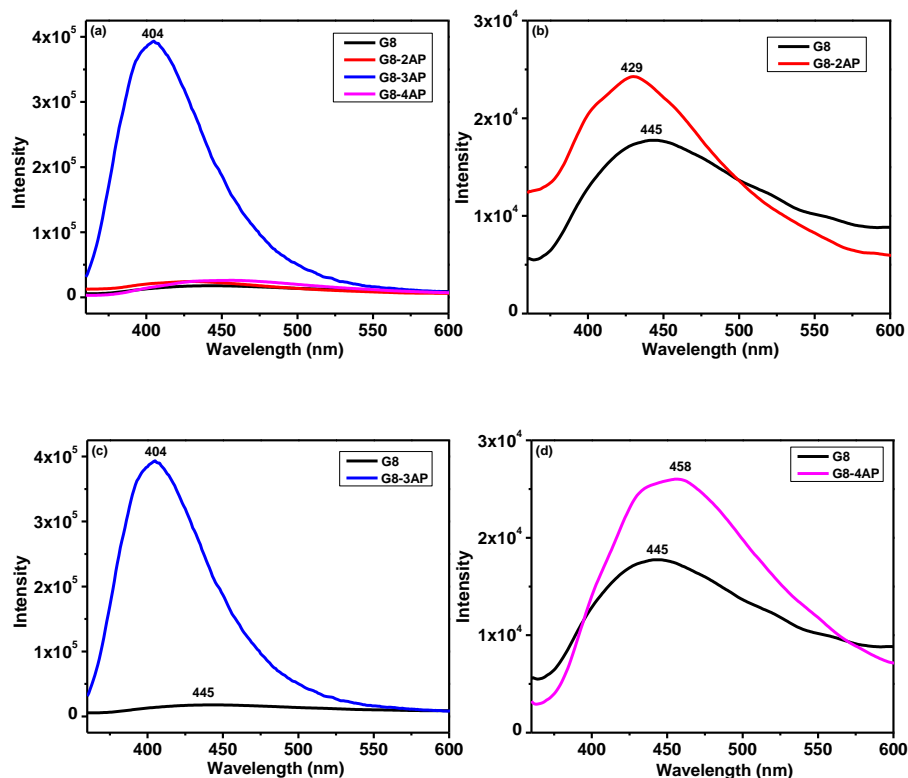


**Figure 3.9.** Fluorescence analysis of interaction of (a) **G8**, **G8-2AP**, **G8-3AP** and **G8-4AP** (b) **G8** and **G8-2AP** (c) **G8** and **G8-3AP** (d) **G8** and **G8-4AP**.

Further fluorescence experiments were performed on **G8** with different pyridine derivatives, i.e., pyridine, 2-pyridine aldehyde, 3-pyridine aldehyde, 4-pyridine aldehyde, aniline, and 4-methyl amino pyridine, and the results show that no fluorescence enhancement occurred in any of these cases (Figure 3.10). A luminophore, an atom or a functional group responsible for the luminescence properties of a compound, can show enhancement or quenching of the fluorescence properties due to aggregation. Two such types of luminophores, viz. ACQphores and AIEgens, are reported.<sup>[28]</sup> In ACQphores, quenching is observed due to aggregation, whereas in AIEgens an enhancement in fluorescence can be seen. In this case, gelator molecule **G8** can act as an AIEgen as an aggregation-induced emission is observed. AIEgens show non-emissive nature in the dilute state, and the emission increases with increasing concentration of the compound.<sup>[29]</sup>

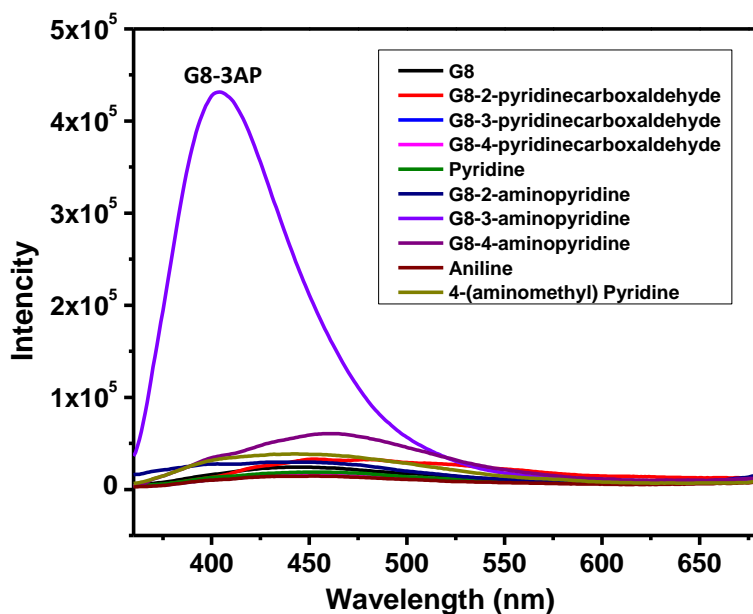


**Figure 3.10.** Controlled experiment of interaction of **G8** with different pyridine compounds.

As per the reported literature, specific organic structures with the possibility of flexible intramolecular motions favor rapid relaxation of excited state of the molecules in a dilute solution by non-radiative decay, like rotational motion, and become non-emissive. Restriction of intramolecular motion (RIM) can be the critical factor behind AIE. Molecules that show AIE or AIEE often have flexible intramolecular motion (IM) or intramolecular rotation (IR) in the dilute state. The aggregation of the molecules restricts these motions generating AIE or AIEE. Generation of AIE can be due to both restriction of intramolecular rotation (RIR) and restriction of intramolecular vibration (RIV) driven by aromaticity.<sup>[30, 31]</sup>

The gelator molecule **G8** is planar in geometry, with one cyanuric core and three tetrazole arms attached to the cyanuric ring by secondary amine ( $-\text{NH}$ ). The molecule is flexible with the possibility of intramolecular rotation. The hetero-aromatic cyanuric ring containing the **G8** molecule shows significant fluorescence in concentrated solution due to intramolecular charge transfer (ICT) from the highest occupied molecular orbital (HOMO) to the lowest unoccupied molecular orbital (LUMO) of **G8**, delocalized on the whole molecule (Figure 3.11).

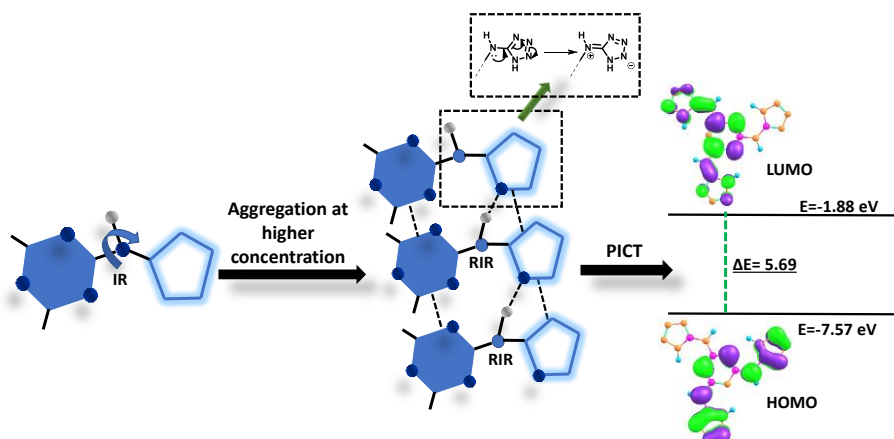


**Figure 3.11.** Schematic representation of intramolecular charge transfer in planar molecule **G8**.

To confirm the ICT, the solvent effects on the fluorescence of **G8** were investigated. When 1 mM solutions of **G8** (6.6 in 20 mL solvent) in DMSO: H<sub>2</sub>O, DMSO: CH<sub>3</sub>CH<sub>2</sub>OH, DMSO: CH<sub>3</sub>CN, DMSO: CHCl<sub>3</sub>, and DMSO: CH<sub>3</sub>COOCH<sub>2</sub>CH<sub>3</sub> were prepared and investigated using a fluorometer, it was found that there were some minor shifts of the peak toward higher wavelengths when the polarity of the used solvent with DMSO was increased (Figure 3.12). This is a piece of evidence to show that intramolecular charge transfer occurs in **G8**.<sup>[32, 33]</sup> The theoretical calculation has been done for **G8**, where the Mulliken atomic charge distribution and ESP diagram show the electrostatic potential surface of gelator molecule **G8**. The magnitude of the dipole moment is 0.0058 Debye, which means the gelator is electronically symmetrical (Figure 3.13 and Figure 3.14).<sup>[34]</sup> The fluorescence was enhanced with increasing concentration of **G8** molecules, and it has been found to be maximum in the gel state due to significant restriction of intramolecular rotation (RIR) of the secondary amine and tetrazole ring attached to the central core. Similarly, enhanced fluorescence occurred in **G8-3AP** due to suitable orientation of -NH<sub>2</sub> and pyridine nitrogen in 3-AP, which are complementary with respect to **G8** hydrogen bonding sites. DFT studies have been conducted based on the possible interactions between the **G8** molecule and different aminopyridines. This reveals that, in the case of **G8-3AP**, there are hydrogen bonds between the secondary amine

of **G8** and the pyridine nitrogen of aminopyridine, which restrict the RIR more effectively than other gel systems.

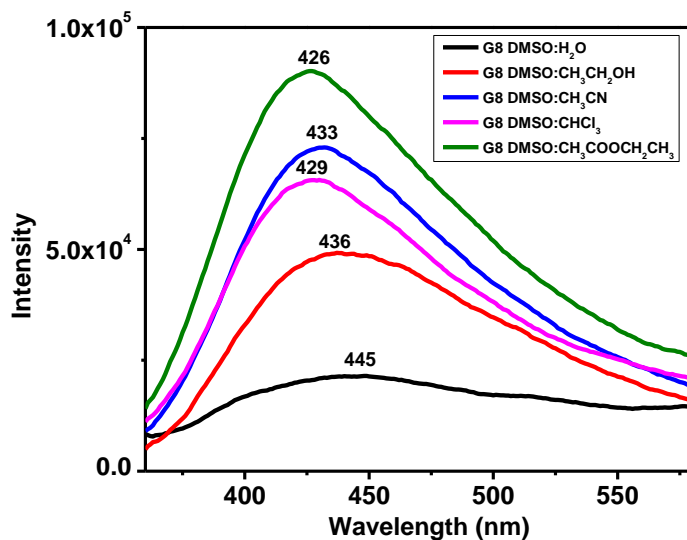


**Figure 3.12.** Effect of solvent on wavelength of **G8** molecule.

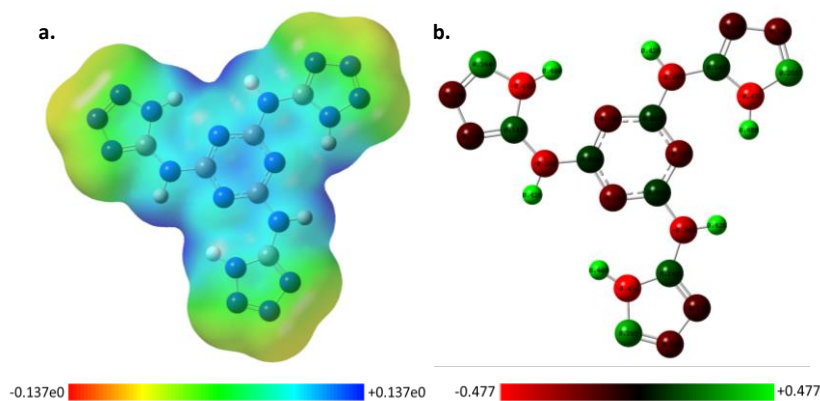


**Figure 3.13.** Gelator molecule **G8** (a) Mapped with ESP and (b) Mulliken atomic charge distribution.

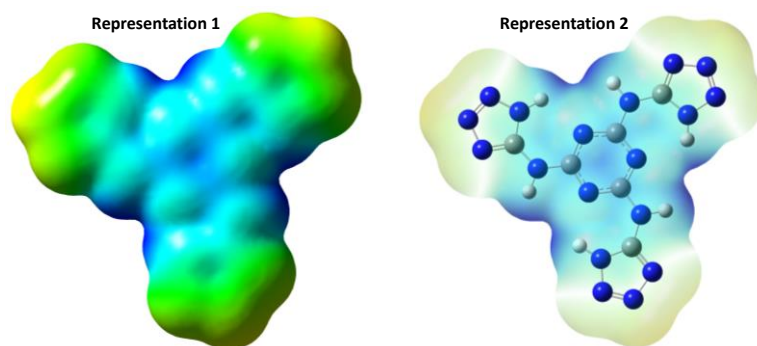


**Figure 3.14.** **G8** molecule Mapped with ESP. Isovalue for new surfaces: MO, 0.04, density 0.001, and Laplacian, 0.00.

**Role of the amino group and pyridine nitrogen in hydrogen bonding and fluorescence study for structure prediction.** The role of hydrogen bonds in the interaction of gelator molecule **G8** with the isomers of aminopyridine has been investigated by concentration-dependent  $^1\text{H}$  NMR spectroscopy. The  $^1\text{H}$  NMR spectrum of 2-aminopyridine shows peaks at 7.90, 7.34, 6.46 and 5.88 ppm for the aromatic protons and  $-\text{NH}_2$  protons, respectively. When the interaction of 2-aminopyridine (0.1 mmol) and **G8** (0.03 mmol) was investigated by  $^1\text{H}$  NMR, the NMR peaks of 2-aminopyridine were found at 7.91, 7.38, 6.49, and 6.10 ppm for aromatic hydrogen and  $-\text{NH}_2$  hydrogen, respectively. When the concentration of **G8** increased (0.06 mmol and 0.09 mmol) in the same amount of solvent (0.5 mL  $\text{DMSO-d}_6$ ), the peak positions were changed for both aromatic and  $-\text{NH}_2$  protons to 7.93, 7.41, 6.51 and 6.50 ppm and 7.93, 7.45, 6.54 and 6.56 ppm, respectively, showing that the 2-aminopyridine  $-\text{NH}_2$  hydrogen and pyridine ring nitrogen both participate in hydrogen bond formation. Similarly, when concentration-dependent  $^1\text{H}$  NMR was done with **G8-3AP** and **G8-4AP**, the downward shift in proton peak positions shows the role of the amino proton and pyridine ring nitrogen in hydrogen bond formation (Table 3.3 and Figure 3.16, 3.18 and 3.20). The structure prediction of **G8-2AP**, **G8-3AP**, and **G8-4AP** was also made using a Job plot based on fluorescence spectroscopy.<sup>[35]</sup> 1 mM stock solutions of both **G8** (6.6 mg in 20 mL) and 2AP/3AP/4AP (1.88 mg in 20 mL) in the mixture of  $\text{DMSO}/\text{H}_2\text{O}$  were prepared. The fluorescence analysis was performed by changing the volume ratio of **G8** and aminopyridine, keeping the total volume constant (2 mL). In the case of **G8-2AP**, it is found that the fluorescence intensity is the highest at a 0.8 mole fraction of 2-AP. In the case of **G8-3AP**, the fluorescence intensity is the highest at a 0.6 mole fraction of 3-AP, while for **G8-4AP** it is found at a 0.7 mole fraction of 4-AP (Figure 3.15, 3.17, and 3.19).

**Table 3.3.**  $^1\text{H}$  NMR data of downward shifting of protons of 2-AP, 3-AP and 4-AP during interactions with gelator molecule **G8**.

$^1\text{H}$ NMR analysis in 0.5 mL DMSO- $d_6$			
2-AP (0.1 mmol)	G8 (0.03 mmol)	G8 (0.06 mmol)	G8 (0.09 mmol)
7.90 ppm (aromatic)	7.91	7.93	7.93
7.34 ppm (aromatic)	7.38	7.41	7.45
6.46 ppm (aromatic)	6.49	6.51	6.54
5.88 ppm (-NH $_2$ )	6.10	6.50	6.56
3-AP (0.1 mmol)	G8 (0.03 mmol)	G8 (0.06 mmol)	G8 (0.09 mmol)
7.95 ppm (aromatic)	7.96	7.97	7.98
7.74 ppm (aromatic)	7.75	7.78	7.80
7.00 ppm (aromatic)	7.06	7.12	7.16
6.91 ppm (aromatic)	6.98	7.05	7.10
5.27 ppm (-NH $_2$ )	5.86	6.55	6.92
4-AP (0.1 mmol)	G8 (0.03 mmol)	G8 (0.06 mmol)	G8 (0.09 mmol)
7.98 ppm (aromatic)	8.00	8.01	8.05
6.46 ppm (aromatic)	6.51	6.56	6.60
5.98 ppm (-NH $_2$ )	6.25	6.51	6.74

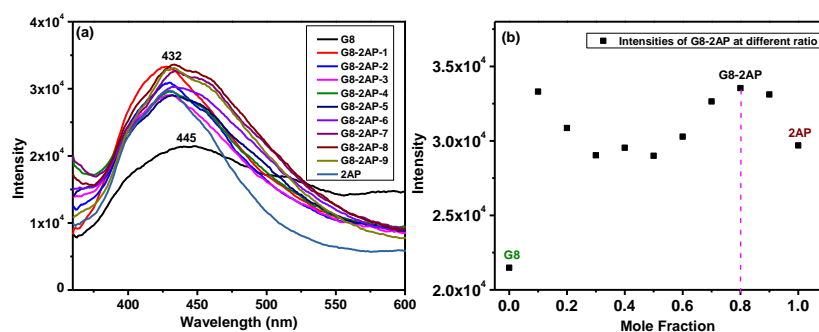


**Figure 3.15.** (a) Fluorescence spectra of **G8-2AP** at different concentration (b) Job plot to shows maximum intensity ratio of **G8-2AP**.

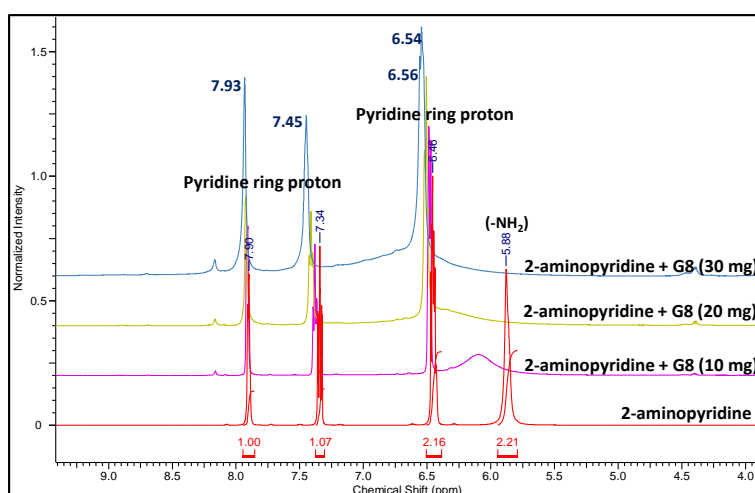


**Figure 3.16.** Concentration dependent  $^1\text{H}$  NMR of 2-aminopyridine with increasing amount of gelator molecule **G8**.

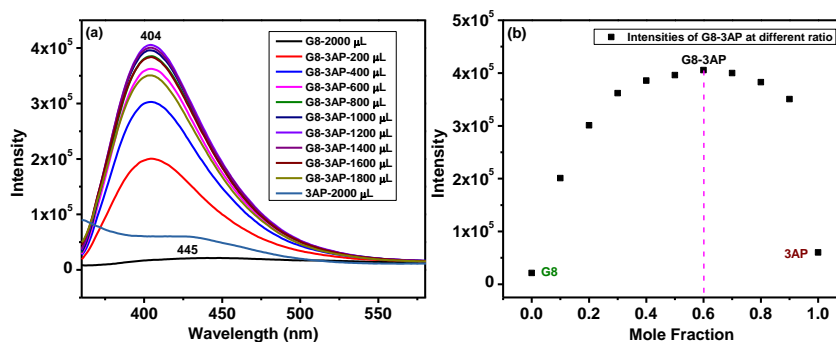


**Figure 3.17.** (a) Fluorescence spectra of **G8-3AP** at different concentration ratio (b) Job plot to shows the maximum intensity ratio of **G8-3AP**.

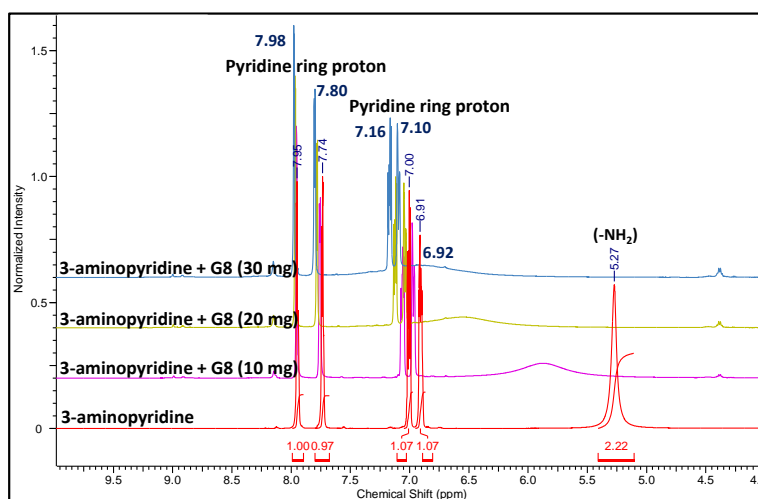


**Figure 3.18.** Concentration dependent  $^1\text{H}$  NMR of 3-aminopyridine with increasing amount of gelator molecule **G8**.

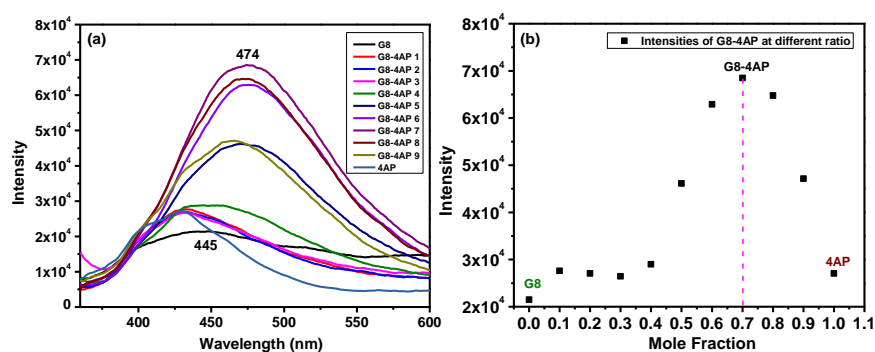


**Figure 3.19.** (a) Fluorescence spectra of **G8-4AP** at different concentration ratio (b) Job plot to shows the maximum intensity ratio of **G8-4AP**.

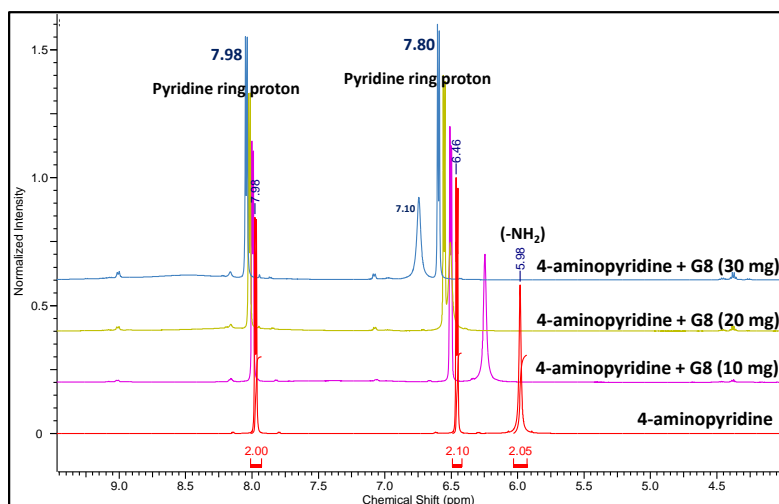


**Figure 3.20.** Concentration dependent  $^1\text{H}$  NMR of 4-aminopyridine with increasing amount of gelator molecule **G8** showing participation of hydrogen and nitrogen for hydrogen bonding.

To analyse the effect of different solvent mixtures on the interaction of **G8** and 3-AP, different solvent mixtures, viz. DMSO:  $\text{H}_2\text{O}$ , DMSO:  $\text{CH}_3\text{CH}_2\text{OH}$ , DMSO:  $\text{CH}_3\text{CN}$ , DMSO:  $\text{CHCl}_3$  and DMSO:  $\text{CH}_3\text{COOCH}_2\text{CH}_3$ , were utilized. In all the cases, the fluorescence intensity has been found to be the highest with a mole fraction of 0.6 with respect to 3-AP, similar to the previous observation. This shows that there is no effect of solvent on the interaction ratio of **G8** and 3AP (Figure 3.21-3.25). Therefore, by concentration-dependent  $^1\text{H}$  NMR and fluorescence studies, the structures of organogels **G8-2AP**, **G8-3AP**, and **G8-4AP** have been predicted as given below and further confirmed by DFT calculations (Figure 3.26).

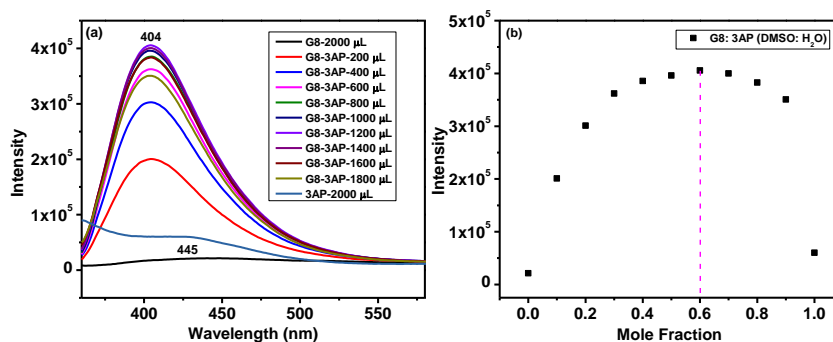


**Figure 3.21.** (a) Fluorescence spectra of **G8-3AP** at different concentration ratio in DMSO:  $H_2O$  (b) Job plot to shows the ratio of amount of interaction of **G8-3AP** at maximum intensity.

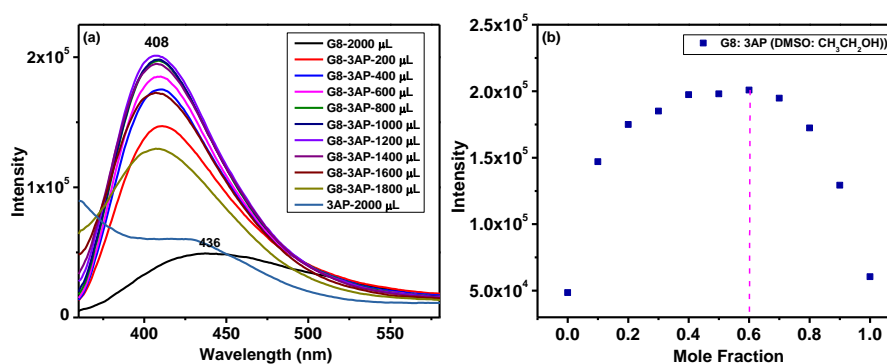


**Figure 3.22.** (a) Fluorescence spectra of **G8-3AP** at different concentration ratio in DMSO:  $CH_3CH_2OH$  (b) Job plot to shows the ratio of amount of interaction of **G8-3AP** at maximum intensity.

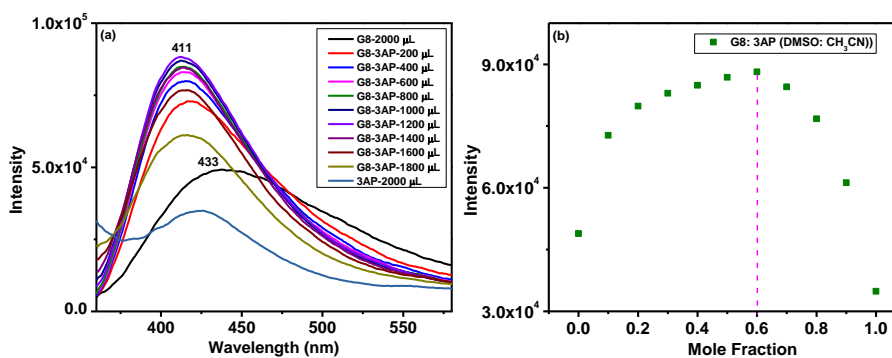


**Figure 3.23.** (a) Fluorescence spectra of **G8-3AP** at different concentration ratio in DMSO:  $CH_3CN$  (b) Job plot to shows the ratio of amount of interaction of **G8-3AP** at maximum intensity.

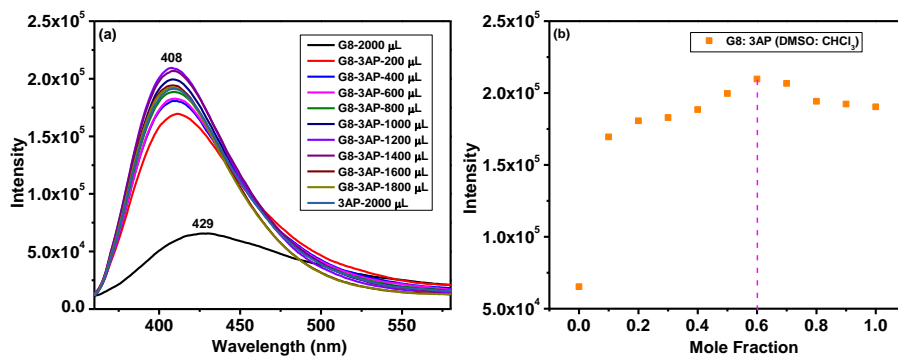


**Figure 3.24.** (a) Fluorescence spectra of **G8-3AP** at different concentration ratio in DMSO:  $\text{CH}_3\text{Cl}$  (b) Job plot to shows the ratio of amount of interaction of **G8-3AP** at maximum intensity.

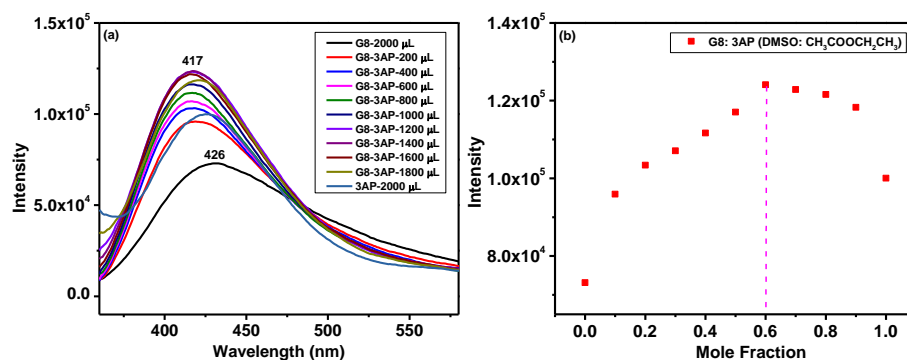


**Figure 3.25.** (a) Fluorescence spectra of **G8-3AP** at different concentration ratio in DMSO:  $\text{CH}_3\text{COOCH}_2\text{CH}_3$  (b) Job plot to shows the ratio of amount of interaction of **G8-3AP** at maximum intensity.

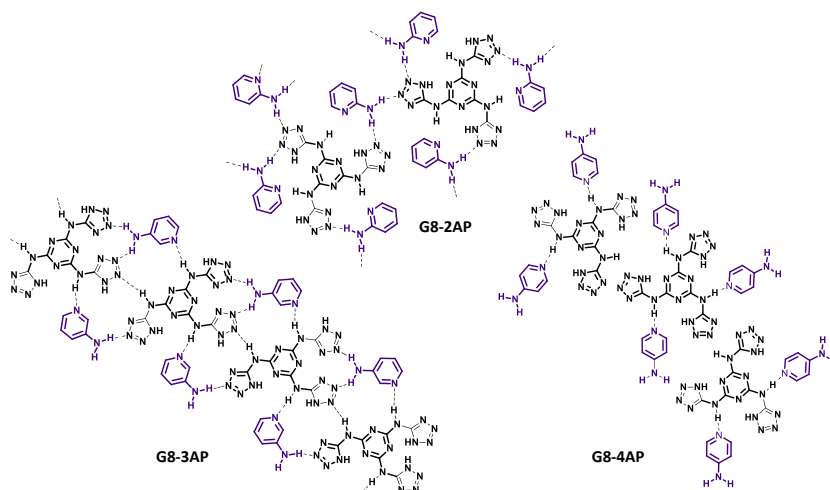


**Figure 3.26.** Possible predicted structure of **G8-2AP**, **G8-3AP** and **G8-4AP** organogels.

**DFT calculations and structure prediction.** The structures of the synthesized gelator molecules **G8** and their organogels have been predicted by density functional theory (DFT) using RB3LYP with the basis set 6-311++G(d,p) and water as a solvent. The bond lengths of C1–N1, N1–C2, C2–N5, N5–H2, C5–N11, N11–N12, N12–N13, N13–N14 and N14–H5 are found to be 1.331, 1.343, 1.369, 1.012, 1.324, 1.356, 1.287, 1.352 and 1.013 Å, respectively. The bond angles of C1–N4–C4 and N4–C4–N10 are found to be 127.111 and 127.201, respectively. All the bond lengths and bond angles are summarized in Table 3.4. From the optimized structure it is evident that **G8** is a planar molecule in which the lone pair of secondary nitrogen is delocalized between the cyanuric ring and tetrazole ring.<sup>[36]</sup> The first HOMO–LUMO energy gap for the **G8** molecule is found to be 5.69 eV (Figure 3.27). The values of the first five HOMO–LUMO energies are 5.69, 5.70, 6.66, 7.82, 8.60 and 8.70 eV, respectively (Figure 3.28). Here, the theoretical (DFT calculated) HOMO-LUMO energy gap (5.69 eV) is different from HOMO-LUMO energy gap calculated by UV visible (200-400 nm) analysis i.e., 5.16 eV (Figure 3.29). The difference came because the DFT analysis was done by using water as a solvent. While the UV-Visible analysis has been performed in DMSO: H<sub>2</sub>O mixture, which shows the decrement in the band gap due to an increment in dipole moment.<sup>[37]</sup>

**Table 3.4.** Bond lengths and bond angles of structure of planer **G8** molecule from DFT Data.

Molecule	Bond	Bond length (Å)	Bond	Bond length (Å)	Bond angle name	Bond angle (°)
G8	C1-N1	1.33	N5-C5	1.37	N3-C1-N4	115.37
	N1-C2	1.34	C5-N11	1.32	N1-C1-N4	118.67
	C2-N2	1.33	N11-N12	1.36	C1-N4-C4	127.12
	N2-C3	1.34	N12-N13	1.29	N4-C4-N10	127.22
	C3-N3	1.33	N13-N14	1.35	N2-C2-N5	115.38
	N3-C1	1.34	N14-H5	1.01	N1-C2-N5	118.67
	C1-N4	1.37	N14-C6	1.34	C2-N5-C5	127.09
	N4-H1	1.01	C3-N6	1.37	N5-C5-N14	127.20
	N4-C4	1.37	N6-H3	1.01	N3-C3-N6	115.38
	C4-N7	1.32	N6-C6	1.37	N2-C3-N6	188.66
	N7-N8	1.36	C6-N15	1.32	C3-N6-C6	127.11
	N8-N9	1.29	N15-N16	1.36	N6-C6-N18	127.20
	N9-N10	1.35	N16-N17	1.29		
	N10-H4	1.01	N17-N18	1.35		
	N10-C4	1.34	N18-H6	1.01		
	C2-N5	1.37	N18-C6	1.34		
	N5-H2	1.02				

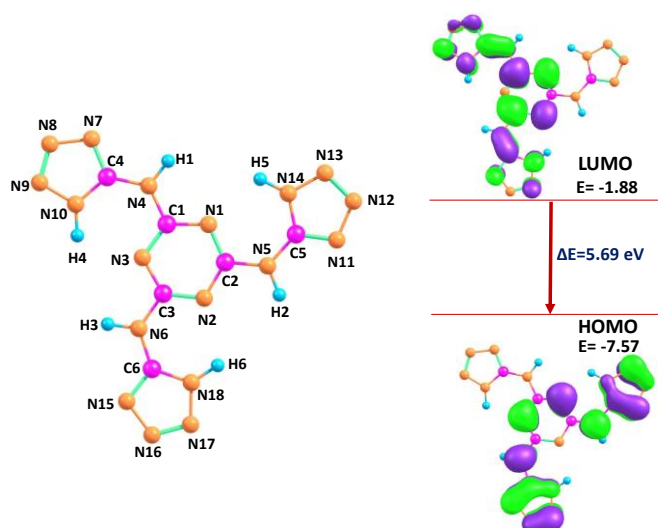


**Figure 3.27.** HOMO and LUMO orbital demonstration of gelator molecule **G8** by DFT study.

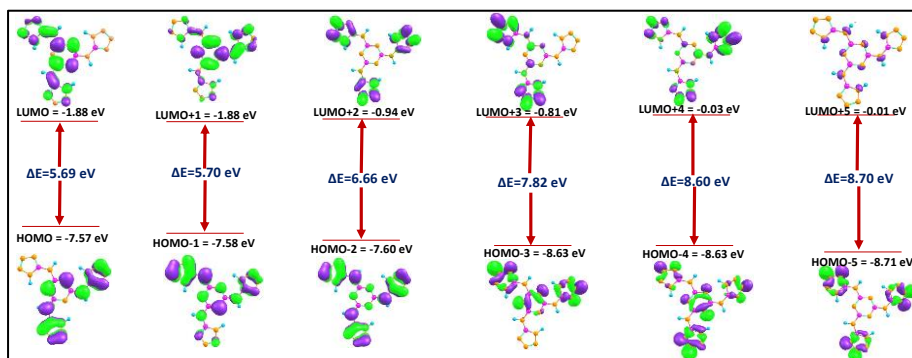


**Figure 3.28.** HOMO-LUMO energy orbitals of gelator molecule **G8** studied by DFT analysis.

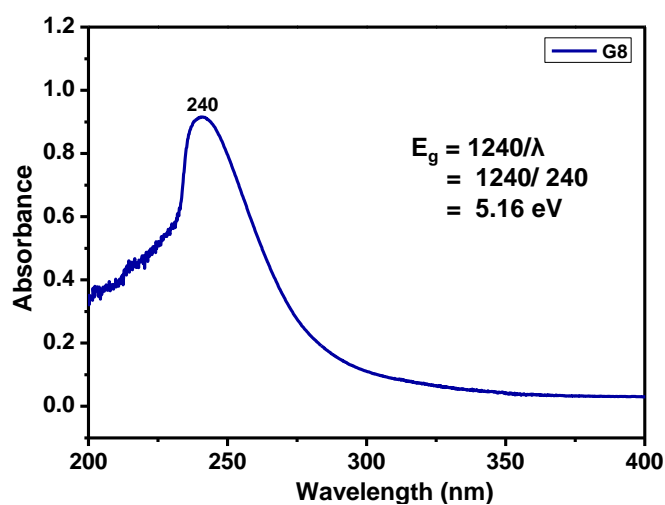


**Figure 3.29.** Energy band gap calculation by UV-Visible analysis (200-400 nm) of **G8** in DMSO: H<sub>2</sub>O mixture.

The structures of **G8-2AP**, **G8-3AP** and **G8-4AP** have been predicted by Job plot and  $^1\text{H}$  NMR studies. This prediction has been confirmed by DFT analysis for **G8-2AP**, **G8-3AP** and **G8-4AP**. The DFT structure of **G8-2AP** shows that the nitrogen of the  $-\text{NH}_2$  group attached with the pyridyl ring interacts via hydrogen bond formation with the hydrogen of the tetrazole ring and the hydrogen of the  $-\text{NH}_2$  group interacts through hydrogen bond formation with the nitrogen of the tetrazole ring. In the case of **G8-3AP**, the hydrogen bonds are formed between  $-\text{NH}_2$  hydrogen and tetrazole nitrogen, and  $-\text{NH}_2$  nitrogen and tetrazole hydrogen. Here, the pyridyl nitrogen also takes part in the formation of hydrogen bonds with the hydrogen of secondary  $-\text{NH}$  bridging between cyanuric and tetrazole rings. In the case of **G8-4AP**, the hydrogen bonds are formed between the pyridyl nitrogen and hydrogen of secondary  $-\text{NH}$ . The DFT data confirmed the more restricted structure in the case of **G8-3AP** in terms of intramolecular rotation (Figure 3.30).

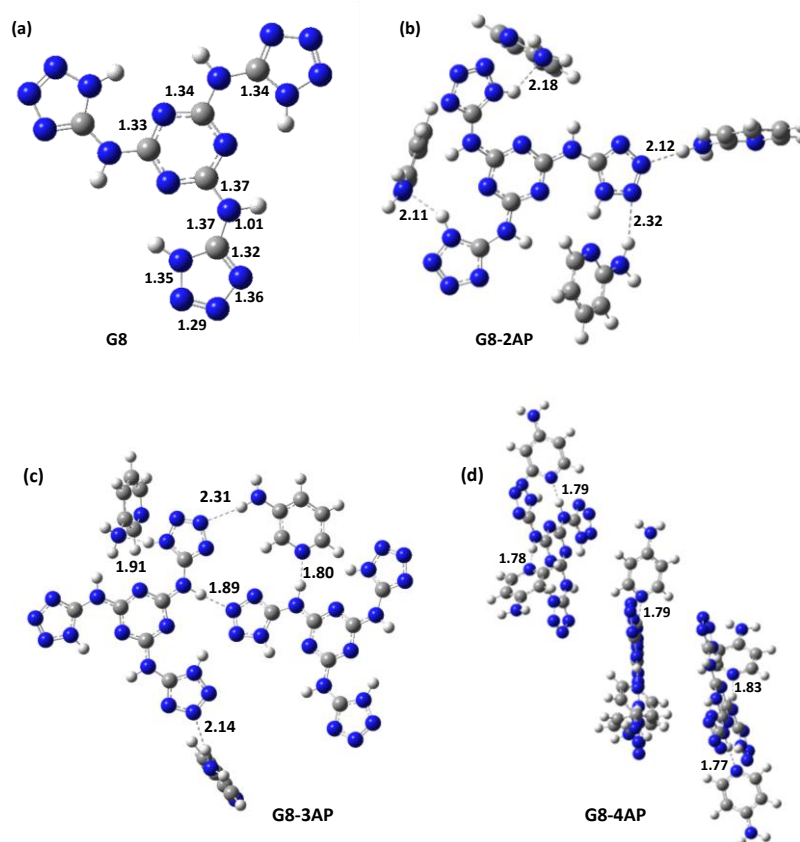


**Figure 3.30.** Structure confirmation of (a) **G8** (b) **G8-2AP** (c) **G8-3AP** (d) **G8-4AP** by DFT study.

The bond angles of the hydrogen bonds in **G8-2AP**, **G8-3AP** and **G8-4AP** are in the range of 137.23°-179.33°. The N–H...N type hydrogen bonds are found to show stronger interactions. The bond length range of hydrogen bonds in **G8-2AP** is between 2.11 and 2.32 Å which is weaker compared to the hydrogen bonds formed in **G8-3AP**, for which the lengths are found to be between 1.80 and 2.31 Å. **G8-4AP** also contained stronger hydrogen bonds in the range of 1.77–1.83 Å but it has a less restricted structure. These results point to the fact that a relatively strong interaction between **G8** and 3-AP might be the reason for the enhanced fluorescence due to more effective restriction in intramolecular rotation.<sup>[38, 39]</sup>

The outcome of the DFT study and correlation with fluorescence shows that in the case of **G8-3AP**, amine hydrogen and pyridine nitrogen of 3-aminopyridine participate as hydrogen bond donor and acceptor sites, respectively, with tetrazole nitrogen and secondary amine hydrogen sites of two different **G8** molecules. While in **G8-2AP**, the orientation of pyridine nitrogen and amine hydrogen is such a way that it can form hydrogen bonds with the same molecule of **G8**. Similarly, in **G8-4AP**, the hydrogen bond formed only between pyridine nitrogen of 4-aminopyridine with hydrogen of secondary amine but with not primary amine hydrogens. Therefore, more restrictions in intramolecular rotation (RIR) occurred in the case of **G8-3AP** compared to **G8-2AP** and **G8-4AP**, which supports the enhancement in fluorescence.

**Rheological study of organogels.** The strength and sol-gel transition behavior of the gel were investigated by rheology.<sup>[40-42]</sup> The average storage modulus ( $G'$ ) for organogel **G8** was  $2.36 \times 10^2$  Pa and the storage modulus ( $G'$ ) was found to be larger than the loss modulus ( $G''$ ) in the whole experimental range. When the strain is increased in the LVE experiment, the values of  $G'$  and  $G''$  deviate from linearity, and the crossover point is observed at approximately 64% of the strain value. The strain sweep test of **G8** also shows weak strain overshoot (WSO) which indicate the formation of complex microstructure inside gel matrix during organogel formation.<sup>[43-45]</sup> When the isomer of

aminopyridine is introduced with gelator **G8**, the values of the storage modulus were found to be  $0.90 \times 10^2$  for **G8-2AP**,  $5.14 \times 10^3$  for **G8-3AP** and  $6.07 \times 10^2$  Pa for the **G8-4AP** organogel (Figure 3.31-3.34). The significant increase in the storage modulus in the case of **G8-3AP** indicates a greater number of noncovalent interactions like hydrogen bonds,  $\pi$ - $\pi$  stacking and intercolumnar stacking. Therefore, the organogel of **G8** with aminopyridine also shows rheological sensing ability toward 3-AP (Figure 3.35). These organogels also have the tendency of sol-gel-sol transition which is indicative of the self-healing property of low molecular weight gels.

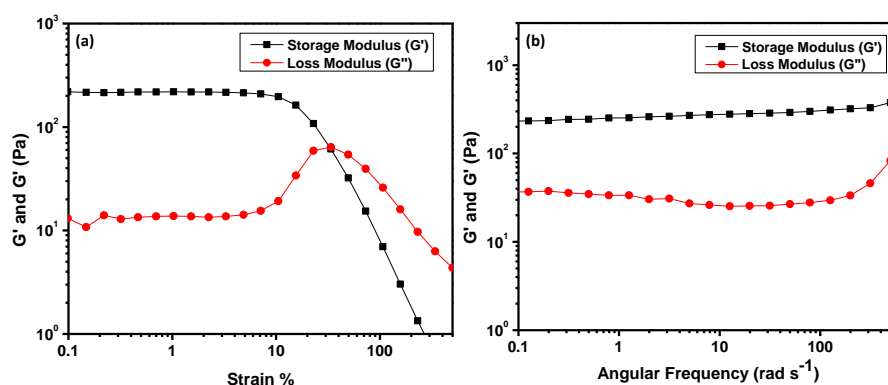


**Figure 3.31.** (a) LVE Angular sweep (AS) and (b) Frequency sweep (FS) of organogel **G8**.

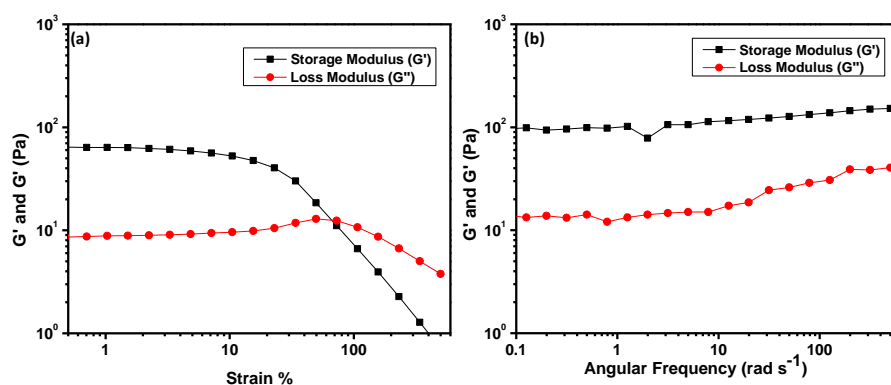


**Figure 3.32.** (a) LVE Angular sweep (AS) and (b) Frequency sweep (FS) of organogel **G8-2AP**.

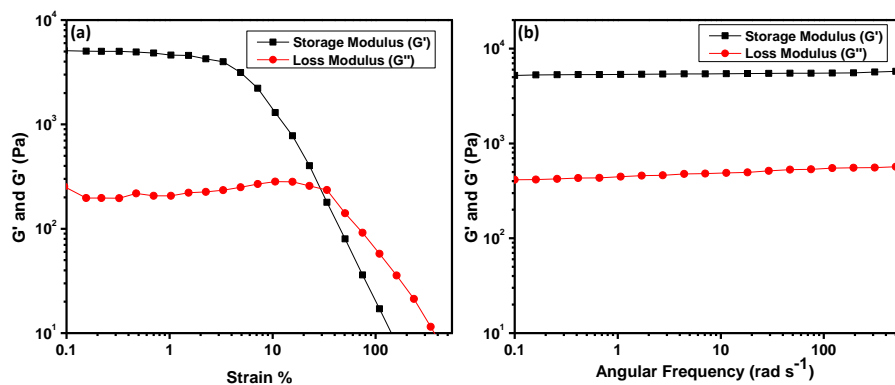


**Figure 3.33.** (a) LVE Angular sweep (AS) and (b) Frequency sweep (FS) of organogel **G8-3AP**.

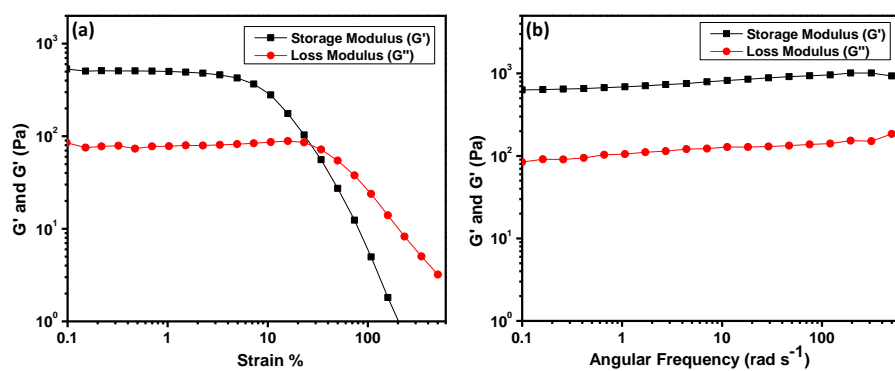


**Figure 3.34.** (a) LVE Angular sweep (AS) and (b) Frequency sweep (FS) of organogel **G8-4AP**.

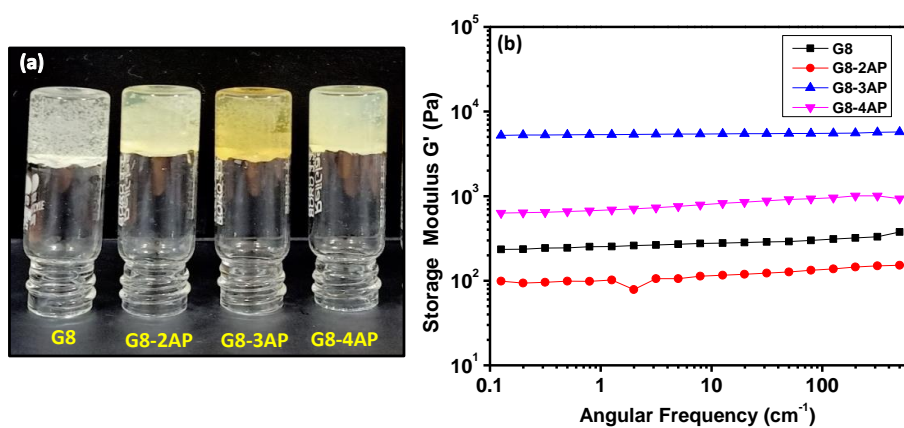


**Figure 3.35.** (a) Series of organogels synthesized from **G8** (b) Comparative study of storage modulus of **G8-2AP**, **G8-3AP** and **G8-4AP** gels with **G8** by Frequency sweep experiment.

**Effect of the gelation component on the thixotropic behavior of organogel G8 (self-healing property of LMWG).** The gel-sol-gel transition or self-healing of low molecular weight gelators or thixotropy of gels can be evaluated by the strain sweep experiment. In the case of organogel **G8**, the strain sweep experiment shows that, during five cycles, at low (1%) and high (200%) strain values, there was no change in the value of storage modulus which shows that it has the capacity for gel-sol-gel transition even after five cycles. During this experiment, the effect of the gelation components with **G8** has been examined. It has been observed that lower value of storage modulus ( $G'$ ) for organogel indicates more flexible or viscous nature. Therefore, lower strength gel shows tendency for gel-sol-gel transition, without considerable changes in the storage modulus ( $G'$ ). The gels (**G8-3AP**) that have higher values of storage modulus show thixotropic behavior, but  $G'$  decreases with an increasing number of cycles (at low 1% and high 100% strain). Therefore, it is confirmed that stronger non-covalent bonding gives a higher storage modulus, and the result is low thixotropic behavior toward a higher number of strain sweep cycles (Figure 3.36 and 3.37).

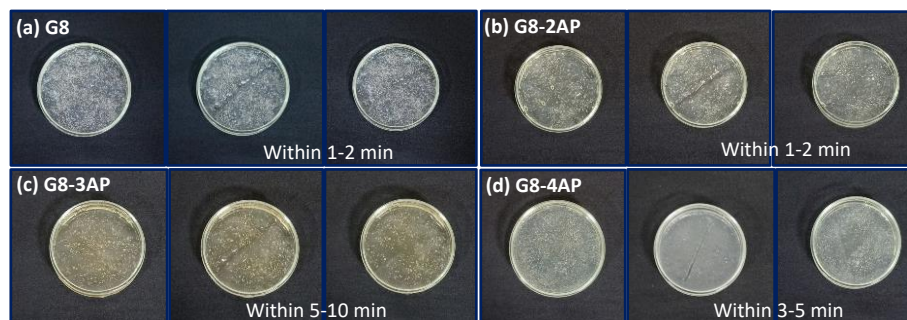


**Figure 3.36.** Images showing the self-healing property of LMWG organogels before and during the cut, and after healing (a) **G8**, (b) **G8-2AP**, (c) **G8-3AP** and (d) **G8-4AP**.

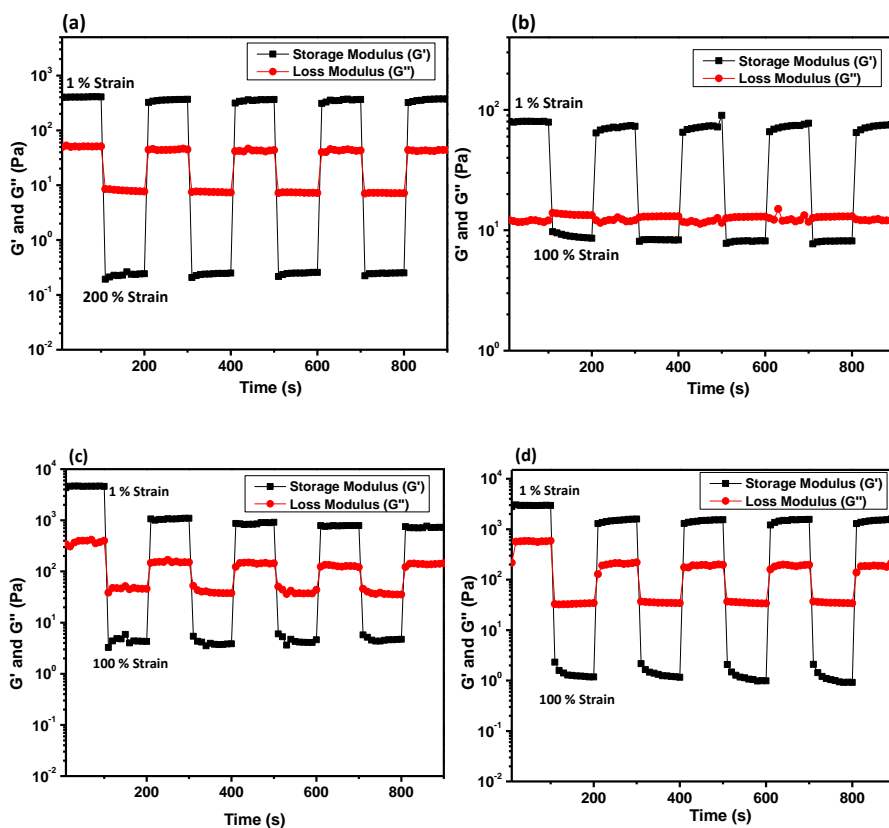


**Figure 3.37.** Strain sweep experiment of (a) Organogel **G8** (b) Organogel **G8-2AP** and (c) Organogel **G8-3AP** (d) Organogel **G8-4AP**.

**Self-assembly of organogels of G8.** Morphological analysis of the organogel of **G8** has been done by FE-SEM. **G8** powder shows nanostructured flower-type morphology. Upon transformation to organogel, **G8** offers a continuous tiny fiber-like structure. When organogels of **G8** are formed with the isomers of aminopyridine, obvious changes are observed. In the case of **G8-3AP**, a nanoflower-like structure of 60–90 nm dimension was observed. For **G8-2AP** a nanofibrous structure of 20–80 nm dimension with the covering of tiny fiber morphology is visible. **G8-4AP** shows nanostructured thread-like morphology also covered by tiny fibers (Figure 3.38). Here the FE-SEM analysis have been done with gel as well as its xerogel form which revealed changes in morphology upon conversion from a gel to a xerogel due to changes in method of drying and sample preparation (Figure 3.39–3.42).<sup>[46, 47]</sup> The FE-SEM images of all the organogels, conclusively confirm the different type of interactions between **G8** and different

aminopyridines lead to different morphologies and bring about differences in the rheological properties of the mixed organogels.

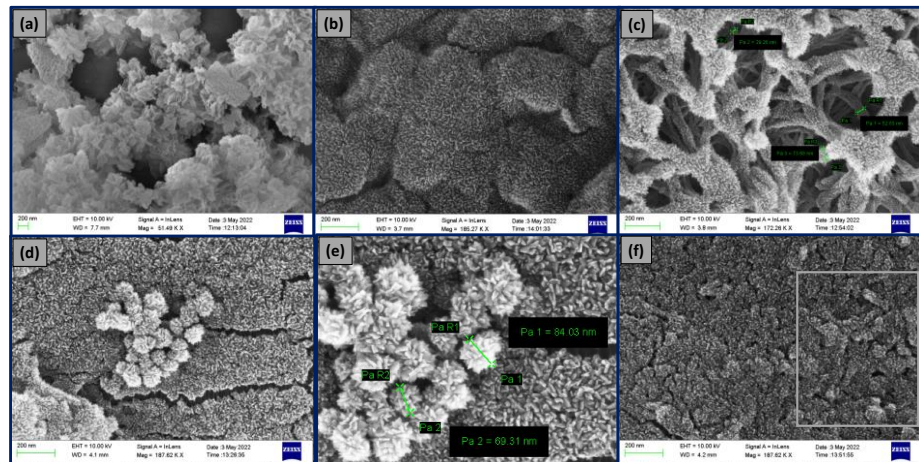


**Figure 3.38.** FE-SEM images of (a) **G8** powder (b) Organogel **G8** (c) Organogel **G8-2AP** (d) Organogel **G8-3AP** (e) **G8-3AP** with nano-measurement and (f) Organogel **G8-4AP** at 200 nm.

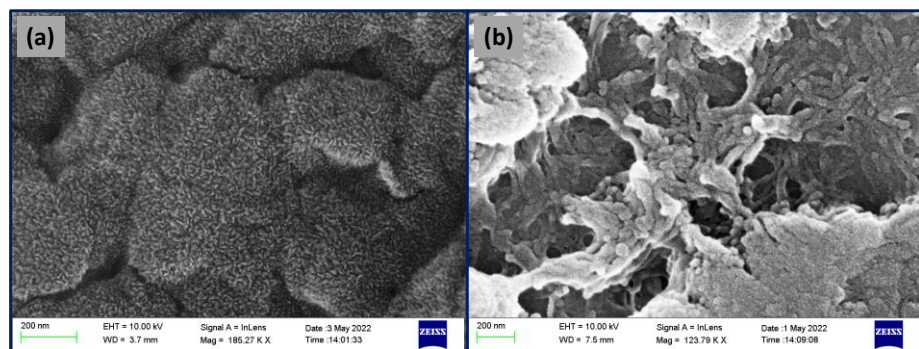


**Figure 3.39.** FE-SEM images of (a) Organogel **G8** and (b) Xerogel of Organogel **G8** at 200 nm.

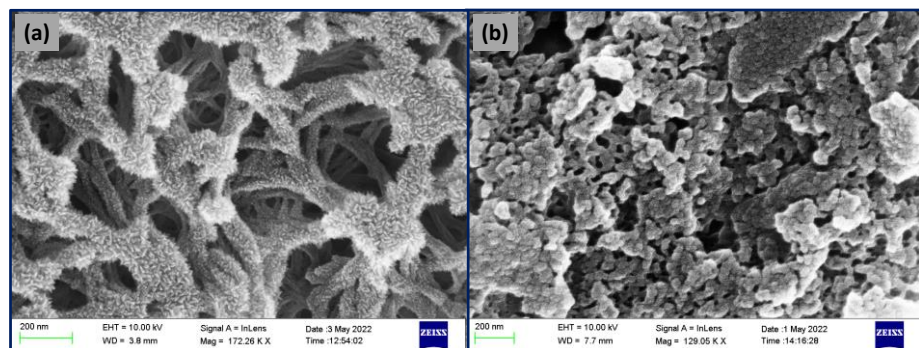


**Figure 3.40.** FE-SEM images of (a) Organogel **G8-2AP** and (b) Xerogel of Organogel **G8-2AP** at 200 nm.

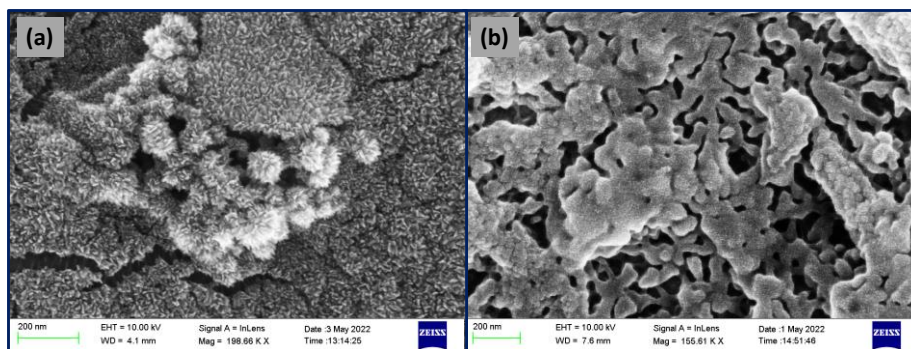


**Figure 3.41.** FE-SEM images of (a) Organogel **G8-3AP** and (b) Xerogel of Organogel **G8-3AP** at 200 nm.

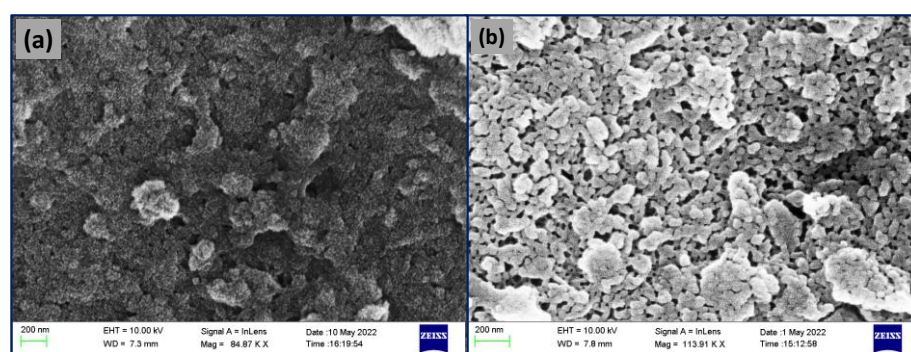


**Figure 3.42.** FE-SEM images of (a) Organogel **G8-4AP** and (b) Xerogel of Organogel **G8-4AP** at 200 nm.

The FTIR spectrum of the xerogel of **G8** shows IR bands at 3413, 1653, 1554, 1427, and 1017  $\text{cm}^{-1}$ , indicating the presence of secondary amines and tetrazole groups. The FTIR bands for the xerogel of **G8-2AP** were observed at 3377, 1660, 1550, 1417 and 1010  $\text{cm}^{-1}$ , for the xerogel of **G8-3AP** at 3370, 1632, 1554, 1413 and 1017  $\text{cm}^{-1}$ , and for the xerogel of **G8-4AP** at 3377, 1646, 1554, 1420 and 1010  $\text{cm}^{-1}$ . In the case of **G8-3AP**, the shift from a higher wavenumber to a lower wavenumber shows the formation of strong hydrogen bonds as compared to other isomeric organogels (Figure 3.43 and Table 3.5).

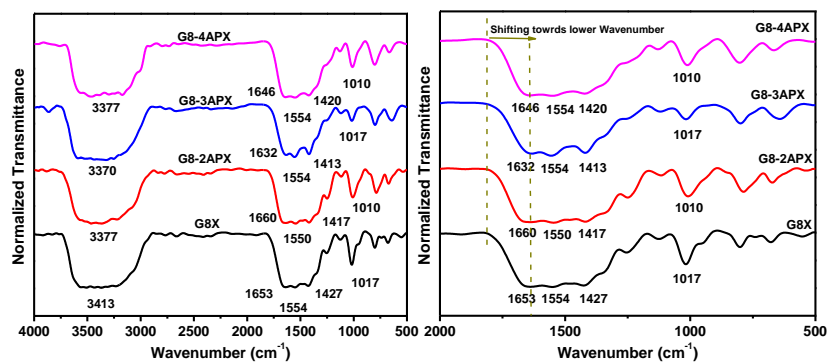


**Figure 3.43.** FT-IR data of xerogel of **G8**, **G8-2APX**, **G8-3APX** and **G8-4APX**.

**Table 3.5.** Comparative wavenumber range to show the participation of amine and tetrazolic ring for gelation.

Gel	N-H Stretching (cm <sup>-1</sup> )	N-H Bending (cm <sup>-1</sup> )	C-N Stretching (aromatic amine) (cm <sup>-1</sup> )	C-N Stretching (amine) (cm <sup>-1</sup> )	C=N Stretching (imine) (cm <sup>-1</sup> )
<b>G8-X</b>	3413	1653	1427	1017	1554
<b>G8-2AP</b>	3377	1660	1427	1010	1550
<b>G8-3AP</b>	3370	1632	1413	1017	1554
<b>G8-4AP</b>	3377	1646	1420	1010	1554

Self-assembly of the organogels was also studied by PXRD analysis of gelator molecules and xerogels of organogels. The drying of gel to xerogel has been done in a controlled manner by lyophilization. Therefore, the gel matrix and interaction between molecules do not get disturbed during drying, which leads to the conservation of basis properties upon conversion. For the gelator powder of **G8**, a relatively broad peak at  $2\theta = 18.90^\circ$  is observed with a d-spacing value of 4.83 Å for intercolumnar stacking, peak at  $2\theta = 27.59^\circ$  (d value of 3.38 Å) revealing the  $\pi$ - $\pi$  stacking between the benzene rings, whereas the peak at  $2\theta = 34.96^\circ$  (d value of 2.73 Å) indicates the H-bond interactions between the NH proton of a secondary amine and tetrazole groups. In the case of the xerogel of **G8**, the higher intensity peak as compared to powder **G8** at  $2\theta = 27.49^\circ$  shows increased  $\pi$ - $\pi$  stacking between gelator molecules. Similarly, in the case of the xerogel of **G8-2AP**, PXRD peaks were found at  $2\theta = 20.41^\circ$  and  $2\theta = 27.49^\circ$ , for **G8-3AP** they were found at  $2\theta = 21.27^\circ$  and  $2\theta = 27.58^\circ$  and for **G8-4AP** they were found at  $2\theta = 20.70^\circ$  and  $2\theta = 27.49^\circ$ , indicating the presence of the highest amount of

intercolumnar stacking, and  $\pi$ - $\pi$  stacking between the gelator molecules and the respective isomers of aminopyridine. Here, the peak for hydrogen bonds has not been clearly observed, which may be due to the possibility that, after the hydrogen bond formation, the molecules get stacked with each other by intercolumnar and  $\pi$ - $\pi$  stacking, which resulted in the dominance of these two interaction peaks over the peak meant for hydrogen bond formation (Figure 3.44).

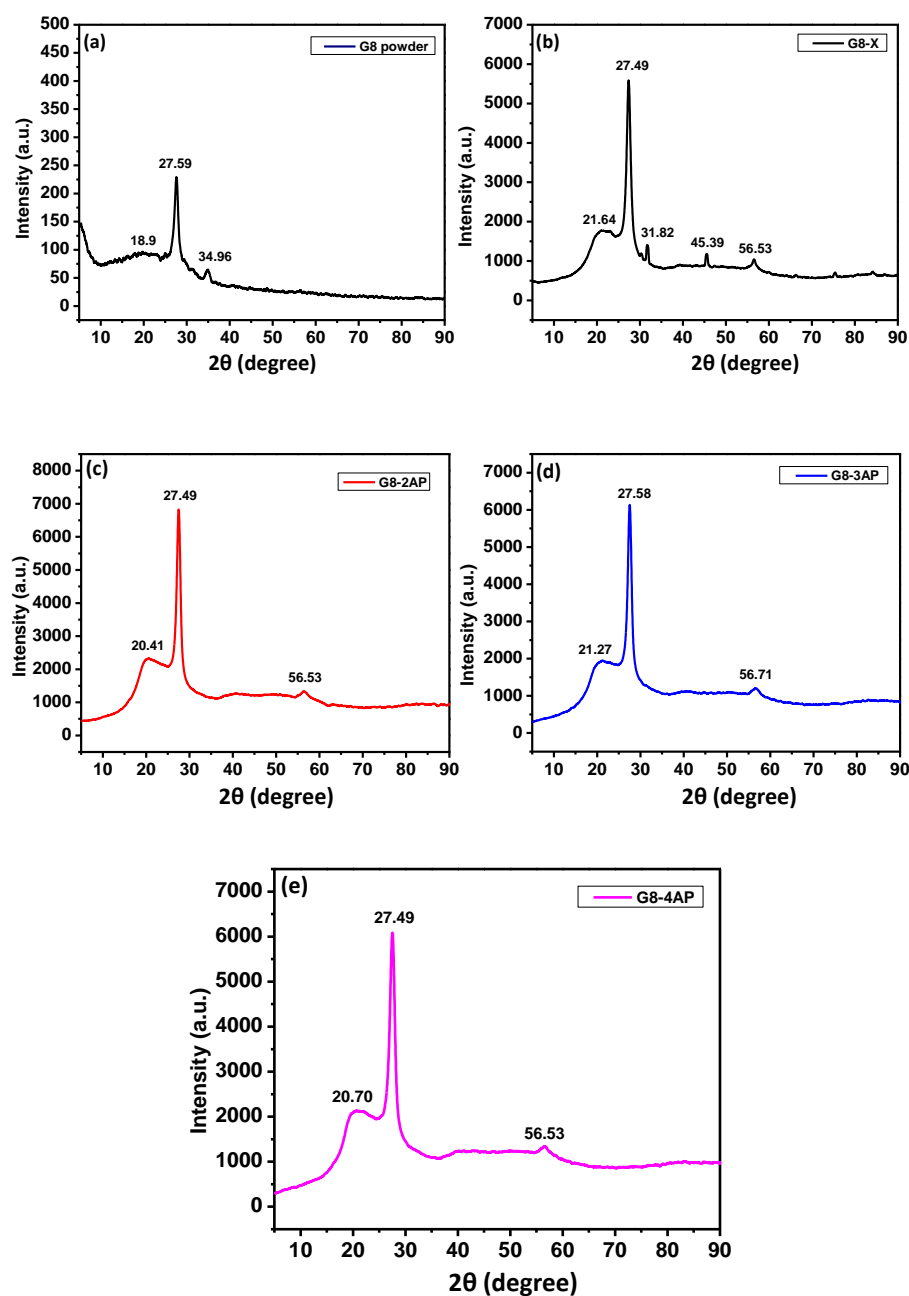


**Figure 3.44.** PXRD data of (a) gelator powder **G8** and Xerogel of (b) **G8**, (c) **G8-2AP**, (d) **G8-3AP**, (e) **G8-4AP**.

**Thermal study of the gelator molecule G8 and xerogels.** The xerogels of organogels **G8**, **G8-2AP**, **G8-3AP**, and **G8-4AP** were used for the thermogravimetric analysis (TGA). This test has also been performed for **G8** in the powder state. During the experiment, it was found that there were three steps of degradation for all the cases. In the case of **G8** powder, some trapped solvent molecules get released from the surface of the compound, which is observable between 36.17 and 219.94 °C with 4.34% weight loss of the material, while in the low volatility range, i.e. 219.94– 347.51 °C, in which the observed weight loss of about 30.78% may be due to the breakage of the C–N bonds of secondary amine between cyanuric and tetrazole rings. The slow combustion of the carbon of the compound is observable between 347.51 and 595.78 °C, and the weight loss is found to be 62.45%. Similarly, in the case of **G8**, **G8-2AP**, **G8-3AP**, and **G8-4AP** organogels, the weight loss occurred in three similar steps, but the difference can be seen in the high volatility range in the case of **G8-2AP**, **G8-3AP**, and **G8-4AP**. In **G8-2AP**, it started from 160.15 °C, in **G8-3AP** from 160.38 °C, and in **G8-4AP** from 168.49 °C, indicating that, due to the strong gel network, the removal of solvents becomes more energy-demanding. After the total combustion, the remaining weight percentage of **G8-3AP** was found to be 7.38%, higher compared to the others. The TGA data show that the combustion of the xerogel of **G8** is slow compared to its precursor **G8** powder. Further, the combustion of the xerogels of **G8-2AP**, **G8-3AP**, and **G8-4AP** is slow as compared to the **G8** xerogel, which may be due to the formation of stronger gel networks (Figure 3.45).

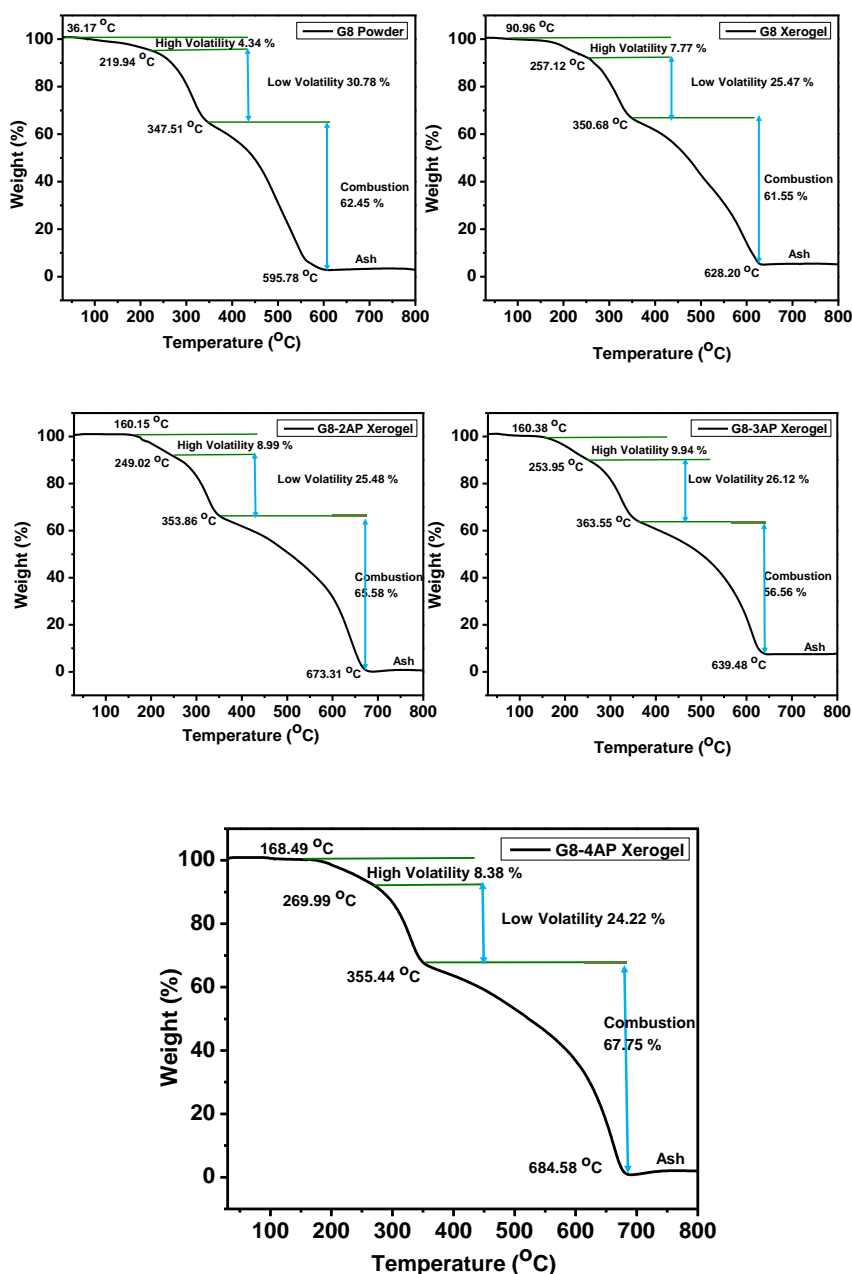


**Figure 3.45.** TGA data of gelator molecule **G8** and xerogels of organogels of **G8**, **G8-2AP**, **G8-3AP** and **G8-4AP**.

### 3.4 Conclusions

The tetrazole-based gelator molecule  $N^2, N^4, N^6$ -tri(1H-tetrazol-5-yl)-1,3,5-triazine-2,4,6-triamine (**G8**) has been synthesized and characterized using various spectroscopic tools. The structure of the molecule **G8** has been optimized through density functional theory (DFT). **G8** gets self-assembled to form an organogel in the DMSO:  $H_2O$  mixture through different non-covalent interactions, viz. hydrogen bond

formation,  $\pi$ - $\pi$  interactions, intra- or intercolumnar stacking, etc. **G8** has been utilized successfully to form mixed organogels with different isomers of aminopyridines in which 3-AP gets distinguished from other isomers in terms of fluorescence enhancement, color changes, and rheological behavior. The enhancement in fluorescence is attributed to the restriction of intramolecular rotation (RIR) due to the stronger hydrogen bond interactions between complementary hydrogen bond donor-acceptor sites of **G8** and 3-AP. The interactions between **G8** and aminopyridines have been investigated by Job plot, concentration dependent  $^1\text{H}$  NMR studies, and DFT studies. An additional hydrogen bond in the case of **G8-3AP** between the secondary -NH of **G8** and the pyridyl nitrogen of 3-AP has been found to be the reason for greater restriction in RIR. The FE-SEM analysis shows tiny fibrous, nano-flower and nano-thread like structures of organogels **G8-2AP**, **G8-3AP**, and **G8-4AP**, respectively. The thermal studies have been performed by TGA showing the slow combustion of the xerogels of organogels compared to **G8** powder due to the stronger non-covalent network inside the gel matrix. Organogels **G8**, **G8-2AP**, **G8-3AP**, and **G8-4AP** show thixotropic behavior which indicates the self-healing property of LMWG. Here, by the strain sweep or time oscillation sweep (TOS) experiment, it has been found that **G8** offers sol-gel-sol transition due to its low storage modulus ( $G'$ ) value, while in the case of **G8-3AP**, sol-gel-sol transition decreases with increasing number of TOS cycles due to its higher  $G'$  value. These analyses indicate that the **G8** organogel can effectively discriminate 3-AP from the other isomers of aminopyridines, i.e., 2-AP and 4-AP, not only by optical processes but also through rheological parameters.

### **3.5 Declaration**

This chapter is adapted from Mater. Chem. Front., 2022, 6, 2835-2847. (D.O.I. 10.1039/D2QM00520D)

### 3.6 References

- [1] Ma, X., Liu, S., Zhang, Z., Niu, Y., Wu, J. (2017), A novel thermo-responsive supramolecular organogel based on dual acylhydrazone: fluorescent detection for  $Al^{3+}$  ions, *Soft Matter*, 13, 8882-8885 (DOI: 10.1039/C7SM02141K)
- [2] Zhang, A., Zhang, Y., Xu, Z., Li, Y., Yu, X., Geng, L. (2017), Naphthalimide-based fluorescent gelator for construction of both organogels and stimuli-responsive metallogels, *RSC adv.*, 7, 25673-25677 (DOI: 10.1039/C7RA03184J)
- [3] Panja, S. and Adams, D.J. (2021), Stimuli responsive dynamic transformations in supramolecular gels, *Chem. Soc. Rev.*, 50, 5165-5200 (DOI: 10.1039/D0CS01166E)
- [4] Liu, G., Sheng, J., Teo, W.L., Yang, G., Wu, H., Li, Y., Zhao, Y. (2018), Control on dimensions and supramolecular chirality of self-assemblies through light and metal ions, *J. Am. Chem. Soc.*, 140, 16275-16283 (DOI: 10.1021/jacs.8b10024)
- [5] Wen, X., Tang, L., Qiang, L. (2014), Stimuli-responsive one-dimensional copolymer nanostructures fabricated by metallogel template polymerization and their adsorption of aspirin, *Soft Matter*, 10, 3960-3969 (DOI: 10.1039/C4SM00121D)
- [6] Maiti, B., Abramov, A., Franco, L., Puiggali, J., Enshaei, H., Alemán, C., Díaz, D.D. (2020), Thermoresponsive shape-memory hydrogel actuators made by phototriggered click chemistry, *Adv. Funct. Mater.*, 30, 2001683 (DOI: 10.1002/adfm.202001683)
- [7] Sebastian, A., Mahato, M.K. and Prasad, E. (2019), A mixed ligand approach towards lanthanide-based gels using citric acid as assembler ligand: white light emission and environmental sensing, *Soft Matter*, 15, 3407-3417 (DOI: 10.1039/C9SM00153K)
- [8] Zhong, Q., Liu, W., Yang, Y., Pan, W., Wu, M., Zheng, F., Lian, X., Niu, H. (2021), Conductive NiMn-based bimetallic metal-

- organic gel nanosheets for supercapacitors, *Mater. Adv.*, 2, 4362-4369 (DOI: 10.1039/D1MA00390A)
- [9] Li, Y.F., Li, Z., Lin, Q., Yang, Y.W. (2020), Functional supramolecular gels based on pillar [n] arene macrocycles, *Nanoscale*, 12, 2180-2200 (DOI: 10.1039/C9NR09532B)
- [10] Haldar, R., Matsuda, R., Kitagawa, S., George, S.J., Maji, T.K. (2014), Amine-Responsive Adaptable Nanospaces: Fluorescent Porous Coordination Polymer for Molecular Recognition, *Angew. Chem. Int. Edition*, 53, 11772-11777 (DOI: 10.1002/anie.201405619)
- [11] Ariga, K., Hill, J.P., Endo, H. (2007), Developments in molecular recognition and sensing at interfaces, *Int. J. Mol. Sci.*, 8, 864-883 (DOI: 10.3390/i8080864)
- [12] Lin, Q., Guan, X.W., Song, S.S., Fan, H., Yao, H., Zhang, Y.M., Wei, T.B. (2019), A novel supramolecular polymer  $\pi$ -gel based on bis-naphthalimide functionalized-pillar [5] arene for fluorescence detection and separation of aromatic acid isomers, *Polymer Chem.*, 10, 253-259 (DOI: 10.1039/C8PY01299G)
- [13] Liu, J., Sun, X.W., Huang, T.T., Zhang, Y.M., Yao, H., Wei, T.B., Lin, Q. (2021), Influence of Monomers' Structure on the Assembly and Material Property of Pillar [5] arene-Based Supramolecular Polymer Gels, *Chin. J. Chem.*, 39, 3421-3428 (DOI: 10.1002/cjoc.202100583)
- [14] Yao, H., Zhou, Q., Zhang, Y., Hu, Y., Kan, X., Chen, Y., Gong, G., Zhang, Q., Wei, T., Lin, Q. (2020), Supramolecular polymer materials based on pillar [5] arene: Ultrasensitive detection and efficient removal of cyanide, *Chin. Chem. Lett.*, 31, 1231-1234 (DOI: 10.1016/j.cclet.2019.09.046)
- [15] Wang, T., Li, Y., Shen, F., Ren, J., Yu, X. (2020), Isomeric effect of solvents on a sugar-based supergelator with self-healing ability, *Appl. Surf. Sci.*, 513, 145814 (DOI: 10.1016/j.apsusc.2020.145814)

- [16] Fang, W., Liu, C., Chen, J., Lu, Z., Li, Z.M., Bao, X., Tu, T. (2015), The electronic effects of ligands on metal-coordination geometry: a key role in the visual discrimination of dimethylaminopyridine and its application towards chemo-switch, *Chem. Commun.*, 51, 4267-4270 (DOI: 10.1039/C5CC00196J)
- [17] Malviya, N., Das, M., Mandal, P., Mukhopadhyay, S. (2017), A smart organic gel template as metal cation and inorganic anion sensor, *Soft Matter*, 13, 6243-6249 (DOI: 10.1039/C7SM01199G)
- [18] Malviya, N., Sonkar, C., Ganguly, R., Mukhopadhyay, S. (2019), Cobalt Metallogel Interface for selectively sensing l-tryptophan among essential amino acids, *Inorg. Chem.*, 58, 7324-7334 (DOI: 10.1021/acs.inorgchem.9b00455)
- [19] Kotova, O., Daly, R., dos Santos, C.M., Boese, M., Kruger, P.E., Boland, J.J., Gunnlaugsson, T. (2012), Europium-directed self-assembly of a luminescent supramolecular gel from a tripodal terpyridine-based ligand, *Angew. Chem. Int. Edition*, 51, 7208-7212 (DOI: 10.1002/anie.201201506)
- [20] Desmarchelier, A., Alvarenga, B.G., Caumes, X., Dubreucq, L., Troufflard, C., Tessier, M., Vanthuyne, N., Idé, J., Maistriaux, T., Beljonne, D., Brocorens, P. (2016), Tuning the nature and stability of self-assemblies formed by ester benzene 1, 3, 5-tricarboxamides: the crucial role played by the substituents, *Soft Matter*, 12, 7824-7838 (DOI: 10.1039/C6SM01601D)
- [21] He, M., Li, J., Tan, S., Wang, R., Zhang, Y. (2013), Photodegradable supramolecular hydrogels with fluorescence turn-on reporter for photomodulation of cellular microenvironments, *J. Am. Chem. Soc.*, 135, 18718-18721 (DOI: 10.1021/ja409000b)
- [22] Lee, J.H., Lee, H., Seo, S., Jaworski, J., Seo, M.L., Kang, S., Lee, J.Y., Jung, J.H. (2011), Fluorescence enhancement of a tetrazole-based pyridine coordination polymer hydrogel, *New J. Chem.*, 35, 1054-1059 (DOI: 10.1039/C0NJ00840K)

- [23] Kyarikwal, R., Malviya, N., Chakraborty, A., Mukhopadhyay, S. (2021), Preparation of tris-tetrazole-based Metallogels and Stabilization of Silver Nanoparticles: Studies on Reduction Catalysis and self-healing Property, *ACS Appl. Mater. Interfaces.*, 13, 59567-59579 (DOI: 10.1021/acsami.1c19217)
- [24] Ding, Z., Ma, Y., Shang, H., Zhang, H., Jiang, S. (2019), Fluorescence regulation and photoresponsivity in AIEE supramolecular gels based on a cyanostilbene modified benzene-1, 3, 5-tricarboxamide derivative, *Chem. Eur. J.*, 25, 315-322 (DOI: 10.1002/chem.201804135)
- [25] Wang, B., Li, J., Shui, S., Xu, J. (2021), An acylhydrazone-based AIE organogel for the selective sensing of submicromolar level Al<sup>3+</sup> and Al (iii)-based metallogel formation to detect oxalic acid, *New J. Chem.*, 45, 1899-1903 (DOI: 10.1039/C9NJ06340D)
- [26] Zhang, Q., Zhang, Y.M., Yao, H., Wei, T.B., Shi, B., Lin, Q. (2021), Supramolecular AIE polymer-based rare earth metallogels for the selective detection and high efficiency removal of cyanide and perchlorate, *Polymer Chem.*, 12, 2001-2008 (DOI: 10.1039/D0PY01630F)
- [27] Jia, W., Yang, P., Li, J., Yin, Z., Kong, L., Lu, H., Ge, Z., Wu, Y., Hao, X., Yang, J. (2014), Synthesis and characterization of a novel cyanostilbene derivative and its initiated polymers: aggregation-induced emission enhancement behaviors and light-emitting diode applications, *Polymer Chem.*, 5, 2282-2292 (DOI: 10.1039/C3PY01550E)
- [28] Shivaji, B.S., Boddula, R., Saeki, A., Singh, S.P. (2022), A phenothiazine-fused electroactive bilayer helicene: design, synthesis, ACQ-to-AIE transformation and photophysical properties, *J. Mater. Chem. C*, 10, 5173-5182 (DOI: 10.1039/D1TC06090B)
- [29] Fang, W., Liu, K., Wang, G., Liang, Y., Huang, R., Liu, T., Ding, L., Peng, J., Peng, H., Fang, Y. (2021), Dual-phase emission

- AI-Egen with ICT properties for VOC chromic sensing, *Anal. Chem.*, 93, 8501-8507 (DOI: 10.1021/acs.analchem.1c00980)
- [30] Leung, N.L., Xie, N., Yuan, W., Liu, Y., Wu, Q., Peng, Q., Miao, Q., Lam, J.W., Tang, B.Z. (2014), Restriction of intramolecular motions: the general mechanism behind aggregation-induced emission, *Chem. Eur. J.*, 20, 15349-15353 (DOI: 10.1002/chem.201403811)
- [31] Liu, J., Lam, J.W., Tang, B.Z. (2009), Aggregation-induced emission of silole molecules and polymers: fundamental and applications, *J. Inorg. Organomet. Polym. Mater.*, 19, 249-285 (DOI: 10.1007/s10904-009-9282-8)
- [32] Rout, Y., Montanari, C., Pasciucco, E., Misra, R., Carlotti, B. (2021), Tuning the fluorescence and the intramolecular charge transfer of phenothiazine dipolar and quadrupolar derivatives by oxygen functionalization, *J. Am. Chem. Soc.*, 143, 9933-9943 (DOI: 10.1021/jacs.1c04173)
- [33] Jeon, K., Jen, M., Lee, S., Jang, T., Pang, Y. (2021), Intramolecular charge transfer of 1-aminoanthraquinone and ultrafast solvation dynamics of dimethylsulfoxide, *Int. J. Mol. Sci.*, 22, 11926 (DOI: 10.3390/ijms222111926)
- [34] Kundu, B.K., Mandal, P., Mukhopadhyay, B.G., Tiwari, R., Nayak, D., Ganguly, R., Mukhopadhyay, S. (2019), Substituent dependent sensing behavior of Schiff base chemosensors in detecting  $Zn^{2+}$  and  $Al^{3+}$  ions: Drug sample analysis and living cell imaging, *Sens. Actuators B: Chem.*, 282, 347-358 (DOI: 10.1016/j.snb.2018.11.076)
- [35] Goswami, S., Chakraborty, S., Paul, S., Halder, S., Panja, S., Mukhopadhyay, S.K. (2014), A new pyrene based highly sensitive fluorescence probe for copper (II) and fluoride with living cell application., *Org. Biomol. Chem.*, 12, 3037-3044 (DOI: 10.1039/C4OB00067F)
- [36] Boogaarts, M.G., von Helden, G., Meijer, G. (1996), A study on the structure and vibrations of diphenylamine by resonance-enhanced multiphoton ionization spectroscopy and ab initio

- calculations, *J. Chem. Phys.*, 105, 8556-8568 (DOI: 10.1063/1.472640)
- [37] Kerru, N., Gummidi, L., Bhaskaruni, S.V., Maddila, S.N., Singh, P., Jonnalagadda, S.B. (2019), A comparison between observed and DFT calculations on structure of 5-(4-chlorophenyl)-2-amino-1, 3, 4-thiadiazole, *Sci. Rep.*, 9, 19280 (DOI: 10.1038/s41598-019-55793-5)
- [38] Desiraju, G.R., Steiner, T. (2001), *The weak hydrogen bond: in structural chemistry and biology*, 9, International Union of Crystal
- [39] Hunt, P.A., Ashworth, C.R., Matthews, R.P. (2015), Hydrogen bonding in ionic liquids, *Chem. Soc. Rev.*, 44, 1257-1288 (DOI: 10.1039/C4CS00278D)
- [40] Stojkov, G., Niyazov, Z., Picchioni, F., Bose, R.K. (2021), Relationship between structure and rheology of hydrogels for various applications, *Gels*, 7, 255 (DOI: 10.3390/gels7040255)
- [41] Priya, M.V., Kumar, R.A., Sivashanmugam, A., Nair, S.V., Jayakumar, R. (2015), Injectable amorphous chitin-agarose composite hydrogels for biomedical applications, *J. Funct. Biomater.*, 6, 849-862 (DOI: 10.3390/jfb6030849)
- [42] Zhang, G., Li, Y., Wang, H., Wang, J. (2019), Rheological properties of polyurethane-based magnetorheological gels, *Front. Mater.*, 6, 56 (DOI: 10.3389/fmats.2019.00056)
- [43] Fan, X., Xu, H., Zhang, Q., Song, Y., Zheng, Q. (2019), Insight into the weak strain overshoot of carbon black filled natural rubber, *Polymer*, 167, 109-117 (DOI: 10.1016/j.polymer.2019.01.076)
- [44] Hyun, K., Kim, S.H., Ahn, K.H., Lee, S.J. (2002), Large amplitude oscillatory shear as a way to classify the complex fluids, *J. Non-Newton. Fluid Mech.*, 107, 51-65 (DOI: 10.1016/S0377-0257(02)00141-6)
- [45] Donley, G.J., Singh, P.K., Shetty, A., Rogers, S.A. (2020), Elucidating the  $G''$  overshoot in soft materials with a yield transition via a time-resolved experimental strain

- decomposition, *Proc. Natl. Acad. Sci.*, 117, 21945-21952 (DOI: 10.1073/pnas.2003869117)
- [46] Liu, F., Feng, D., Yang, H., Guo, X. (2020), Preparation of macroporous transition metal hydroxide monoliths via a sol-gel process accompanied by phase separation, *Sci. Rep.*, 10, 4331 (DOI: 10.1038/s41598-020-61195-9)
- [47] Mears, L.L., Draper, E.R., Castilla, A.M., Su, H., Zhuola, Dietrich, B., Nolan, M.C., Smith, G.N., Douth, J., Rogers, S., Akhtar, R. (2017), Drying affects the fiber network in low molecular weight hydrogels, *Biomacromolecules*, 18, 3531-3540 (DOI: 10.1021/acs.biomac.7b00823)

## **Chapter 4**

### **Palladium Nanoparticles and Palladium Ions Embedded Nanostructured Metallogel: Effective Catalyst for Suzuki-Miyaura Coupling and Cycloaddition Reaction for Tetrazole Formation**



## Chapter 4

# Palladium Nanoparticles and Palladium Ions Embedded Nanostructured Metallogel: Effective Catalyst for Suzuki-Miyaura Coupling and Cycloaddition Reaction for Tetrazole Formation

## 4.1 Introduction

Catalysis is one of the fascinating areas of chemistry research that has been explored since the development of modern chemistry.<sup>[1]</sup> Many catalysts have been reported based on transition metal complexes, metal-organic frameworks, and nanocomposite materials over the years.<sup>[2-7]</sup> However, using soft materials, particularly metallogels, as catalysts is a topic of recent interest. The fundamental properties of gels and their semisolid nature make them interesting candidates for catalysis. The semisolid porous nature of the gel network can provide a scaffold for the interactions between substrate and reagent to obtain a product in a kinetically driven pathway. The insoluble nature of the gel or the derived composite can make the recovery of the catalyst easier.<sup>[8]</sup> There are some notable reports based on the use of gels as catalysts. Some Pd(II)-coordinated metallogels are used for organic reactions like the oxidative reaction of benzyl alcohol, Suzuki-Miyaura coupling, Heck coupling, etc. At the same time, some PdNPs based gels are also used as catalysts for Suzuki-Miyaura and other C-C coupling reactions.<sup>[9, 10]</sup> Other than palladium, there are some reports where Cd(II), Cu(I), Cu(II), AgNPs based nanostructured metallogels are used as active catalysts of various organic transformations like Huisgen cycloaddition reaction, asymmetric Diels-Alder cycloaddition, reduction of p-nitrophenol, degradation of dyes, etc.<sup>[11-24]</sup> Other than metallogels, LMW organogels also shows their catalytic activities for various organic transformation.  
[25-28]

Organic moieties are essential for the preparation of various necessary products related to pharmaceuticals, food additives, pesticides, fertilizers, and many more. For preparing these necessary products,

some chemical processes are involved many times. The maximum procedure contained high temperature, pressure, toxic solvent, catalyst, and chemicals and generated toxic chemical waste, adversely impacting the environment and health.<sup>[29, 30]</sup> Notably, the use of suitable catalysts can control the reaction system and decrease the limitation. Catalysts are of two types homogeneous and heterogeneous catalysts. Due to the solubility of the Homogenous catalyst in the reaction medium, it shows higher selectivity and better yield. However, the limitation is the difficulty separating the homogenous catalyst from the reaction medium. Therefore, the transformation of the homogenous catalytic process by heterogeneous catalysts is in light to overcome the limitation. The introduction of nanomaterials as catalysts have been studied for the last two decades that can be used as an excellent alternative to the conventional catalytic system. The nanomaterials could provide the properties of both homogeneous and heterogeneous catalysis. The formation of nanomaterials as catalysts is also helpful because of the possibilities of tuning the morphology, shape, and size, which must affect the catalytic pathway. Nanomaterials-based catalytic systems are helpful because the interaction between nanocatalyst and reactant is significantly higher due to the large surface area, high surface area-to-volume ratio, and can be reused many times, which makes this catalyst economically and environmentally suitable.

Nitrogen-containing heterocyclic tetrazole-based molecules have greater attention due to their applicability towards antifungal,<sup>[31, 32]</sup> anti-HIV,<sup>[33]</sup> antitubercular,<sup>[34]</sup> antibacterial,<sup>[35]</sup> antiulcer,<sup>[36, 37]</sup> antiallergic,<sup>[38]</sup> antihypertensive,<sup>[39]</sup> antileishmanial,<sup>[40]</sup> anticancer,<sup>[41, 42]</sup> antibacterial and antiproliferative,<sup>[43]</sup> activities. Tetrazole derivatives are also used to increase lipophilicity, bioavailability, and pharmacokinetic properties and reduce drug molecule side effects. Furthermore, they are used as high-energy material, bioimaging, explosives, organometallic chemistry, etc.<sup>[44, 45]</sup> Tetrazole derivatives are also effective for organogel and metallo gel formation due to their multifunctional sites, which can participate in adequate hydrogen bonding.

Palladium-catalyzed cross-couplings have played an increasingly important role in the synthesis of agrochemicals. The palladium-catalyzed cross-coupling reaction between organoboron compounds and organic halides or triflates is referred to as Suzuki–Miyaura cross-coupling. Commercially available, nontoxic, and stable organoboron compounds used as coupling reactants in Suzuki–Miyaura coupling. This coupling reaction shows high yield and selectivity, suitable conditions, and broad substrate scope.<sup>[46, 47]</sup> The reaction is used in organic synthesis, pharmaceutical, and pesticide industries.<sup>[48]</sup> Many reports are there with transition metal catalysts participating in tetrazole formation reactions, out of which the palladium catalyst dominated as the most potential candidate due to its application at laboratory and industrial scale.<sup>[49-53]</sup>

Here, the palladium ion and palladium nanoparticle-based nanostructured catalysts have been prepared and stabilized by gel formation, where the same gelator molecule **G8** is used to form both metallogel **G8PdCl<sub>2</sub>** and **G8PdNPs**. Xerogel of **G8PdCl<sub>2</sub>** was used as a catalyst for the 2+3 cycloaddition reaction of nitrile and sodium azide to form tetrazoles. While xerogel of **G8PdNPs** is used as a catalyst for the Suzuki–Miyaura coupling reaction. The reactions have been applied on a number of substrates and show good product yield. Both catalysts offer recyclability till five continuous cycles of reactions without much depreciation in product yield.

## **4.2 Experimental section**

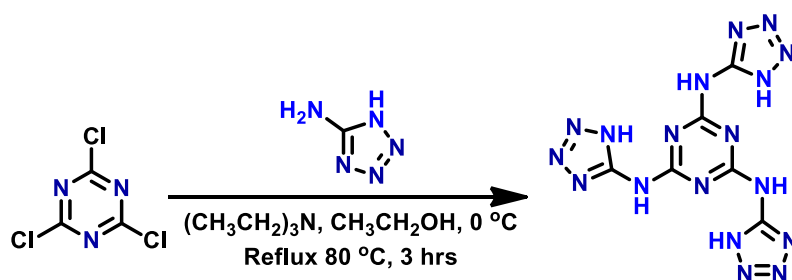
### **4.2.1 Materials and methods**

The chemicals used in this work, *viz.*, cyanuric chloride, i.e., 5-amino tetrazole monohydrate and palladium chloride, have been taken from commercial sources. DMSO/MQ-water or a mixture of solvents was used for experimental analysis. Instruments used for FTIR, NMR, ESI-MS and FE-SEM experiments have already been mentioned in section 2.2.1 of chapter 2.

The formation of nanostructured metallogels with PdNPs inside the gel matrix of **G8** has been analyzed by TEM, PXRD, and XPS techniques. The synthesis of the organic substrate of tetrazole formation and Suzuki-Miyaura coupling reaction has been characterized by ESI-MS, FTIR,  $^1\text{H}$ , and  $^{13}\text{C}$  NMR spectroscopy.

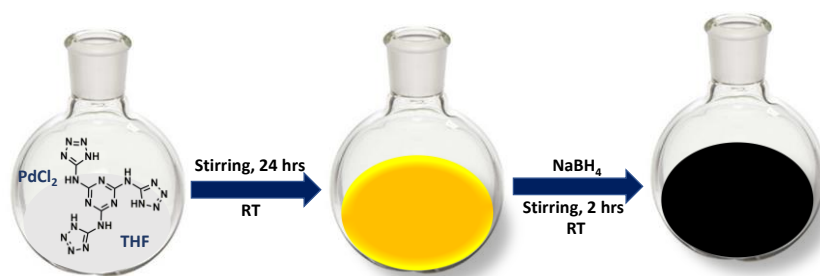
#### 4.2.2 Synthesis of **G8**, **G8PdCl<sub>2</sub>** and **G8PdNPs**

The gelator molecule **G8** was synthesized as reported in chapter 3 (Scheme 4.1).



*Scheme 4.1. Synthesis of gelator **G8**.*

The metallogel formation of **G8PdCl<sub>2</sub>**, has been done in DMSO:  $\text{H}_2\text{O}$  mixture. After the fabrication of **G8PdCl<sub>2</sub>** metallogel, it was converted into xerogel by lyophilization. This xerogel acts as a catalyst for the cycloaddition reaction of nitrile substituent and sodium azide to form respective tetrazoles. For the formation of the nanocatalyst, 0.5 mmol (165 mg) gelator molecule **G8** and 0.5 mmol (88.50 mg)  $\text{PdCl}_2$  were taken in 60 mL of THF and stirred for 24 hrs at room temperature. After that, 3M, 500  $\mu\text{L}$  aqueous solution of  $\text{NaBH}_4$  was added and the mixture is again stirred for 2 hrs at room temperature (Scheme 4.2). The black color precipitate of **G8PdNPs** formed, which was washed by THF and dried in a desiccator.



*Scheme 4.2. Synthesis of nanocomposite material **G8PdNPs**.*

### 4.2.3 Gels preparation

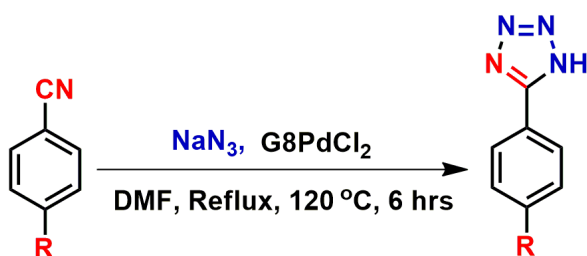
For the fabrication of metallogel **G8PdCl<sub>2</sub>**, 0.1 mmol (33 mg) of **G8** was dissolved in 1 mL of DMSO and added into 0.1 mmol (18 mg) 1 mL aqueous solution of PdCl<sub>2</sub>. The yellow metallogel formed instantaneously, but it became more stable over time. Further, the nanometallogel **G8PdNPs** has been fabricated by adding 1 mL 1.8 weight % **G8PdNPs** powder into 1 mL solution of 0.1 mmol (33 mg) of **G8** dissolved in DMSO. Stable greenish-black color nano-metallogel has been formed instantaneously. The gels have been stable at room temperature.

### 4.2.4 Characterization

The ESI-MS analysis, FTIR spectra, NMR studies, powder X-ray diffraction, morphological and rheological analysis of organogel **G8**, metallogels **G8PdCl<sub>2</sub>** and **G8PdNPs** have been done as similar to analysis mentioned in section 2.2.5 of chapter 2.

The synthesis of palladium nanoparticles inside gel matrix of **G8** has also been analysed by XPS analysis. The catalytic reaction of 2+3 cycloaddition reaction of tetrazole formation has been examined by ESI-MS, FTIR and NMR technologies. Similarly, the Suzuki-Miyaura coupling reaction was also examined by FTIR and NMR spectroscopy.

**4.2.5 General method of synthesis of tetrazole substituent (3+2 cycloaddition reaction).** Benzonitrile substrate (1 mmol) has been taken in 5 mL DMF. After that 2 mmol of NaN<sub>3</sub> and 20 mg of palladium (II) catalyst (**G8PdCl<sub>2</sub>**) were added into it at stirring condition. The reaction mixture was refluxed at 120 °C for six hours (Scheme 4.3). After that, the reaction mixture was extracted with ice-cooled water (20 mL) and ethyl acetate (30 mL) two times. The organic layer was evaporated by the rotatory evaporator, and the isolated product was washed further with hexane to find a fine solid as a pure product. The product has been characterized by ESI-MS and NMR spectroscopy.



**Scheme 4.3:** 2+3 cycloaddition reaction for synthesis of tetrazole substituent by catalyst **G8PdCl<sub>2</sub>**.

**Synthesis of 5-phenyl-1H-tetrazole:** The product has been Synthesized as general method mentioned above. Product: yield: 74 %. ESI-MS: m/z [M-H]<sup>-</sup> calculated for C<sub>7</sub>H<sub>5</sub>N<sub>4</sub><sup>-</sup>: 145.05, found 145.03 (Figure 4.1). The FTIR band for nitrile -CN found at 2230 cm<sup>-1</sup> in benzonitrile. This band diminished in product shows the formation of tetrazole from nitrile. FTIR: 3397 cm<sup>-1</sup>, 2927 cm<sup>-1</sup>, 2856 cm<sup>-1</sup>, 1714 cm<sup>-1</sup>, 1448 cm<sup>-1</sup>, 1369 cm<sup>-1</sup>, 1252 cm<sup>-1</sup>, 1046 cm<sup>-1</sup> and 693 cm<sup>-1</sup> (Figure 4.2). <sup>1</sup>H NMR (500 MHz, DMSO-*d*<sub>6</sub>) δ ppm 8.10 (2H, d) and 7.52 (3H, m) for aromatic protons (Figure 4.3). <sup>13</sup>C NMR (126 MHz, DMSO-*d*<sub>6</sub>) δ ppm 151.91 (1 C), 132.16 (1 C), 131.11 (2 C), 129.18 (2 C) and 127.34 (1 C) (Figure 4.4).

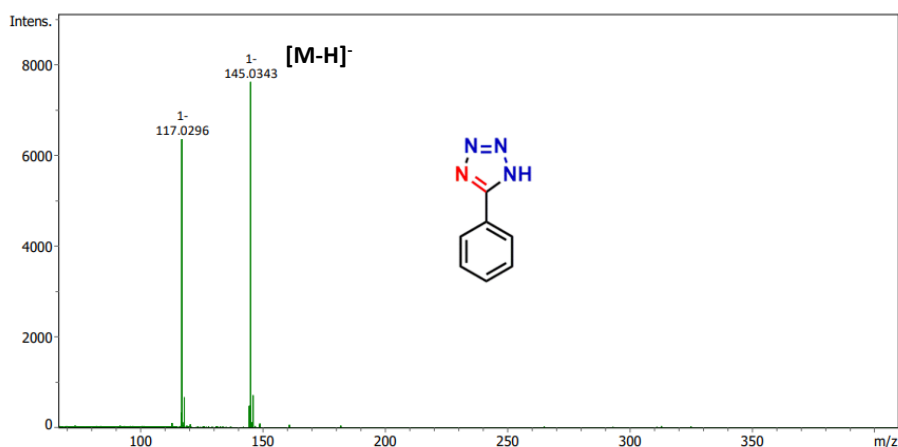


**Figure 4.1.** ESI-MS of 5-phenyl-1H-tetrazole in negative mode.

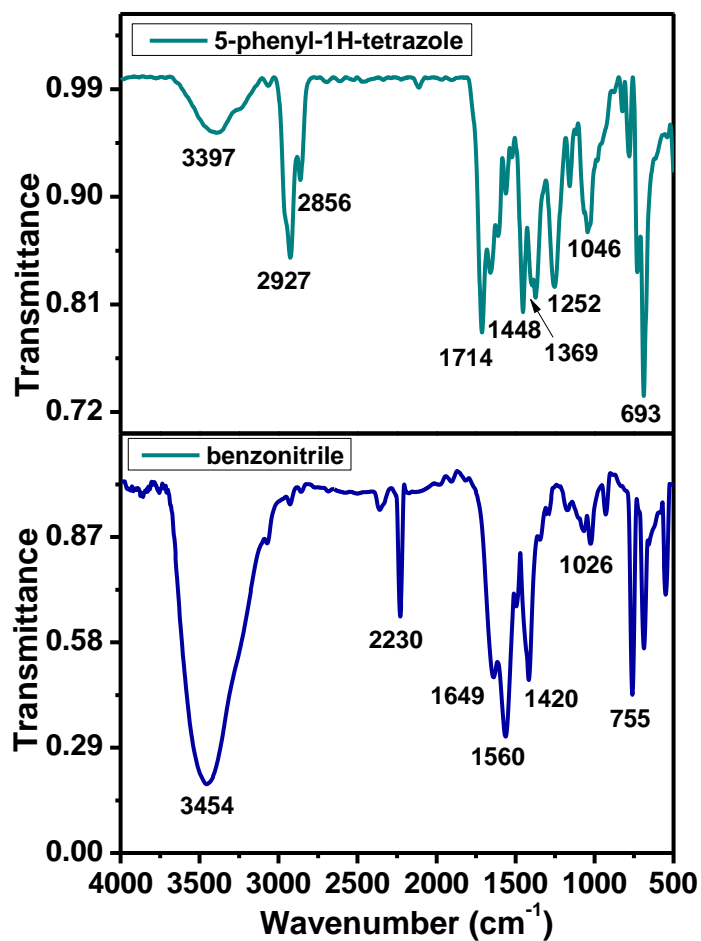


Figure 4.2. FTIR data of benzonitrile and 5-phenyl-1H-tetrazole.

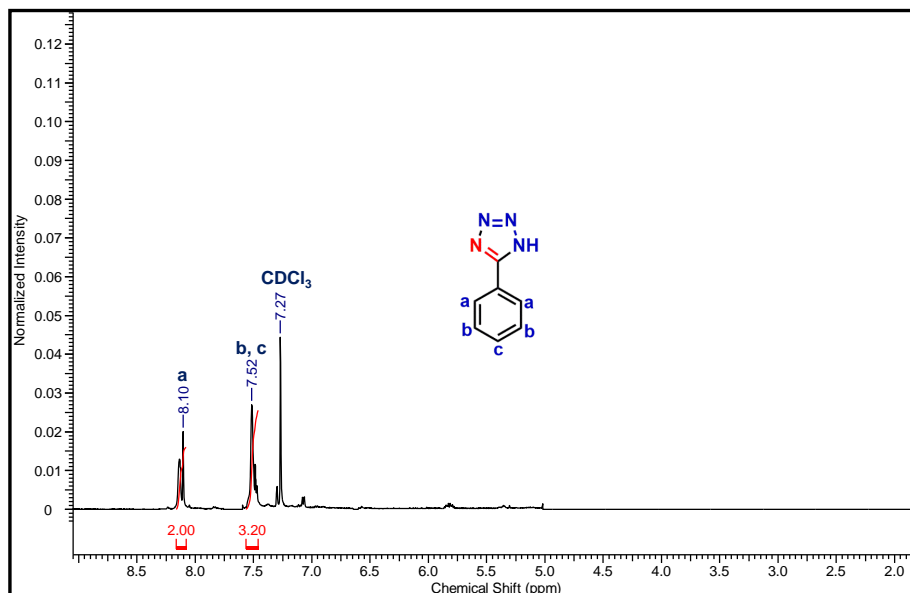


Figure 4.3. <sup>1</sup>H NMR data of 5-phenyl-1H-tetrazole.

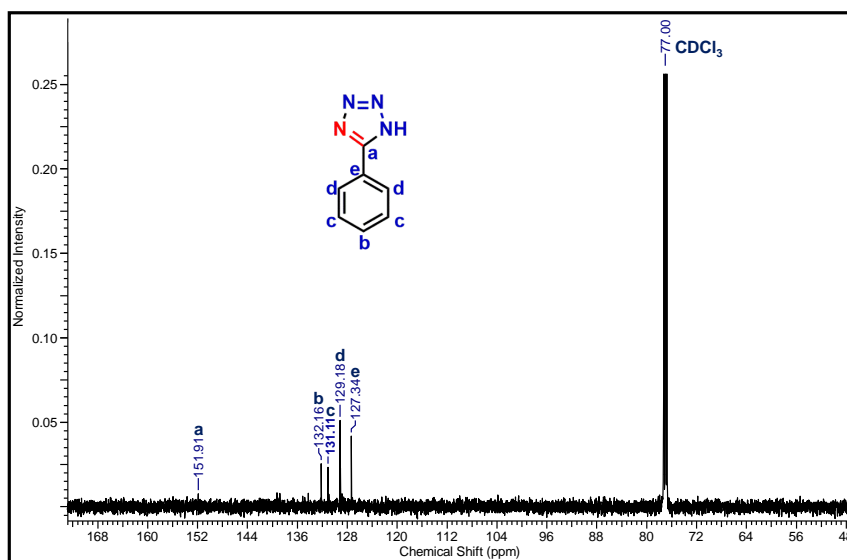


Figure 4.4.  $^{13}\text{C}$  NMR data of 5-phenyl-1H-tetrazole.

**Synthesis of 4-(1H-tetrazol-5-yl)aniline:** Product: yield:86 %. ESI-MS:  $m/z$  [M] calculated for  $\text{C}_7\text{H}_7\text{N}_5$ : 161.07, found 161.07 (Figure 4.5). The FTIR band for nitrile  $-\text{CN}$  found at  $2210\text{ cm}^{-1}$  in 4-aminobenzonitrile. This band diminished in product shows the formation of tetrazole from nitrile. FTIR:  $3459\text{ cm}^{-1}$ ,  $3356\text{ cm}^{-1}$ ,  $2917\text{ cm}^{-1}$ ,  $2861\text{ cm}^{-1}$ ,  $1600\text{ cm}^{-1}$ ,  $1514\text{ cm}^{-1}$ ,  $1313\text{ cm}^{-1}$ ,  $1264\text{ cm}^{-1}$ ,  $825\text{ cm}^{-1}$  and  $545\text{ cm}^{-1}$  (Figure 4.6).  $^1\text{H}$  NMR (500 MHz,  $\text{DMSO}-d_6$ )  $\delta$  ppm 7.42-7.40 (2H, d), 6.66-6.64 (2H, d) for aromatic protons and 4.19 (2H, s) for amide  $-\text{NH}_2$  proton (Figure 4.7).  $^{13}\text{C}$  NMR (126 MHz,  $\text{DMSO}-d_6$ )  $\delta$  ppm 150.38 (2 C), 133.76 (2 C), 120.10 (1 C), 114.39 (2 C) (Figure 4.8).

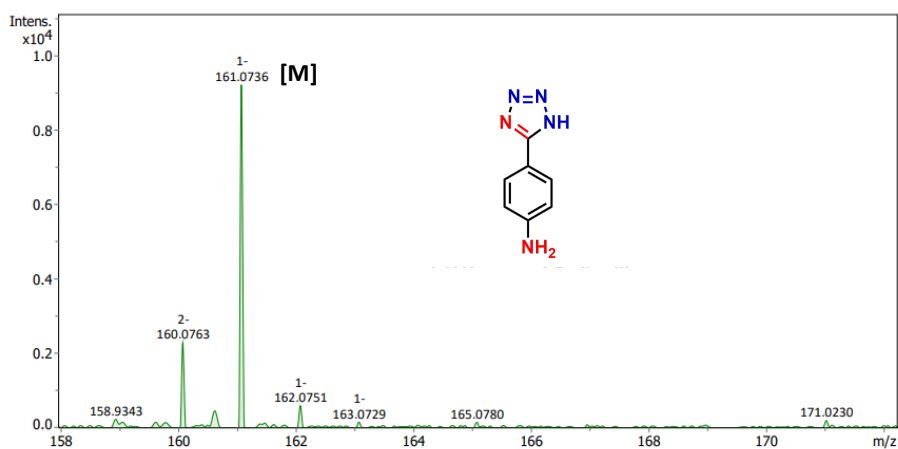


Figure 4.5. ESI-MS data of 4-(1H-tetrazol-5-yl)aniline in negative mode.

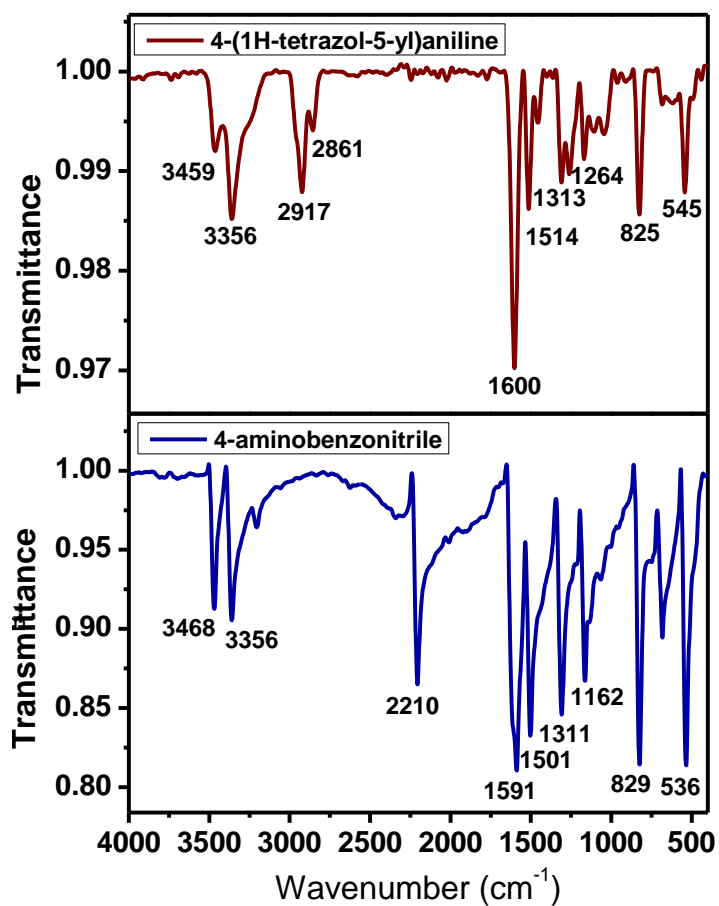


Figure 4.6. FTIR data of 4-aminobenzonitrile and 4-(1H-tetrazol-5-yl)aniline.

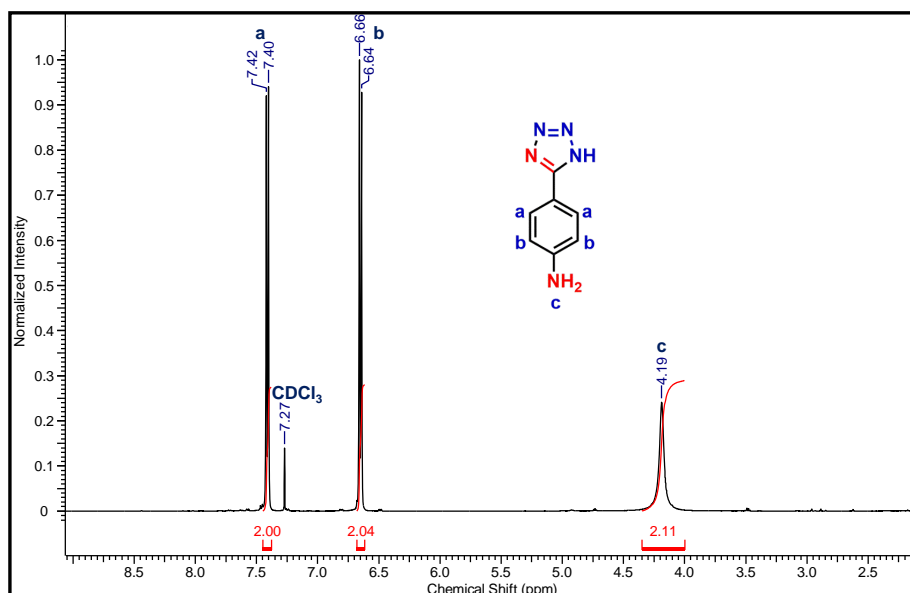
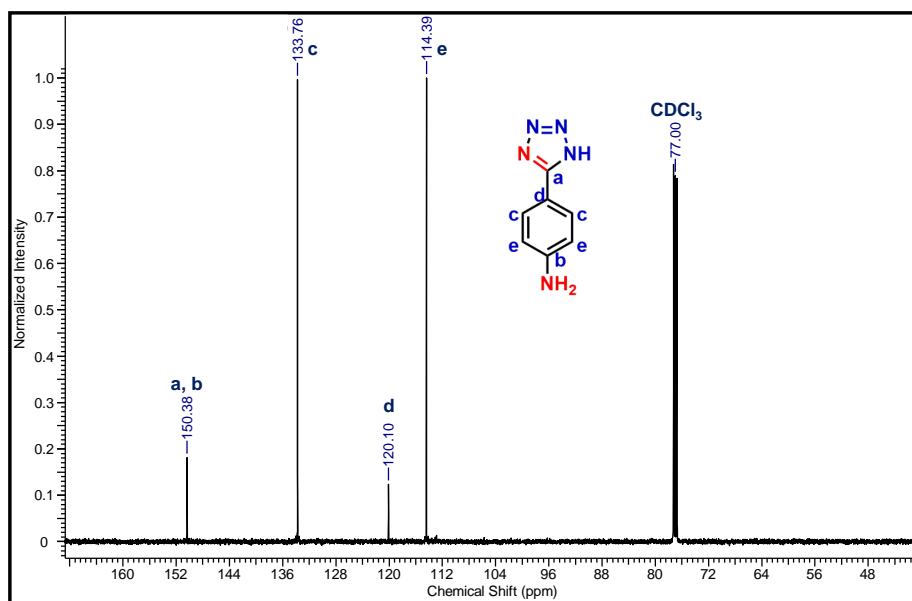
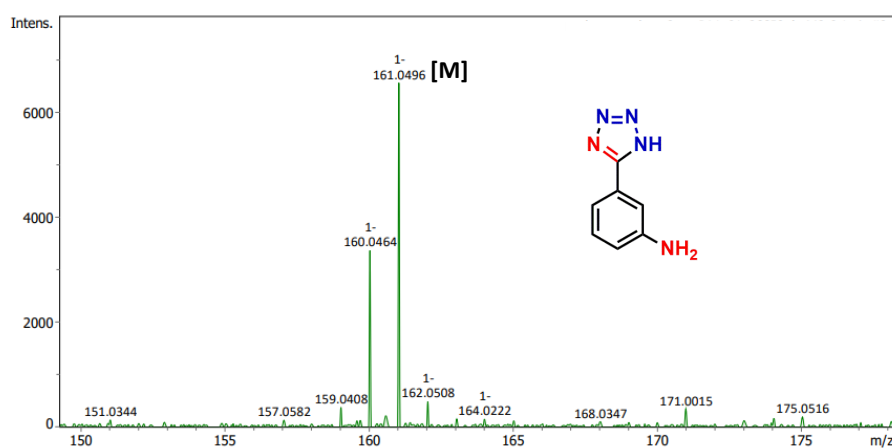


Figure 4.7. <sup>1</sup>H NMR data of 4-(1H-tetrazol-5-yl)aniline.



**Figure 4.8.**  $^{13}\text{C}$  NMR data of 4-(1H-tetrazol-5-yl)aniline.

**Synthesis of 3-(1H-tetrazol-5-yl)aniline:** Product: yield: 75 %. ESI-MS:  $m/z$  [M] calculated for  $\text{C}_7\text{H}_7\text{N}_5$ : 161.07, found 161.05 (Figure 4.9). FTIR:  $3356\text{ cm}^{-1}$ ,  $2945\text{ cm}^{-1}$ ,  $2833\text{ cm}^{-1}$ ,  $1648\text{ cm}^{-1}$ ,  $1451\text{ cm}^{-1}$ ,  $1405\text{ cm}^{-1}$ ,  $1022\text{ cm}^{-1}$  and  $629\text{ cm}^{-1}$  (Figure 4.10).  $^1\text{H}$  NMR (500 MHz,  $\text{DMSO-}d_6$ )  $\delta$  ppm 7.22 (1H, d), 7.02 (1H, m), 6.90 (1H, s), 6.88 (1H, d) for aromatic protons and 3.91 (2H, s) for amide -NH proton (Figure 4.11).  $^{13}\text{C}$  NMR (126 MHz,  $\text{DMSO-}d_6$ )  $\delta$  ppm 146.91 (2C), 130.00 (1C), 121.91 (1C), 119.15 (1C), 117.38 (1C) and 112.85 (1C) (Figure 4.12).



**Figure 4.9.** ESI-MS data of 3-(1H-tetrazol-5-yl)aniline in negative mode.

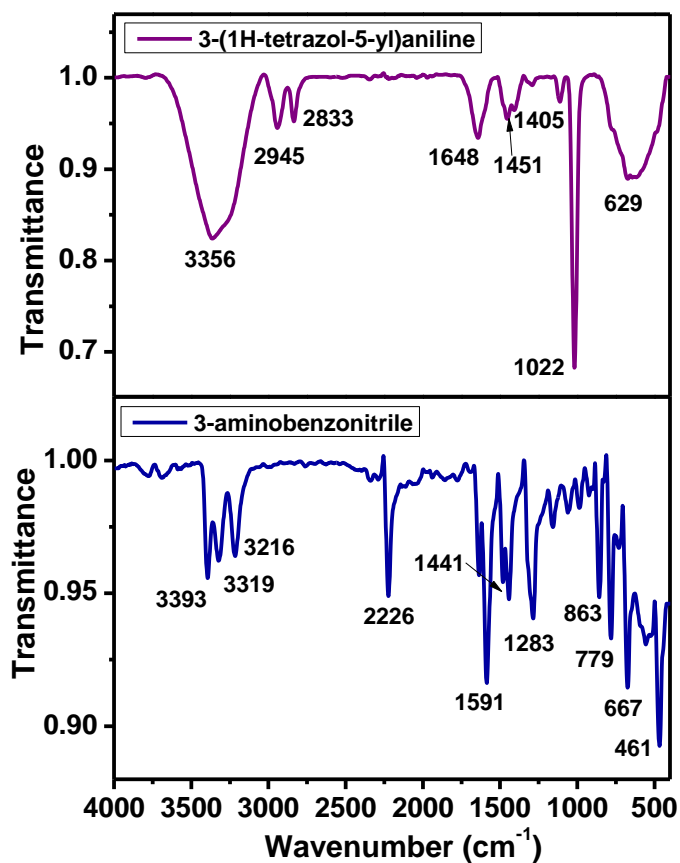


Figure 4.10. FTIR data of 3-aminobenzonitrile and 3-(1H-tetrazol-5-yl)aniline.

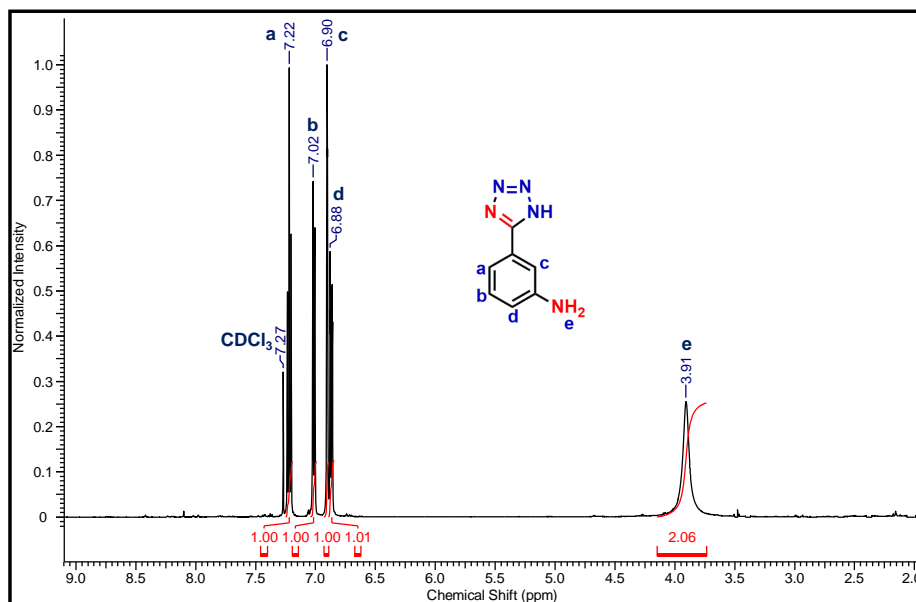
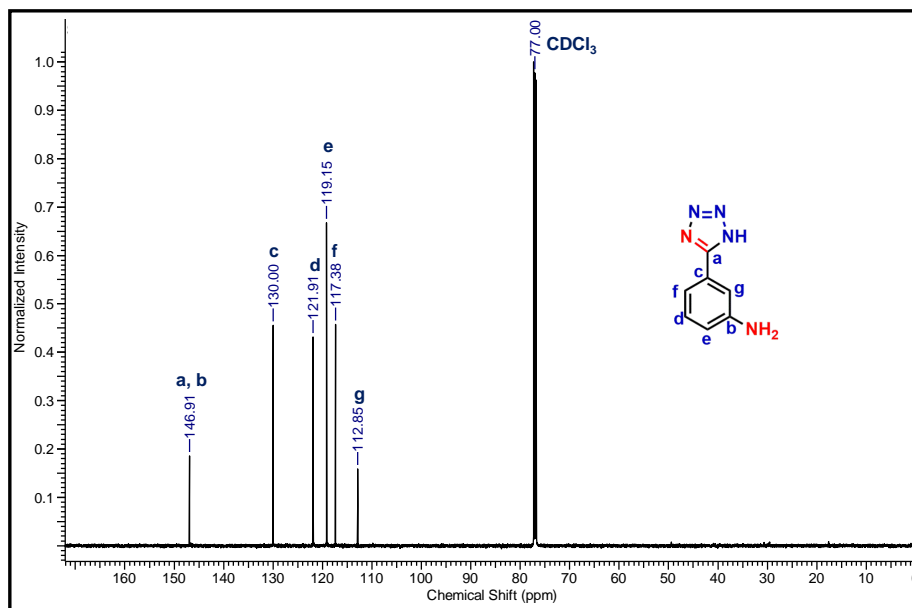
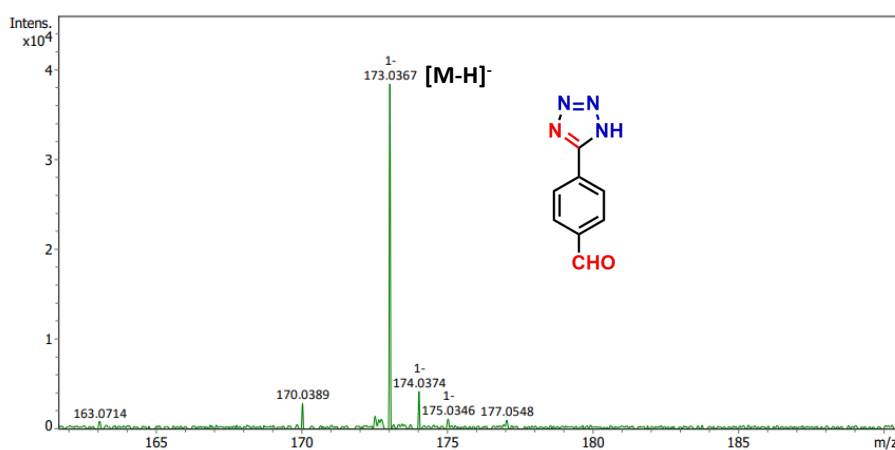


Figure 4.11.  $^1\text{H}$  NMR data of 3-(1H-tetrazol-5-yl)aniline.



**Figure 4.12.**  $^{13}\text{C}$  NMR data of 3-(1H-tetrazol-5-yl)aniline.

**Synthesis of 4-(1H-tetrazol-5-yl)benzaldehyde:** Product: yield: 85 %. ESI-MS:  $m/z$   $[\text{M}-\text{H}]^-$  calculated for  $\text{C}_8\text{H}_5\text{N}_4\text{O}^-$ : 173.04, found, 173.04 (Figure 4.13). FTIR:  $3375\text{ cm}^{-1}$ ,  $2927\text{ cm}^{-1}$ ,  $2852\text{ cm}^{-1}$ ,  $1694\text{ cm}^{-1}$ ,  $1283\text{ cm}^{-1}$ ,  $1189\text{ cm}^{-1}$ ,  $825\text{ cm}^{-1}$  and  $536\text{ cm}^{-1}$  (Figure 4.14).  $^1\text{H}$  NMR (500 MHz,  $\text{DMSO}-d_6$ )  $\delta$  ppm 10.10 (1H, s) for aldehyde proton and 8.00 (2H, d), 7.86 (2H, d) for aromatic protons (Figure 4.15).  $^{13}\text{C}$  NMR (126 MHz,  $\text{DMSO}-d_6$ )  $\delta$  ppm 190.60 (1C), 162.74 (1C), 138.70 (2C), 132.88 (2C) and 129.87 (2C) (Figure 4.16).



**Figure 4.13.** ESI-MS data of 4-(1H-tetrazol-5-yl)benzaldehyde in negative mode.

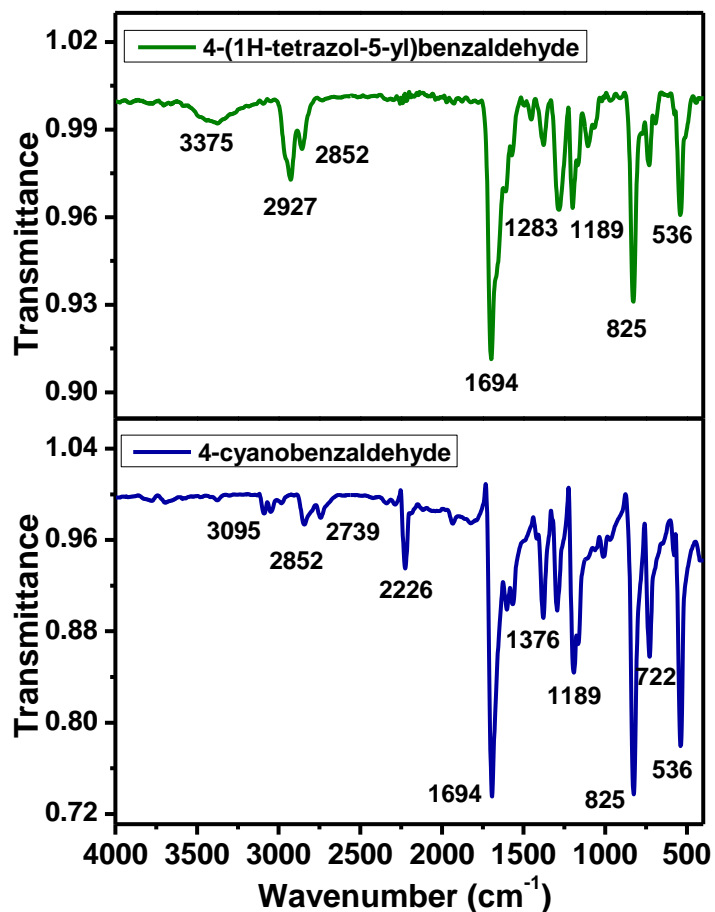


Figure 4.14. FTIR data of 4-cyanobenzaldehyde and 4-(1H-tetrazol-5-yl)benzaldehyde.

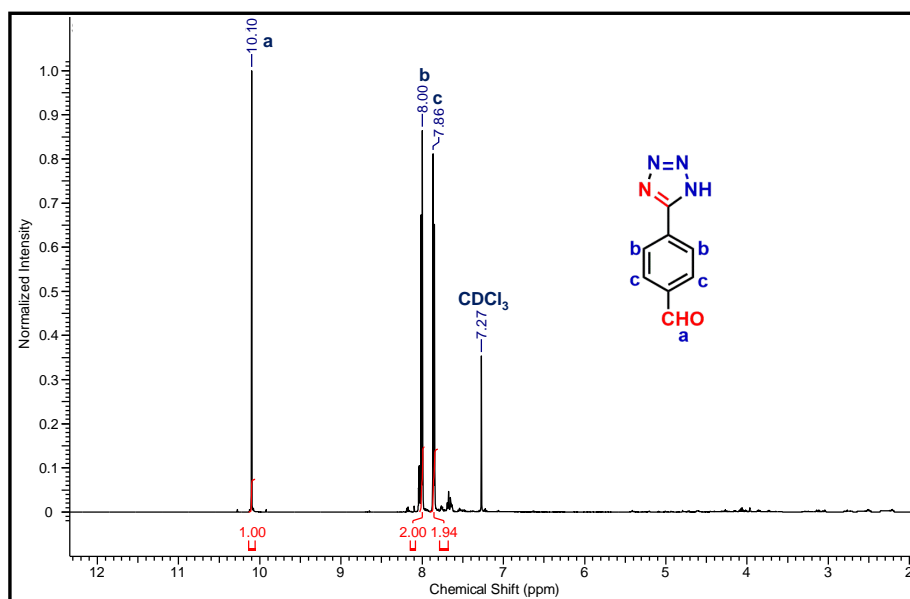
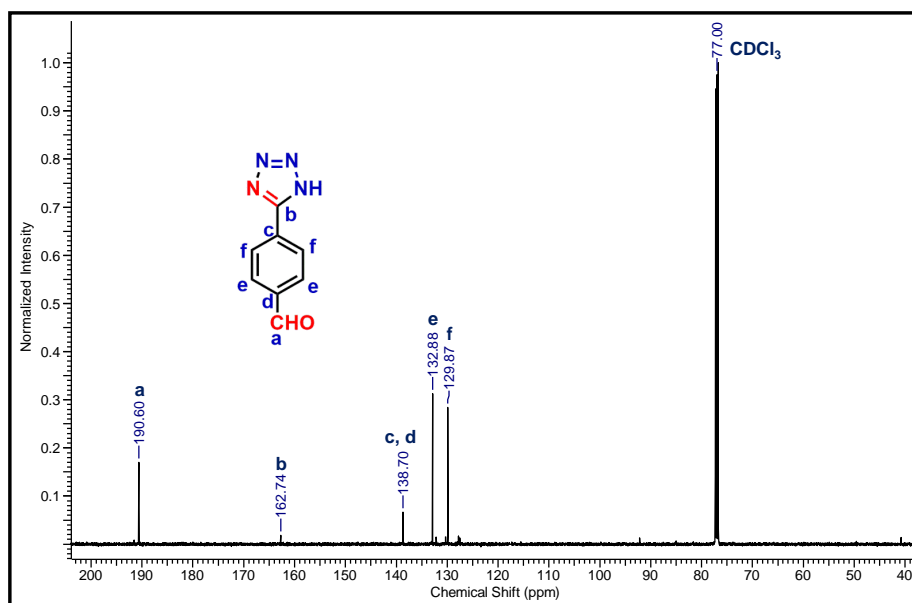
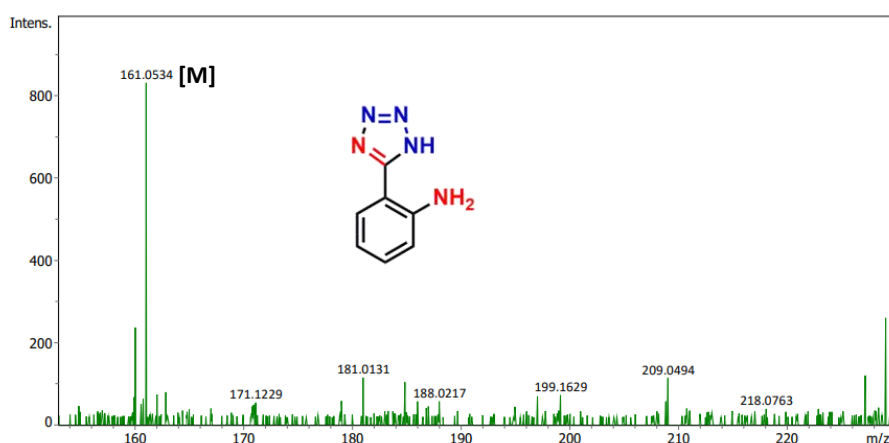


Figure 4.15. <sup>1</sup>H NMR data of 4-(1H-tetrazol-5-yl)benzaldehyde.



**Figure 4.16.**  $^{13}\text{C}$  NMR data of 4-(1H-tetrazol-5-yl)benzaldehyde.

**Synthesis of 2-(1H-tetrazol-5-yl)aniline:** Product: yield: 72 %. ESI-MS:  $m/z$  [M] calculated for  $\text{C}_7\text{H}_7\text{N}_5$ : 161.07, found 161.05 (Figure 4.17). FTIR:  $3368\text{ cm}^{-1}$ ,  $2917\text{ cm}^{-1}$ ,  $2858\text{ cm}^{-1}$ ,  $1722\text{ cm}^{-1}$ ,  $1604\text{ cm}^{-1}$ ,  $1448\text{ cm}^{-1}$ ,  $1262\text{ cm}^{-1}$ ,  $1104\text{ cm}^{-1}$  and  $742\text{ cm}^{-1}$  (Figure 4.18).  $^1\text{H}$  NMR (500 MHz,  $\text{DMSO-}d_6$ )  $\delta$  ppm 7.40 (1H, d), 7.33 (1H, m), 6.76 (1H, s), 6.74 (1H, m) for aromatic protons and 4.38 (2H, s) for amide -NH proton (Figure 4.19).  $^{13}\text{C}$  NMR (126 MHz,  $\text{DMSO-}d_6$ )  $\delta$  ppm 149.55 (2C), 133.98 (1C), 132.34 (1C), 117.98 (2C) and 115.11 (1C) (Figure 4.20).



**Figure 4.17.** ESI-MS data of 2-(1H-tetrazol-5-yl)aniline in negative mode.

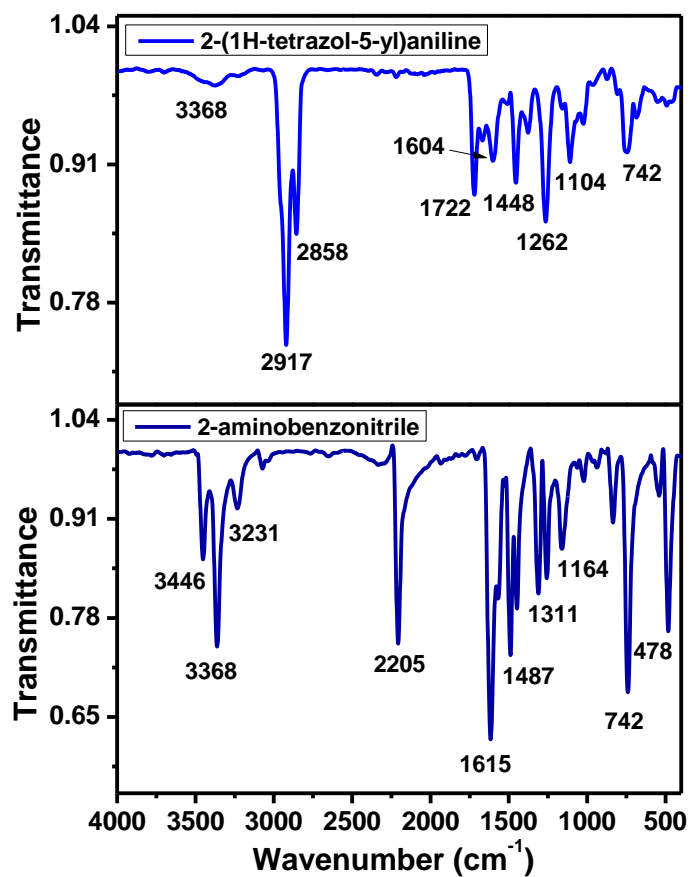


Figure 4.18. FTIR data of 2-aminobenzonitrile and 2-(1H-tetrazol-5-yl)aniline.

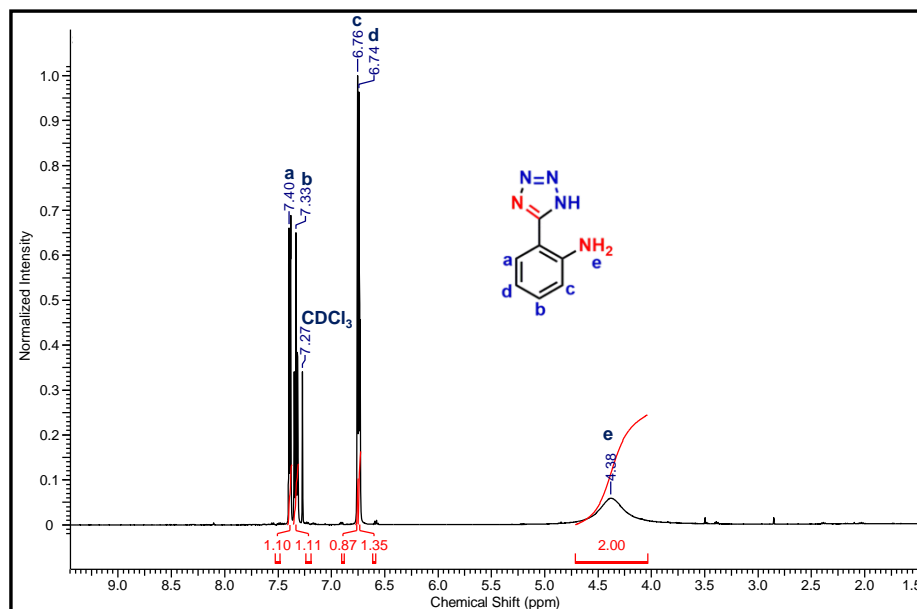
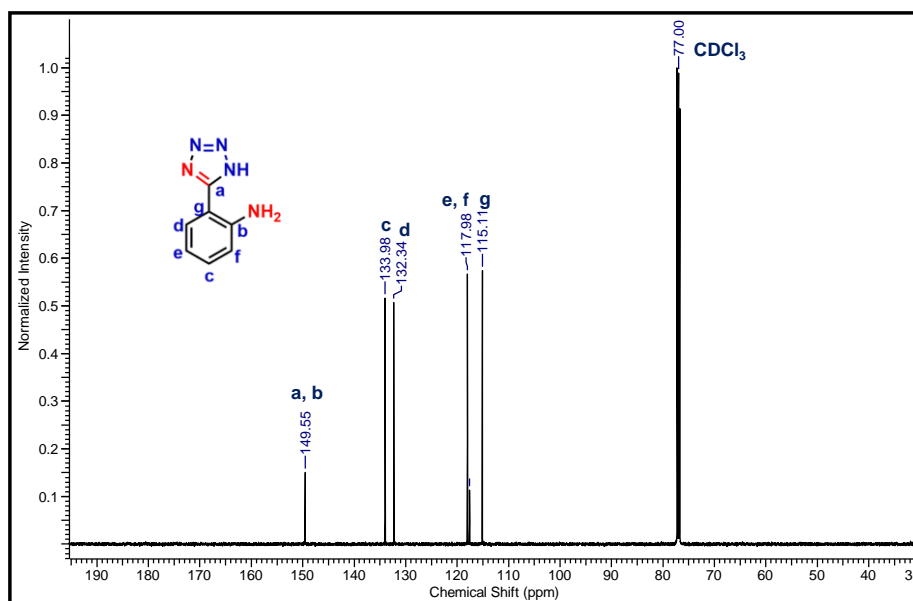
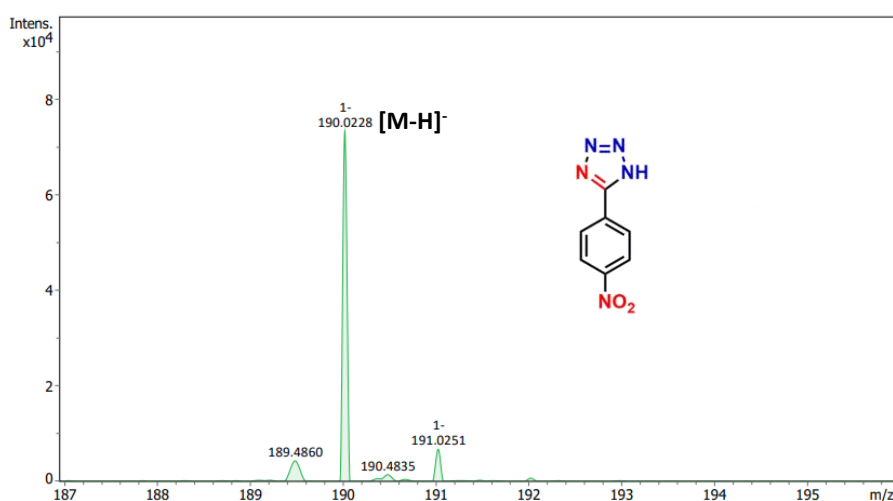


Figure 4.19.  $^1\text{H}$  NMR data of 2-(1H-tetrazol-5-yl)aniline.



**Figure 4.20.**  $^{13}\text{C}$  NMR data of 2-(1H-tetrazol-5-yl)aniline.

**Synthesis of 5-(4-nitrophenyl)-1H-tetrazole:** Product: yield: 73 %. ESI-MS:  $m/z$   $[\text{M-H}]^-$  calculated for  $\text{C}_7\text{H}_4\text{N}_5\text{O}_2^-$ : 190.04, found 190.02 (Figure 4.21). FTIR:  $2914\text{ cm}^{-1}$ ,  $2850\text{ cm}^{-1}$ ,  $1604\text{ cm}^{-1}$ ,  $1506\text{ cm}^{-1}$ ,  $1291\text{ cm}^{-1}$ ,  $1095\text{ cm}^{-1}$ ,  $831\text{ cm}^{-1}$  and  $615\text{ cm}^{-1}$  (Figure 4.22).  $^1\text{H}$  NMR (500 MHz,  $\text{DMSO-}d_6$ )  $\delta$  ppm 7.64 (2H, d) and 7.12 (2H, d) for aromatic protons (Figure 4.23).  $^{13}\text{C}$  NMR (126 MHz,  $\text{DMSO-}d_6$ )  $\delta$  ppm 162.74 (1C), 144.92 (1C), 133.83 (1C), 128.09 (2C) and 124.30 (2C) (Figure 4.24).



**Figure 4.21.** ESI-MS data of 5-(4-nitrophenyl)-1H-tetrazole in negative mode.

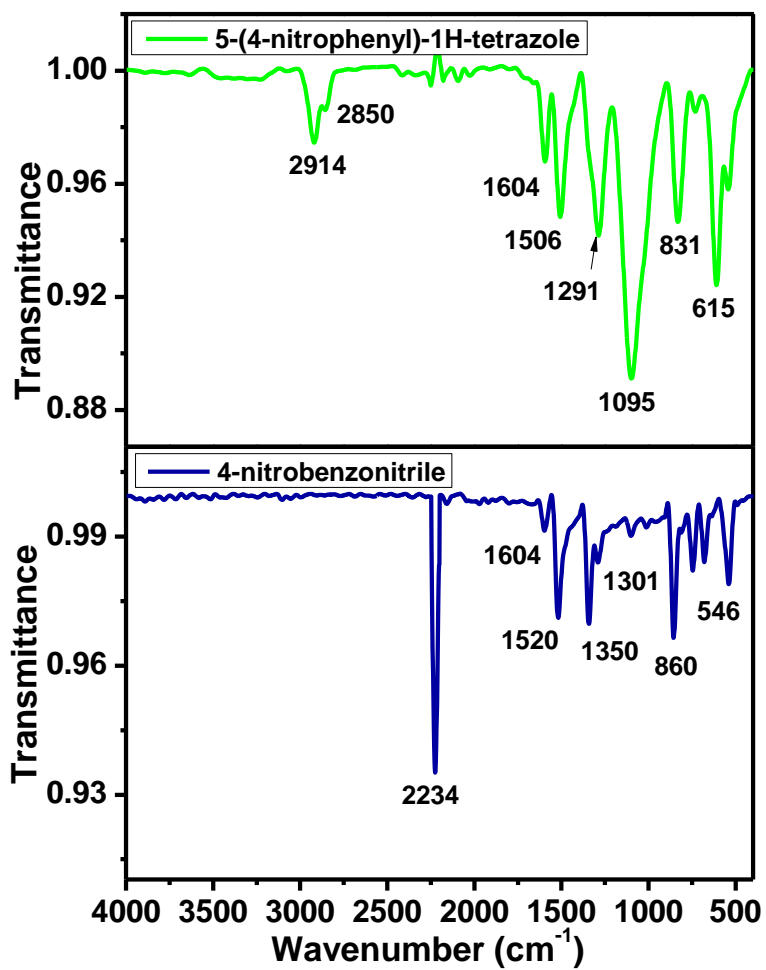


Figure 4.22. FTIR data of 4-nitrobenzonitrile and 5-(4-nitrophenyl)-1H-tetrazole.

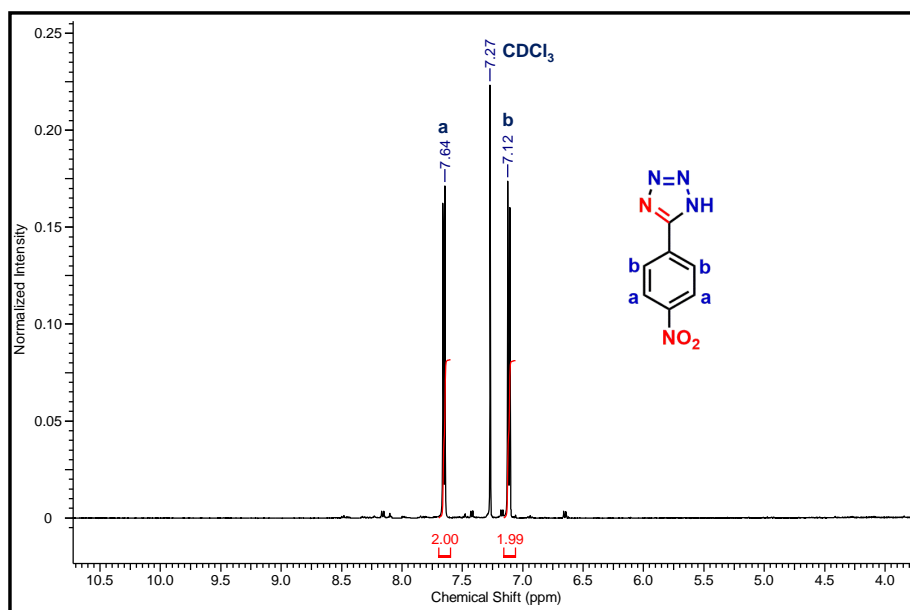
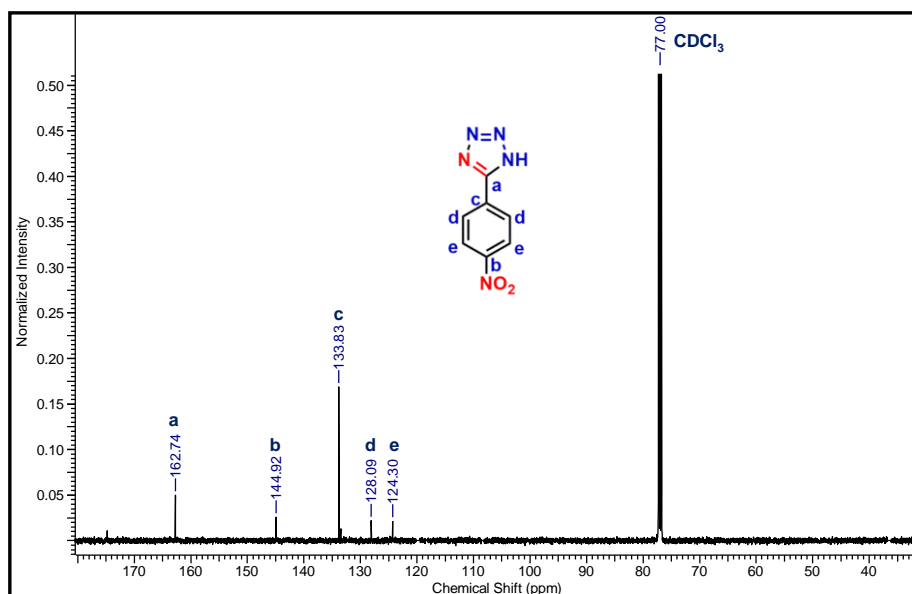


Figure 4.23. <sup>1</sup>H NMR data of 5-(4-nitrophenyl)-1H-tetrazole.



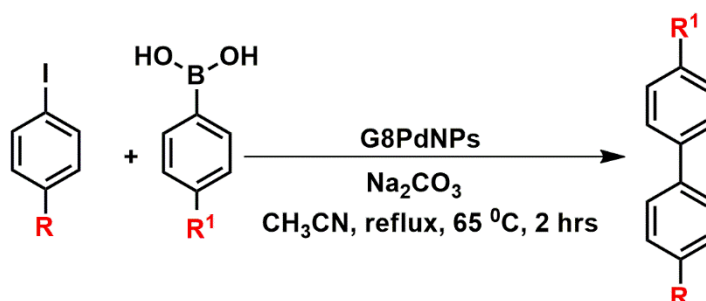
**Figure 4.24.**  $^{13}\text{C}$  NMR data of 5-(4-nitrophenyl)-1H-tetrazole.

Several methods and catalysts containing different metal ions/nanoparticles of Pd, Cu, Fe, etc., have been reported to form tetrazoles. However, using gel or xerogel as a catalyst for tetrazole formation is rare. Nanocomposite materials, MOFs, and dual metal systems are known to catalyze tetrazole formation. Table 4.1 presents some of the reports,<sup>[49-53]</sup> where tetrazole formation of nitrile substituent (nitrobenzene) is taken up by previously reported catalysts along with the xerogel catalyst **G8PdCl<sub>2</sub>** reported in this Chapter. The use of xerogel **G8PdCl<sub>2</sub>** as a heterogenous catalyst with significant yields presents the gel as a promising material for tetrazole formation by an easy and convenient method.

**Table 4.1.** Activity of different reported catalyst and synthesized catalyst **G8PdCl<sub>2</sub>** for tetrazole formation.

Entry	Catalyst used for tetrazole formation from benzonitrile	Amount of catalyst	Temperature (°C)	Solvent	Time (h)	Yield (%)	Ref.
1	Pd-isatin@boehmite	35 mg	120	PEG-400	7	96	49
2	Fe <sub>3</sub> O <sub>4</sub> -CNT-SO <sub>3</sub> H	20 mg	80	Solvent free	2.5	90	50
3	Fe <sub>3</sub> O <sub>4</sub> @silica sulfonic acid	20 mg	100	Solvent free	50	97	51
4	Cu-MOFs-1(Cu-TMU-1-NH <sub>2</sub> )	50 mg	110	PEG	5	94	52
5	ZnO/ Co <sub>3</sub> O <sub>4</sub>	50 mg	120	DMF	12	90	53
6	G8PdCl <sub>2</sub> Xerogel	20 mg	120	DMF	6	99	This work

**4.2.6 General method of Suzuki-Miyaura coupling reaction:** The following optimization has been done to follow the Suzuki-Miyaura coupling reaction. For this reaction, substituents of iodobenzene (0.5 mmol), phenylboronic acid (1 mmol), sodium carbonate (1.5 mmol), and **G8PdNPs** nanocomposite powder as a catalyst have been taken in 15 mL acetonitrile (MeCN) and the reaction mixture was reflux at 65° C for 2 hours in nitrogenous environment (Scheme 4.4). After two hours, the solvent was removed by a rotatory evaporator, and the mixture was extracted with 30 mL ethyl acetate and 30 mL water mixture (two times). The organic layer was evaporated, and the product was treated with hexane to obtain pure product. The product has been characterized by FTIR and NMR spectroscopy.



**Scheme 4.4.** Suzuki-Miyaura coupling reaction catalyzed by nanocomposite catalyst xerogel **G8PdNPs**.

**Optimization of C-C coupling reaction.** The solvent system has been changed for reaction with methanol, ethanol, acetonitrile, tetrahydrophenol, and dimethylformamide (Figure 4.25-4.34). It was found that the most suitable solvent for Suzuki-Miyaura coupling, when **G8PdNPs** are used as catalyst, is acetonitrile.

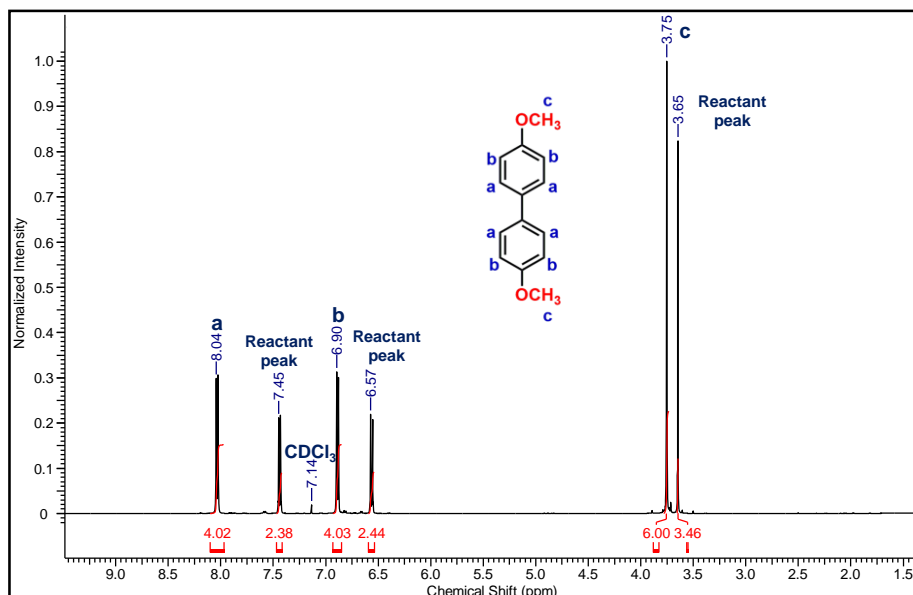


**Figure 4.25.**  $^1\text{H}$  NMR data of 4,4'-dimethoxy-1,1'-biphenyl when reaction done in methanol.

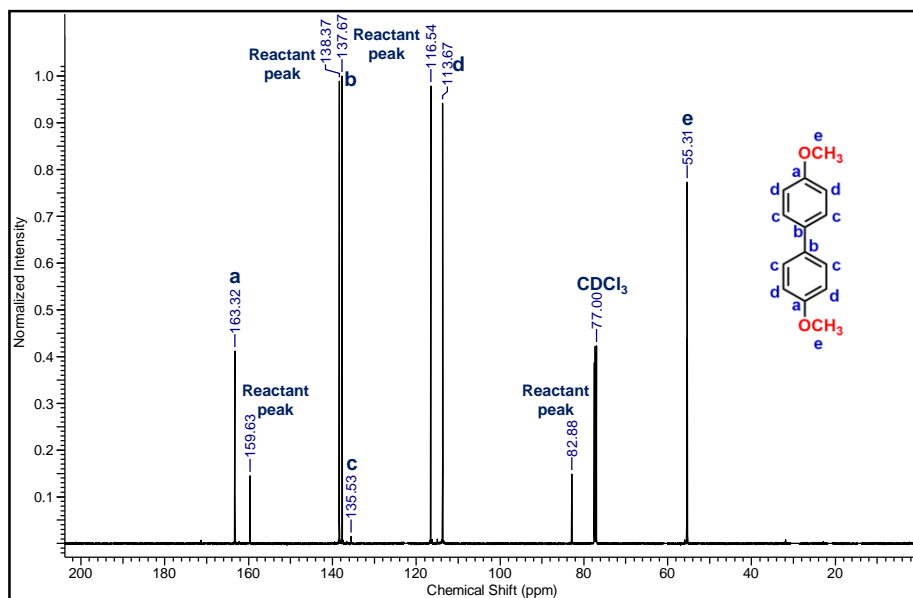


**Figure 4.26.**  $^{13}\text{C}$  NMR data of 4,4'-dimethoxy-1,1'-biphenyl when reaction done in methanol.

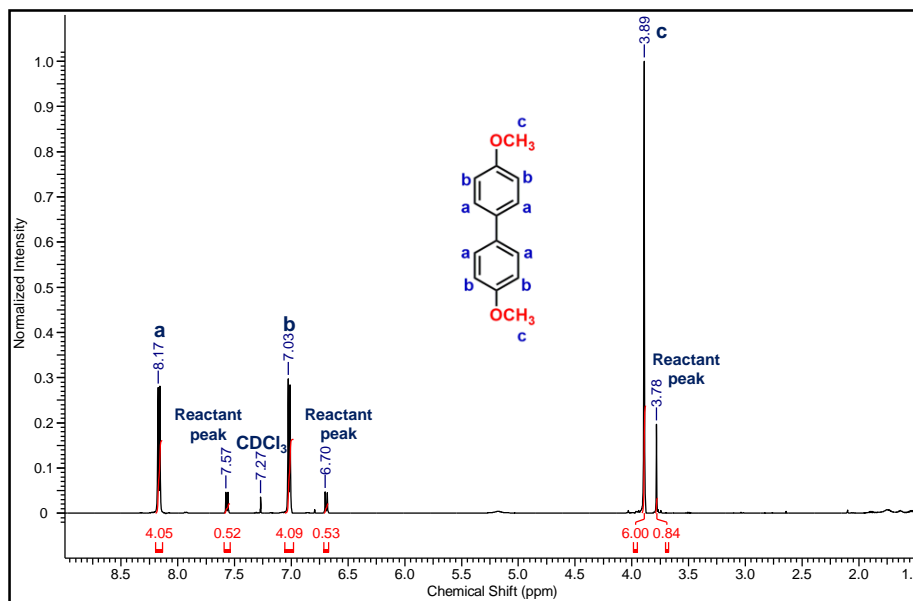


**Figure 4.27.**  $^1\text{H}$  NMR data of 4,4'-dimethoxy-1,1'-biphenyl when reaction done in DMF.

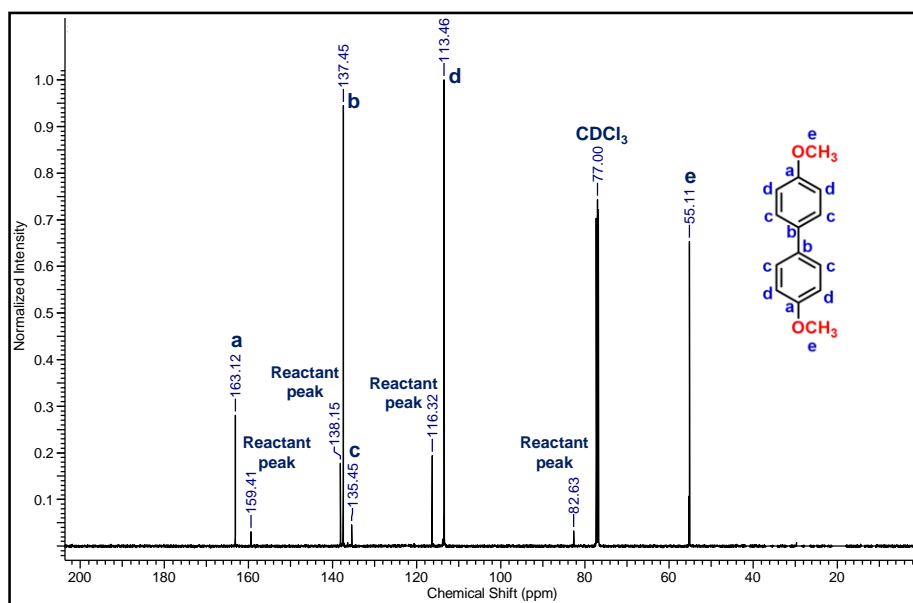


**Figure 4.28.**  $^{13}\text{C}$  NMR data of 4,4'-dimethoxy-1,1'-biphenyl when reaction done in DMF.

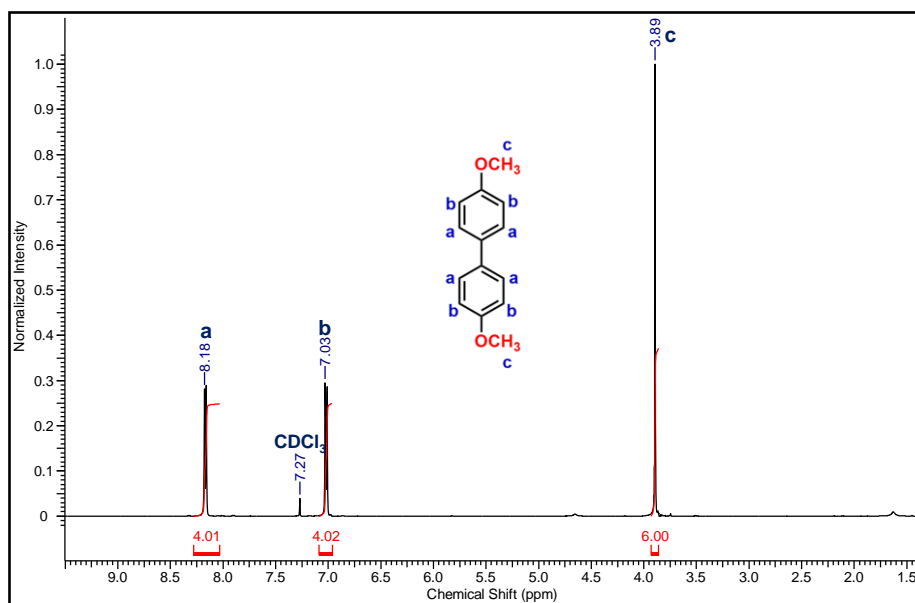


**Figure 4.29.**  $^1\text{H}$  NMR data of 4,4'-dimethoxy-1,1'-biphenyl when reaction done in acetonitrile.

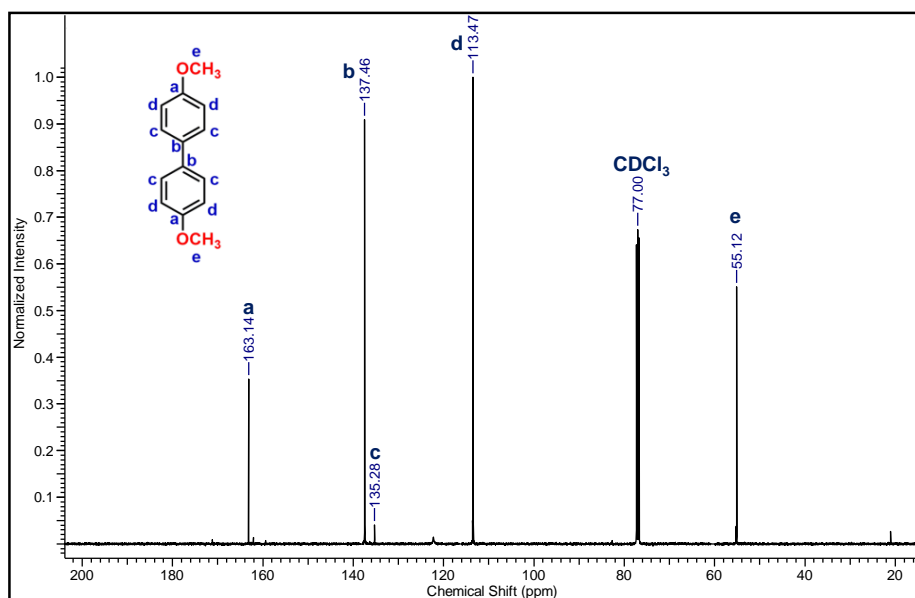


**Figure 4.30.**  $^{13}\text{C}$  NMR data of 4,4'-dimethoxy-1,1'-biphenyl when reaction done in acetonitrile.

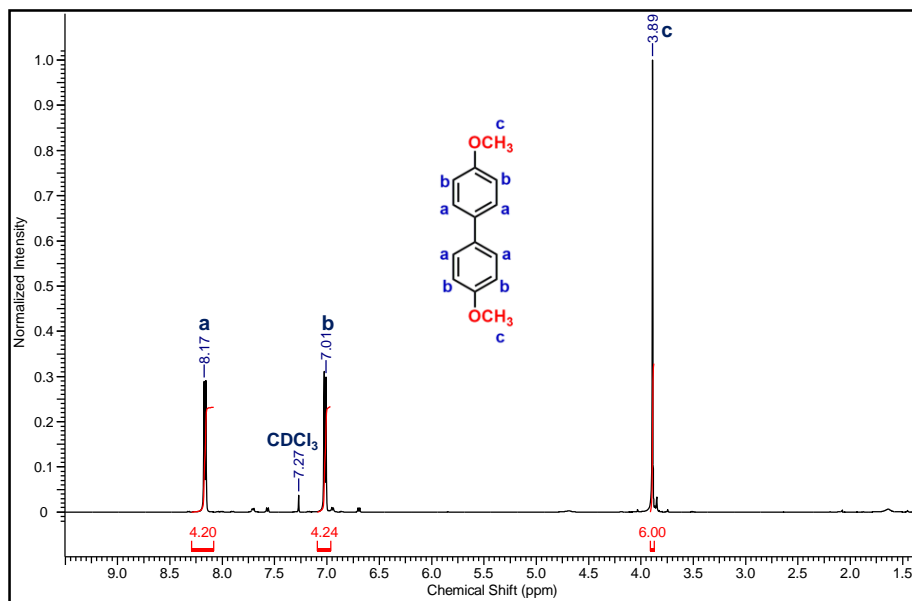


**Figure 4.31.**  $^1\text{H}$  NMR data of 4,4'-dimethoxy-1,1'-biphenyl when reaction done in ethanol.

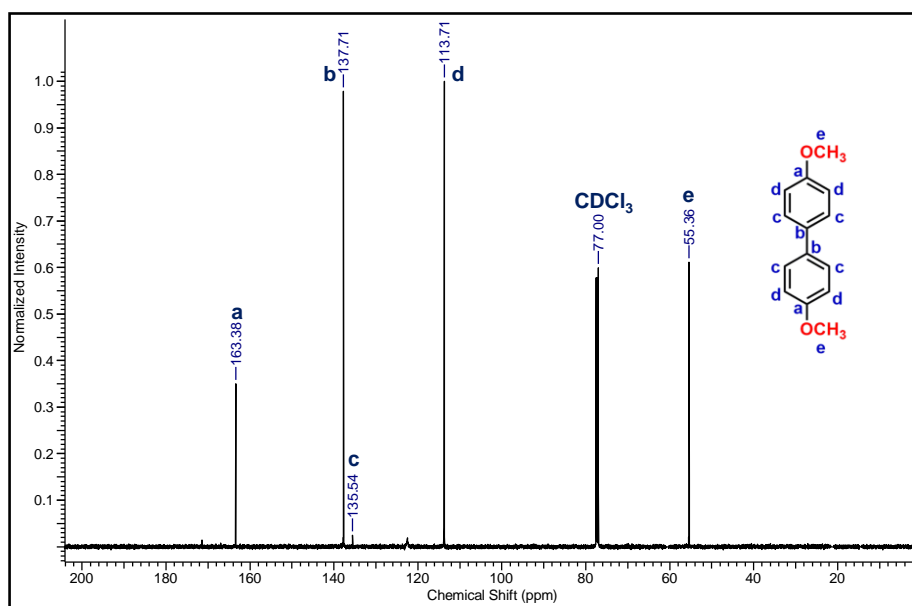


**Figure 4.32.**  $^{13}\text{C}$  NMR data of 4,4'-dimethoxy-1,1'-biphenyl when reaction done in ethanol.

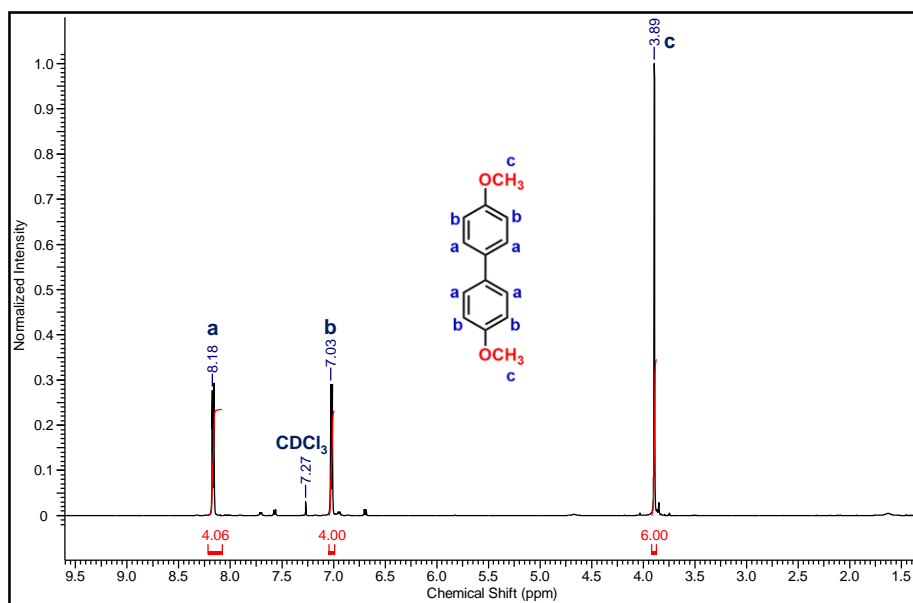


Figure 4.33.  $^1\text{H}$  NMR data of 4,4'-dimethoxy-1,1'-biphenyl when reaction done in tetrahydrofuran.

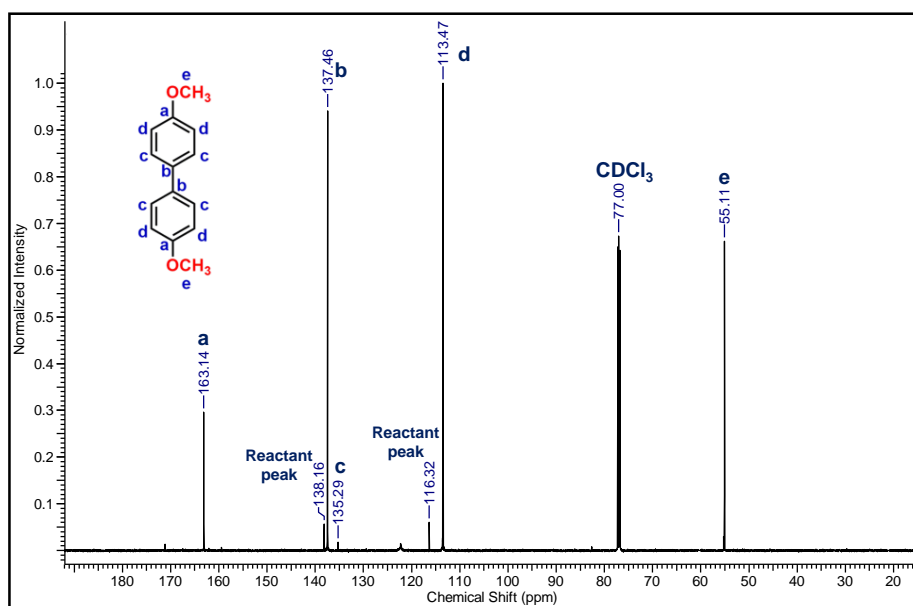
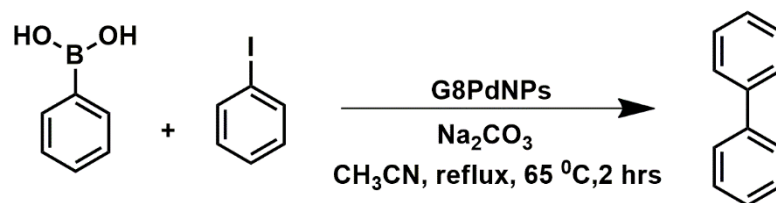


Figure 4.34.  $^{13}\text{C}$  NMR data of 4,4'-dimethoxy-1,1'-biphenyl when reaction done in tetrahydrofuran.

### Synthesis of 1,1'-biphenyl:

The synthesis of 1,1'-biphenyl (Scheme 4.5) has been done as mentioned above in “General method of Suzuki-Miyaura coupling reaction”.



**Scheme 4.5.** Suzuki-Miyaura coupling for synthesis of 1,1'-biphenyl.

The synthesis of coupling product has been confirmed by FTIR and NMR spectroscopy. The diminished FTIR band of aromatic iodo group at  $445\text{ cm}^{-1}$  in product from  $445\text{ cm}^{-1}$  shows C-C coupling product formation. Product: isolated yield: 60 %. FTIR:  $1606\text{ cm}^{-1}$ ,  $1450\text{ cm}^{-1}$ ,  $1332\text{ cm}^{-1}$ ,  $690\text{ cm}^{-1}$  and  $573\text{ cm}^{-1}$  (Figure 4.35).  $^1\text{H}$  NMR (500 MHz,  $\text{DMSO-}d_6$ )  $\delta$  ppm 8.28-8.26 (4H, d), 7.63 (2H, m) and 7.54 (4H, m) for aromatic protons (Figure 4.36).  $^{13}\text{C}$  NMR (126 MHz,  $\text{DMSO-}d_6$ )  $\delta$  ppm 135.68 (2C), 132.73 (4C) and 128.02 (6C) (Figure 4.37). ESI-MS:  $m/z$   $[\text{M}+\text{H}]^+$  calculated for  $\text{C}_{12}\text{H}_{11}^+$ : 155.08, found 155.14.

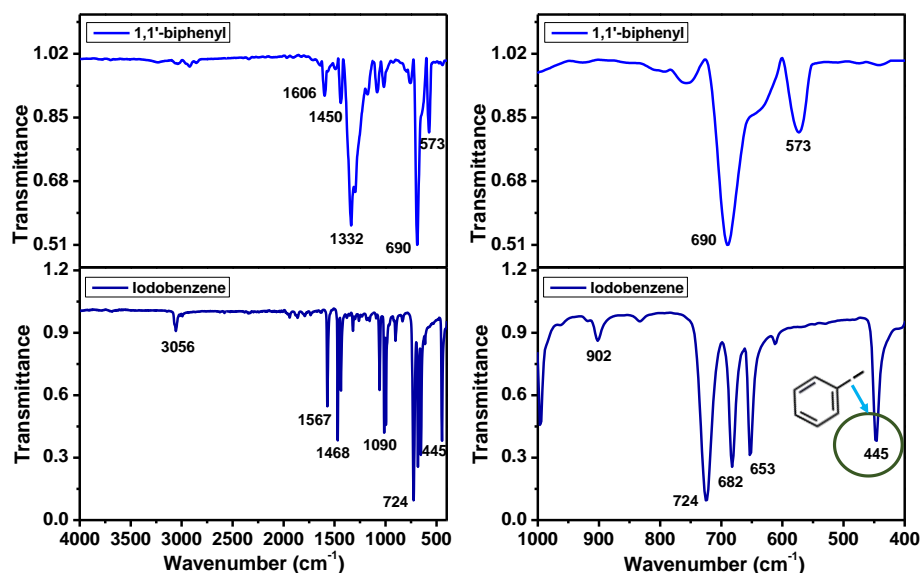


**Figure 4.35.** FTIR analysis of formation of 1,1'-biphenyl from iodobenzene and phenylboronic acid.

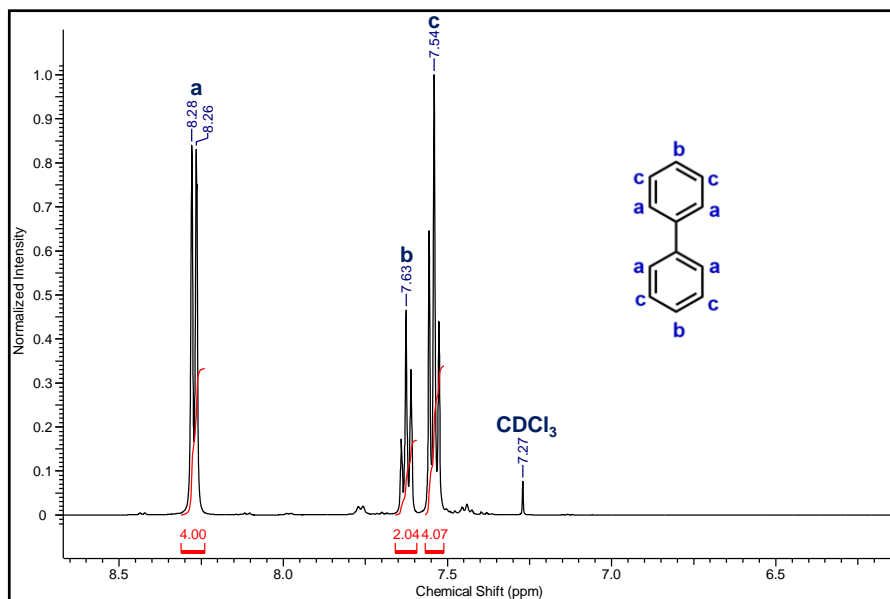


Figure 4.36.  $^1\text{H}$  NMR analysis of 1,1'-biphenyl.

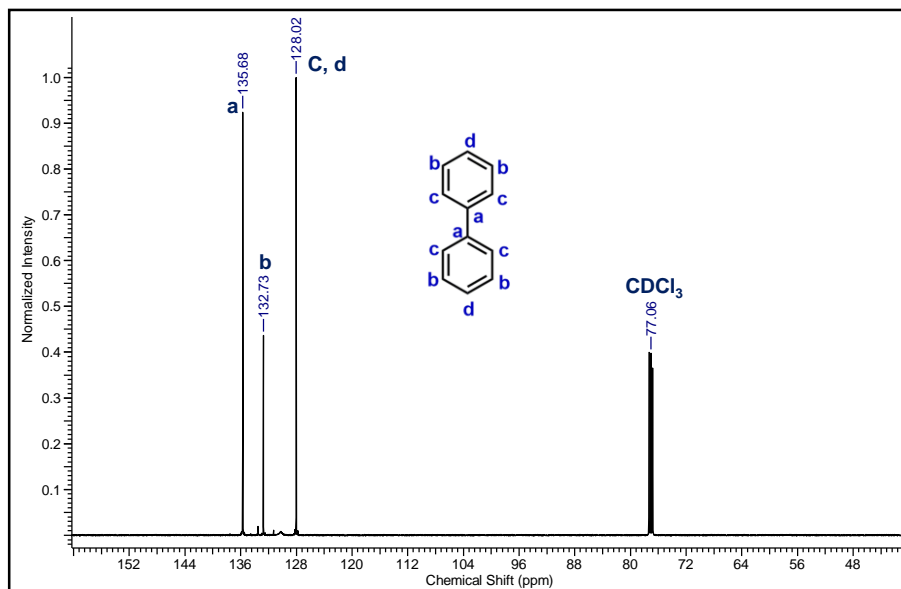
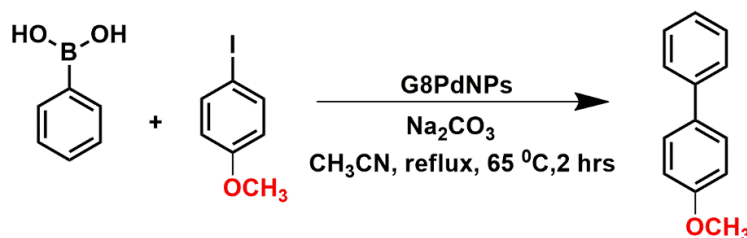


Figure 4.37.  $^{13}\text{C}$  NMR analysis of 1,1'-biphenyl.

### Synthesis of 4-methoxy-1,1'-biphenyl:

The synthesis of 4-methoxy-1,1'-biphenyl (Scheme 4.6) has been done as mentioned above in “General method of Suzuki-Miyaura coupling reaction”.



**Scheme 4.6.** Suzuki-Miyaura coupling for synthesis of 4-methoxy-1,1'-biphenyl.

Product: isolated yield: 85 %. FTIR: 2928  $\text{cm}^{-1}$ , 1586  $\text{cm}^{-1}$ , 1439  $\text{cm}^{-1}$ , 1332  $\text{cm}^{-1}$ , 1029  $\text{cm}^{-1}$ , 690  $\text{cm}^{-1}$  and 569  $\text{cm}^{-1}$  (Figure 4.38).  $^1\text{H}$  NMR (500 MHz,  $\text{DMSO-}d_6$ )  $\delta$  ppm 8.28 (2H, d), 7.62 (1H, m), 7.57 (2H, d), 7.54 (2H, m), 6.71 (2H, d) for aromatic protons and 3.79 (3H, s) for methoxy proton (Figure 4.39).  $^{13}\text{C}$  NMR (126 MHz,  $\text{DMSO-}d_6$ )  $\delta$  ppm 159.42 (1C), 138.17 (1C), 135.62 (1C), 132.67 (4C), 127.96 (3C), 116.33 (2C) and 55.27 (1C) (Figure 4.40). ESI-MS:  $m/z$   $[\text{M}+\text{H}]^+$  calculated for  $\text{C}_{13}\text{H}_{13}\text{O}^+$ : 185.09, found 185.12.

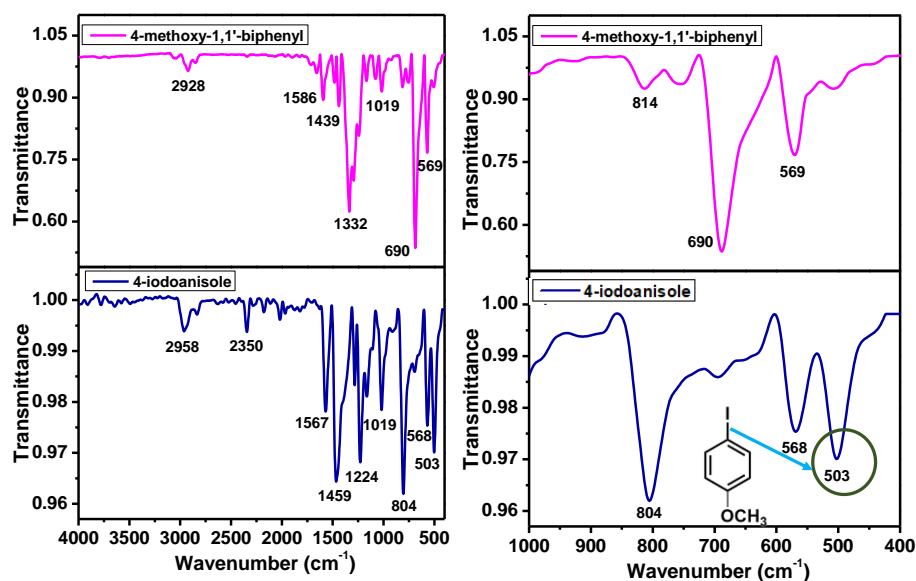


**Figure 4.38.** FTIR analysis of formation of 4-methoxy-1,1'-biphenyl from 1-iodo-4-methoxybenzene and phenylboronic acid.

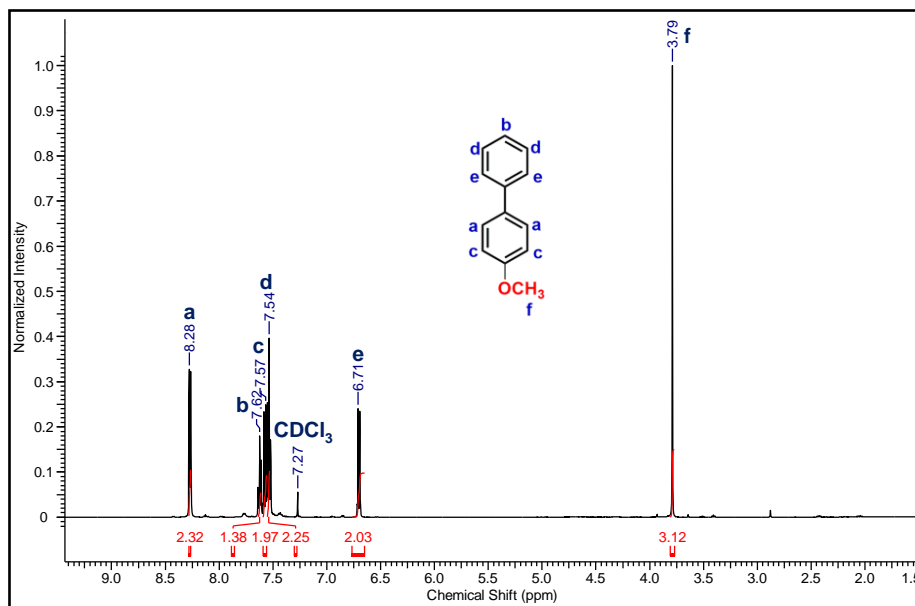


Figure 4.39.  $^1\text{H}$  NMR analysis of 4-methoxy-1,1'-biphenyl.

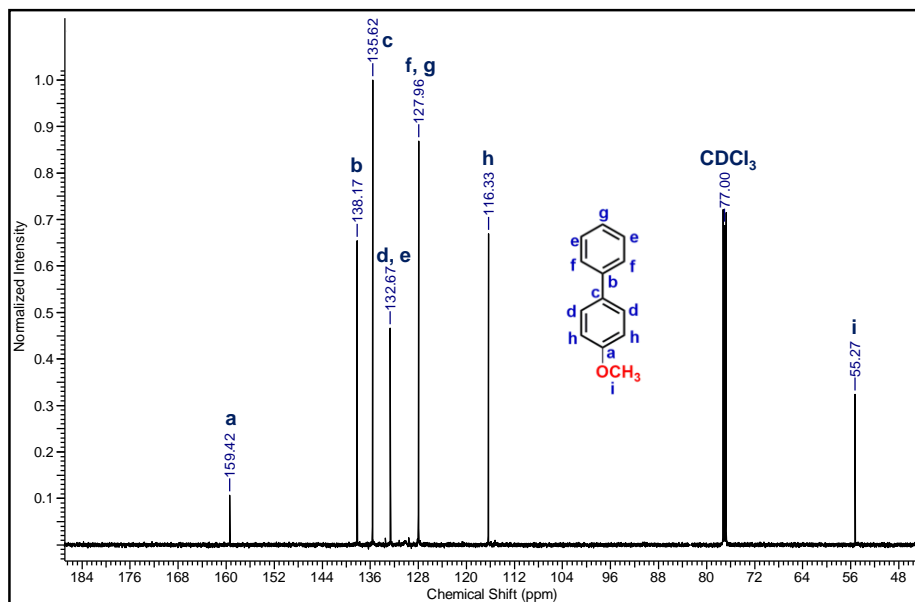
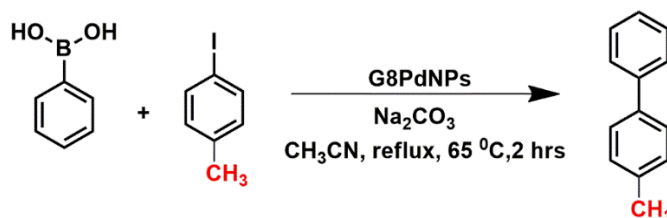


Figure 4.40.  $^{13}\text{C}$  NMR analysis of 4-methoxy-1,1'-biphenyl.

### Synthesis of 4-methyl-1,1'-biphenyl:

The synthesis of 4-methyl-1,1'-biphenyl (Scheme 4.7) has been done as mentioned above in “General method of Suzuki-Miyaura coupling reaction”.



**Scheme 4.7.** Suzuki-Miyaura coupling for synthesis of 4-methyl-1,1'-biphenyl.

Product: isolated yield: 75 %. FTIR: 1596  $\text{cm}^{-1}$ , 1439  $\text{cm}^{-1}$ , 1332  $\text{cm}^{-1}$ , 1019  $\text{cm}^{-1}$ , 799  $\text{cm}^{-1}$ , 690  $\text{cm}^{-1}$  and 573  $\text{cm}^{-1}$  (Figure 4.41).  $^1\text{H}$  NMR (500 MHz,  $\text{DMSO-}d_6$ )  $\delta$  ppm 8.28 (4H, d, m), 7.62 (1H, m), 7.53 (4H, d, d) for aromatic protons and 2.31 (3H, s) for methyl proton (Figure 4.42).  $^{13}\text{C}$  NMR (126 MHz,  $\text{DMSO-}d_6$ )  $\delta$  ppm 137.44 (1C), 137.21 (1C), 135.63 (1C), 132.70 (2C), 132.68 (2C), 131.17 (2C), 127.97 (3C) and 20.99 (1C) (Figure 4.43). ESI-MS:  $m/z$   $[\text{M}+\text{Na}]^+$  calculated for  $\text{C}_{13}\text{H}_{12}\text{Na}^+$ : 191.08, found 191.09.

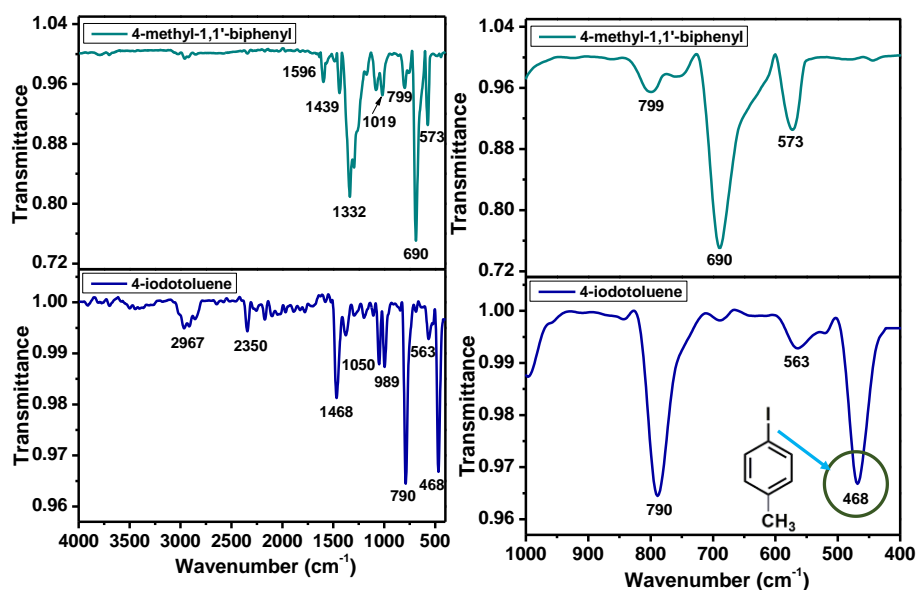


**Figure 4.41.** FTIR analysis of formation of 4-methyl-1,1'-biphenyl from 4-iodotoluene and phenylboronic acid.

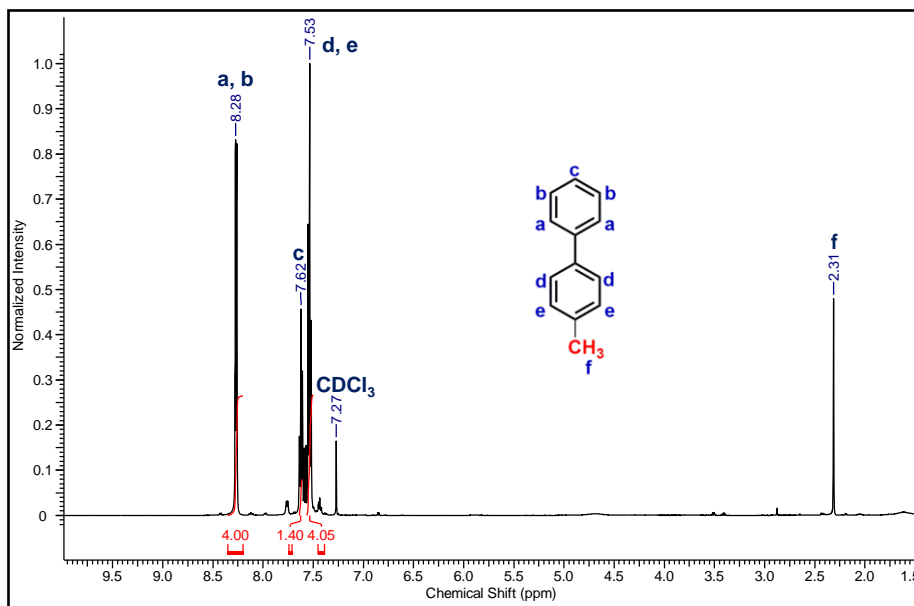


Figure 4.42.  $^1\text{H}$  NMR analysis of 4-methyl-1,1'-biphenyl.

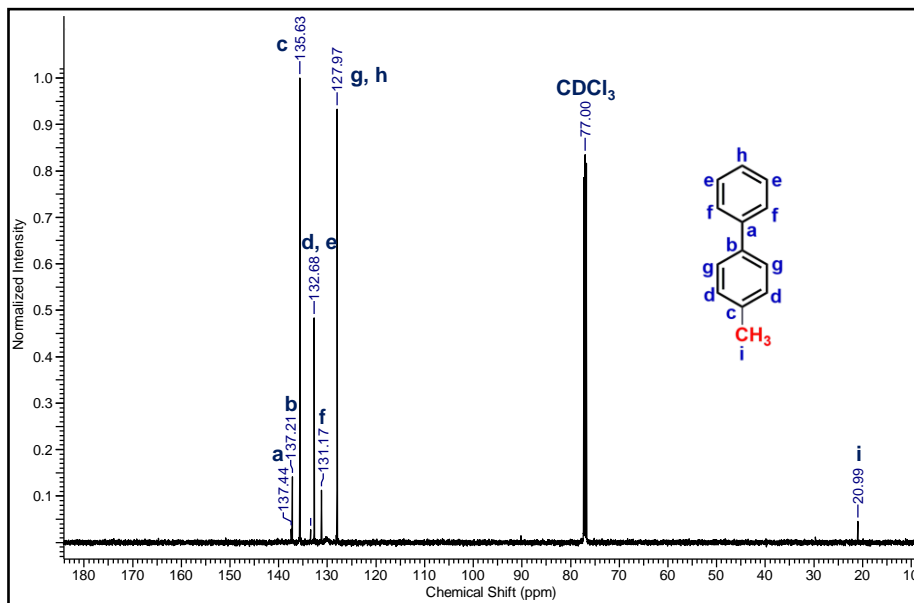
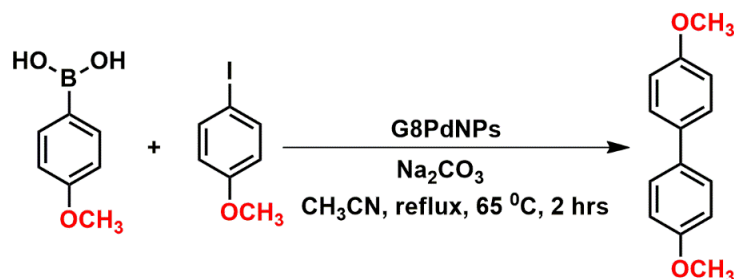


Figure 4.43.  $^{13}\text{C}$  NMR analysis of 4-methyl-1,1'-biphenyl.

### Synthesis of 4,4'-dimethoxy-1,1'-biphenyl:

The synthesis of 4,4'-dimethoxy-1,1'-biphenyl (Scheme 4.8) has been done as mentioned above in “General method of Suzuki-Miyaura coupling reaction”.



**Scheme 4.8.** Suzuki-Miyaura coupling for synthesis of 4,4'-dimethoxy-1,1'-biphenyl.

Product: isolated yield: 88 %. FTIR: 1596  $\text{cm}^{-1}$ , 1332  $\text{cm}^{-1}$ , 1234  $\text{cm}^{-1}$ , 1155  $\text{cm}^{-1}$ , 1019  $\text{cm}^{-1}$ , 685  $\text{cm}^{-1}$  and 544  $\text{cm}^{-1}$  (Figure 4.44).  $^1\text{H}$  NMR (500 MHz, DMSO- $d_6$ )  $\delta$  ppm 8.18 (4H, d), 7.03 (4H, d) for aromatic protons and 3.89 (6H, s) for methoxy proton (Figure 4.45).  $^{13}\text{C}$  NMR (126 MHz, DMSO- $d_6$ )  $\delta$  ppm 163.14 (2C), 137.46 (2C), 135.28 (4C), 113.47 (4C) and 55.12 (2C) (Figure 4.46). ESI-MS:  $m/z$   $[\text{M}+\text{H}]^+$  calculated for  $\text{C}_{14}\text{H}_{15}\text{O}_2^+$ : 215.11, found 215.12.

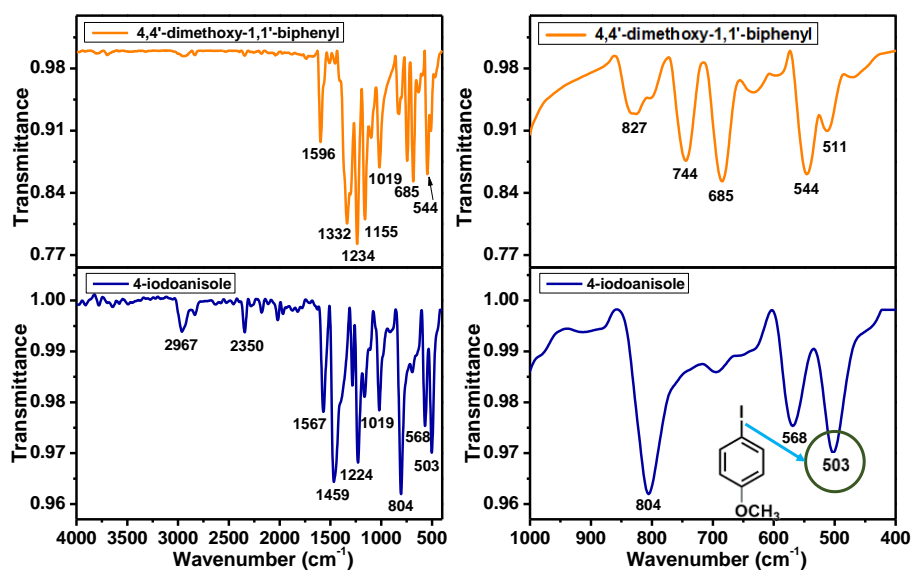


**Figure 4.44.** FTIR analysis of formation of 4,4'-dimethoxy-1,1'-biphenyl from 1-iodo-4-methoxybenzene and (4-methoxyphenyl) boronic acid.

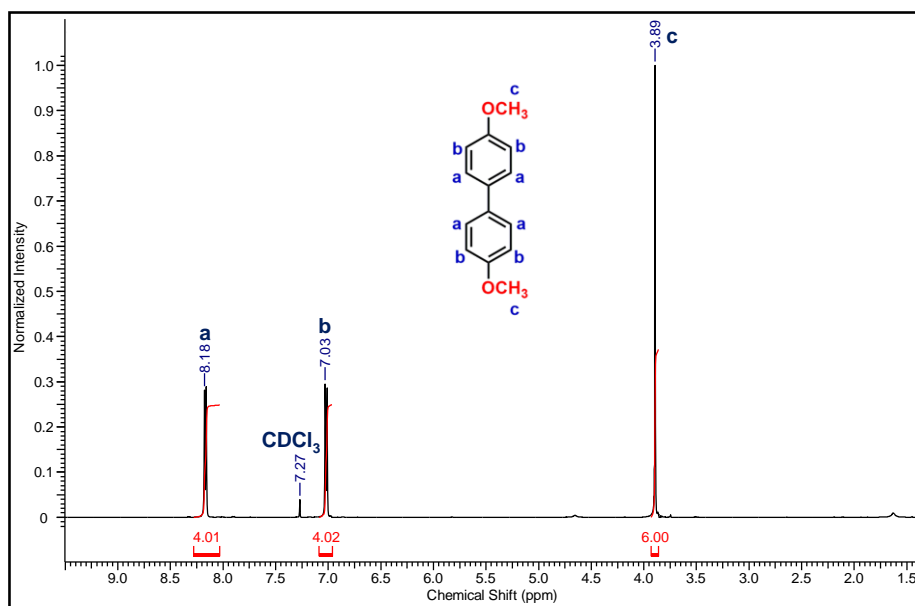


Figure 4.45.  $^1\text{H}$  NMR analysis of 4,4'-dimethoxy-1,1'-biphenyl.

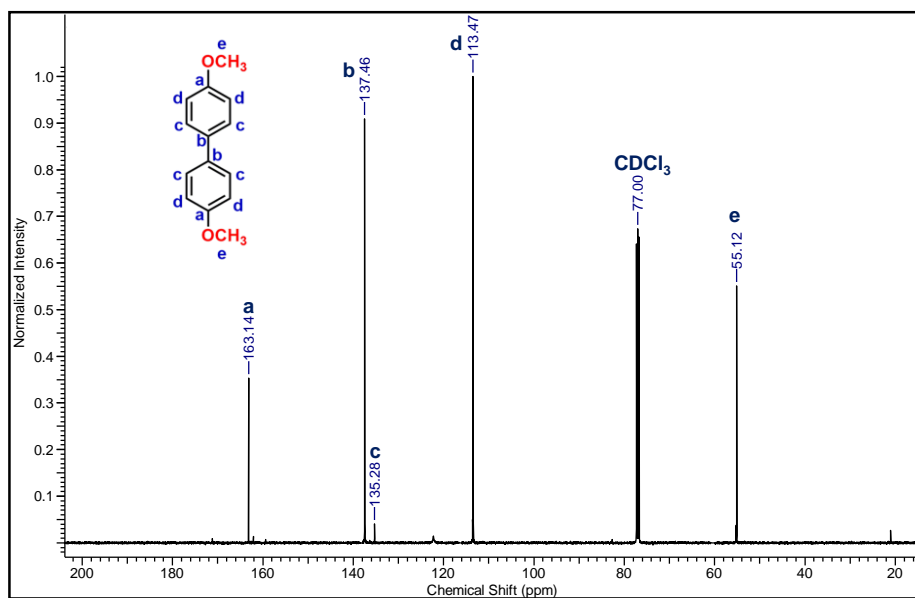
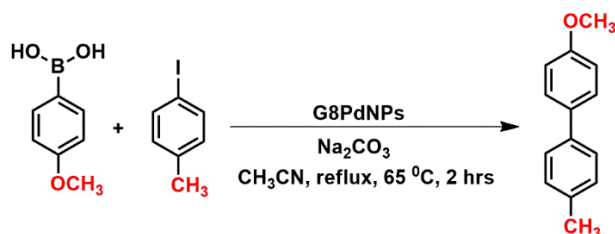


Figure 4.46.  $^{13}\text{C}$  NMR analysis of 4,4'-dimethoxy-1,1'-biphenyl.

### Synthesis of 4-methoxy-4'-methyl-1,1'-biphenyl:

The synthesis of 4-methoxy-4'-methyl-1,1'-biphenyl (Scheme 4.9) has been done as mentioned above in “General method of Suzuki-Miyaura coupling reaction”.



**Scheme 4.9.** Suzuki-Miyaura coupling for synthesis of 4-methoxy-4'-methyl-1,1'-biphenyl.

Product: isolated yield: 75 %. FTIR: 2918  $\text{cm}^{-1}$ , 1596  $\text{cm}^{-1}$ , 1332  $\text{cm}^{-1}$ , 1234  $\text{cm}^{-1}$ , 1155  $\text{cm}^{-1}$ , 1019  $\text{cm}^{-1}$ , 741  $\text{cm}^{-1}$ , 679  $\text{cm}^{-1}$  and 542  $\text{cm}^{-1}$  (Figure 4.47).  $^1\text{H}$  NMR (500 MHz,  $\text{DMSO}-d_6$ )  $\delta$  ppm 8.18 (2H, d), 7.59 (2H, d), 7.03 (2H, d), 6.95 (2H, d) for aromatic protons and 3.89 (3H, s), 2.31 (3H, s) for methoxy and methyl proton respectively (Figure 4.48).  $^{13}\text{C}$  NMR (126 MHz,  $\text{DMSO}-d_6$ )  $\delta$  ppm 163.12 (1C), 137.46 (1C), 137.19 (1C), 135.30 (1C), 131.16 (4C), 122.26 (2C), 113.46 (2C), 55.11 (1C) and 20.97 (1C) (Figure 4.49). ESI-MS:  $m/z$   $[\text{M}+\text{Na}]^+$  calculated for  $\text{C}_{14}\text{H}_{14}\text{NaO}^+$ : 221.09, found 221.10.

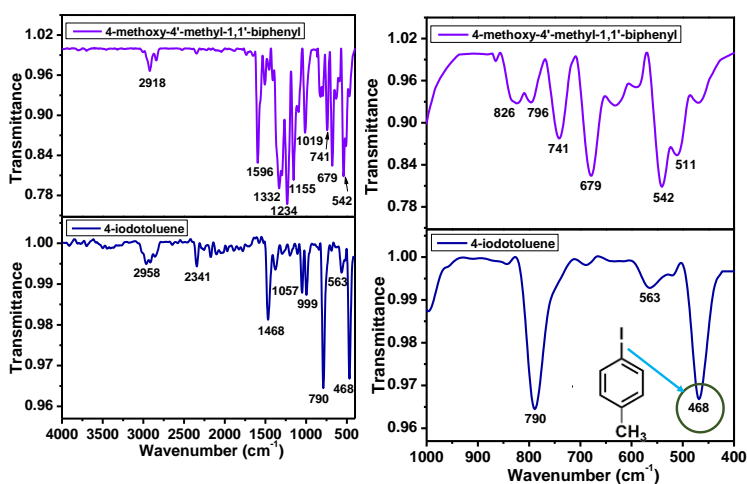


**Figure 4.47.** FTIR analysis of formation of 4-methoxy-4'-methyl-1,1'-biphenyl from 1-iodo-4-methylbenzene and (4-methoxyphenyl)boronic acid.

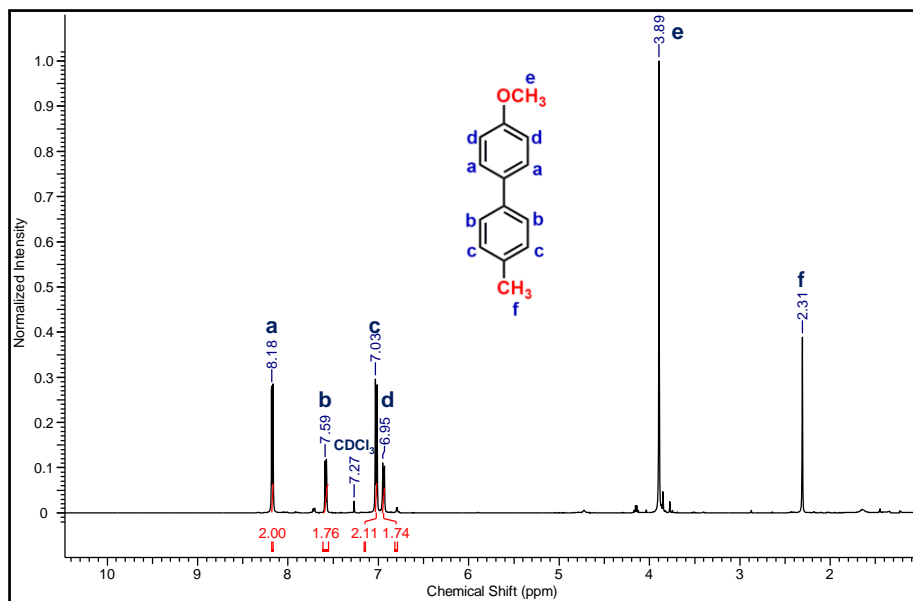


Figure 4.48.  $^1\text{H}$  NMR analysis of 4-methoxy-4'-methyl-1,1'-biphenyl.

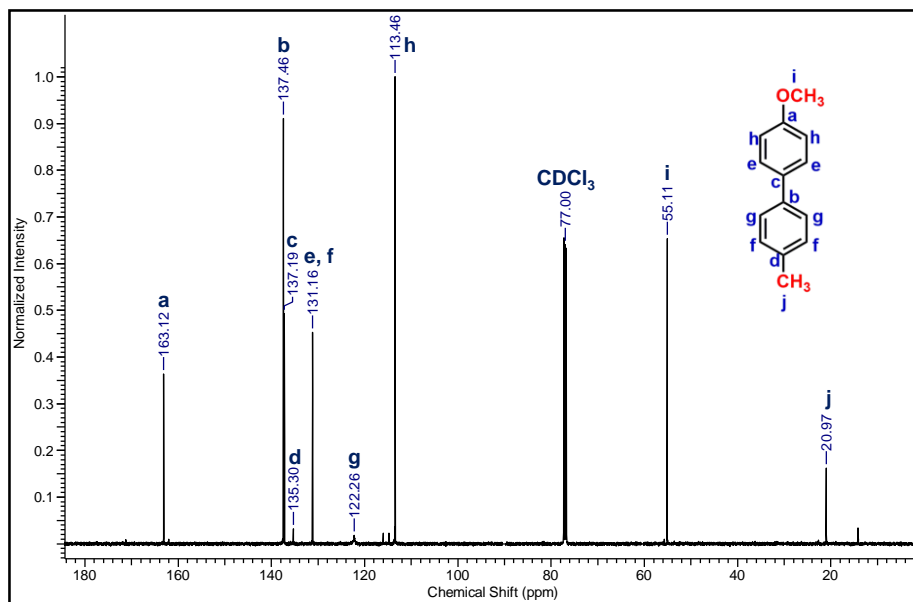
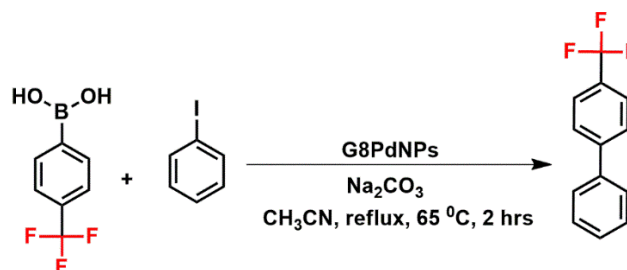


Figure 4.49.  $^{13}\text{C}$  NMR analysis of 4-methoxy-4'-methyl-1,1'-biphenyl.

### Synthesis of 4-(trifluoromethyl)-1,1'-biphenyl:

The synthesis of 4-(trifluoromethyl)-1,1'-biphenyl (Scheme 4.10) has been done as mentioned above in “General method of Suzuki-Miyaura coupling reaction”.



**Scheme 4.10.** Suzuki-Miyaura coupling for synthesis of 4-(trifluoromethyl)-1,1'-biphenyl.

Product: isolated yield: 75 %. FTIR: 3251 cm<sup>-1</sup>, 2350 cm<sup>-1</sup>, 1959 cm<sup>-1</sup>, 1322 cm<sup>-1</sup>, 1106 cm<sup>-1</sup>, 1008 cm<sup>-1</sup>, 630 cm<sup>-1</sup> and 553 cm<sup>-1</sup> (Figure 4.50). <sup>1</sup>H NMR (500 MHz, DMSO-*d*<sub>6</sub>) δ ppm 7.80 (4H, d), 7.72 (2H, d), 7.34 (1H, m) and 7.12 (2H, m) for aromatic protons (Figure 4.51). <sup>13</sup>C NMR (126 MHz, DMSO-*d*<sub>6</sub>) δ ppm 139.28 (1C), 135.77 (1C), 134.04 (1C), 127.11 (2C), 124.76 (2C), 124.56 (2C), 122.93 (1C), 115.48 (2C) and 114.05 (1C) (Figure 4.52). ESI-MS: m/z [M+H]<sup>+</sup> calculated for C<sub>13</sub>H<sub>10</sub>F<sub>3</sub><sup>+</sup>: 223.07, found 223.09.

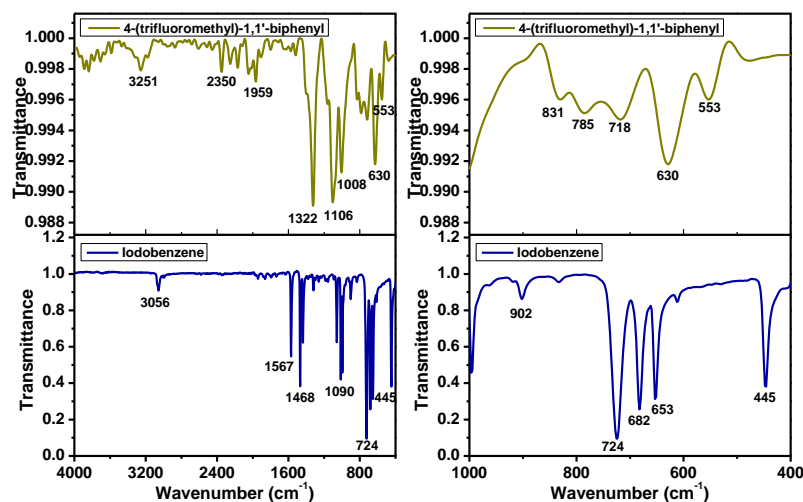


**Figure 4.50.** FTIR analysis of formation of 4-(trifluoromethyl)-1,1'-biphenyl from iodobenzene and 4-(trifluoromethyl)phenylboronic acid.

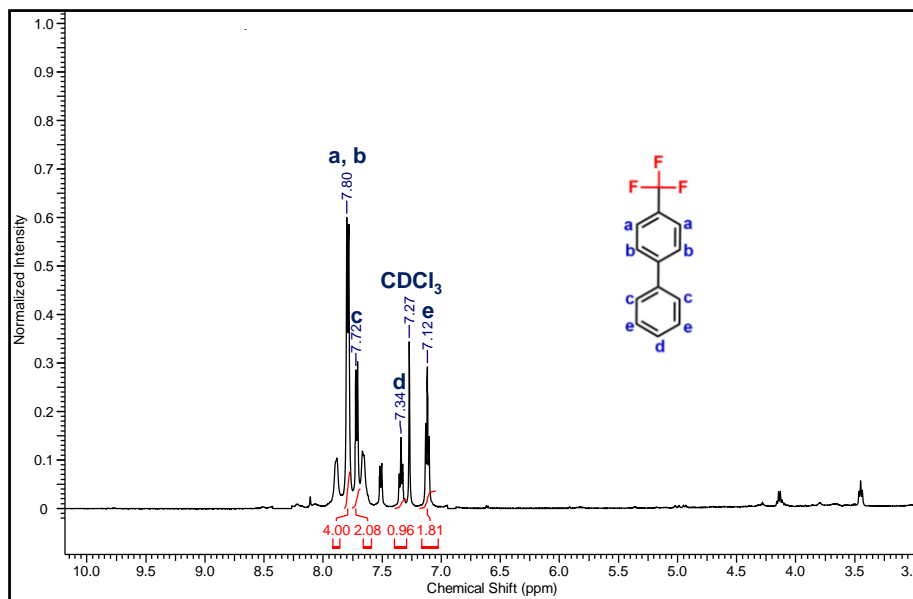


**Figure 4.51.**  $^1\text{H}$  NMR analysis of 4-(trifluoromethyl)-1,1'-biphenyl.

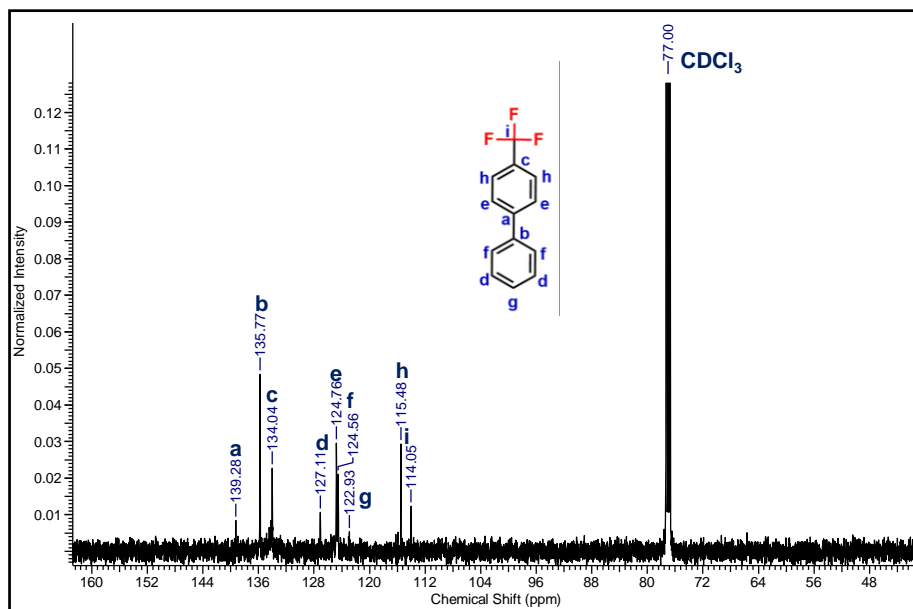


**Figure 4.52.**  $^{12}\text{C}$  NMR analysis of 4-(trifluoromethyl)-1,1'-biphenyl.

The synthesized nanocatalyst **G8PdNPs** act as an active heterogenous catalyst for Suzuki-Miyaura coupling reactions. Although some reported gels are there which has been used for coupling reactions, numbers are very few.<sup>[54-57]</sup> The synthesized catalyst has the tendency to provide good product yield (75-88 % for maximum products) with minimum reaction time. The activity of some notable gels and synthesized **G8PdNPs** gel as catalysts have been mentioned in Table 4.2.

**Table 4.2.** Activity of different reported gel catalyst and synthesized catalyst **G8PdNPs** for Suzuki-Miyaura coupling reaction.

Entry	Catalyst	Amount of catalyst	Base used	Temperature (°C)	Solvent	Time (h)	Yield (%)	Ref.
1	GP1-Pd gel	1 mmol %	Na <sub>2</sub> CO <sub>3</sub>	60	Methanol or Water	0.5-3.5	25-90	54
2	Pd/ L gel	1 mmol %	Na <sub>2</sub> CO <sub>3</sub>	60	Methanol	7	26-99	55
3	PMHS-Pd gel	20-40 mg/g gel beds	K <sub>2</sub> CO <sub>3</sub>	65-95	Ethanol: Water	0.5	40-60	56
4	Peptide 1 hybrid gel	1 mmol %	NaOH	RT	Water	3.5	81-96	57
6	<b>G8PdNPs Xerogel</b>	20 mg	Na <sub>2</sub> CO <sub>3</sub>	65	DMF	2	75-88	This work

### 4.3 Results and discussion

The gelator molecule **G8** contains many nitrogen and hydrogen sites for non-covalent interactions, primarily for hydrogen bond formation. Here, these sites are used for the stabilization of palladium nanoparticles. Many palladium-based catalysts are known to be active for many organic reactions, such as coupling reactions, tetrazole formation, and other catalytic reactions.<sup>[58]</sup> However, only a few reports are available where palladium-based metallogels are used for catalysis.<sup>[9]</sup> In this Chapter, **G8** is used to form two types of catalyst based on palladium ions and palladium nanoparticles, i.e., **G8PdCl<sub>2</sub>** and **G8PdNPs**, respectively (Figure 4.53). Both catalysts originated from the nanostructured metallogel of **G8** and **Pd**. The **G8PdCl<sub>2</sub>** xerogel was used as a catalyst for the 2+3 cycloaddition reaction of nitrile and azide to form tetrazole substituents. In contrast, **G8PdNPs** xerogel is used as a catalyst for Suzuki-Miyaura coupling reactions. The use of a single gelator system for the formation of two different catalysts for different reactions is most valuable for developing the future of soft materials as effective catalysts for various catalytic organic reactions.

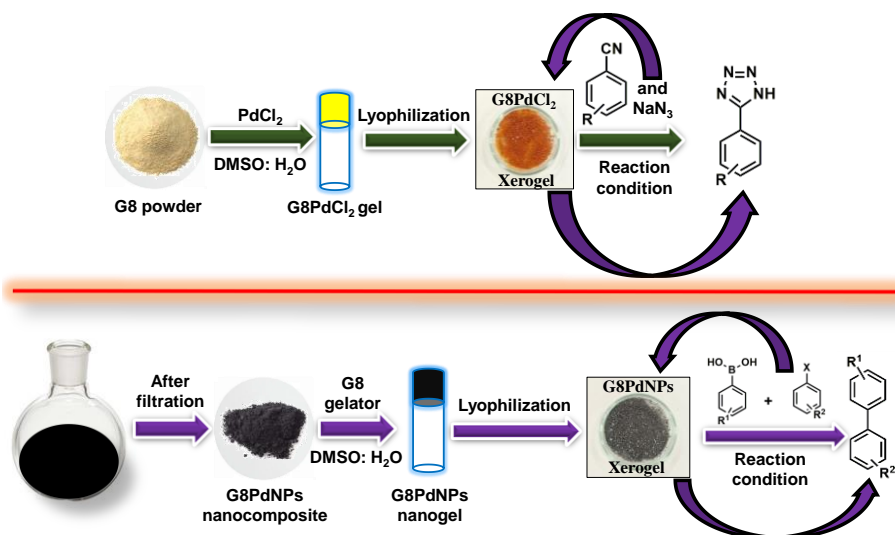


**Figure 4.53.** Use of **G8** for the formation of two type of catalyst i.e., used in two different types of reactions.

**Critical gel concentration (CGC) for metallogel PdCl<sub>2</sub> and G8PdNPs formation.** The nanostructured metallogels formation of **G8PdCl<sub>2</sub>** and **G8PdNPs** have been performed with different concentrations of **PdCl<sub>2</sub>** and **PdNPs** by taking a fixed concentration of **G8** and a fixed volume of solvents ratio of DMSO: H<sub>2</sub>O. The inverted vial method has been applied for each gel set and found the critical gel concentration (CGC) where the gel does not come down from the inverted vial. The experiments show that the CGC for **G8PdCl<sub>2</sub>** gel is 2.15 wt % (w/v), while an ideal condition of strong metallogel formation is 0.1 mmol (33 mg) of **G8** and 0.1 mmol (18 mg) of **PdCl<sub>2</sub>** in 2 mL of DMSO: H<sub>2</sub>O solvent mixture (1 mL each) (Table 4.3). Similarly, the CGC experiment has been done with the nanometallogel formation of **G8PdNPs**. Here, the value of CGC for **G8PdNPs** is 1.9 wt %, while an ideal concentration for strong gel formation is 0.1 mmol (33 mg) of **G8** and 18 mg of **G8PdNPs** in 2 mL of DMSO: H<sub>2</sub>O solvent mixture (1 mL each) (Table 4.4).

**Table 4.3.** CGC experiment for formation of **G8PdCl<sub>2</sub>** nanostructured metallogel.

Concentration of G8	Concentration of PdCl <sub>2</sub>	Solvent amount DMSO:H <sub>2</sub> O	Gelation
0.1 mmol (33 mg)	0.03 mmol (5 mg)	1 mL: 1 mL	Gelatinous solution
0.1 mmol (33 mg)	0.06 mmol (10 mg)	1 mL: 1 mL	Weak strength gel
0.1 mmol (33 mg)	0.09 mmol (16 mg)	1 mL: 1 mL	Weak strength gel
0.1 mmol (33 mg)	0.1 mmol (18 mg)	1 mL: 1 mL	Strong strength gel

**Table 4.4.** CGC experiment for formation of **G8PdNPs** nanostructured metallogel.

Concentration of G8	Amount of G8PdNPs	Solvent amount DMSO:H <sub>2</sub> O	Gelation
0.1 mmol (33 mg)	5 mg	1 mL: 1 mL	Weak gel
0.1 mmol (33 mg)	10 mg	1 mL: 1 mL	Weak strength gel
0.1 mmol (33 mg)	16 mg	1 mL: 1 mL	Moderate strength gel
0.1 mmol (33 mg)	18 mg	1 mL: 1 mL	Strong strength gel

**Analysis of xerogels of G8PdCl<sub>2</sub> and G8PdNPs nanostructured metallogel.** The synthesis, characterization, and analysis of **G8** has been mentioned in previous Chapter. The FTIR data analysis has been performed for **G8**, **G8PdCl<sub>2</sub>**, and **G8PdNPs** xerogels. In the case of **G8**, the FTIR band found at 1637 cm<sup>-1</sup> indicates the presence of secondary amine -NH, 1523 cm<sup>-1</sup> for tetrazole -NH, while the bands at 1422, and 1339 cm<sup>-1</sup> indicate the presence of tetrazole ring -C-N groups. In the case of xerogel of **G8PdCl<sub>2</sub>**, the IR bands at 1624, 1505, 1418, and 1318 cm<sup>-1</sup> show the presence of secondary amine -NH, tetrazole amine -NH and tetrazole -C-N, respectively. Similarly, with **G8PdNPs**, the IR band for secondary amine -NH is found at 1620 cm<sup>-1</sup>, for tetrazole -NH, it is at 1518 cm<sup>-1</sup> and for tetrazole ring-C-N, the IR bands found at 1418 and

1327  $\text{cm}^{-1}$  (Figure 4.54). The shifting in the peak positions of **G8** functional groups in **G8PdCl<sub>2</sub>** and **G8PdNPs** indicates the presence of non-covalent interactions between **G8** and Pd(II)/ PdNPs.

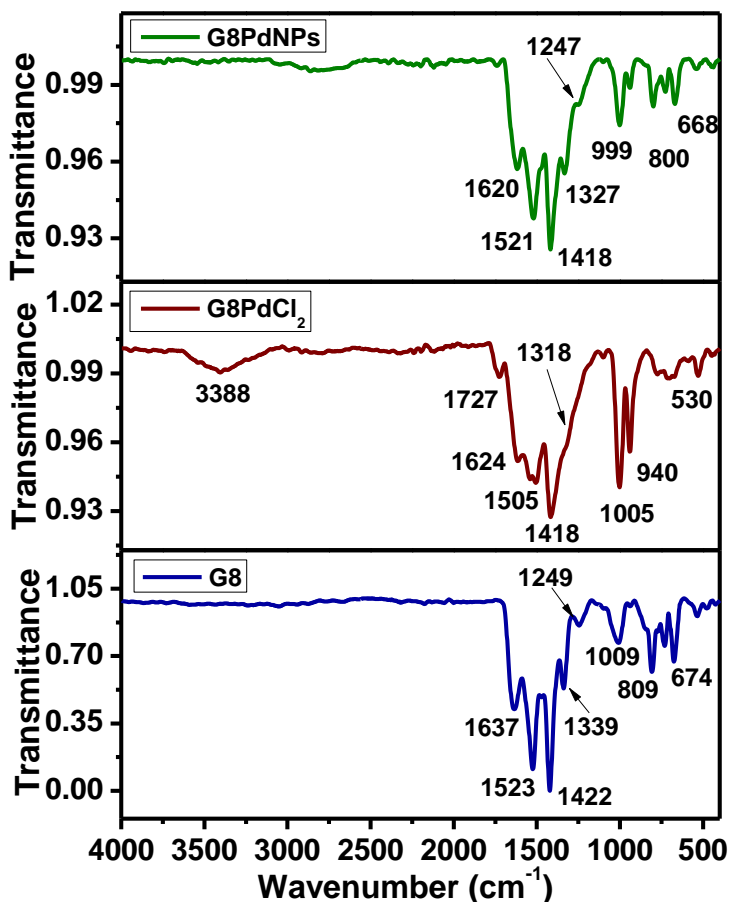


**Figure 4.54.** FTIR analysis of xerogels of **G8**, **G8PdCl<sub>2</sub>** and **G8PdNPs**.

The synthesized **G8PdCl<sub>2</sub>** and **G8PdNPs** are also characterized by PXRD analysis. The PXRD analysis of **G8** shows three peaks at 20.12°, 27.64°, and 34.35° due to intercolumnar stacking,  $\pi$ - $\pi$  stacking and hydrogen bond formation, respectively. When **G8** interacts with PdCl<sub>2</sub> to form metallogel **G8PdCl<sub>2</sub>**, it shows PXRD peaks at 11.21°, 19.58°, 27.14°, 32.04°, and 47.96°, in which 19.58°, 27.14°, and 32.04° indicate the presence of **G8** in **G8PdCl<sub>2</sub>**. The PXRD analysis of **G8PdNPs** shows the characteristic diffraction peaks of synthesized PdNPs at 40.19° (111), 45.67° (200), 66.58° (220) and 75.70° (311). The spectrum also indicates two PXRD peaks at 15.45° (100) and 20.61° (001) which are characteristic peaks for PdO due to partial oxidation of PdNPs (Figure 4.55).<sup>[59-61]</sup>

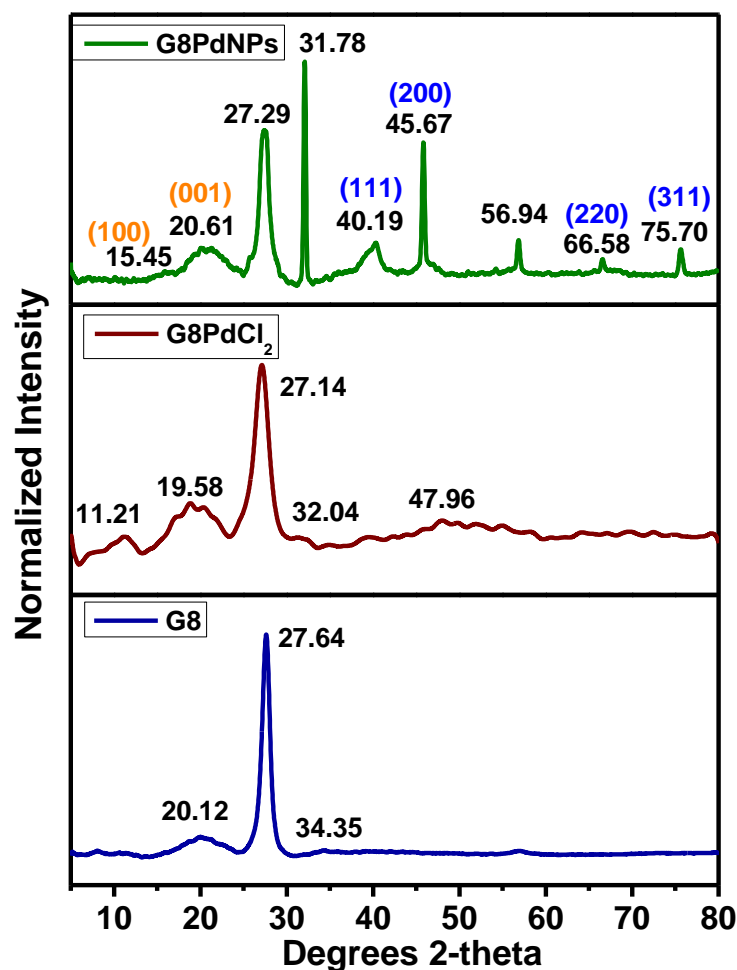


*Figure 4.55. PXRD analysis of xerogels of G8, G8PdCl<sub>2</sub> and G8PdNPs.*

The xerogel of synthesized nanometallogel **G8PdNPs** has also been examined by XPS analysis. The survey spectrum of **G8PdNPs** shows peaks at 285.06 eV for C 1s, 336.45 eV, and 341.71 eV for Pd 3d, 399.14 eV for N 1s, 532.45 eV for O 1s, and 561.76 eV for Pd 3P elements. The XPS spectrum of C 1s shows three types of carbon atoms, i.e., =C-NH- at 287.55 eV, -C=N- at 284.84 eV, and =C-N= at 284.04 eV, which indicates the presence of **G8** molecules with PdNPs. The N 1s spectrum also supports the stability of PdNPs by **G8** gelator molecules where four types of nitrogen atoms are present, i.e., C-NH-N at 402.52 eV, C-NH-C at 400.84 eV, N-N=N at 399.48 eV and C-N=C at 398.83 eV. The Pd 3d spectrum shows four peaks at 343.42 eV, 341.71 eV, 338.23 eV, and 336.45 eV. Here, the 341.71 eV and 336.45 eV peaks confirmed the presence of Pd 3d<sub>3/2</sub> and Pd 3d<sub>5/2</sub>, respectively. While the peaks at 343.42 eV and 338.23 eV indicate the presence of Pd 3d<sub>3/2</sub> and Pd 3d<sub>5/2</sub>,

respectively, due to the presence of PdO. The presence of PdO is also confirmed by the XPS spectrum of O 1s, where three peaks are available at 535.09 eV, 533.05 eV, and 531.19 eV for Pd 3p<sub>3/2</sub>, PdO, and molecular oxygen, respectively (Figure 4.56).<sup>[62-69]</sup>

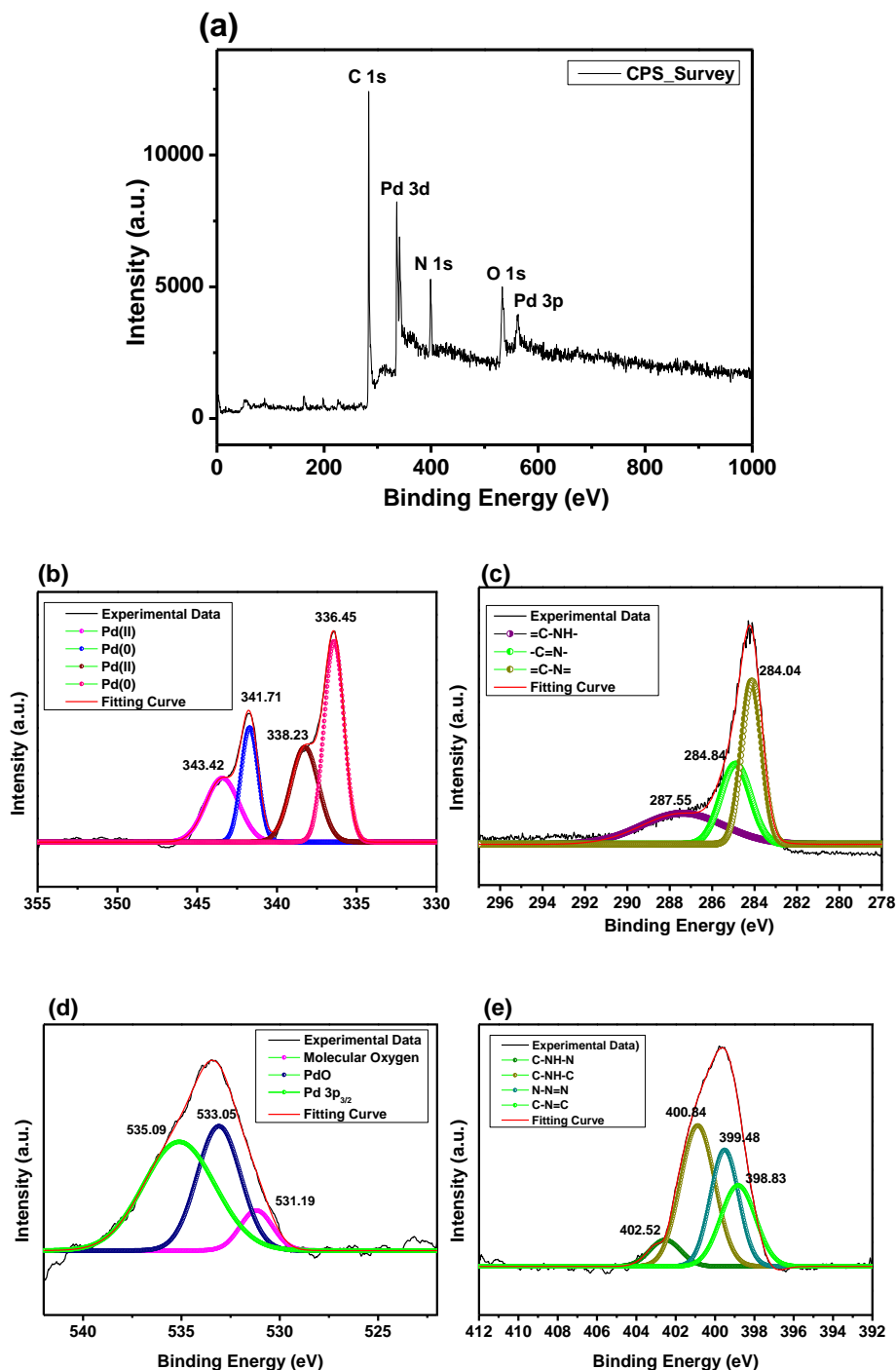


**Figure 4.56.** (a) XPS survey spectra of xerogel of **G8PdNPs** and XPS analysis of (b) Pd 3d (c) C 1s (d) PdO (e) N 1s.

**Morphological analysis of nanostructured metallo gels.** The morphological studies for organogel **G8** have been mentioned in previous chapter. Organogel **G8** shows a continuous tiny nanofibers-like structure. When  $\text{PdCl}_2/\text{PdNPs}$  interact with **G8** molecules in  $\text{DMSO}:\text{H}_2\text{O}$  (1:1) mixture (**G8PdCl<sub>2</sub>/G8PdNPs gels**), it shows 3D changes in morphology. The metallo gel **G8PdCl<sub>2</sub>** shows a nanofibrous-like structure with a flower-like appearance. **G8PdNPs** powder shows a dense structure with flowery nodes, while it has been converted into a denser form when metallo gel **G8PdNPs** have been fabricated (Figure 4.57). The EDX and mapping analysis confirmed PdNPs inside the gel matrix (Figure 4.58). The presence and size of PdNPs have been confirmed by TEM analysis of nanometallo gel **G8PdNPs**. The TEM analysis indicated the size of palladium nanoparticles between 10-50 nm in range (Figure 4.59).

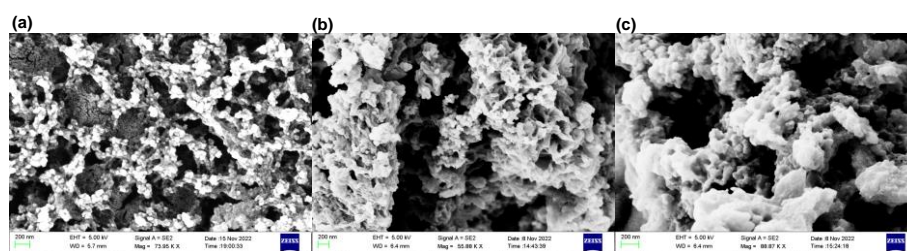


**Figure 4.57.** FE-SEM images of (a) **G8PdCl<sub>2</sub>** gel (b) **G8PdNPs** powder and (c) **G8PdNPs** gel.

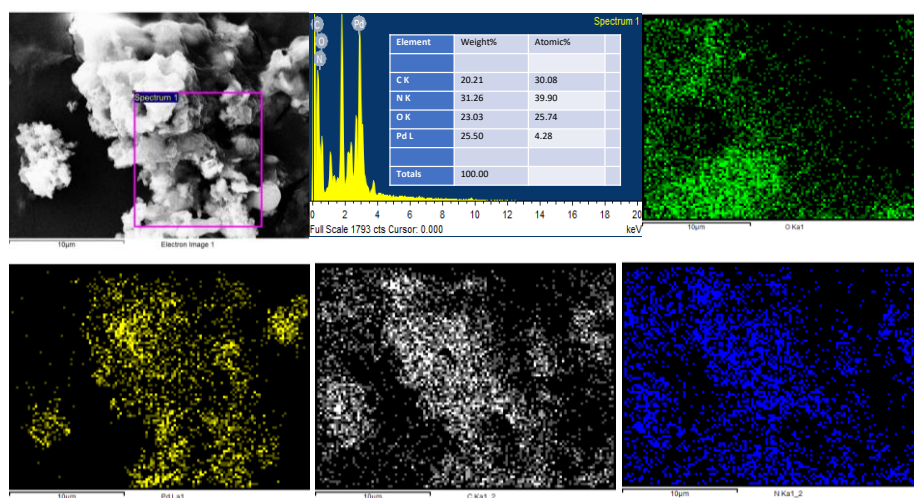


**Figure 4.58.** EDX and mapping analysis of **G8PdNPs** gel.

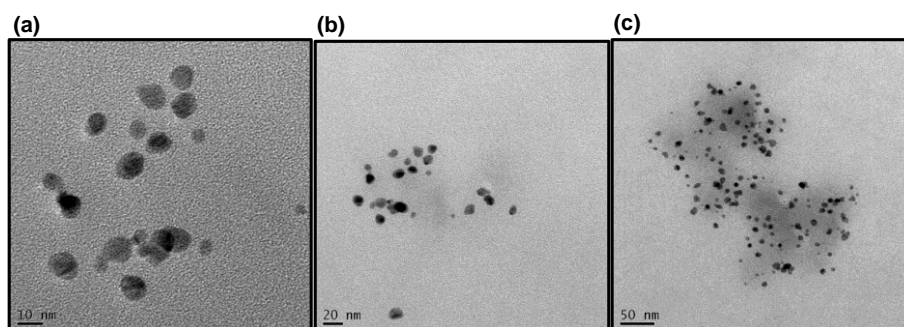


**Figure 4.59.** TEM analysis of **G8PdNPs** gel.

**Investigation of rheological properties of nanostructured metallo gels.** Angular sweep (AS), frequency sweep (FS), and time oscillation sweep (TOS)/ thixotropic behavior experiment has been performed for organogel **G8**, metallo gels **G8PdCl<sub>2</sub>** and **G8PdNPs**. The FS experiments have been done at 1 % strain taken from between the non-deformation range (0.1 to 5 % strain for **G8**) for AS experiment of organogel **G8**. The non-deformation range is the range of applied strain percentage on gel on which gel shows no loss in the storage modulus value ( $G'$ ). The frequency test is done with the range of value for non-deformation strain percentage. For **G8PdCl<sub>2</sub>** metallo gel, the non-deformation range was between 0.1-1 % strain. Therefore, the FS has been done at 0.5 % strain. While for **G8PdNPs**, it is from 0.1 to 8 % strain. Both are metallo gel of Pd, therefore the FS has been performed at similar strain % i.e., 0.5 % strain. The TOS experiment was tested at a minimum 1 % and maximum 200 % strain for **G8**, while for **G8PdCl<sub>2</sub>** and **G8PdNPs**, the minimum and maximum strain % values were 0.5 % and 100 %, respectively. The values of storage modulus ( $G'$ ) for **G8**, **G8PdCl<sub>2</sub>** and **G8PdNPs** are found to be 236 Pa, 6595 Pa and 950 Pa, respectively. The strength (measured in the term of storage modulus  $G'$ ) of nanostructured metallo gels was greater than organogel **G8** due to additional metal coordinated bond formation between **G8** and palladium ion/ palladium nanoparticle. However, the storage modulus value is more significant in the case of **G8PdCl<sub>2</sub>** than **G8PdNPs**, while the value of the non-deformation range is higher for **G8PdNPs**. So, the nanometallo gel **G8PdNPs** have a

more viscoelastic nature than **G8PdCl<sub>2</sub>** due to their moderate strength (950 Pa) (Figure 4.60). The strain test of **G8** shows weak strain overshoot as mentioned in previous chapter. The reason behind the increment in  $G''$  at certain strain % might be the formation of complex microstructure during the fabrication of organogel. This phenomenon appeared little bit in nanostructured metallogels *viz.* **G8PdCl<sub>2</sub>** and **G8PdNPs** which indicate the formation of some complex microstructure inside metallogel matrix.

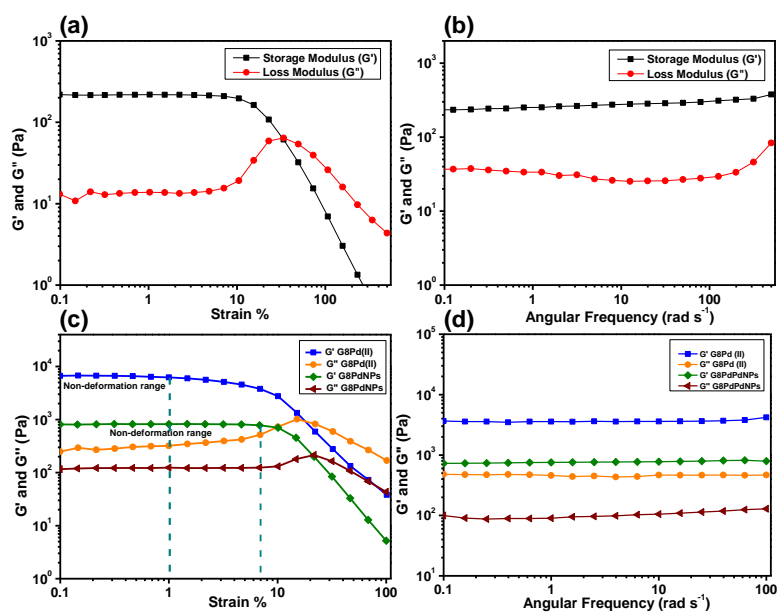


**Figure 4.60.** Angular sweep experiment of (a) **G8** (c) **G8PdCl<sub>2</sub>** and **G8PdNPs**, frequency sweep experiment of (b) **G8** and (d) **G8PdCl<sub>2</sub>** and **G8PdNPs**.

The effect of its viscoelastic nature can also be seen in TOS experiments. The experiment indicates that the gel-sol-gel transition at a minimum and maximum strain percentage for organogel **G8** and nanometallogel **G8PdNPs** was constant without losing the value of  $G'$ . At the same time, in the case of **G8PdCl<sub>2</sub>**, its storage modulus decreases after the first cycle of the TOS experiment, i.e., when the maximum strain (100 %) released and minimum strain (0.5 %) applied on gel did not show its initial  $G'$  value. The reason for this decrescent might be the higher storage modulus value of **G8PdCl<sub>2</sub>**, which increases the strength

of the gel, but maximum time decreases the flexibility of the gel (Figure 4.61).

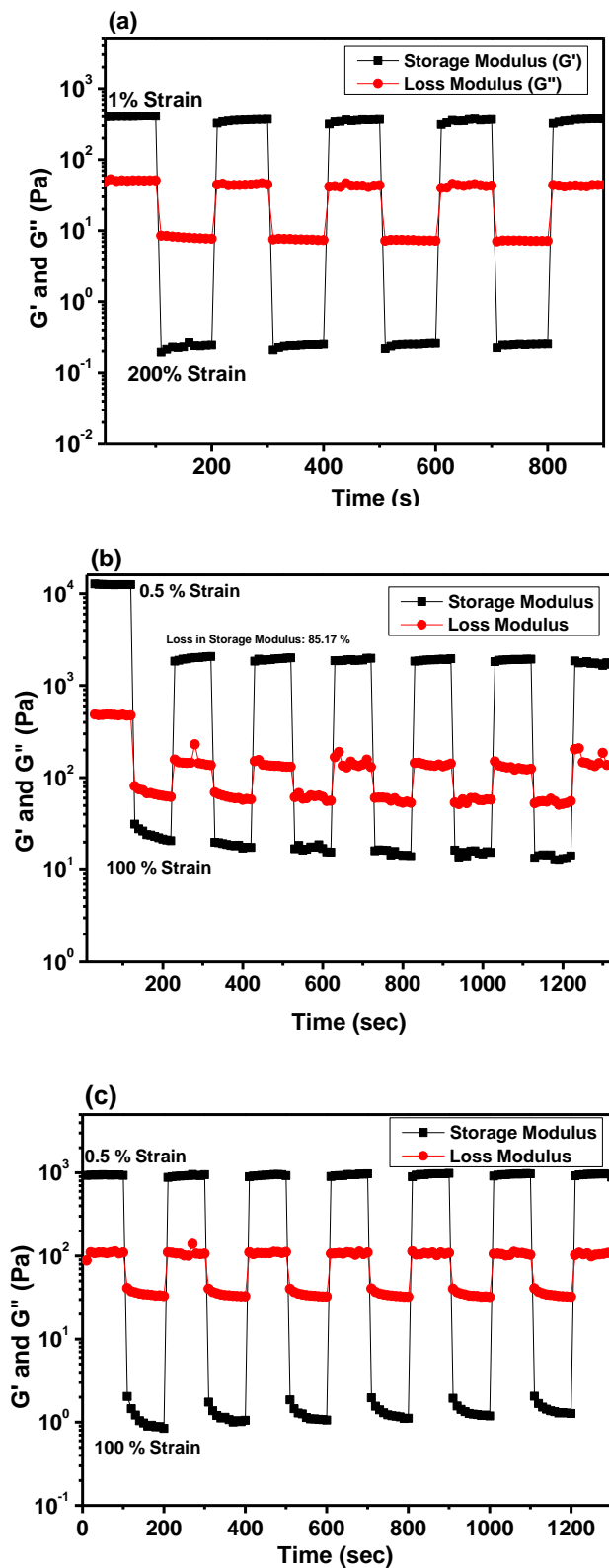
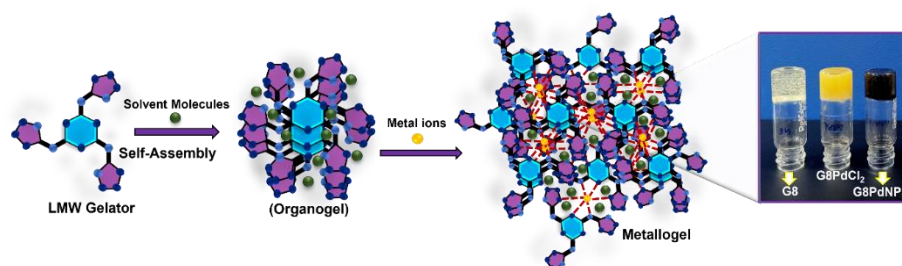


Figure 4.61. Time oscillation sweep experiment of (a) G8 (b) G8PdCl<sub>2</sub> and (c) G8PdNPs.

**Study on self-assembly of G8 gelator molecule and their metal components.** The main important factor of gel formation by gelator molecules is the self-assembly of gelator molecules with each other or gel components. The reason behind self-assembly is the formation of non-covalent interactions, *viz.*  $\pi$ - $\pi$  interactions between aromatic rings or electron clouds, hydrogen bond between electronegative-electropositive functional sites and intercolumnar stacking between  $\pi$ - $\pi$  stacked branches of gelator molecules (Figure 4.62).



**Figure 4.62.** Schematic representation of self-assembly of G8 molecules and their components for gel formation.

The self-assembly between gelator molecules can be predicted by FE-SEM, FTIR, and PXRD analysis. The self-assembly between gelator molecules can be predicted by FE-SEM, FTIR, and PXRD analysis. Here, the morphological 3D changes from organogel **G8** to nanostructured metallogels **G8PdCl<sub>2</sub>** and **G8PdNPs** indicate that the gelator components self-assembled to each other with different modes of interactions to form different types of morphologies (Figure 4.5). The FTIR data of **G8**, **G8PdCl<sub>2</sub>**, and **G8PdNPs** also indicates the interactions of **G8** with PdCl<sub>2</sub> and G8PdNPs. In the case of **G8PdCl<sub>2</sub>**, the FTIR band for secondary -NH was found at 1624 cm<sup>-1</sup> in the place of 1637 cm<sup>-1</sup>, which was found in xerogel of organogel **G8**. Similarly, the FTIR band for tetrazole -NH was found at 1505 cm<sup>-1</sup> in the place of 1523 cm<sup>-1</sup>, and for tetrazole C-N groups were found at 1418 and 1318 cm<sup>-1</sup> in the place of 1422 and 1339 cm<sup>-1</sup>. Same as, in the case of **G8PdNPs**, the FTIR band for secondary -NH is found at 1620 cm<sup>-1</sup>; for tetrazole -NH, it is at 1518 cm<sup>-1</sup>, and for tetrazole C-N groups, the bands are at 1418 and 1327 cm<sup>-1</sup>. The shifting in wavenumbers of these groups

from higher wavenumber to lower wavenumber indicates the strong interactions between **G8** molecules and with palladium metal ions or nanoparticles. These interactions denote the formation of self-assembled structure to formed gel materials (Figure 4.2). The self-assembly of gelator components can also be explored by PXRD data. The PXRD analysis of **G8** shows three peaks at  $20.12^\circ$ ,  $27.64^\circ$ , and  $34.35^\circ$  due to various non-covalent interactions between **G8** molecules. **G8PdCl<sub>2</sub>** shows PXRD peaks at  $11.21^\circ$ ,  $19.58^\circ$ ,  $27.14^\circ$ ,  $32.04^\circ$ , and  $47.96^\circ$ , where the peaks at  $19.58^\circ$ ,  $27.14^\circ$  and  $32.04^\circ$  appear due to the non-covalent interaction between **G8** molecules which is present in **G8PdCl<sub>2</sub>**. The PXRD analysis of **G8PdNPs** indicates the characteristic diffraction peaks of synthesized PdNPs at  $40.19^\circ$  (111),  $45.67^\circ$  (200),  $66.58^\circ$  (220) and  $75.70^\circ$  (311) and two PXRD peaks at  $15.45^\circ$  (100) and  $20.61^\circ$  (001) due to presence of PdO. Here, two other peaks can be seen at  $27.29^\circ$  and  $31.78^\circ$  representing the interactions of **G8** molecules with **PdNPs** (Figure 4.3).

Therefore, the reliable changes in FE-SEM, FTIR and PXRD data of **G8**, **G8PdCl<sub>2</sub>** and **G8PdNPs** confirmed the self-assembly between respective gelator components.

**Recyclability of catalyst G8PdCl<sub>2</sub>.** Catalyst **G8PdCl<sub>2</sub>** is used in the form of xerogel. It acts as a heterogeneous catalyst in cycloaddition reactions. Therefore, it is easy to separate the catalyst by filtering. The filtrate was extracted by ethyl acetate and ice-cooled water, and the product was isolated by evaporation of the organic layer in the rotary evaporator. The obtained solid in the filter paper can be used further for another cycle of catalytic reaction. Here, the recyclability was tested with tetrazole formation of 4-cyanobenzaldehyde for five cycles, and it was found that till the third cycle, the isolated yield of the product remained almost the same. It decreases slowly after the third cycle of the reaction (Figure 4.63). The recyclability of the catalyst has been confirmed by comparing the FTIR data of the original catalyst and the catalyst isolated after the fifth cycle of reaction (Figure 4.64). Almost

similar IR pattern of FTIR data, even after the fifth cycle of repetition, indicates the stability and applicability of the catalyst.

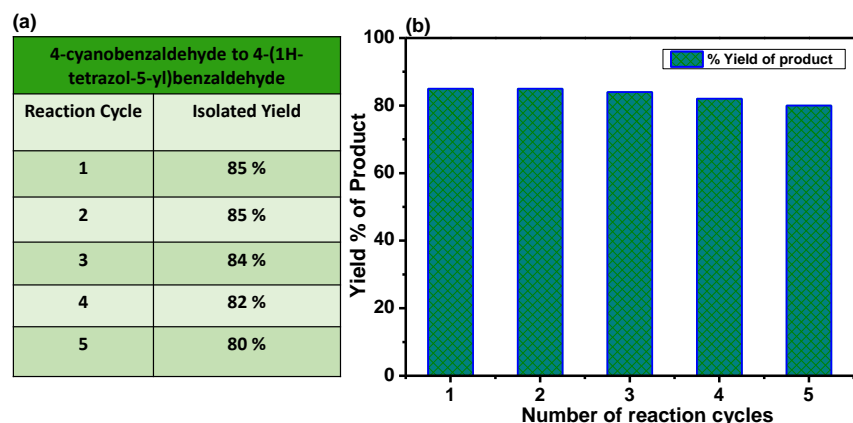


**Figure 4.63.** (a) Isolated yield of product 4-(1H-tetrazol-5-yl)benzaldehyde during recyclability of catalyst  $G8PdCl_2$  till five cycle of reaction (b) Bar graph showing the recyclability of catalyst.

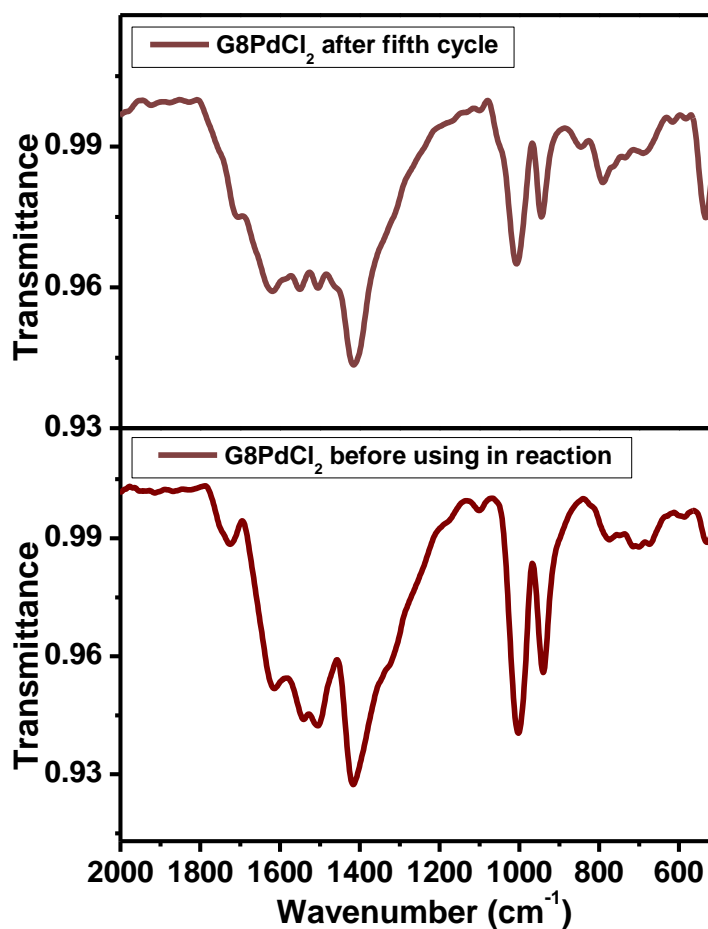


**Figure 4.64.** FTIR data of catalyst  $G8PdCl_2$  before use and after using till five cycles of reaction.

**Recyclability of catalyst G8PdNPs.** Catalyst G8PdNPs is also used in the form of xerogel. It acts as a heterogenous catalyst with minimum reaction time and is easily separated. Here, also the catalyst is removed by filtration. During filtration, the remaining amount of sodium carbonate can also be there, so filtration must be done by decaying the reaction system. The filtrate was extracted by ethyl acetate and water, and the product was isolated by evaporation of the organic layer in a rotary evaporator. The filtered solid, which is greyish black in colour is identified as an original catalyst, which can be used further after drying for another cycle of the same reaction. Here, the recyclability has been tested for the Suzuki-Miyaura coupling reaction of (4-methoxyphenyl)boronic acid and 1-iodo-4-methoxybenzene to form the product 4,4'-dimethoxy-1,1'-biphenyl. The recyclability was tested for five cycles, and it was found that till the second cycle, the isolated yield of the product was almost the same. It decreases slowly after the second cycle of reaction (Figure 4.65). The stability of the catalyst has been confirmed by the FTIR data of the catalyst before and after use till the fifth cycle of the reaction (Figure 4.66). The FTIR data show that there is no change in the FTIR band pattern, which indicates that the xerogel is in a stable state during the reaction.

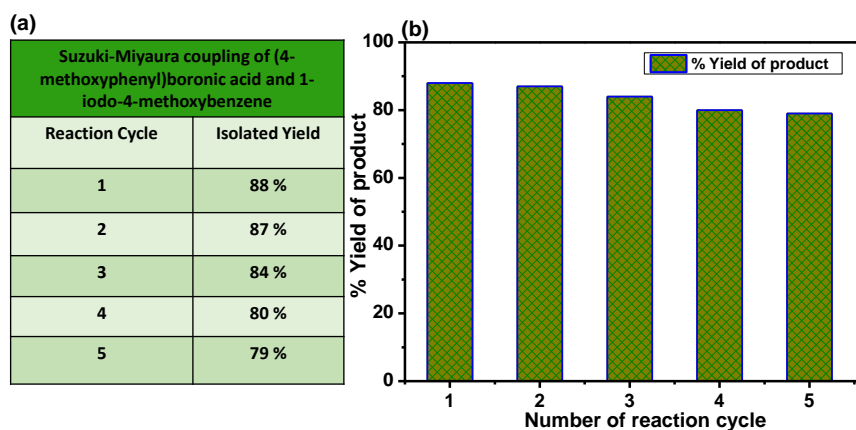


**Figure 4.65.** (a) Isolated yield of Suzuki-Miyaura coupling product 4,4'-dimethoxy-1,1'-biphenyl during, recyclability of catalyst G8PdNPs till five cycles of reaction. (b) Bar graph showing the recyclability of catalyst.

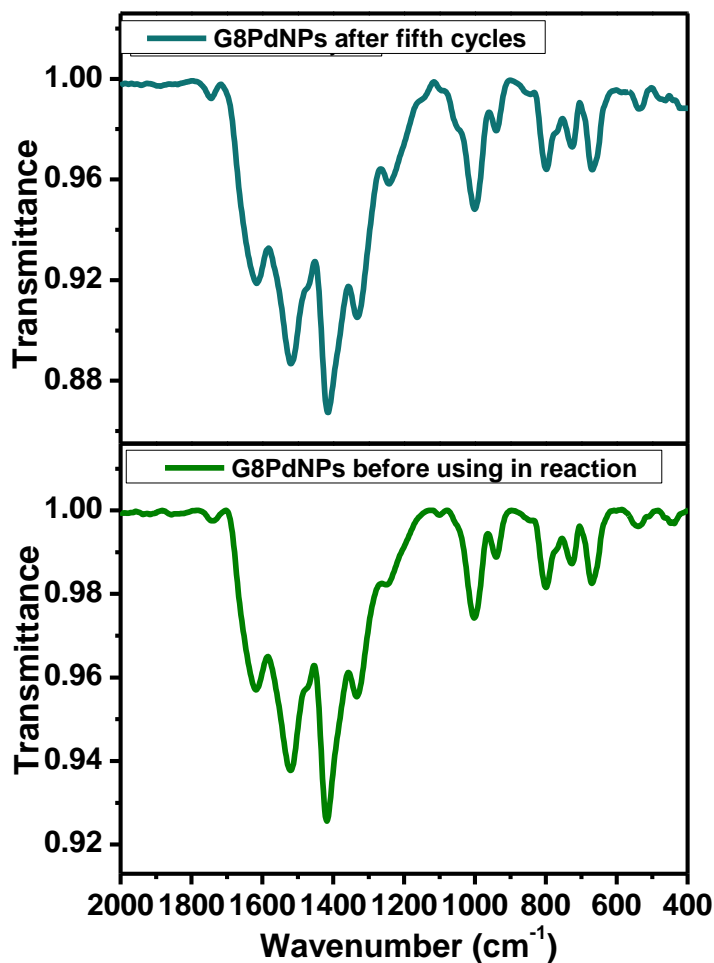


*Figure 4.66. FTIR data of catalyst G8PdNPs before use and after using up to five cycles of reaction.*

#### **4.4 Conclusion**

Gelator molecule **G8** has been synthesized and characterized by various spectroscopic tools. **G8** contains many functional sites as secondary amine -NH, tetrazole -NH, and triazine ring nitrogen. **G8** was used to stabilize palladium nanoparticles using these sites, and a palladium nanocomposite powder **G8PdNPs** was synthesized. Further, for the formation of a Pd(0) catalyst, **G8PdNPs** nanometallogel has been fabricated in DMSO: H<sub>2</sub>O mixture with **G8**. Similarly, the fabrication of **G8PdCl<sub>2</sub>** metallogel was done in DMSO: H<sub>2</sub>O mixture using **G8** and PdCl<sub>2</sub> as gel components. After the fabrication of **G8PdCl<sub>2</sub>** and **G8PdNPs** metallogel, both were converted into xerogels by lyophilization. The synthesis and fabrication of palladium nanocomposite, metallogels, and its xerogels have been analyzed by

FTIR, PXRD, XPS, SEM, TEM, and UV-Vis analysis. Xerogels **G8PdCl<sub>2</sub>** and **G8PdNPs** both act as heterogenous catalyst and show good catalytic activity for the cycloaddition reaction of nitrile substituent and sodium azide to form respective tetrazoles and for the Suzuki-Miyaura coupling reaction for various substrates, respectively. Both nanostructured catalysts worked as active catalysts and provided notable product yields. The catalytic reaction products were examined by ESI-MS, FTIR, <sup>1</sup>H, and <sup>13</sup>C NMR techniques. Both the catalysts show good recyclability till five cycles of reactions without much change in the yield of the reaction products.

#### 4.5 References

- [1] Melian-Cabrera, I. (2021), Catalytic materials: Concepts to understand the pathway to implementation., *Ind. Eng. Chem. Res.*, 60, 18545-18559 (DOI: 10.1021/acs.iecr.1c02681)
- [2] Bavykina, A., Kolobov, N., Khan, I.S., Bau, J.A., Ramirez, A., Gascon, J. (2020), Metal–organic frameworks in heterogeneous catalysis: recent progress, new trends, and future perspectives, *Chem. Rev.*, 120, 8468-8535 (DOI: 10.1021/acs.chemrev.9b00685)
- [3] Takaya, J. (2021), Catalysis using transition metal complexes featuring main group metal and metalloid compounds as supporting ligands, *Chem. Sci.*, 12, 1964-1981 (DOI: 10.1039/D0SC04238B)
- [4] Liao, G., Fang, J., Li, Q., Li, S., Xu, Z., Fang, B. (2019), Ag-Based nanocomposites: synthesis and applications in catalysis, *Nanoscale*, 11, 7062-7096 (DOI: 10.1039/C9NR01408J)
- [5] Rizzo, C., Marullo, S., Billeci, F., D'Anna, F. (2021), Catalysis in supramolecular systems: the case of gel phases, *Eur. J. Org. Chem.*, 2021, 3148-3169 (DOI: 10.1002/ejoc.202100372)
- [6] Biffis, A., Centomo, P., Del Zotto, A., Zecca, M. (2018), Pd metal catalysts for cross-couplings and related reactions in the

- 21st century: a critical review, *Chem. Rev.*, 118, 2249-2295 (DOI: 10.1021/acs.chemrev.7b00443)
- [7] Mohammadi, L., Hosseini-fard, M., Vaezi, M.R. (2023), Stabilization of Palladium-Nanoparticle-Decorated Postsynthesis-Modified Zr-UiO-66 MOF as a Reusable Heterogeneous Catalyst in C–C Coupling Reaction, *ACS omega*, 8, 8505-8518 (DOI: 10.1021/acsomega.2c07661)
- [8] Hawkins, K., Patterson, A.K., Clarke, P.A., Smith, D.K. (2020), Catalytic gels for a prebiotically relevant asymmetric aldol reaction in water: From organo-catalyst design to hydrogel discovery and back again, *J. Am. Chem. Soc.*, 142, 4379-4389 (DOI: 10.1021/jacs.9b13156)
- [9] Fang, W., Zhang, Y., Wu, J., Liu, C., Zhu, H., Tu, T. (2018), Recent advances in supramolecular gels and catalysis, *Chem. Asian J.*, 13, 712-729 (DOI: 10.1002/asia.201800017)
- [10] Kori, D.K., Ghosh, T., Das, A.K. (2023), Electrochemical Suzuki–Miyaura cross-coupling using peptide bolaamphiphile hydrogel-supported Pd NPs as heterogeneous electrocatalyst, *Catal. Sci. Technol.*, 13, 2540-2550 (DOI: 10.1039/D3CY00108C)
- [11] Xing, B., Choi, M.F., Xu, B. (2002), Design of coordination polymer gels as stable catalytic systems, *Chem. Eur. J.*, 8, 5028-5032 (DOI: 10.1002/1521-3765)
- [12] Liu, Y.R., He, L., Zhang, J., Wang, X., Su, C.Y. (2009), Evolution of spherical assemblies to fibrous networked Pd (II) metallogels from a pyridine-based tripodal ligand and their catalytic property, *Chem. Mater.*, 21, 557-563 (DOI: 10.1021/cm802841r)
- [13] Liao, Y., He, L., Huang, J., Zhang, J., Zhuang, L., Shen, H., Su, C.Y. (2010), Magnetite nanoparticle-supported coordination polymer nanofibers: synthesis and catalytic application in Suzuki-Miyaura coupling, *ACS Appl. Mater. Interfaces*, 2, 2333-2338 (DOI: 10.1021/am100354b)

- [14] Lee, H.H., Jung, S.H., Park, S., Park, K.M., Jung, J.H. (2013), A metal–organic framework gel with  $\text{Cd}^{2+}$  derived from only coordination bonds without intermolecular interactions and its catalytic ability, *New J. Chem.*, 37, 2330-2335 (DOI: 10.1039/C3NJ00164D)
- [15] He, Y., Bian, Z., Kang, C., Cheng, Y., Gao, L. (2010), Chiral binaphthylbisbipyridine-based copper (I) coordination polymer gels as supramolecular catalysts, *Chem. Commun.*, 46, 3532-3534 (DOI: 10.1039/B926936C)
- [16] Yang, L., Luo, L., Zhang, S., Su, X., Lan, J., Chen, C.T., You, J. (2010), Self-assembly from metal–organic vesicles to globular networks: metallo-gel-mediated phenylation of indole with phenyl boronic acid, *Chem. Commun.*, 46, 3938-3940 (DOI: 10.1039/C0CC00112K)
- [17] Araújo, M., Díaz-Oltra, S., Escuder, B. (2016), Triazolyl-based molecular gels as ligands for autocatalytic ‘Click’ reactions, *Chem. Eur. J.*, 22, 8676-8684 (DOI: 10.1002/chem.201600594)
- [18] Mallick, A., Schön, E.M., Panda, T., Sreenivas, K., Díaz, D.D., Banerjee, R. (2012), Fine-tuning the balance between crystallization and gelation and enhancement of  $\text{CO}_2$  uptake on functionalized calcium-based MOFs and metallo-gels, *J. Mater. Chem.*, 22, 14951-14963 (DOI: 10.1039/C2JM30866E)
- [19] Yamada, Y.M., Maeda, Y., Uozumi, Y. (2006), Novel 3D coordination palladium-network complex: A recyclable catalyst for Suzuki-Miyaura reaction, *Org. Lett.*, 8, 4259-4262 (DOI: 10.1021/ol0615026)
- [20] Miravet, J.F., Escuder, B. (2005), Pyridine-functionalised ambidextrous gelators: towards catalytic gels, *Chem. Commun.*, 46, 5796-5798 (DOI: 10.1039/B510874H)
- [21] Jin, Q., Zhang, L., Cao, H., Wang, T., Zhu, X., Jiang, J., Liu, M. (2011), Self-assembly of copper (II) ion-mediated nanotube and its supramolecular chiral catalytic behavior, *Langmuir*, 27, 13847-13853 (DOI: 10.1021/la203110z)

- [22] Lee, J.H., Kang, S., Lee, J.Y., Jung, J.H. (2012), A tetrazole-based metallogel induced with  $\text{Ag}^+$  ion and its silver nanoparticle in catalysis, *Soft Matter*, 8, 6557-6563 (DOI: 10.1039/C2SM25316J)
- [23] Wen, X., Tang, L., Li, B. (2014), Metallogel template fabrication of pH-responsive copolymer nanowires loaded with silver nanoparticles and their photocatalytic degradation of methylene blue, *Chem. Asian J.*, 9, 2975-2983 (DOI: 10.1002/asia.201402575)
- [24] Wen, X., Tang, L. (2015), One-dimensional copolymer nanostructures loaded with silver nanoparticles fabricated via metallogel template copolymerization and their pH dependent photocatalytic degradation of methylene blue, *J. Mol. Catal. A: Chem.*, 399, 86-96 (DOI: 10.1016/j.molcata.2015.01.025)
- [25] Notz, W., Tanaka, F., Barbas, C.F. (2004), Enamine-based organocatalysis with proline and diamines: the development of direct catalytic asymmetric aldol, Mannich, Michael, and Diels–Alder reactions, *Acc. Chem. Res.*, 37, 580-591 (DOI: 10.1021/ar0300468)
- [26] Rodríguez-Llansola, F., Escuder, B., Miravet, J.F. (2009), Remarkable increase in basicity associated with supramolecular gelation, *Org. Biomol. Chem.*, 7, 3091-3094 (DOI: 10.1039/B904523F)
- [27] Mazzier, D., Carraro, F., Crisma, M., Rancan, M., Toniolo, C., Moretto, A. (2016), A terminally protected dipeptide: From crystal structure and self-assembly, through co-assembly with carbon-based materials, to a ternary catalyst for reduction chemistry in water, *Soft Matter*, 12, 238-245 (DOI: 10.1039/C5SM02189H)
- [28] Guler, M.O., Stupp, S.I. (2007), A self-assembled nanofiber catalyst for ester hydrolysis, *J. Am. Chem. Soc.*, 129, 12082-12083 (DOI: 10.1021/ja075044n)
- [29] Corma, A., Garcia, H. (2006), Silica-bound homogenous catalysts as recoverable and reusable catalysts in organic

- synthesis, *Adv. Synth. Catal.*, 348, 1391-1412 (DOI: 10.1002/adsc.200606192)
- [30] Gawande, M.B., Monga, Y., Zboril, R., Sharma, R.K. (2015), Silica-decorated magnetic nanocomposites for catalytic applications, *Coord Chem Rev.*, 288, 118-143 (DOI: 10.1016/j.ccr.2015.01.001)
- [31] Łukowska-Chojnacka, E., Mierzejewska, J., Milner-Krawczyk, M., Bondaryk, M., Staniszevska, M. (2016), Synthesis of novel tetrazole derivatives and evaluation of their antifungal activity, *Bioorg. Med. Chem.*, 24, 6058-6065 (DOI: 10.1016/j.bmc.2016.09.066)
- [32] Qian, A., Zheng, Y., Wang, R., Wei, J., Cui, Y., Cao, X., Yang, Y., (2018), Design, synthesis, and structure-activity relationship studies of novel tetrazole antifungal agents with potent activity, broad antifungal spectrum and high selectivity, *Bioorganic Med. Chem. Lett.*, 28, 344-350 (DOI: 10.1016/j.bmcl.2017.12.040)
- [33] Zhan, P., Li, Z., Liu, X., De Clercq, E. (2009), Sulfanyltriazole/tetrazoles: a promising class of HIV-1 NNRTIs, *Mini-Rev. Med. Chem.*, 9, 1014-1023 (DOI: 10.2174/138955709788681618)
- [34] Chauhan, K., Sharma, M., Trivedi, P., Chaturvedi, V., Chauhan, P.M. (2014), New class of methyl tetrazole based hybrid of (Z)-5-benzylidene-2-(piperazin-1-yl) thiazol-4 (% H)-one as potent antitubercular agents, *Bioorganic Med. Chem. Lett.*, 24, 4166-4170 (DOI: 10.1016/j.bmcl.2014.07.061)
- [35] DeMarinis, R.M., Hoover, J.R., Dunn, G.L., Actor, P., Uri, J.V., Weisbach, J.A. (1975), A new parenteral cephalosporin. SK&F 59962: 7-Trifluoromethylthioacetamido-3-(1-methyl-1H-tetrazol-5-ylthiomethyl)-3-cephem-4-carboxylic acid. Chemistry and structure activity relationships, *J. Antibiot.*, 28, 463-470 (DOI: 10.7164/antibiotics.28.463)
- [36] Uchida, M., Komatsu, M., Morita, S., Kanbe, T., Nakagawa, K. (1989), Studies on gastric antiulcer active agents. II.: synthesis

- of tetrazole alkanamides and related compounds, *Chem. Pharm. Bull.*, 37, 322-326 (DOI: 10.1248/cpb.37.322)
- [37] Uchida, M., Komatsu, M., Morita, S., Kanbe, T., Yamasaki, K., Nakagawa, K. (1989), Studies on gastric antiulcer active agents. III.: synthesis of 1-substituted 4-(5-tetrazolyl) thio-1-butanones and related compounds, *Chem. Pharm. Bull.*, 37, 958-961 (DOI: 10.1248/cpb.37.958)
- [38] Ford, R.E., Knowles, P., Lunt, E., Marshall, S.M., Penrose, A.J., Ramsden, C.A., Summers, A.J., Walker, J.L., Wright, D.E. (1986), Synthesis and quantitative structure-activity relationships of antiallergic 2-hydroxy-N-(1H-tetrazol-5-yl) benzamides and N-(2-hydroxyphenyl)-1H-tetrazole-5-carboxamides, *J. Med. Chem.*, 29, 538-549 (DOI: 10.1021/jm00154a019)
- [39] Hayao, S., Havera, H.J., Strycker, W.G., Leipzig, T.J., Rodriguez, R. (1967), New antihypertensive aminoalkyltetrazoles, *J. Med. Chem.*, 10, 400-402 (DOI: 10.1021/jm00315a025)
- [40] Purohit, P., Pandey, A.K., Singh, D., Chouhan, P.S., Ramalingam, K., Shukla, M., Goyal, N., Lal, J., Chauhan, P.M. (2017), An insight into tetrahydro- $\beta$ -carboline-tetrazole hybrids: synthesis and bioevaluation as potent antileishmanial agents, *Med. chem. comm.*, 8, 1824-1834 (DOI: 10.1039/C7MD00125H)
- [41] Neochoritis, C.G., Zhao, T., Dömling, A. (2019), Tetrazoles via multicomponent reactions, *Chem. Rev.*, 119, 1970-2042 (DOI: 10.1021/acs.chemrev.8b00564)
- [42] Gao, F., Xiao, J., Huang, G. (2019), Current scenario of tetrazole hybrids for antibacterial activity, *Eur. J. Med. Chem.*, 184, 111744 (DOI: 10.1016/j.ejmech.2019.111744)
- [43] Dileep, K., Polepalli, S., Jain, N., Buddana, S.K., Prakasham, R.S., Murty, M. S. R. (2018), Synthesis of novel tetrazole containing hybrid ciprofloxacin and pipemidic acid analogues and preliminary biological evaluation of their antibacterial and

- antiproliferative activity, *Mol. Divers.*, 22, 83-93 (DOI: 10.1007/s11030-017-9795-y)
- [44] Gupta, A.K., Song, C.H., Oh, C.H. (2004), 1-(2-Iodophenyl)-1H-tetrazole as a ligand for Pd (II) catalyzed Heck reaction, *Tetrahedron Lett.*, 45, 4113-4116 (DOI: 10.1016/j.tetlet.2004.03.162)
- [45] Patil, D.R., Wagh, Y.B., Ingole, P.G., Singh, K., Dalal, D.S. (2013),  $\beta$ -Cyclodextrin-mediated highly efficient [2+ 3] cycloaddition reactions for the synthesis of 5-substituted 1 H-tetrazoles, *New J. Chem.*, 37, 3261-3266 (DOI: 10.1039/C3NJ00569K)
- [46] Suzuki, A. (1999), Recent advances in the cross-coupling reactions of organoboron derivatives with organic electrophiles, 1995–1998, *J. Organomet. Chem.*, 576, 147-168 (DOI: 10.1016/S0022-328X(98)01055-9)
- [47] Koudehi, M.F., Zibaseresht, R. (2020), One-Pot Suzuki–Miyaura C–C Coupling Reaction versus Stepwise Reaction Involving Isolated Synthesized Catalyst Addition, *J. Chem. Educ.*, 97, 3822-3828 (DOI: 10.1021/acs.jchemed.0c00357)
- [48] Magano, J., Dunetz, J.R. (2011), Large-scale applications of transition metal-catalyzed couplings for the synthesis of pharmaceuticals, *Chem. Rev.*, 111, 2177-2250 (DOI: 10.1021/cr100346g)
- [49] Jabbari, A., Tahmasbi, B., Nikoorazm, M., Ghorbani-Choghamarani, A. (2018), A new Pd-Schiff-base complex on boehmite nanoparticles: Its application in Suzuki reaction and synthesis of tetrazoles, *Appl. Organomet. Chem.*, 32, e4295 (DOI: 10.1002/aoc.4295)
- [50] Akbarzadeh, P., Koukabi, N., Hosseini, M.M. (2020), Magnetic carbon nanotube as a highly stable and retrievable support for the heterogenization of sulfonic acid and its application in the synthesis of 2-(1H-tetrazole-5-yl) acrylonitrile derivatives, *J. Heterocycl. Chem.*, 57, 2455-2465 (DOI: 10.1002/jhet.3961)

- [51] Naeimi, H., Mohamadabadi, S. (2014), Sulfonic acid-functionalized silica-coated magnetic nanoparticles as an efficient reusable catalyst for the synthesis of 1-substituted 1H-tetrazoles under solvent-free conditions, *Dalton Trans.*, 43, 12967-12973 (DOI: 10.1039/C4DT01664E)
- [52] Salahshournia, B., Hamadi, H., Nobakht, V. (2018), Engineering a Cu-MOF Nano-Catalyst by using Post-Synthetic Modification for the Preparation of 5-Substituted 1H-Tetrazoles, *Appl. Organomet. Chem.*, 32, e4416 (DOI: 10.1002/aoc.4416)
- [53] Agawane, S.M., Nagarkar, J.M. (2012), Synthesis of 5-substituted 1H-tetrazoles using a nano ZnO/Co<sub>3</sub>O<sub>4</sub> catalyst, *Catal. Sci. Technol.*, 2, 1324-1327 (DOI: 10.1039/C2CY20094E)
- [54] Zhang, J., Wang, X., He, L., Chen, L., Su, C.Y., James, S.L. (2009), Metal-organic gels as functionalisable supports for catalysis, *New J. Chem.*, 33, 1070-1075 (DOI: 10.1039/B822104A)
- [55] Liu, Y.R., He, L., Zhang, J., Wang, X., Su, C.Y. (2009), Evolution of spherical assemblies to fibrous networked Pd (II) metallogels from a pyridine-based tripodal ligand and their catalytic property, *Chem. Mater.*, 21, 557-563 (DOI: 10.1021/cm802841r)
- [56] Bennett, J.A., Davis, B.A., Ramezani, M., Genzer, J., Efimenko, K., Abolhasani, M. (2021), Continuous ligand-free Suzuki-Miyaura cross-coupling reactions in a cartridge flow reactor using a gel-supported catalyst, *Ind. Eng. Chem. Res.*, 60, 9418-9428 (DOI: 10.1021/acs.iecr.1c01531)
- [57] Roy Chowdhury, S., Nandi, S.K., Halder, D. (2022), Proof of concept: Interface of recyclable organogels with embedded palladium nanoparticles catalyzing Suzuki-Miyaura coupling in water at room temperature, *ACS omega*, 7, 21566-21573 (DOI: 10.1021/acsomega.2c01360)
- [58] Ruiz-Castillo, P., Buchwald, S.L. (2016), Applications of palladium-catalyzed C-N cross-coupling reactions, *Chem. Rev.*, 116, 12564-12649 (DOI: 10.1021/acs.chemrev.6b00512)

- [59] Xu, Y.L., Li, C.T., Cao, Q.Y., Wang, B.Y., Xie, Y. (2017), A pyrenyl-appended organogel for fluorescence sensing of anions, *Dyes Pigm.*, 139, 681-687 (DOI: 10.1016/j.dyepig.2016.12.068)
- [60] Zhang, Y., Liang, C., Shang, H., Ma, Y., Jiang, S. (2013), Supramolecular organogels and nanowires based on a V-shaped cyanostilbene amide derivative with aggregation-induced emission (AIE) properties, *J. Mater. Chem. C*, 1, 4472-4480 (DOI: 10.1039/C3TC30545G)
- [61] Kadam, J., Madiwale, S., Bashte, B., Dindorkar, S., Dhawal, P., More, P. (2020), Green mediated synthesis of palladium nanoparticles using aqueous leaf extract of *Gymnema sylvestre* for catalytic reduction of Cr (VI), *SN Appl. Sci.*, 2, 1-13 (DOI: 10.1007/s42452-020-03663-5)
- [62] Artemenko, A., Shchukarev, A., Štenclová, P., Wågberg, T., Segervald, J., Jia, X., Kromka, A. (2021), Reference XPS spectra of amino acids, *IOP Conf. Ser. Mater. Sci. Eng.*, 1050, 012001 (DOI: 10.1088/1757-899X/1050/1/012001)
- [63] Zhao, Z., Sun, S., Wu, D., Zhang, M., Huang, C., Umemura, K., Yong, Q. (2019), Synthesis and characterization of sucrose and ammonium dihydrogen phosphate (SADP) adhesive for plywood, *Polymers*, 11, 1909 (DOI: 10.3390/polym11121909)
- [64] Huang, X., Xie, Z., Li, K., Chen, Q., Chen, Y., Gong, F. (2020), Thermal stability of CrWN glass molding coatings after vacuum annealing, *Coatings*, 10, 198 (DOI: 10.3390/coatings10030198)
- [65] Wang, Y., Yu, J., Peng, W., Tian, J., Yang, C. (2019), Novel multilayer TiO<sub>2</sub> heterojunction decorated by low g-C<sub>3</sub>N<sub>4</sub> content and its enhanced photocatalytic activity under UV, visible and solar light irradiation, *Sci. Rep.*, 9, 5932 (DOI: 10.1038/s41598-019-42438-w)
- [66] Yang, S., Dong, J., Yao, Z., Shen, C., Shi, X., Tian, Y., Lin, S., Zhang, X. (2014), One-pot synthesis of graphene-supported monodisperse Pd nanoparticles as catalyst for formic acid electro-oxidation, *Sci. Rep.*, 4, 4501 (DOI: 10.1038/srep04501)

- [67] Gholinejad, M., Bahrami, M., Najera, C. (2017), A fluorescence active catalyst support comprising carbon quantum dots and magnesium oxide doping for stabilization of palladium nanoparticles: Application as a recoverable catalyst for Suzuki reaction in water, *Mol. Catal.*, 433, 12-19 (DOI: 10.1016/j.mcat.2016.12.010)
- [68] Jindal, A., Basu, S., Aby, C.P. (2015), Electrospun carbon nitride supported on poly (vinyl) alcohol as an electrocatalyst for oxygen reduction reactions, *RSC Adv.*, 5, 69378-69387 (DOI: 10.1039/C5RA10884E)
- [69] Militello, M.C., Simko, S.J. (1994), Palladium oxide (PdO) by XPS, *Surf. Sci. Spectra*, 3, 395-401 (DOI: 10.1116/1.1247784)



## Chapter 5

### **Design and Synthesis of Hydrophobic Mixed Organogel with Complementary Hydrogen-bond Donor-acceptor Sites: Removal of Heavy Metal Ions $\text{Hg}^{2+}$ , $\text{Cd}^{2+}$ and $\text{Pb}^{2+}$ from Aqueous Solution**



## Chapter 5

# Design and Synthesis of Hydrophobic Mixed Organogel with Complementary Hydrogen-bond Donor-acceptor Sites: Removal of Heavy Metal Ions $\text{Hg}^{2+}$ , $\text{Cd}^{2+}$ and $\text{Pb}^{2+}$ from Aqueous Solution

### 5.1 Introduction

Low molecular weight gels (LMWGs) present a new opportunity to utilize the intermediate state in favour of various applications in diverse fields. The organic molecules with carboxamide and tetrazole moieties have shown greater tendencies to form gel.<sup>[1-4]</sup> While gels have been seen to have prospective applications in tissue engineering,<sup>[5,6]</sup> sensing,<sup>[7,8]</sup> drug delivery,<sup>[9,10]</sup> self-healing materials,<sup>[11,12]</sup> etc., incorporating metal ions in gel structure can further enrich the materialistic properties by introducing optical,<sup>[13,14]</sup> magnetic,<sup>[15,16]</sup> catalytic,<sup>[17-19]</sup> and conductive properties.<sup>[20,21]</sup> Interestingly, though LMWGs have shown extensive metallogel formation properties, there are only limited reports where LMWGs are being used in water remediation through the adsorption of heavy metals. However, some reports show that alginate or cellulose-based gels<sup>[22-24]</sup> have been used for water remediation. Recently a metalloprotein-based hybrid hydrogel is reported for Cd(II) removal.<sup>[25]</sup> Some other reports used glucolipid biosurfactant or cryogel for heavy metal removal from wastewater.<sup>[26-28]</sup> These limited studies of heavy metal removal by gel materials are basically related to polymeric gels or high molecular weight gels. Contrary, in this report, a modified hydrophobic LMW organogel with a second component has been used for water remediation with increased adsorption capacity compared to previous limited reports. One major challenge to utilizing gels for water remediation is to stabilize the gels in the presence of excess water. Furthermore, the interactions of metal ions with a gelator system could be of two different types. One could be through forming covalent bonds and making coordination complexes, and the other could be loosely bound metal ions, mainly through non-covalent interactions. In the first case, recovering the heavy metal ions

are difficult after initial adsorption. So, for an application like water remediation, non-covalent interactions between gel materials and metal ions can be more helpful.

Out of many contaminations in water, heavy metal salts are very serious to human health. Heavy metals are considered to be those with a 5 gm/cm<sup>3</sup> density or more.<sup>[29]</sup> These are found to be toxic and carcinogenic, even at very low concentrations. This pollution mainly gets originates from the dumping of animal manure, sewage sludge, fertilizer, petroleum distillates waste, and pesticides. Many studies noted hazards of heavy metals impurities like Hg, Cd, Cu, Pb, Zn, etc., in contaminated water,<sup>[30,31]</sup> out of which the impurities of mercury, cadmium, and lead are the major health concerns for life. Hg<sup>2+</sup> can damage the nervous system and kidneys, Cd<sup>2+</sup> can cause damage to kidneys, bone, liver, and blood with its continuous exposure, and Pb<sup>2+</sup> causes damage to kidneys, liver, and learning difficulties.<sup>[32]</sup> As purification methods, adsorption by porous materials, membrane separation, electricity-driven removal, and several other chemical processes are reported,<sup>[33]</sup> adsorption is the most significant method because of no side product formation and is easy to prepare. Some notable ligand-based composite materials and optical sensors have also been reported to detect and remove Pb(II) and Cd(II) ions from contaminated water.<sup>[34-37]</sup> With constant endeavour to investigate metallogel formations and properties,<sup>[38-41]</sup> the potential applications of utilizing LMWGs for water remediation through heavy metal adsorption has been taken here. With a porous network that entraps solvent molecules, gels provide attractive scaffolds that capture various ions and molecules within the cavity, particularly when the entrapped solvent is driven off.<sup>[33]</sup> This can open the door to utilizing gels in environmental applications, specifically water remediation. Removing heavy metal ions from water is an important aspect that has been extensively studied recently.<sup>[24-27]</sup> However, while employing gels for such applications, it is required to fabricate a robust material that is not soluble in water, even partially.

In the recent past, one LMWG viz.  $N^2, N^4, N^6$ -tri(1*H*-tetrazol-5-yl)-1,3,5-triazine-2,4,6-triamine (**G8**) has been reported, which can be utilized to discriminate between isomers of amino pyridines through fluorometric investigations.<sup>[42]</sup> Interestingly the gel strength of **G8** is found to be moderate. However, **G8** is found to be non-stable when treated with excess water. This might be due to the presence of non-hydrogen bonded tetrazole rings in the periphery that interact extensively with excess water. It is strategized that the incorporation of a second organic molecule with hydrogen-bond donor-acceptor sites complementary to **G8** may enhance the gel strength and stability in water by reducing the excessive hydrogen bond interactions of **G8**. With this background a new molecule viz. 3,3',3''-(benzenetricarbonyltris(azanediyl))tris(4-aminobenzoic acid) (**Gel Enhancer or GE**) has been designed and synthesized. This work discusses the effect on gel formation and properties with **G8** in the presence of equimolar amounts of **GE**. As the resultant organogel is found to be stable in water, it tends to form metallogels with toxic heavy metal ions like Hg(II), Cd(II), and Pb(II); the gel was explored for capturing those heavy metal ions from their aqueous solutions as an effort towards water remediation. Interestingly, during the adsorption study, the properties of metallogels obtained were found to vary with different methods adopted for gel fabrication. Slow diffusion of metal ions through the gel was found to be more efficient than mixing the gelators and metal ions for the fabrication of metallogels in terms of the strength and stability of the resultant gels. There are no previous literature reports where modified hydrophobic organogel was used to remove Cl<sup>-</sup>, CH<sub>3</sub>COO<sup>-</sup>, and SO<sub>4</sub><sup>2-</sup> salts of Hg<sup>2+</sup>, Cd<sup>2+</sup>, and Pb<sup>2+</sup> with notable adsorption capacity. Other than this, the study has shown correlations between metallogel strengths and their fabrication methods. Herein, the remediation of water by xerogel **G8GE** has been further investigated by ICP-AES, PXRD, BET and XPS techniques.

## 5.2 Experimental section

### 5.2.1 Materials and methods

The chemicals used in this work, *viz.*, cyanuric chloride, i.e., 5-amino tetrazole monohydrate, 3, 4-diaminobenzoic acid, trimesoyl chloride, and heavy metal salts have been taken from commercial sources. DMSO/MQ-water or a mixture of solvents was used for experimental analysis. All the instruments used for experimental analysis related to FTIR, NMR, ESI-MS and FE-SEM are mentioned in section 2.2.1 of Chapter 2.

The removal of heavy metal ions from contaminated water has also been confirmed by analysis of the surface area of xerogel, done by Quantachrome, Autosorb iQ2 Brunauer–Emmett– Teller (BET) surface area analyzer. It is also examined by PXRD, XPS, and ICP-AES techniques.

### 5.2.2 Synthesis of gelator component **G8** [ $N^2, N^4, N^6$ -tri(1H-tetrazol-5-yl)-1,3,5-triazine-2,4,6-triamine] and **GE** [3,3',3''-(benzenetricarbonyltris(azanediyl)) tris (4-aminobenzoic acid)]

The gelator molecule **G8** was synthesized as a previously reported method<sup>38</sup>. For the synthesis of **G8**, 2.47 g (24 mmol) of the 5-amino tetrazole monohydrate and 3.34 mL, (24 mmol) of triethylamine were taken in 80 mL ethanol at ice-cooled condition, and 8 mmol (1.472 g) of solid cyanuric chloride was added into it by small portions. The reaction mixture was refluxed for 3 hrs at 80 °C. After the reaction was completed, the precipitate was filtered and washed with 3N HCl, water, and methanol before being dried at room temperature under vacuum, and the desired gelator molecule **G8** was obtained. Product yield 80%.

The synthesis of an organic molecule (**GE**) with carboxamide, amine, and carboxylic acid groups, has been designed, which can strategically enhance the physical and chemical properties of organogel **G8** by forming extensive hydrogen bonds. For the synthesis of 3,3',3''-(benzenetricarbonyltris(azanediyl))tris(4-aminobenzoic acid) as

gelation enhancer (**GE**) 1.82 g (12 mmol) of 3,4-diaminobenzoic acid and 1.67 mL (12 mmol) of triethylamine were taken in 50 mL of dry DCM and the mixture was added drop wise into 50 mL chloroform solution of 1.06 g (4 mmol) of trimesoyl chloride in ice-cooled condition. The reaction mixture was kept in this condition for one hour, and then the mixture was refluxed for 12 hours. After the reaction was completed, the precipitate was filtered and washed with 3N HCl and water before being dried at room temperature under vacuum. Product: yield: 83 %.  $^1\text{H}$  NMR (500 MHz, DMSO- $d_6$ )  $\delta$  ppm 10.46 (3 H), 8.69-8.62 (9 H), 8.19 (3 H), 7.81 (amine 6 H) and 6.82 (amide -NH proton).  $^{13}\text{C}$  NMR (126 MHz, DMSO- $d_6$ )  $\delta$  ppm 113.48 (6 C) 116.78 (6 C) 118.81 (3 C) 121.79 (3 C) 132.55 (3 C) 141.09 (3 C) 167.73 (3 C) 168.35 (3 C). FTIR of **GE**: 1700  $\text{cm}^{-1}$ , 1659  $\text{cm}^{-1}$ , 1602  $\text{cm}^{-1}$ , 1520  $\text{cm}^{-1}$ , 1428  $\text{cm}^{-1}$ , 1301  $\text{cm}^{-1}$ , 1225  $\text{cm}^{-1}$ . ESI-MS:  $m/z$   $[\text{M}+\text{H}]^+$  calculated for **GE** ( $\text{C}_{30}\text{H}_{25}\text{N}_6\text{O}_9^+$ ): 613.16, found 613.17.

### 5.2.3 Gels preparation

The synthesized molecule **3,3',3''-(benzenetricarbonyltris(azanediyl))tris(4-aminobenzoic acid)** behave like a gelation enhancer (**GE**) along with **G8**, which enhanced the strength and stability of gel even in water in comparison with the previously synthesized gel only out of **G8** ( $\text{N}^2, \text{N}^4, \text{N}^6$ -tri(1H-tetrazol-5-yl)-1,3,5-triazine-2,4,6-triamine). For the formation of **G8GE** organogel, 0.03 mmol of **G8** and 0.03 mmol of **GE** were solubilised in 1 mL of DMSO by heating. After a clear red-brown solution of **G8GE** was obtained, 1 mL Milli Q water was added. Instantaneously yellowish-brown coloured organogel has been formed. Similarly, 0.03 mmol of each gelation component (i.e., **G8** and **GE**) was dissolved in 1 mL DMSO by heating, and 0.03 mmol of heavy metal salt dissolved in 1 mL Milli Q water was added separately. After mixing red brown metallogels of **M1G8GECl<sub>2</sub>**, **M1G8GE(OAc)<sub>2</sub>**, **M1G8GESO<sub>4</sub>**, **M2G8GECl<sub>2</sub>**, **M3G8GECl<sub>2</sub>**, **M3G8GE(OAc)<sub>2</sub>**, have been fabricated where **M1**=  $\text{Hg}^{+2}$ , **M2**=  $\text{Cd}^{+2}$  and **M3**=  $\text{Pb}^{+2}$ . However, by this method, no metallogels formation was observed with  $\text{Cd}(\text{OAc})_2$  and  $\text{CdSO}_4$ . Similarly, for

metallogel formation by adsorption method, firstly, organogel **G8GE** was fabricated, and then 1 mmol of individual metal salt dissolved in 1 mL milli Q water was slowly added into the upper layer of the organogel of **G8GE**. After 24 hours, strong metallogels *viz.* **M1G8GECl<sub>2</sub>Ads**, **M1G8GE(OAc)<sub>2</sub>Ads**, **M1G8GESO<sub>4</sub>Ads**, **M2G8GECl<sub>2</sub>Ads**, **M2G8GE(OAc)<sub>2</sub>Ads**, **M2G8GESO<sub>4</sub>Ads**, **M3G8GECl<sub>2</sub>Ads** and **M3G8GE(OAc)<sub>2</sub> Ads** have been formed. All the gel formation has been confirmed by the test tube inversion method, where gels do not flow under the effect of gravitational force.

#### 5.2.4 Gel melting temperature

The melting temperatures of organogel and metallogels were obtained with the help of a silicon oil bath. 2 mL v/v gels in DMSO: H<sub>2</sub>O were formed in a 5 mL glass vial, a steel ball was placed on the gel surface, and the system was immersed in an oil bath. When the temperature started rising, and the gel started to melt (when any downward moment of steel ball is seen), that temperature was noted down as the melting temperature of the gel ( $T_{gel}$ ). The temperature at which gels start getting converted into sols can be seen with the help of a thermometer, which was dipped in an oil bath. After the complete conversion of the gel into sol, heating was turned off. After 10 min the sol was again converted into a gel, showing the gel-sol-gel transition property of gel.

#### 5.2.5 Characterization

The FTIR spectra, UV-vis analysis, NMR studies, powder X-ray diffraction, morphological and rheological analysis of gelator molecules **G8** and **GE**, xerogel of organogel **G8GE**, metallogels **M1G8GECl<sub>2</sub>**, **M1G8GE(OAc)<sub>2</sub>**, **M1G8GESO<sub>4</sub>**, **M2G8GECl<sub>2</sub>**, **M3G8GECl<sub>2</sub>**, **M3G8GE(OAc)<sub>2</sub>**, have been done in similar ways as mentioned in section 2.2.5 of chapter 2.

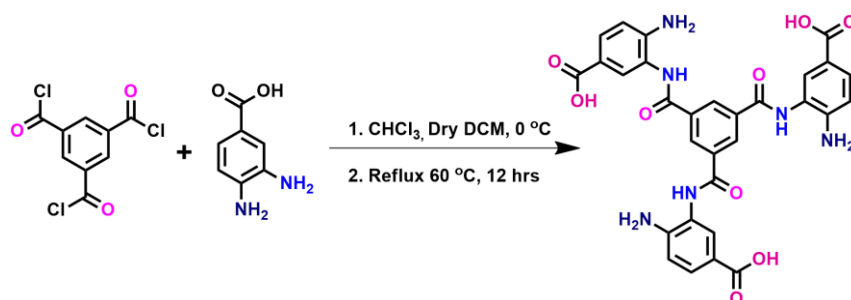
The interaction ratio between **G8:GE** and all the studies related to fluorescence data have been recorded with a Fluoromax-4 spectrofluorometer (HORIBA Jobin Yvon, model FM-100) in a quartz cuvette (10 mm × 10 mm). Removal of heavy metal ions from

contaminated water, recyclability of **G8GE** towards separation, and water remediation at different pH, from acidic to basic, have been studied by ICP-AES analysis. The surface area changes during the removal of heavy metal ions have been analysed by BET and XPS analysis.

### **5.3 Results and discussion**

Water is an essential part of our life. Contamination of water bodies by various pollutants like heavy metals is a challenging issue, and developing suitable materials to reduce such pollution is getting researchers' attention worldwide. There are many reports on removing heavy metal contamination from water by nanocomposite powder and other hybrid materials.<sup>[43-46]</sup> Out of those adsorbents, the new material for water purification as adsorbent, i.e., gels, is introduced with its great sensitivity towards metal ions and its heterogenous nature within the water system. In this Chapter, the synthesis of the organic molecule **GE** is strategized as it contains carboxamide, amine, and carboxylic acid sites with the chances of generating extensive hydrogen bonds. For the synthesis of gelation enhancer (**GE**), diaminobenzoic acid and triethylamine were taken in 50 mL of dry DCM, and the mixture was added dropwise into 50 mL of a chloroform solution of trimesoyl chloride in an ice-cooled condition. The reaction mixture was kept in this condition for one hour, and then the mixture was refluxed for 12 hours. After the reaction was completed, the precipitate was filtered and washed with 3N HCl and water before being dried at room temperature under a vacuum (Scheme 5.1). **GE** is characterized by ESI-MS, FTIR, CHN elemental analysis, <sup>1</sup>H, and <sup>13</sup>C NMR spectroscopy. The IR spectrum of **GE** molecule reveals characteristic band for carboxylic acid C=O at 1700 cm<sup>-1</sup>, carboxamide C=O at 1659 cm<sup>-1</sup>, amide N-H at 1602 cm<sup>-1</sup>, primary amine N-H at 1520 cm<sup>-1</sup>, and presence of C-O at 1225 cm<sup>-1</sup> (Figure 5.1). In <sup>1</sup>H NMR spectrum, the carboxylic acid proton was observed at 10.46 ppm, aromatic protons were observed within the range of 8.69- 8.19 ppm, primary amine protons observed at 7.81 ppm and amide -NH proton was found at 6.82 ppm (Figure 5.2). In <sup>13</sup>C NMR, the

peak for carboxylic carbon was found at 168.35, for carboxamide carbon at 167.73, and all the aromatic carbons were found between 141.09 to 113.48 ppm (Figure 5.3). The ESI-MS spectrum shows the molecular ion peak at 613.17 in positive mode, confirming the synthesis of **GE** (Figure 5.4). The CHN elemental analysis has been done for **GE**. The calculated values for C, N, and H are 58.82 %, 13.72 %, 3.95 % respectively and the found values for C, N, and H are 58.63 %, 13.75 % and 3.91 % respectively.



*Scheme 5.1. Synthesis of gelator enhancer **GE**.*

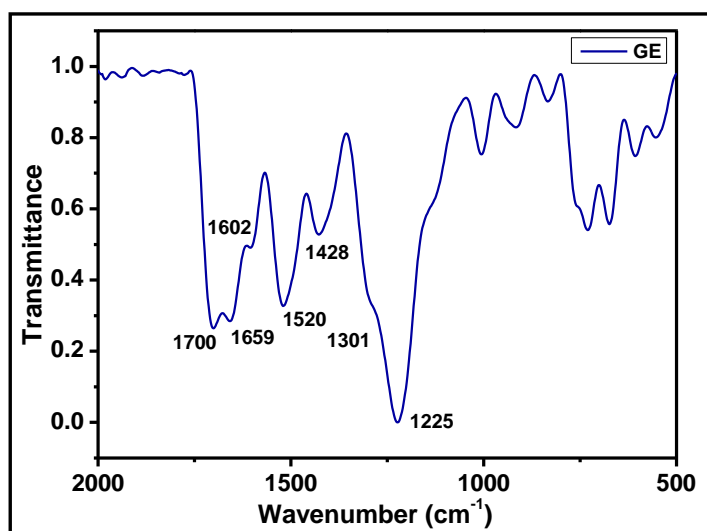


*Figure 5.1. FTIR data of gelator enhancer molecule **GE**.*

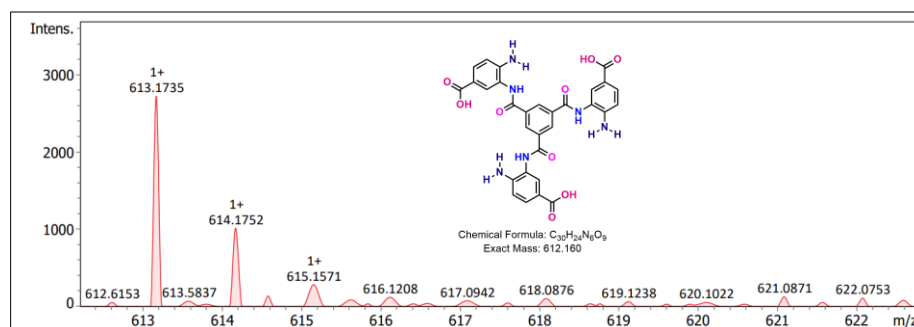


*Figure 5.2. ESI-MS data of gelator component **GE**.*

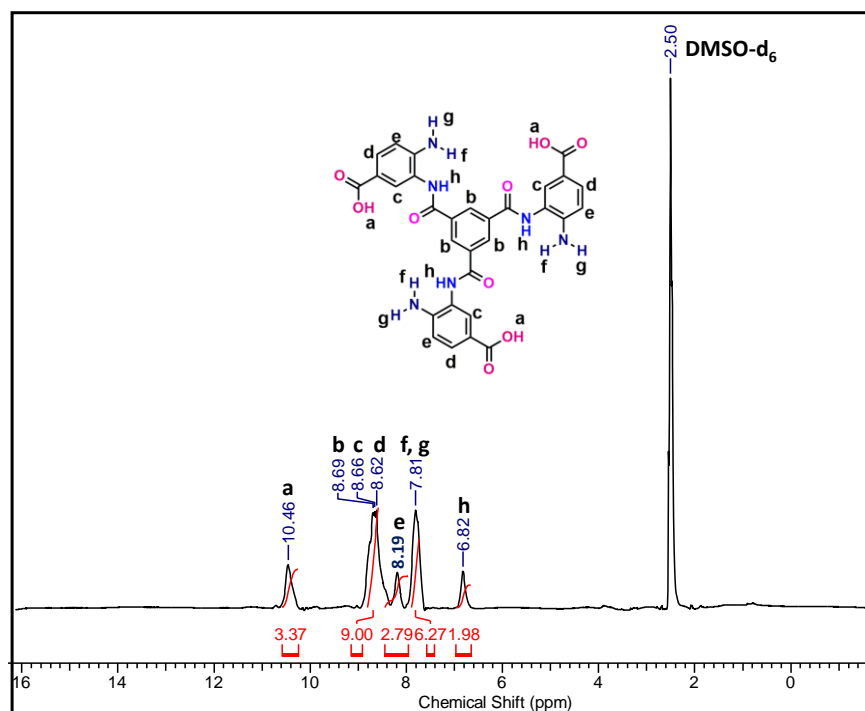


Figure 5.3.  $^1\text{H}$  NMR data of gelator component **GE**.

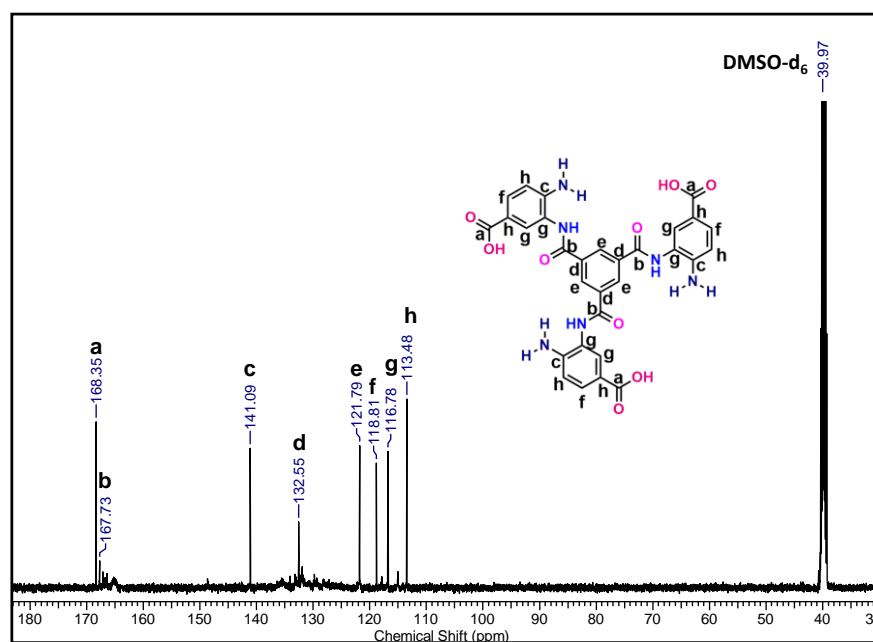
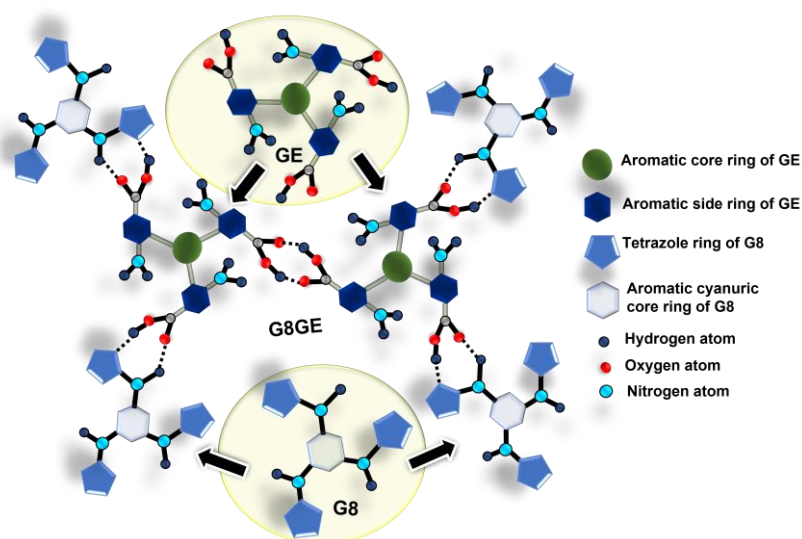


Figure 5.4.  $^{13}\text{C}$  NMR data of gelator component **GE**.

However, no suitable solvent or solvent composition was found that can allow **GE** to form a stable gel, albeit a robust one. Therefore, the study of the influence of **GE** in the fabrication of gel with previously synthesized gelator molecule **G8** has been investigated. This could be easily noted that the hydrogen-bond formations could be complementary between **G8** and **GE** (Scheme 5.2). As expected, the interaction of **G8**

with **GE** gave a water-stable organogel **G8GE**. It also shows metallo gel fabrication with heavy metal salts by mixing gel components in DMSO: H<sub>2</sub>O mixture and metallo gels **M1G8GECl<sub>2</sub>**, **M1G8GE(OAc)<sub>2</sub>**, **M1G8GESO<sub>4</sub>**, **M2G8GECl<sub>2</sub>**, **M3G8GECl<sub>2</sub>**, **M3G8GE(OAc)<sub>2</sub>** are obtained. Interestingly in these cases, the strength of the gel was found to be decreased with the incorporation of metal ions, which is the reverse of the general trend.<sup>[47,48]</sup> It signifies that the non-covalent interactions between **G8** and **GE** molecules get disturbed by the insertion of metal salts with mixing. To overcome this disturbance, the unique approach of allowing the metal ions to diffuse through the bulk gel materials has taken in a layering technique, revealing the increased storage modulus of metallo gels compared to organogel and mixed metallo gels. This observation also led to the application of mixed organogel in heavy metal adsorption from aqueous solution. This will open the door to utilizing this untapped technique for water remediation.



*Scheme 5.2. G8 and GE showing alternative hydrogen bond donor-acceptor sites.*

**Critical gel concentration, hydrophobic and shape forming nature of organogel G8GE and their metallo gel formation with heavy metal salts.** In Chapter 3, it is mentioned that **G8** could form a gel with DMSO and H<sub>2</sub>O mixture, but it has also been observed to become soluble in water after sonication. When **G8** and **GE** are dissolved in 1 mL of DMSO, and 1 mL of H<sub>2</sub>O is added into it, rapid gel formation occurs.

This gel has been found to be hydrophobic in nature. It was not soluble in water, even after sonication or stirring for an extended period. Notably, very minimum concentrations of **G8** and **GE** can also show gel formation. To get the CGC values of organogel **G8GE**, different amounts of **G8** and **GE** were taken from 0.01 to 0.1 mmol with a constant volume ratio of DMSO: H<sub>2</sub>O, taking each solvent of 1 mL of volume. It was found that even 0.01 mmol (3 mg) of **G8** and 0.01 mmol (6 mg) of **GE** in 2 mL DMSO: H<sub>2</sub>O mixture formed a transparent yellowish-brown gel. Therefore, the CGC for **G8GE** is 10 mM (0.01 mmol per mL) (Figure 5.5). Attempts to fabricate gel with a lower concentration of **G8** and **GE** were unsuccessful.

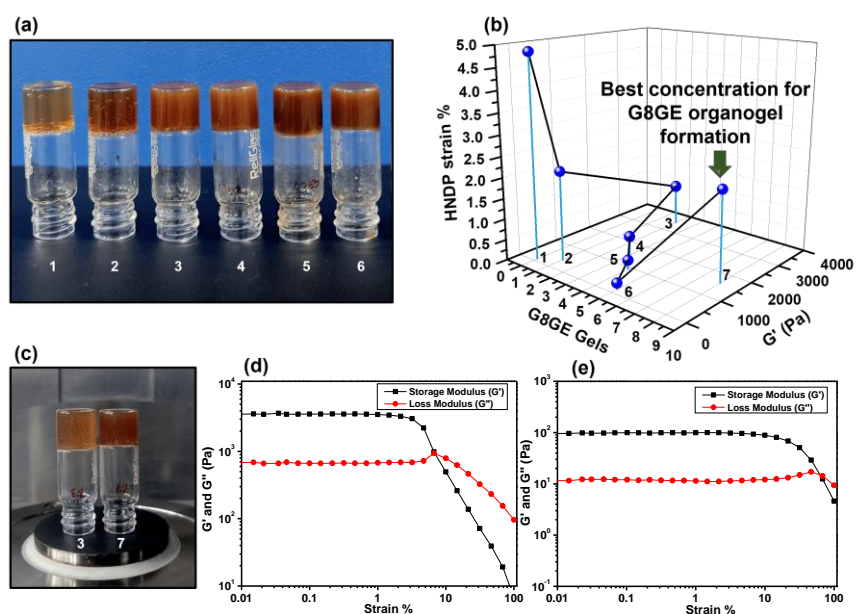


**Figure 5.5.** (a) Formation of gel **G8GE** at different concentration (b) 3D graph showing best gelation concentration for **G8GE** organogel (c) images of organogel **G8GE** at 1:1 and 3:2 ratio (d) linear viscoelastic (LVE) experiment for **G8GE** at 0.03: 0.03 mmol condition (e) LVE experiment for **G8GE** at 0.03: 0.02 mmol condition.

The Job plot, for which the fluorescence experiment has been done, has suggested that the ratio of the interaction of **G8:GE** is maximum at 3:2, so the **G8GE** organogel was fabricated at a 3:2 ratio, i.e., with 0.03 and 0.02 mmol, respectively. However, the rheological experiments done with organogel **G8GE** in different concentrations starting from 0.01 to

0.1 mmol indicated that the most effective concentration for the strongest gel formation is a 1:1 ratio of **G8** and **GE** with 0.03 mmol of each in 2 mL of DMSO: H<sub>2</sub>O mixture (Figure 5.6-5.8, Table 5.1).

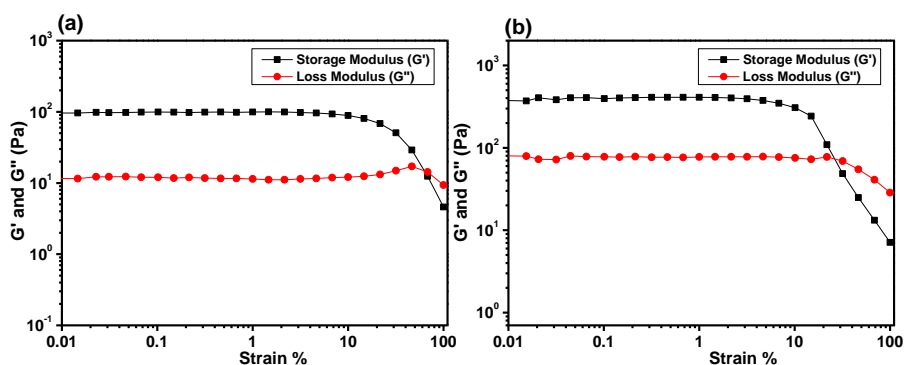


**Figure 5.6.** Angular sweep experiment of organogel **G8GE** with (a) 0.01: 0.01 mmol (b) 0.02: 0.02 mmol in 1:1 ratio of 2 mL DMSO: H<sub>2</sub>O mixture.

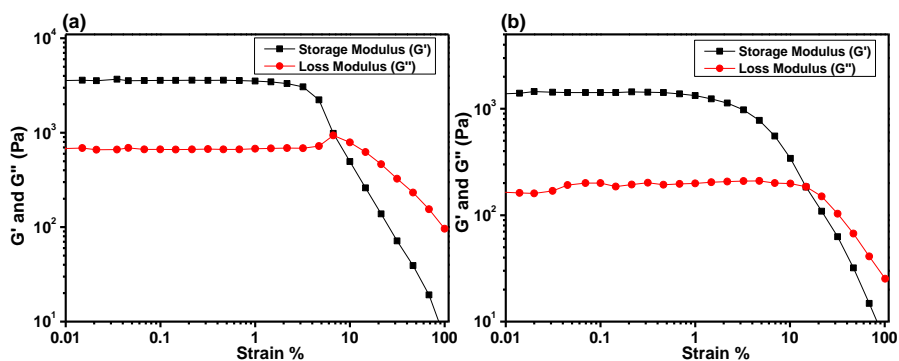


**Figure 5.7.** Angular sweep experiment of organogel **G8GE** with (a) 0.03: 0.03 mmol (b) 0.04: 0.04 mmol in 1:1 ratio of 2 mL DMSO: H<sub>2</sub>O mixture.

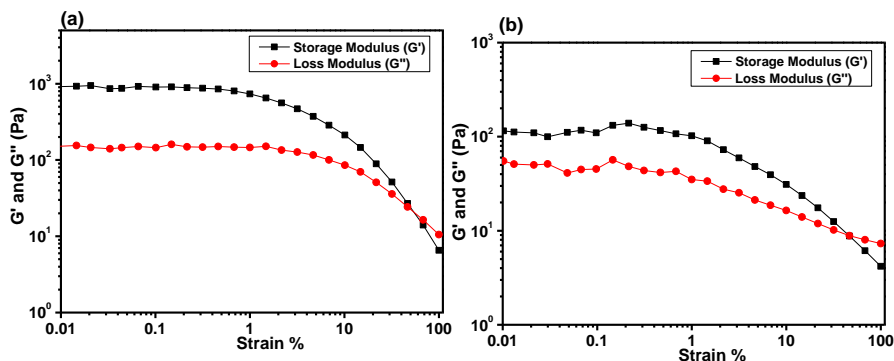


**Figure 5.8.** Angular sweep experiment of organogel **G8GE** with (a) 0.07: 0.07 mmol (b) 0.1: 0.1 mmol in 1:1 ratio of 2 mL DMSO: H<sub>2</sub>O mixture.

**Table 5.1.** Concentration dependent rheological study of organogel **G8GE**.

S. No.	mmol of G8	mmol of GE	Ratio of G8 and GE	Observation in DMSO: H <sub>2</sub> O (1: 1 mL)	Value of G'	Value of crossover point	Non- deformation range
1	0.01	0.01	1:1	Gel	95 Pa	68 strain %	0.01- 4.85 strain %
2	0.02	0.02	1:1	Gel	392 Pa	26 strain %	0.01- 2.16 strain %
3	0.03	0.03	1:1	Strong Gel	3517 Pa	6 strain %	0.01- 1.01 strain %
4	0.04	0.04	1:1	Strong Gel	1456 Pa	14 strain %	0.01- 0.47 strain %
5	0.07	0.07	1:1	Gel	922 Pa	47 strain %	0.01- 0.22 strain %
6	0.1	0.1	1:1	Gel	144 Pa	46 strain %	0.01- 0.15 strain %
7	0.03	0.02	3:2	Strong Gel	1593 Pa	25 strain %	0.01- 2.16 strain %

Previously, organogel **G8** has been fabricated, which was found to be less stable in water than the mixed organogel **G8GE** reported here. The hydrophobicity of the fabricated gel was checked with the addition of **G8GE** gel in water in a beaker with the help of a syringe, and it was found that the drops of gel formed a flat circular disc-like shape within the water layer. After adding several drops, many such disc-shaped structures can be seen inside the water and separated from each other. Its hydrophobicity was also checked by making a circle with gel in a Petridis containing water. The formed structures within the water layer remain as such, with no apparent change in shape or size, indicating the hydrophobic nature of the gel system. The organogel **G8GE** has soft, flexible nature, because of which it can be shaped into different structures. The metallogel formation has been explored with **G8GE**, and it was found that with a suitable proportion of gelator components and metal salts, the fabrication of gels can be achieved with HgCl<sub>2</sub>, Hg(OAc)<sub>2</sub>, HgSO<sub>4</sub>, CdCl<sub>2</sub>, PbCl<sub>2</sub> and Pb(OAc)<sub>2</sub>. However, no gel formation was observed with Cd(OAc)<sub>2</sub> and CdSO<sub>4</sub>; instead, gelatinous solutions were obtained, indicating the involvement of the counter-anions as well. Another method has been used to form metallogels, i.e., the adsorption method by which the metallogel fabrication has been

carried out with all three heavy metals (Hg, Cd, and Pb) salts. It is fascinating to note that in these cases, the metallogels formed by the adsorption method have shown much higher strengths with respect to the metallogels obtained by simple mixing (Figure 5.9).

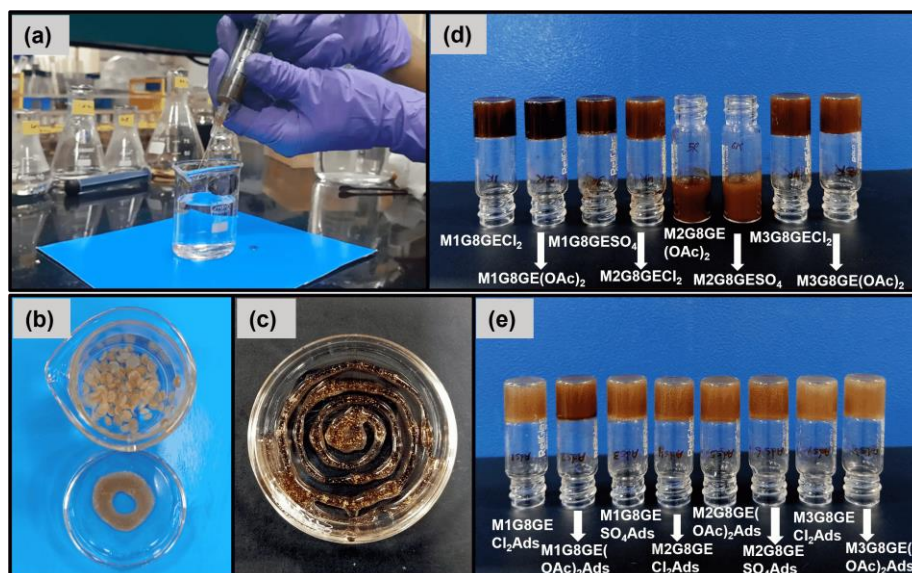


**Figure 5.9.** (a) Addition of organogel **G8GE** in water by syringe (b) Image showing hydrophobic nature of **G8GE** gels in water (c) shape formation showing soft and viscoelastic nature of gel (d) formation of metallogel of **G8GE** with heavy metal salts by mixing (e) formation of metallogel of **G8GE** with heavy metal salts by adsorption method.

**Fluorescence behaviour of gelator components, organogel, metallogels and notable difference by gelation method.** The spectroscopic study of each **G8**, **GE**, and **G8GE** gives interesting results. The molecule **G8** with a broad UV-Vis peak in solution around 335 nm has shown a fluorescence peak at 445 nm with moderate intensity when excited at 350 nm.<sup>[42]</sup> The UV-Vis data of **GE** also shows a broad UV-Vis peak around 328 nm, and at 350 nm excitation, it gives a fluorescence peak at 428 nm in DMSO: H<sub>2</sub>O solvent system. When the UV-Vis analysis was done for the gel made from **G8GE**, a broad UV-Vis peak was found at around 330 nm, which shows an emission peak at 431 nm when excited at 350 nm excitation wavelength. (Figure 5.10). The synthesized gelator enhancer **GE** shows moderate fluorescence

(emission wavelength 428 nm), which is a little bit stronger than the **G8** molecule (emission wavelength 435 nm) (Figure 5.11).

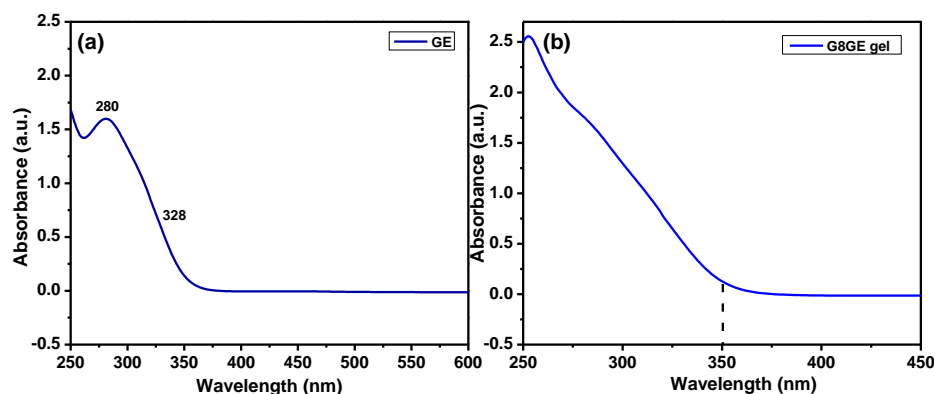


**Figure 5.10.** UV-Vis spectrum of (a) **GE** and (c) **G8GE**.

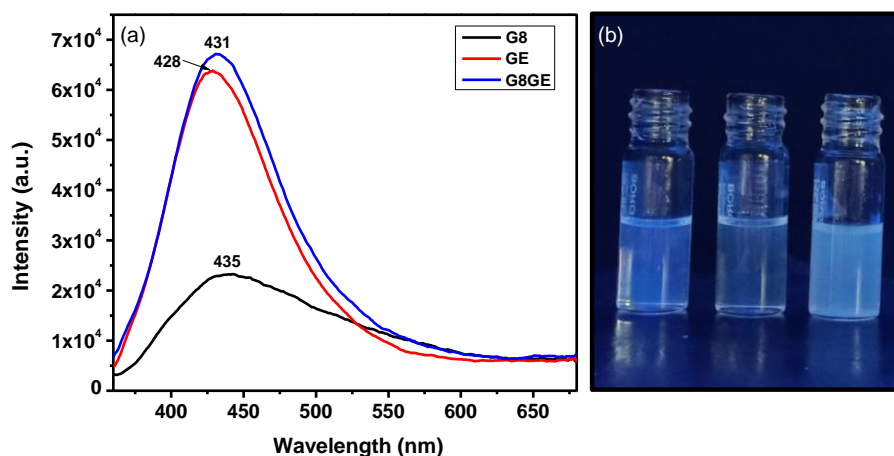


**Figure 5.11.** Fluorescence spectrum of (a) **G8**, **GE**, **G8GE** at excitation wavelength of 350 nm (b) 1 mM solution of **G8**, **GE** and **G8GE** under UV chamber.

However, in **G8GE** where the interaction of **G8** and **GE** occurs, some intramolecular motions get restricted due to the formation of non-covalent interactions between these two gelator components. As a result, the fluorescence gets increased. The data were recorded with **G8GE** solution, **G8GE** gel, and metallogels. It was found that the fluorescence intensity was different with different conditions. When 1 mM DMSO: H<sub>2</sub>O solution of **G8** (2 mL), **GE** (2 mL), and **G8GE** (1:1 mL) was analysed by fluorescence experiment, the relative intensity was found in the order of **G8**<**GE**<**G8GE** with the  $\lambda_{\text{max}}$  values at 435 nm, 428 nm,

431 nm, respectively (Figure 5.12, a). While the same experiment, when done only in DMSO, the relative intensity order remains the same while the  $\lambda_{\max}$  values change to 432 nm, 409 nm, 419 nm, respectively (Figure 5.12, b). The values of  $\lambda_{\max}$  are greater in the case of DMSO: H<sub>2</sub>O as compared to only DMSO, indicating intramolecular charge transfer (ICT) within the molecules where the wavelength increases with increasing the polarity of the solvent.<sup>[49-51]</sup> The fluorescence intensity and wavelength got affected by the solvents system, which has been confirmed by fluorescence analysis of 0.3 mM **G8GE** solution in DMSO and in the solvent combinations (1:1) of DMSO: EA, DMSO: DMF, DMSO: MeCN, DMSO: MeOH, DMSO: EtOH and DMSO: H<sub>2</sub>O. In the case of polar aprotic solvents, the intensity was much higher than polar protic solvents with lower wavelengths of  $\lambda_{\max}$  values (Figure 5.13). The driving force behind such observation might be the hydrogen bond formation in polar protic solvents with **G8** and **GE** gelation components. This led to disturbances in the interactions of **G8** and **GE**, resulting in a decrement in fluorescence. The solution of **G8GE** also shows aggregation-induced enhanced emission (AIEE).<sup>[52]</sup> For this, 1 mM solution of **G8GE** in DMSO: H<sub>2</sub>O mixture has been taken as a stock solution, and the fluorescence intensity has been found to be increased with increasing concentration. This might be due to the restriction in intermolecular rotation with the aggregation of **G8GE** molecules (Figure 5.12c). Interaction of **G8** with **GE** by Job plot indicated that 0.4 mole fraction of **GE** shows higher fluorescence intensity. Therefore, the interaction ratio for **G8:GE** is 3: 2 (Figure 5.12d).

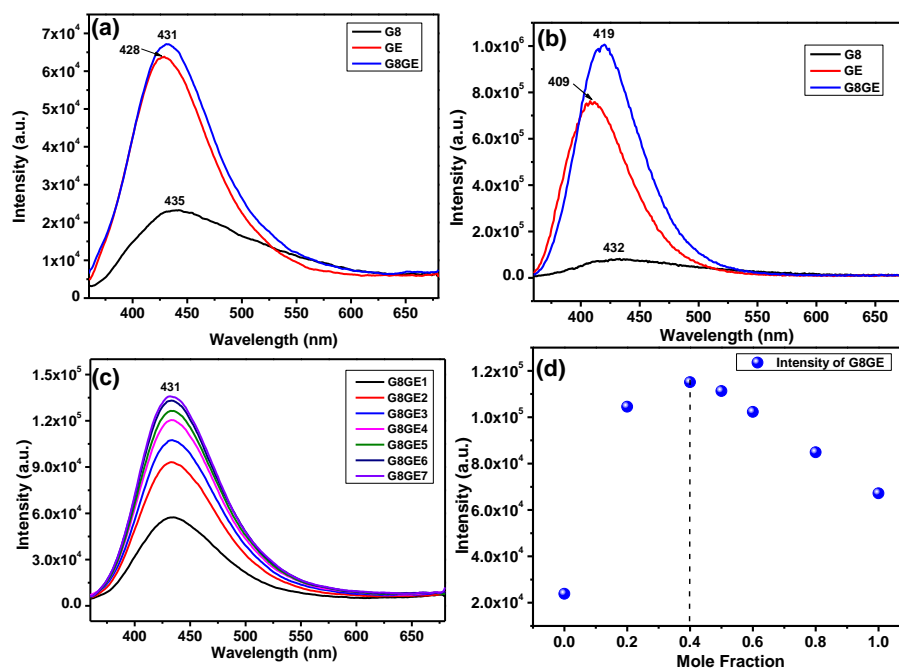


**Figure 5.12.** (a) Fluorescence analysis of **G8**, **GE** and **G8GE** in DMSO:  $H_2O$  mixture (b) Fluorescence analysis of **G8**, **GE** and **G8GE** in DMSO (c) AIEE phenomenon for **G8GE** gelation component and (d) Job plot showing ratio of interaction between **G8** and **GE**.

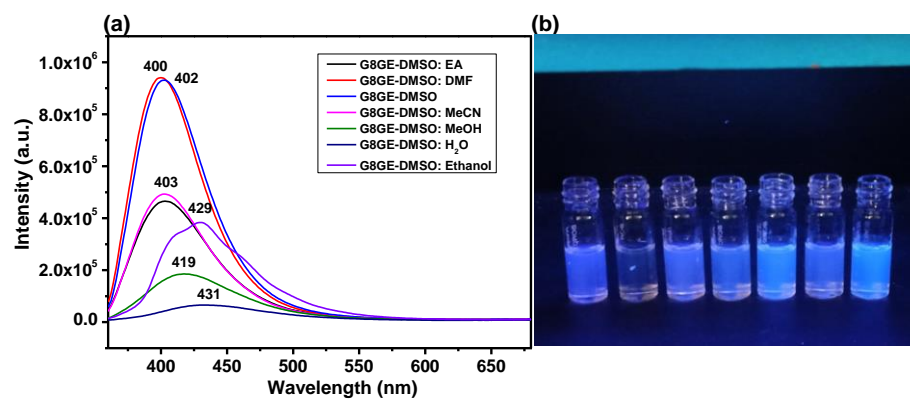


**Figure 5.13.** (a) Fluorescence study of **G8GE** gelator component with different polar protic and polar aprotic solvents (b) 0.03 mM solution of **G8GE** component in different solvents under UV chamber.

Fluorescence experiments were also done with dissolving organogel and metallogels in DMSO. As a general methodology, 50 mg of gel which was formed by mixing, was dissolved in 3 mL of DMSO, and fluorescence data were recorded with 350 nm excitation. It was found that the intensity of **G8GE** gel was greater than other metallogels, and

in the case of **M1G8GE(OAc)<sub>2</sub>**, it was almost quenched. However, the fluorescence data of metallo gels formed by adsorption shows increased fluorescence intensities compared to mixed metallo gels (Figure 5.14). The reason might be the disturbances created by the metal insertion in the assembly of **G8GE** molecules during its mixing. However, in the case of adsorption-based gels, metal ions are allowed to take favourable positions within the gel matrix without much disturbance and, thus, reinforcing the assembled structures making the fluorescence intensities stronger. To understand the influence of Hg(II) on the fluorescence property of **G8GE**, 1 mM solution of organogel in DMSO was treated with increasing concentration of Hg(II) by gradual addition of 1 mM solution of HgCl<sub>2</sub> in H<sub>2</sub>O in a constant volume. With the decreasing amount of **G8GE** and an increasing amount of HgCl<sub>2</sub>, a significant decrement in fluorescence with a slight bathochromic shift is observed. Similarly, when the same experiment was carried out by dissolving **G8GE** and mercury salt in a 1: 1 mixture of DMSO and H<sub>2</sub>O, a similar observation was recorded (Figure 5.15). The data indicate that the incorporation of metal ions interferes with the non-covalent bonding between **G8** and **GE**.

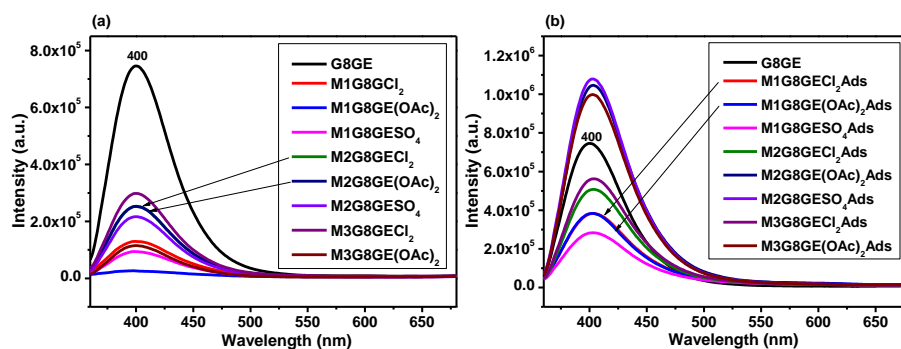


**Figure 5.14.** Fluorescence study of **G8GE** organogel and metallo gels formed by (a) mixing method and (b) adsorption method.

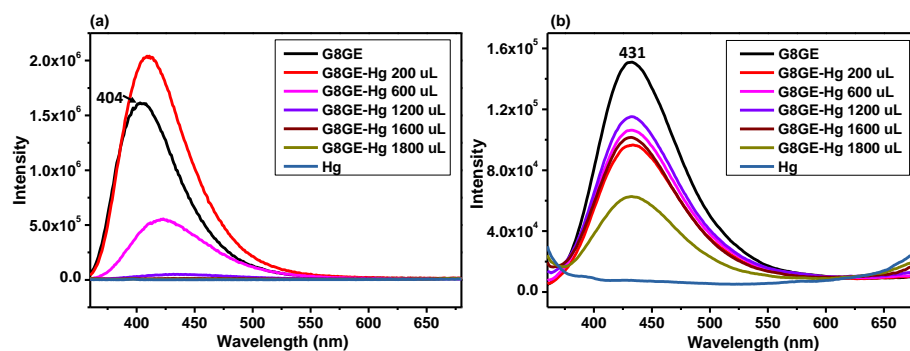


**Figure 5.15.** Fluorescence study of (a) 1 mM solution of **G8GE** (in DMSO) and  $\text{HgCl}_2$  (in  $\text{H}_2\text{O}$ ) and (b) 1 mM solution of **G8GE** (in DMSO:  $\text{H}_2\text{O}$ ) and  $\text{HgCl}_2$  (in DMSO:  $\text{H}_2\text{O}$ ).

**Morphological analysis of organogel and metallogel of G8GE.** The morphology of **G8** organogel was found to be a continuous tiny fibres-like structure, as reported in previous work.<sup>[42]</sup> When the **G8** molecules are combined with **GE**, a drastic change was observed in the morphology. Interestingly, morphology changes are also observed with the **G8** and **GE** ratio alteration. When the gel is formed with 0.03 mmol of each of **G8** and **GE** in 2 mL of DMSO- $\text{H}_2\text{O}$  solution, the morphology reveals nano-branched thread-like structures connecting to make a net of gel fibers. However, in higher concentrations with 0.1 mmol of each of **G8** and **GE**, it shows nano threads-like structures which are closely packed within the 3D network of gel. These indicate that branches in higher concentrations of gel are closely packed to cover a wider area as connected with nano-threads (Figure 5.16). These 3D changes in morphology from organogel **G8** (continuous tiny fibres-like structure) to mixed organogel **G8GE** (nano-branched threads) reveal that the self-assembly of **G8GE** forms a more robust gel network.

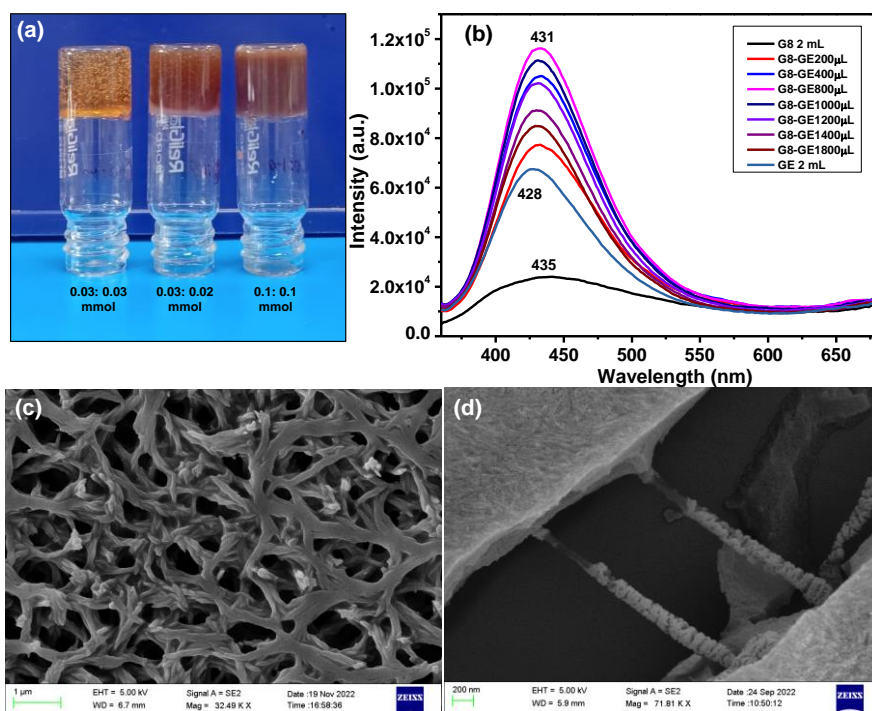


**Figure 5.16.** (a) Organogel **G8GE** at different concentration (b) Ratio of interaction of **G8** and **GE** (c) FE-SEM image of **G8GE** (gel of 0.03: 0.03 mmol of **G8** and **GE**) and (d) FE-SEM image of **G8GE** (gel of 0.1: 0.1 mmol of **G8** and **GE**).

Further, the formation of metallo gels of **G8GE** with heavy metal salts also shows 3D nanostructured metallo gel fabrication. The FE-SEM images confirmed that the metallo gel morphologies are different when fabricated following different methods, i.e., mixing and adsorption methods. The mixing method furnished metallo gel **M1G8GECl<sub>2</sub>** with sharp leaf and flower pattern, **M1G8GE(OAc)<sub>2</sub>** with flowers-like morphology, **M1G8GESO<sub>4</sub>** and **M2G8GECl<sub>2</sub>** with network structure of threads. Leaf-like closely packed structure attached to each other was obtained for **M2G8GE(OAc)<sub>2</sub>** while in **M2G8GESO<sub>4</sub>**, **M3G8GECl<sub>2</sub>** and **M3G8GE(OAc)<sub>2</sub>** dense fibrous morphology are recorded (Figure 5.17). The metallo gel fabricated by adsorption methods shows dense fibrous morphology for all the cases. This signifies that with this method, metal ions do not disturb the **G8GE** gel matrix significantly (Figure 5.18). EDX and mapping analysis has been done and found the presence of respective elements inside the gel matrix (Figure 5.19-5.26).

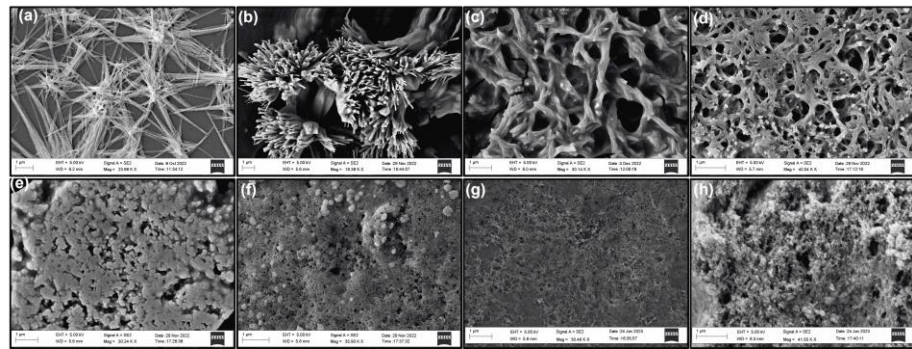


**Figure 5.17.** FE-SEM images of (a)  $M1G8GEC1_2$  (b)  $M1G8GE(OAc)_2$  (c)  $M1G8GESO_4$  (d)  $M2G8GEC1_2$  (e) Gelatinous solution of  $M2G8GE(OAc)_2$  (f) Gelatinous solution of  $M2G8GESO_4$  (g)  $M3G8GEC1_2$  and (h)  $M3G8GE(OAc)_2$ .

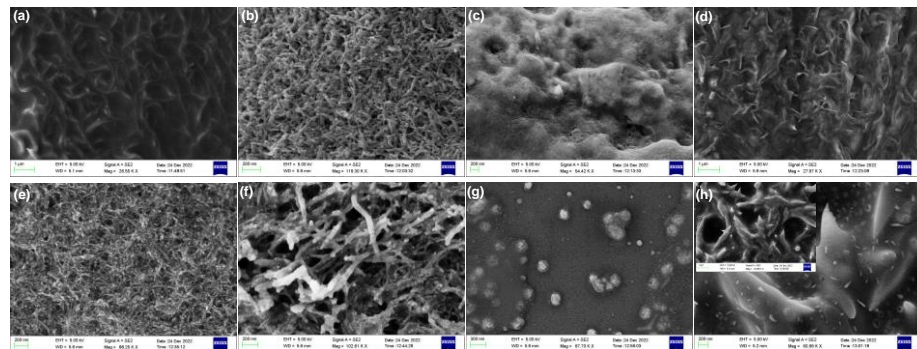


**Figure 5.18.** FE-SEM images of (a)  $M1G8GEC1_2Ads$  (b)  $M1G8GE(OAc)_2Ads$  (c)  $M1G8GESO_4Ads$  (d)  $M2G8GEC1_2Ads$  (e)  $M2G8GE(OAc)_2Ads$  (f)  $M2G8GESO_4Ads$  (g)  $M3G8GEC1_2Ads$  and (h)  $M3G8GE(OAc)_2Ads$  formed by adsorption method.

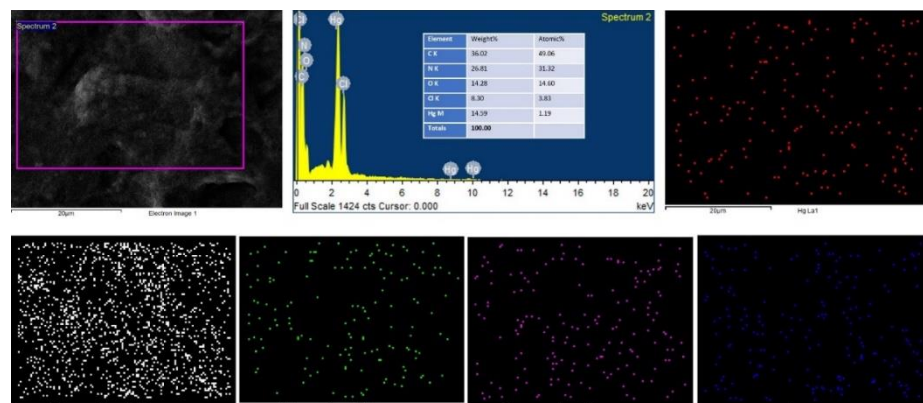


**Figure 5.19.** EDX and Mapping analysis of  $M1G8GEC1_2$  showing the presence of C, N, O, Hg and Cl inside gel matrix.

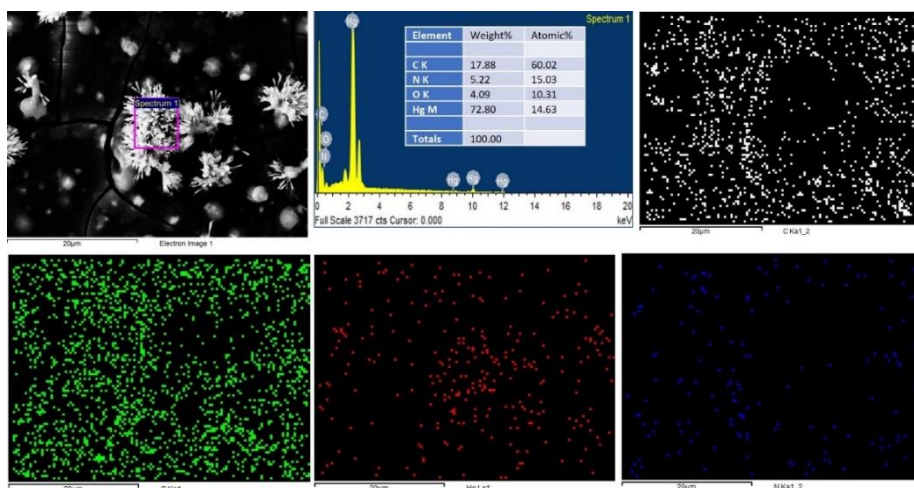


**Figure 5.20.** EDX and Mapping analysis of  $MIG8GE(OAc)_2$  showing the presence of C, N, O and Hg inside gel matrix.

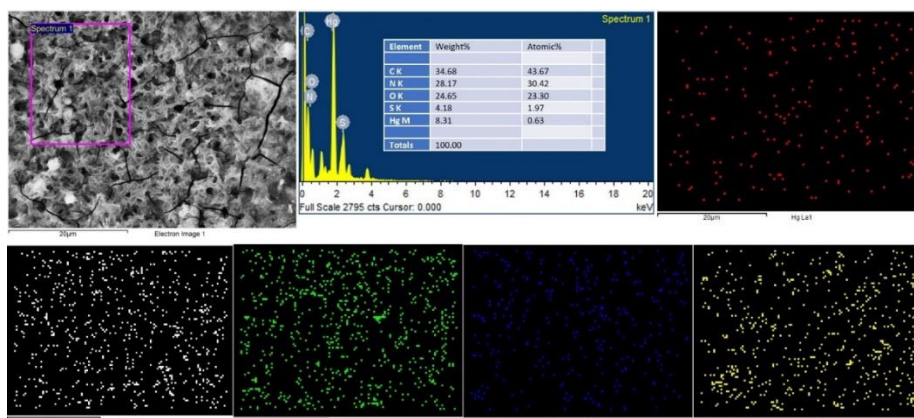


**Figure 5.21.** EDX and Mapping analysis of  $MIG8GESO_4$  showing the presence of C, N, O, Hg and S inside gel matrix.

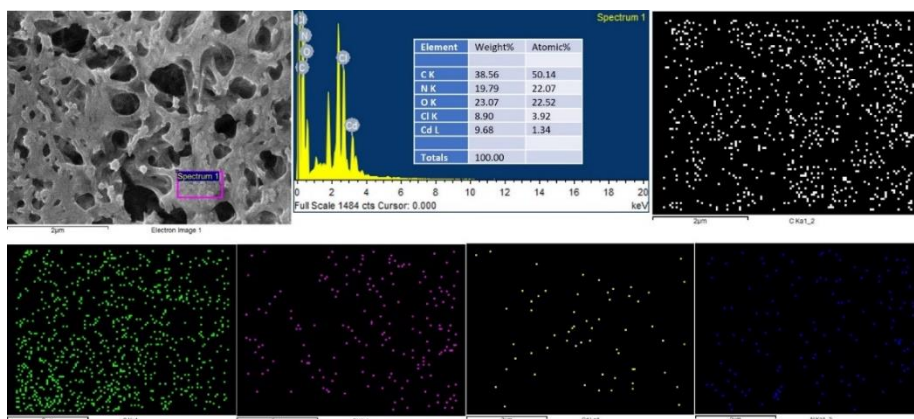


**Figure 5.22.** EDX and Mapping analysis of  $M2G8GECl_2$  showing the presence of C, N, O, Cd and Cl inside gel matrix.

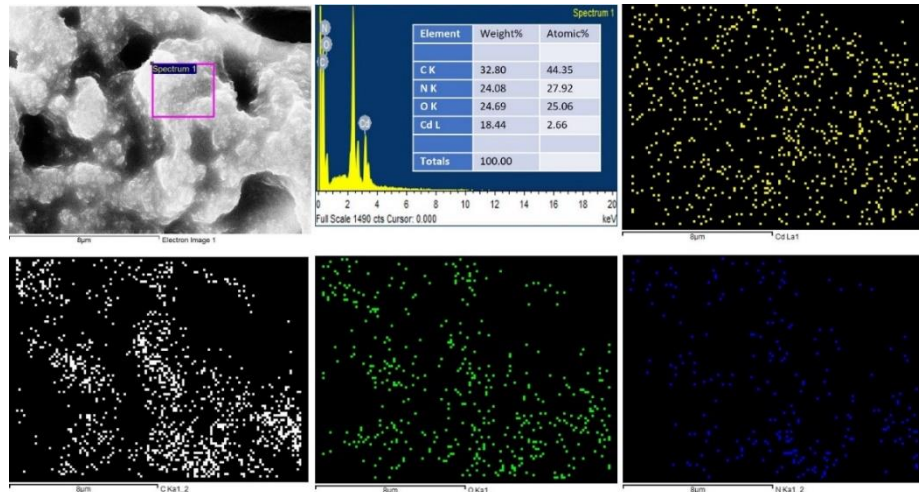


**Figure 5.23.** EDX and Mapping analysis of  $M2G8GE(OAc)_2$  showing the presence of C, N, O and Cd inside gel matrix.

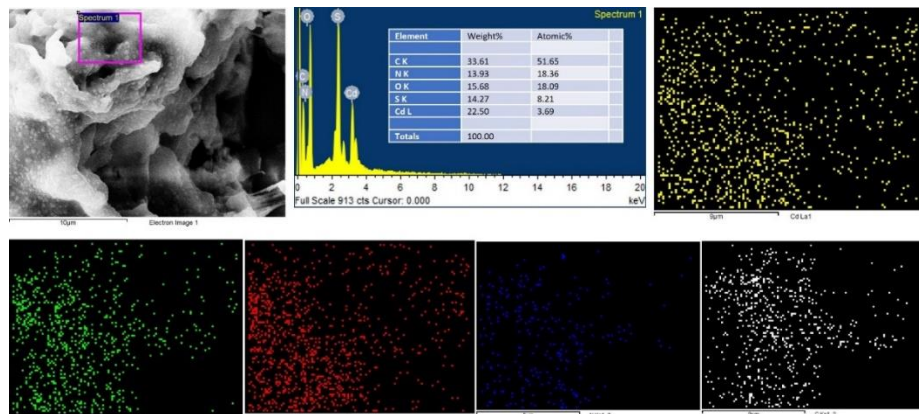


**Figure 5.24.** EDX and Mapping analysis of  $M2G8GESO_4$  showing the presence of C, N, O, Cd and S inside gel matrix.

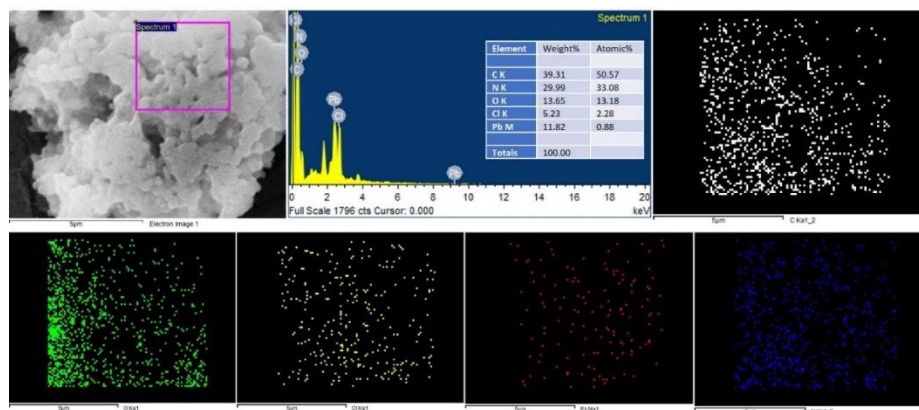


**Figure 5.25.** EDX and Mapping analysis of  $M3G8GECI_2$  showing the presence of C, N, O, Pb and Cl inside gel matrix.

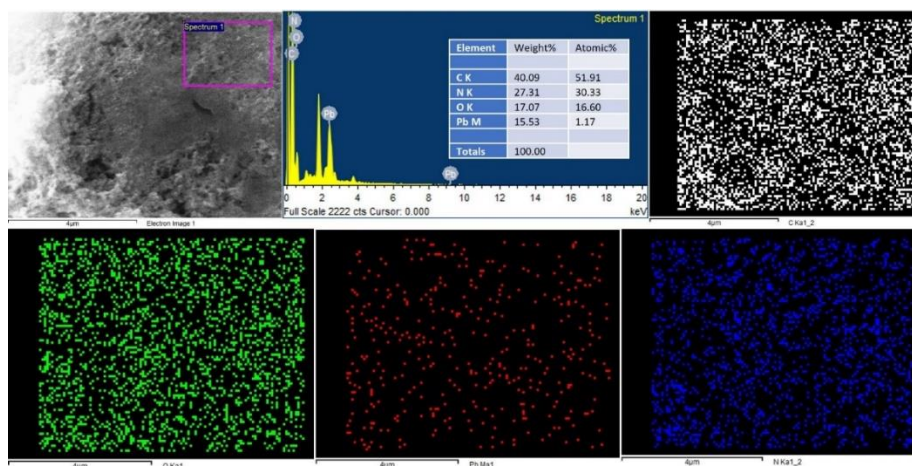


**Figure 5.26.** EDX and Mapping analysis of  $M3G8GE(OAc)_2$  showing the presence of C, N, O and Pb inside gel matrix.

### Effect of method of gel formation on their rheological properties.

The rheological study was taken up to find out the relative gel strength. A significant difference was found between the gel strength of previously fabricated organogel **G8** and the modified organogel **G8GE**. The value of storage modulus ( $G'$ ) for **G8** was  $236 \text{ Pa}$ <sup>[42]</sup> while the value for **G8GE** (0.03: 0.03 mmol, 1:1 ratio) is  $3517 \text{ Pa}$  and  $1593 \text{ Pa}$  for 3:2 (0.03: 0.02 mmol) of **G8**: **GE** (Figure 5.27). When metallogels were formed by the mixing method, the value of storage modulus ( $G'$ ) for **M1G8GECl<sub>2</sub>**, **M1G8GE(OAc)<sub>2</sub>**, **M1G8GESO<sub>4</sub>**, **M2G8GECl<sub>2</sub>**, **M3G8GECl<sub>2</sub>** and **M3G8GE(OAc)<sub>2</sub>** are found to be  $1976$ ,  $189$ ,  $4838$ ,  $176$ ,  $140$  and  $2646 \text{ Pa}$  respectively indicating the role of counter anions in the gel strength (Figure 5.28- 5.33 and Table 5.2).

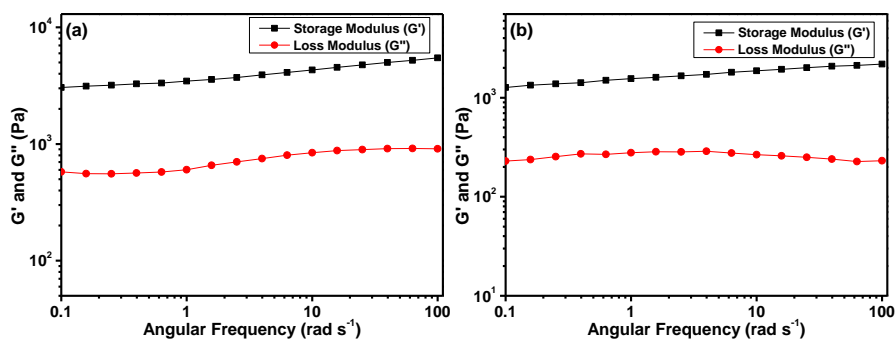


**Figure 5.27.** Frequency sweep experiment of organogel **G8GE** at (a) 1:1 molar ratio (0.03: 0.03 mmol) (b) 3: 2 molar ratio (0.03: 0.02 mmol).

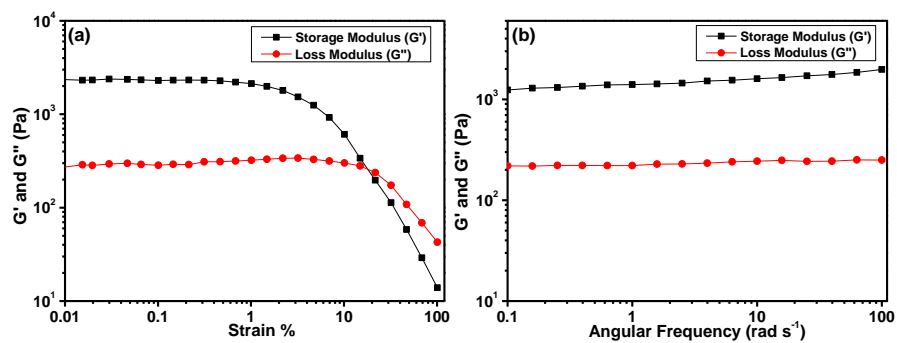


**Figure 5.28.** (a) Angular sweep experiment of metallogel  $\text{MIG8GECl}_2$   
(b) Frequency sweep experiment of metallogel  $\text{MIG8GECl}_2$ .

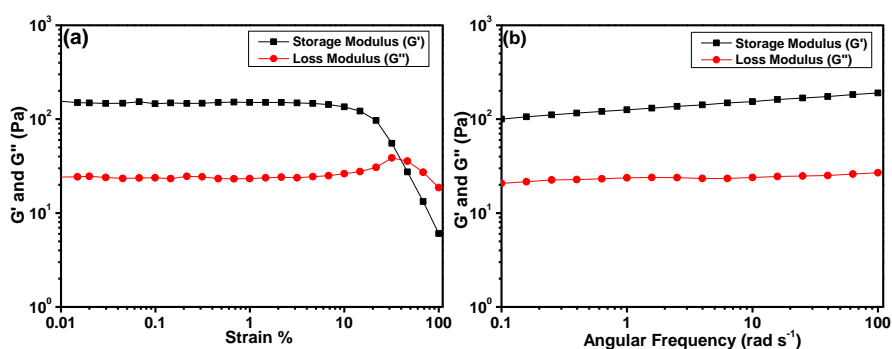


**Figure 5.29.** (a) Angular sweep experiment of metallogel  $\text{MIG8GE(OAc)}_2$   
(b) Frequency sweep experiment of metallogel  $\text{MIG8GE(OAc)}_2$ .

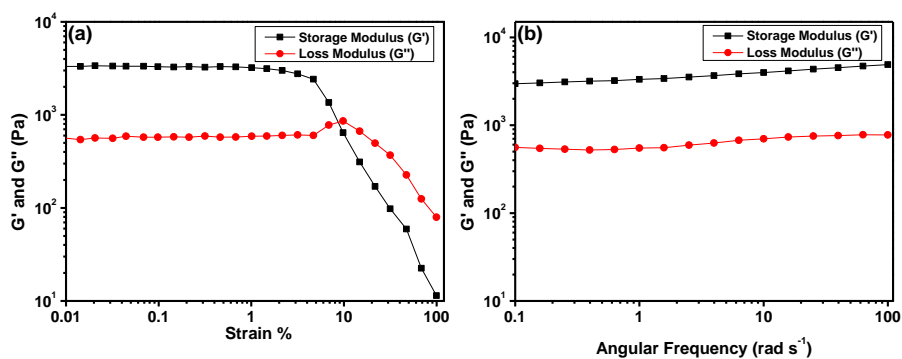


**Figure 5.30.** (a) Angular sweep experiment of metallogel  $\text{MIG8GESO}_4$   
(b) Frequency sweep experiment of metallogel  $\text{MIG8GESO}_4$ .

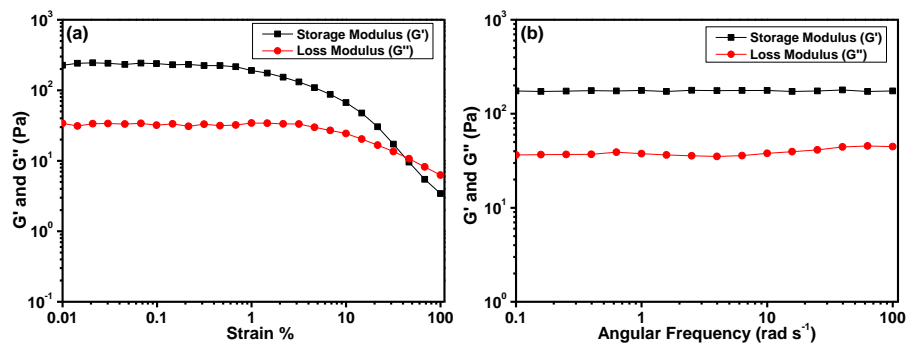


Figure 5.31. (a) Angular sweep experiment of metallogel  $M2G8GEC1_2$   
(b) Frequency sweep experiment of metallogel  $M2G8GEC1_2$ .

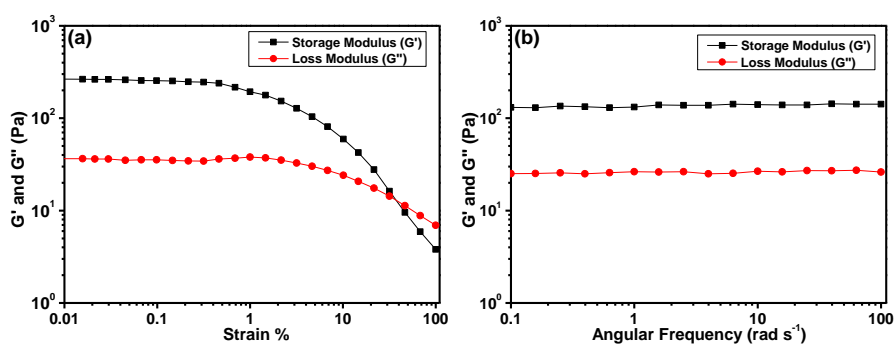


Figure 5.32. (a) Angular sweep experiment of metallogel  $M3G8GEC1_2$   
(b) Frequency sweep experiment of metallogel  $M3G8GEC1_2$ .

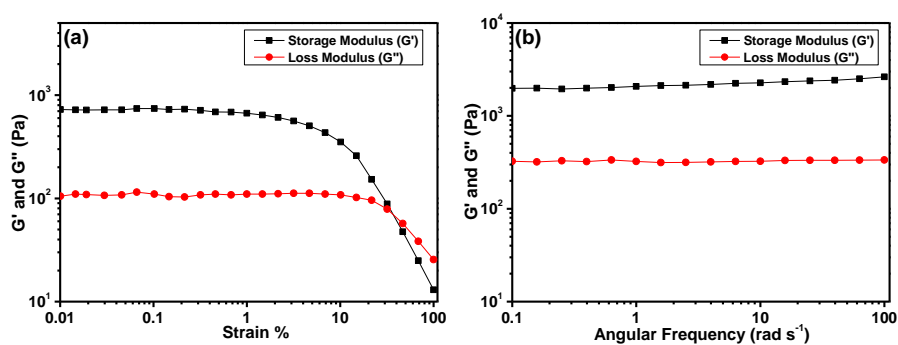


Figure 5.33. (a) Angular sweep experiment of metallogel  $M3G8GESO_4$   
(b) Frequency sweep experiment of metallogel  $M3G8GESO_4$ .

**Table 5.2.** Storage modulus and loss modulus of metallogels formed by mixing method.

Metallogel	Storage Modulus (G')	Loss Modulus (G'')
M1G8GECl <sub>2</sub>	1976 Pa	247 Pa
M1G8GE(OAc) <sub>2</sub>	189 Pa	27 Pa
M1G8GESO <sub>4</sub>	4838 Pa	792 Pa
M2G8GECl <sub>2</sub>	176 Pa	44 Pa
M2G8GE(OAc) <sub>2</sub>	Gelatinous Solution	Gelatinous Solution
M2G8GESO <sub>4</sub>	Gelatinous Solution	Gelatinous Solution
M3G8GECl <sub>2</sub>	140 Pa	26 Pa
M3G8GE(OAc) <sub>2</sub>	2646 Pa	338 Pa

While gel formation was done by adsorption method, the value of storage modulus for M1G8GECl<sub>2</sub>Ads, M1G8GE(OAc)<sub>2</sub>Ads, M1G8GESO<sub>4</sub>Ads, M2G8GECl<sub>2</sub>Ads, M2G8GE(OAc)<sub>2</sub>Ads, M2G8GESO<sub>4</sub>Ads, M3G8GECl<sub>2</sub>Ads and M3G8GE(OAc)<sub>2</sub>Ads are found to be 11730, 3055, 10872, 11830, 13815, 13635, 10747 and 13119 Pa respectively (Figure 5.34- 5.41 and Table 5.3). This indicates that the adsorption method provides stronger metallogels with respect to the mixing method. This might be due to disturbances in the assembled structure between the gelator components G8 and GE, while metal ions are incorporated through mixing (Figure 5.42). However, the adsorption method allows the metal ions to diffuse through the gel network without any disturbance to take up the preferred positions inducing a more robust gel fabrication.

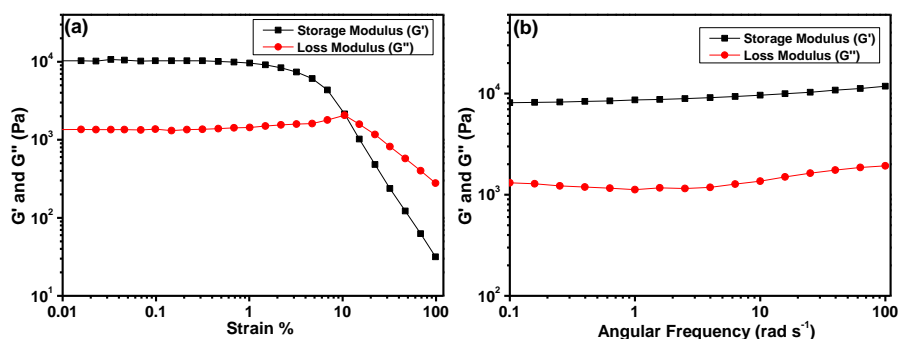


Figure 5.34. (a) Angular sweep experiment of metallogel  $\text{MIG8GECl}_2\text{Ads}$  (b) Frequency sweep experiment of metallogel  $\text{MIG8GECl}_2\text{Ads}$ .

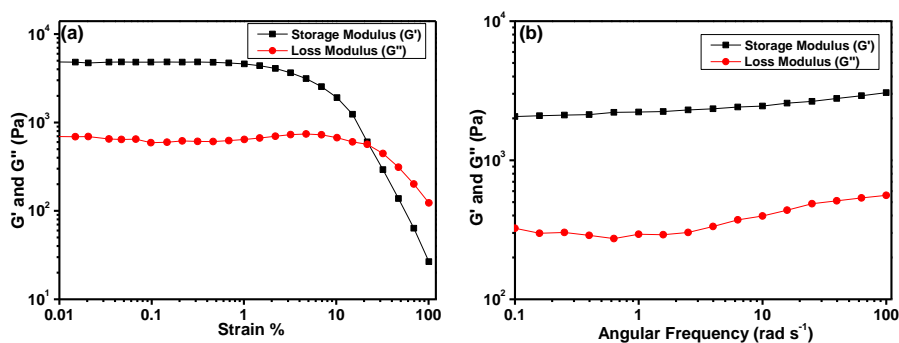


Figure 5.35. (a) Angular sweep experiment of metallogel  $\text{MIG8GE(OAc)}_2\text{Ads}$  (b) Frequency sweep experiment of metallogel  $\text{MIG8GE(OAc)}_2\text{Ads}$ .

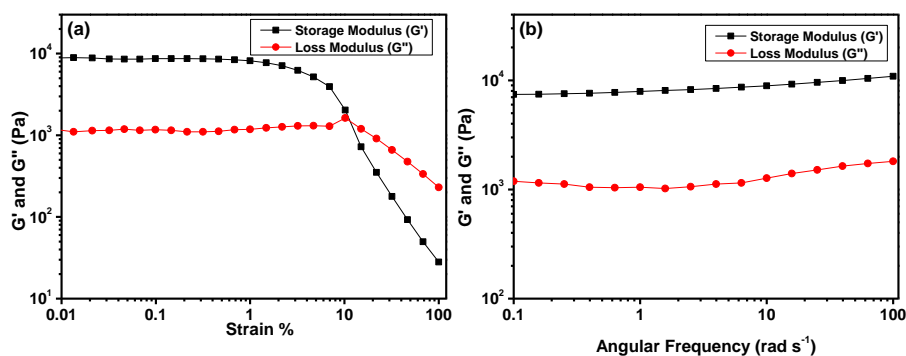


Figure 5.36. (a) Angular sweep experiment of metallogel  $\text{MIG8GESO}_4\text{Ads}$  (b) Frequency sweep experiment of metallogel  $\text{MIG8GESO}_4\text{Ads}$ .

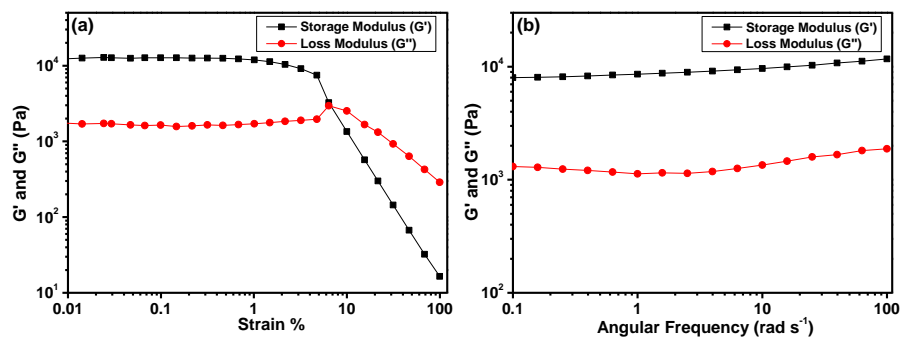


Figure 5.37. (a) Angular sweep experiment of metallogel  $M2G8GECl_2Ads$  (b) Frequency sweep experiment of metallogel  $M2G8GECl_2Ads$ .

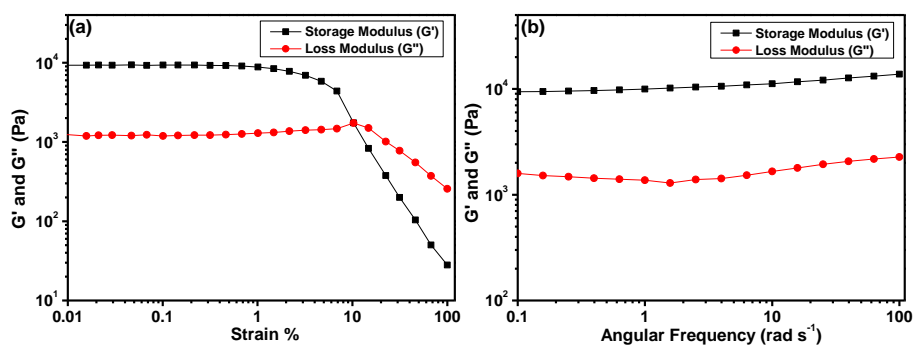


Figure 5.38. (a) Angular sweep experiment of metallogel  $M2G8GE(OAc)_2Ads$  (b) Frequency sweep experiment of metallogel  $M2G8GE(OAc)_2Ads$ .

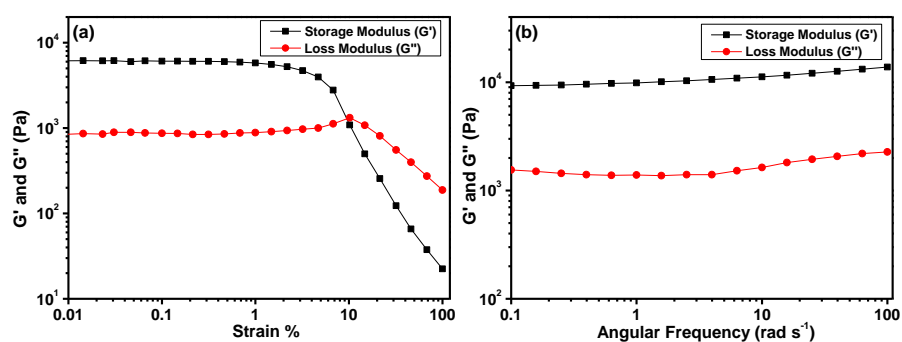
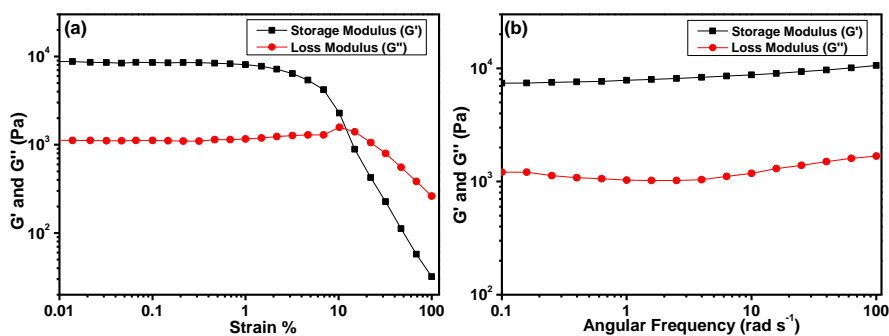
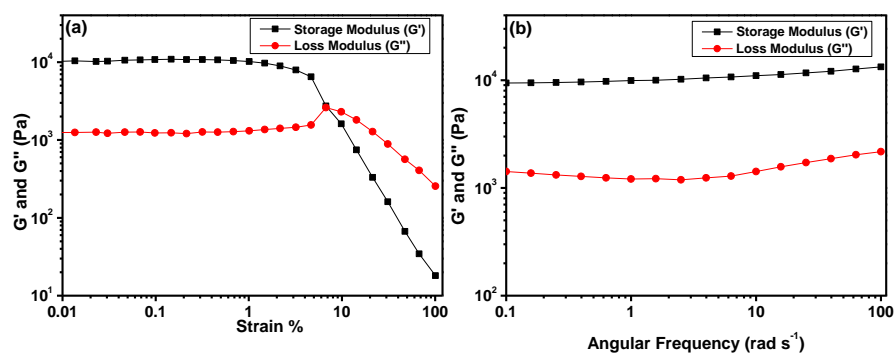


Figure 5.39. (a) Angular sweep experiment of metallogel  $M2G8GESO_4Ads$  (b) Frequency sweep experiment of metallogel  $M2G8GESO_4Ads$ .



**Figure 5.40.** (a) Angular sweep experiment of metallogel  $M3G8GECl_2Ads$  (b) Frequency sweep experiment of metallogel  $M3G8GECl_2Ads$ .



**Figure 5.41.** (a) Angular sweep experiment of metallogel  $M3G8GE(OAc)_2Ads$  (b) Frequency sweep experiment of metallogel  $M3G8GE(OAc)_2Ads$ .

**Table 5.3.** Storage modulus and loss modulus of metallogels formed by adsorption method.

Metallogel	Storage Modulus ( $G'$ )	Loss Modulus ( $G''$ )
$M1G8GECl_2Ads$	11730 Pa	1943 Pa
$M1G8GE(OAc)_2Ads$	3055 Pa	559 Pa
$M1G8GESO_4Ads$	10872 Pa	1803 Pa
$M2G8GECl_2Ads$	11830 Pa	1855 Pa
$M2G8GE(OAc)_2Ads$	13815 Pa	2291 Pa
$M2G8GESO_4Ads$	13635 Pa	2266 Pa
$M3G8GECl_2Ads$	10747 Pa	1688 Pa
$M3G8GE(OAc)_2Ads$	13119 Pa	2179 Pa

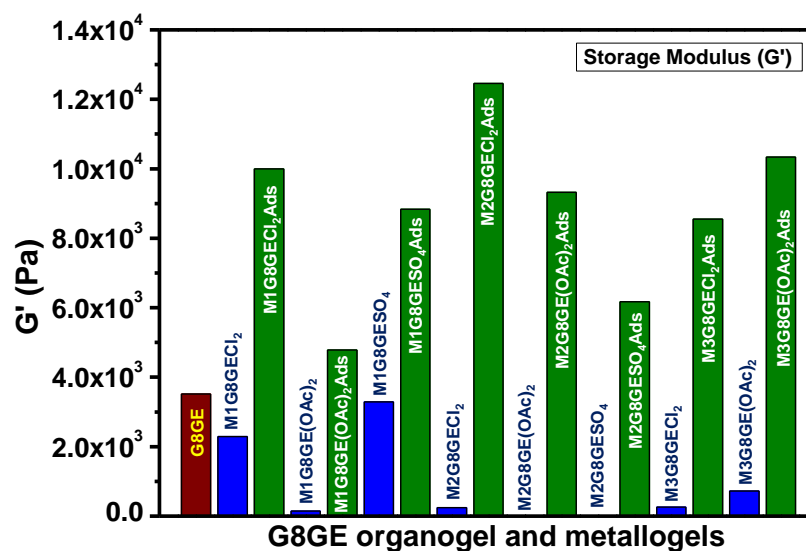


*Figure 5.42. Comparative study of value of storage modulus ( $G'$ ) of all the metallogels formed by mixing and adsorption methods.*

#### **Study on self-assembly of G8GE gelator components and their gels.**

Based on Job plot, which has been analysed by fluorescence method, the ratio of maximum interaction between **G8** and **GE** was found to be 3: 2. Organogel was formed with this ratio, and the IR data of the xerogel revealed that the carboxylic acid group, tetrazole -NH and secondary amine of **G8** and **GE** participate in the formation of hydrogen bonds providing strong gel network of **G8GE**. It is already reported that the gelator molecule **G8** shows the IR band at  $1339\text{ cm}^{-1}$  for the presence of cyclic -C-N=C- group, at  $1523, 1422\text{ cm}^{-1}$  for tetrazole. The presence of a secondary -NH group was verified with the band at  $1637\text{ cm}^{-1}$ . Gelator component **GE** shows IR band at  $1225\text{ cm}^{-1}$  for C-O,  $1520\text{ cm}^{-1}$  for primary amine,  $1602\text{ cm}^{-1}$  for amide -NH,  $1659\text{ cm}^{-1}$  for amide -C=O and  $1700\text{ cm}^{-1}$  carboxylic -C=O groups. Now, in the case of **G8GE** xerogel, IR band of amide -C=O was observed at  $1640\text{ cm}^{-1}$  in the place of  $1659\text{ cm}^{-1}$ , and carboxylic acid group shows a broad feature at  $1693\text{ cm}^{-1}$ . Also, the IR band at  $1422$  for tetrazole C-N shifted toward  $1415\text{ cm}^{-1}$ . The downward shifts in wavenumbers of these groups strongly recommend their involvement in hydrogen bond formation between **G8** and **GE**. The fabrication of gels was also studied by PXRD technique. In the case of **G8** peaks observed with the value of  $2\theta = 20.12^\circ$  ( $d = 4.48\text{ \AA}$ ) for intercolumnar stacking,  $2\theta = 27.64^\circ$  ( $d = 3.32\text{ \AA}$ ) for  $\pi$ - $\pi$  stacking

and  $2\theta = 34.35^\circ$  ( $d = 2.73 \text{ \AA}$ ) for hydrogen bonding while for **GE** peaks are at  $2\theta = 25.52^\circ$  ( $d = 3.57 \text{ \AA}$ ) and  $2\theta = 42.39^\circ$  ( $d = 2.28 \text{ \AA}$ ) for  $\pi$ - $\pi$  stacking and hydrogen bonding respectively. When the organogel **G8GE** has been formed, the PXRD peaks found at  $2\theta = 21.30^\circ$  ( $d = 4.24 \text{ \AA}$ ) indicated the presence of intercolumnar stacking,  $2\theta = 25.66^\circ$  ( $d = 3.56 \text{ \AA}$ ) and  $2\theta = 27.50^\circ$  ( $d = 3.33 \text{ \AA}$ ) shows the presence of  $\pi$ - $\pi$  stacking between **G8** and **GE**.<sup>[53-55]</sup> The PXRD pattern of **G8**, **GE**, and **G8GE** shows that these are crystalline in nature. Based on the interaction ratio between **G8** and **GE**, i.e., 3: 2, and the downward shift in the IR band of carboxylic acid, secondary amine, and tetrazole nitrogen, a plausible structure with probable hydrogen bonding interaction has been proposed for the organogel **G8GE** (Figure 5.43).

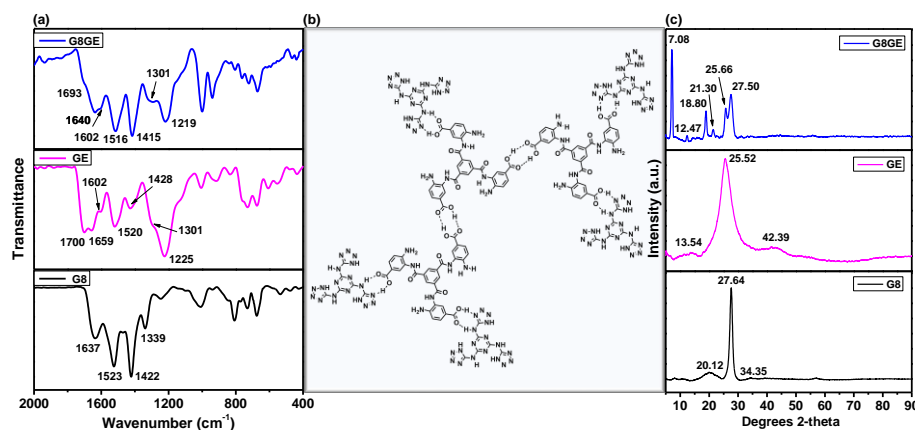


**Figure 5.43.** (a) FTIR data of **G8**, **GE** and **G8GE** xerogel (b) possible structure of gelator components **G8GE** interaction (c) PXRD data of **G8**, **GE** and **G8GE** xerogel.

To confirm the probability of the given structure DFT study was done. Stable ground-state geometries of **GE** and **G8** were obtained using the hybrid density functional – B3LYP-D3<sup>[56, 57]</sup> in combination with the 6-31G(d) basis set. The true minimum was confirmed based on the absence of imaginary frequencies. The binding of **GE** and **G8** was studied by optimizing the complex, and the binding energy was computed using the following equation:

$$\text{Binding energy} = E_{\text{Complex}} - (2E_{\text{GE}} + 2*E_{\text{G8}}) \dots \text{For Structure } \mathbf{G8GE}$$

where  $E_{\text{Complex}}$ ,  $E_{\text{GE}}$  and  $E_{\text{G8}}$  are the energies of the **GE-G8** complex, **GE** and **G8**, respectively. All calculations were performed using the polarizable continuum model (PCM) with water as the solvent as incorporated in Gaussian 16 program package. To estimate the strength of hydrogen bonding in the composite gel, the H-bond binding energy (HBE) was calculated based on the bond critical points (BCP of type [3, -1]) according to Bader's atoms in molecules (AIM) theory using Multiwfn.<sup>[58]</sup> The HBE was estimated using the following equation<sup>[59]</sup>:

$$\text{HBE} = -223.08 \cdot \rho(r_{\text{BCP}}) + 0.7423$$

where HBE is in kcal/mol, and  $\rho(r_{\text{BCP}})$  is in atomic units (a.u.).

The binding of **GE** with **G8** (with two molecules of **G8** and two molecules of **GE**) leads to a stabilization energy of  $\sim 60$  kcal/mol. The stabilization is largely due to multiple intermolecular hydrogen bonds between N-H...O, O-H...N, and O-H...O (Figure 5.44). The estimated average intermolecular hydrogen bond strength of  $\sim -9.14$  kcal/mol (the hydrogen bond energy per site is provided in Table 5.4 and strong hydrogen bonds in the range of 1.66-1.86 Å. The structures of **G8**, **GE**, and **G8GE** are also shown by DFT (Figure 5.45). The HOMO-LUMO energy orbitals for **G8** and **GE** are mentioned in ESI (Figure 5.46).

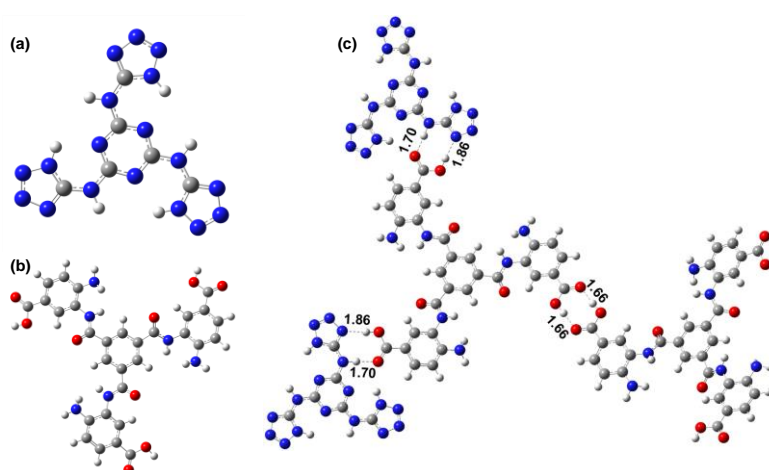


**Figure 5.44.** (a) DFT structure of (a) **G8** (b) **GE** and (c) plausible structure of interaction of **G8** and **GE**.

**Table 5.4.** Intermolecular H-bond binding energies of individual sites along with the associated bond lengths of structure **G8GE**.

Binding Site	H-bond length (Å)	$\rho(r_{BCP})$ (a.u.)	HBE (kcal/mol)
O-H...O	1.66	0.0497	-10.33
O-H...O	1.66	0.0497	-10.34
O-H...N	1.86	0.0367	-7.44
O-H...N	1.86	0.0368	-7.46
N-H...O	1.70	0.0466	-9.65
N-H...O	1.70	0.0466	-9.66

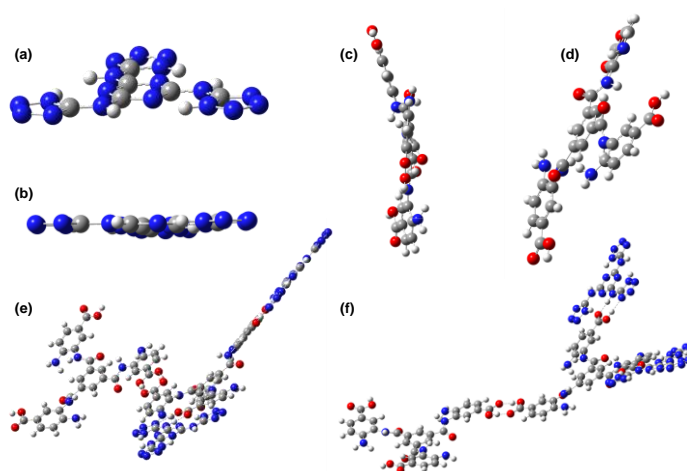


**Figure 5.45.** DFT structure showing (a, b) Planarity and (c, d) Tilted structure of **GE**, (e, f) Less tilted structure of **G8GE**.

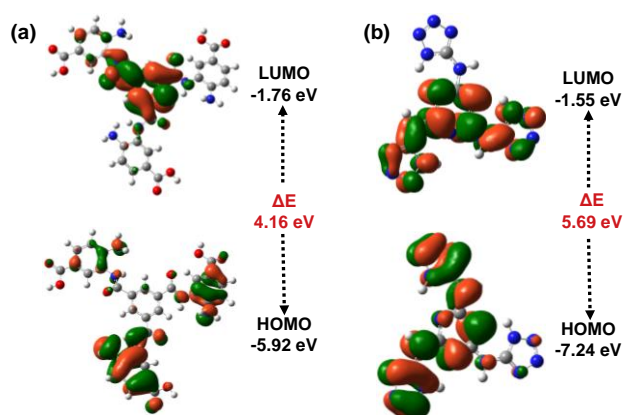


**Figure 5.46.** HOMO-LUMO energy orbitals of (a) **G8** and (b) **GE**.

FTIR analyses of xerogels of all the metallo gels have been done and found the changes in carboxylic, amide, and amine groups, which shows the changes in noncovalent interaction inside the gel system by the insertion of metal ions (Figure 5.47).

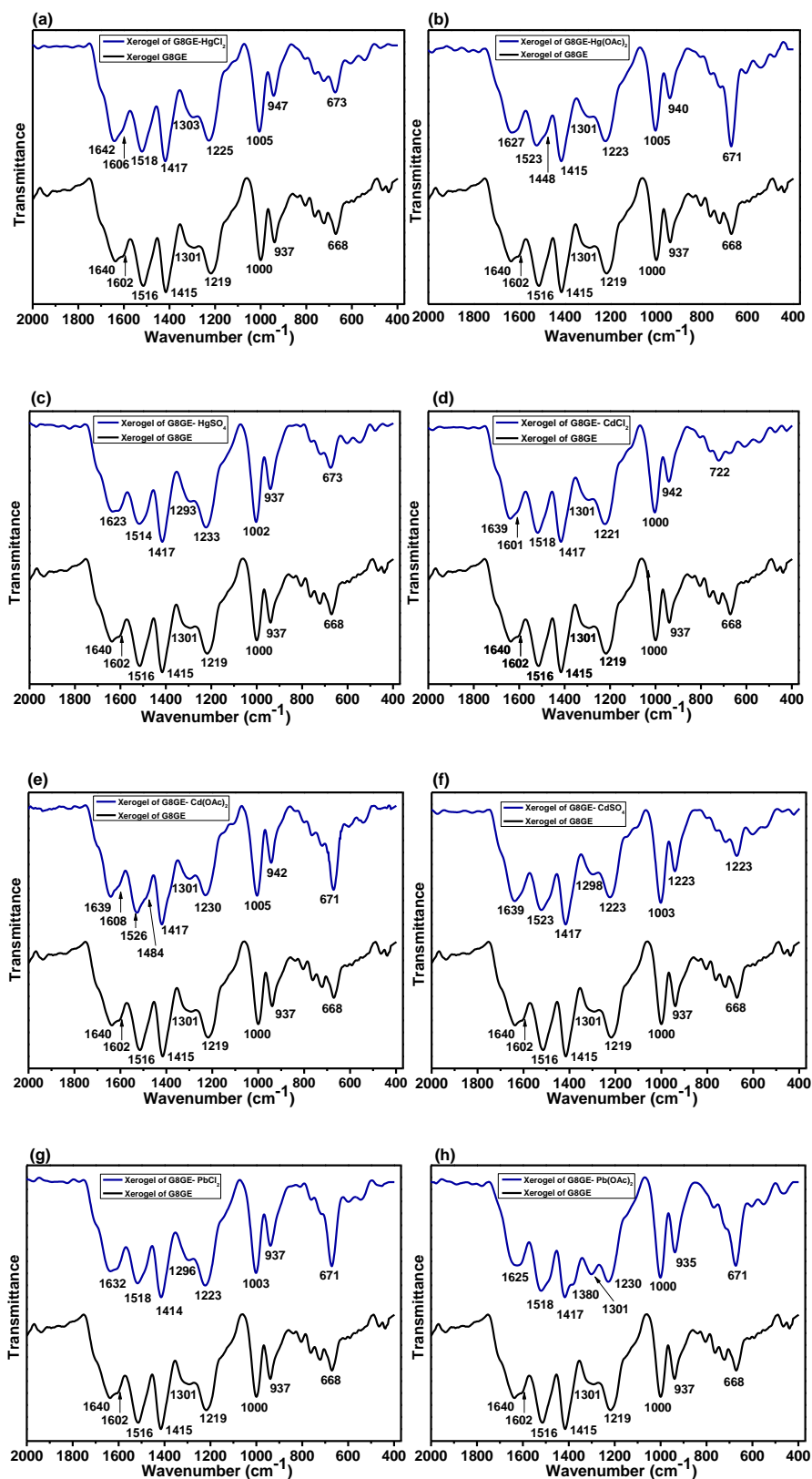


**Figure 5.47.** FTIR data of (a)  $M1G8GECl_2$  (b)  $M1G8GE(OAc)_2$  (c)  $M1G8GESO_4$  (d)  $M2G8GECl_2$  (e) precipitate of  $M2G8GE(OAc)_2$  (f) precipitate of  $M2G8GESO_4$  (g)  $M3G8GECl_2$  (h)  $M3G8GE(OAc)_2$ .

To know the effect of metal insertion on noncovalent interactions in gel matrix, PXRD data analysis has been done. All the xerogels of metallogels formed by mixing and adsorption methods show basically three PXRD peaks in the range of 20-23° for intercolumnar stacking, 26-28° for  $\pi$ - $\pi$  stacking, and 32-45° for hydrogen bonding interactions. PXRD patterns of all the metallogels are almost the same, showing similar interactions of heavy metal ions with gelator system **G8GE** (Figure 5.48 and 5.49).

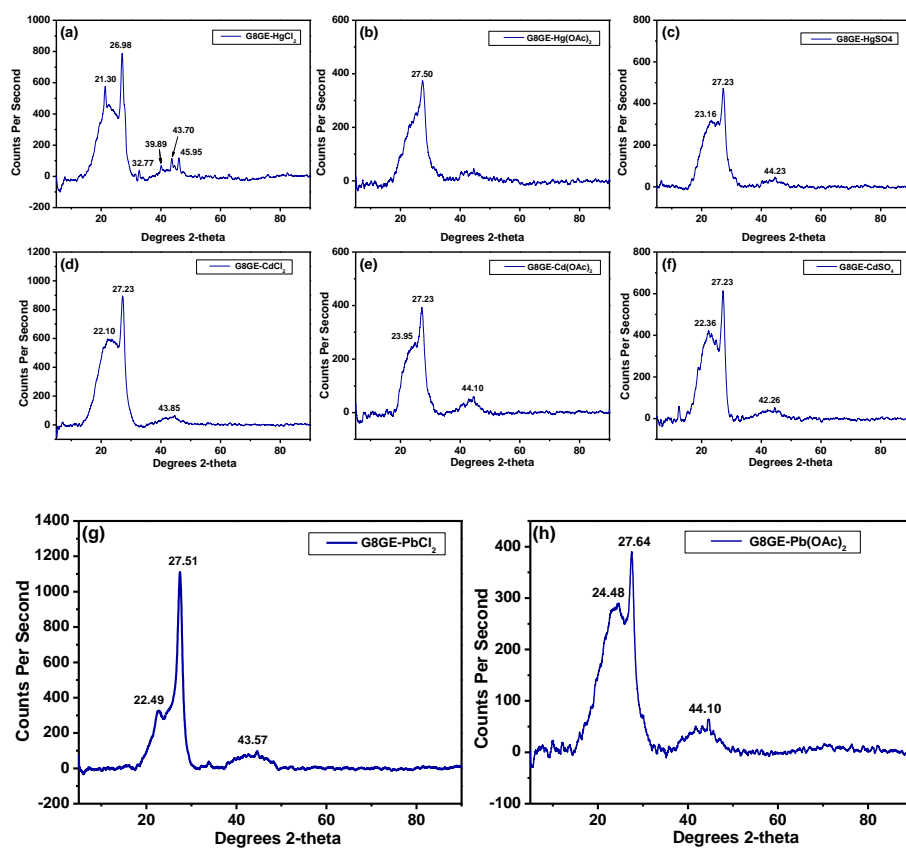


**Figure 5.48.** PXRD data of metallogels (a) *M1G8GECl<sub>2</sub>* (b) *M1G8GE(OAc)<sub>2</sub>* (c) *M1G8GESO<sub>4</sub>* (d) *M2G8GECl<sub>2</sub>* (e) precipitate of *M2G8GE(OAc)<sub>2</sub>* (f) precipitate of *M2G8GESO<sub>4</sub>* (g) *M3G8GECl<sub>2</sub>* (h) *M3G8GE(OAc)<sub>2</sub>*.

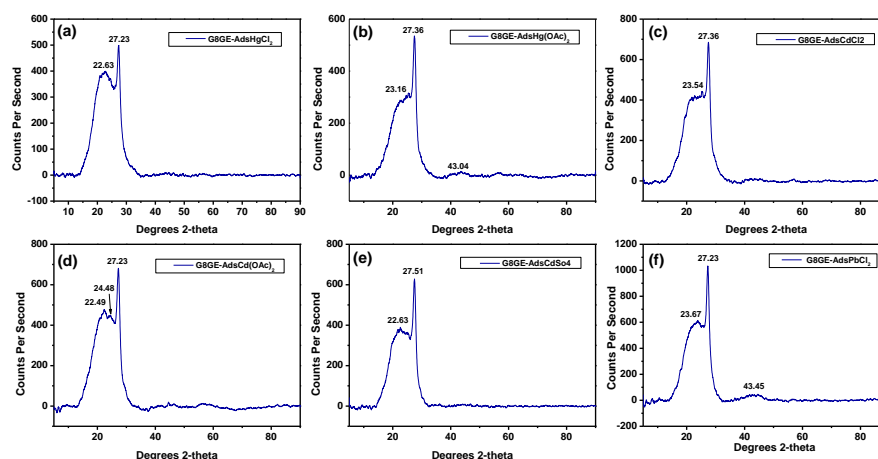


**Figure 5.49.** PXRD data of metallogels (a) **M1G8GECl<sub>2</sub>Ads** (b) **M1G8GE(OAc)<sub>2</sub> Ads** (c) **M2G8GECl<sub>2</sub> Ads** (d) **M2G8GE(OAc)<sub>2</sub> Ads** (e) **M2G8GESO<sub>4</sub> Ads** (f) **M3G8GECl<sub>2</sub> Ads**.

**Remediation of water (contaminated water treatment).** Organogel **G8GE** is found to be hydrophobic in nature. It does not get dissolved in water even after the sonication of organogel inside a large quantity of water (i.e., 2 mL gel by volume in around 20 mL of water). The organogel can show shape-forming properties even inside water. After sonication, organogel gets dispersed in water and remains as a separated layer of gel inside the mixture. The hydrophobic nature of the gel and the ability to capture metal ions to fabricate metallogels open the idea of applying the organogel for capturing toxic heavy metal ions in the remediation process of water. The optimization condition for the removal of heavy metal salt has been analysed with  $\text{Hg}(\text{OAc})_2$  (1 mM, 20 mL  $\text{H}_2\text{O}$ ) with changes in the amount of adsorbent (xerogel) and time of removal reaction (Table 5.5). Optimization shows the best condition for removal reaction for 1 mM heavy metal salt in 20 mL water was six hours stirring with 40 mg of xerogel gives almost 99 % removal. Therefore, for the separation of heavy metal ions from water, 20 mL, 1 mM solution of different metal salts was taken separately and treated with 40 mg of xerogel of **G8GE**. The solution was kept stirring at room temperature for six hours. After that, the solutions were filtered, and filtrates were checked by Inductively coupled plasma atomic emission spectroscopy (ICP-AES) to analyse the remaining amount of metal ions

in the aqueous system. It was found that xerogel **G8GE** adsorbs 56 % of mercury chloride, 99 % of mercury acetate, 99 % of mercury sulphate, 52 % of cadmium chloride, 99 % cadmium acetate, 84 % of cadmium sulphate, 60 % of lead chloride and 99 % of lead acetate from heavy metal contaminated water (Figure 5.50). The adsorption capacities ( $q_e$ ) of **G8GE** xerogel for different heavy metal salts are given in Table 5.6. The results show that xerogel **G8GE** adsorbed metal acetate and metal sulphate salts more as compared to metal chloride salt. The reason behind this might be the stronger hydrogen bonding of acetate and sulphate ions with **G8GE** molecules. The more electronegative oxygen atom of acetate and sulphate ion must act as a stronger hydrogen bond acceptor with hydrogen atoms of primary amine of **G8GE**, while chloride might form a less strong hydrogen bond due to its comparatively less electronegativity. The whole experiments and results indicate that xerogel of organogel **G8GE** can be a water remediation material for heavy metal removal from an aqueous solution. There are very few reports where gel materials are utilized for capturing heavy metal ions from aqueous solutions. Among them, the current system shows significant efficiency, and the data are presented in Table 5.7.

**Table 5.5.** Optimization of heavy metal removal reaction by xerogel of organogel **G8GE**, analysed by ICP-AES.

S. No.	Volume of solvent (H <sub>2</sub> O) used	Metal salt and concentration used	Amount of xerogel used	Time	Removal %
1	20 mL water	Hg(OAc) <sub>2</sub> , 1 mM	10 mg	3	57
2				6	60
3			20 mg	3	72
4				6	80
5			40 mg	3	90
6				6	99

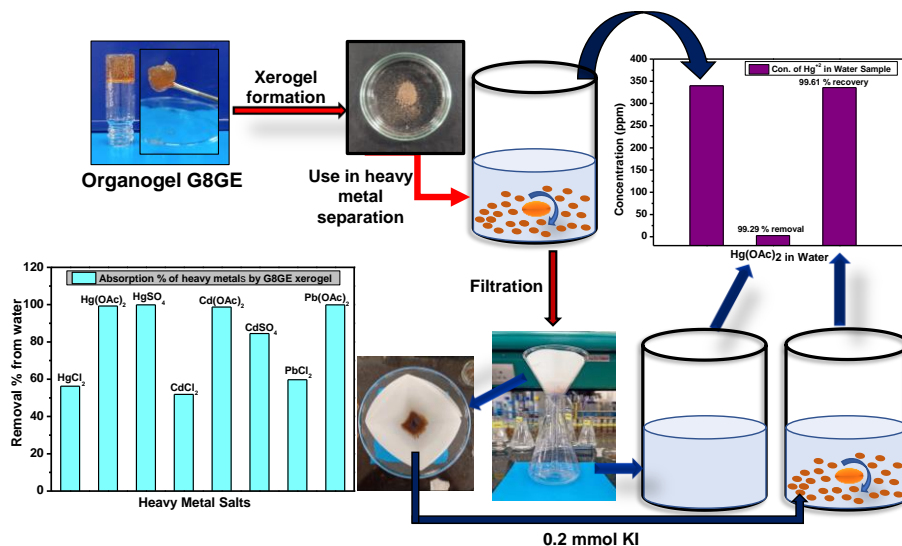


Figure 5.50. Systematic representation of removal of heavy metal salts from contaminated water and their ICP-AES analysis.

Table 5.6. ICP-AES analysis of study of adsorption property of organogel G8GE.

Heavy metal salt	Concentration in ppm before treatment in 20 mL water	Concentration in ppm after treatment by xerogel G8GE (ppm)	Adsorption capacity (q) in (mg/g)	% of heavy metal separation from water
HgCl <sub>2</sub>	271 ppm (1 mM)	118.517	76.24	56 %
Hg(CH <sub>3</sub> COO) <sub>2</sub>	318 ppm (1 mM)	2.42	157.79	99 %
HgSO <sub>4</sub>	296 ppm (1 mM)	0.289	147.81	99 %
CdCl <sub>2</sub>	201 ppm (1 mM)	96.818	52.09	52 %
Cd(CH <sub>3</sub> COO) <sub>2</sub>	266 ppm (1 mM)	3.501	131.25	99 %
CdSO <sub>4</sub>	769 ppm (1 mM)	119.437	284.93	84 %
PbCl <sub>2</sub>	278 ppm (1 mM)	112.033	83	60 %
Pb(CH <sub>3</sub> COO) <sub>2</sub>	443 ppm (1 mM)	0.432	221.02	99 %

Table 5.7. Adsorption capacity of various gel-based adsorbent.

S. No.	Adsorbent	Adsorbate	Adsorption capacity (q)	References
1	Bi-component supramolecular gel (RQ)	Hg <sup>2+</sup>	59 mg/g	60
2	Alginate cryogel of sweet lime-derived activated carbon (SLACC)	Cr <sup>6+</sup> , Cd <sup>2+</sup> , Pb <sup>2+</sup> , Hg <sup>2+</sup> and As <sup>3+</sup>	3.71, 4.22, 20.04, 4.37 and 7.31 mg/g	61
3	Xerogel of BTG organogel	Cu <sup>2+</sup> and Hg <sup>2+</sup>	99.02 % and 99.46 % (1 × 10 <sup>-5</sup> M metal salt by 1 mg of xerogel)	62
4	G-L organogel	Pb <sup>2+</sup> and Hg <sup>2+</sup>	85.63 % and 99.95 % ( For Pb <sup>2+</sup> it is from 301.5 mg/L to 43.34 mg/L and for Hg <sup>2+</sup> , it is from 24.12 to 0.011 mg/L) with xerogel 1 wt. % in 2 mL	63
5	Xerogel of G8GE organogel	Chloride, acetate and sulphate salt of Hg <sup>2+</sup> and Cd <sup>2+</sup> , Chloride and acetate of Pb <sup>2+</sup>	76.24, 157.79, 147.81, 52.09, 131.25, 284.93, 83 and 221.02 mg/g respectively.	This work

After the mercury adsorption by xerogel **G8GE**, it can be activated and recycled further. For this purpose,  $\text{Hg}(\text{OAc})_2$  treated xerogel **G8GE** was taken in 20 mL of water, and a small amount of KI (0.2 mmol, 34 mg) was added. The mixture was stirred for three hours at room temperature and then filtered. The filtrate was found to contain 99 % of mercury, which was captured within the xerogel during the remediation of water by xerogel **G8GE**. It means almost 1 % mercury could not be recovered from the xerogel **G8GE**. This recovery was analysed by ICP-AES analysis. The activated xerogel was further used successfully for another cycle of heavy metal removal. This regeneration method of adsorbent (xerogel **G8GE**) is cost-effective because here, a common laboratory salt, i.e., potassium iodide was sufficient to recover xerogel **G8GE**. Further, the changes between the fabricated xerogel and the treated xerogel after the recovery of mercury have been analysed by the BET technique. BET experiments have been performed by  $\text{N}_2$  adsorption-desorption analysis at 80 °C and 8 hours of degassing time. The BET multipoint surface area for **G8GE** xerogel before use for heavy metal removal is 6.651  $\text{m}^2/\text{g}$ . After the treatment with  $\text{Hg}(\text{OAc})_2$  the multipoint BET is found to be 4.010  $\text{m}^2/\text{g}$  which is less than the original due to the presence of mercury inside the gel matrix. However, after the recovery of mercury from xerogel **G8GE** by treatment with KI, this value founds to be 6.549  $\text{m}^2/\text{g}$ . These changes in multipoint BET clearly indicate the adsorption and removal of mercury from water by xerogel **G8GE** (Figure 5.51).

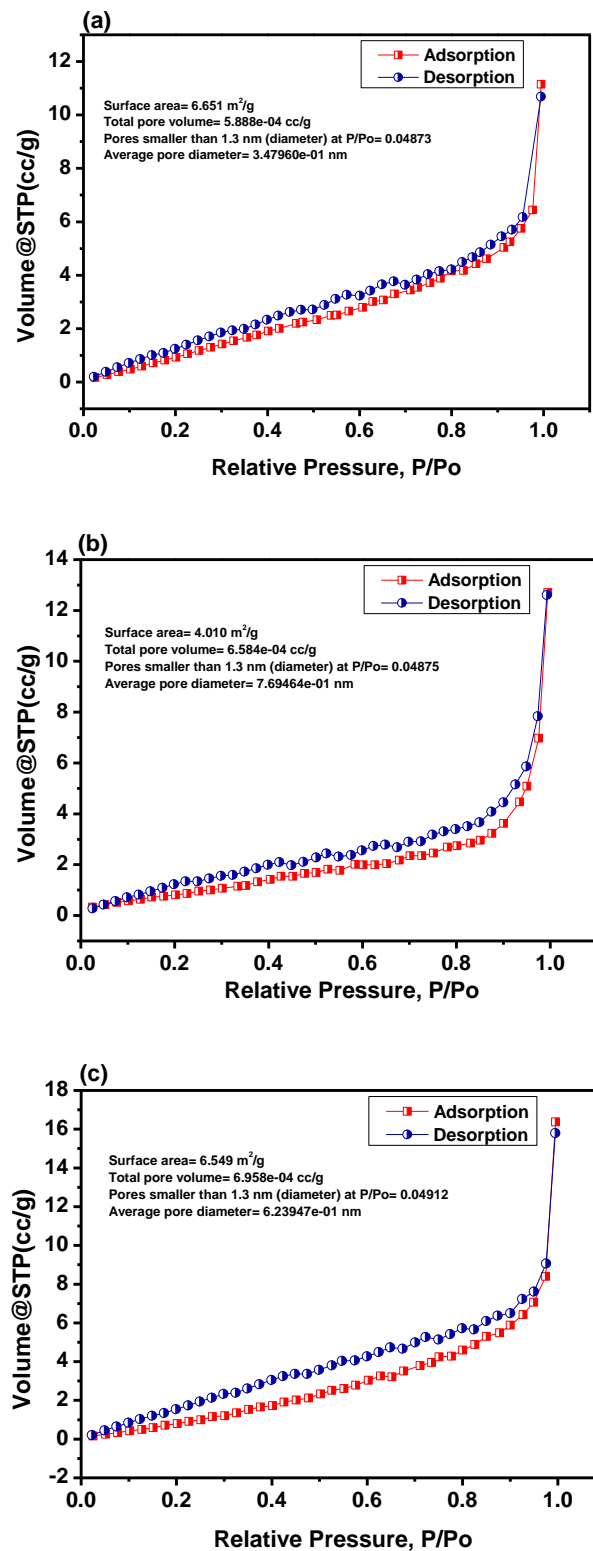


**Figure 5.51.** BET analysis data of (a) Xerogel G8GE (b) mercury-treated G8GE (*mtG8GE*) (c) mercury-recovered G8GE (*mrG8GE*).

The removal of heavy metal salts by xerogel G8GE has been further examined by XPS analysis. XPS analysis has been carried out for

xerogel **G8GE**, mercury-treated **G8GE** (**mtG8GE**), and mercury-recovered **G8GE** (**mrG8GE**). XPS survey spectrum of **G8GE** shows the presence of C1s, N1s, and O1s at 285, 399, and 533 eV, respectively. Similarly, in **mtG8GE**, the peaks at 285, 399, and 533 eV indicated the presence of C1s, N1s, and O1s, respectively, with the addition of two new peaks at 100.9 and 104 eV for Hg 4f<sub>7/2</sub> and Hg 4f<sub>5/2</sub>, respectively. Further, the survey spectrum of **mrG8GE** shows similar peaks for C1s, N1s, and O1s with small intensity peaks at 101 and 104 eV for Hg 4f, which indicates that a small amount of Hg remains inside the **G8GE** system (Figure 5.52). C1s spectrum of xerogel **G8GE** reveals peaks at 284.4, 285.2, 287.9, and 288.9 eV for C=C/ C-C, C-N/ C-O, N-C=N and -COOH/ C=O respectively. N1s shows the XPS peaks at 398.8, 399.8, 400.6, and 402.0 eV for -NH<sub>2</sub>, -C=N, C-NH-C, and -NH, respectively. The O1s spectrum shows the peaks at 530.9, 531.5, and 532.9 eV for -C-OH, -C=O, and -COOH groups, respectively.<sup>[64-69]</sup> The XPS analysis of **G8GE**, **mtG8GE**, and **mrG8GE** has been mentioned in Figure 5.53-5.55 and Table 5.8.

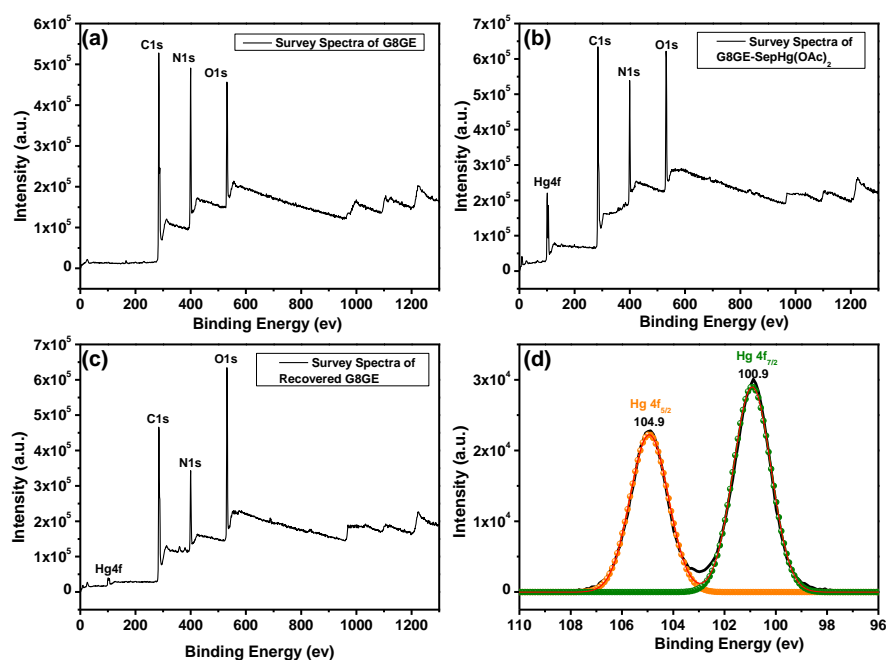


**Figure 5.52.** XPS survey spectra of (a) xerogel **G8GE** (b) **mtG8GE** (c) **mrG8GE** and (d) XPS spectrum of **mtG8GE** showing the presence of Hg 4f.

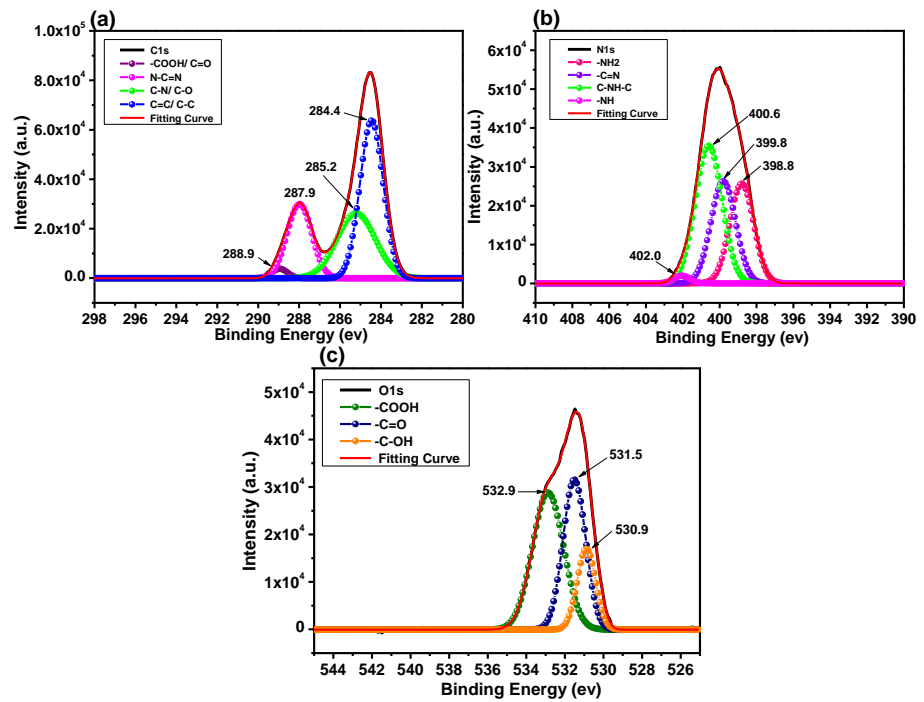


Figure 5.53. XPS analysis of xerogel G8GE showing (a) C1s spectrum (b) N1s spectrum and (c) O1s spectrum.

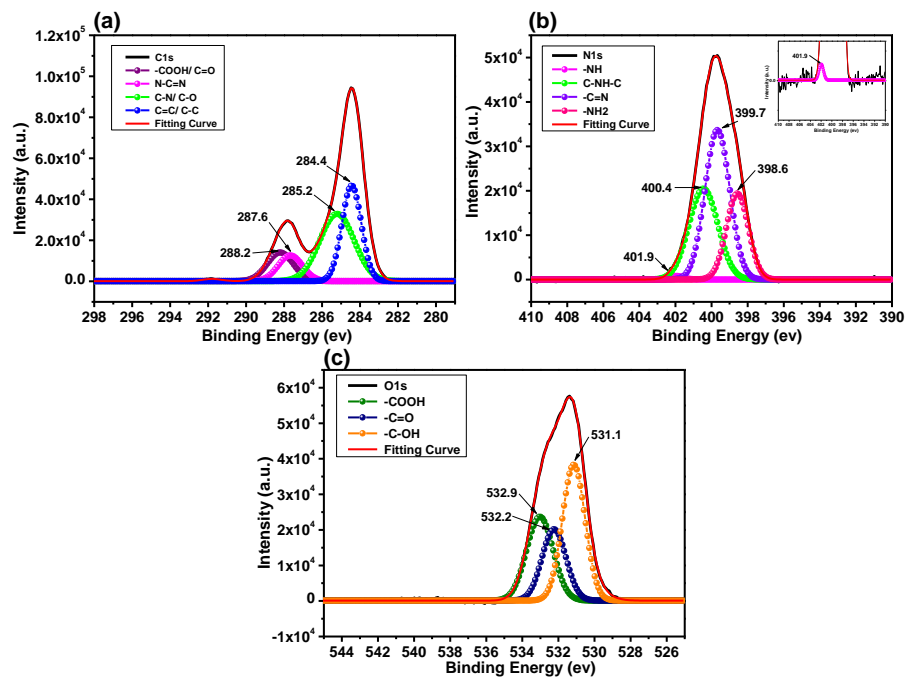
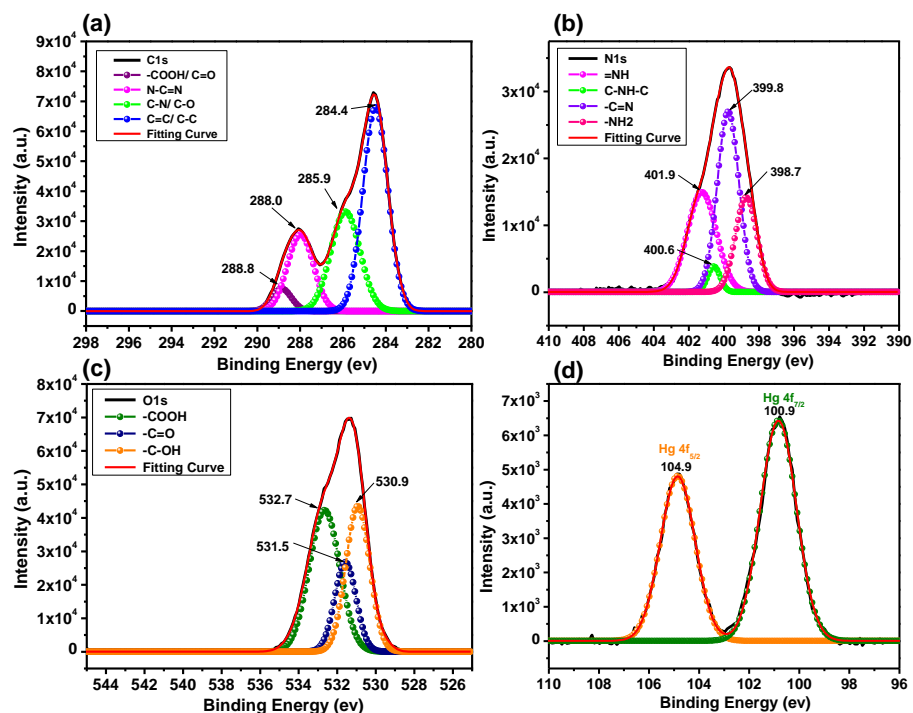


Figure 5.54. XPS analysis of xerogel mtG8GE showing (a) C1s spectrum (b) N1s spectrum and (c) O1s spectrum.



**Figure 5.55.** XPS analysis of xerogel *mrG8GE* showing (a) *C1s* spectrum (b) *N1s* spectrum and (c) *O1s* spectrum and (d) *Hg 4f* spectrum.

**Table 5.8.** XPS peaks position of various groups for *G8GE*, *mtG8GE* and recovered *mrG8GE*.

Groups or Element present	Xerogel G8GE Binding Energy (eV)	mtG8GE Binding Energy (eV)	mrG8GE Binding Energy (eV)
-COOH/ C=O	288.9	288.2	288.8
N-C=N	287.9	287.6	288.0
C-N/ C-O	285.2	285.2	285.9
C=C/ C-C	284.4	284.4	284.4
-NH	402.0	401.9	401.9
C-NH-C	400.6	400.4	400.6
-C=N	399.8	399.7	399.8
-NH <sub>2</sub>	398.8	398.6	398.7
-COOH	532.9	532.9	532.7
C=O	531.5	532.2	531.5
C-OH	530.9	531.1	530.9
Hg <sup>2+</sup> (Hg 4f <sub>7/2</sub> )	-	100.9	100.9
Hg <sup>2+</sup> (Hg 4f <sub>5/2</sub> )	-	104.9	104.9

The effect on the morphology of the gel after utilization for mercury capture from aqueous solution was also investigated by FE-SEM image analysis (Figure 5.56). The microscopy reveals a circular-shaped morphology comprised of a nanofibrous network. It is quite evident that after capturing mercury when treated with an aqueous solution, the original morphology gets altered due to the interactions of the metal ion with the gel network.

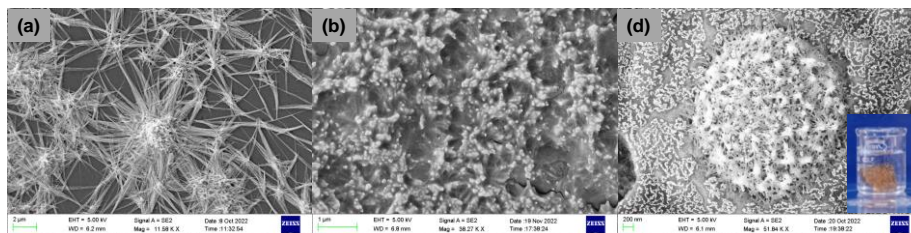


**Figure 5.56.** FE-SEM images of (a) *MIG8GECI<sub>2</sub>* gel by mixing (b) *MIG8GECI<sub>2</sub>Ads* by adsorption (c) *MIG8GECI<sub>2</sub>Ads* when *G8GE* inserted inside the aqueous solution of *HgCl<sub>2</sub>*.

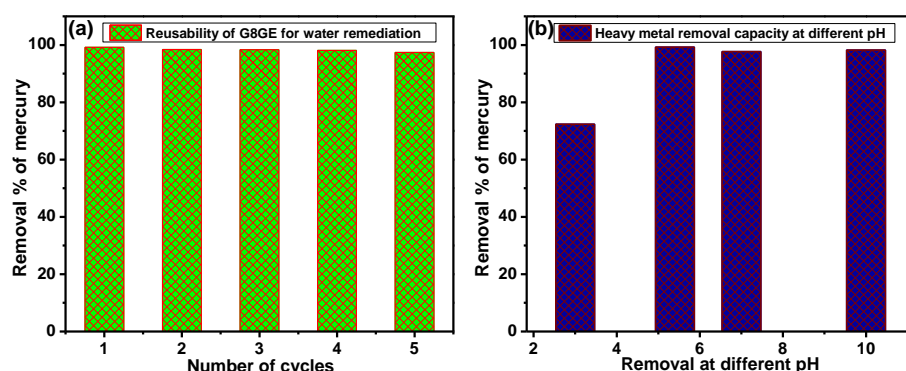
**Reusability of xerogel and effect of pH on removal of heavy metal ions.** To check the reusability of xerogel *G8GE* as water remediation material, *G8GE* was used for five consecutive cycles to remove mercury, and the removal percentages are recorded as 99, 98, 98, 98, and 97 from first to fifth cycle. At the end of every cycle, used xerogel *G8GE* was recovered by its treatment with KI to remove the adsorbed amount of mercury. These experiments show the reusability of xerogel, where removal percentages are found to be in the range of 97 to 99 % (Table 5.9). The heavy metal separation capability of *G8GE* has been checked in four different pH values of 3, 5.4 (DI water), 7, and 10. The results indicate 72, 99, 97, and 98 percent removal of mercuric acetate from aqueous solution respectively (Figure 5.57 and Table 5.10)

**Table 5.9.** Recyclability of xerogel **G8GE** for heavy metal separation.

Concentration of $\text{Hg}(\text{CH}_3\text{COO})_2$ in ppm before treatment (20 mL water)	Concentration in ppm after treatment by xerogel <b>G8GE</b> (ppm)	Removal % from water
318 ppm (1 mM)	2.514	99
318 ppm (1 mM)	5.092	98
318 ppm (1 mM)	5.271	98
318 ppm (1 mM)	6.003	98
318 ppm (1 mM)	8.311	97

**Table 5.10.** Water remediation at different pH by xerogel **G8GE**.

Concentration of $\text{Hg}(\text{CH}_3\text{COO})_2$ in ppm before treatment (20 mL water)	pH of contaminated water system	Concentration in ppm after treatment by xerogel <b>G8GE</b> (ppm)	Removal % from water
318 ppm (1 mM)	3	87.876	72
318 ppm (1 mM)	5.4	2.405	99
318 ppm (1 mM)	7	7.338	97
318 ppm (1 mM)	10	5.514	98

**Figure 5.57.** (a) Reusability of **G8GE** for water remediation (b) Heavy metal removal at different pH from 3-10.

**Thixotropic modification of metallogels by adsorption method.** Self-healing property or thixotropic behaviour of low molecular weight gels show gel-sol-gel transition for many cycles. Organogel **G8GE** also shows good self-healable properties. The time oscillation sweep (TOS) experiment has done with three concentrations organogel at 0.02: 0.02, 0.03: 0.03, and 0.04: 0.04 mmol of **G8: GE** and found that in the case of 0.03: 0.03 mmol of **G8:GE** the recovery of storage modulus is

continuous and unaffected (Figure 5.58). The metallogels, which have been fabricated by mixing, show low capacities as thixotropic gels, but metallogels which have been fabricated by the adsorption method, displayed a much better thixotropic nature. More significant decrement of  $G'$  values after the first cycle of TOS was observed in the cases of **M1G8GECl<sub>2</sub>**, **M1G8GE(OAc)<sub>2</sub>**, **M1G8GESO<sub>4</sub>**, and **M3G8GE(OAc)<sub>2</sub>**. It has been reported that within similar gel systems, when the value of  $G'$  increases, thixotropic behaviour decreases because of the less viscous nature of gels. However, in this case, when the metallogels have been formed by the adsorption method, the thixotropic nature increases. This is because, during adsorption, the metal ions interact with gelator components without making any disturbance within the **G8GE** gel network. This leads to the viscous nature of the gel being unaffected (Figure 5.59- 5.63).

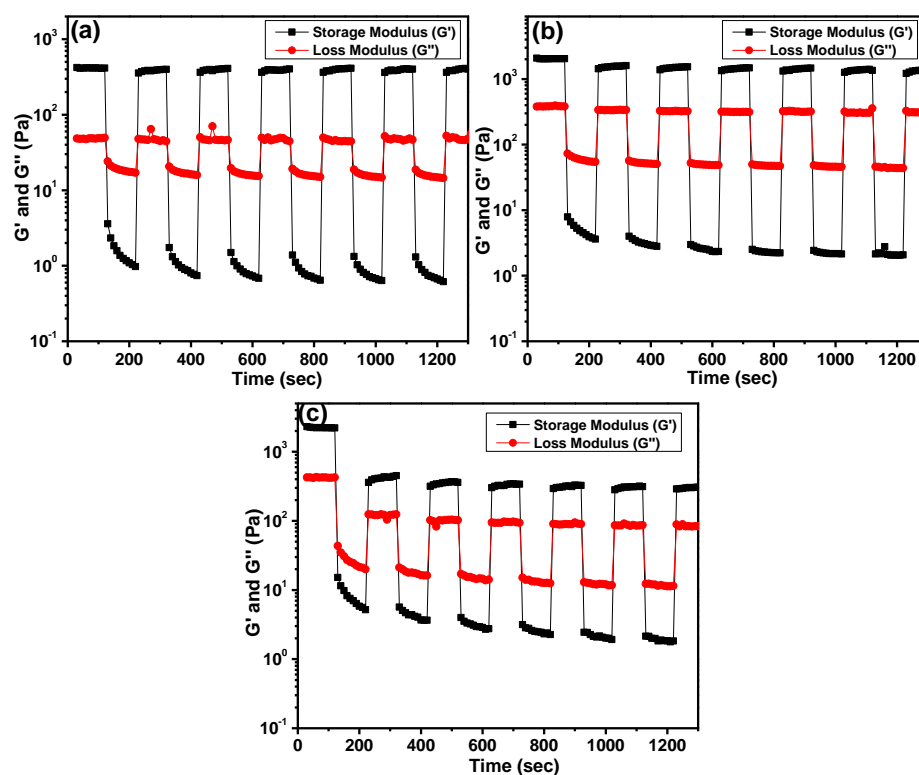


**Figure 5.58.** Time oscillation sweep experiment of organogel **G8GE** at (a) 0.02: 0.02 mmol (b) 0.03: 0.03 mmol and (c) 0.04: 0.04 mmol.

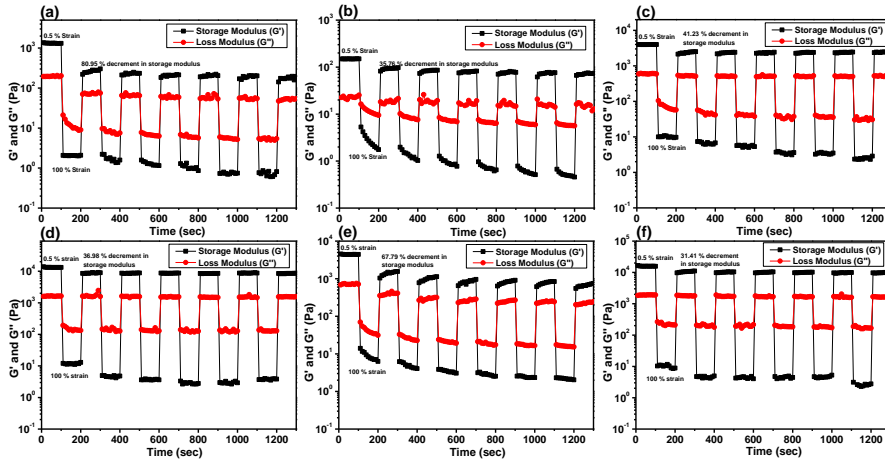


Figure 5.59. Thixotropic behaviour by Time oscillation sweep experiments for metallogels (a)  $MIG8GECl_2$  (b)  $MIG8GE(OAc)_2$  (c)  $MIG8GESO_4$ , and metallogels (d)  $MIG8GECl_2Ads$  (e)  $MIG8GE(OAc)_2Ads$  and (f)  $MIG8GESO_4Ads$ .

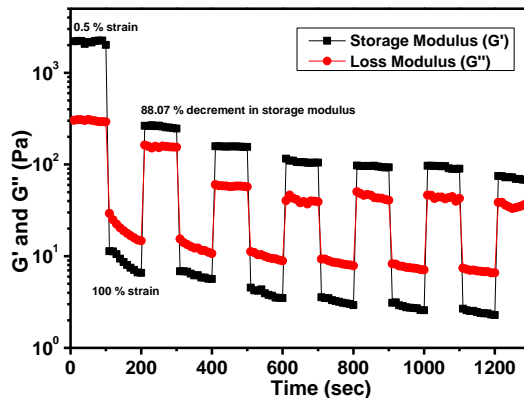


Figure 5.60. Time oscillation sweep experiment of metallogel  $M3G8GECl_2$ .

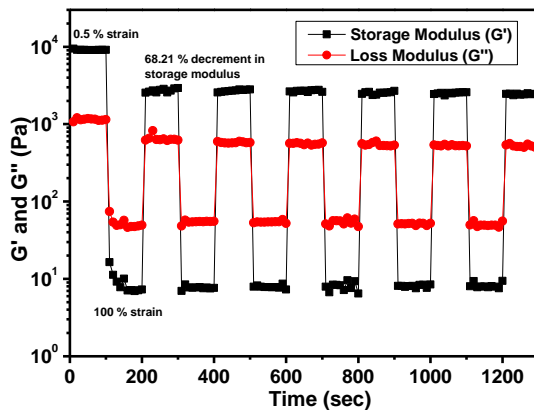
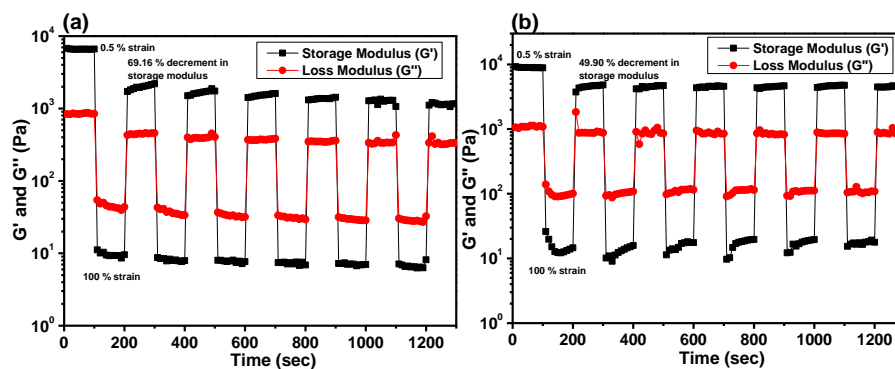
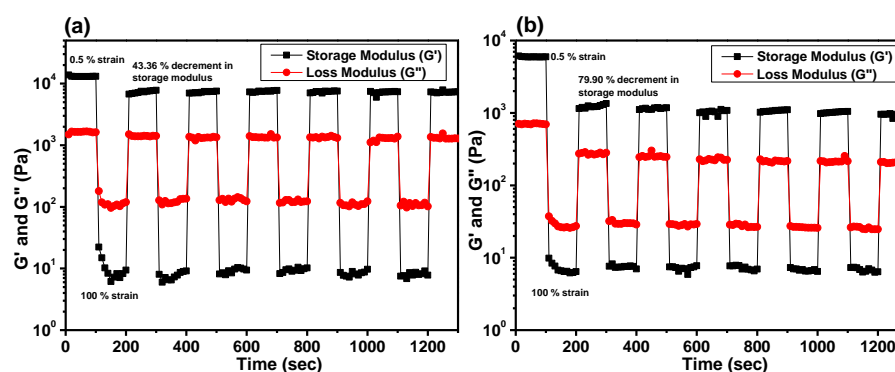


Figure 5.61. Time oscillation sweep experiment of metallogel  $M2G8GECl_2Ads$ .



**Figure 5.62.** Time oscillation sweep experiment of metallogel (a)  $M2G8GE(OAc)_2Ads$  and (b)  $M2G8GESO_4Ads$ .



**Figure 5.63.** Time oscillation sweep experiment of metallogel (a)  $M3G8GECl_2Ads$  and (b)  $M3G8GE(OAc)_2Ads$ .

## 5.4 Conclusion

This Chapter is focused on utilizing  $N^2$ ,  $N^4$ ,  $N^6$ -tri(1*H*-tetrazol-5-yl)-1,3,5-triazine-2,4,6-triamine (**G8**), an LMWG as the prospective heavy metal adsorbing material for water remediation. In an earlier report, it was observed that **G8** is not stable while treated with excess water, thus unsuitable for water remediation. Herein, the development of another organic molecule, viz. 3,3',3''-(benzenetricarbonyltris(azanediyl))tris(4-aminobenzoic acid) (**GE**) has been done with complementary hydrogen bond donor-acceptor sites with respect to **G8** as the gel strength enhancer to impart stability even in the aqueous medium. The resultant organogel **G8GE** has shown the ability to form metallogels with Hg(II), Cd(II), and Pb(II) salts. The hydrophobicity of the gel was evident from the retention of the disc-shaped gel structure in aqueous medium for an

extended period. With these hydrophobic and metal adsorption properties, mixed organogel **G8GE** has been found to efficiently remove toxic heavy metal salts  $\text{HgCl}_2$ ,  $\text{Hg}(\text{OAc})_2$ ,  $\text{HgSO}_4$ ,  $\text{CdCl}_2$ ,  $\text{Cd}(\text{OAc})_2$ ,  $\text{CdSO}_4$ ,  $\text{PbCl}_2$  and  $\text{Pb}(\text{OAc})_2$  from aqueous solution with effective adsorption capacity ( $q_e$ ) of 76.24, 157.79, 147.81, 52.09, 131.25, 284.93, 83 and 221.02 mg/g respectively. The adsorbent xerogel **G8GE** can be recycled for further utilization for five cycles with almost 99 % recovery, which has been tested for Hg(II) by treatment with KI.

Other than the use of **G8GE** for water remediation, the effect of the method of gel formation on the rheological and fluorescence properties of the gel has also been described here. From Jobs plot, the maximum interactions between **G8** and **GE** have been found to be 3:2; however, the rheological experiment indicates the fabrication of the strongest gel at a 1:1 ratio. Two different methods have been applied for metallogel formation, viz., mixing and adsorption method. The fluorescence spectrum of **G8GE** has shown a stronger fluorescence peak with respect to **G8** and **GE** due to the extended non-covalent interactions and, consequently, the reduction in the non-radiative decay process. At lower concentrations, **G8GE** has shown nano-branched thread-like structures in SEM. However, at higher concentrations, a closely packed 3D network of gel is fabricated. Several experiments, including fluorescence properties, morphology determination, and rheological studies, indicated that the adsorption method of fabrication of metallogels does not disturb the **G8GE** network significantly, while metal ions diffuse through the gel network. Thus, it has been proven to be a more efficient process for gel formation than the mixing method. The DFT optimization study has supported the complementary hydrogen bond formation hypothesis between **G8** and **GE**. The limitation of this work is that the adsorption capacities are different with different salts of Hg(II), Cd(II), and Pb(II), which have to be analyzed further. Also, the effect of different metal ions which might be present in contaminated water with Hg(II), Cd(II), and Pb(II) in the adsorption process needs to be found.

Conclusively, a hydrophobic organogel **G8GE** has been fabricated with a tendency to form strong metallogels by the adsorption method with heavy metal salts of mercury, cadmium, and lead. This property of mixed organogel makes it suitable for water remediation resulting in the notable adsorption capacity of **G8GE** xerogel toward heavy metals. This idea of using a gel strength enhancer for different applications of gel materials might create new possibilities in the near future.

### **5.5 Declaration**

This chapter is adapted from Mater. Adv., 2023, 4, 3603 - 3618 (D.O.I. 10.1039/D2QM00520D)

### **5.6 References**

- [1] Malviya, N., Sonkar, C., Ganguly, R., Bhattacharjee, D., Bhabak, K.P., Mukhopadhyay, S. (2019), Novel approach to generate a self-deliverable Ru (II)-based anticancer agent in the self-reacting confined gel space, ACS Appl. Mater. Interfaces, 11, 47606-47618 (DOI: 10.1021/acsami.9b17075)
- [2] Malviya, N., Ranjan, R., Sonkar, C., Mobin, S.M., Mukhopadhyay, S. (2019), Self-healable lanthanoid-based metallogels: dye removal and crystallization in the confined gel state, ACS Appl. Nano Mater., 2, 8005-8015 (DOI: 10.1021/acsnm.9b02064)
- [3] He, M., Li, J., Tan, S., Wang, R., Zhang, Y. (2013), Photodegradable supramolecular hydrogels with fluorescence turn-on reporter for photomodulation of cellular microenvironments, J. Am. Chem. Soc., 135, 18718-18721 (DOI: 10.1021/ja409000b)
- [4] Lee, J.H., Lee, H., Seo, S., Jaworski, J., Seo, M.L., Kang, S., Lee, J.Y., Jung, J.H. (2011), Fluorescence enhancement of a tetrazole-based pyridine coordination polymer hydrogel, New J. Chem., 35, 1054-1059 (DOI: 10.1039/C0NJ00840K)
- [5] Xavier, J.R., Thakur, T., Desai, P., Jaiswal, M.K., Sears, N., Cosgriff-Hernandez, E., Kaunas, R., Gaharwar, A.K. (2015),

- Bioactive nanoengineered hydrogels for bone tissue engineering: a growth-factor-free approach, *ACS nano*, 9, 3109-3118 (DOI: 10.1021/nn507488s)
- [6] Zhao, T., Wang, G., Hao, D., Chen, L., Liu, K., Liu, M. (2018), Macroscopic layered organogel–hydrogel hybrids with controllable wetting and swelling performance, *Adv. Funct. Mater.*, 28, 1800793 (DOI: 10.1002/adfm.201800793)
- [7] Yang, Y., Liu, W., Zhong, Q., Zhang, J., Yao, B., Lian, X., Niu, H. (2021), Self-assembly of lanthanide-based metallogel nanoplates into microcubic blocks as self-calibrating luminescent methanol sensors, *ACS Appl. Nano Mater.*, 4, 4735-4745 (DOI: 10.1021/acsanm.1c00343)
- [8] Roy, S.G., Kumar, A., Misra, N., Ghosh, K. (2022), Pyridoxal-based low molecular weight progelator as a new chemosensor for the recognition of  $\text{Ag}^+$  and  $\text{Hg}^{2+}$  under different conditions, *Mater. Adv.*, 3, 5836-5844 (DOI: 10.1039/D2MA00358A)
- [9] Biswas, P., Datta, H.K., Dastidar, P. (2022), Multi-NSAID-based Zn (II) coordination complex-derived metallogelators/metallogels as plausible multi-drug self-delivery systems, *Chem. Commun.*, 58, 969-972 (DOI: 10.1039/D1CC05334E)
- [10] Singh, B., Sharma, V., Kumar, R., Sharma, D. (2023), Designing biphasic gels from dietary fiber sterculia gum by green approach using high energy radiation for biomedical applications, *Food Hydrocoll. Health.*, 3, 100137 (DOI: 10.1016/j.fhfh.2023.100137)
- [11] Alam, N., Ojha, N., Kumar, S., Sarma, D. (2023), Self-Templated Conversion of a Self-Healing Metallogel into an Active Carbon Quasiaerogel: Boosting Photocatalytic  $\text{CO}_2$  Reduction by Water, *ACS Sustain. Chem. Eng.*, 11, 2658-2669 (DOI: 10.1021/acssuschemeng.2c07079)
- [12] Dhibar, S., Dey, A., Dey, A., Majumdar, S., Mandal, A., Ray, P.P., Dey, B. (2019), The development of a rapid self-healing

- semiconducting monoethanolamine-based Mg(OH)<sub>2</sub> metallogel for a Schottky diode application with a high ON/OFF ratio, *New J. Chem.*, 43, 15691-15699 (DOI: 10.1039/C9NJ03457A)
- [13] Lepcha, G., Singha, T., Majumdar, S., Pradhan, A.K., Das, K.S., Datta, P.K., Dey, B. (2022), Adipic acid directed self-healable supramolecular metallogels of Co (II) and Ni (II): intriguing scaffolds for comparative optical-phenomenon in terms of third-order optical non-linearity, *Dalton Trans.*, 51, 13435-13443 (DOI: 10.1039/D2DT01983C)
- [14] Su, H., Zhu, S., Qu, M., Liu, R., Song, G., Zhu, H. (2019), 1, 3, 5-Triazine-based Pt (II) metallogel material: Synthesis, photophysical properties, and optical power-limiting performance, *J. Phys. Chem. C*, 123, 15685-15692 (DOI: 10.1021/acs.jpcc.9b02168)
- [15] Su, H., Zhu, S., Qu, M., Liu, R., Song, G., Zhu, H. (2019), 1, 3, 5-Triazine-based Pt (II) metallogel material: Synthesis, photophysical properties, and optical power-limiting performance, *J. Phys. Chem. C*, 123, 15685-15692 (DOI: 10.1021/acs.jpcc.9b02168)
- [16] Lalitha, K., Prasad, Y.S., Sridharan, V., Maheswari, C.U., John, G., Nagarajan, S. (2015), A renewable resource-derived thixotropic self-assembled supramolecular gel: magnetic stimuli responsive and real-time self-healing behaviour, *Rsc Adv.*, 5, 77589-77594 (DOI: 10.1039/C5RA14744A)
- [17] Zhao, T., Chen, S., Kang, K., Ren, J., Yu, X. (2022), Self-assembled copper metallogel bearing terpyridine and its application as a catalyst for the click reaction in water, *Langmuir*, 38, 1398-1405 (DOI: 10.1021/acs.langmuir.1c02568)
- [18] Kyarikwal, R., Malviya, N., Chakraborty, A., Mukhopadhyay, S. (2021), Preparation of tris-tetrazole-based Metallogels and Stabilization of Silver Nanoparticles: Studies on Reduction Catalysis and self-healing Property, *ACS Appl. Mater. Interfaces*, 13, 59567-59579 (DOI: 10.1021/acsami.1c19217)

- [19] Fang, W., Zhang, Y., Wu, J., Liu, C., Zhu, H., Tu, T. (2018), Recent advances in supramolecular gels and catalysis, *Chem. Asian J.*, 13, 712-729 (DOI: 10.1002/asia.201800017)
- [20] Feng, Q., Wan, K., Zhu, T., Fan, X., Zhang, C., Liu, T. (2022), Stretchable, environment-stable, and knittable ionic conducting fibers based on metallo gels for wearable wide-range and durable strain sensors, *ACS appl. Mater. interfaces*, 14, 4542-4551 (DOI: 10.1021/acsami.1c22099)
- [21] Dhibar, S., Dey, A., Dey, A., Majumdar, S., Ghosh, D., Ray, P.P., Dey, B. (2019), Development of supramolecular semiconducting Mn (II)-metallo gel based active device with substantial carrier diffusion length, *ACS Applied Electron. Mater.*, 1, 1899-1908 (DOI: 10.1021/acsaelm.9b00410)
- [22] Wang, H., Zhang, Y., Xiong, J., Zhang, D., Lin, H., Chen, Y. (2022), Regenerated cellulose microspheres-aerogel enabled sustainable removal of metal ions for water remediation, *J. Mater. Sci.*, 57, 8016-8028 (DOI: 10.1007/s10853-022-07175-y)
- [23] Li, Y., Wen, J., Xue, Z., Yin, X., Yuan, L., Yang, C. (2022), Removal of Cr (VI) by polyaniline embedded polyvinyl alcohol/sodium alginate beads– Extension from water treatment to soil remediation, *J. Hazard. Mater.*, 426, 127809 (DOI: 10.1016/j.jhazmat.2021.127809)
- [24] El Kurdi, R., Chebl, M., Sillanpää, M., El-Rassy, H., Patra, D. (2021), Chitosan oligosaccharide/silica nanoparticles hybrid porous gel for mercury adsorption and detection, *Mater. Today Commun.*, 28, 102707 (DOI: 10.1016/j.mtcomm.2021.102707)
- [25] Huang, S., Liu, X., Hu, Q., Wei, T., Wang, J., Chen, H., Wu, C. (2019), Temperature-driven metalloprotein-based hybrid hydrogels for selective and reversible removal of cadmium (II) from water, *ACS appl. Mater. interfaces*, 12, 2991-2998 (DOI: 10.1021/acsami.9b19306)
- [26] Yang, H.L., Sun, X.W., Zhang, Y.M., Wang, Z.H., Zhu, W., Fan, Y.Q., Wei, T.B., Yao, H., Lin, Q. (2019), A bi-component supramolecular gel for selective fluorescence detection and

- removal of  $\text{Hg}^{2+}$  in water, *Soft Matter*, 15, 9547-9552 (DOI: 10.1039/C9SM01652J)
- [27] Türkmen, D., Bakhshpour, M., Akgönüllü, S., Aşır, S., Denizli, A. (2022), Heavy metal ions removal from wastewater using cryogels: A review. *Frontiers in Sustainability*, 3, 765592 (DOI: 10.3389/frsus.2022.765592)
- [28] Huseynli, S., Bakhshpour, M., Qureshi, T., Andac, M., Denizli, A. (2020), Composite polymeric cryogel cartridges for selective removal of cadmium ions from aqueous solutions, *Polymers*, 12, 1149-1163 (DOI: 10.3390/polym12051149)
- [29] Nagajyoti, P.C., Lee, K.D., Sreekanth, T.V.M. (2010), Heavy metals, occurrence and toxicity for plants: a review, *Environ. Chem. Lett.*, 8, 199-216 (DOI: 10.1007/s10311-010-0297-8)
- [30] Sobhanardakani, S. (2017), Potential health risk assessment of heavy metals via consumption of caviar of Persian sturgeon, *Mar. Pollut. Bull.*, 123, 34-38 (DOI: 10.1016/j.marpolbul.2017.09.033)
- [31] Hosseini, N.S., Sobhanardakani, S., Cheraghi, M., Lorestani, B., Merrikhpour, H. (2020), Heavy metal concentrations in roadside plants (*Achillea wilhelmsii* and *Cardaria draba*) and soils along some highways in Hamedan, west of Iran, *Environ. Sci. Pollut. Res.*, 27, 13301-13314 (DOI: 10.1007/s11356-020-07874-6)
- [32] Mitra, S., Chakraborty, A.J., Tareq, A.M., Emran, T.B., Nainu, F., Khusro, A., Idris, A.M., Khandaker, M.U., Osman, H., Alhumaydhi, F.A., Simal-Gandara, J. (2022), Impact of heavy metals on the environment and human health: Novel therapeutic insights to counter the toxicity, *J. King Saud Univ. Sci.*, 34, 101865 (DOI: 10.1016/j.jksus.2022.101865)
- [33] Ganesamoorthy, R., Vadivel, V.K., Kumar, R., Kushwaha, O.S., Mamane, H. (2021), Aerogels for water treatment: A review, *J. Clean. Prod.*, 329, 129713 (DOI: 10.1016/j.jclepro.2021.129713)
- [34] Salman, M.S., Znad, H., Hasan, M.N., Hasan, M.M. (2021), Optimization of innovative composite sensor for Pb (II)

- detection and capturing from water samples, *Microchem. J.*, 160, 105765 (DOI: 10.1016/j.microc.2020.105765)
- [35] Hasan, M.N., Salman, M.S., Islam, A., Znad, H., Hasan, M.M. (2021), Sustainable composite sensor material for optical cadmium (II) monitoring and capturing from wastewater, *Microchem. J.*, 161, 105800 (DOI: 10.1016/j.microc.2020.105800)
- [36] Awual, M.R. (2019), An efficient composite material for selective lead (II) monitoring and removal from wastewater, *J. Environ. Chem. Eng.*, 7, 103087 (DOI: 10.1016/j.jece.2019.103087)
- [37] Awual, M.R. (2019), A facile composite material for enhanced cadmium (II) ion capturing from wastewater, *J. Environ. Chem. Eng.*, 7, 103378 (DOI: 10.1016/j.jece.2019.103378)
- [38] Malviya, N., Sonkar, C., Ganguly, R., Bhattacharjee, D., Bhabak, K.P., Mukhopadhyay, S. (2019), Novel approach to generate a self-deliverable Ru (II)-based anticancer agent in the self-reacting confined gel space, *ACS appl. Mater. interfaces*, 11, 47606-47618 (DOI: 10.1021/acsami.9b17075)
- [39] Malviya, N., Ranjan, R., Sonkar, C., Mobin, S.M., Mukhopadhyay, S. (2019), Self-healable lanthanoid-based metallogels: dye removal and crystallization in the confined gel state, *ACS Appl. Nano Mater.*, 2, 8005-8015 (DOI: 10.1021/acsanm.9b02064)
- [40] Malviya, N., Sonkar, C., Kundu, B.K., Mukhopadhyay, S. (2018), Discotic organic gelators in ion sensing, metallogel formation, and bioinspired catalysis, *Langmuir*, 34, 11575-11585 (DOI: 10.1021/acs.langmuir.8b02352)
- [41] Malviya, N., Sonkar, C., Ganguly, R., Mukhopadhyay, S. (2019), Cobalt Metallogel Interface for selectively sensing l-tryptophan among essential amino acids, *Inorganic chemistry*, 58, 7324-7334 (DOI: 10.1021/acs.inorgchem.9b00455)

- [42] Kyarikwal, R., Kundu, B.K., Chakraborty, A., Mukhopadhyay, S. (2022), A tris-tetrazole based nanostructured soft material: Studies on self-healing, AIEE, and rheological and fluorometric detection of 3-aminopyridine, *Mater. Chem. Front.*, 6, 2835-2847 (DOI: 10.1039/D2QM00520D)
- [43] Awual, M.R., Hasan, M.N., Hasan, M.M., Salman, M.S., Sheikh, M.C., Kubra, K.T., Islam, M.S., Marwani, H.M., Islam, A., Khaleque, M.A., Waliullah, R.M. (2023), Green and robust adsorption and recovery of Europium (III) with a mechanism using hybrid donor conjugate materials, *Sep. Purif. Technol.*, 319, 124088 (DOI: 10.1016/j.seppur.2023.124088)
- [44] Kubra, K.T., Hasan, M.M., Hasan, M.N., Salman, M.S., Khaleque, M.A., Sheikh, M.C., Rehan, A.I., Rasee, A.I., Waliullah, R.M., Awual, M.E., Hossain, M.S. (2023), The heavy lanthanide of Thulium (III) separation and recovery using specific ligand-based facial composite adsorbent, *Colloids Surf. A Physicochem. Eng. Asp.*, 667, 131415 (DOI: 10.1016/j.colsurfa.2023.131415)
- [45] Salman, M.S., Hasan, M.N., Hasan, M.M., Kubra, K.T., Sheikh, M.C., Rehan, A.I., Waliullah, R.M., Rasee, A.I., Awual, M.E., Hossain, M.S., Alsukaibi, A.K. (2023), Improving copper (II) ion detection and adsorption from wastewater by the ligand-functionalized composite adsorbent, *J. Mol. Struct.*, 1282, 135259 (DOI: 10.1016/j.molstruc.2023.135259)
- [46] Hasan, M.N., Salman, M.S., Hasan, M.M., Kubra, K.T., Sheikh, M.C., Rehan, A.I., Rasee, A.I., Awual, M.E., Waliullah, R.M., Hossain, M.S., Islam, A. (2023), Assessing sustainable Lutetium (III) ions adsorption and recovery using novel composite hybrid nanomaterials, *J. Mol. Struct.*, 1276, 134795 (DOI: 10.1016/j.molstruc.2022.134795)
- [47] Mohammed, M., Chakravarthy, R.D., Lin, H.C. (2022), Influence of metal ion crosslinking on the nanostructures, stiffness, and biofunctions of bioactive peptide hydrogels, *Mol. Syst. Des. Eng.*, 7, 1336-1343 (DOI: 10.1039/D2ME00062H)

- [48] Zhang, A., Zhang, Y., Xu, Z., Li, Y., Yu, X., Geng, L. (2017), Naphthalimide-based fluorescent gelator for construction of both organogels and stimuli-responsive metallogels, *RSC advances*, 7, 25673-25677 (DOI: 10.1039/C7RA03184J)
- [49] Haidekker, M.A., Brady, T.P., Lichlyter, D., Theodorakis, E.A. (2005), Effects of solvent polarity and solvent viscosity on the fluorescent properties of molecular rotors and related probes, *Bioorg. Chem.*, 33, 415-425 (DOI: 10.1016/j.bioorg.2005.07.005)
- [50] Bhat, H.R., Jha, P.C. (2017), Intramolecular Charge Transfer: Mechanism Behind Cyanide Anion Sensing of 3, 5-Diformylborondipyrromethene, *Chem. Select*, 2, 2732-2739 (DOI: 10.1002/slct.201601998)
- [51] Sowmiya, M., Tiwari, A.K., Saha, S.K. (2011), Study on intramolecular charge transfer fluorescence properties of trans-4-[4'-(N, N'-dimethylamino) styryl] pyridine: Effect of solvent and pH, *J. Photochem. Photobiol. A: Chem.*, 218, 76-86 (DOI: 10.1016/j.jphotochem.2010.12.006)
- [52] Liu, J., Fan, Y.Q., Song, S.S., Gong, G.F., Wang, J., Guan, X.W., Yao, H., Zhang, Y.M., Wei, T.B., Lin, Q. (2019), Aggregation-induced emission supramolecular organic framework (AIE SOF) gels constructed from supramolecular polymer networks based on tripodal pillar [5] arene for fluorescence detection and efficient removal of various analytes, *ACS Sustain. Chem. Eng.*, 7, 11999-12007 (DOI: 10.1021/acssuschemeng.9b00452)
- [53] Xu, Y.L., Li, C.T., Cao, Q.Y., Wang, B.Y., Xie, Y. (2017), A pyrenyl-appended organogel for fluorescence sensing of anions, *Dyes Pigm.*, 139, 681-687 (DOI: 10.1016/j.dyepig.2016.12.068)
- [54] Zhang, Y., Liang, C., Shang, H., Ma, Y., Jiang, S. (2013), Supramolecular organogels and nanowires based on a V-shaped cyanostilbene amide derivative with aggregation-induced emission (AIE) properties, *J. Mater. Chem. C*, 1, 4472-4480 (DOI: 10.1039/C3TC30545G)

- [55] Beltrán, E., Garzoni, M., Feringán, B., Vancheri, A., Barberá, J., Serrano, J.L., Pavan, G.M., Giménez, R., Sierra, T. (2015), Self-organization of star-shaped columnar liquid crystals with a coaxial nanophase segregation revealed by a combined experimental and simulation approach, *Chem. Commun.*, 51, 1811-1814 (DOI: 10.1039/C4CC08602C)
- [56] Lee, C. T., Yang, W. T. & Parr, R. G. (1988), Development of the Colle-Salvetti correlation-energy formula into a functional of the electron density, *Phys. Rev. B.* 37, 785–789 (DOI: 10.1103/PhysRevB.37.785)
- [57] Grimme, S., Antony, J., Ehrlich, S., Krieg, H. (2010), A consistent and accurate ab initio parametrization of density functional dispersion correction (DFT-D) for the 94 elements H-Pu, *J. Chem. Phys.*, 132, 154104 (DOI: 10.1063/1.3382344)
- [58] Lu, T., Chen, F. (2012), Multiwfn: A multifunctional wavefunction analyzer, *J. Comput. Chem.* 33, 580-592 (DOI: 10.1002/jcc.22885)
- [59] Emamian, S., Lu, T., Kruse, H., Emamian, H. (2019), Exploring nature and predicting strength of hydrogen bonds: A correlation analysis between atoms-in-molecules descriptors, binding energies, and energy components of symmetry-adapted perturbation theory, *J. Comput. Chem.*, 40, 2868-2881 (DOI: 10.1002/jcc.26068)
- [60] Yang, H.L., Sun, X.W., Zhang, Y.M., Wang, Z.H., Zhu, W., Fan, Y.Q., Wei, T.B., Yao, H., Lin, Q. (2019), A bi-component supramolecular gel for selective fluorescence detection and removal of Hg<sup>2+</sup> in water, *Soft Matter*, 15, 9547-9552 (DOI: 10.1039/C9SM01652J)
- [61] Kumar, A., Das, T., Thakur, R.S., Fatima, Z., Prasad, S., Ansari, N.G., Patel, D.K. (2022), Synthesis of biomass-derived activated carbons and their immobilization on alginate gels for the simultaneous removal of Cr (VI), Cd (II), Pb (II), As (III), and Hg (II) from water, *ACS omega*, 7, 41997-42011 (DOI: 10.1021/acsomega.2c03786)

- [62] Wei, T.B., Zhao, Q., Li, Z.H., Dai, X.Y., Niu, Y.B., Yao, H., Zhang, Y.M., Qu, W.J., Lin, Q. (2021), Supramolecular organogel with aggregation-induced emission for ultrasensitive detection and effective removal of  $\text{Cu}^{2+}$  and  $\text{Hg}^{2+}$  from aqueous solution, *Dyes Pigm.*, 192, 109436 (DOI: 10.1016/j.dyepig.2021.109436)
- [63] De, A., Mondal, R. (2018), Toxic metal sequestration exploiting a unprecedented low-molecular-weight hydrogel-to-metallogel transformation, *ACS omega*, 3, 6022-6030 (DOI: 10.1021/acsomega.8b00758)
- [64] Ding, Y., Zhang, F., Xu, J., Miao, Y., Yang, Y., Liu, X., Xu, B. (2017), Synthesis of short-chain passivated carbon quantum dots as the light emitting layer towards electroluminescence, *RSC adv.*, 7, 28754-28762 (DOI: 10.1039/C7RA02421E)
- [65] Chowdhury, A., Das, S.K., Mondal, S., Ruidas, S., Chakraborty, D., Chatterjee, S., Bhunia, M.K., Chandra, D., Hara, M., Bhaumik, A. (2021), Sulfur-containing nitrogen-rich robust hierarchically porous organic polymer for adsorptive removal of mercury: experimental and theoretical insights, *Environ. Sci. Nano*, 8, 2641-2649 (DOI: 10.1039/D1EN00448D)
- [66] Ding, Y., Zhang, F., Xu, J., Miao, Y., Yang, Y., Liu, X., Xu, B. (2017), Synthesis of short-chain passivated carbon quantum dots as the light emitting layer towards electroluminescence, *RSC adv.*, 7, 28754-28762 (DOI: 10.1039/C7RA02421E)
- [67] Artemenko, A., Shchukarev, A., Štenclová, P., Wågberg, T., Segervald, J., Jia, X., Kromka, A. (2021), Reference XPS spectra of amino acids. In *IOP Conference Series: Materials Science and Engineering*, 1050, 012001) IOP Publishing (DOI: 10.1088/1757-899X/1050/1/012001)
- [68] Martínez-Iniesta, A.D., Morelos-Gómez, A., Muñoz-Sandoval, E., López-Urías, F. (2021), Nitrogen-phosphorus doped graphitic nano onion-like structures: experimental and theoretical studies, *RSC adv.*, 11, 2793-2803 (DOI: 10.1039/D0RA10019F)

- [69] Liu, Y., Tang, X., Deng, M., Cao, Y., Li, Y., Zheng, H., Li, F., Yan, F., Lan, T., Shi, L., Gao, L. (2019), Nitrogen doped graphene quantum dots as a fluorescent probe for mercury (II) ions, *Microchim. Acta*, 186, 1-8 (DOI: 10.1007/s00604-019-3249-4)



**Chapter 6**  
**General Conclusions and Future Scope**



---

## Chapter 6

### General Conclusions and Future Scope

#### 6.1 General Conclusion

Design and fabrication of low molecular weight gelators (LMWGs) and modification in their fundamental properties have become popular methods for soft material applications as advanced functional materials. The formation of gels is occurred by supramolecular self-assembly of LMWGs. The driving factors behind self-assembly are the engagements of non-covalent interactions, *viz.* hydrogen bonds,  $\pi$ - $\pi$  stacking, and intercolumnar stacking between  $\pi$  cloud and functional groups of gelator molecules. Non-covalent interactions make gel materials stimuli-responsive, thermo-reversible, biodegradable, and easy to fabricate within the favourable synthetic path. The role of the positions of hydrogen bonds forming donor-acceptor sites on gel properties is explored in this thesis. With the broad area of applicability of organogels, metallogels also provide specific advanced applicability due to the additional properties of introduced metal centers. The fabrications of nanostructured and nanoparticle-containing gels are emerging as a dynamic field among soft materials. The present work is focused on the synthesis and applications of LMWGs containing carboxamide (1,3,5-benzene tricarboxamide /BTA), tetrazole, and triazine moieties. Here, the synthesized molecules are employed to fabricate nanostructured organo- and metallogels. Also, the gelator molecules are used for the formation of nanocomposite materials by stabilization of metal nanoparticles inside the gelator matrix. The concept of induced gelation is also introduced here to modify the properties of gels. This modification explained the effect of the method of gel formation, used gelator components, and the role of gelator concentration on strength (storage modulus,  $G'$ ) and the thixotropic behavior of gels. Other than rheological studies, work has also been done to explain fluorometric behaviours, morphological changes, and the induced hydrophobic nature of mixed organogel.

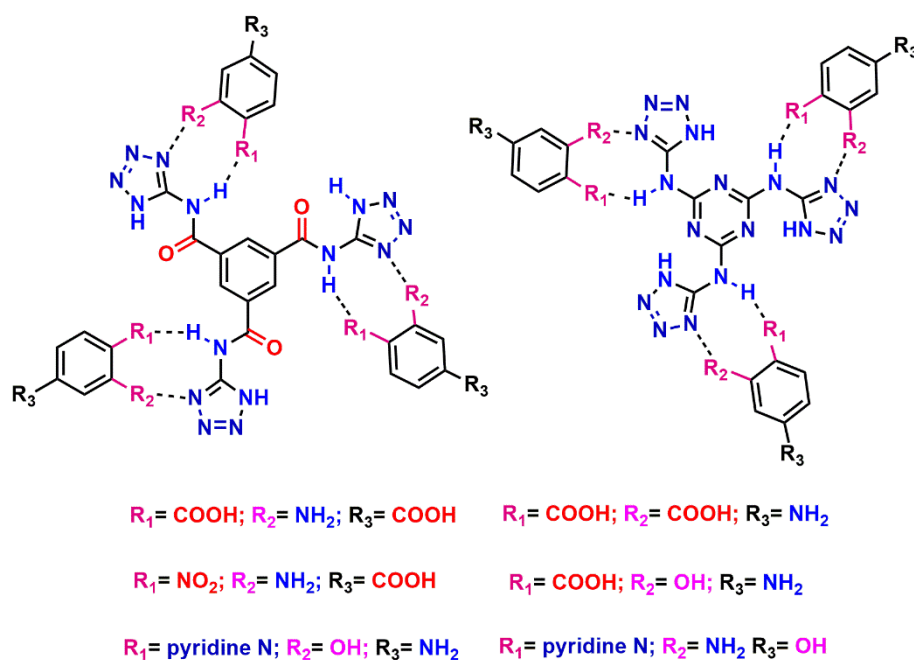
Chapters 2, 3, and 4 explored the synthesis of tetrazole-based gelator molecules **G7** (triethylammonium 5-(3,5-bis((1H-tetrazol-5-yl) carbamoyl) benzamido) tetrazol-1-ide) and **G8**. ( $N^2$ ,  $N^4$ ,  $N^6$ -tri (1H-tetrazol-5-yl)-1,3,5-triazine-2,4,6-triamine). Gelator molecule **G7** contains the benzene tricarboxamide (BTA) core ring and three tetrazole side rings. While **G8** contains a triazine ring in the place of BTA. Both gelators can form organogels with DMSO: H<sub>2</sub>O mixture. In the second chapter, the fabrication of metallogels with Fe(III), Co(II), Ni(II), Cu(II), Zn(II), Ag(I), and Fe(II) is explored in the presence of **G7**. These metallogels stabilize silver nanoparticles (AgNPs) within the gel matrices to form a nanocomposite system with dual metal. The stabilization of smaller-size AgNPs without much aggregation has been achieved by Fe(III)G7 (**M<sup>1</sup>G7**), and nanocomposite Fe(III)G7AgNPs (**M<sup>1</sup>G7AgNPs**) is obtained. The nanocomposite **M<sup>1</sup>G7AgNPs** act as an active catalyst for the reduction of nitro substituent to respective amino products. The catalyst shows good recyclability for five consecutive cycles. **M<sup>1</sup>G7** shows gel-to-crystal transition during metallogel formation by absorption method. Additionally, nanocomposite **M<sup>1</sup>G7AgNPs** offers nanometallogel formation ability with self-healing property. In the third chapter, gelator molecule **G8** was used to explore the effect of the isomeric position of hydrogen bond donor-acceptor sites on gel properties. For this, the mixed-organogel of **G8** has been fabricated in the presence of isomers of aminopyridine, which contain both hydrogen bond donor and acceptor sites. Various spectroscopic tools are used to study the fabricated organogel **G82AP**, **G83AP**, and **G84AP**, which found the effective and robust hydrogen bond formation exclusively between **G8** and 3AP. This discrimination has been confirmed by visual, rheological, and fluorometric analysis of organogels, indicating the effective orientation of hydrogen bond donor-acceptor sites of 3-aminopyridine (3-AP) with hydrogen bond donor-acceptor sites of **G8**. Here, the work explored the notable role of the isomeric position of functional groups on the physical and chemical properties of gels. In the fourth chapter, gelator molecule **G8** is used to stabilize palladium

nanoparticles (PdNPs) within the gelator matrix (**G8PdNPs**). Here, the synthesized nanocomposite **G8PdNPs** are further used to fabricate nanometallogel of **G8PdNPs**. To explore the possibility of incorporation of Pd(II) ion in a gel system, the metallogel **G8PdCl<sub>2</sub>** was fabricated using **G8** and PdCl<sub>2</sub> in DMSO: H<sub>2</sub>O mixture. Xerogels of **G8PdNPs** and **G8PdCl<sub>2</sub>** were used as an active catalyst for Suzuki-Miyaura coupling and 2+3 cycloaddition reaction for tetrazole formation, respectively. Both the catalyst shows good product yield and almost constant recyclability till five consecutive cycles of reaction.

To explore the synthesized gelator molecule and fabricated gel system in various applicable fields, it was envisaged to synthesize a water-stable organogel that can be used further for water remediation. From the second chapter, adding a second component as a gelator component can increase the strength of the gel, can be seen. Therefore, to utilize this finding, in the fifth chapter, the synthesis of an organic molecule **GE** (3,3',3''-(benzenetricarbonyltris(azanediyl))tris(4-aminobenzoic acid) has taken up. The gelator components **G8** and **GE** are used here to fabricate an organogel **G8GE** that shows notable water stability even after the sonication of gel material. The mixed organogel **G8GE** shows strong metallogel formation with heavy metal salts of HgCl<sub>2</sub>, Hg(OAc)<sub>2</sub>, HgSO<sub>4</sub>, CdCl<sub>2</sub>, Cd(OAc)<sub>2</sub>, CdSO<sub>4</sub>, PbCl<sub>2</sub>, and Pb(OAc)<sub>2</sub> by adsorption method. These two properties, i.e., hydrophobic nature and metallogel formation by adsorption, make the organogel **G8GE** suitable for remediation of water by adsorption of heavy metal salts of Hg(II), Cd(II), and Pb(II). Here, the xerogel of **G8GE** used as adsorbent for removal of toxic heavy metal salts HgCl<sub>2</sub>, Hg(OAc)<sub>2</sub>, HgSO<sub>4</sub>, CdCl<sub>2</sub>, Cd(OAc)<sub>2</sub>, CdSO<sub>4</sub>, PbCl<sub>2</sub> and Pb(OAc)<sub>2</sub> from aqueous solution with adequate adsorption capacity (qe) of 76.24, 157.79, 147.81, 52.09, 131.25, 284.93, 83 and 221.02 mg/g respectively. Xerogel **G8GE** can be recycled until five cycles with almost 99 % recovery.

## 6.2 Future scope

Although organogels can have broad applicability in different fields, incorporating metal ions or nanoparticles inside the gel matrix can diversify it further. Though several studies on the fabrication and application of soft materials have been reported, the controlled modification of fabricated organogels and metallogels according to the need is still an elusive area of research. As an example, if a synthesized gelator molecule forms organogel or metallogel with low storage modulus value or less strength, more data is required on what kinds of additives can be used to increase its strength according to the requirement. It should be noted that the second gelation component must provide the sites for non-covalent interactions with the already available gelator molecule (Scheme 6.1).



**Scheme 6.1.** Possibilities of addition of second component with **G7** and **G8** gelator components to increase the hydrogen bonding interactions.

The formation of nanostructured metallogels and metal nanoparticles containing nanocomposite systems can be applied for various fields like heterogenous catalysis, water remediation, smart drug delivery system, photoelectric and conductive materials, and intelligent sensors. The method for the fabrication of organogels and metallogels is flexible and

mostly depends on trials. This finding leads to the formation of gel materials. Sometimes, the gel formation has occurred by mixing method, but applying some modifications in the technique of gel formation or gelator components can make the gel more stable and applicable. Therefore, first finding and further tuning of the system can deliver the desired properties and applicabilities (Figure 6.1).

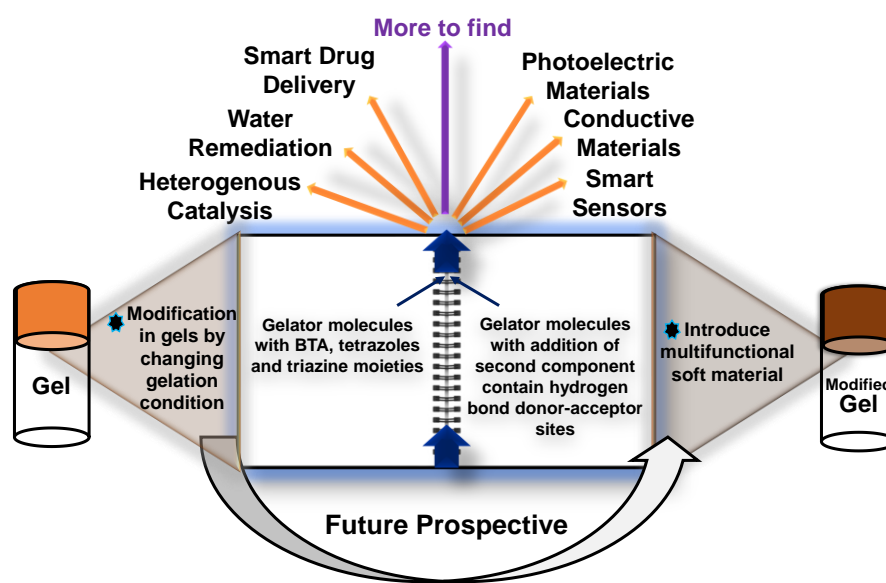


**Figure 6.1.** Future prospective of application of BTA, tetrazole and triazine based gels and their properties modification for different fields.

Finding new gelator molecules is always challenging because it is not precise which molecules can form a gel. The gelator component can be designed by incorporating possibilities of prospective aromatic ring-based  $\pi$ - $\pi$  stacking interactions, functional groups with hydrogen bond formation and intercolumnar stacking formation possibilities, etc. However, its gelation tendency only can be found by experimental analysis. Therefore, a more understanding of the reasons behind gel formation, the effect of different methods for gel fabrication, and the incorporation of various types of metal nanoparticles inside gel matrix can enrich this field further and make it ready for future applications.

